Kirkland & Ellis Library
5 0628 01144179 4

# Silicon Processing

## for the VLSI Era

## Volume 3 - The Submicron MOSFET

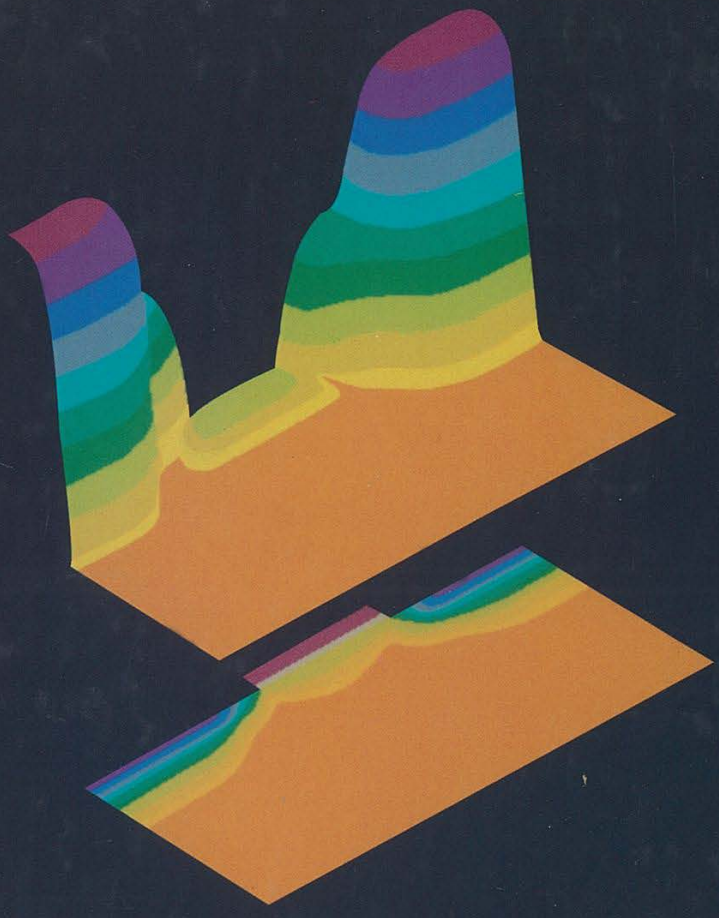

S. Wolf

THE COMPANION VOLUMES TO THIS BOOK

# Silicon Processing
## for the VLSI Era

### Volume 1 - Process Technology
**By STANLEY WOLF and RICHARD N. TAUBER**

**TABLE of CONTENTS - Ch.1** Silicon: Single-Crystal Growth and Wafering; **Ch. 2** Crystalline Defects, Thermal Processing, and Gettering; **Ch. 3** Vacuum Technology for VLSI Applications; **Ch. 4** Basics of Thin Films; **Ch. 5** Silicon Epitaxial Film Growth; **Ch. 6** Chemical Vapor Deposition of Amorphous and Polycrystalline Films; **Ch. 7** Thermal Oxidation of Silicon **Ch. 8** Diffusion in Silicon; **Ch. 9** Ion Implantation for VLSI; **Ch. 10** Aluminum Thin Films and Physical Vapor Deposition in VLSI; **Ch. 11** Refractory Metals and Their Silicides in VLSI; **Ch. 12** Lithography I: Optical Photoresists - Material Properties and Process Technology; **Ch. 13** Lithography II: Optical Aligners and Photomasks; **Ch. 14** Advanced Lithography: E-Beam and X-Ray; **Ch. 15** Wet Processing: Cleaning, Etching, and Lift-Off; **Ch. 16** Dry Etching for VLSI; **Ch. 17** Material Characterization Techniques for VLSI Fabrication; **Ch. 18** Structured Approach to Design of Experiments for Process Optimization.

**1986 LATTICE PRESS 660 pp. ISBN 0-9616721-3-7**

### Volume 2 - Process Integration
**By STANLEY WOLF**

**TABLE of CONTENTS - Ch. 1** Process Integration for VLSI and ULSI; **Ch. 2** Isolation Technologies for Integrated Circuits; **Ch. 3** Contact Technology and Local Interconnects for VLSI; **Ch. 4**; Multilevel Interconnect Technology for VLSI and ULSI; **Ch. 5** NMOS Devices and Process Integration; **Ch. 6** CMOS Process Integration; **Ch. 7** Bipolar and BiCMOS Process Integration; **Ch. 8** Semiconductor Memory Process Integration; **Ch. 9** Process Simulation.

**1990 LATTICE PRESS 752 pp. ISBN 0-9616721-4-5**

**on last page of book**

0961672153 (249884)
Silicon Processing for the VLSI Era
Vol. 3: The Submicron MOSFET

BOOK

ing

hnology

HARD N. TAUBER

Single-Crystal Growth and Wafering;
essing, and Gettering; **Ch. 3** Vacuum
4 Basics of Thin Films; **Ch. 5** Silicon
Vapor Deposition of Amorphous and
idation of Silicon **Ch. 8** Diffusion in
**Ch. 10** Aluminum Thin Films and
**11** Refractory Metals and Their
Optical Photoresists - Material
**h. 13** Lithography II: Optical Aligners
nography: E-Beam and X-Ray;
ning, and Lift-Off; **Ch. 16** Dry Etching
on Techniques for VLSI Fabrication;
of Experiments for Process

p. ISBN 0-9616721-3-7

tegration

cess Integration for VLSI and ULSI;
rated Circuits; **Ch. 3** Contact Technology
**4**; Multilevel Interconnect Technology
ices and Process Integration;
**h. 7** Bipolar and BiCMOS
uctor Memory Process Integration;

pp. ISBN 0-9616721-4-5

e of book

# Silicon Processing for the VLSI Era

Volume 3

The Submicron MOSFET

S. Wolf

TK
7874
.W635
2000
V. 3

Kirkland & Ellis Librar
5 0628 01144

Sili

Volu

# CONTENTS


## PREFACE

## Chap. 1 - THE ROLE OF PROCESS AND DEVICE MODELS IN MICROELECTRONICS TECHNOLOGY 1

### 1.1 MODELS IN MICROELECTRONIC TECHNOLOGY 1

1.1.1 Development of Physically Based Models 3
1.1.2 Development of Empirically Based Models 4
*1.1.2.1 Empirically Based versus Physically Based Models.*
*1.1.2.2 Deriving Empirically Based Models.*
*1.1.2.3 Role of Empirical Models in Semiconductor Simulation.*
*1.1.2.4 Examples of Quantitative Empirically Based Models.*
*1.1.2.5 PREDICT-1: A Process Simulator Based on Empirical Models.*

### 1.2 MATHEMATICAL FORMULATION OF THE PHYSICALLY-BASED MODELS OF SEMICONDUCTOR PROCESSES AND DEVICES 9

1.2.1 The Physically Based Model of Impurity Diffusion in Silicon - Fick's Second Law Equation 11
1.2.2 The Physically Based Model of Semiconductor Device Behavior 12
1.2.3 The Poisson Equation 15

### 1.3 CLOSED-FORM ANALYTICAL SOLUTIONS VERSUS NUMERICAL SOLUTIONS OF THE PDES THAT ARE THE PHYSICALLY BASED MODELS OF MICROELECTRONICS 16

1.3.1 Closed-Form Analytical Solutions - Mathematical Aspects 16
1.3.2 Numerical Solutions - Mathematical Aspects 16
1.3.3 Comparing the Analytical and Numerical Solutions in Semiconductor Simulation Applications 17
1.3.4 Role of Analytical Solutions in Submicron Semiconductor Technology 17
1.3.5 Analytic Solutions of Fick's 2nd Law Equation 19




MPS EX. 1008C - 4/295

1.3.6 Analytical Solutions of the One-Dimensional Form of the Poisson Equation in the Depletion Approximation 23

**1.4 CIRCUMSTANCES UNDER WHICH THE ANALYTIC SOLUTIONS OF THESE PDES BECOME INADEQUATE FOR SIMULATION PURPOSES 24**

1.4.1 The Inadequacy of the Analytic Solutions of Fick's 2nd Law Equation for Simulating Diffusion in Submicron Device Structures 24
1.4.2 The Inadequacy of Using a One-Dimensional Form of the Poisson Equation and the Depletion Approximation to Model Submicron MOSFET Behavior 27

**REFERENCES 28**

***Chap. 2 - NUMERICAL METHODS FOR SOLVING THE PARTIAL DIFFERENTIAL EQUATIONS WHICH MODEL THE PHYSICS OF SUBMICRON DEVICES AND PROCESSES 29***

**2.1 NUMERICAL SOLUTIONS OF DIFFERENTIAL EQUATIONS 31**

**2.2 NUMERICAL METHODS FOR SOLVING NONLINEAR PARTIAL DIFFERENTIAL EQUATIONS 32**

**2.3 GRID GENERATION AND REFINEMENT PROCEDURES 34**

**2.4 DISCRETIZATION OF DIFFERENTIAL EQUATIONS 36**

2.4.1 Space Discretization 39
2.4.2. The Finite-Difference Method 39
*2.4.2.1 The Difference Operator Method*
*2.4.2.2 Taylor Series.*
*2.4.2.3 One-Dimensional Finite Difference Approximations of Derivatives.*
*2.4.2.4 Two-Dimensional Space Discretization.*
2.4.3 The Finite Element Method 45
2.4.4 Time Discretization 47
*2.4.4.1 Explicit Time Discretization.*
*2.4.4.2 Implicit Time Discretization.*

**2.5 ORDERING THE SET OF DISCRETIZED PDEs INTO APPROPRIATE MATRIX FORM 50**

**2.6 LINEARIZING NONLINEAR ALGEBRAIC EQUATIONS** 52

**2.7 MATRIX METHODS FOR SOLVING SIMULTANEOUS LINEAR ALGEBRAIC EQUATIONS** 55

**2.8 VISUALIZATION OF THE RESULTS** 57

**2.9 DATA BASE OF THE SIMULATION PACKAGES** 58

**2.10 EXAMPLES OF THE PROCEDURES USED TO NUMERICALLY SOLVE THE MODEL PARTIAL-DIFFERENTIAL EQUATIONS OF MICROELECTRONICS** 59

2.10.1 Outline of a Numerical Analysis Procedure for Solving the Two-Dimensional Poisson Equation to Simulate the Electrostatic Potential in a MOSFET 59

*2.10.1.1 Example of How Device Simulation Programs are Used to Obtain the Two-Dimensional Solution of the Poisson Equation in a MOSFET Structure Operating in Subthreshold.*

2.10.2 Example of a Numerical Procedure for Solving the One-Dimensional Form of Fick's 2nd Law Equation as a Model for Impurity Diffusion in Silicon 70

**2.11 SYSTEMS OF COUPLED EQUATIONS** 74

2.11.1 Gummel's Iterative Method 75
2.11.2 Newton's Direct Method 76

**2.12 EVOLUTION OF MOSFET DEVICE SIMULATORS** 77

2.12.1 CADDET 78
2.12.2 MINIMOS 78
2.12.3 GEMINI 78
2.12.4 PISCES-II 80
2.12.5 Three-Dimensional Device Simulators 80

**REFERENCES** 81

***Chap. 3 - MOS TRANSISTOR DEVICE PHYSICS: PART 1 - BASICS MOS PHYSICS and THE MOS CAPACITOR*** 83

**3.1 BASIC MOS THEORY and PHYSICS of IDEAL MOS CAPACITORS (MOS-C)** 84

3.1.1 The Structure of the MOS-C and the MOSFET 85

*3.1.1.1 Comparison of MOS-Cs and Conventional Capacitor Structures.*

*3.1.1.2 Why is the MOS-C Studied First?*

**3.2 QUALITATIVE DESCRIPTION OF MOS-C DEVICE BEHAVIOR** 89

3.2.1 Energy-Band Diagram Representation of Semiconductor Devices 90
3.2.2 Energy Band Diagram of the Ideal MOS Capacitor 91
*3.2.2.1 Accumulation.*
*3.2.2.2 Depletion.*
*3.2.2.3 Inversion.*
*3.2.2.4 Strong Inversion.*
*3.2.2.5 Microscopic Perspective of the Mobile Charge Behavior in a MOS-C.*

**3.3 QUANTITATIVE DESCRIPTION OF MOS-C BEHAVIOR** 96

3.3.1 The Electrostatic Potential in MOS Structures 98
3.3.2 General Approach to Deriving MOS-C Characteristics 100
3.3.3 Finding the Quantitative Characteristics of a MOS-C when the Depletion Approximation is Invoked 103
3.3.4 More Accurate and General Model for MOS-C Behavior 106
3.3.5 Charge-Sheet Model for Determining the Characteristics of the Ideal MOS-C 112
*3.3.5.1 Approximation of $Q_I$ in Weak Inversion.*
*3.3.5.2 Approximation of $Q_I$ in Strong Inversion.*

**3.4 THRESHOLD VOLTAGE OF IDEAL MOS CAPACITORS** 116

**3.5 PHYSICS OF NON-IDEAL MOS CAPACITORS ($n^+$PolySi-$SiO_2$-Si MOS Capacitors)** 117

3.5.1 Workfunction Difference Between Gate and Semiconductor 117
3.5.2 Oxide Charges and Traps 119
*3.5.2.1 Mobile Ionic Charges.*
*3.5.2.2 Fixed Oxide Charge.*
*3.5.2.3 Interface Trapped Charge.*
*3.5.2.4 Oxide Trapped Charge.*
*3.5.2.5 Combined Effect of Oxide Charges on $V_T$ of Submicron MOSFETs.*

**3.6 THE THRESHOLD VOLTAGE EQUATION OF Si-$SiO_2$ MOS CAPACITORS** 127

**3.7 VISUALIZATION OF MOS-C AND MOSFET PHENOMENA USING POTENTIAL VERSUS POSITION DIAGRAMS** 129

**REFERENCES** 130

*Chap. 4 - MOS TRANSISTOR DEVICE PHYSICS: PART 2 - LONG-CHANNEL MOSFETS* 134

**4.1 TERMINOLOGY OF MOSFET DEVICE STRUCTURES** 135

4.1.1 Basics of MOSFET Operation 136

**4.2 BIASING THE INVERSION LAYER (BODY EFFECT)** 138

4.2.1 Qualitative Discussion of the Effect of Applying a Bias to the Inversion Layer of a MOS Structure 138

*4.2.1.1 Case When Both $V_{GB}$ and $V_{CB} = 0V$.*

*4.2.1.2. Case When $V_{GB} \geq V_T$ and $V_{CB} = 0V$.*

*4.2.1.3. Case When $V_{GB} = 0V$, But $V_{CB} > 0V$.*

*4.2.1.4. Case When $V_{GB} \geq V_T$ and $V_{CB} > 0V$.*

*4.2.1.5 Summary of the Behavior of the Three-Terminal MOS Structure and the Significance of Such Behavior on the Operation of the MOSFET.*

*4.2.1.6 Body Effect.*

4.2.2 Quantitative Description of Effects of Biasing the Inversion Layer of MOS Structures 144

*4.2.2.1 General Case.*

*4.2.2.2 Strong Inversion Case.*

**4.3 DEFINITION OF THE TERM: LONG-CHANNEL MOSFET** 147

4.3.1 The Gradual Channel Approximation (GCA) 149

*4.3.1.1 Verifying the Validity of the GCA as a Function of the Geometrical Factors of the MOSFET Device Structure and Bias Conditions.*

4.3.2 Circuit Characteristics of Long-Channel MOSFETs 152

**4.4 QUALITATIVE DESCRIPTION OF MOSFET OPERATION** 153

4.4.1 MOSFET Behavior in Response to Gate Bias Alone 153

4.4.2 Qualitative MOSFET Behavior when both Gate and Drain Bias are Applied 158

**4.5 QUANTITATIVE BEHAVIOR OF MOSFETS: DC CIRCUIT MODELS OF LONG-CHANNEL MOSFETS** 162

4.5.1 General Approach to Deriving the DC Drain-Current Relationships in Long-Channel MOSFETs 163

4.5.2 Pao-Sah Model 166

4.5.3 The Charge Sheet Model 170

4.5.4 Variable Depletion-Charge (or Bulk-Charge) Model 173

4.5.5 Square-Law Model 175
4.5.6 Comparison of the Four MOSFET Circuit Models 177
*4.5.6.1 MOSFET Models of the SPICE Circuit Simulator.*

**4.6 THRESHOLD-VOLTAGE CONTROL IN MOSFETS** 182

4.6.1 Measuring Threshold Voltage 182
4.6.2 Adjusting Threshold Voltage 182
4.6.3 Ion Implantation for Adjusting Threshold Voltage 183
*4.6.3.1 Impact of the $V_T$-adjust Implant on the Body Effect.*
4.6.4 Impact of $V_T$-Adjust Implant on Other MOSFET Characteristics 188

**4.7 SUBTHRESHOLD CURRENTS IN LONG-CHANNEL MOSFETs ($I_{DST}$ when $V_{GS} < |V_T|$)** 191

4.7.1 Subthreshold Swing $S_t$ 196
4.7.2 Gate-Induced Drain Leakage (GIDL) 198

**4.8 SUMMARY OF LONG-CHANNEL MOSFET BEHAVIOR** 200

**REFERENCES** 201

***Chap. 5 - MOS TRANSISTOR DEVICE PHYSICS: PART 3 - THE SUBMICRON MOSFET*** 205

**5.1 DEVICE CHARACTERISTICS OF LONG-CHANNEL VERSUS SHORT-CHANNEL MOSFETS** 207

**5.2 EFFECT OF GATE DIMENSIONS ON THRESHOLD VOLTAGE** 208

5.2.1 Short-Channel Threshold-Voltage Shift 208
*5.2.1.1 Numerical Solution of the 2-D Poisson Equation for Calculating $\Delta V_{TSC}$.*
*5.2.1.2 Charge-Sharing Models.*
*5.2.1.3 Barrier-Lowering Models and DIBL.*
*5.2.1.4 Quasi-Two-Dimensional Analytical Solution for $\Delta V_{TSC}$.*
*5.2.1.5 Measuring Surface-DIBL Effects.*
*5.2.1.6 Dependence of $V_T$ on $V_{BS}$ in Short-Channel MOSFETs.*
5.2.2 Narrow Gate-Width Effects on Threshold Voltage 222
*5.2.2.1 Devices Exhibiting Both Short- and Narrow-Width Effects.*

5.2.3 Reverse Short-Channel Effects on Threshold Voltage 226

*5.2.3.1 Model which Proposes RSCE is Due to Lateral Dopant Nonuniformity at the Channel Si-$SiO_2$ Interface (Arising from Enhanced Diffusion of Channel Dopants Caused by Interstitial Injection During Poly Reox, Salicide Formation, or Implant Damage).*

*5.2.3.2 Model Which Proposes RSCE Arises from Boron Segregation to Implant Damaged Regions at the Edge of the Channel.*

*5.2.3.3 Model Which Attributes RSCE to Transient Enhanced Diffusion of Channel Dopants to the Silicon Surface Arising from Implant Damage.*

*5.2.3.4 Model which Attributes RSCE to Silicon Interstitial Capture in the Gate Oxide.*

**5.3 SHORT-CHANNEL EFFECTS ON SUBTHRESHOLD SWING, $S_t$ (Subsurface Punchthrough)** 232

5.3.1 Experimentally Characterizing Punchthrough 240

5.3.2 Modeling Punchthrough 242

5.3.3 Modeling the Simultaneous Occurrence of Surface-DIBL and Subsurface-DIBL 245

**5.4 SHORT-CHANNEL EFFECTS ON THE I-V CHARACTERISTICS OF MOSFETS OPERATED IN THE STRONG THRESHOLD REGIME** 247

5.4.1 Impact of the MOSFET Electric Fields on Mobility 248

*5.4.1.1 Models of Mobility Degradation Due to Gate-Induced Electric Fields.*

*5.4.1.2 Models of the Carrier-Velocity Dependence on Drain Electric Field (Velocity Saturation).*

5.4.2 A Simple, Analytic DC Circuit Model of the Short-Channel MOSFET in Strong Inversion 254

*5.4.2.1 DC Circuit Model of the Short-Channel MOSFET in the Linear Regime.*

*5.4.2.2 Effects of Scaling on $g_{msat}$.*

*5.4.2.3 Comparing the Values of $I_D$ Calculated with the Long- and Short-Channel MOSFET Models as a Function of Channel Length.*

5.4.3 Modeling the Saturation Region of Operation in Short-Channel MOSFETs 260

*5.4.3.1 Modeling Short-Channel MOSFET Saturation Behavior Using the Abrupt Junction and Depletion Approximations.*

*5.4.3.2 Constant Field-Gradient Model.*

*5.4.3.3 Pseudo-Two-Dimensional Model.*

**5.5. SHORT-CHANNEL MOSFET MODELS USED IN THE *SPICE* CIRCUIT SIMULATOR** 271

5.5.1 BSIM Model Equations 272
*5.5.1.1 BSIM Threshold Voltage Equation.*
*5.5.1.2 BSIM Equations for $I_D$ when the MOSFET is Operated in Strong Inversion.*
*5.5.1.3 BSIM Equations for $I_D$ when the MOSFET is Operated in Weak Inversion (Subthreshold Regime).*

**5.6 MOSFET SCALING** 274

5.6.1 Design of Submicron MOSFETs: Scaling Guidelines 274
*5.6.1.1 Constant Electric-Field, Constant Voltage & Electrostatic Scaling.*
*5.6.1.2 Subthreshold Scaling.*
*5.6.1.3 Off-Current Scaling Approach.*
5.6.2 Manufacturing Considerations in Submicron MOSFET Device Design 285

**5.7 DESIGN OF SUBMICRON MOSFETS** 286

5.7.1 Design Methodology Based on the Subthreshold Scaling Equation 286
5.7.2 Design Methodology Based on Required Off-Current Value 287

**5.8 *p*-CHANNEL DEVICES IN CMOS** 288

5.8.1 PMOS Devices with $n^+$-Polysilicon Gates 289
*5.8.1.1 Punchthrough Susceptibility.*
5.8.2 Why PMOS Devices with $n^+$-Polysilicon Gates and Implanted *p*-Surface Layers Exhibit Enhanced Susceptibility to Short-Channel Effects 291
*5.8.2.1 Threshold-Voltage Roll-Off in Buried-Channel PMOS.*
*5.8.2.2 Subthreshold Swing ($S_t$) in Buried-Channel PMOS.*
*5.8.2.3 Punchthrough Susceptibility of Buried-Channel PMOS.*
5.8.3 Techniques Used to Suppress Short-Channel Effects in Buried-Channel PMOS 305
*5.8.3.1 Techniques Used to Keep the Implanted p-Layer as Thin as Possible.*
*5.8.3.2 Shallow $p^+$ Source/Drain Junctions to Suppress Punchthrough in PMOSFETs.*
*5.8.3.3 LDD Structures in PMOS to Limit Punchthrough.*
*5.8.3.4 New PMOS Device Structures Designed to Suppress Punchthrough.*
5.8.4 PMOS Devices with $p^+$--Polysilicon Gates 311

**REFERENCES** 313

**Chap. 6 - ISOLATION STRUCTURES IN SUBMICRON CMOS** 321

**6.1 CHARACTERIZING MOS ISOLATION**

6.1.1 Test Structures for NMOS Isolation Structures 322
6.1.2 Punchthrough Prevention between Adjacent Devices in MOS Circuits 325

**6.2 THE BASIC LOCOS ISOLATION PROCESS** 330

6.2.1 Details of the Basic Semi-recessed LOCOS Process 332
*6.2.1.1 Pad-Oxide Layer.*
*6.2.1.2 CVD of Silicon Nitride Layer.*
*6.2.1.3 Mask and Etch Pad-Oxide/Nitride Layer to Define Active Regions.*
*6.2.1.4 Channel-Stop Implant.*
*6.2.1.5 Problems Arising from the Channel-Stop Implants.*
*6.2.1.6 Grow Field Oxide.*
*6.2.1.7. Factors Which Impact Bird's Beak Length and Shape.*
*6.2.1.8 Use of High-Energy Ion Implantation to Introduce the Channel-Stop Dopant After Field Oxide Growth.*
*6.2.1.9 Strip the Masking Nitride/Pad-Oxide Layer.*
*6.2.1.10 Regrow Sacrificial Pad Oxide and Strip (Kooi Effect).*
6.2.2. Planarizing Semirecessed LOCOS Structures 348

**6.3 MODELING THE TOPOGRAPHY OF LOCOS STRUCTURES** 349

6.3.1 Empirical Models of 2-D Thermal Oxidation 350
6.3.2 Physically Based Models of 2-D Oxidation 351
6.3.3 Simulating Thermal Oxidation in 3-D Using Physical Models 355

**6.4 POLY-BUFFERED LOCOS** 357

6.4.1. Modified Poly-Buffered LOCOS Processes 361
*6.4.1.1 Framed-Mask PBL (FMPBL)*
*6.4.1.2 Polysilicon-Encapsulated LOCOS (PELOX)*
*6.4.1.3 Nitride-Clad LOCOS (NCL)*
*6.4.1.4 Mitigating the Field-Thinning Problem of LOCOS*

**6.5 SHALLOW TRENCH AND REFILL ISOLATION** 367

6.5.1 Early Shallow Trench and Refill Isolation 368
6.5.2 Improved Shallow Trench and Refill Isolation Processes 371

**6.6 CMOS ISOLATION TECHNOLOGY** 373

6.6.1 Qualitative Description of Isolation in CMOS 374

*6.6.1.1 Leakage Currents in CMOS Gates Due to Active Device Phenomena and Intra-Well Isolation Loss*

*6.6.1.2 Leakage Currents in CMOS Gates Due to Loss of Isolation Among Opposite-Type FETs*

*6.6.1.3 Why $n^+$-to-$p^+$ Isolation Spacing is Greater than $n^+$-to-$n^+$ Spacing in NMOS (or $p^+$-to-$p^+$ Spacing in PMOS)*

*6.6.1.4 Effects on $n^+$-to-$p^+$ Spacing of Dopant Redistribution at the Well Borders*

*6.6.1.5 Threshold Voltage Rolloff, DIBL, and Lateral Punchthrough in Submicron CMOS Parasitic Field FETs*

6.6.2 Quantitative Modeling of CMOS Isolation 384

6.6.3 Experimental Characterization of Isolation in CMOS 387

*6.6.3.1 Experimental Characterization of Isolation in $n^+$-to-n-well Parasitic FETs.*

*6.6.3.2 Experimental Characterization of Isolation in $p^+$-to-p-substrate Parasitic FETs.*

6.6.4 Establishing the Minimum $n^+$-to-$p^+$ Isolation Spacing in CMOS from Modeling and Experimental Data 398

*6.6.4.1 Isolation Spacing Design Rules for 0.35 and 0.25 μm CMOS.*

6.6.5 Vertical Isolation in CMOS 402

6.6.6 LOCOS-Based Isolation in CMOS 405

6.6.7 Trench Isolation for CMOS 407

**REFERENCES** 414

***Chap. 7 - THIN GATE OXIDES: GROWTH AND RELIABILITY*** 421

**7.1 GATE OXIDE CHARACTERISTICS NEEDED FOR SUBMICRON MOSFETS** 422

**7.2 PHYSICAL PICTURE OF $SiO_2$ AND THE $Si/SiO_2$ INTERFACE** 423

7.2.1 Physical and Chemical Properties of $SiO_2$ 423

7.2.2 The $Si/SiO_2$ Interface 425

**7.3 CARRIER INJECTION IN THE $Si/SiO_2$ SYSTEM** 429

7.3.1 Channel Hot Electrons (CHE) 430

7.3.2 Injection of Drain Avalanche Hot Carriers (DAHC) 434

7.3.3 Fowler-Nordheim (FN) Tunneling 435

7.3.4 Direct Tunneling 437

**7.4 TESTS FOR GATE OXIDE RELIABILITY 438**

7.4.1 Measuring Dielectric Strength 438
7.4.2 Measuring Time-Dependent Breakdown Behavior 440
*7.4.2.1 Time-to-Breakdown under Constant-Voltage Stressing.*
*7.4.2.2 Time-to-Breakdown under Constant-Current Stressing.*
*7.4.2.3 Charge to Breakdown ($Q_{BD}$).*
7.4.3 Mathematics of Reliability Characteristics 441
*7.4.3.1 The Failure Unit (FIT).*
*7.4.3.2. The Cumulative Distribution Function.*
*7.4.3.3 Probability Density Function.*
*7.4.3.4 The Instantaneous Failure Rate.*
*7.4.3.5 The Mean Time to Failure.*
*7.4.3.6 The Weibull Cumulative Distribution Function.*
*7.4.3.7 The Log-Normal Cumulative Distribution Function.*
*7.4.3.8 Characterizing the Reliability of Oxides in Terms of the Mathematical Reliability Functions.*

**7.5 THE PHENOMENON OF OXIDE BREAKDOWN 448**

7.5.1 Qualitative Physical Models of Intrinsic Oxide Breakdown 451
*7.5.1.1 Hole Generation and Trapping Model.*
*7.5.1.2 Wolters' Electron Lattice-Damage Model.*
7.5.2 Qualitative Models for the Physical Origin of B-Mode Failures in Oxides 458
*7.5.2.1 Test Structure for Intrinsic Oxide Breakdown Measurements.*
*7.5.2.2 Damage at the Gate Periphery Resulting from the Polysilicon Etch Process.*
7.5.3 Empirical Quantitative Model of Intrinsic Oxide Breakdown 462
7.5.4 Quantitative Models for B-Mode Failures 467
*7.5.4.1 Reduced Barrier Height Model.*
*7.5.4.2 Oxide Thinning Model.*
*7.5.4.3. The Cumulative Defect Density Function $D(\Delta t_{ox})$.*
*7.5.4.4. Using $D(\Delta t_{ox})$ to Predict Oxide Breakdown Reliability.*
*7.5.4.5. Ramp-Voltage Breakdown Test for Obtaining $D(\Delta t_{ox})$ Data.*
*7.5.4.6. Correlating Ramp-Voltage Test Data and Constant-Voltage TDDB Data.*
*7.5.4.7 Interface Trap Generation as a Measure of Oxide Damage Due to Charge Injected into the Oxide.*
7.5.5 Applications of the Oxide Breakdown Reliability Model 477
*7.5.5.1 Projecting the Reliability of Gate Oxides with Various Thicknesses.*

*7.5.5.2 If a MOS IC is to have a Specific Lifetime (e.g., 10-Years), What is the Minimum Oxide Thickness that can be Used? (Assume the Maximum Cumulative Failure Percentage, Operating Temperature, and Oxide Area are Specified.)*

**7.6 SCREENING TESTS FOR OXIDE BREAKDOWN (BURN-IN)** 482

7.6.1 Modeling the Effect of the Burn-In Stress on the Post-Burn-In Reliability of the Oxides 485
7.6.2 Procedure for Selecting an Optimal Set of Burn-In Conditions for Oxide Breakdown Screening 486
7.6.3 Example of Applying the Procedure for Determining an Optimal Set of Burn-In Conditions 489

**7.7 OXIDE BREAKDOWN MODULE IN BERKELEY RELIABILITY TOOL (BERT)** 492

**7.8 MODELS OF THIN OXIDE GROWTH** 492

**7.9 TECHNOLOGY OF THIN OXIDE GROWTH** 495

7.9.1 Oxidation Furnaces 495
7.9.2 Control of Gate Oxide Growth Rates 495
7.9.3 Factors Impacting Gate-Oxide Thickness Uniformity 496
7.9.4 Gate Oxide Growth Processes for 10-20 nm thick Gate Oxides on 150-200 mm Wafers 499
7.9.5 Alternative Gate Oxide Growth Processes 502
*7.9.5.1 Stacked Gate Oxide Films (Thermally Grown Layer and CVD Layer).*

**7.10 GATE OXIDE DAMAGE FROM PLASMA PROCESSING** 504

7.10.1 How Isolated Conductor Regions on a Wafer Surface Can be Charged Up by an RF Plasma 504
7.10.2 Causes of Non-Uniformities in Plasmas 506
7.10.3 Test Structures used to Characterize Plasma-Induced Oxide Damage 507
7.10.4 Electrical Tests for Measuring Oxide Damage 509
*7.10.4.1 Wafer Mapping to Determine Positional Dependence of Damage on the Wafer Surface.*
7.10.5 Oxide Damage Models in Various Plasma Etching Processes 511
*7.10.5.1 Oxide Damage During Polysilicon or Metal Etch Processes.*
*7.10.5.2 Oxide Damage During Resist Stripping.*
*7.10.5.3 Radiation Induced Oxide Damage.*
7.10.6 Procedures for Reducing Plasma-Induced Oxide Damage 514

**REFERENCES** 515

*Chap. 8 - WELL FORMATION IN CMOS* 523

**8.1 *p*-WELL, *n*-WELL, and TWIN-WELL TECHNOLOGIES** 524

8.1.1 *p*-Well CMOS 525
8.1.2 *n*-Well CMOS 527
8.1.3 CMOS on Epitaxial Substrates 528
8.1.4 Twin-Well CMOS 530
8.1.5 Summary of CMOS Well-Technology Issues 532

**8.2 CONVENTIONAL FORMATION OF WELLS AND CHANNEL STOPS** 532

8.2.1 Aligning Subsequent Patterns to the Wells 532
8.2.2 Twin-Well and Channel-Stop Formation 535
8.2.3 Split Well-Drive-In Process 538

**8.3 RETROGRADE-WELL CMOS** 539

8.3.1 Retrograde Well Technologies to Improve Isolation 546

**8.4 FUTURE TRENDS IN WELL FORMATION** 552

**8.5 AFTER-GATE IMPLANTATION (AGI)** 554

**REFERENCES** 555

*Chap. 9 - HOT-CARRIER RESISTANT PROCESSING AND DEVICE STRUCTURES* 559

**9.1 MODEL FOR THE MAXIMUM LATERAL ELECTRIC FIELD $\mathcal{E}_{ymax}$ IN NON-GRADED-DRAIN MOSFETS** 561

**9.2 SUBSTRATE CURRENTS DUE TO HOT CARRIERS** 563

**9.3 MODELS OF HOT-CARRIER DEGRADATION PHENOMENA** 566

9.3.1. Si-H Bond Breaking Model 569
9.3.2 Hot-Hole and Hot-Electron Trapping Model 569
9.3.3 Location of the Hot-Carrier Damaged Region 571

**9.4 CHARACTERIZING MOSFET DEGRADATION DUE TO HOT-CARRIER EFFECTS** 572

9.4.1 Device Parameters that are Impacted by Hot-Carrier Damage 573

9.4.2 How to Determine if a MOSFET Can be Operated with out Failing due to Hot-Carrier Effects Under Normal Operating Conditions? 574
*9.4.2.1 Selecting a Criterion that Identifies Device Failure Due to Hot-Carrier Damage.*
9.4.3 Accelerated Testing of Hot-Carrier Device Lifetime 576
9.4.4 Hot-Carrier Lifetime Under AC Stressing 580
9.4.5 Effect of Device Degradation on Circuit Performance 581
9.4.6 Hot-Carrier Reliability Simulation 582
*9.4.6.1 SCALE.*
*9.4.6.2 Simulators that Relate the Device-Level Degradation Parameters to Circuit Performance (CAS and HOTRON).*

**9.5 DECREASING HOT CARRIER DEGRADATION BY MODIFYING THE MOSFET STRUCTURE 586**

9.5.1 Phosphorus-Drain Structure 588
9.5.2 Double Diffused Drain (DDD) 588

**9.6 LIGHTLY DOPED DRAIN (LDD) STRUCTURES 591**

9.6.1 Modeling $\mathcal{E}_{ymax}$ in LDD MOSFETs 592
*9.6.1.1 Simple Model for Estimating $\mathcal{E}_{ymax}$ in LDD MOSFETs*
*9.6.1.2 Analytical Model for Calculating $\mathcal{E}_{ymax}$ in LDD MOSFETs Using the Pseudo-2D Approach to Solving the Poisson Equation.*
*9.6.1.3 Model for the Series Resistance Introduced by the $n^-$ Region of the LDD.*
9.6.2 Overview of the Process Sequence to Form LDDs 595

**9.7 PERFORMANCE AND HOT-CARRIER LIMITATIONS OF THE CONVENTIONAL LDD 598**

9.7.1 Performance Degradation in LDD MOSFETs 599
*9.7.1.1 $I_D$ Decrease Due to Added Resistance of $n^-$ Regions.*
*9.7.1.2 Doping Compensation Effects that can Increase $R_{n^-}$ in Deep Submicron LDD MOSFETs.*
*9.7.1.3 Increase of $R_{sh}$ by Weak Overlap of the Gate and Drain.*
*9.7.1.4 The Impact of Poly Re-Ox on Weak Overlap in MOSFETs.*
*9.7.1.5 Off-Axis Implant Effects in MOSFETs, Leading to Weak Overlap Problems and Asymmetrical MOSFET Device Characteristics.*
*9.7.1.6 Implanter Issues that Impact the LDD Process Sequence.*
*9.7.1.7 Process integration issues which arise when an LDD is integrated into a CMOS Technology.*
9.7.2 Hot Carrier Reliability Issues in Early LDDs 606

**9.8 DISPOSABLE SPACERS** 608

**9.9 SUMMARY OF THE LIMITATIONS OF EARLY LDD DEVICES** 611

**9.10 SUMMARY OF THE METHODS TO BE USED IN DESIGNING EFFECTIVE LDD STRUCTURES** 612

**9.11 IMPROVED CONVENTIONAL (OXIDE-SPACER-BASED) LDD STRUCTURES** 613

9.11.1 Increasing the Doping in the $n^-$ Region of the LDD 614
*9.11.1.1 Moderate Lightly Doped Drain (M-LDD).*
*9.11.1.2 Metal-coated LDD (MLD).*
9.11.2 Tailoring the Vertical Doping Profile of the $n^-$ Implant to Improve the Conventional LDD 616
*9.11.2.1 Buried-LDD (B-LDD).*
*9.11.2.2 Profiled-LDD (P-LDD).*
9.11.3 Improving the Short-Channel Performance of the Conventional NMOS LDD 621

**9.12 FULLY OVERLAPPED LDD STRUCTURES** 623

9.12.1 Inverse-T Gate LDD (ITLDD) and Gate-Drain Overlapped Device (GOLD) Structures 623
*9.12.1.1 Inverse-T Gate LDD Structure.*
*9.12.1.2 Gate-Drain Overlapped LDD (GOLD).*
*9.12.1.3 Modified IT-LDD Structures.*
9.12.2 Large-Angle-Tilt Implanted Drain (LATID) 630
9.12.3 High Dielectric Spacers 634
9.12.4 Asymmetrical MOSFET Structure: Halo-Source-GOLD (HS-GOLD) 636

**9.13 HOT-CARRIER EFFECTS IN PMOS TRANSISTORS** 637

9.13.1 Model for Hot-Carrier Damage in PMOSFETs 638
9.13.2 Hot-Electron Induced Punchthrough (HEIP) 638
9.13.3 Hot-Electron Induced Degradation in $p^+$-Poly PMOSFETs 641

**9.14 STRENGTHENING OXIDES AGAINST HOT-CARRIER INJECTION** 641

9.14.1 Minimizing Hydrogen and $H_2O$ at the Si-$SiO_2$ Interface 643
*9.14.1.1. The role of hydrogen in hot-carrier degradation.*

*9.14.1.2 Hydrogen introduced at high temperatures.*
*9.14.1.3 Moisture in Gate Oxides as a Contributor to Hot-Carrier Degradation.*
9.14.2 Gate-Oxide Damage by Metal Etching 647
9.14.3 Nitrided Oxides 648
*9.14.3.1 Thermal nitridation of $SiO_2$.*
*9.14.3.2 $NH_3$ Oxides as MOSFET Gate Dielectrics.*
*9.14.3.3 Low-Pressure and RTP $NH_3$ Oxides (Lightly Nitrided Reoxidized $NH_3$-Nitrided Oxides).*
*9.14.3.4 Oxynitridation of Silicon in $N_2O$ Ambients.*
*9.14.3.5. Oxynitridation of Oxides in $N_2O$.*
*9.14.3.6 Fluorinated Oxides.*

**REFERENCES** 661

***APPENDIX A*** **- MATRIX METHODS** 675

**A.1 INTRODUCTION TO MATRICES** 675
**A.2 MATRIX MULTIPLICATION** 677
**A.3 MATRIX INVERSION** 678
**A.4 MATRIX METHODS FOR SOLVING SIMULTANEOUS LINEAR ALGEBRAIC EQUATIONS** 680
**A.5 NON-LINEAR ALGEBRAIC EQUATIONS** 691

***APPENDIX B*** **- MAXIMIZING THE CIRCUIT PERFORMANCE OF LONG-CHANNEL MOSFETS THROUGH DEVICE DESIGN AND PROCESSING TECHNOLOGY** 695

**B.1 CHARACTERISTICS OF DIGITAL IC MOSFETS** 695
**B.2 DESIRED CIRCUIT CHARACTERISTICS OF IC INTERCONNECTS** 697

***APPENDIX C*** **- DERIVATION OF THE BSIM $I_D$ MODEL** 705

***APPENDIX D*** **- DERIVATION OF THE DISCRETIZED 2-D POISSON EQUATIONS USING THE BOX-INTEGRATION METHOD** 708

**INDEX** 709

# PREFACE

SILICON PROCESSING FOR THE VLSI ERA now represents a series of texts designed to provide a comprehensive and up-to-date treatment of this important and rapidly changing field. The volume in hand is the third of this series. Volumes 1 (*Process Technology*) and 2 (*Process Integration*) were published in 1986 and 1990, respectively. Volume 1 deals with the individual processes employed in the fabrication of silicon VLSI circuits, such as epitaxial growth, thermal oxidation of silicon, CVD and PVD of amorphous and polycrystalline films, diffusion and ion implantation of dopants in silicon, microlithography, and patterning technology. Volume 2 describes how the individual processes of Volume 1 are combined in various ways to produce MOS and bipolar VLSI and ULSI circuits. The task of integrating these various fabrication processes together is referred to as *process integration.*

Here, we treat the topics of submicron MOSFET device physics and the relationship between such device physics and submicron MOSFET fabrication. That is, an understanding of device physics has become even more important now that MOSFETs have crossed the long-channel frontier into the submicron realm. Device aspects that could once be ignored (because they cause only second-order effects in large MOS devices) are now significant. Many device effects observed in submicron MOSFETs are impacted by the process technology used to fabricate them. Some of such effects include: short-channel effect on $V_T$; RSCE (reverse-short-channel effect on $V_T$); DIBL (drain-induced barrier lowering); narrow-width effect; reverse-narrow-width effect; subsurface punchthrough in NMOSFETs; punchthrough in PMOSFETs; impact of the $V_T$-adjust implant on subthreshold swing, $S_t$; boron penetration of gate oxides in $p^+$-poly-gate PMOSFETs - and the polysilicon depletion effect that this causes; GIDL (gate-induced drain leakage); impact of process technology on the reliability and wearout of thin gate oxides, including damage from plasma processing; hot-carrier degradation and drain-engineered MOSFET structures developed to combat the problem (including LDDs, LATID, "halo" implants, and asymmetrical MOSFETs); well-engineering by high-energy implants (including retrograde-well CMOS); ROXNOX (re-oxidized-nitrided oxides); and very-lightly-nitrided gate oxides. These and many other phenomena associated with submicron MOS fabrication can only be understood in the context of short-channel MOSFET physics. Only with such an understanding can the relationship between circuit behavior, device design, and process technology of submicron MOSFETs be grasped. Consequently, by gaining such an understanding process engineers (and other microelectronic professionals) will be better able to contribute to the task of successfully designing and manufacturing submicron ICs. One of our main purposes is thus to provide a text that treats both the topics of submicron MOSFET device physics and the phenomena associated with fabricating such devices.

Chapter 1 introduces the process and device models employed in the early days of the semiconductor industry. Such models were based on empirical data and/or simplified physical equations (e.g., differential equations in their one-dimensional form). In the



MPS EX. 1008C - 20/295

submicron era, however, the more general forms of these differential equations must be used to obtain accurate predictive capability of both the fabrication processes and the device physics. Since this generally means that partial differential equations in two- or three-dimensional form must be solved, this can only be carried out by numerical analysis, performed with the aid of high-speed digital computers. Thus, chapter 2 outlines the methodology of this approach.

To facilitate the discussion of submicron MOSFET device physics, we divide the topic up into three chapters: The first of these, chapter 3, deals with basic MOS theory and the MOS capacitor. The next, chapter 4, covers long-channel MOSFETs and the circuit models developed to predict the drain current characteristics of such devices. Finally, chapter 5 describes the characteristics of the short-channel (i.e., submicron) MOSFET. This is the longest chapter of the book, and it includes the following topics: DIBL, subsurface punchthrough, the drain current in saturation, simplified short-channel MOSFET circuit models, MOSFET scaling, and submicron PMOSFETs.

Chapter 6 is concerned with isolation issues in integrated circuits with an emphasis on CMOS technology. Chapter 7 covers thin gate oxides, primarily with respect to their reliability and growth. Chapter 8 deals with well formation in CMOS. Chapter 9 focuses on hot-carrier effects in MOS ICs, as well as on device structures and processing techniques that mitigate the detrimental aspect of such phenomena on MOSFETs. Problems are included at the end of each chapter to assist readers in gauging how well they have assimilated the material in the text.

A book of this length and diversity would not have been possible without the indirect and direct assistance of many other workers. From an indirect perspective, virtually all the information presented here is based on the research efforts of countless numbers of scientists and engineers. Their contributions are recognized to a small degree by citing some of their articles in the references given at the end of each chapter. Likewise, the direct help came in a variety of forms, and was generously provided by many people. The text is a much better work as a result of this aid, and the author expresses heartfelt thanks to those who gave of their time, energy, and intellect.

Roy Montibon of Visionary Art Resources, Inc., Los Angeles, CA designed this cover, as well as those of Volumes 1 and 2.

Stanley Wolf

P.S. Additional copies of the books can be obtained from:

**Lattice Press**
Post Office Box 340-V
Sunset Beach, CA 90742

For your convenience an order form is provided on the final leaf of the book.

# CHAPTER 3

## MOS TRANSISTOR DEVICE PHYSICS: PART 1
## BASICS MOS PHYSICS
## and
## THE MOS CAPACITOR

A basic goal of IC manufacture is to produce circuits having the highest performance at lowest cost. For digital CMOS ICs (the largest category of silicon ICs in the mid-1990s), the main performance criteria are speed, power dissipation, and device packing density. Reduction in device size has been the chief vehicle for achieving these goals. Smaller devices also produce the twin benefits of decreased die size (more chips per wafer and higher fractional yield) which exert downward pressure on die cost. However, the mere reduction of all device dimensions by a constant factor, for example, without paying attention to other processing parameters can adversely impact IC performance. That is, power dissipation may worsen because of increased device leakage currents, or circuit speed may be degraded. Reliability problems which afflict submicron MOSFETs might also be exacerbated, including hot-carrier degradation, gate-oxide wearout, and electromigration. As a result, it is necessary to employ more sophisticated scaling guidelines for device design to ensure that the shrunken devices exhibit electrical behavior comparable to that of previous generations of larger devices. In the case of MOSFETs, the aim of such scaling guidelines is to provide a design path to *short-channel devices* which continue to exhibit the ideal characteristics of *long-channel devices*. (These terms are defined later in the chapter.)

Our purpose here is to present the issues of submicron MOS device design for semiconductor process engineers. An understanding of device physics has become even more important now that MOSFETs have crossed the long-channel frontier into the short-channel (submicron) realm. Device aspects which could once be ignored (because they cause only second-order effects in large MOS devices) are now significant - such as source/drain doping profiles, channel doping profiles, and the device geometry around the gate periphery. Furthermore, if the degree of process control is not increased, variations in these parameters will become larger (on a percentage basis) as the devices become even smaller. Since the uniformity of device characteristics will be adversely impacted, process control must be improved. In addition, better processes will need to



MPS EX. 1008C - 22/295

be developed and devices will have to be designed with less process sensitivity. All of these issues can only be discussed in the context of short-channel MOSFET physics. By understanding the relationship between circuit behavior, device design, and process technology of submicron MOSFETs process engineers will be better able to contribute to the task of successfully designing and manufacturing submicron ICs.

The discussion of MOS device physics also serves to set the stage for some later topics of this book (and others of this series), namely the process technology developed to fabricate silicon ICs. To facilitate the understanding of the submicron MOSFET, we divide the topic of *MOS device physics* into three chapters. The first (chap. 3) deals with basic MOS theory and MOS capacitors The second (chap. 4) covers long-channel MOSFETs and the circuit models developed to predict the drain current characteristics of such devices. The last (chap. 5) describes short-channel (i.e., submicron) MOSFETs and issues of MOSFET device scaling.

In each of these chapters the following general approach is adopted. As each new topic is introduced it is first considered from a *qualitative* perspective, using visualization analogies whenever possible. This is intended to provide an intuitive, rudimentary grasp of the device phenomenon being presented. Then the same device effects are analyzed from a *quantitative* perspective, and mathematical relationships that describe the physical effects are developed. Where applicable, as a final task, quantitative models of the device behavior in terms of the terminal voltages and currents are derived. Where possible complicated mathematics and derivations are minimized to prevent them from standing in the way of conceptual explanations. Where such complications cannot be completely circumvented many of the intermediate steps are given. Hopefully this will make the material somewhat more digestible.

## 3.1 BASIC MOS THEORY and PHYSICS of IDEAL MOS CAPACITORS (MOS-C)

As noted in the introduction, the ultimate purpose of this and the next two chapters is to provide an understanding of short-channel MOSFET behavior (extending to devices with submicron channel lengths). Since the behavior of submicron MOSFETs is complex, the subject is best approached in a step-by-step fashion. That is, the device behavior of the simplest MOS structure (i.e., the two-terminal MOS capacitor, to be referred henceforth as the MOS-C) is considered first. The MOS-C exhibits behavior which is the foundation of both long- and short-channel MOSFET operation. Such behavior is easier to describe in the MOS-C since some of the device phenomena exhibited in more complex MOS structures (i.e., multi-dimensional electric fields and drain currents) are absent in the MOS-C. Once the reader acquires a good understanding of MOS-C behavior, these effects can be added, allowing a relatively straightforward explanation of long-channel MOSFET operation. Thereafter, submicron MOSFET behavior can be explored by showing how the long-channel MOSFET behavior is altered as the channel length is reduced. With this rationale in mind, we begin by describing the behavior of the MOS capacitor in this chapter - initially dealing with the *ideal* MOS capacitor, but later incorporating *nonideal* effects. We should also point out

that the MOS-C itself is quite a complex and subtle structure. In fact, a lengthy and rigorous text that deals comprehensively with these subtleties has been written by Nicollian and Brews.[1]

### 3.1.1 The Structure of the MOS-C and the MOSFET

Although we begin by studying the MOS-C, it is useful to compare its structure with that of the MOSFET. To do this, an even-more-fundamental configuration, the generic MOS structure is first defined. The *MOS* or *metal-oxide-semiconductor* structure is a three-layered object. It consists of a conducting layer (referred to as the *gate*), atop an insulator layer (usually silicon dioxide), and a semiconductor substrate beneath the insulator (termed either the *substrate* or *body*). The substrate can be doped either *n*-type or *p*-type. Note that the acronym MOS stems from the early days of MOS fabrication when all gates were made of metal (aluminum). While heavily doped polysilicon has replaced aluminum as the standard gate material, the name MOS continues to be used.

The structure of the *MOS capacitor* (or *MOS-C*) is shown in Fig. 3-1a. It consists of the generic MOS structure with terminals G and B connected to the gate and substrate, respectively, making it a *two-terminal device*. An external bias can be applied across these terminals, called the *gate-substrate (or gate-body) voltage* $V_{GB}$. In Fig. 3-1a1 we show a perspective view of a MOS-C having a *p*-type Si substrate. Then in Fig. 3-1a2 we show the cross-section of this device cut along the middle of the gate. This cross-section is shown lying flat Fig. 3-1a3, and in Fig. 3-1a4 the same structure with only the Si beneath the oxide is shown.

The structure of the *MOS field-effect transistor* (or *MOSFET*) is given in Fig. 3-1b. It has two regions of doping opposite that of the substrate, one at each edge of the MOS structure. These regions are called the *source* and *drain*, and a *pn* junction exists between them and the substrate. When terminals are connected to all the various regions of the MOSFET a *four-terminal device* results, with the terminals designated as G (gate), S (source), D (drain), and B (substrate).

We next observe that since one of these terminals can be designated as the common (or reference) terminal, three independent terminal voltages can be applied to the MOSFET (e.g., if B is chosen as common we will have $V_{GB}$, $V_{SB}$, and $V_{DB}$). However, only one significant current exists in an ideal MOSFET. That is, we assume that the gate current is zero ($I_G = 0$), and that the source and drain junctions are always kept under reverse bias during normal MOSFET operation. Since reverse bias current in a *pn* junction can be considered negligible (and $I_G = 0$), substrate current will also be inconsequential ($I_{sub} \approx 0$).* Thus, only the drain current $I_D$ which flows between the source and drain in the MOSFET needs to be considered. In summary, three independent terminal voltages and one current (i.e., $I_D$) are generally associated with the operation of the ideal MOSFET. In Fig. 3-1b1 we show the MOSFET in perspective, then in cross-section (Fig. 3-1b2), and finally (in Fig. 3-1b3), with the cross-section lying flat.

Figure 3-1 also defines the axes to be used in our discussion of both the MOS-C and the MOSFET structures. That is, the *x*-direction is perpendicular to the Si-$SiO_2$

* We'll remove these restrictions in chaps. 7 and 9.

interface (*vertical* direction), with $x = 0$ at the Si surface. The $y$-direction is parallel to the Si surface in the direction from source to drain (*lateral* or *longitudinal* direction). Since the source and drain are separated by a distance $L$ (termed the *channel length*), we usually choose $y = 0$ at the source end of the channel, and $y = L$ at the drain end. The $z$-direction is the other direction parallel to the Si surface (perpendicular to the $y$-direction), and defines the channel width.

**3.1.1.1. Comparison of MOS-Cs and Conventional Capacitor Structures.** It should be noted at the outset that the structure and behavior of the MOS-C differs from that of the more conventional metal-dielectric-metal capacitor structure. That is, in the latter structure both terminals are highly conductive, but in the MOS-C the semiconductor terminal is not of high conductivity. Consequently, if a potential difference is applied across the terminals of the conventional capacitor, an electric field arises within the dielectric, but is zero outside the dielectric. This implies that the "metal-dielectric-metal" capacitor stores all of the charge at the interfaces of the respective metal electrodes and the dielectric.

The situation is different in the MOS-C where one of the terminals of the capacitor is a semiconductor, not a metal. If we consider the case of a $p$-type semiconductor, then the application of a *negative* bias will induce a negative charge on the gate and a positive charge on the substrate. The high conductivity of the gate requires that the electric field within the dielectric again terminates at the gate-dielectric interface. Here, the charge on which the field lines terminate is the negative charge stored on the gate. At the substrate-dielectric interface, however, the semiconductor must supply positive charge to balance the gate's negative charge. This can readily occur because the majority mobile charge carriers in $p$-type Si are holes, implying that (1) they exist in great abundance and (2) that they are capable of moving to the interface in response to the negative bias on the gate. In this case, the $p$-type silicon MOS-C and the conventional capacitor structure behave identically. Furthermore, as we will describe in more detail in the next section, this bias condition is known as "accumulation" because it causes majority carriers to accumulate at the semiconductor surface.

On the other hand, if a *positive* gate bias is applied to this MOS-C, a somewhat different set of phenomena occur. That is, a positive gate potential produces a positive charge on the gate, and a negative charge must arise in the substrate to balance the gate charge. In this case, there are very few mobile negative charge carriers (electrons) in the $p$-substrate. Thus, their scarcity prevents them from supplying enough of the required negative charge, especially at small positive gate-bias values. Instead, the repulsion of holes (the majority carriers) by the positive bias drives the holes away from the substrate-dielectric interface. This forms a region depleted of mobile carriers (i.e., a *depletion region*) that penetrates from the surface into the substrate. The departure of holes from this surface region leaves it negatively charged because the immobile, ionized acceptor impurities remain within the region. This negative "background" charge thus becomes the negative charge induced by the positive gate potential. As a result, the electric field lines terminate on these negative charges. Unlike in the case of accumulation, however, the terminal charge of the MOS-C in the semiconductor is no

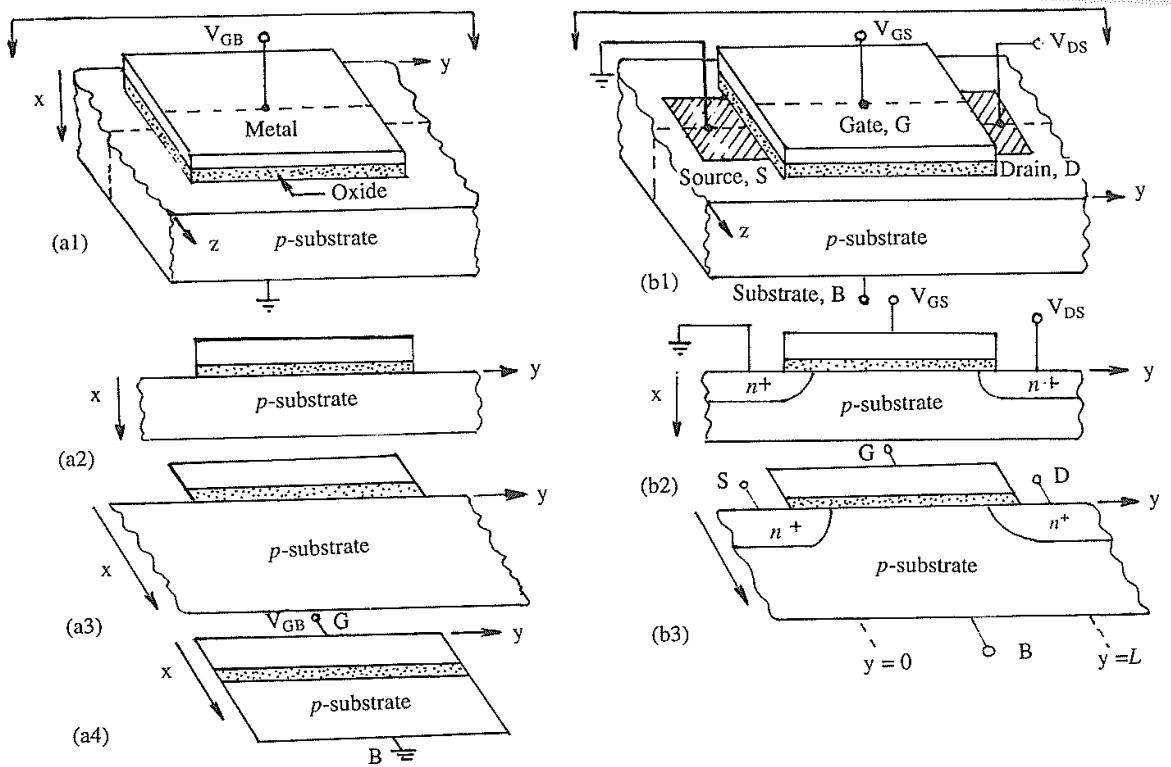


**Fig. 3-1** (a1) Perspective view of the MOS-C, (a2) Cross-section of the MOS-C cut along the middle of the structure, (a3) Cross-section shown lying flat, (a4) Cross-section with only the Si beneath the oxide shown. (b1) Perspective view of the MOSFET structure, (b2) Cross-section of the MOSFET cut down the middle of the channel, (b3) Cross-section of the MOSFET lying flat.

longer confined to the substrate-dielectric interface (i.e., to the Si surface). Instead, the charge is spread over some distance extending to the depth of the depletion region. This added distance increases the "effective" dielectric thickness and thus decreases the capacitance of the structure. Thus, unlike a conventional capacitor, whose capacitance is constant regardless of the applied bias, the capacitance of the MOS-C varies with the applied bias under some bias conditions.

Note, however, that if the value of the positive gate bias becomes sufficiently large, a large number of minority carrier electrons will be attracted to the surface. They will collect there and come to dominate the negative charge in the substrate. This induced charge due to the electrons at the surface is called an *inversion layer*. Note also that these phenomena will be described in more detail in the upcoming section, but the purpose of briefly introducing them here is to point out the fact that MOS-Cs indeed behave in a somewhat different fashion than conventional capacitor structures.

**3.1.1.2 Why is the MOS-C Studied First?** As illustrated above, the MOS-C forms the heart of the MOSFET. Yet it is a fundamental structure in its own right, just as the *pn* junction is a fundamental structure apart from the bipolar transistor. Yet, much in the same way that understanding *pn* junctions is central to understanding the operation of the bipolar transistor, an understanding of the MOS-C is central to understanding of MOSFETs. Hence, it seems logical that the behavior of MOS-Cs should be studied first, before considering the physics of the MOSFET.

We can see this by noting that the basis of MOSFET behavior essentially involves two phenomena: (1) the action of mobile carriers in the semiconductor in response to the application of a gate bias; and (2) the transport of these mobile carriers between the source and drain (in the form of a drain current, $I_D$) in response to the application of a drain bias. Therefore, to quantitatively describe MOSFET operation, initially we need to establish a quantitative model which allows the first of these two phenomena to be treated (i.e., we need to be able to determine the mobile charge distribution in a MOS structure for a given gate bias). Once this charge distribution is known, it can be used to develop a model for the relationship between $I_D$ and the terminal voltages (i.e., the gate and drain biases). Such a model for mobile-charge versus gate-bias is most easily developed in MOS-C structures for the following reasons:

**1.** We noted that the MOS capacitor is a two-terminal device. If we assume the oxide is a perfect insulator, then the current through the oxide $I_G$ is zero for dc biases between the gate and substrate. Since this is the only possible current in the MOS-C - and its value in ideal structures is zero - the redistribution of charges in the semiconductor with respect to changes in $V_{GB}$ can be analyzed without the complication of current flow. Furthermore, since no current flows under dc bias, the behavior of MOS-Cs in such cases represents an electrostatic problem. Thus, only one of the five classical device equations introduced in chap. 1 needs to be solved (i.e., the Poisson equation) to completely characterize the potential and mobile charge distribution in the ideal MOS-C (i.e., even if $V_{GB} \neq 0$).

**2.** The electric field in the MOS-C is perpendicular to the silicon surface, making it essentially uni-directional (vertical). The electrostatic potential in the device can thus be found by solving the Poisson equation in its least complex (e.g., one-dimensional) form. On the other hand, if a bias is also applied between the source and drain of a MOSFET, the direction of the electric field in the semiconductor region of the MOSFET is no longer perpendicular to the silicon surface. That is, it generally contains components parallel as well as vertical to the silicon surface. Hence, to calculate the electrostatic potential in a MOSFET, it is in general necessary to solve the Poisson equation in its two- or three-dimensional form.

**3.** The absence of current flow in a MOS-C implies that equilibrium is maintained in the semiconductor region even if a dc $V_{GB}$ is applied.* Thus, the equations used to calculate carrier concentrations in terms of equilibrium concepts (e.g., the Fermi level) can be used. This makes the solution of the Poisson equation simpler as well.

**4.** The MOS-C is widely used as the test structure for characterizing the reliability of the gate oxide film with respect to oxide breakdown and hot-electron degradation (as described in chaps. 7 and 9, respectively). Thus, the study of the MOS-C behavior is intrinsically useful for interpreting data obtained from such structures.

**5.** The quantitative relationships we develop for the mobile charge concentration in the channel region of the MOS-C under inversion are used in the $I_D$ models of the long-channel MOSFET by invoking the *gradual-channel approximation.* This approximation will be examined in more detail in chap. 4.

## 3.2 QUALITATIVE DESCRIPTION OF MOS-C DEVICE BEHAVIOR

The behavior of the MOS-C from a qualitative perspective is considered first, namely a verbal description is given of how the mobile charge distribution in the semiconductor depends on the applied dc gate bias. To help visualize these phenomena we make use of energy-band and potential representations, as well as electric-field and charge distribution diagrams.

* The term *equilibrium* should be considered here to mean *thermal equilibrium,* as viewed from the microscopic perspective. That is, the net energy in the semiconductor is stored in the crystal-lattice vibrations (phonons) as well as by free carrier motion. Although external sources of energy (such as incident photoelectric radiation) may also excite a crystal, many situations exist where no such external forces act. In such cases, the total energy is a function of only the crystal temperature, and the semiconductor will spontaneously reach a state referred to as thermal equilibrium. In thermal equilibrium every process is exactly balanced by its inverse process. One such set of competing processes in a semiconductor involves carrier generation and recombination. At thermal equilibrium the rates of these two processes are equal (and are also assumed to be driven only by thermal processes). This makes it valid to use the equilibrium carrier concentration expressions (i.e., Eqs. 3-1a and 3-1b) to calculate the carrier concentrations in the MOS-C even when $V_{GB} \neq 0V$.

### 3.2.1 Energy-Band Diagram Representation of Semiconductor Devices

One of the most helpful tools for visualizing semiconductor phenomena is the *energy-band diagram.* In such diagrams, the vertical axis represents the energy possessed by electrons when they occupy energy levels at a given location in the device. (In one-dimensional representations, a location in the device is generally specified by a point x, which is designated as the distance along the horizontal axis of the diagram). Such one-dimensional representations are adequate for treating the MOS-C (with the *x*-direction representing the direction perpendicular to the silicon surface).

In the energy-band representation of a semiconductor (Fig. 3-2), $E_C$ and $E_V$ are the conduction and valence band edges, respectively. The intrinsic Fermi level $E_i$ is at the middle of the band gap (i.e., $E_i \cong [E_C+E_V]/2$), corresponding to the Fermi-level of an intrinsic (undoped) semiconductor (Fig. 3-2a). In *n*-type doped silicon the Fermi level $E_F$ is closer to $E_C$ than to $E_V$ (Fig. 3-2b), but in *p*-type it is closer to $E_V$ (Fig. 3-2c) If an electron occupies a state at the bottom edge of the conduction band ($E_C$), its kinetic energy is defined to be zero (point A in Fig. 3-2d). As the kinetic energy of such an electron increases, it occupies energy levels higher in the conduction band (e.g., point B in Fig. 3-2d). If a semiconductor is in equilibrium, the Fermi level is invariant with position in the material, and this is depicted in a one-dimensional energy-band-versus-distance diagram as $E_F$ being a straight, horizontal line (as in all of Fig. 3-2).

Assuming Maxwell-Boltzmann statistics, the electron and hole concentrations in a semiconductor at equilibrium ($n_O$ and $p_O$, respectively) can be expressed in terms of quantities found in the energy-band diagram ($E_F$, $E_i$), as well as T, and $n_i$ (the intrinsic carrier concentration at T) according to the following expressions:

$$n_O = n_i \exp (E_F - E_i)/kT \qquad (3 - 1a)$$

$$p_O = n_i \exp (E_i - E_F)/kT \qquad (3 - 1b)$$

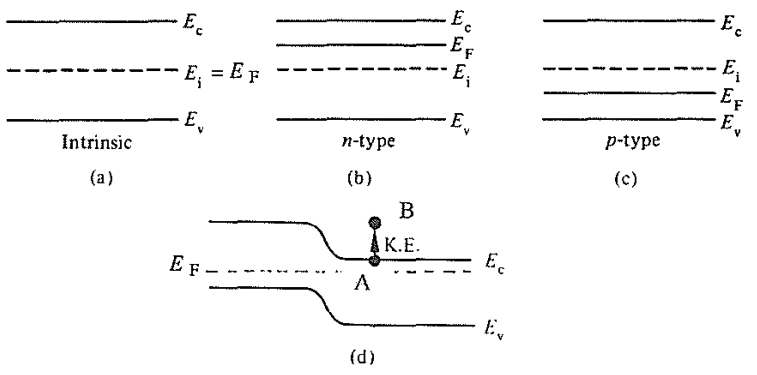


**Fig. 3-2** Energy band representation of a semiconductor: (a) intrinsic; (b) *n*-type; (c) *p*-type; (d) Depicting the kinetic energy of an electron in the energy band diagram.

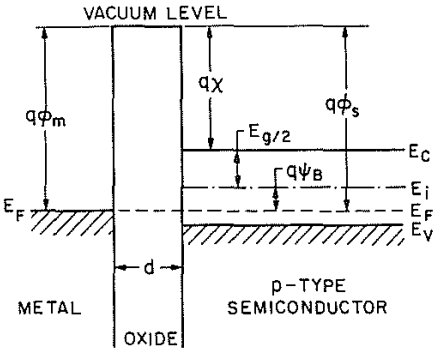


**Fig. 3-3** Energy band diagram of an ideal MOS-C when $V_{GB} = 0V$ (*flat-band condition*).

Note also that at equilibrium

$$n_o p_o = n_i^2 \qquad (3 - 1c)$$

## 3.2.2 Energy Band Diagram of the Ideal MOS Capacitor

Using the energy-band diagram representation we now consider the qualitative behavior of an *ideal* MOS-C subjected to dc bias. The following assumptions are assumed to be valid in an ideal MOS-C:

1. The energy difference between the work function of the gate material (metal), $q\varphi_m$ and that of the semiconductor, $q\varphi_s$ is zero (i.e., $q\varphi_{ms} = 0$);
2. No charges exist in the MOS-C under any biasing conditions, other than those existing in the semiconductor and those with equal but opposite sign on the gate, i.e., within the oxide there are no mobile charge carriers nor any charge centers;
3. No current can flow through the oxide under dc-biasing conditions ($I_G = 0$);
4. The semiconductor region is uniformly doped;
5. The gate layer is considered to be an equipotential region.

For our example we will consider an ideal MOS-C with a *p*-type semiconductor region.

First consider the case when no bias is applied ($V_{GB} = 0V$). The energy-band diagram for this case is shown in Fig. 3-3. We note that since equilibrium exists in the semiconductor and $q\varphi_{ms} = 0$ (Assumption #1), the Fermi level throughout the semiconductor must be invariant with position, and it must also line up with the Fermi level in the gate. This also implies that $E_c$, $E_v$, and $E_i$ in the semiconductor are horizontal and straight (i.e., flat). An energy-band diagram in which $E_c$, $E_v$, and $E_i$ are flat is said to be in a *flat-band condition. Thus, when $V_{GB} = 0$ in an ideal MOS capacitor, it's energy-band diagram is in a flat-band condition.* Note also that in *p*-type Si, $E_F$ is below $E_i$, by an amount expressed as $|E_F - E_i|$.

Next let a dc bias be applied between the gate and substrate. Since $I_G = 0$ (Assumption #3), the silicon region remains in equilibrium, implying that $E_F$ remains flat. This aspect of MOS-C behavior is unique, since the application of a dc bias across the electrodes of other semiconductor devices will cause at least some current to flow. Hence, MOS-C analysis remains simple under dc bias because the Fermi-level concept is still valid. Although the semiconductor region remains in equilibrium under dc bias (and $E_F$ remains flat), the other bands are altered from that of the $V_{GB} = 0V$ case. This is seen in Fig. 3-4 where four different gate-bias conditions are depicted. Here in Fig. 3-4a we depict the MOS-C in cross-section, as was also shown in Fig. 3-1b2. This structure is then rotated as shown in Fig. 3-4b, and the energy-band and charge distribution versus $x$ diagrams we show next refer to the MOS-C cross-section oriented in the manner of Fig. 3-4b.

**3.2.2.1 Accumulation.** In the first biasing case a *negative* bias is applied ($V_{GB}<0V$, Fig. 3-4c). The negative bias causes holes (the majority carriers in *p*-type Si) to be attracted to the silicon surface adjacent to the oxide. More holes accumulate near the Si surface than if $V_{GB} = 0V$. The effect of attracting additional majority carriers to the semiconductor surface is called *accumulation*. The conductivity of the region near the Si surface is increased by the presence of the extra holes.

Note that in the energy-band representation, extra holes at one location of a semiconductor (e.g., in this case, at the Si surface) implies that $E_F$ must be closer to $E_V$ than in a region containing fewer holes (e.g., the region deeper below the surface [bulk region]). However, since the *Fermi level* in the semiconductor must remain flat, the energy bands in the semiconductor ($E_C$, $E_V$, and $E_i$) near the surface must bend upward to reflect the presence of the extra holes at that location compared to the *bulk* (Fig. 3-4c1)

The applied gate bias also causes the Fermi levels in the gate and semiconductor regions to be separated by an amount equal to $qV_{GB}$, or

$$E_F(\text{gate}) - E_F(\text{semiconductor}) = -qV_{GB} \qquad (3 - 2)$$

Although the capacitance of the MOS-C varies with applied dc voltage under some bias conditions, in the accumulation mode it does not. That is, in this mode the capacitance per unit area remains constant as $V_{GB}$ is changed, and is given by $C_{ox} = \kappa_{ox}\varepsilon_o/t_{ox}$, where $\kappa_{ox}$ and $t_{ox}$ are the dielectric constant and thickness of the oxide, and $\varepsilon_o$ is the permittivity of free space.

We now introduce the *charge-distribution versus distance* diagram as an additional visualization tool. This allows us to depict the approximate charge distribution inside the MOS structure. For the case of accumulation, applying a negative bias causes more electrons to move onto the gate. Holes are attracted toward the silicon surface in response. Thus, the charge inside the device as a function of position can be approximated as shown in Fig. 3-4c2. Note that a squared-off (or block) representation of the charge is used in this simple plot. Such block approximations are only intended to be a qualitative representation of the actual charge distribution, which, in general, is not distributed so simply. When interpreting the magnitude and spatial extent of the charge using such simplified diagrams this fact should be kept in mind.

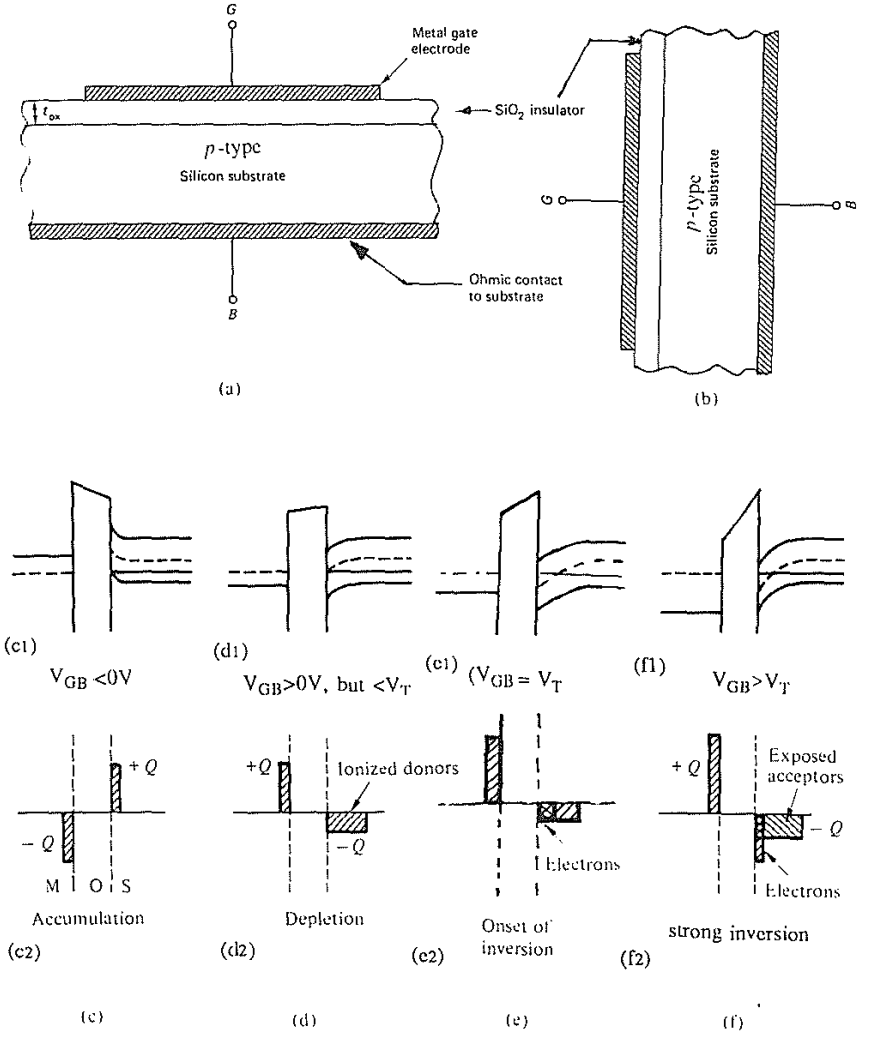


**Fig. 3-4** (a) Cross-section of a MOS-C with $p$-substrate; (b) Cross-section of the same MOS-C, but rotated 90°; (c1) and (c2) Energy band and block charge diagrams when the MOS-C is biased to accumulation ($V_{GB}<0V$); (d1) and (d2) Same diagrams for depletion biasing ($V_{GB}>0V$, but $<V_T$); (e1) and (e2) Same diagrams at onset of inversion ($V_{GB} = V_T$); (f1) and (f2) Same diagrams at strong inversion ($V_{GB}>V_T$).

**3.2.2.2 Depletion.** In the second bias condition (Fig. 3-4d), a *small positive* voltage is applied to the gate of the *p*-type MOS capacitor. This causes holes in the semiconductor to be pushed away from the surface, creating a depletion region of width d, consisting primarily of negatively charged acceptor ions. In the energy-band representation of this phenomenon the bands bend downward near the surface (Fig. 3-4d1). In this mode of operation, known as *depletion,* the MOS capacitor exhibits two capacitances in series - the oxide capacitance per unit area $C_{ox}$ and the depletion capacitance per unit area $C_d = \kappa_{Si}\varepsilon_o/d$. While $C_{ox}$ is constant, $C_d$ is not. That is, $C_d$ decreases as $V_{GB}$ is made larger (more positive). The approximate charge distribution for this bias condition is shown in Fig. 3-4d2.

**3.2.2.3 Inversion.** If the positive voltage applied to the gate is increased, the bands are bent further downward, eventually causing $E_F$ to cross over $E_i$ and to be closer to $E_c$ than to $E_v$ at the surface. At this point the semiconductor surface is *inverted* (i.e., it has been changed from *p*-type to *n*-type) because there are now more electrons than holes at the surface.*

Another way to view this situation is to remember that the kinetic energy of an electron is zero when it occupies an energy state at the conduction band edge (corresponding to an energy $E_c$). Thus, under depletion or inversion biasing electrons near the Si surface having zero kinetic energy occupy energy states of lower *total* energy than electrons deeper in the Si having zero kinetic energy. Hence, when a positive bias is applied to the gate, electrons are more likely to fill such states near the surface. Consequently, electrons will be found at higher concentrations closer to the surface when $V_{GB}>0V$.

**3.2.2.4 Strong Inversion.** If $V_{GB}$ is made even more positive, the bands will continue to bend further downward, until $E_i$ at the surface is eventually below $E_F$ by an energy equal to $|E_F - E_i|$. At this point the electron density per unit volume at the surface $n_{surf}$ (located in a thin layer known as the *inversion layer*) is equal to the hole density in the bulk. This is known as the point of *onset of strong inversion*, and in this condition

$$E_i(\text{bulk}) - E_i(\text{surface}) = 2[E_i(\text{bulk}) - E_F] \qquad (3-3)$$

Solving this equation for $E_i$(surface), and using the result in Eq. 3-1a, the concentration of electrons at the Si surface at the onset of strong inversion, $n_{surf}$(inv) is

$$n_{surf}(\text{inv}) = n_i \exp[E_F - E_i(\text{surface})]/kT = n_i \exp[E_i(\text{bulk}) - E_F]/kT = p_{obulk} \approx N_A \qquad (3-4)$$

Figure 3-4e1 is the energy-band diagram depicting the condition of onset of strong

* The surface is actually inverted as soon as $E_F$ crosses over $E_i$. However, the density of electrons at the surface remains small until $E_F$ is considerably greater than $E_i$. The mode of operation when the electron density is smaller than the hole density in the substrate bulk is referred to as *weak inversion.* Weak inversion is important in submicron MOSFET behavior and will be discussed in detail in section 4.7.

inversion. In this diagram the width of the depletion region is denoted by $d_{max}$. The block charge diagram at the onset of strong inversion is shown in Fig. 3-4e2. Note that the voltage applied between the gate and substrate at the onset of strong inversion is known as the threshold voltage, $V_T$.

For further increases in positive bias, the electron concentration in the inversion layer at the surface exceeds the bulk equilibrium hole concentration, $p_o = N_A$. This is referred to as *strong inversion.* The energy-band and block-charge diagrams depicting the strong inversion condition are shown in Figs. 3-4f1 and 3-4f2, respectively.

In general, the charges on the gate $Q_G$ of a MOS-C must be balanced by the charges in the semiconductor $Q_C$

$$Q_G\ (C/cm^2) = -Q_C\ (C/cm^2) \qquad (3 - 5)$$

In strong inversion, the charge per unit area $Q_C$ in a *p*-type semiconductor is the sum of the electrons in the inversion layer ($Q_I$) and the negative charges in the depletion region ($Q_{Bmax}$). Thus, in strong inversion

$$Q_G = -Q_C = -(Q_I + Q_{Bmax}) \qquad (3 - 6)$$

where $Q_{Bmax} = -qN_A d_{max}$. (Note that Q's in this chapter are expressed in units of charge/unit area - specifically, $C/cm^2$.) The total capacitance per unit area at strong inversion is the oxide capacitance $C_{ox}$ in series with the depletion capacitance at the maximum depletion width in equilibrium $C_{dmax} = \kappa_{si}\varepsilon_o/d_{max}$. While the above discussion applies to a MOS-C with a *p*-type semiconductor, similar results can be obtained for an *n*-type semiconductor, with the polarity of the voltages and charges being reversed. A typical value of $Q_I$ in a MOS-C or MOSFET in strong inversion is on the order of $10^{12}$ $cm^{-2}$.

**3.2.2.5 Microscopic Perspective of the Mobile Charge Behavior in a MOS-C.** It is also useful to consider from a (qualitative) microscopic perspective the phenomena involving charge carriers near the silicon surface of the MOS-C under conditions of depletion and inversion biasing. That is, when the MOS-C is thus biased, a potential difference between the surface and the bulk exists, giving rise to a potential energy barrier (PEB) with respect to the majority carriers. The majority carriers (holes in our example) are thereby repelled from the surface, and minority carriers (i.e., electrons in this example) are attracted toward it. In either inversion or depletion a region largely devoid of carriers is established (depletion region), and in this region thermal generation of carriers continuously produces holes and electrons in an attempt to re-establish the mobile charge concentration values present in the charge-neutral regions at equilibrium. The holes so produced, however, are continuously repelled from the surface, while the generated electrons are likewise drifted toward the surface.

In a state of thermal equilibrium, some holes in the bulk nevertheless still possess sufficient energy to overcome the PEB at the surface, and they are able to penetrate the depletion region so that recombination with the electrons attracted to the surface can occur. At thermal equilibrium, the rate of such recombination at the surface exactly equals the rate of electron generation in the depletion region, and the electron and hole

concentrations are thus maintained at a fixed, specific value, dependent on the temperature, doping concentration, and gate bias.

If the gate bias is instantaneously changed from one fixed value to another, the carrier concentrations must also change to reflect this new bias value. However, since an increase in the electron concentration relies essentially on their generation in the depletion region by thermal processes, some time must elapse before the new equilibrium electron concentration can be established. In fact, the response of a silicon MOS-C due to instantaneous changes in $V_{GB}$ is relatively slow because thermal generation and recombination processes in the silicon substrate occur at low rates at room temperature. The situation that exists in a MOSFET, as we will describe in chap. 4, is quite different. That is, the presence of diffused regions of doping type opposite that of the substrate (i.e., the source/drain regions) permit electrons (under favorable bias conditions) to be injected into (or removed from) this surface region much more rapidly than if only thermal processes are responsible for contributing carriers (see section 4.2).

## 3.3 QUANTITATIVE DESCRIPTION OF MOS-C BEHAVIOR

We now consider the behavior of the ideal MOS-C from a quantitative perspective. Specifically, we seek to obtain mathematical relationships that permit us to calculate the following parameters in terms of the applied dc gate bias $V_{GB}$, the device structure parameters (i.e., $t_{ox}$ and the doping concentration in the silicon), and the material parameters (i.e., $\varepsilon_{si}$ and $\varepsilon_{ox}$):

1. The electrostatic potential as a function of position $\varphi(x)$;
2. The surface potential, $\varphi_{surf}$, which is the potential at $x = 0$, or $\varphi(0)$
3. The electric field as a function of position $\mathcal{E}(x)$;
4. The mobile charge concentrations $n(x)$ and $p(x)$ in the silicon;
5. The bulk charge per unit area $Q_B$ in the silicon;
6. The inversion layer charge per unit area $Q_I$

Later, we will treat the nonideal MOS-C in which we will also include the effects due to the properties of the gate material and the charges in the oxide and at the $Si\text{-}SiO_2$ interface. We will also describe how to calculate the threshold voltage of MOS structures.

Three quantitative models of MOS-C behavior will be developed, differing in their complexity, accuracy, and generality. The simplest MOS-C model, based on the *depletion approximation* will be derived first. It is also the least general and least accurate of the three models, and provides accurate values of the mobile charge concentrations in the silicon only beyond strong inversion. Nevertheless, this model offers easy-to-interpret analytical expressions of MOS-C behavior, and is the model developed in most basic device physics texts. It is also the basis of the simpler long-channel MOSFET models described in chap. 4.

The second MOS-C model we derive is the most general and accurate model (in that it is valid for the accumulation, depletion, and inversion regimes of MOS-C operation), but it provides these benefits only at the expense of much greater mathematical complexity. That is, the second model does not provide analytical expressions for the quantities listed above, but requires numerical analysis for specific values to be obtained. Despite its mathematical complexity, this model is presented for several important reasons:

1. The MOS-C parameters listed above when calculated using this model are so accurate compared to experimental measurements that the model represents a benchmark to which the results of the other models can be compared to establish their accuracy.

2. It is the basis for the most general long-channel MOSFET model we present in chap. 4 (i.e., the Pao-Sah model).

3. It illustrates the principle that numerical analysis must be relied upon to obtain the most accurate quantitative representations even for the cases of the MOS-C and the long-channel MOSFET.

4. It implies that numerical analysis must certainly be employed to obtain accurate predictions of submicron MOSFET behavior.

However, the complexity of this model is such that it is not feasible to use it for constructing models of MOSFET circuit behavior, nor does it provide analytical expressions for the MOS-C quantities listed above. Thus, quantitative insights about MOS-C behavior are difficult to extract from this model, making it a poor tool for learning about MOS-C behavior. As a result, the previous simple model and a third model (which we describe last), find much wider use than this one.

The third MOS-C model is intermediate in accuracy, generality, and complexity between the other two models. It is referred to as the *charge sheet model,* and it calculates the characteristics of the MOS-C quite accurately over the entire range of inversion (i.e., from weak to strong inversion). It requires more computational effort than the simple model, but far less than the general model. Unlike the general model it provides analytical expressions for the mobile charge density which also extend beyond the operating regimes treated by the simple model. These expressions provide quantitative insight about the behavior of device operating regions that become more important in short-channel MOSFETs.

Note that we will designate the externally applied (i.e., terminal) voltages with the symbol V (e.g., $V_{GB}$), while the voltage drops internal to the MOS structure will be expressed with the symbol $\varphi$ (e.g., the voltage drop across the oxide $\varphi_{ox}$ and the voltage drop across the semiconductor from the Si surface to the bulk, $\varphi_{surf}$). Note, however, that both the external and internal voltage drops have units of volts.

### 3.3.1 The Electrostatic Potential in MOS Structures

Before setting out to derive the expressions listed above, let us make some introductory remarks about the *electrostatic potential* $\varphi$. First, we note that since the bias voltages applied to MOS devices are expressed in units of volts, it would be preferable if the quantitative MOS-C relationships we seek were also expressed in the same units (rather than in terms of units of energy, which would result if we used the energy-band representation of MOS behavior). In addition, one of the five classical semiconductor device equations is the Poisson equation, and its solution yields the electrostatic potential in the device. Hence, two of the relationships we obtain when solving the 1-D Poisson equation in the semiconductor region of a MOS-C involve the electrostatic potential, i.e.,

**a.** The relationship between $V_{GB}$ and the *surface electrostatic potential* $\varphi_{surf}$ (henceforth referred to as the *surface potential*), and;

**b.** An expression for the electrostatic potential versus position $\varphi(x)$ [which uses $\varphi_{surf}$ obtained from **a** as one of the boundary values for calculating this function].

It turns out that the electrostatic potential at any location in a MOS device is related to the potential energy an electron possesses at that location. That is, the electrostatic potential-difference $\Delta\varphi$ observed in moving from one position to another in the semiconductor (assuming the kinetic energy of the electron is the same at both positions) can be computed (in terms of an electron) from

$$\Delta\varphi = \Delta E/(-q) \qquad (3 - 7)$$

where $q$ is the magnitude of the electron's charge. It is evident from Eq. 3-7 that if an electron undergoes a *potential energy* decrease, it means that a *potential* increase exists between two locations, because of the algebraic sign of the electron charge. Thus, for the case of an electron, an energy-band diagram can be converted to a potential diagram by merely inverting one of the bands $E_c$, $E_i$, or $E_v$ (as shown in Fig. 3-7, which depicts both representations).* Note that *downward* band bending while going, for example, from the bulk to the surface in a MOS structure, implies an *increase* in the electrostatic potential when moving between those same locations.

Since the potential is a relative quantity, the zero value of $\varphi$ can be arbitrarily chosen. In our discussion we select the zero value as the electrostatic potential in the bulk (i.e., at $x = \infty$). We also choose the energy level of the intrinsic Fermi level $E_i$ in the bulk [$E_i$(bulk)] to designate this level of zero on an energy-band diagram. Thus, elsewhere, the value of $\varphi(x)$ is measured with respect to $E_i$(bulk) according to

$$\varphi(x) = [E_i(\text{bulk}) - E_i(x)]/q \qquad (3 - 8)$$

* Note that since an electron at $E_c$ will have the same kinetic energy (zero) at any location, the bending of the $E_c$ band directly indicates the change in potential energy versus location.

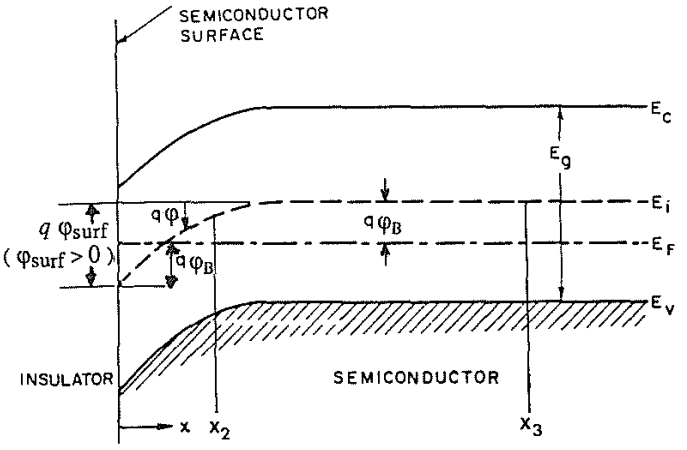


**Fig. 3-5** The energy-band and potential diagram representations of the MOS-C (in this figure a MOS-C with a *p*-type substrate and biased to inversion is depicted).

as depicted in the figure. For example, in the bulk of the semiconductor (position $x_3$ in Fig. 3-5), $E_i(x_3) = E_i(\text{bulk})$. Hence, from Eq. 3-8 the potential at $x_3$ is 0. At $x_2$, however, $\varphi(x_2) \neq 0$, but instead is $\varphi(x_2) = [E_i(\text{bulk}) - E_i(x_2)]/q$.

Another consequence of choosing $\varphi\ (x = \infty) = 0$ is this: If we apply a bias to the gate of a MOS-C, part of the voltage will be dropped across the oxide $\varphi_{ox}$ and part across the silicon $\varphi_{si}$ , or,

$$V_{GB} = \varphi_{ox} + \varphi_{si} \tag{3-9}$$

If $\varphi(x = \infty) = 0$, then the potential at the surface of the silicon ($\varphi_{surf}$) represents the voltage drop from the bulk ($x = \infty$) to the silicon surface ($x = 0$) in a MOS structure. In that case we can write Eq. 3-9 as

$$V_{GB} = \varphi_{ox} + \varphi_{surf} \tag{3-10}$$

Now we see that if we can derive an expression for $\varphi_{ox}$ in terms of $\varphi_{surf}$, an equation relating $V_{GB}$ and $\varphi_{surf}$ results. We show how this is done in the next section.

Let us also introduce another dimensionless parameter called the *doping parameter* $\varphi_B$ which relates the potential of an electron at the Fermi level (in the bulk of the silicon in a MOS structure) to the doping concentration. The doping parameter is defined as

$$\varphi_B = [E_i(\text{bulk}) - E_F]/q \approx (kT/q)\ln(N_A/n_i)_{p\text{-type Si}} \approx (kT/q)\ln(n_i/N_D)_{n\text{-type Si}} \tag{3-11}$$

in the bulk region of the Si in the MOS capacitor, see Fig. 3-5). Note that $\varphi_B>0$ for a *p*-type semiconductor and $\varphi_B<0$ for an *n*-type semiconductor. For substrate doping concentrations usually encountered in MOSFETs ($10^{14}$-$10^{17}$ cm$^{-3}$), the magnitude of $\varphi_B$ is between $9kT/q$ and $16kT/q$ (where $kT/q$ at 300K is ~0.025 V); that is, the magnitude of $\varphi_B$ is between 225 and 400 mV at 300K for this range of doping concentrations.

Also, the value of the surface potential at the onset of weak and strong inversion can be expressed in terms of $\varphi_B$. That is, in section 3.2 we defined the onset of *weak inversion* as the condition when the electron concentration at the surface of *p*-type Si equals $n_i$. At that point, $\varphi_{surf} = \varphi_B$. Since the onset of *strong inversion* is the condition when the surface electron concentration equals $N_A$, at that point $E_i$ (surf) - $E_i$ (bulk) = 2 [$E_F$ - $E_i$ (bulk)]. By combining this fact with Eqs. 3-4 and 3-11, we see that the surface potential at the onset of strong inversion $\varphi_{surf}(inv) = 2\varphi_B$.

Note that it is also possible to express the equilibrium concentrations of electrons $n_p$ (x) and $p_p$ (x) in terms of $\varphi(x)$. That is, when the zero value of $\varphi$ is defined as above

$$n_p(x) = n_{po} \exp[q\varphi(x)/kT] \quad (3 - 12a)$$

$$p_p(x) = p_{po} \exp[-q\varphi(x)/kT] \quad (3 - 12b)$$

where $n_{po}$ and $p_{po}$ are the equilibrium concentrations of electrons and holes in the bulk of the silicon (in this case in *p*-type Si). At the surface of the silicon, the concentrations $n_{surf}$ and $p_{surf}$ are given by

$$n_{surf} = n_{po} \exp(q\varphi_{surf}/kT) \quad (3 - 13a)$$

$$p_{surf} = p_{po} \exp(-q\varphi_{surf}/kT) \quad (3 - 13b)$$

Using Eq. 3-11 in Eq. 3-13a, we can express the electron concentration at the surface in terms of $N_A$ and $\varphi_B$ as:

$$n_{surf} = N_A \exp[q(\varphi_{surf} - 2\varphi_B)/kT] \quad (3 - 13c)$$

This expression is plotted versus $\varphi_{surf}$ in Fig. 3-6. This figure reiterates several aspects of MOS behavior established with the energy-band representation of MOS characteristics. First, using Eq. 3-11 we see that when $\varphi_{surf} = \varphi_B$, $n_{surf}$ becomes equal to the intrinsic concentration, $n_i$. Thus, $\varphi_{surf} = \varphi_B$ is defined as the limit point between the regions of depletion and weak inversion. Second, as $\varphi_{surf}$ increases above $\varphi_B$, $n_{surf}$ grows very rapidly. Eventually, when $\varphi_{surf} = 2\varphi_B$, $n_{surf} = N_A$. This is commonly defined as the demarcation point between weak and strong inversion. Finally, beyond this point (i.e., $\varphi_{surf}>2\varphi_B$), $n_{surf}$ continues to increase rapidly, becoming much greater than $N_A$ for small increases of $\varphi_{surf}$ beyond $2\varphi_B$. This implies that in strong inversion the inversion layer charge density $Q_I$ is generally much larger than the ionic charge density in the depletion region $Q_B$. An additional important point can also be inferred from this figure. That is, if the potential as a function of x is known we can calculate $n_p(x)$ from Eq. 3-12a.

## 3.3.2 General Approach to Deriving MOS-C Characteristics

Now we can set out to derive the expressions listed at the beginning of section 3.3. This can be done in four stages, assuming we are given $V_{GB}$, the oxide thickness $t_{ox}$, and the doping concentration $N_A$.

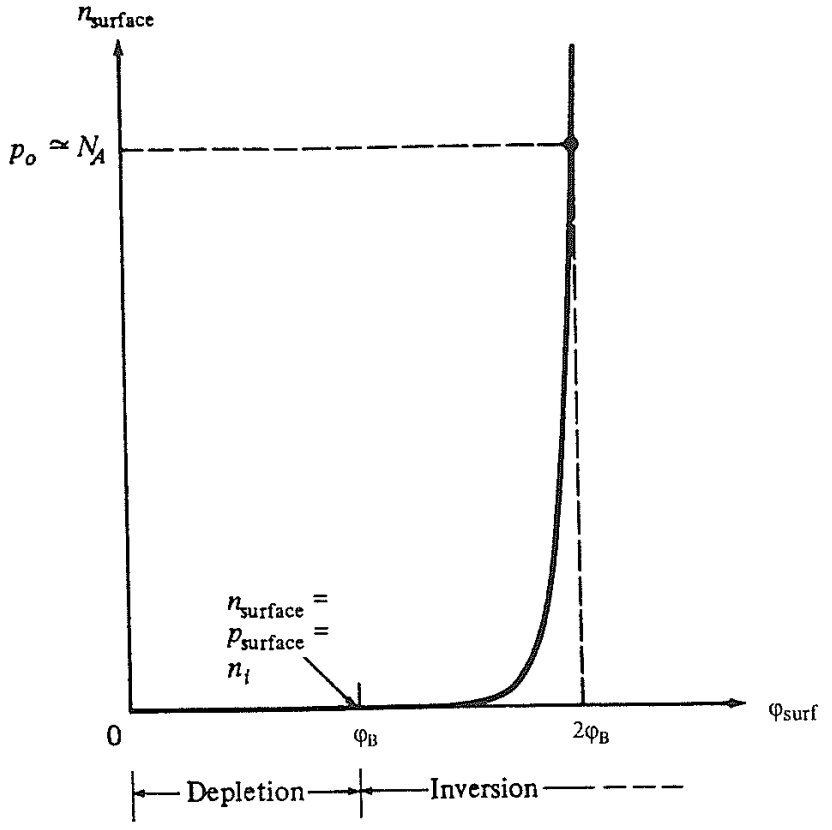


**Fig. 3-6** Electron concentration at the surface of a MOS-C (with a *p*-type substrate) as a function of $\varphi_{surf}$.[6] Linear axes are used. Reprinted with permission of McGraw-Hill Book Co.

**1.** We first find a relationship between $V_{GB}$ and $\varphi_{surf}$ in the MOS structure. This is done by recalling that if we have an expression for $\varphi_{ox}$ in terms of $\varphi_{surf}$, it can be substituted in Eq. 3-10 to yield an equation for $\varphi_{surf}$ in terms of $V_{GB}$.

We begin the derivation of such an expression by noting that the oxide is considered to be an ideal insulator, with no mobile carriers or charge centers. Hence, the electric field in the oxide must be constant, or $\mathcal{E}_{ox} = - d\varphi_{ox}/dx =$ constant. Thus, the voltage across the oxide $\varphi_{ox}$ is found from:

$$\varphi_{ox} = -\int_{-t_{ox}}^{0} \mathcal{E}_{ox}\, dx = t_{ox}\mathcal{E}_{ox} \qquad (3 - 14)$$

The next step is to relate $\mathcal{E}_{ox}$ to the electric field in the semiconductor. Since the charge per unit area located at the Si-$SiO_2$ interface of an ideal MOS-C is assumed to be zero, the electric displacement, $D = \varepsilon\mathcal{E}$ perpendicular to the interface, is continuous [i.e., $D_{ox} = D_{si}(x = 0)$]. The field in the oxide is therefore related to the field at the surface of the silicon $\mathcal{E}_{si}$ (x = 0) by the equation

$$\mathcal{E}_{ox} = (\kappa_{si}/\kappa_{ox})\, \mathcal{E}_{si}\ (x = 0) \qquad (3 - 15)$$

Now, using Eq. 3-15 in Eq. 3-14 we can write $\varphi_{ox}$ as

$$\varphi_{ox} = t_{ox}\, (\kappa_{si}/\kappa_{ox})\, \mathcal{E}_{si}\ (x = 0) \qquad (3 - 16)$$

and this result can be substituted for $\varphi_{ox}$ in Eq. 3-10. In order to complete our goal of finding an expression for $\varphi_{surf}$ in terms of $V_{GB}$ we see that an expression for $\mathcal{E}_{si}$ (x = 0) in terms of $\varphi_{surf}$ is needed. Since $\mathcal{E}(x) = -\, d\varphi/dx$, such expression can be obtained by integrating the one-dimensional form of the Poisson equation once, using the appropriate total charge density $\rho(x)$, and the boundary conditions $\mathcal{E}\ (x = \infty) = 0$, and $\varphi\ (x = 0) = \varphi_{surf}$. We will carry out this integration for three cases in the upcoming sections.

**2.** We next solve the Poisson equation to find $\varphi(x)$. Since we have noted that the electric field is normal to the oxide surface in a MOS-C (neglecting fringing fields at the edges of the capacitor), we can consider the variation in electrostatic potential $\varphi$ in a MOS-C to be one-dimensional (i.e., we assume $\partial\varphi/\partial y$ and $\partial\varphi/\partial z = 0$). Thus, it is only necessary to solve the Poisson equation in its one-dimensional form. We use the value of $\varphi_{surf}$ from step **1** as one boundary condition [$\varphi\ (x = 0) = \varphi_{surf}$], and [$\varphi\ (x = \infty) = 0$] as the other, when we solve the Poisson equation to find $\varphi\ (x)$.

**3.** To calculate the mobile charge concentrations $n_p(x)$ and $p_p(x)$, we can use the values of $\varphi\ (x)$ found from step (2) in Eqs. 3-12.

**4.** To find expressions for $Q_B$ and $Q_I$ as a function of gate bias we proceed as follows:

**a.** First, we recall Gauss' law, which states that the charge contained in a volume equals the permittivity times the electric field emanating from the volume. Applying Gauss' law to a volume extending from the silicon surface to the field-free bulk region, which contains a total charge per unit area $Q_C$, we can write*

$$Q_C = -\, \kappa_{si}\varepsilon_o\, \mathcal{E}_{si}\ (x = 0) \qquad (3 - 17)$$

* Note that only the $\mathcal{E}$-field at the Si-$SiO_2$ interface (which represents the top surface of the volume in which the charge in the semiconductor exists) must be included in Eq. 3-17 because the $\mathcal{E}$-field does not emanate from any other surfaces of the volume. This is because: (1) the $\mathcal{E}$–field emanating from the bottom of the volume under consideration (i.e., at x = d) is assumed to be zero, and; (2) since the $\mathcal{E}$-field in the MOS-C is assumed to be unidirectional, $\mathcal{E}_y = \mathcal{E}_z = 0$. Thus, the $\mathcal{E}$-field emanating from the sides of the volume is also zero.

We also note from Eq. 3-16 and from the fact that $C_{ox} = \kappa_{ox}\varepsilon_o/t_{ox}$ that

$$\varphi_{ox} = t_{ox}\,(\kappa_{si}/\kappa_{ox})\,\mathcal{E}_{si}\,(x = 0) = \{\kappa_{si}\varepsilon_o\,\mathcal{E}_{si}\,(x = 0)\}/C_{ox} \quad (3 - 18)$$

Thus, we can also write

$$Q_C = -\varphi_{ox}\,C_{ox} \quad (3 - 19)$$

**b.** Next, we note that the charge per unit area in the semiconductor $Q_C$ is the sum of the inversion layer charge per unit area $Q_I$ and the ionic charge per unit area $Q_B$. So we can write

$$Q_C = Q_I + Q_B \quad (3 - 20)$$

In general, $Q_I$ can be found by calculating the total mobile charge in the inversion layer (in our example, the electrons). In other words, to get $Q_I$, we could integrate Eq. 3-12a from $x = 0$ to the depth $x_c$ at which the electron concentration becomes negligible, or

$$Q_I(x) = -q\int_0^{x_c} n(x)\,dx \quad (3 - 21)$$

Then, $Q_B$ could be found by subtracting $Q_I$ from $Q_C$.

However, this approach to calculating $Q_I$ and $Q_B$ is quite complex, in fact, it requires that $\varphi(x)$ be computed first, and then this result be used to integrate $n(\varphi)$. Both of these calculations, in general, require numerical integration. Although we shall outline this approach in more detail, we will also illustrate simpler methods for calculating $Q_I$ and $Q_B$ which still provide values accurate enough for many applications.

### 3.3.3 Finding the Quantitative Characteristics of a MOS-C when the Depletion Approximation is Invoked

Let us derive the quantitative characteristics of the ideal MOS-C under some assumptions that simplify the mathematical treatment outlined above, but still provide expressions that are accurate enough for many applications. The simplest of such quantitative analyses assumes that we deal with the ideal uniformly doped MOS-C, and this analysis is also the one carried out in most basic device textbooks. Here we invoke the following approximations: (1) the *depletion approximation* is assumed to be valid; (2) the *one-sided abrupt junction approximation* is assumed; and (3) other simplifying approximations are assumed which allow the depletion region width d, the surface potential $\varphi_{surf}$, and the inversion layer charge $Q_I$ to be simply computed beyond the point of strong inversion.

The *depletion approximation* invoked in this case is based on the following simplifying assumptions:

1. The mobile charges in the depletion region are totally absent in the depletion region for values of $V_{GB}$ smaller than those needed to cause inversion (i.e., $n = p = 0$ in the depletion region over this range of gate-bias values).

2. For values of gate-bias voltages beyond inversion, the depletion region is still totally devoid of mobile carriers, except in the inversion layer, which is assumed to be a very thin layer near the silicon surface.

The *one-sided abrupt-junction approximation* assumes that the depletion region extends to a depth d, beyond which the silicon returns abruptly to a condition in which the mobile carrier densities are again equal to their equilibrium values [i.e., at $x = d$, $p = N_A = p_{po}$, and $n = n_{po}$].

The simplifying assumptions dealing with the d (depletion region width), $\varphi_{surf}$ (surface potential), and $Q_I$ (mobile charges in the inversion layer) are the following:

1. Beyond strong inversion, additional positive bias on the gate simply draws more electrons into the inversion layer. This negative electron charge balances the additional positive gate charge, and the depletion-region width d no longer increases. That is, d remains fixed at the value attained at the onset of strong inversion, and this value is denoted as $d_{max}$.

2. Since the depletion region no longer increases once the inversion layer is formed, the bands of the energy band diagram are not bent any further with increasing positive bias. Hence, $\varphi_{surf}$ also remains fixed (or is *clamped*) at the value it has at the onset of inversion, namely at $\varphi_{surf}$ (inv) = $2\varphi_B$.

3. Beyond strong inversion, the ionic charge per unit area $Q_B$ contained in the depletion region remains unchanged, since $d = d_{max}$. Hence, we can compute $Q_B$ beyond inversion simply from a knowledge of $N_A$ and $d_{max}$. Also if $V_{GB}$ is given, and we know $\varphi_{surf}$ beyond strong inversion, we can compute $\varphi_{ox}$ from Eq. 3-10, and from this we can obtain $Q_C$. Then, $Q_I$ can be found by subtracting $Q_B$ from $Q_C$.

Using these assumptions, we set out to find the desired expressions. We initially solve the Poisson equation in the semiconductor region for $\varphi(x)$. That is, under depletion biasing conditions we have assumed $n = p = 0$, and so the charge density $\rho(x)$ is merely a constant term ($q\, N_A/\kappa_{si}\varepsilon_o$). In this case, the Poisson equation has the form:

$$\begin{aligned} d^2\varphi/dx^2 &= q\, N_A/\kappa_{si}\varepsilon_o \qquad & 0 < x < d \\ &= 0 & x > d \end{aligned} \qquad (3\text{-}22)$$

This is an ordinary, linear differential equation that can easily be integrated twice to yield a closed-form solution of $\varphi(x)$ in the semiconductor. That is, assuming the boundary conditions $\varphi(x = d) = 0$, and $\varphi(x = 0) = \varphi_{surf}$ we get,

$$\varphi(x) = \varphi_{surf}(1 - x/d)^2 \qquad (3\text{-}23)$$

where d is the depletion-region depth. The electric field $\mathcal{E}$ (x) is given by $-d\varphi/dx$ or

$$\mathcal{E}(x) = -d\varphi/dx = 2\varphi_{surf}(1 - x/d)(-1/d) \qquad (3-24)$$

and

$$d^2\varphi/dx^2 = 2\varphi_{surf}/d^2 \qquad \text{[from (3 - 23)]} \qquad (3-25)$$

$$= q N_A/\kappa_{si}\varepsilon_o \qquad \text{[from (3 - 22)]} \qquad (3-26)$$

Then from (3 - 25) and (3 - 26) we can find d in terms of $\varphi_{surf}$ and $N_A$

$$d = [\kappa_{si}\varepsilon_o(2\varphi_{surf})/qN_A]^{1/2}. \qquad (3-27)$$

Beyond the point of strong inversion $\varphi_{surf}(inv) = 2\varphi_B$, and so $d_{max}$ is then

$$d_{max} = (4\kappa_{si}\varepsilon_o\varphi_B/qN_A)^{1/2} \qquad (3-28)$$

Next, we solve Eq. 3-10 for $\varphi_{surf}$. In this case, let us initially assume that the MOS-C is biased into depletion, but below inversion. In that case, no inversion layer exists ($Q_I = 0$), thus, $Q_C = Q_B$ and $Q_B$ is given by

$$Q_B = q N_A d \qquad (3-29)$$

Since $\varphi_{ox} = -Q_C/C_{ox} = -Q_B/C_{ox}$, by using Eq. 3-29 in this result, we get

$$\varphi_{ox} = -q N_A d/C_{ox} = \{[\kappa_{si}\varepsilon_o(2\varphi_{surf})qN_A]^{1/2}\}/C_{ox} \qquad (3-30)$$

Now if we let $\eta = \{[2\kappa_{si}\varepsilon_o qN_A]^{1/2}\}/C_{ox}$, we can write $\varphi_{ox} = \eta\sqrt{\varphi_{surf}}$. Substituting this into Eq. 3-10 we get

$$V_{GB} = \varphi_{surf} + \eta\sqrt{\varphi_{surf}} \qquad (3-31)$$

If we let $\alpha = \sqrt{\varphi_{surf}}$, we can write Eq. 3-31 as a quadratic equation

$$0 = \alpha^2 + \eta\alpha - V_{GB} \qquad (3-32)$$

We can now easily solve this for $\alpha$, using the quadratic formula. Once we have $\alpha$ we can find $\varphi_{surf}$, since $\varphi_{surf} = \alpha^2$.

Now that $\varphi_{surf}$ has been obtained, we can find $Q_B$ (from Eq. 3-29) and $\varphi(x)$ (from Eq. 3-23). Below inversion we do not need to find $n$ (x) and $p$ (x), since for this case we have assumed them to be zero for x<d.

Beyond inversion we can calculate $d_{max}$ from Eq. 3-28, and $Q_{Bmax}$ from Eq. 3-29, (using $d = d_{max}$). Then, since $\varphi_{ox} = V_{GB} - 2\varphi_B$, we can find $Q_C$ from

$$Q_C = -(V_{GB} - 2\varphi_B) C_{ox} \qquad (3-33)$$

Now, since $Q_I = Q_C - Q_{Bmax}$

$$Q_I = -[(V_{GB} - 2\varphi_B) C_{ox}] - q N_A d_{max} \qquad (3-34)$$

$$Q_I = -[(V_{GB} - 2\varphi_B)\, C_{ox}] + \sqrt{4\kappa_{si}\varepsilon_o\varphi_B q N_A} \qquad (3-35)$$

The results of this analysis are summarized in Fig. 3-7. Here the energy band diagrams of an ideal MOS capacitor (*p*-type Si substrate) are shown for the case of $V_{GB} = 0V$ (Fig. 3-7a). In Fig. 3-7b the case when sufficient gate voltage is applied to strongly invert the silicon surface is shown. Also depicted in these figures are the charge (Fig. 3-7c), $\mathcal{E}$-field (Fig. 3-7d) and electrostatic potential versus distance diagrams (Fig. 3-7e) for these two conditions. We note that since there are no charges in the oxide, the electric field is constant in the oxide, and that the slope of $\varphi$ is thus constant in the oxide. In Fig. 3-7f we show the electrostatic potential versus distance diagram for an ideal MOS-C with an *n*-type substrate biased into strong inversion. It is useful to note that since a positive bias is needed to invert the *p*-type MOS-C, the $\varphi$ versus x diagram curves upward, with the maximum value of $\varphi$ at the surface. However, for the *n*-type MOS-C a negative gate bias is needed. Thus, in such cases the $\varphi$ versus x diagram curves downward, with its minimum at the surface.

Another important point to which we will refer when discussing the so-called *gradual-channel approximation* (GCA) involves the gradient of the vertical electric field in the silicon, i.e., $\partial\mathcal{E}/\partial x$. In strong inversion $\partial\mathcal{E}/\partial x$ in the silicon is greatest in the inversion layer thickness, since $Q_I >> Q_B$ in strong inversion and the inversion layer is quite thin (~30-300Å thick). Hence, $\partial\mathcal{E}/\partial x$ can be estimated by approximating the vertical electric field value to be zero at the bottom edge of the inversion layer thickness $t_{inv}$. Then, $\partial\mathcal{E}/\partial x \sim [\mathcal{E}_{si}(x = 0) - 0]/t_{inv} = \mathcal{E}_{si}(x = 0)/t_{inv}$. We will make use of this result when examining the GCA in chap. 4.

### 3.3.4 More Accurate and General Model for MOS-C Behavior

The assumption that no mobile charges exist in the depletion region of the MOS-C (depletion approximation) does not accurately reflect the actual charge distribution condition in the silicon, especially below inversion. Thus, the expressions for $\varphi(x)$, $\varphi_{surf}$, $\mathcal{E}(x)$, and $Q_I$, obtained using this assumption are not accurate. In order to obtain a more accurate quantitative model of the MOS-C, we need to use the Poisson equation in which *p* and *n* have non-zero values. This will allow us to obtain more accurate expressions of the above quantities. As noted in the introduction of this section, this analysis is complicated. The complexity arises in part because it provides a model that is valid in all regimes (accumulation, depletion, and all ranges of inversion). Although the accumulation and depletion regions are not very important regimes of operation in most MOSFET applications, we nevertheless present this complex MOS-C model here for the several reasons listed in the introduction.

In this more accurate and general representation of the MOS-C, we treat the Poisson equation in the following form:

$$\frac{d^2\phi}{dx^2} = -\left(\frac{q}{\kappa_{Si}\varepsilon_o}\right)[-N_A + N_D + p - n] \qquad (3-36)$$

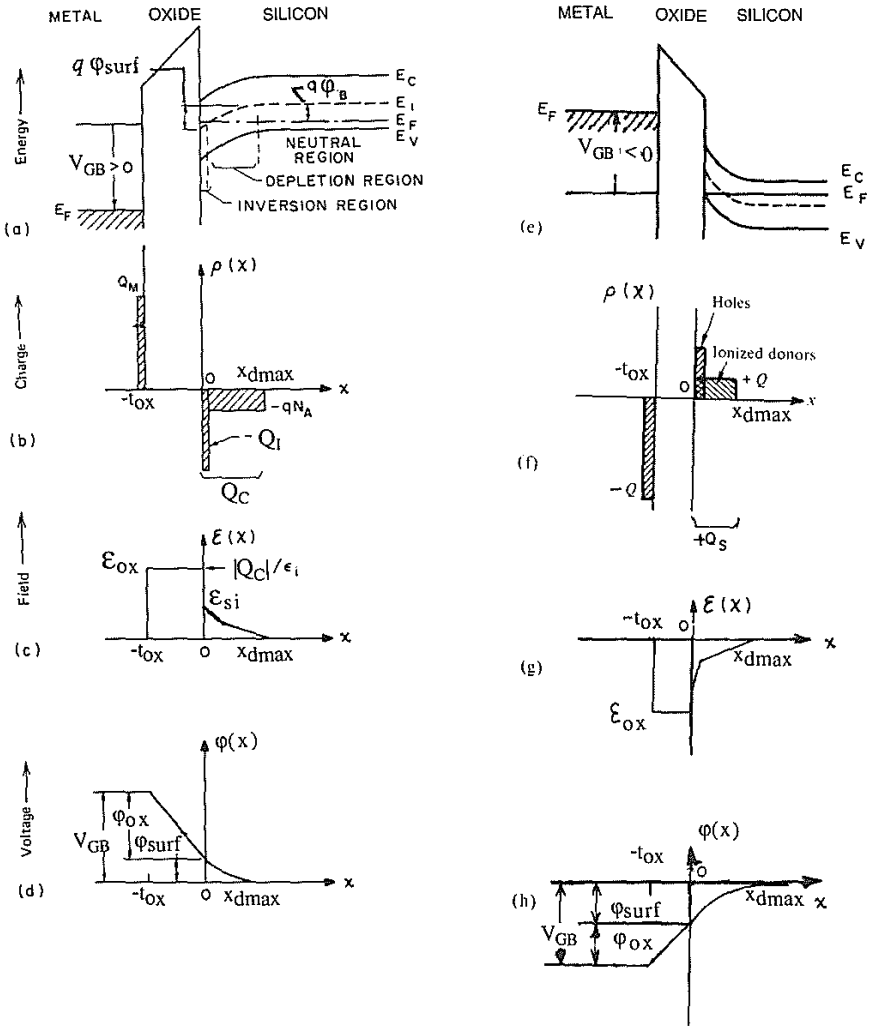


**Fig. 3-7** Ideal *p*-type Si MOS-C when biased into inversion [$V_{GB}>V_T$]: (a) Energy-band diagram; (b) Charge distribution; (c) Electric field; and (d) Potential distribution; (e) - (h) Comparable diagrams for an ideal *n*-type Si MOS-C.

Equations 3-12a and 3-12b for $n(\varphi)$ and $p(\varphi)$ are substituted for $n$ and $p$ to give

$$\frac{d^2\phi}{dx^2} = -\left(\frac{q}{\kappa_{Si}\varepsilon_o}\right)\left[-N_A + p_{po}\, e^{-q\varphi/kT} + N_D - n_{po}\, e^{q\varphi/kT}\right] \qquad (3 - 37)$$

In general, Eq. 3-37 can be integrated once to give an analytic expression for the electric field, $\mathcal{E} = -\, d\varphi/dx$. This is accomplished by first multiplying both sides of Eq. 3-37 by $2(d\varphi/dx)$. The left-hand side is then recognized as $(d/dx)(d\varphi/dx)^2$, and we can write the result as

$$\frac{1}{2}\frac{d}{dx}\left(\frac{d\phi}{dx}\right)^2 = -\left(\frac{q}{\kappa_{Si}\varepsilon_o}\right)\left[-N_A + p_{po}\, e^{-q\varphi/kT} + N_D - n_{po}\, e^{q\varphi/kT}\right]\left(\frac{d\varphi}{dx}\right) \qquad (3 - 38)$$

Integrating this expression from the bulk ($x = \infty$, where $\varphi = 0$) to an arbitrary point x, we get

$$\left(\frac{d\phi}{dx}\right)^2_{\infty} - \left(\frac{d\phi}{dx}\right)^2_{x} = -\left(\frac{2q}{\kappa_{Si}\varepsilon_o}\right)\int_0^{\varphi}\left[-N_A + p_{po}\, e^{-q\varphi/kT} + N_D - n_{po}\, e^{q\varphi/kT}\right]d\varphi \qquad (3 - 39)$$

If we note that $p_{po} \approx N_A$, then $n_{po} = n_i^2/N_A$. In addition, since $\varphi_t = q/kT$, and $\mathcal{E} = -\, d\varphi/dx$, and $\mathcal{E}_{si}(x = \infty) = 0$, the first term on the left hand side of Eq. 3-39 is zero. Thus, after integrating the right-hand side we get

$$-\frac{d\varphi}{dx} = \mathcal{E}_{si}(x) = \sqrt{\frac{2q\,N_A}{\kappa_{Si}\varepsilon_o}}\sqrt{\varphi_t e^{-\varphi/\varphi_t} + \varphi - \varphi_t + e^{-2\varphi_B/\varphi_t}\left(\varphi_t e^{-\varphi/\varphi_t} - \varphi - \varphi_t\right)} \qquad (3 - 40)$$

This result allows us to obtain the electric field at the surface ($x = 0$) if $\varphi_{surf}$ is known

$$\mathcal{E}_{si}(x = 0) = \sqrt{\frac{2q\,N_A}{\kappa_{Si}\varepsilon_o}}\sqrt{\varphi_t e^{-\varphi_{surf}/\varphi_t} + \varphi_{surf} - \varphi_t + e^{-2\varphi_B/\varphi_t}\left(\varphi_t e^{-\varphi_{surf}/\varphi_t} - \varphi_{surf} - \varphi_t\right)} \qquad (3 - 41)$$

In addition, by applying Gauss' law we can use Eq. 3-41 to find $Q_C$ - i.e., from Eq. 3-17 [$Q_C = -\,\kappa_{Si}\varepsilon_o\mathcal{E}_{si}(x = 0)$] we get:

$$Q_C = \sqrt{2q\,N_A\kappa_{Si}\varepsilon_o}\sqrt{\varphi_t e^{-\varphi_{surf}/\varphi_t} + \varphi_{surf} - \varphi_t + e^{-2\varphi_B/\varphi_t}\left(\varphi_t e^{-\varphi_{surf}/\varphi_t} - \varphi_{surf} - \varphi_t\right)} \qquad (3 - 42)$$

This equation is valid for all regimes (accumulation, depletion, and inversion). Figure 3-8 depicts the variation of total charge concentration $Q_C$ with $\varphi_{surf}$ as calculated using Eq. 3-42.[6] It provides a quantitative representation of the total charge dependence on $\varphi_{surf}$ that was qualitatively described in section 3.2.* We see that for negative values of $\varphi_{surf}$, $Q_C$ is positive, corresponding to the accumulation regime. For $\varphi_{surf} = 0$, we

* Note that in section 3.3.1 we also examined the variation of the mobile charge concentration at the silicon surface $n_{surf}$ versus $\varphi_{surf}$ for depletion and inversion ($\varphi_{surf} > 0V$).

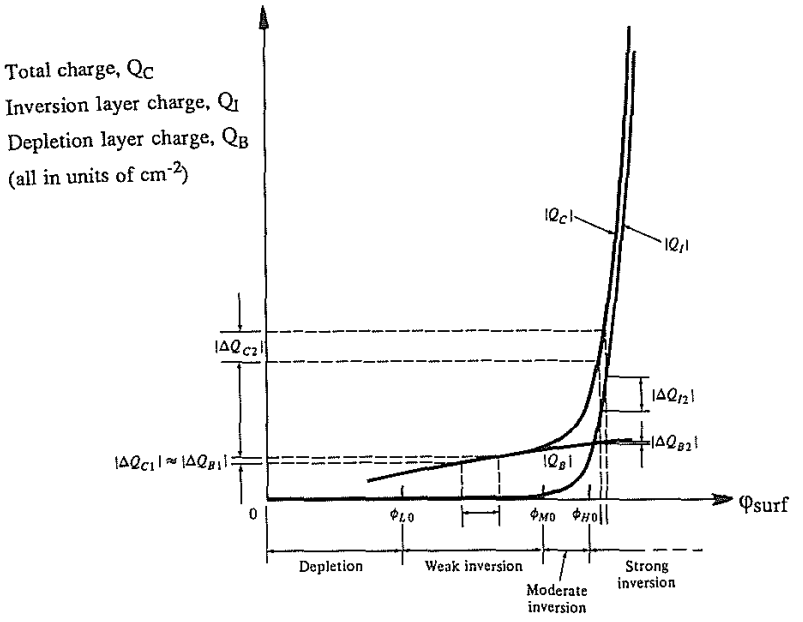


**Fig. 3-8** Magnitude of inversion layer charge, depletion layer charge, and their sum (all per unit area) versus $\varphi_{surf}$. [6] Reprinted with permission of McGraw-Hill Book Company.

have the flat-band condition, in which $Q_C = 0$. When $\varphi_{surf}$ is positive, and its value lies between 0 and $2\varphi_B$, $Q_C$ is negative and is $\sim\sqrt{\varphi_{surf}}$. This means that in depletion and weak inversion the mobile charge density is much smaller than the ionic charge density. For $\varphi_{surf}>2\varphi_B$, strong inversion occurs, and $Q_C \cong -\exp(q\varphi_{surf}/2kT$, indicating that the mobile charge density is now much greater than the ionic charge density.

To calculate $\varphi_{surf}$, assuming we are given $V_{GB}$, $C_{ox}$ and $N_A$, we use

$$V_{GB} = \varphi_{ox} + \varphi_{surf} \tag{3-43}$$

and

$$\varphi_{ox} = \{\kappa_{si}\varepsilon_o\, \mathcal{E}_{si}\,(x = 0)\}/C_{ox} \tag{3-44}$$

$$V_{GB} = \varphi_{surf} + \frac{\sqrt{2q\, N_A \kappa_{si}\varepsilon_o}}{C_{ox}}\sqrt{\varphi_t e^{-\varphi_{surf}/\varphi_t} + \varphi_{surf} - \varphi_t + e^{-2\varphi_B/\varphi_t}\left(\varphi_t e^{-\varphi_{surf}/\varphi_t} - \varphi_{surf} - \varphi_t\right)} \tag{3-45}$$

* (cont.) The conclusions we drew concerning the mobile charge concentration in the silicon in that case for these regions are reiterated here. However, in Fig. 3-8 the contribution of $Q_B$ to the change in $Q_C$ as $\varphi_{surf}$ is varied is also included.

Note that to find $\varphi_{surf}$ from this equation we must perform a numerical iteration.

To calculate $Q_I$ accurately we must follow the procedure outlined in section 3.3.2. That is, we must use Eq. 3-21. Here we also change the variable of integration to $\varphi$

$$Q_I = -q\int_0^{x_c} n(x)\,dx = -q\int_{\varphi_{surf}}^{\varphi_c} \frac{n(\varphi)\,d\varphi}{d\varphi/dx} \qquad (3-46)$$

By using Eqs. 3-12a and 3-40 in Eq. 3-46 (since $\mathcal{E} = -d\varphi/dx$), we get

$$Q_I = q\int_{\varphi_{surf}}^{\varphi_c} \frac{n_{po}\, e^{\varphi/\varphi_t}}{\sqrt{\frac{2q\,N_A}{\kappa_{Si}\varepsilon_o}}\sqrt{\varphi_t e^{-\varphi/\varphi_t} + \varphi - \varphi_t + e^{-2\varphi_B/\varphi_t}\left(\varphi_t e^{-\varphi/\varphi_t} - \varphi - \varphi_t\right)}}\,d\varphi \qquad (3-47)$$

A similar procedure gives $Q_B$ (consisting of ionized acceptor atoms and holes)

$$Q_B = q\,p_{po}\int_{\varphi_{surf}}^{\varphi_c} \frac{e^{-\varphi/\varphi_t} - 1}{\sqrt{\frac{2q\,N_A}{\kappa_{Si}\varepsilon_o}}\sqrt{\varphi_t e^{-\varphi/\varphi_t} + \varphi - \varphi_t + e^{-2\varphi_B/\varphi_t}\left(\varphi_t e^{-\varphi/\varphi_t} - \varphi - \varphi_t\right)}}\,d\varphi \qquad (3-48)$$

To get $\varphi(x)$ we must integrate the Poisson equation a second time. That is, to find $\varphi$ at some point x we start with Eq. 3-40, separate variables and integrate from x to 0 on the right hand side, and from $\varphi$ to $\varphi_{surf}$ on the left:

$$-\int_{\varphi}^{\varphi_{surf}} \frac{d\varphi}{\sqrt{\frac{2q\,N_A}{\kappa_{Si}\varepsilon_o}}\sqrt{\varphi_t e^{-\varphi/\varphi_t} + \varphi - \varphi_t + e^{-2\varphi_B/\varphi_t}\left(\varphi_t e^{-\varphi/\varphi_t} - \varphi - \varphi_t\right)}} = x \qquad (3-49)$$

However, unlike the first integration which yielded the analytical expression for $\mathcal{E}(x)$ given by Eq. 3-40, this second integration cannot be carried out analytically. That is, we must use numerical procedures to calculate $\varphi(x)$ in this case. This was first done by Young in 1961.[2] Numerical integration must also be used to find the electron and hole densities using Eqs. 3-12 a and 3-12b. Sample plots of $[\rho/qN_A]$ versus x and $\varphi(x)$ versus x calculated using such numerical analysis techniques are shown for accumulation (Fig. 3-9a), depletion (Fig. 3-9b), onset of strong inversion, $\varphi_{surf} = 2\varphi_B$ (Fig. 3-9c), and strong inversion, $\varphi_{surf} = 2\varphi_B + 0.15V$ (Fig. 3-9d) for a MOS-C with $\varphi_B = 0.3V$.[3]

We observe from these curves that: (1) the mobile charge in the inversion layer is confined to a very thin layer near the surface; and (2) the depletion-region edge is fairly abrupt, with the charge concentration dropping to negligible values over a distance of ~0.5 $\mu$m. The first observation supports the use of the following two approximations

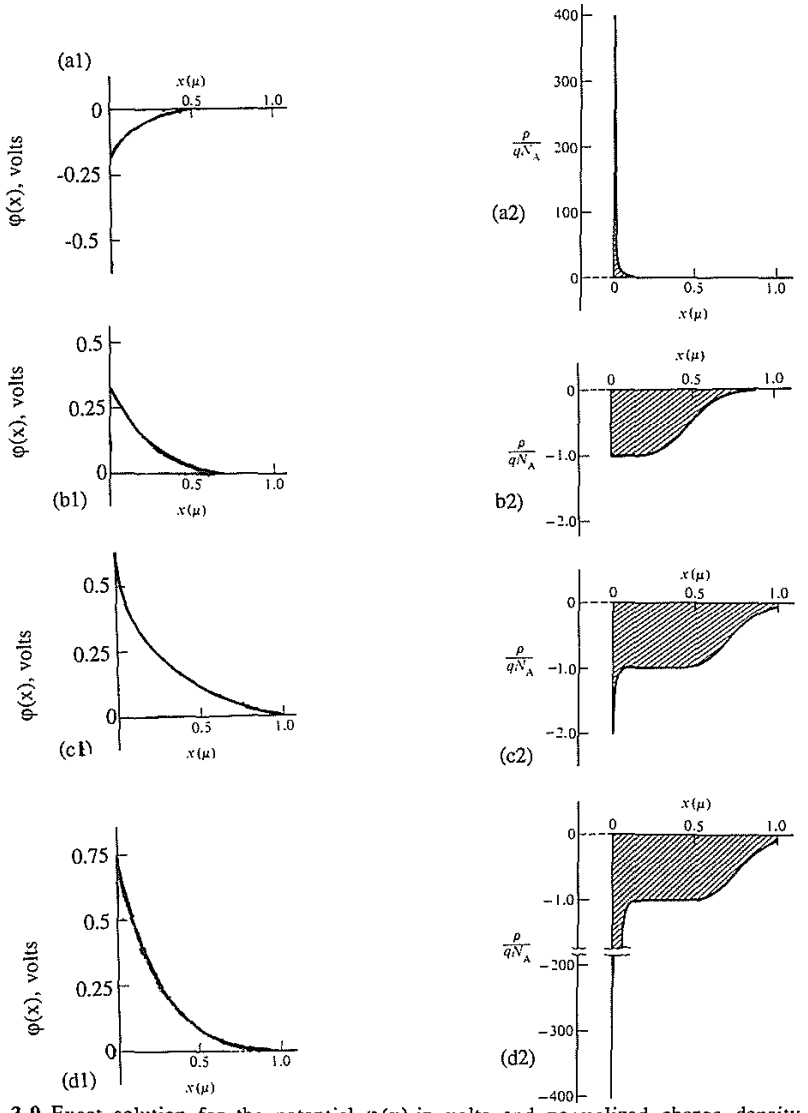


**Fig. 3-9** Exact solution for the potential $\varphi(x)$ in volts and normalized charge density ($\rho/qN_A$), respectively, in the semiconductor region of a MOS-C with a *p*-type Si substrate, as a function of depth, x. Here we assume $\varphi_B = 0.3V$ and T = 300K: (a1 and a2) Accumulation ($\varphi_{surf} = -0.15V$); (b1 and b2) middle of depletion ($\varphi_{surf} = \varphi_B = 0.3V$); (c1 and c2) Onset of inversion ($\varphi_{surf} = 2\varphi_B = 0.6V$); and (d1 and d2) strong inversion ($\varphi_{surf} = 2\varphi_B + 0.15V = 0.75V$). The charge concentration $\rho/N_A$ diagrams are drawn on a linear scale.[3] (Compare Figs. a2 - d2 to the simpler representation of charge in the silicon shown in Figs. 3-4c2 - f2.)

invoked in both the simplified and charge sheet models of the MOS-C: (a) the inversion layer can be treated as an infinitesimally-thin sheet of charge at the interface; and (b) the presence of mobile charge in the depletion region can be ignored (the depletion approximation). The second observation indicates it is reasonable to assume that transition from the bulk to the depletion region occurs abruptly.

In summary, the complicated procedure outlined above involves the following steps to get exact values of MOS-C parameters. For an ideal, uniformly doped *p*-type MOS-C, if we are given $N_A$, $t_{ox}$, and $V_{GB}$

1. Calculate $\varphi_{surf}$ using Eq. 3-45.

2. With this value of $\varphi_{surf}$ we can get $Q_I$ from Eq. 3-47, $\mathcal{E}(x)$ from Eq. 3-40, and $\varphi(x)$ from Eq. 3-49.

3. Once $\varphi(x)$ is known we can calculate $n(x)$ and $p(x)$ using Eqs. 3-12a and b.

From the sample plots of the charge distribution we see that in accumulation and inversion the mobile charge resides in an extremely narrow portion of the semiconductor immediately adjacent to the oxide-semiconductor surface. This substantiates the validity of the assumption used in the depletion approximation analysis that the inversion layer charge is confined to a very thin layer near the silicon surface. Thus, a third model based on this approximation (that is intermediate in complexity between the two models just described) has been developed by Baccarani et al.,[4] and Brews.[5] It is called the *charge-sheet model* and will be presented next.

### 3.3.5 Charge-Sheet Model for Determining the Characteristics of the Ideal MOS-C

The third quantitative model of the MOS-C is the *charge-sheet model.* It is more accurate than the simple depletion approximation model, but does not require the numerical analysis of the general model to obtain $Q_I$. Since it includes mobile charge carriers in the Poisson equation it provides information about the charge distribution in the MOS-C below strong inversion (unlike the depletion approximation model, which assumes that no mobile charges are present below strong inversion). Since the charge-sheet model assumes that the mobile charge concentrations are zero in the depletion region outside of the thin layer at the surface (that would contain the inversion layer - see assumption 2 below), this model is not as accurate for characterizing the MOS-C in depletion or accumulation as the general model. However, since inversion is responsible for current conduction in MOSFETs, accurate quantitative characteristics of the depletion and accumulation regimes in MOS-Cs and MOSFETs are usually not of much concern. Hence, this does not represent a significant limitation for most applications.

To begin the derivation, we list the assumptions upon which the charge-sheet model is based:

1. Mobile charge can exist in the silicon beyond the onset of *weak* inversion i.e., when $\varphi_{surf}>\varphi_B$ (unlike the previous model that assumed that no mobile charge exists in the channel until strong inversion, i.e., until $\varphi_{surf}>2\varphi_B$);

**2.** All this mobile charge is confined to a negligibly thin inversion layer at the silicon surface, so that the remainder of the depletion region contains no mobile charges ($n = p = 0$, for $0 < x \leq d$);

**3.** The depletion region is defined by a sharp boundary at a depth d (i.e., an abrupt transition between the depletion region and the bulk exists), in the same manner as was invoked the depletion approximation model;

**4.** The voltage drop across the inversion layer in the $x$-direction is zero, hence $V_{GB}$ (in an ideal MOS-C) is still the sum of $\varphi_{surf}$ and $\varphi_{ox}$;

**5.** The value of $\varphi_{surf}$ beyond strong inversion is not clamped at exactly $2\varphi_B$. Instead its exact value can be calculated from the model equations;

**6.** The depletion width at strong inversion is calculated using Eq. 3-28, so that the ionic charge in the depletion region can be calculated using Eq. 3-29;

**7.** The value of $Q_I$ can be found by subtracting $Q_B$ from $Q_C$.

Since both holes and electrons are included in the charge density term of the Poisson equation, we start the development of the charge sheet model again with Eq. 3-37. The first integration of the Poisson equation is also carried out in the same way as in the general model analysis, yielding the identical value for $\mathcal{E}_{si}(x = 0)$. $Q_C$ is also expressed by Eq. 3-42. However, since the goal of the charge sheet model is to provide accurate MOS-C expressions only for the case of inversion (including weak inversion), $Q_C$ can be simplified for this operating range. That is, if $\varphi_{surf} \geq \varphi_B$ (where, as we noted in section 3.3.1, $\varphi_B$ is $9\varphi_t$ to $16\varphi_t$ for the range of doping concentrations used in MOSFETs), several terms in Eq. 3-42 become insignificant and can be dropped, yielding

$$Q_C \approx \sqrt{2q\, N_A \kappa_S \varepsilon_o} \sqrt{\varphi_{surf} + \varphi_t\, e^{(\varphi_{surf} - 2\varphi_B)/\varphi_t}} \qquad (3 - 50)$$

Now, since we assume that in the depletion region there are no mobile charges present (i.e., all the mobile charge is in the inversion layer, which is infinitesimally thin), the depth of the depletion region is again given by Eq. 3-27

$$d = [\kappa_{si}\varepsilon_o(2\varphi_{surf})/qN_A]^{1/2} \qquad (3 - 51)$$

Then, $Q_B$ will consist only of the uncovered acceptor atoms in the depletion region, and can again be expressed by Eq. 3-29, repeated here:

$$Q_B = q\, N_A\, d = (2\kappa_{si}\varepsilon_o q N_A \varphi_{surf})^{1/2} \qquad (3 - 52)$$

To get $Q_I$ we can now subtract $Q_B$ from $Q_C$ as given by Eq. 3-50 to get

$$Q_I = \sqrt{2q\, N_A \kappa_S \varepsilon_o}\left(\sqrt{\varphi_{surf} + \varphi_t\, e^{(\varphi_{surf} - 2\varphi_B)/\varphi_t}} - \sqrt{\varphi_{surf}}\right) \qquad (3 - 53)$$

Also note that if we use Eq. 3-50 to approximate $Q_C$ in Eq. 3-19 for $\varphi_{ox}$, and insert this into Eq. 3-10, the expression relating $\varphi_{surf}$ and $V_{GB}$ is now

$$V_{GB} = \varphi_{surf} - Q_C/C_{ox} \tag{3 - 54}$$

or

$$V_{GB} = \varphi_{surf} + \frac{\sqrt{2q\, N_A K_S \varepsilon_0}}{C_{ox}} \sqrt{\varphi_{surf} + \varphi_t e^{(\varphi_{surf} - 2\varphi_B)/\varphi_t}} \tag{3 - 55}$$

We note, however, that this equation cannot be solved explicitly for $\varphi_{surf}$, but requires a numerical iteration approach to solve for $\varphi_{surf}$.

Nevertheless, the charge sheet model provides analytical expressions for $Q_I$ and $Q_B$ in a MOS-C that are quite accurate over the entire range of inversion (i.e., $\varphi_{surf}>\varphi_B$). This makes it more useful in many applications than the more general MOS-C model.

It should also be noted that when the equation for $Q_I$ from the charge sheet model is plotted versus the surface potential (i.e., using a log-linear plot, as shown in Fig. 3-10),[6] two inversion regimes can be identified: (1) weak inversion; and (2) strong inversion. In each of these regimes we can simplify the expression for $Q_I$ given by Eq. 3-53.

**3.3.5.1 Approximation of $Q_I$ in Weak Inversion.** First, we recall from section 3.3.4 that $Q_I$ is much smaller than $Q_B$ in weak inversion. Therefore, we can simplify $Q_I$ by treating the term $\varphi_t \exp(\varphi_{surf} - 2\varphi_B)/\varphi_t$ in Eq. 3-53 as small compared to

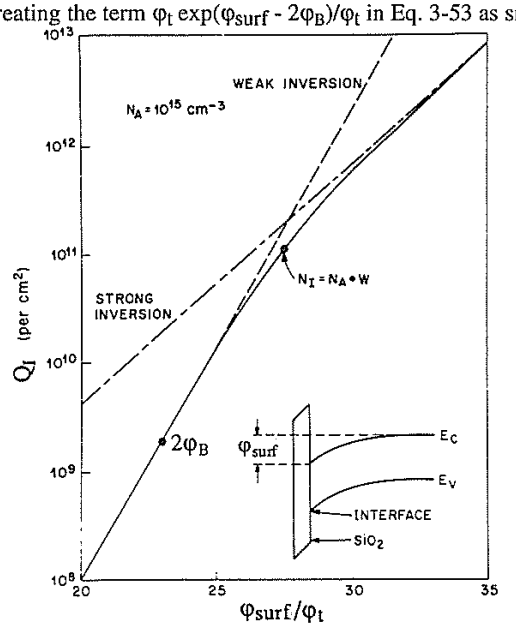


**Fig. 3-10** Inversion layer carrier density per unit area versus $\varphi_{surf}/\varphi_t$ as computed from Eq. 3-53 and from approximations to this equation for the case of weak inversion (Eq. 3-58), and strong inversion (Eq. 3-62).[5] (© IEEE 1978).

the term $\varphi_{surf}$. Then, if we let

$$\zeta = \varphi_t \exp(\varphi_{surf} - 2\varphi_B)/\varphi_t \qquad (3-56)$$

the first square root term in the parentheses in Eq. 3-53 becomes $\sqrt{\varphi_{surf}} + \zeta$. Since $\zeta$ is smaller than $\varphi_{surf}$, we can approximate the function $\sqrt{\varphi_{surf}} + \zeta$ by the first two terms of its Taylor expansion about $\zeta = 0$:

$$\sqrt{\varphi_{surf} + \xi} \approx \sqrt{\varphi_{surf}} + \frac{1}{2\sqrt{\varphi_{surf}}}\xi \qquad (3-57)$$

Using Eq. 3-56 and Eq. 3-57 in Eq. 3-53 we get

$$Q_I\,(\text{weak inv}) \approx \frac{\sqrt{2q\,N_A\kappa_{Si}\varepsilon_o}}{2\sqrt{\varphi_{surf}}}\varphi_t\, e^{(\varphi_{surf} - 2\varphi_B)/\varphi_t} \qquad (3-58)$$

This expression implies that in weak inversion the inversion layer charge is essentially an exponential function of $\varphi_{surf}$. Note from Fig. 3-10 that the weak inversion approximation of $Q_I$ from Eq. 3-53 is quite accurate up to $2\varphi_B$, but becomes increasingly inaccurate beyond strong inversion.

We can easily solve for $\varphi_{surf}$ in weak inversion as well. That is, since $Q_I \ll Q_B$, we can write Eq. 3-10 as

$$V_{GB} = \varphi_{surf} - Q_B/C_{ox} \qquad (3-59)$$

or using Eq. 3-52

$$V_{GB} = \varphi_{surf} + [(\sqrt{2\kappa_{Si}\varepsilon_o q N_A})/C_{ox}]\sqrt{\varphi_{surf}} \qquad (3-60)$$

$$= \varphi_{surf} + \gamma\sqrt{\varphi_{surf}} \qquad (3-60a)$$

where $\gamma = (\sqrt{2\kappa_{Si}\varepsilon_o q N_A})/C_{ox}$. Equation 3-60a can be solved for $\varphi_{surf}$ to yield

$$\varphi_{surf} = \left[-\frac{\gamma}{2} + \left(\frac{\gamma^2}{4} + V_{GB}\right)^{1/2}\right]^2 \qquad (3-61)$$

To relate $Q_I$ to $V_{GB}$, we can substitute the value of $\varphi_{surf}$ from Eq. 3-61 into Eq. 3-58.

**3.3.5.2 Approximation of $Q_I$ in Strong Inversion.** In strong inversion $Q_I \gg Q_B$. As a result, the exponential term in Eq. 3-53 is the only significant term within the parentheses. Thus, $Q_I$ in strong inversion can be well approximated as

$$Q_I\,(\text{strong inv}) \approx (\sqrt{2\kappa_{Si}\varepsilon_o q}\; n_i \exp(\varphi_{surf}/2\varphi_t) \qquad (3-62)$$

The inversion-layer charge in strong inversion is thus seen to be an exponential function of the surface potential with a slope of $1/(2\varphi_t)$. Therefore, a small increase in the surface potential induces a large change in $Q_I$ (strong inv). This implies that $\varphi_{surf}$ will remain almost unchanged even in the face of a large increase in $V_{GB}$ or $Q_I$ beyond strong inversion. The approximation that $\varphi_{surf}$ (inv) is clamped at $2\varphi_B$ made in the depletion approximation model is thus seen to be reasonably accurate for actual MOSFETs. If the gate voltage corresponding to value needed to produce $\varphi_{surf}$(inv) is

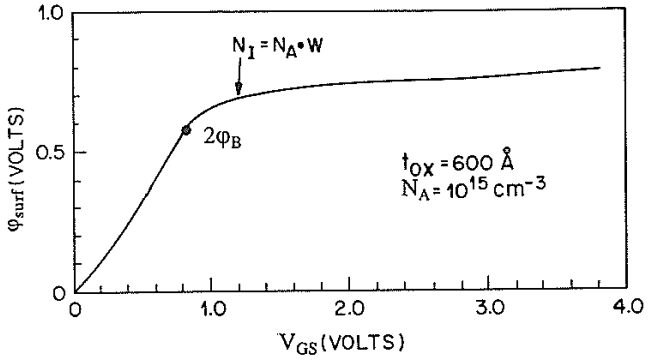


**Fig. 3-11** $\varphi_{surf}$ versus $V_{GB}$ calculated from the charge sheet model for an oxide thickness of 60 nm, and a substrate doping level of $N_A = 10^{15}$ cm$^{-3}$. The dot indicates $\varphi_{surf} = 2\varphi_B$.[5] (© IEEE 1978).

termed the threshold voltage $V_T$ (see next section for how to compute this value), then the $Q_I$ (strong inv) dependence on $V_{GB}$ can be approximated by

$$Q_I \approx - C_{ox} (V_{GB} - V_T) \qquad (3 - 63)$$

We should mention that $\varphi_{surf}$(inv) does change slightly as $V_{GB}$ is increased beyond strong inversion, as shown in Fig. 3-11, where $\varphi_{surf}$ from Eq. 3-55 is plotted versus $V_{GB}$. We see that $\varphi_{surf}$ in strong inversion actually increases beyond $2\varphi_B$ by ~150 mV before leveling off. Thus, models of $Q_I$ that use $\varphi_{surf}(inv) = 2\varphi_B$ underestimate the actual value. This has an impact on the accuracy of predicted drain current values in MOSFET circuit models based on this approximation. We will discuss this further in chap. 4.

## 3.4 THRESHOLD VOLTAGE of IDEAL MOS CAPACITORS

*Strong* inversion in MOSFETs occurs in essentially the same manner as in MOS-Cs. In fact, one of the most important parameters of a MOSFET is the gate voltage at the onset of strong inversion. This parameter is known as the *threshold voltage* $V_T$. We can obtain an expression for $V_T$ using an ideal MOS-C in which we assume the depletion approximation is valid. Then we follow the same analysis as in section 3.3.3.

* Note that a third inversion regime, intermediate to the two mentioned above, namely *moderate inversion*, has been defined by Tsividis (see Fig. 3-6).[6] This allows an even more careful representation of MOS behavior to be developed. Interested readers can consult ref. 6 for more details.

That is, we begin with Eq. 3-10:

$$V_{GB} = \varphi_{ox} + \varphi_{surf} \qquad (3 - 64)$$

At the *onset* of strong inversion (i.e., implying that the inversion layer is just at the verge of forming, so $Q_I$ is still zero), the magnitude of the charge on the gate is balanced by just the charge in depletion region of the semiconductor $Q_B$ due to the ionized dopants, or:

$$Q_G = - Q_B = q\, N_{SUB}\, d_{max} \qquad (3 - 65)$$

where $N_{SUB}$ is the substrate doping (i.e., $N_A$ in *p*-type and $N_D$ in *n*-type substrates), respectively. Then, $\varphi_{surf}$ at the onset of inversion = $2\varphi_B$. It can also be expressed in terms of $d_{max}$ using Eq. 3-27. Setting these two equal, we have for a *p*-type substrate

$$\varphi_{surf}(inv) = 2\varphi_B = qN_A\,(d_{max})^2/2\kappa_{si}\varepsilon_o) \qquad (3 - 66)$$

Solving this for $d_{max}$, and substituting into Eq. 3-65 we get $Q_B$ in terms of $N_A$ and $\varphi_B$. Finally, using this expression for $Q_B$ in Eqs. 3-19 and 3-20 ($\varphi_{ox} = -Q_B/C_{ox}$), and putting this into Eq. 3-64 we obtain the gate voltage value at the onset of strong inversion in an ideal MOS capacitor ($V_T$) expressed as a single equation in terms of $t_{ox}$, T, $n_i$, and $N_A$:

$$V_T \text{ (of an ideal MOS capacitor)} = 2\sqrt{\kappa_{si}\varepsilon_o q N_A \varphi_B}/C_{ox} + 2\varphi_B \qquad (3 - 67)$$

## 3.5 PHYSICS OF NON-IDEAL MOS CAPACITORS ($n^+$-PolySi-$SiO_2$-Si MOS Capacitors)

Although the ideal MOS capacitor is a useful structure for introducing MOS behavior, from the perspective of this text the most important MOS capacitor structure is the metal (Al, or heavily-doped polysilicon)-$SiO_2$-Si structure. In the metal-$SiO_2$-Si structure (and other "real" MOS capacitors), the work function difference $\varphi_{ms}$ is virtually never zero, and various charges are also always present inside the oxide or at the Si-$SiO_2$ interface. These phenomena exhibited by "real" MOS capacitors significantly alter ideal MOS behavior. They are also inherent in "real" MOSFETs, and must therefore be included to accurately describe actual device behavior.

### 3.5.1 Workfunction Difference Between Gate and Semiconductor

We noted earlier that the energy-band diagram of an *ideal* MOS capacitor is in a flat band condition when $V_{GB} = 0$. In real MOS capacitors, however, a flat band condition with $V_{GB} = 0$ is essentially never observed. Instead, when $V_{GB} = 0$ the bands are almost always bent as a result of the work function difference between the gate and semiconductor regions, as well as the charges that exist in the MOS capacitor.

The *work function* of a material is defined as the minimum energy required to bring an electron from the Fermi level to the vacuum level. In MOS structures, however, it

is more useful to deal with the *modified* work function. This is defined as the minimum energy required to bring an electron from the Fermi level in the gate $E_{Fm}$ or the semiconductor $E_{Fs}$ to the oxide conduction-band edge ($q\varphi_m'$ or $q\varphi_s'$, respectively), as shown in Fig. 3-12. Note also that $q\varphi_s' = q[\chi' + (E_C - E_F)_\infty] = q(\chi' + E_G/2 + \varphi_B)$ for a *p*-type semiconductor, where $\chi'$ is the *modified electron affinity* (defined as the energy difference between the conduction band edges of the semiconductor and the oxide). In the Si-$SiO_2$ case, $q\chi' = 3.23$ eV.

Figure 3-12a shows the energy-band diagram for an Al-$SiO_2$-*p*-type-Si structure before contact. For Al-$SiO_2$, $q\varphi_m' = 3.2$ eV, while for *p*-type Si-$SiO_2$ $q\varphi_s' = (3.23 + 0.55 + q\varphi_B) \sim 4.1$ eV. Obviously, $q\varphi_m'$ and $q\varphi_s'$ are not equal. Hence, if a MOS structure could be formed by bringing the 2 regions in contact, the effect of this difference on the energy-band diagram of the MOS capacitor would be as shown in Fig. 3-12b. That is, if such a MOS capacitor was unbiased ($V_{GB} = 0$), the Fermi levels would have to "line up" (be at the same energy level) everywhere in the capacitor, Fig.

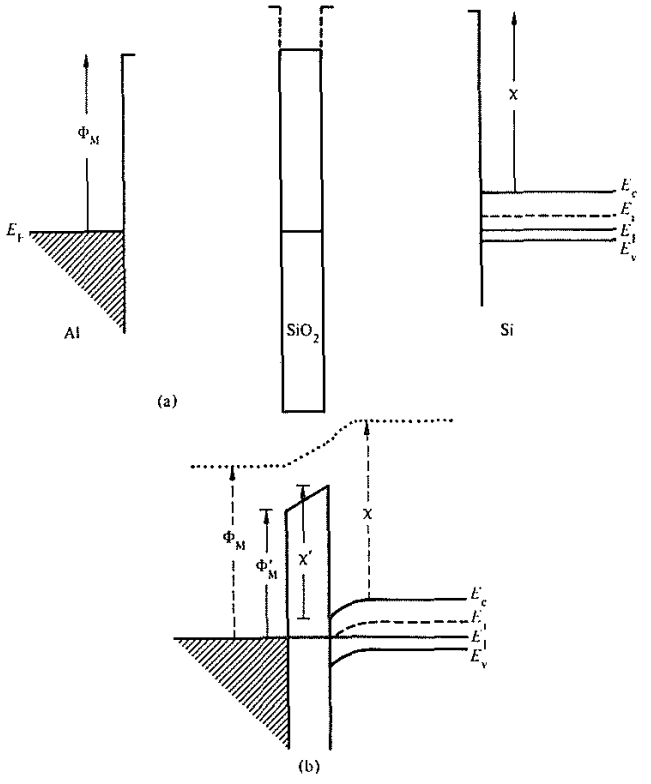


**Fig. 3-12** The MOS capacitor structure and idealized energy-band diagram (a) before contact and (b) after contact.[12] Reprinted with permission of Addison-Wesley.

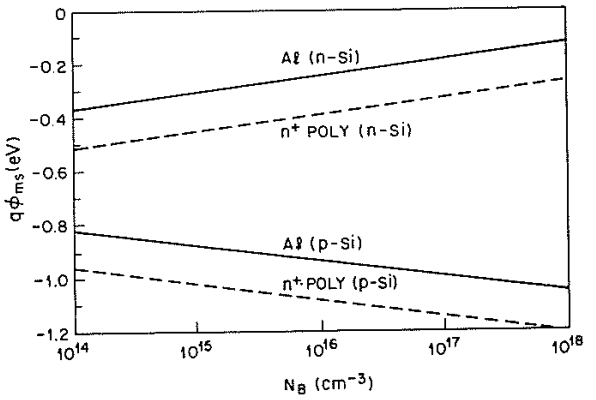


**Fig. 3-13** Work-function difference $\phi_{ms}$ (V) versus doping for $n^+$ and $p^+$ polysilicon, and Al gate electrodes.[7] Reprinted with permission of Solid-State Electronics.

3-12). Since the modified work functions in this structure are different, the $E_c$, $E_i$, and $E_v$ bands would be bent downward when $V_{GB} = 0$ to satisfy the requirement of a constant Fermi level. To achieve a flat-band condition in this structure, a negative voltage [equal to $(\varphi_m - \varphi_s)$], would have to be applied to the gate (in this example $\cong$ - 0.9 V).

In submicron ICs, however, the gate material is normally heavily-doped polysilicon. The Fermi level in heavily doped $n$-type polysilicon resides at the conduction band edge (and in heavily doped $p$-type poly, at the valence band edge). Hence, for an $n$-channel device with $n^+$ poly on a $p$-type substrate $\varphi_{ms}(n\text{-ch}) = (\varphi_m - \varphi_s) = (-E_G/2q) - \varphi_B$ (with its value between -0.9 to -0.95V for $10^{16}\,cm^{-3}<N_A<10^{17}\,cm^{-3}$ - the appropriate doping range for submicron technologies if $L>0.5\ \mu m$). Likewise, the $p$-channel $\varphi_{ms}$ for an $n^+$ poly on an $n$-type substrate is $\varphi_{ms}(p\text{-ch}) = (\varphi_m - \varphi_s) = (-E_G/2q) + |\varphi_B|$, with its value between -0.15 to -0.2V for the same doping range. Finally, for a $p$-channel device having a $p^+$ poly on an $n$-substrate, $\varphi_{ms}(p\text{-ch}) = (\varphi_m - \varphi_s) = (E_G/2q) + |\varphi_B|$. Figure 3-13 shows the value of $\varphi_{ms}$ for various substrate-doping values if an aluminum, $n^+$-poly, or $p^+$-poly gate electrode is used.

## 3.5.2 Oxide Charges and Traps

Four different types of charges are associated with the oxide and Si-$SiO_2$ interface as shown schematically in Fig. 3-14. The effective net (i.e., total) charge per unit area at the Si-$SiO_2$ interface (in $C/cm^2$) is denoted by the symbol $Q_{tot}$, whereas the net (total) number of charges per unit area ($Q_{tot}/q$) is given by $N_{tot}$. The standardized terminology and symbols used to differentiate the various individual charge types are as follows:

**1.** Mobile ionic charge per unit area $Q_m$ ($C/cm^2$), and $N_m$ (no. of mobile charges/$cm^2$);

2. Fixed oxide charge per unit area $Q_f$ (C/cm$^2$), and $N_f$ (no. of fixed oxide charges/cm$^2$);

3. Interface trap charge per unit area $Q_{it}$ (C/cm$^2$), and $N_{it}$ (no. of interface trapped charges/cm$^2$); $D_{it}$ - number of interface trapped charges per unit area *and* energy (no. of interface trapped charges/cm$^2$-eV);

4. Oxide trapped charge $Q_{ot}$ (C/cm$^2$), and $N_{ot}$ (no. of oxide trapped charges/cm$^2$).

Since issues relating to the reliability of submicron MOSFETs also involve these charges, a brief review concerning the origin of the charges, their effect on device behavior, and techniques to minimize their presence is given here. A more detailed description of their characteristics can be found in Vol. 1 and refs. 1 and 7.

**3.5.2.1 Mobile Ionic Charges.** Mobile ionic charges $Q_m$ in the oxide layer arise mostly from the presence of sodium or potassium ions, which have very high diffusivities in the oxide (even at temperatures of less than 200°C). Their presence leads to threshold instabilities and to a deterioration of the oxide reliability. After it was confirmed that sodium in even very small concentrations is ruinous to MOSFET operation, stringent procedures were developed to keep the level below $N_m = 10^9$ cm$^{-2}$. At such levels, the instabilities in $V_T$ are negligibly small. Procedures to counteract Na contamination include: using clean processing techniques; employing gettering techniques; neutralization of the sodium in the oxide by growing the oxide in ambients containing chlorine compounds; and using SiN (or oxynitride) passivation films. (Such films are impervious to the transport of Na.) Tests for Na contamination are also routinely performed (using MOS-C monitor structures) to detect any accidental contamination. Steps can then be taken to find and eliminate the contamination source. More information on the details of these techniques can be found in Vol. 1, Chap. 7.

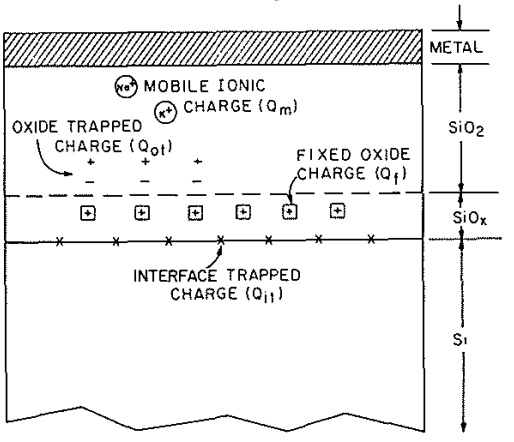


**Fig. 3-14** Standardized terminology for oxide charges associated with thermally oxidized silicon.[13] (© IEEE 1980).

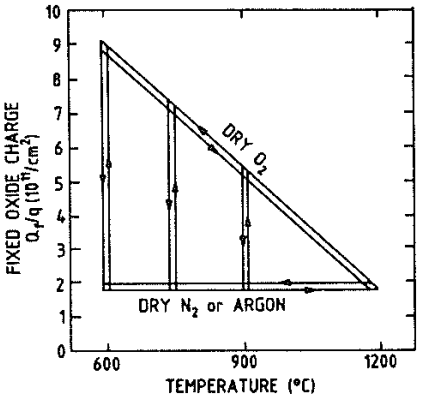


**Fig. 3-15** The *Deal triangle,* which specifies the expected $Q_f/q$ after dry $O_2$ oxidation and after inert ambient annealing.[9] Reprinted by permission of the publisher, The Electrochemical Society, Inc.

**3.5.2.2 Fixed Oxide Charge.** The fixed oxide charge $Q_f$ (usually positive) is located in the oxide within approximately 30Å of the Si-$SiO_2$ interface. Since its density does not vary with surface potential (unlike interface trapped charge $Q_{it}$), it is termed *fixed* oxide charge. It is generally accepted that $Q_f$ is associated with the structure of the interfacial transition region between the silicon and $SiO_2$. One hypothesis is that $Q_f$ is due to *excess ionic silicon* which has broken away from the silicon proper and is waiting to react in the vicinity of the Si-$SiO_2$ interface when the oxidation process is abruptly terminated.

Regardless of the origin, it has been experimentally confirmed that the magnitude of $Q_f$ is influenced by substrate orientation, oxidation temperature, and anneal conditions after oxide growth. These factors were carefully studied by Deal et al., and their results are summarized by the well-known "Deal-triangle" shown in Fig. 3-15. In this figure $N_f$ ($Q_f/q$) is plotted for (111) Si against final oxidation or anneal temperature. It can be seen that the minimum $N_f$ value for (111) material is ~$2\times10^{11}$ cm$^{-2}$. The time required to reach a minimum value of $N_f$ is less than 5 min at 1200°C and about an hour at 550°C. In addition, after an oxide growth step, wafers are annealed in an inert ambient (part of the annealing step occurring during the slow withdrawal from the furnace). It should be noted, however, that continued annealing in inert ambients (e.g., $N_2$) at high temperatures leads to a marked increase of $N_f$. Fig. 3-16 shows how $N_f$ changes as a function of time during a nitrogen anneal at 950, 1100 or 1200°C.

The value of $N_f$ also depends on the orientation of the Si surface, and is lowest on (100) orientations (in which the minimum $N_f$ value is ~$1.1\times10^{10}$ cm$^{-2}$). As the lowest values of $N_f$ are desired, (100) material is used to build MOS ICs.

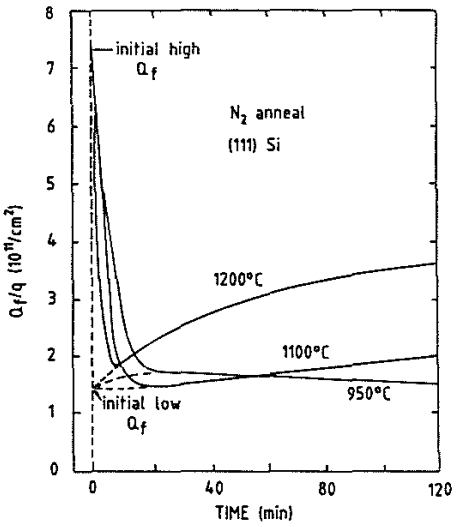


**Fig. 3-16** Variation of fixed oxide charge as a function of time during nitrogen anneal at 950, 1100 or 1200°C.[10] Reprinted by permission of the publisher, The Electrochemical Society, Inc.

Since $Q_f$ is located at the Si-$SiO_2$ interface, the change in $V_T$ that it causes ($\Delta V_T$) is simply calculated as the shift in $V_T$ that would be produced by a sheet of positive charge placed at the interface, or

$$\Delta V_T = -Q_f/C_{ox} = q\, N_f / C_{ox} \qquad (3\text{-}68)$$

**3.5.2.3 Interface Trapped Charge.** Interface trapped charge $Q_{it}$ arises from allowed energy states (also referred to as *surface states*, *interface states*, or *interface traps*) that somehow exist in the forbidden gap of the Si in the region very close to the Si-$SiO_2$ interface. Although models exist that detail the *electrical* behavior of interface traps, their *physical origin* has not been totally clarified. The weight of experimental evidence supports the view that the interface traps arise primarily from unsatisfied chemical bonds or so-called "dangling bonds" at the surface of the semiconductor. When a silicon lattice is abruptly terminated along a given plane to form a surface, one of the four surface-atom bonds will be left dangling as pictured in Fig. 3-17. It seems plausible that most, but maybe not all, of such Si-surface bonds would be tied up as a result of thermally growing an $SiO_2$ layer (Fig. 3-17b). The remaining dangling bonds might become interfacial traps. Other possible interfacial trap-formation effects include Si-Si bond stretching - due to the absence of an oxygen atom (Fig. 3-17c), Si-O bond stretching (Fig. 3-17d), and the presence of a metallic impurity at the Si surface (Fig. 3-17e).[11] These interface traps are also considered further in chaps. 7 and 8.

Based on the wide-ranging and degrading effects they cause in the operational behavior of MOSFETs (and the fact that $Q_m$ and $Q_f$ can generally be acceptably

minimized), interface trapped charges must be considered to be the most perfidious of the oxide charges. Because they are not usually caused by the presence of foreign impurities, but instead are due to a disruption of the periodicity of the crystal lattice, they are not associated with well-defined energy levels. Instead, interface trapped charges are distributed throughout the entire band gap at closely spaced levels. (Interface levels

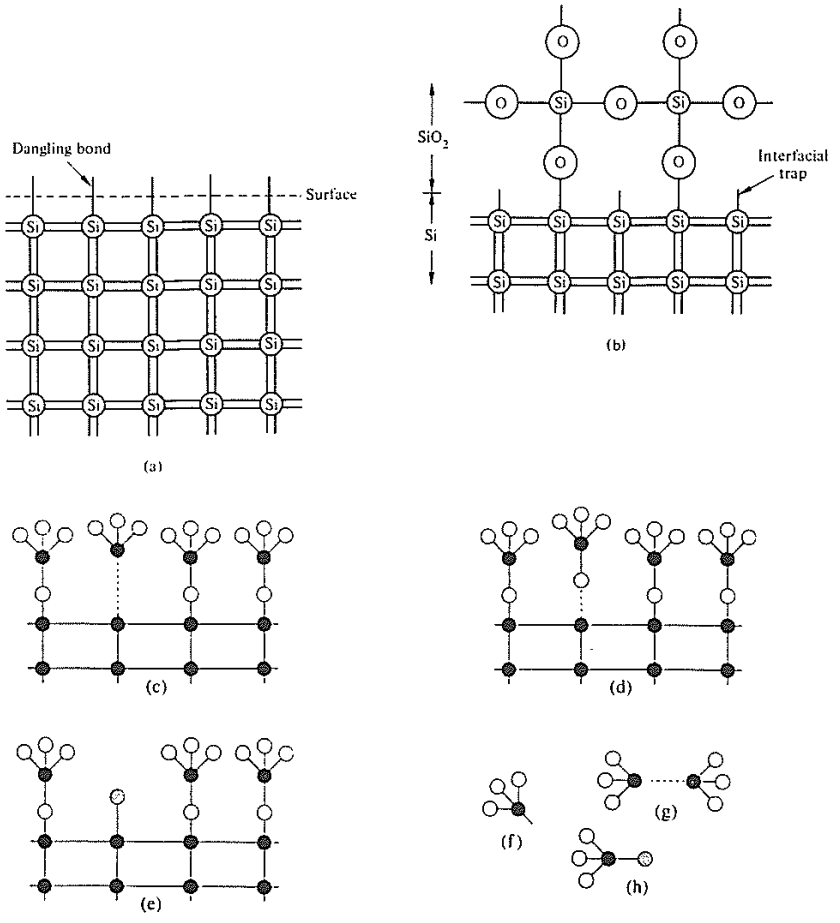


**Fig. 3-17** Physical model for the interfacial traps. (a) "Dangling bonds" which occur when the Si lattice is abruptly terminated along a given plane to form a surface. (b) Post oxidation dangling bonds (relative number greatly exaggerated) that become the interfacial traps. (c) Si-Si bond stretching. (d) Si-O bond stretching. (e) presence of a metallic impurity at the Si surface. (f) - (h) possible defects in the $SiO_2$ bulk that may give rise to oxide trapped charge.

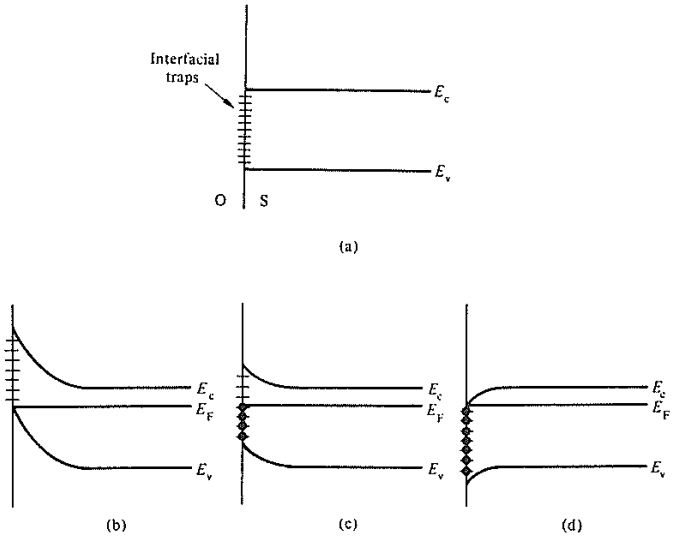


**Fig. 3-18** (a) Electrical modeling of interfacial traps as allowed electronic levels localized in space at the oxide-semiconductor interface. (b) - (d) Filling of the interface levels under (b) inversion, (c) depletion, and (d) accumulation biasing in an *n*-type device. From R.F. Pierret, *Modular Series on Solid-State Devices*; *Vol. IV - Field Effect Devices.* Copyright, 1983, Addison-Wesley. Reprinted with permission.

can also occur at energies greater than $E_C$ or less than $E_V$, but such levels are usually obscured by the much larger density of conduction- or valence-band states.) By using an energy-band diagram to show how these energy levels are distributed throughout the forbidden gap (Fig. 3-18a), we can more easily visualize their impact on a MOS-C.

That is, if an *n*-doped Si MOSFET (PMOS) is biased into inversion (Fig. 3-18b), the Fermi level at the surface will be close to $E_V$. In this case, the interfacial traps will mostly be empty, as they lie in energies above $E_F$. Furthermore, if these empty trap sites are assumed to be donorlike (that is, positively charged when empty and neutral when filled with an electron), the net charge per unit area associated with the interfacial traps ($Q_{it}$) will be positive. Changing the gate bias to achieve depletion conditions (Fig. 3-18c) positions $E_F$ near the middle of the band gap at the surface. Since the interface levels always remain fixed in energy relative to $E_C$ and $E_V$ at the surface, depletion biasing obviously draws electrons into the lower interface state levels, and $Q_{it}$ reflects the added negative charge. If the MOS capacitor is biased into the accumulation mode, most of the traps will be filled with electrons (Fig. 3-18d), and $Q_{it}$ will approach its minimum value. The purpose of the above discussion is to show that the interface traps charge and discharge as a function of bias, thereby affecting the charge distribution inside the device, as well as the device characteristics in a complex but somewhat predictable manner.

Once again, however, since $Q_{it}$ is located at the Si-$SiO_2$ interface, the change in $V_T$ due to $Q_{it}$ can be simply calculated from

$$\Delta V_T = -Q_{it}(\varphi_{surf})/C_{ox} \tag{3-69}$$

Since Eq. 3-69 shows that $Q_{it}$ depends upon the bias condition (and is therefore a function of $\varphi_{surf}$), its value will change as $V_{GB}$ changes. Under conditions of inversion $Q_{it}$ takes on its largest positive value, and decreases as the bias progresses from depletion to accumulation. The distribution of trap levels as a function of energy in the band gap has a U-shaped distribution (see Fig. 3-19). The minimum level of $D_{it}$ at midgap is usually the density used to characterize their presence.

The overall value of $Q_{it}$, as well as the precise density of states as a function of energy, makes the value of $D_{it}$ sensitive to a variety of process conditions used to fabricate the MOSFET. Nevertheless, certain definite trends concerning these values have been uncovered. First, $Q_{it}$, like $Q_f$, is greatest on (111) surfaces, and smallest on (100) surfaces, and the ratio of midgap-$D_{it}$ values on the two surfaces is ~3:1. Second,

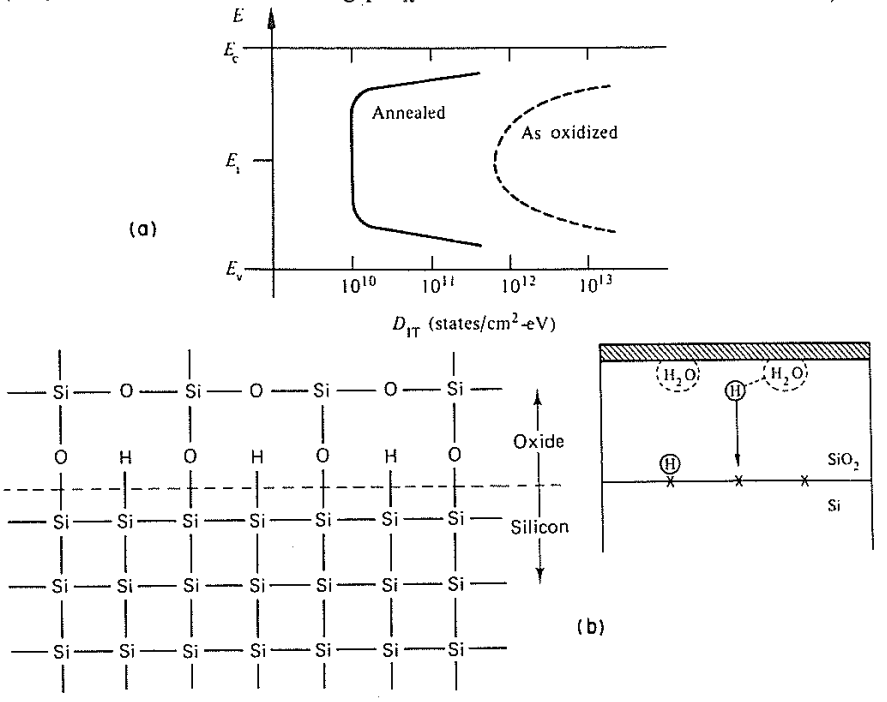


**Fig. 3-19** (a) Energy distribution of interface states within the band gap. General form and magnitude of the interfacial trap density observed before and after interface state anneal. (b) Conceptual picture of how hydrogen is thought to passivate dangling bonds.

after oxidation in a dry $O_2$ ambient, the midgap value of $D_{it}$ is relatively high ($\sim 10^{11}$-$10^{12}$ states/cm$^2$-eV), with the values decreasing as the oxide temperature is increased (this is also the case with $Q_f$). However, annealing at lower temperatures in inert ambients *does not* reduce the value of $D_{it}$. Instead, annealing in the presence of hydrogen at relatively low temperatures (≤500°C) for 5-10 minutes minimizes $D_{it}$. $D_{it}$ at midgap under an optimum set of processing conditions is $\sim 10^{10}$/cm$^2$-eV. See Fig. 3-19b for a conceptual picture of how hydrogen is thought to passivate the dangling bonds at the silicon surface and how this thus reduces the interface trap density.

**3.5.2.4 Oxide Trapped Charge.** The oxide trapped charge $Q_{ot}$ is due to holes or electrons trapped in the *bulk* of the oxide, and hence can be positive or negative. $Q_{ot}$ is associated with defects in the $SiO_2$, which may arise from ionizing radiation, hot carrier injection, or high currents through the oxide (e.g., due to Fowler-Nordheim tunneling - as described in chap. 7), or other reactions which either tend to break Si-O bonds in the oxide or otherwise lead to carrier trapping on sites or traps somehow already present in the oxide. Figure 3-17 f - h shows possible defects in the $SiO_2$ bulk that may give rise to such traps. For example, a trivalent Si atom in the $SiO_2$ will introduce a deep trap level in the $SiO_2$ bandgap ($\bullet Si{\equiv}O_3$), and stretched Si-O or Si-Si bonds (in the latter a missing bridging oxygen atom leads to a defect, $(O_3{\equiv}Si\bullet\bullet S{\equiv}O_3)$ introduce a continuum of shallow or deep trap levels in the $SiO_2$ bandgap when located in the bulk of the $SiO_2$.

$Q_{ot}$ can be annealed out by low-temperature treatments (450-550°C) although some neutral traps may remain. Therefore, oxide trapped charge has been considered relatively less important than the other oxide charges in just-completed MOSFETs. In early generations of MOSFET ICs, exposure of the devices to ionizing radiation encountered in space flights was the main concern involving $Q_{ot}$. However, more recently-introduced processing techniques such as ion-implantation, electron-beam evaporation of metal films, reactive-ion etching, and x-ray lithography are all potential sources for creating charged and neutral traps in the gate dielectric (all of which may not be completely annealed out at the end of the fabrication process). This may result in long-term reliability problems, especially if hot carriers are injected in these oxides and get trapped (see chap. 9). Another reliability concern involves gate oxide degradation due to high oxide electric fields (and subsequent Fowler-Nordheim tunneling currents in the oxide). This has become more of a concern as oxide thickness has been scaled down.

**3.5.2.5 Combined Effect of Oxide Charges on $V_T$ of Submicron MOSFETs.** It is now possible to control the level of $Q_m$ in modern IC fabrication processes so that it has an insignificant effect on $V_T$ stability. Thus, $Q_f$ and $Q_{it}$ are the remaining important charges that must be controlled during fabrication. For this discussion, let the sum of $Q_f$ and $Q_{it} = Q_{tot}$. Then, combining Eqs. 3-68 and 3-69,

$$\Delta V_T = -Q_{tot}/C_{ox} = -(Q_f + Q_{it})/C_{ox}. \qquad (3-70)$$

If $N_{tot} = Q_{tot}/q$ is maintained at $<5\times10^{10}$/cm$^2$, for oxides <200Å thick:

$$\Delta V_T = Q_{tot}/C_{ox} = qN_{tot}\, t_{ox}/3.9\, \varepsilon_o$$

$$= (1.6\text{x}10^{-19}\ \text{C})(5\text{x}10^{10}\ \text{cm}^{-2})(2\text{x}10^{-6}\ \text{cm})\ /(3.5\text{x}10^{-13}\ \text{F/cm})$$

$$= 0.05\ \text{V}$$

Thus, for routine submicron process technology, it may seem that these charges are no longer a major problem. However, this is not true as far as the problems of gate oxide reliability and MOSFET degradation due to hot-carrier injection effects are concerned. That is, due the high electric fields present in submicron MOSFETs, phenomena occur that give rise to the generation of additional $Q_{ot}$ and $Q_{it}$ during normal device operation. Thus, the value of these charges can rise during the lifetime of the device, and cause performance degradation or failure. This topic will be revisited in more detail in chaps. 7 and 9.

## 3.6 THE THRESHOLD VOLTAGE EQUATION OF Si-SiO$_2$ MOS CAPACITORS

To obtain a flat-band condition in a real (non-ideal) MOS capacitor, a voltage must be applied to the gate to overcome the effects of $\varphi_{ms} \neq 0$ and $Q_{tot} \neq 0$. The total voltage needed to offset these effects is referred to as the *flat-band voltage* $V_{FB}$ and is given as

$$V_{FB} = \varphi_{ms} - Q_{tot}/C_{ox} \qquad (3\text{-}71)$$

The gate voltage that must then be applied to a real MOS capacitor structure to achieve the onset of strong inversion (i.e., threshold voltage, $V_T$) must include the flat band voltage as well. Thus, the $V_T$ equation for real MOS capacitors (and long-channel MOSFETs when the source-to-substrate voltage $V_{SB} = 0$V) is given as

$$V_{T\ (\text{uniform doping, long-channel})} = V_{T(ud,lc)} = V_{FB} + 2\sqrt{\kappa_{si}\varepsilon_o q N_{sub}\varphi_B}/C_{ox} + 2\varphi_B$$

$$= \varphi_{ms} - Q_{tot}/C_{ox} + 2\sqrt{\kappa_{si}\varepsilon_o q N_{sub}\varphi_B}/C_{ox} + 2\varphi_B \qquad (3\text{-}72)$$

Figure 3-20 plots Eq. 3-72 for $n^+$ silicon-gate MOSFETs (both PMOS and NMOS) versus substrate doping concentration for several values of $t_{ox}$ (i.e., 65, 25, and 15 nm thick) as the parameter, and assuming also that $Q_{tot} = 0$.

Note that Eq. 3-72 also assumes that the Si substrate is uniformly doped. In practical MOSFETs, however, $V_T$ is normally adjusted by implanting a thin layer of impurity atoms (boron or arsenic) at the Si surface. Thus, the substrate becomes non-uniformly doped, and the $V_T$ equation must be modified to take this into account. To a first order this is done by treating the implanted impurity atoms as if they are an additional layer of charge very close to the Si-SiO$_2$ interface. Their presence is accounted for by adding a term to the $V_T$ equation similar to the term used to describe

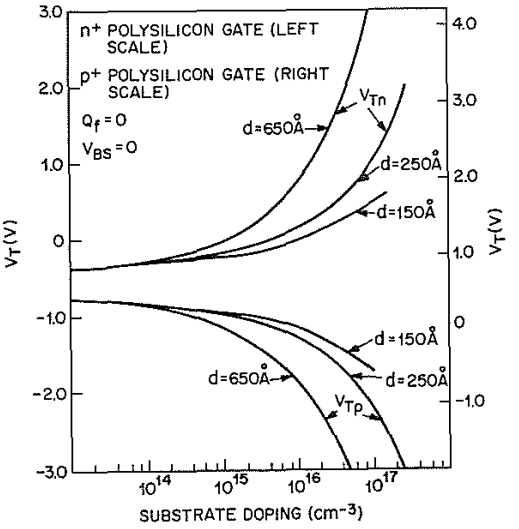


**Fig. 3-20** Calculated threshold voltages of $n$-channel ($V_{Tn}$) and $p$-channel ($V_{Tp}$) transistors as a function of their substrate's doping, assuming $n^+$ polysilicon gate (left scale) and $p^+$ polysilicon gate (right scale). Curves for gate oxide thicknesses $d$ of 150 Å, 250 Å, and 650Å are shown. From S.M. Sze Ed. *VLSI Technology,* 2nd Ed., Chap. 11, "VLSI Process Integration." Copyright, 1988 Bell Telephone Laboratories. Reprinted with permission.

the presence of oxide charge $Q_{tot}$. Details of $V_T$ adjustment and the term used to modify Eq. 3-72 are discussed in chap. 4.

**Example 3-1**: Find $V_{T(ud,lc)}$ of an ideal MOS-C ($\varphi_{ms}$ = 0V, $Q_{tot}$ = 0) with a uniform substrate doping $N_A = 10^{15}/cm^2$. The gate-oxide thickness is $t_{ox}$ = 15 nm.

**Solution**: $\varphi_B(\text{sub}) = (E_i - E_F)/q = 0.29$ V

$$\varepsilon_{ox} = 3.9\varepsilon_o = 3.5\text{x}10^{-13}\ \text{F/cm};\quad C_{ox} = \varepsilon_{ox}/1.5\text{x}10^{-6} = 2.3\text{x}10^{-7}\ \text{F/cm}^2$$

$$2\sqrt{\kappa_{si}\varepsilon_o q N_A \varphi_B} = 2\,[1.02\ \text{x}10^{-12}\ \text{x}\ 1.6\text{x}10^{-19}\ \text{x}\ 10^{15}\ \text{x}\ 0.29]^{1/2} = 1.4\text{x}10^{-8}\ \text{C/cm}^2$$

$$2\sqrt{\kappa_{si}\varepsilon_o q N_A \varphi_B}/C_{ox} = 1.4\ \text{x}\ 10^{-8}/2.3\ \text{x}\ 10^{-7} = 0.06\ \text{V}$$

$$V_{T(ud,lc,\ ideal)} = 0.58\text{V} + 0.06\text{V} = 0.64\ \text{V}$$

**Example 3-2**: Find $V_{T(ud,lc)}$ of a 'real' MOS-C just like the one of Example 3-1, except that it has a heavily-doped silicon gate (doped to $N_D = 10^{20}/cm^3$), and $Q_{tot} = q\,(5\ \text{x}\ 10^{10}/cm^2)$.

**Solution:** According to Eq. 3-72, the threshold voltage of the 'real' MOS-C is shifted from that of the 'ideal' MOS-C by the value of $V_{FB}$. This term is the sum of $\varphi_{ms}$ + $Q_{tot}/C_{ox}$. Thus, since

$$\varphi_{ms} \text{ (from Fig. 3-13)} = -1.02 \text{ V}$$

and

$$Q_{tot}/C_{ox} = -1.6\text{x}10^{-19} \text{ x } 2\text{x}10^{10} / 2.3\text{x}10^{-7} = -0.01 \text{ V}$$

$$V_{T(ud,lc)} = V_{T(ud,lc,\ ideal)} + V_{FB}$$

$$= 0.64\text{V} + (-1.03\text{V}) = -0.39 \text{ V}$$

Note that a negative value of $V_{T(ud,lc)}$ is yielded, implying that this MOSFET would be ON at $V_{GB} = 0$V (and would therefore behave as a depletion-mode device). The parameters used in this calculation of $V_{T(ud,lc)}$ are typical of the NMOS device parameters encountered in the early days of MOS ICs. Hence, at that time it was not possible to easily and/or reliably fabricate enhancement-mode NMOS transistors. In chap. 4 we shall show how this problem was overcome by the development of ion implantation. With this process it became possible to introduce dopants into the channel region near the silicon surface, such that the threshold voltage is shifted from the value it has in the case of a uniformly doped substrate, to the desired value. This enabled enhancement-mode NMOSFETs to be manufactured with appropriate threshold voltage values.

The typical value of $V_T$ in NMOSFETs is 0.7V. This means that $V_T$ of the MOS-C structure of Example 3-2 must be shifted by 1.11V. Equation 4-73 indicates that a shallow implant with a dose of ~$1.6\text{x}10^{12}$ boron ions/cm$^2$ will produce such a $V_T$ shift in the MOSFET of Example 3-2.

## 3.7 VISUALIZATION OF MOS-C AND MOSFET PHENOMENA USING POTENTIAL VERSUS POSITION DIAGRAMS

Many aspects of the behavior of the MOS-C and the MOSFET are described in terms of the variation of the electrostatic potential in the silicon as a function of position. By plotting such relationships in a graphical format, a visual model is obtained which helps to portray many of the phenomena associated with MOS-C and MOSFET behavior.

When describing the MOS-C most graphical representations are one-dimensional, reflecting the one-dimensional nature of the behavior of such structures [i.e., usually $\varphi(x)$ versus x plots are presented]. However, when the potential in the MOSFET is being depicted, a two-dimensional representation is needed to appropriately depict the MOSFET behavior. Thus, we have decided to illustrate the potential versus position in the MOS-C using both the 2-D plot (as is needed for the MOSFET), as well as the 1-D potential plots more usually encountered when MOS-C behavior is being studied. This is done in Fig. 3-21, in which both 1-D and 2-D potential plots for a MOS-C cross-section are depicted. We note that $\varphi_{surf} = \varphi\ (x = 0)$ is constant versus $y$ in the MOS-C, and thus the 1-D representation of the potential in the MOS-C would be

adequate. However, when the 2-D potential versus position diagrams of the MOSFET are presented (i.e., in chaps. 4 and 5), it will be easier to interpret their details by comparing them to the simpler 2-D cases introduced here.

In Fig. 3-21a we show the 2-D cross-section of a *p*-substrate MOS-C, with a bias $V_{GB}$ connected between the gate and body. In Fig. 3-21b we show the case of the *ideal* MOS-C described in Example 3-1. We observe that when $V_{GB} = 0$ (Fig. 3-21b1), $\varphi(x,y) = 0$ everywhere, corresponding to the flat-band condition in the energy-band representation. In Fig. 3-21b2 we portray the case of $V_{GB} = V_T = 0.64V$ for the MOS-C of Example 3-1. Here we note that $\varphi_{surf} = 2\varphi_B = 0.58V$, with the variation of $\varphi(x)$ expressed by Eq. 3-23.

In Fig. 3-21c we note that the *real* MOSFET of Example 3-2 is depicted for the bias condition of $V_{GB} = 0V$. Since we noted that $V_T = -0.39V$, implying that a negative voltage of -0.39V must be applied to cause a condition of $\varphi_{surf} = 2\varphi_B = 0.58V$, which corresponds to the onset of strong inversion. Thus, when $V_{GB} = 0V$, $\varphi_{surf} = 0.97V$, which is larger than $2\varphi_B$, as shown in Fig. 3-21c1.

In order for this MOS-C to exhibit a value of $V_T = 0.7V$, we indicated in the previous section that a dose of $1.6 \times 10^{12}$ boron ions/cm$^2$ must be implanted into the channel region. If this is done, when $V_{GB} = 0V$, $\varphi_{surf}$ will then equal -0.05V, and the potential versus position diagram will as shown in Fig. 3-21d1. Note that when $V_{GB} = 0.7V$, $\varphi_{surf} = 0.58V$, but the potential versus x variation is different from that of the uniformly doped case of Fig. 3-21b. The effect of the implant dose on the depletion region width of the channel and other MOSFET phenomena are discussed in chap. 4.

## REFERENCES


1. E.H. Nicollian and J.R. Brews, *MOS Physics and Technology,* Wiley-Interscience, New York, 1982.
2. C.E. Young, "Extended Curves of the Space Charge, Electric Field, and Electrostatic Potential Inside a Semiconductor," *J. Appl. Phys.,* **32**, p. 329, (1961).
3. R.F. Pierret and J.A. Shields, "Simplified long-channel MOSFET theory," *Solid-State Electronics,* vol. 26, p. 143, 1983.
4. G. Baccarani et al., "Analytical i.g.f.e.t.model including drift and diffusion currents," *IEE Journal on Solid-State and Electron Devices,* vol. 2, p. 62, March 1978.
5. J.R. Brews, "A Charge-Sheet Model of the MOSFET," *Solid-State Electronics,* vol. 21, p. 345, 1978.
6. Y.P. Tsividis, *Operation and Modeling of the MOS Transistor,* McGraw-Hill, New York, 1987.
7. W.M. Werner, "The Work Function Difference of the MOS-System with Aluminum Field Plates and Polysilicon Field Plates," *Solid-State Electronics,* **17**, 769 (1974).
8. P. Balk Ed., *The Si-SiO$_2$ System,* Elsevier, New York, 1988.
9. B.E. Deal et al., "Characteristics of the Surface State Charge of Thermally Oxidized Silicon," *J. Electrochem. Soc.,* **114**, p. 266 (1967).
10. B.E. Deal et al., *J. Electrochem. Soc.,* **121**, p. 198C (1974).

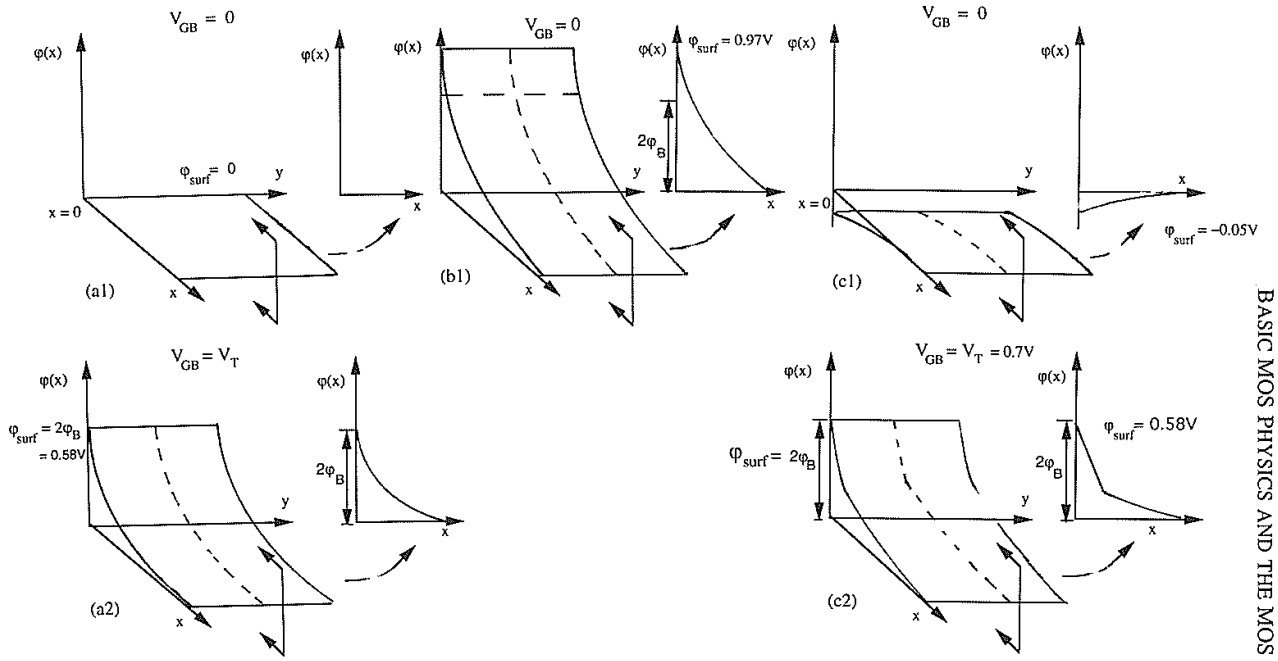


**Fig. 3-21** Visualization of the electrostatic potential in *p*-type MOS-Cs with $N_A = 10^{15}$ cm$^{-3}$, and $t_{ox} = 150$Å. (a1) φ(x,y) in an *ideal* MOS-C ($\varphi_{ms} = 0$ and $Q_{tot} = 0$) when $V_{GB} = 0$V (flatband condition); and (a2) when $V_{GB} = V_T$. (b1) φ(x,y) in *real* MOSFET with uniformly doped substrate and $n^+$ polysilicon gate ($\varphi_{ms} = 1.02$V), and $Q_{tot} = 2\times10^{10}$ cm$^{-2}$, when $V_{GB} = 0$V. (c1) φ(x,y) in *real* MOSFET with $n^+$ polysilicon gate and $V_T$-adjust implant into substrate such that $V_T = 0.7$V, when $V_{GB} = 0$V. (c2) φ(x,y) when $V_{GB} = V_T$.

11. P. Roblin, S. Samman, and S. Bibyk, "Simulation of Hot-Electron Trapping and Aging in nMOSFETs," *IEEE Trans. Electron Dev.*, **ED-35**, December 1988, p. 2229.

12. R.F. Pierret, *Modular Series on Solid-State Devices; Vol. IV - Field Effect Devices.*, R.F. Pierret and G.W. Neudeck, Eds., Addison-Wesley Publ. Co., Reading MA, 1983.

13. B.E. Deal, "Standardized Terminology for Oxide Charges Associated with Thermally Oxidized Silicon," *IEEE Trans. Electron Dev.*, **ED-27**, p. 606, (1980).

## PROBLEMS

1. Explain why it is useful to study the behavior of the MOS-C prior to studying the behavior of the MOSFET.

2. Sketch the energy-band diagrams of a MOS-C with a heavily-doped *n*-polysilicon gate when (a) $V_{GB} = 0$, and (b) in the flat band condition when the Si substrate: (1) 1-Ω-cm *n*-type, and (2) 1-Ω-cm, *p*-type.

3. For an ideal MOS-C with $t_{ox} = 30$ nm and $N_A = 5\times10^{15}$ cm$^{-3}$, find the applied voltage and electric field at the interface needed to: (a) make the silicon surface intrinsic; and (b) to bring about strong inversion.

4. Using Eq. 3-13c prove that for $n_{surf} = 10N_A$, $\varphi_{surf}$ is only 58 mV greater than $2\varphi_B$.

5. Calculate the flatband voltage and the threshold voltage (a) in 1 Ω-cm *p*-type silicon and (b) in 1 Ω-cm *p*-type silicon. The MOS-Cs for each case have : (i) aluminum gate for which $q\varphi_m = 4.3$ eV, (ii) $t_{ox} = 100$ nm; and (iii) the oxide is free of charge except for a surface density of $Q_f = 5\times10^{10}$ cm$^{-2}$. The electron affinity of silicon is 4.05 eV.

6. Use the "threshold" statement in SUPREM III to extract and plot $V_T$ vs. $V_{SB}$ for increments of 0.25V between 0 and 5V for the device specified in Prob. 4. Compare the zero bias ($V_{BS} = 0$V) value with the two corresponding values of $V_T$ found in Prob. 4.

7. Consider Poisson's equation in the substrate of a MOS-C. Using the condition that there is charge neutrality in the substrate, show that the impurity doping terms $N_D - N_A$ can be written as $n_i$ (exp ($u_B$) - exp ($-u_B$)] = 2 $n_i$ sinh $u_B$ , where $u$ represents the potential normalized to (kT/$q$) and $u_B$ is the substrate potential ($u_B = -q\varphi_B/kT$) in a *p*-type substrate.

8. Using the form derived in Problem 6, show that the Poisson equation can be written in terms of $u$ as:

$$d^2u/dx^2 = (1/L_{Di})^2 [\sinh(u) - \sinh(u_B)]$$

where $L_{Di}$ is the intrinsic Debye length

$$L_{Di} = (\varepsilon_{Si}\, k\, T/2q^2 n_i)^{1/2}$$

9. Calculate the maximum depletion layer depth in a MOS-C with a *p*-type substrate doped uniformly at $2\times10^{15}$ cm$^{-3}$ if T = 77K and 300K.

**10.** Consider the establishment of a $p$-type inversion layer in a MOS-C. Show that for a nondegenerate $n$-type semiconductor, the surface charge density $Q_C$ needed to make $p_{surf} = n_o$ (the equilibrium electron concentration in the bulk) is given by

$$Q_C = \sqrt{2\varepsilon_{si}\, q\, N_D\, (\varphi_B)}.$$

# CHAPTER 4

## MOS TRANSISTOR DEVICE PHYSICS: PART 2

## LONG-CHANNEL MOSFETS

A description of the physics of the MOS capacitor (MOS-C, chap. 3) provides a solid foundation for analyzing the behavior of the MOSFET. Hence, in this chapter the device physics of long-channel MOSFETs is undertaken. In chap. 5 we examine the behavior of short-channel (i.e., submicron) MOSFETs.

Long-channel MOSFETs are discussed first for the following reasons:

**1.** The derivation of accurate long-channel-MOSFET drain-current models can be achieved by solving both the *Poisson equation* and the *drift-diffusion current density equations* in one-dimensional form, whereas accurate modeling of short-channel MOSFET behavior requires the solution of these equations in two (or even three) dimensions. Thus, it is logical to undertake the simpler analysis first.

**2.** The long-channel drain-current MOSFET models derived from the solution of the 1-D device equations can be expressed in analytical form. Hence, these models are widely used in circuit-design applications. In addition, quantitative insight about the device physics of MOSFET operation can also be obtained by examining these models. On the other hand, physically based analytical models of short-channel MOSFET behavior do not arise from the solution of the two-dimensional device equations, and thus it is harder to gain quantitative insight into MOSFET operation from them.

**3.** The analytical expressions for $I_D$ from two of the four long-channel MOSFET models derived in this chapter are the $I_D$ expressions used in SPICE for simulating MOSFET behavior in IC circuit design applications.

**4.** As MOSFETs are scaled down, they eventually become prone to 'short-channel' effects. In most cases, however, these effects are considered detrimental. That is, it is the task of the device designer to suppress them when scaling-down MOSFET structures. The goal is to produce 'short-channel' MOSFETs with 'long-channel' behavior. Thus, it is important to define long-channel behavior and to describe the physics that produce such characteristics in MOSFETs. This understanding provides insight into the measures that must be employed to suppress unwanted short-channel effects.



MPS EX. 1008C - 73/295

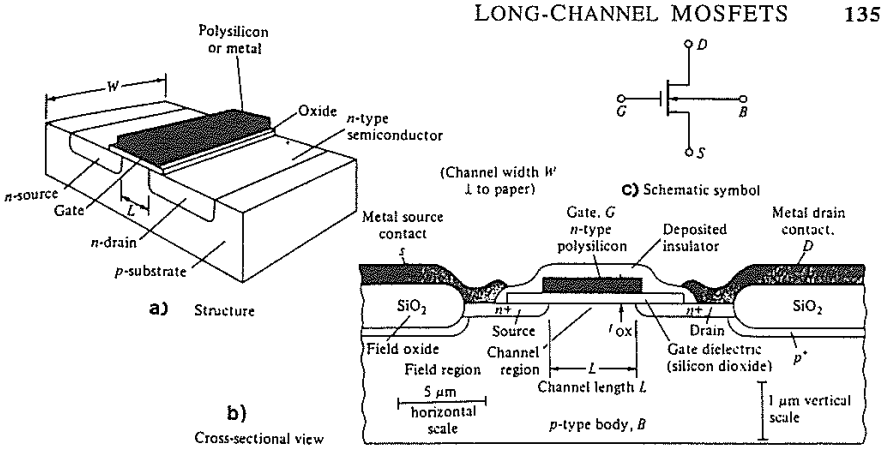


**Fig. 4-1** (a) Structure of an MOS device. (b) Cross sectional view. (c) Schematic symbol.[1] From D. A. Hodges and H. G. Jackson, Analysis and Design of Digital Integrated Circuits, Copyright, 1983 McGraw-Hill Book Co. Reprinted with permission.

In this chapter the following topics dealing with MOSFETs are covered:

- **a.** Introduction to the terminology of MOSFETs and their behavior
- **b.** Effect of Applying a Bias to the Inversion Layer of the MOS-C
- **c.** Definition of the Long-Channel MOSFET and the Gradual-Channel Approximation
- **d.** Qualitative Description of Long-Channel MOSFETs
- **e.** Quantitative Models of dc Long-Channel MOSFET Behavior
  - **i.** Pao-Sah Model
  - **ii.** Charge-Sheet Model
  - **iii.** Variable-Depletion-Charge Model
  - **iv.** Square-Law Model
- **f.** Threshold-Voltage Control in Long-Channel MOSFETs
  - **i.** Body Effect
  - **ii.** Threshold-voltage adjustment by ion-implantation
- **g.** Subthreshold behavior of Long-Channel MOSFETs
  - **i.** Physics and modeling of subthreshold current flow
  - **ii.** Subthreshold swing
  - **iii.** Gate-induced leakage current (GIDL)

## 4.1 TERMINOLOGY OF MOSFET DEVICE STRUCTURES

Figure 4-1 shows the cross-section of the MOSFET, as introduced in chap. 3. The important difference between the MOS-C and the MOSFET is that in the latter a *pn*

junction exists at each side of the MOS-C channel region. Each of these junctions are also close enough to make contact with the inversion layer. By making external connections to each of these edge junctions, the MOSFET becomes a four-terminal device (with the terminals designated respectively as the *gate* G, *body* B, *source* S, and *drain* D). The MOS-C, on the other hand, remains a two terminal device (*gate* and *body*). The source and drain terminals of the MOSFET allow a bias $V_{DS}$ to be applied across the ends of the channel region, giving rise to a *drain current* $I_D$.

As described in chap. 3, the inversion layer can be established by applying an appropriate bias to the gate. For the device shown in Fig. 4-1a, the induced charge in the channel inversion layer is *n*-type, and the device is known as an *n*-channel MOSFET (or simply an NMOS transistor). A *p*-channel MOSFET (or PMOS) is obtained by interchanging the *n* and *p* regions. Just as in the ideal MOS-C it is assumed that current in the gate oxide (*gate current,* $I_G$) is negligible. We also assume that the MOSFET is a symmetrical device, insofar as connecting the two junction terminals to a circuit (i.e., the drain current should remain the same if the two terminals are interchanged). Regardless of the way a MOSFET is connected, the terminal tied to the more positive voltage (in NMOS circuits) is defined to be the *drain*, and the other is the *source*.

### 4.1.1 Basics of MOSFET Operation

In simplest terms, the operation of a MOS transistor involves the application of an input voltage to the gate electrode. This establishes an electric field perpendicular (or transverse) to the Si-$SiO_2$ interface in the channel region of the device (Fig. 4-2a). The conductance of the channel region (in which the device output current $I_D$ flows) can be modulated by varying this electric field. Since an electric field is responsible for controlling the output current flow, such devices are termed *field-effect transistors* (FETs).

If no gate bias is applied, however, the circuit path between source and drain consists of two back-to-back *pn* junctions in series. In this case, if $V_{DS}$ is applied (such that the drain and source *pn* junctions are reverse biased), $I_D$ will consist of only the reverse-bias diode leakage current, which is normally negligible.

When positive bias is applied to an NMOS transistor gate, however, electrons will be attracted to the channel region and holes will be repelled (as is the case in the MOS-C). Once the positive gate voltage becomes strong enough to form an inversion layer, an *n*-type channel is formed that connects the source and drain regions (Fig. 4-2a). A drain current $I_D$ can then flow if a voltage $V_{DS}$ is applied between the source and drain terminals. In the simplest analysis we assume that the voltage-induced *n*-type channel does not form unless the voltage applied to the gate exceeds the threshold voltage $V_T$.

MOS devices such as those just described (in which no conducting channel exists when $V_{GS} = 0$), are referred to as *enhancement-mode* (or *normally OFF*) transistors (see Fig. 4-2b). With NMOS enhancement-mode transistors, a positive gate voltage, $V_{GS}$, greater than $V_T$ must be applied to create the channel (or to turn them ON), while to turn ON PMOS enhancement-mode devices, a negative gate voltage (whose magnitude is $>V_T$) must be applied. Note that in NMOS transistors a positive voltage must also

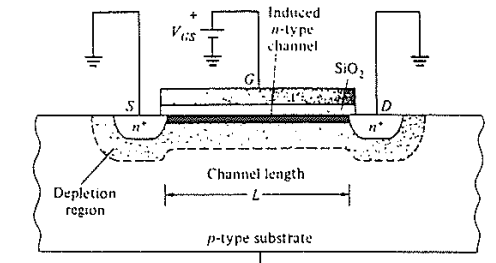


a)

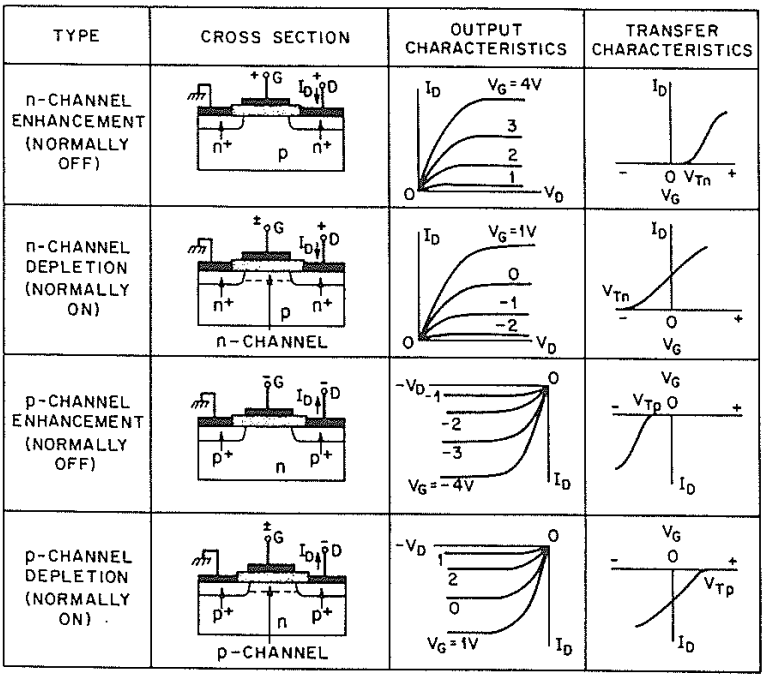


b)

**Fig. 4-2** (a) Idealized NMOS cross section with positive $V_{GS}$ applied showing depletion regions and induced channel. From D. A. Hodges and H. G. Jackson, Analysis and Design of Digital Integrated Circuits, Copyright, 1983 McGraw-Hill Book Co. Reprinted with permission. (b) Cross sections and output and transfer characteristics of four types of MOSFETs. From S.M.Sze, Semiconductor Devices - Physics and Technology, 1985, John Wiley & Sons. Reprinted with permission.

be applied to the drain to keep the drain-substrate reverse-biased, while in PMOS devices this voltage must be negative.

On the other hand, it is also possible to build MOS devices in which a conducting channel region exists when $V_{GS} = 0V$ (see also Fig. 4-2b), and such MOS devices are described as being *normally ON*. Since a bias voltage to the gate electrode is needed to deplete the channel region of majority carriers, and thus turn them OFF, such devices are also commonly called *depletion-mode MOSFETs*. NMOS depletion-mode devices require a negative gate voltage to be turned OFF, while corresponding PMOS devices require positive gate voltages.

## 4.2 BIASING THE INVERSION LAYER (BODY EFFECT)

Before undertaking a detailed discussion of MOSFET behavior, we first study the consequences of *applying a dc bias to the inversion layer of a MOS-structure*. This topic is actually an extension of the subject of MOS-C behavior, but also serves as an important prelude to the discussion of MOSFET operation. Consequently, when we discuss the operation of the MOSFET we will refer back to the results developed in this section.

We examine the effect of biasing the inversion layer from both the qualitative and quantitative perspectives. In the latter we will show how the expressions for the mobile charge concentrations in the inversion layer of the MOS structure are altered when a such bias is applied, as well as how the application of a bias to the inversion layer modifies the threshold voltage equation derived for the MOS-C.

Biasing the inversion layer is accomplished by the application of a dc voltage between the substrate and a diffused region adjacent to, and in contact with, the inversion layer. This implies that a modified MOS-C structure must be used. Specifically, a diffused region must be added to the edge of the MOS-C channel region (see Fig. 4-3a), and a terminal must be connected to this region (designated by the letter C). The result, as shown, is the *three-terminal MOS device* depicted in Fig. 4-3a.

If we choose the substrate (body or B) terminal as the reference, the voltage applied between terminal C and the substrate (body) is denoted by $V_{CB}$, and the voltage between the gate (terminal G) and substrate by $V_{GB}$ (see Fig. 4-3a).* For simplicity we also assume an ideal *p*-type Si-substrate MOS structure (i.e., $\varphi_{ms} = 0$ and $Q_{tot} = 0$).

### 4.2.1 Qualitative Discussion of the Effect of Applying a Bias to the Inversion Layer of a MOS Structure

If a MOS-C with a *p*-type substrate is biased into inversion by a gate voltage $V_{GB}$, a *pn* junction exists between the surface and the bulk of the silicon (as a result of the region near the silicon surface having been inverted to *n*-type). If there is an adjacent *n-doped* region in contact with the *induced* *n*-type inversion layer, it is possible to apply a bias to the induced junction by applying a bias $V_{CB}$ between terminal C and B (the substrate)

* As elsewhere, we use the convention that the second letter of the voltage subscript designates the reference terminal.

as shown in Fig. 4-3a. (Note that here we have a MOS structure in which the induced junction is contacted only at one end of the channel.*) We also assume that the polarity of $V_{CB}$ is such that the induced *pn* junction is either unbiased or under reverse bias (i.e., $V_{CB}$ in Fig. 4-3a is ≥0V). We will refer to $V_{CB}$ as the *channel voltage.*

Before presenting the equations relevant to this structure, let us first consider the qualitative effect of applying various $V_{CB}$ bias values.

**4.2.1.1 Case When Both $V_{GB}$ and $V_{CB}$ = 0V.** In Fig. 4-3b we show the two-dimensional potential φ versus position diagram for the three-terminal MOS structure when both $V_{GB}$ and $V_{CB}$ = 0V. We note that the channel region is in a flat-band condition and that a built-in voltage $\varphi_{bi}$ exists across the $n^+p$ (doped) junction. We also recall that even if $V_{GB} \neq 0V$, as long as $V_{CB}$ remains at 0V, the structure is still in equilibrium, because $I_G$ is assumed to be zero and there is no current in the $n^+p$ junction if $V_{CB}$ = 0V. Hence, this implies that when $V_{CB}$ = 0V the channel region of this structure exhibits the same behavior as that of the MOS-C described in chap. 3.

**4.2.1.2 Case When $V_{GB} \geq V_T$ and $V_{CB}$ = 0V.** If we now consider the case where $V_{CB}$ = 0V, but $V_{GB} \geq V_T$, we encounter a situation as shown in Fig. 4-3c. That is, the channel region is now inverted, and a *field-induced junction* now exists between the *n*-type inversion layer and the underlying *p*-type substrate. Since a bias is not applied across the field-induced junction, it is in equilibrium and is again characterized by the same Fermi level as in the diffused junction. The surface depletion region in the field-induced junction under these conditions is also described by the equilibrium theory presented in chap. 3.

Note, however, that the potential difference between the inversion layer and the $n^+$ region is now much smaller than in the case when $V_{GB}$ = 0V. Specifically, this potential difference is now ~($\varphi_{bi}$ - $2\varphi_B$). This implies that the inversion layer is in "communication" with the $n^+$ region adjacent to it. The term "communication" means that once the inversion layer is formed and a bias $V_{CB}$ is applied between terminals C and B, this bias will appear across the entire length of the field-induced junction (i.e., no longer just across the doped $n^+p$ junction at the edge of the channel). Thus, *if an inversion layer exists in the channel, then $V_{CB}$ does have an influence on $\varphi_{surf}$.*

For example, if $V_{CB}$ is suddenly allowed to increase from 0V to some non-zero value (while $V_{GB}$ is held fixed), electrons will be observed to flow out of the inversion layer through the C terminal. Why this happens, and what the effects are on the behavior of the MOS structure are described next.

**4.2.1.3 Case When $V_{GB}$ = 0V, But $V_{CB}$>0V.** If we next apply a non-zero $V_{CB}$ bias while keeping $V_{GB}$ = 0V, equilibrium will cease to exist in the three-terminal structure. This is because $V_{CB}$ causes a small reverse-bias leakage current to flow in the $n^+p$ junction. (Although this reverse-bias leakage current is extremely small, its

* However, in a MOSFET, contact to the inversion layer can be made at both ends of the induced junction since a diffused region exists at each end of the channel. In the MOSFET these two regions are called the source and drain, and the terminals are designated by the abbreviations S and D.

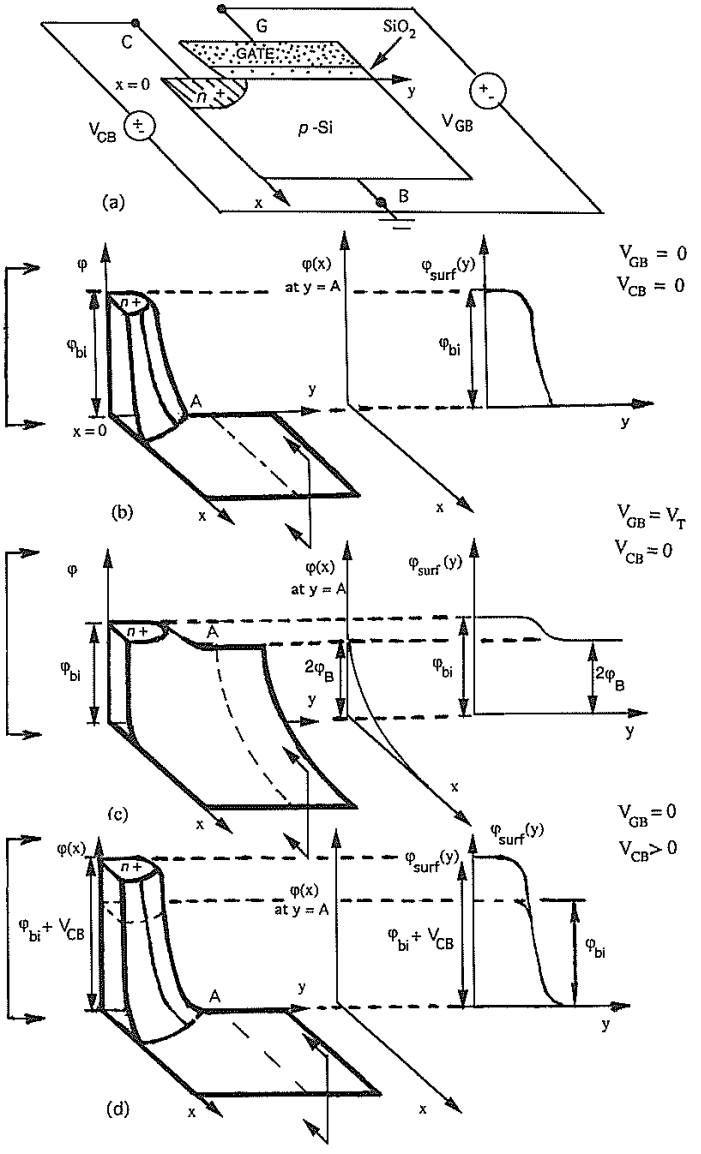


**Fig. 4-3** (a) Applying a bias $V_{CB}$ to an induced channel beneath the gate oxide by applying this bias $V_{CB}$ between terminal C and the substrate of a three-terminal MOS structure. Two-dimensional potential φ versus position diagrams in the three terminal MOS structure when: (b) both $V_{GB}$ and $V_{CB} = 0$; (c) $V_{GB} > V_T$ and $V_{CB} = 0V$; (d) $V_{GB} = 0V$ and $V_{CB} > 0V$.

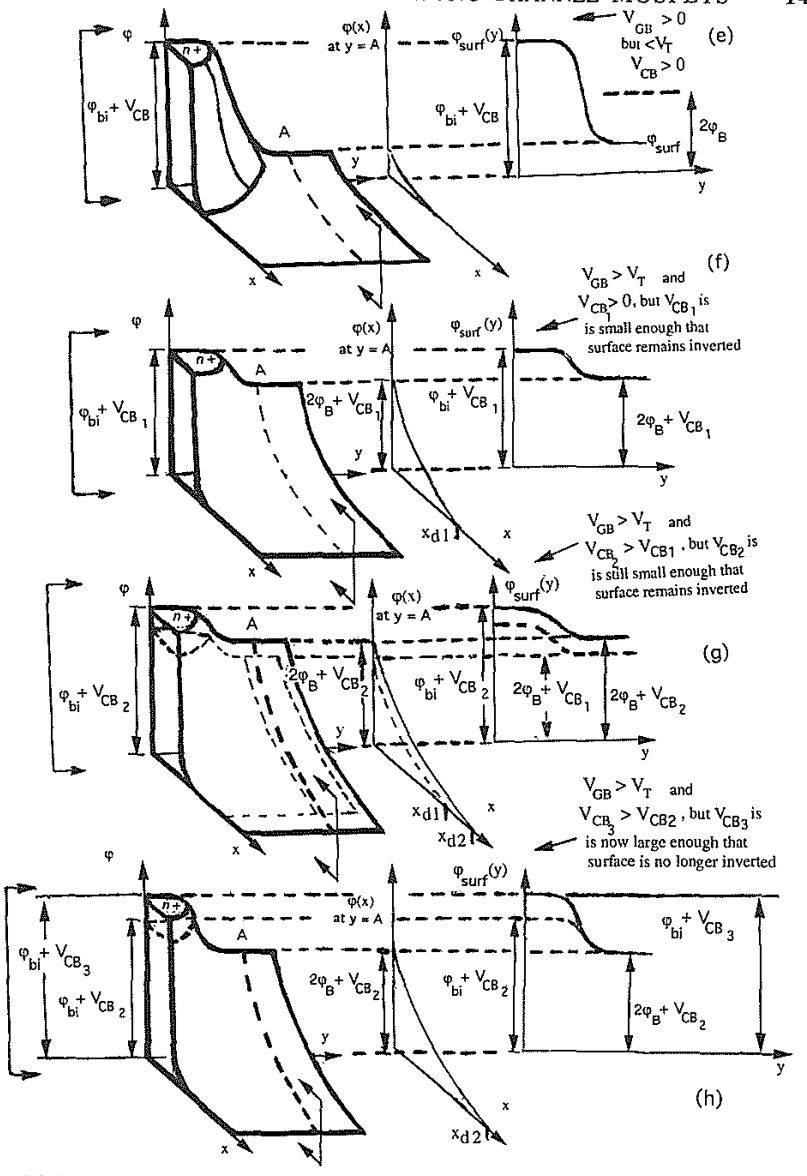


**Fig. 4-3** (cont.) (e) $V_{GB}>0$, but is $<V_T$, and $V_{CB} >0$; (f) $V_{GB}>V_T$ and $V_{CB}>0$, but $V_{CB} = V_{CB1}$, which we assume is small enough so that inversion still exists. (g) $V_{GB}$ is the same as in part (f), but $V_{CB} = V_{CB2}$, where $V_{CB2}>V_{CB1}$, but $V_{CB2}$ is still small enough to keep surface inverted. (g) $V_{GB} = V_T$, $V_{CB} = V_{CB3}$ (large enough to suppress the channel inversion layer).

existence implies that the MOS structure is no longer in equilibrium because some of the carrier energy now depends on an externally applied force, namely the extra electric field created in the depletion region by $V_{CB}$.) However, if $V_{GB}$ remains fixed at 0V, $V_{CB}$ is dropped entirely across the $n^+p$ junction. Hence, the surface potential along the channel is not altered from when $V_{CB}$ = 0V. Instead, only the potential difference between the $n^+$ and $p$ (substrate) regions is increased by $V_{CB}$ (as shown in Fig. 4-3d), leaving the channel region to the right of the $n^+p$ junction in a flat-band state. In addition, Fig. 4-3d indicates that *if no inversion layer is present, changing $V_{CB}$ has negligible impact on the surface potential $\varphi_{surf}$ along the channel.* This last statement also applies to the case illustrated in Fig. 4-3e (i.e., $V_{GB}$>0V, but is less than $V_T$, and $V_{CB}$ is increased from 0V to some value greater than 0V). Here we observe that there is still no impact on $\varphi_{surf}$ as long as no inversion layer is present in the channel.

**4.2.1.4 Case When $V_{GB} \geq V_T$ and $V_{CB}$>0V.** Let us now consider the case when $V_{GB}>V_T$ and a reverse-bias voltage $V_{CB}$ is applied to the induced *pn* junction (such that the surface remains inverted even after $V_{CB}$ is applied). Since the surface is inverted, the potential in the inversion region is very close to the potential value in the diffused region, as shown in Fig. 4-3f (and as exists in the case shown in Fig. 4-3c). That is, a point at the surface is at about the same potential (with respect to the substrate deep in the bulk) as a point in the $n^+$ region. Therefore, the surface is about as "attractive" for electrons as is the $n^+$ region. Consequently, electrons have no reason to prefer only the $n^+$ region as opposed to the "surface" at the right. As a result, the $n^+$ region can "communicate" with the inversion layer (implying that a bias applied to the $n^+$ region is also applied to the inversion layer). In addition, just as in the case of a MOS-C, the value of the surface potential $\varphi_{surf}$ remains clamped at the value it has at the onset of strong inversion (i.e., for the case of Fig. 4-3f, at a value of $\varphi_{surf} \sim 2\varphi_B + V_{CB1}$). That is, as $V_{GB}$ is increased beyond $V_T$, $\varphi_{surf}$ remains unchanged, but the mobile charge concentration in the inversion layer continues to increase.

We also recall from *pn* junction theory that if a reverse-bias voltage is applied to a previously unbiased *pn* junction, the junction depletion-region width will increase. Thus, the depletion region on the *p*-side of the induced junction will also increase if a reverse-bias is applied between terminals C and B. However, if $V_{GB}$ is kept fixed (such that $V_{GS} \geq V_T$) as the reverse-bias voltage $V_{CB}$ is increased (see Fig. 4-3g), the charge on the gate terminal will remain the same as when $V_{CB}$ = 0V. Therefore, the *total* charge in the semiconductor must also remain unchanged to maintain balance with the unchanged value of charge on the gate. However, since the application of $V_{CB}$ widens the depletion region (thereby uncovering more charge in this region of the induced junction), fewer electrons are needed in the inversion layer to balance the unchanged gate charge. Consequently, electrons must exit the inversion layer, resulting in a lower level of inversion. (Looking at it in another way, the increased positive potential at terminal C will attract electrons from the inversion layer, which will start flowing toward the $n^+$ region, and from it into the top terminal of the voltage source.) However, if a sufficiently large value of $V_{CB}$ is applied (while holding $V_{GB}$ fixed), this effect can entirely extinguish the charge in the inversion layer. In other words, a gate voltage

capable of causing inversion in the three-terminal MOS structure when $V_{CB} = 0V$ may no longer be able to sustain inversion if a non-zero value of $V_{CB}$ is applied.

As also shown in Figs. 4-3f and g, as long as the surface remains in inversion as $V_{CB}$ is increased, the depletion region under the field induced junction increases (from $x_{d1}$ in Fig. 4-3f to $x_{d2}$ in Fig. 4-3g). This means that the bands are bent more, and thus $\varphi_{surf}$ also increases. This supports the statement that as $V_{CB}$ increases, the $n^+$ region communicates this change in $V_{CB}$ to the field-induced junction. However, once a sufficiently large number of electrons depart from the inversion layer so that it essentially disappears, further increases in $V_{CB}$ no longer influence the channel region, and the depletion region no longer widens (as shown in Fig. 4-3h), and remains fixed at a value dependent on $V_{CB}$ (e.g., at $x_{d2}$, see Figs. 4-3g and h) as expressed by Eq. 4-8.

If a non-zero $V_{CB}$ is applied and it is desired to re-establish inversion, $\varphi_{surf}$ must be increased to a value larger than that needed when $V_{CB} = 0$. Specifically, at the onset of inversion, it is necessary to increase $V_{GB}$ so that $q\varphi_{surf} \sim q(V_{CB} + 2\varphi_B)$. Note that the effect just described can also be exploited as a technique for raising the threshold voltage of a MOSFET, as will be discussed in section 4.6.2.

**4.2.1.5 Summary of the Behavior of the Three-Terminal MOS Structure and the Significance of Such Behavior on the Operation of the MOSFET.** In summary, it is possible to establish "communication" with the channel region (i.e., an external bias voltage can be applied to the channel region of a MOS structure) if an inversion layer has been induced there. On the other hand, if the channel region is not inverted, the application of a bias voltage to a diffused region adjacent to the channel region will have no effect on the surface potential in the channel. Such "communication" (or lack of) has the following impact on the behavior of a MOSFET:

**1.** If the gate voltage applied to a MOSFET is less than the threshold voltage, the device is said to be operating in the subthreshold regime. From our discussion, this means that if a bias is applied to the drain ($V_{DS}$) of a MOSFET being operated in subthreshold, this voltage will be dropped entirely across the diffused $n^+p$ junction (i.e., the drain-substrate junction), and it will have no impact on $\varphi_{surf}$. Hence, $\varphi_{surf}$ will be determined by the gate potential, which is constant everywhere on the gate. Consequently, the potential drop along the $y$ direction at the surface of the channel will be essentially zero. We will use this information when we discuss subthreshold current flow in MOSFETs in section 4.7.

**2.** If the channel is inverted, and $V_{CB}$ is increased (and the channel remains in inversion for the range of applied $V_{CB}$ values), the depletion region of the field-induced channel increases. If $V_{GB}$ is held fixed, the number of electrons in the inversion layer will decrease as $V_{CB}$ is increased. At some value of $V_{CB}$ the inversion layer charge will entirely disappear. These effects occur when a drain bias $V_{DS}$ is applied to a MOSFET. That is, for a fixed gate voltage (greater than the threshold voltage value), as $V_{DS}$ is increased, the depletion region of

will correspondingly decrease, making it less inverted. Thus, in a MOSFET operating in inversion and with $V_{DS}>0$, the depletion region near the drain will be wider than at the source (i.e., assuming the source is the common terminal).

3. "Communication" with the channel also permits the diffused region to become an additional source (or sink) of mobile carriers to the channel (i.e., in addition to the carriers thermally generated in the depletion regions). As noted, two such diffused regions exist in a MOSFET, one which supplies mobile carriers (the source), and the other which removes them (the drain). Specifically, if a drain bias is applied to a MOSFET in inversion, the channel carriers will be attracted to and move into the drain. These are replenished by carriers entering the channel from the source. The resultant flow of charge in the channel constitutes a current in the drain terminal $I_D$. Since the channel is not a perfect conductor, this current also gives rise to a potential drop along the direction of the channel.

**4.2.1.6 Body Effect.** Until now we have chosen the substrate to be the reference terminal in the three-terminal MOS structure. However, when MOSFETs are used in circuits, the source terminal S (corresponding here to terminal C), is normally chosen to be the reference. Hence, *body effect* is the term used to describe the increase in the threshold voltage of a MOSFET (with reference to the source) upon the application of a reverse bias to the inversion layer. If, as shown in Fig. 4-4b, we choose terminal C to be the reference terminal (instead of the body terminal), the bias voltages are now applied between the gate and C ($V_{GC}$), and between the body and C ($V_{BC}$). In this case, for a given value of $V_{BC}$, a value of $V_{GC}$ greater than that needed when $V_{BC} = 0V$ must be applied to the MOS structure to establish strong inversion. In section 4.2.2.2 we will derive an expression that determines the increase in $V_T$ as a function of $V_{BC}$.

## 4.2.2 Quantitative Description of Effects of Biasing the Inversion Layer of MOS Structures

For the three-terminal MOS structure introduced above, it is possible to develop the quantitative relationships in a general manner for all cases of inversion. However, these can also be simplified somewhat for the more limited (but still most widely used form) of the strong inversion case. Note that in deriving these expressions we also include $V_{FB}$, which accounts for the work-function difference and oxide charge that can exist in 'real' MOS structures.

**4.2.2.1 General Inversion Case.** In the general inversion case (which covers weak as well as strong inversion), five equations characterize the phenomena in the channel region (i.e., the Si region in the vicinity of the Si-$SiO_2$ interface to the right of the $n^+$ junction in Fig. 4-3a) of three-terminal MOS structure (as they do for the MOS-C). If we invoke the charge-sheet and depletion approximations, four of these equations are identical to those for the expressions derived for the charge-sheet model of the MOS-C, and are repeated here for the readers convenience:

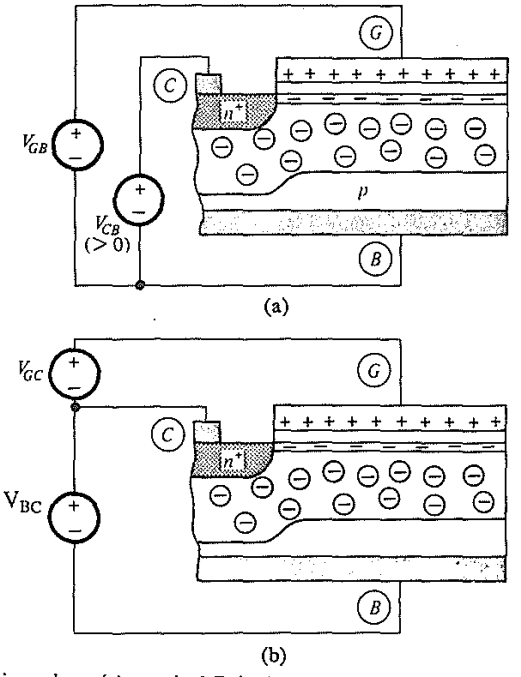


**Fig. 4-4** Bias notation when: (a) terminal B is the reference terminal; (b) terminal C as the reference terminal instead of terminal B.[5] Reprinted with permission of McGraw-Hill Co.

$$V_{GB} = \varphi_{surf} + V_{FB} + \varphi_{ox} \qquad (3\text{-}10) \qquad (4\text{-}1a)$$

$$Q_C = Q_I + Q_B \qquad (3\text{-}20) \qquad (4\text{-}1b)$$

$$Q_C = -C_{ox}\varphi_{ox} \qquad (3\text{-}19) \qquad (4\text{-}1c)$$

$$Q_B = -\gamma C_{ox}\sqrt{\varphi_{surf}} \qquad (3\text{-}29) \qquad (4\text{-}1d1)$$

$$= [2qN_A\kappa_{si}\varepsilon_o(\varphi_{surf})]^{1/2} \qquad (4\text{-}1d2)$$

The fifth equation is a modified form of Eq. 3-53, in which we replace $2\varphi_B$ by $(2\varphi_B + V_{CB})$ to get

$$Q_I = \sqrt{2q\,N_A\kappa_{Si}\varepsilon_o}\left(\sqrt{\varphi_{surf} + \varphi_t\, e^{(\varphi_{surf} - 2\varphi_B - V_{CB})/\varphi_t}} - \sqrt{\varphi_{surf}}\right) \qquad (4\text{-}2)$$

Then, combining Eqs. 4-1a, 4-1c, and 4-1b we get

$$V_{GB} = \varphi_{surf} + V_{FB} - [Q_I(\varphi_{surf}) + Q_B(\varphi_{surf})]/C_{ox} \qquad (4\text{-}3)$$

Next, using Eqs. 4-1d1 and 4-2 in Eq. 4-3, $V_{GB}$ can be written as

$$V_{GB} = \varphi_{surf} + V_{FB} + \gamma\sqrt{\varphi_{surf} + \varphi_t e^{(\varphi_{surf} - 2\varphi_B - V_{CB})/\varphi_t}} \qquad (4 - 4)$$

Now, if $V_{GB}$ and $V_{CB}$ are given, Eq. 4-4 can be solved iteratively for $\varphi_{surf}$. This value can then be inserted into Eq. 4-2 to calculate $Q_I$, or into Eq. 4-1d2 to calculate $Q_B$.

An expression for $Q_I$ in terms of $\varphi_{surf}$ and $V_{GB}$ can also be derived from the above equations. That is, by inserting Eqs. 4-1c and 4-1d1 into Eq. 4-1b above, we get

$$- C_{ox}\varphi_{ox} = Q_I + \gamma C_{ox}\sqrt{\varphi_{surf}} \qquad (4 - 5)$$

Then, solving for $\varphi_{ox}$, and substituting the result into Eq. 4-1a, we obtain

$$Q_I = - C_{ox} (V_{GB} - V_{FB} - \varphi_{surf} - \gamma \sqrt{\varphi_{surf}}) \qquad (4 - 6)$$

**4.2.2.2 Strong Inversion Case.** For the three-terminal structure biased to strong inversion, the above general analysis can be simplified. That is, with $V_{CB} = 0V$, $\varphi_{surf}$ of the three-terminal MOS structure at the onset of inversion is $2\varphi_B$. With a reverse bias applied to the induced junction, the surface potential at the onset of strong inversion becomes

$$\varphi_{surf}(inv) \approx 2\varphi_B + V_{CB} \qquad (4 - 7)$$

Since the applied $V_{CB}$ extends the range of gate voltages under which the surface region remains in depletion, $d_{max}$ is now larger. The expression for $d_{max}$ for the case of an applied $V_{CB}$ is (assuming the depletion approximation):

$$d_{max} = [2\kappa_{si}\varepsilon_o(2\varphi_B + V_{CB})/qN_A]^{1/2} \qquad (4 - 8)$$

and the depletion layer charge (per unit area), $Q_{Bmax}$, when $d = d_{max}$ is expressed as

$$Q_{Bmax} = [2q\kappa_{si}\varepsilon_o N_A (2\varphi_B + V_{CB})]^{1/2} \qquad (4 - 9)$$

The expression for the inversion layer charge per unit area $Q_I$ in strong inversion in terms of $V_{GB}$ and $V_{CB}$ is

$$Q_I = - C_{ox} [V_{GB} - V_{FB} - 2\varphi_B - V_{CB} - \gamma (2\varphi_B + V_{CB})^{1/2}] \qquad (4 - 10)$$

Assuming again that $Q_I$ is negligible at the onset of inversion, the total charge per unit area in the semiconductor is given by $Q_B$. Hence, the gate-substrate bias at the onset of strong inversion is

$$V_{GB} = V_{FB} + \varphi_{surf} + \varphi_{ox} = V_{FB} + (2\varphi_B + V_{CB}) + \gamma (2\varphi_B + V_{CB})^{1/2} \qquad (4 - 11)$$

Noting that $V_{GC} = V_{GB} - V_{CB}$, the threshold voltage, referenced to terminal C, is given by the expression

$$V_T\,(\text{with ref. to term C}) = V_{T(ud,lc)} = V_{FB} + 2\varphi_B + \gamma\,(2\varphi_B + V_{CB})^{1/2} \quad (4 - 12)$$

Note that the term $\gamma$, which was defined in Eq. 3-60a as $[\sqrt{2qN_A\kappa_{Si}\varepsilon_O}]/C_{OX} = [\sqrt{2qN_A\kappa_{Si}\varepsilon_O}]t_{OX}/\varepsilon_{OX}$ is a factor which determines how much $V_T$ will increase when $V_{CB}$ is increased. Hence, $\gamma$ has been given the name *body effect coefficient.* By inspecting the expression for $\gamma$ we note that it predicts the body effect is stronger for heavier substrate dopings and/or thicker gate oxides. Conversely, the body effect can be made smaller by using lower doping concentrations and/or thinner gate oxides. Figure 4-5 shows the threshold voltage shift versus substrate bias for various $\gamma$ values.[26]

## 4.3 DEFINITION OF TERM: LONG-CHANNEL MOSFET

It is appropriate at this point to provide a detailed definition of the term *long-channel MOSFET.* From a qualitative perspective, long-channel MOSFETs are assumed to have channel regions sufficiently long and wide so that "edge" effects along the four sides of the channel can be neglected. Insofar as the channel length is concerned, we assume the channel length $L$ is much longer than the sum of the source and drain

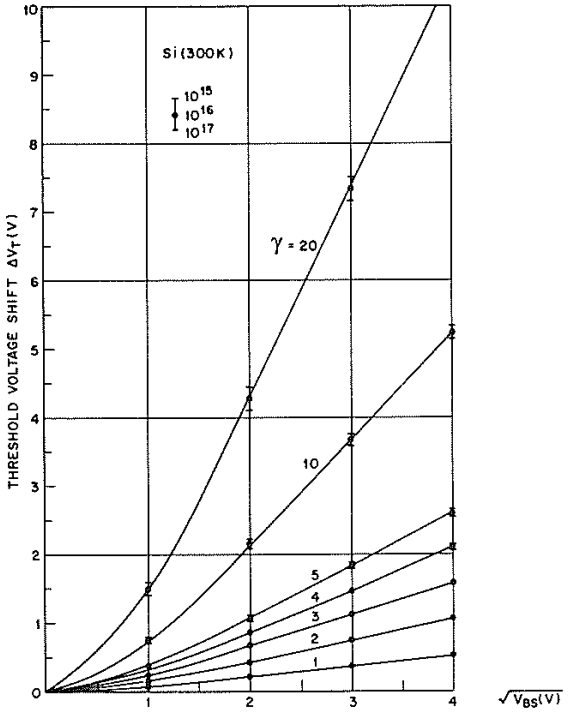


**Fig. 4-5** Threshold voltage shift versus substrate reverse bias for various $\gamma$ values.[2] Reprinted with permission of John Wiley & Sons.

depletion-region widths, or $L >> (d_{source} + d_{drain})$. The channel width, on the other hand is assumed to be much greater than the gate depletion-region depth, d (or Z>>d).

Even when the above criteria are well-satisfied, however, it is apparent that the electric fields and potential in the MOSFET still vary in at least two dimensions.* It seems that to accurately model device characteristics, the semiconductor device equations in their two-, or even three-dimensional forms must be solved. But in modeling long-channel MOSFET behavior this complexity can in fact be circumvented. That is, in such structures the solutions of the semiconductor device equations in their one-dimensional form yield drain-current device characteristics that are quite close to those obtained from measurements of actual long-channel MOSFETs.

Why is it possible to treat long-channel MOSFET behavior as a one-dimensional problem and still obtain relationships that give accurate estimates of $I_D$ as a function of the applied the terminal voltages? First, consider the case of the MOSFET in which no drain bias is applied, and $V_{GB}$ is the only external bias. We know that $V_{GB}$ produces an electric field perpendicular to the device surface. Now, if $L >> (d_{source} + d_{drain})$ the junctions extend over such a small fraction of $L$ that the $\mathcal{E}$-fields of these junctions have negligible impact on the $\mathcal{E}$-field due to the gate. Likewise, insofar as the channel width is concerned, if Z >>d the extension of the gate depletion region beyond the sides of the channel along which there is no source or drain hardly alters the total ionic charge uncovered by the gate voltage. Thus, the fringing field effect in the $z$ direction can also be ignored. If both of these conditions are met, we can approximate the $\mathcal{E}$-field in a long-channel MOSFET when $V_{DS}$ = 0V as being perpendicular to the surface everywhere along the channel. In this case, the one-dimensional analysis we applied to the MOS-C can also be used to determine $Q_I$, $\mathcal{E}$, $\varphi$ and $V_T$ in a long-channel MOSFET.

Next, if a drain bias $V_{DS}$ is simultaneously applied, we assume that in long-channel MOSFETs the *gradual-channel approximation* is valid. This approximation assumes that the two aspects of drain current flow can be treated as strictly one-dimensional, independent problems. The two aspects are: (1) that the gate field acts approximately vertically to induce the channel (i.e., the mobile charge concentration that participates in $I_D$), and; (2) that the drain-to-source voltage acts approximately horizontally to move these mobile charges, and thus to drive the current $I_D$ in the channel. The assumption that these two one-dimensional effects are independent of one another permits the results of the MOS-C analysis (shown to be valid in the case of a MOSFET with no drain bias), to also be applied when deriving the $I_D$-$V_{DS}$ relationship of the MOSFET. Since the gradual-channel approximation is such a key simplification invoked when developing the models of long-channel MOSFET behavior, we need to examine it more rigorously.

* This is the case whether or not a drain current flows in the MOSFET. That is, if a gate bias is applied, but $I_D$ = 0, there will still be electric fields arising from the source and drain junctions at the edges of the channel. If a drain current flows, it is obvious that there must be a component of the electric field along the y-direction. In fact, each of these cases should be examined separately when considering our definition in detail.

### 4.3.1 The Gradual Channel Approximation (GCA)

If a drain bias $V_{DS}$ is applied to a MOSFET in inversion, drain current $I_D$ flows. Owing to the channel's finite resistance and the passage of current, a potential variation occurs along the channel length (i.e., if the source is grounded, the channel potential near the source is close to ground, whereas near the drain it is close to $V_{DS}$). This causes the inversion-layer (mobile) charge density to decrease with position toward the drain because the gate is assumed to be an equipotential region (i.e., the voltage along the gate is invariant with position $y$ along the channel), making the gate-to-channel voltage decrease with position toward the drain. Since $I_D$ must remain constant at all points in the channel under dc biasing conditions, the electric field parallel to the flow of $I_D$ ($\mathcal{E}_y$) must increase toward the drain to offset the decrease in mobile charge density. Thus, a gradient in the $\mathcal{E}_y$ value must exist in the channel (i.e., $\partial\mathcal{E}_y/\partial y \neq 0$). The *gradual-channel approximation* (GCA), however, assumes that this gradient $\partial\mathcal{E}_y/\partial y$ is much smaller than the $\mathcal{E}$-field. gradient in the $x$-direction, $\partial\mathcal{E}_x/\partial x$ (i.e., $\partial\mathcal{E}_x/\partial x >> \partial\mathcal{E}_y/\partial y$).

The two-dimensional form of the Poisson equation with $\partial^2\varphi/\partial x^2$ and $\partial^2\varphi/\partial y^2$ replaced respectively by $-\partial\mathcal{E}(x,y)/\partial x$ and $-\partial\mathcal{E}(x,y)/\partial y$) can be written as:

$$\frac{\partial\mathcal{E}(x,y)}{\partial x} + \frac{\partial\mathcal{E}(x,y)}{\partial y} = \frac{\rho(x,y)}{\kappa_{si}\,\varepsilon_o} \qquad (4 - 13)$$

If the GCA approximation is valid, the $\partial\mathcal{E}(x,y)/\partial y$ term in Eq. 4-13 can be neglected. Then, Eq. 4-13 can be approximated as a one dimensional differential equation with the form:

$$\frac{d\mathcal{E}_x(x)}{dx} \approx \frac{\rho(x,y)}{\kappa_{si}\,\varepsilon_o} \qquad (4 - 13a)$$

The GCA is generally valid when the channel of the MOSFET is long enough (e.g., $L$ ~2 $\mu$m or longer), in which case the electric field strength along the $y$-direction $\mathcal{E}_y$ changes gradually from a small value near the source to values of the order of $V_{DS}/L$ near the drain. Thus, neglecting the $\partial\mathcal{E}(x,y)/\partial y$ term in such devices is appropriate, and the one-dimensional form of the Poisson equation is sufficiently accurate for calculating $Q_I$ used in the expressions for $I_D$. However, at large drain biases, the GCA always becomes invalid (even in long-channel MOSFETs), at least in a certain section of the channel near the drain where the gradient of the longitudinal field $\mathcal{E}_y$ becomes comparable to or larger than the gradient of the transverse field $\mathcal{E}_x$. In such cases, as will be described later, the drain current then becomes nearly independent of drain bias, and the MOSFET is said to be in *saturation*. This implies that under conditions of bias that cause saturation, the $I_D$ behavior of long-channel MOSFETs can no longer be adequately modeled by invoking the GCA along the entire length of the channel. Instead, modifications to the long-channel models must be made (as described in chap. 5).

The importance of being able to invoke the gradual channel approximation should be emphasized, as this is the basis of the derivation of the long-channel MOSFET $I_D$-$V_{DS}$ models. That is, by invoking the GCA, the problem of having to treat the semiconductor equations in their two-dimensional form to calculate $I_D$ in a MOSFET is

avoided. Instead, the task is broken down into two one-dimensional analyses, each independent of the other. As a result, $I_D$ is determined by the superposition of two one-dimensional solutions. Namely, by assuming that the *gradient* of the "horizontal" field in the channel is negligible, the one-dimensional *Poisson equation* can be solved to get the total charge in the silicon at each point $y$ along the channel (i.e., the sum of the inversion layer charge $Q_I$ [see Fig. 3-8] and the ionic charge $Q_B$ in the depletion region). This means that the same formulas derived for the MOS-C are also applicable for calculating the local values of $Q_I(y)$ and $Q_B(y)$ in the long-channel MOSFET (provided, of course, that the effect of the channel voltage caused by the drain-source bias is also included in the MOS-C formulas). Then we note that within the conducting channel of a MOSFET the current flows almost exclusively in the $y$-direction. Thus, we can ignore the fact that there must be a slight $x$-component in the "horizontal" $\mathcal{E}$-field. This allows us to solve the one-dimensional *drift-diffusion current-density equation* in the $y$ direction for $I_D$ as a function of the terminal voltages [using the local $Q(y)$ values obtained from the solution of the Poisson equation in this current-density equation].

Note, however, that if the GCA is not valid, but it is still invoked in order to enable one-dimensional analysis to be used for calculating $Q_I$, it is unlikely that accurate values of $I_D$ will be yielded This is the situation that arises in so-called short-channel devices (as described in chap. 5). In such cases, to obtain good agreement between calculated and measured values of $I_D$, the two-dimensional forms of the semiconductor equations must be solved (usually numerically).

**4.3.1.1 Verifying the Validity of the GCA as a Function of the Geometrical Factors of the MOSFET Device Structure and Bias Conditions.** The validity of the GCA for a particular MOSFET structure can be checked by making rough estimates of $\partial\mathcal{E}_x/\partial x$ and $\partial\mathcal{E}_y/\partial y$ values under given bias conditions. Since we are most interested in $I_D$ when the MOSFET is in strong inversion, we will establish expressions that allow the GCA to be tested if the MOSFET is being operated in strong inversion.*

We begin this derivation by recalling that under strong inversion the inversion layer charge density $Q_I$ is much larger than the ionic charge density $Q_B$ in the depletion region (see section 3.3.3), and that the inversion layer is very thin (~30-300Å). Thus, in strong inversion $\partial\mathcal{E}_x/\partial x$ in the silicon is greatest in the inversion layer region (see Fig. 4-6). Now $\partial\mathcal{E}_x/\partial x$ can be estimated by approximating the vertical electric field value at the bottom edge of the inversion layer as zero. Using this assumption implies that $\partial\mathcal{E}_x/\partial x \sim [\mathcal{E}_{si}(x=0) - 0]/t_{inv} = [\mathcal{E}_{si}(x=0)]/t_{inv}$, where $t_{inv}$ is the effective inversion layer

* Note that in weak inversion the surface potential $\varphi_{surf}(y)$ along the channel in long-channel MOSFETs is almost constant (see section 4.7). Thus, $\partial\mathcal{E}_y/\partial y$ is very small, implying that $\partial\mathcal{E}_x/\partial x >> \partial\mathcal{E}_y/\partial y$, because $\mathcal{E}_x$ drops from its value at $x = 0$ to zero at the bottom edge of the channel depletion region, which is a relatively small distance. Thus, in long-channel MOSFETs the GCA is also valid in weak inversion. However, in short-channel MOSFETs, this will no longer necessarily be the case, as we shall see in chap. 5.

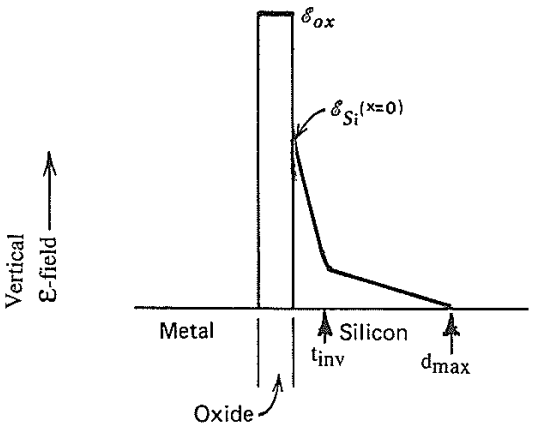


**Fig. 4-6** The vertical electric field in a MOS-C (or MOSFET channel) when a large enough gate bias to cause inversion is applied. Note that since $Q_I > Q_B$ in inversion, that the gradient of the $\mathcal{E}$-field over the inversion layer thickness $t_{inv}$ is larger than that over the depletion region width $d_{max}$, and we can therefore approximate the $\mathcal{E}$-field value at the bottom of the inversion layer thickness as being equal to zero for the purposes of estimating $t_{inv}$.

thickness. From Eq. 3-15, $\mathcal{E}_{si}(x=0) = \varepsilon_{ox}\mathcal{E}_{ox}/\kappa_{si}\varepsilon_o$, and from Eq. 3-14, $\mathcal{E}_{ox}$ is $\sim(V_{GS} - V_T)/t_{ox}$. Thus,

$$\frac{\partial \mathcal{E}_x}{\partial x} \approx \left(\frac{\varepsilon_{ox}}{\kappa_{si}\varepsilon_o t_{inv}}\right) \frac{(V_{GS} - V_T)}{t_{ox}} \qquad (4 - 14a)$$

Now, according to Eq. 3-12a, the concentration of electrons at some point in the semiconductor at equilibrium is exponentially dependent on the potential, with the exponential constant being $1/\varphi_t = kT/q$. This implies that the majority of the charges is contained within a distance from the surface over which $\varphi$ drops by $kT/q$ (i.e., since Eq. 3-12a predicts that if the electron concentration at the surface [x = 0] is $n_{surf}$, then at the point where the potential drops below $\varphi_{surf}$ by an amount $kT/q$, $n_{surf}$ will have dropped to a value 1/e of its value at x = 0, or to $0.37n_{surf}$). Thus, we assume that $t_{inv}$ is roughly equal to that distance below x = 0. If we also assume that the vertical electric field $\mathcal{E}_x$ in the inversion layer is roughly the potential difference across the inversion layer $\Delta\varphi_{inv}$ divided by its thickness $t_{inv}$ ($\mathcal{E}_x \sim \Delta\varphi_{inv}/t_{inv}$) we get $t_{inv} \sim (kT/q)/\mathcal{E}_{si}(x=0)$. Thus, substituting this expression for $t_{inv}$ into Eq. 4-14a we finally obtain the following expression for roughly estimating $\partial\mathcal{E}_x/\partial x$:

$$\frac{\partial \mathcal{E}_x}{\partial x} \approx \left(\frac{\varepsilon_{ox}}{\kappa_{si}\varepsilon_o}\right)^2 \frac{q\,(V_{GS} - V_T)^2}{kT\, t_{ox}^2} \qquad (4 - 14b)$$

If we also assume that the value of $\mathcal{E}_y$ varies gradually from a small value near the source to values of the order of $V_{DS}/L$ near the drain, $\partial\mathcal{E}_y/\partial y$ can be roughly estimated as $\partial\mathcal{E}_y/\partial y \sim V_{DS}/L^2$. Thus, if we assume that the GCA is valid when the ratio $(\partial\mathcal{E}_x/\partial x)/\partial\mathcal{E}_y/\partial y$ is large, then it is also valid if the following inequality is large

$$\frac{\partial\mathcal{E}_x/\partial x}{\partial\mathcal{E}_y/\partial y} = \left(\frac{\varepsilon_{ox}\, L}{\kappa_{si}\varepsilon_o}\right)^2 \frac{q\,(V_{GS} - V_T)^2}{kT\, t_{ox}^2\, V_{DS}} >> 1 \qquad (4 - 15)$$

For a MOSFET at 300K with $L = 1.0\ \mu m$, $t_{ox} = 300Å$, $V_{GS} - V_T = 0.5V$, and $V_{DS} = 0.5V$, the left-hand side of the inequality (4-15) is ~2300, indicating that the GCA is a very good approximation for such a MOSFET. This also implies that the GCA can be valid even in submicron MOSFETs, provided that $V_{GS} - V_T$ is not too small.

However, as we will see in chap. 5, $\mathcal{E}_y$ is quite non-uniform along the length of the channel at high values of $V_{DS}$, becoming much stronger near the drain. Furthermore, from Eq. 4-10 we note that the inversion layer charge density can be approximated as $Q_I \sim [V_{GS} - V_T - V(y)]$, if we replace $V_{GB}$ with $V_{GS}$, and $V_{CB}$ with $V(y)$ [where $V(y)$ is the channel voltage induced by $V_{DS}$]. However, this approximation is only valid when $Q_I$ is positive, i.e., when $V_{GS} - V_T > V(y)$. Thus, if $V_{DS}$ exceeds $V_{GS} - V_T$ (i.e., the condition which occurs in the region of the channel near the drain when the MOSFET is operated in saturation), the GCA becomes invalid in this region of the channel. [Because, when $V(y)$ is greater than $V_{GS} - V_T$, this implies that $\mathcal{E}_y > \mathcal{E}_x$, and that $\partial\mathcal{E}_y/\partial y$ is therefore at least comparable to, if not greater than, $\partial\mathcal{E}_x/\partial x$].

In summary, the GCA appears to be valid for MOSFETs operated in strong inversion even if the channel length is shorter than 1 $\mu m$ - provided that $V_{DS}$ is small enough that the MOSFET is not being operated in saturation (i.e., $V_{DS} \leq V_{DSsat}$, where $V_{DSsat}$ is the voltage at the onset of saturation). On the other hand, if the MOSFET is operated in saturation, use of the GCA to calculate $I_D$ will not yield accurate results, and alternative approximations (as described in chap. 5) must be employed to get good agreement with experimental $I_D$-$V_{DS}$ characteristics.

### 4.3.2 Circuit Characteristics of Long-Channel MOSFETs

From the perspective of the MOSFET as a circuit component, long-channel behavior has been specified in a number of ways. A list of device parameters from a circuit perspective deemed to be characteristic of long-channel MOSFETs include the following:

1. The threshold voltage $V_T$ is independent of channel length $L$.
2. The threshold voltage $V_T$ is independent of drain bias voltage, $V_{DS}$.
3. The drain current in saturation $I_{Dsat}$ is independent of $V_{DS}$.
4. The drain current has a linear dependence on $1/L$ (i.e., one quantitative criterion is that there should be no more than a 10% departure from linearity as the channel length is decreased).

5. The subthreshold current $I_{Dst}$ is independent of drain bias.
6. The subthreshold swing $S_t$ is independent of gate length.

As the behavior of the MOSFET is described later in this chapter, the terms associated with these device characteristics will be defined and discussed in more detail.

## 4.4 QUALITATIVE DESCRIPTION OF MOSFET OPERATION

The operation of the MOSFET is first described from a qualitative perspective. Specifically, our goal is to qualitatively explain the so-called *static characteristics* of the MOSFET; i.e., the drain current characteristics of the MOSFET as a function of the applied dc terminal voltages $V_{GS}$ and $V_{DS}$. This behavior is normally depicted using an $I_D$-$V_{DS}$ plot, with $V_{GS}$ as the parameter.

For simplicity we consider an ideal (i.e., $V_{FB} = 0$) long-channel NMOSFET (*p*-type substrate) as our example device structure, with the source being chosen as the reference terminal (Fig. 4-4b). We also assume that the source-substrate and drain-substrate junctions are always kept under reverse bias and that the resulting reverse-bias leakage currents are negligible (this is valid as long as the bias voltage is kept smaller than the junction breakdown voltage), and that $V_{SB} = 0V$. We also use energy-band versus position and potential versus position diagrams to help depict the qualitative MOSFET behavior. Note that in the case of the MOS-C one-dimensional diagrams were adequate. Here, however, two-dimensional energy-band and potential diagrams must be used. Axes and terminal voltage designations are the same as in Fig. 4-2a.

### 4.4.1 MOSFET Behavior in Response to Gate Bias Alone

We begin by describing how a MOSFET behaves in response to a gate bias $V_{GS}$ alone. In this case, the region under the oxide responds in the same way as does an ideal MOS-C. However, because the source and drain regions are present in a MOSFET the overall device behavior differs from that of a MOS-C with a $V_{GB}$ applied.

To analyze the MOSFET behavior, let us assume that all three bias voltages are initially set to zero (i.e., $V_{GS} = V_{DS} = V_{BS} = 0V$). In this case a flat band condition in exists in the gated region of the MOSFET (as is also observed when $V_{GB} = 0V$ in an ideal MOS-C). The two-dimensional energy-band diagram corresponding to this condition is shown in Fig. 4-7b. We observe that $E_c$ in the *x*-direction at the cut A-A is indeed flat. (The potential versus position diagram in the MOSFET for this bias condition is also shown in Fig. 4-8b). Assuming that $\varphi(x = \infty) = 0$, in this case $\varphi_{surf} = 0$ as well.)

At the surface ($x = 0$), however, a potential energy barrier of value $qV_{bi}$ exists between the *p* region and each of the $n^+$ regions (where $V_{bi}$ is the built-in potential of the *doped* $pn^+$ junction). This is shown in the $E_c$ versus *y* direction plot for $x = 0$ in Fig. 4-7b. For this case (and for cases of when a reverse bias exists across the doped junctions) only the very small leakage current of a reverse-biased *pn* junction flows.

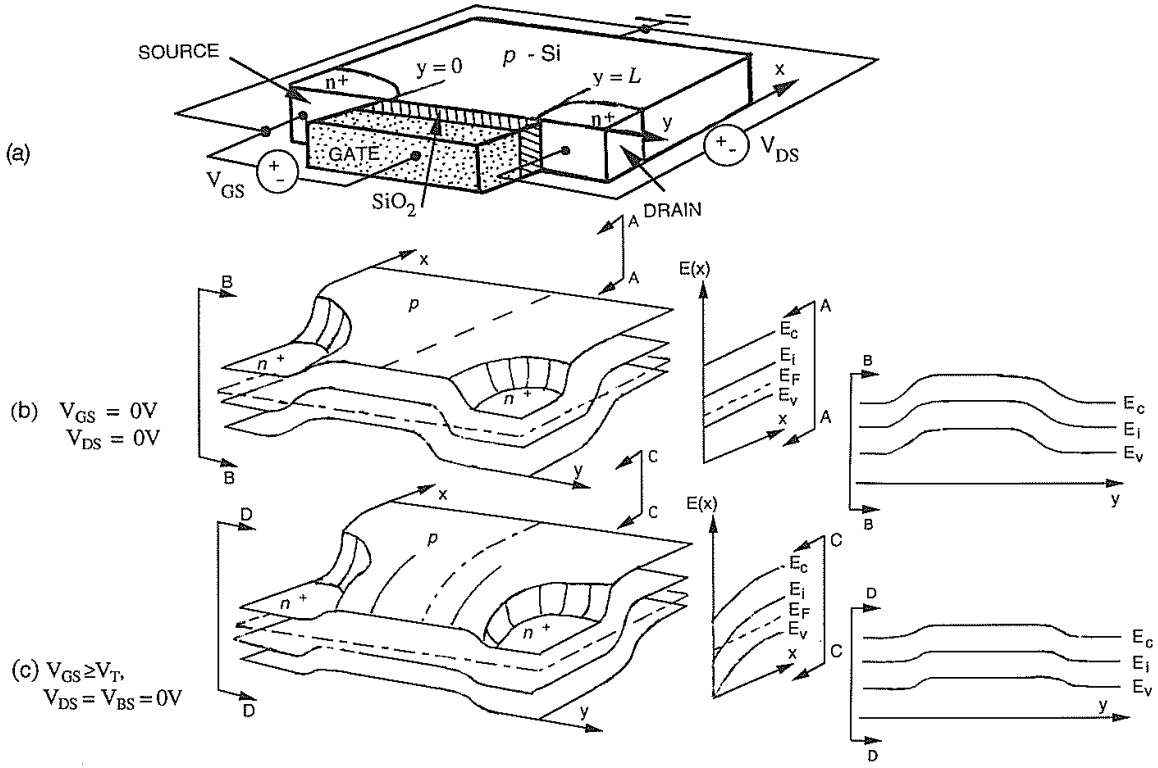


**Fig. 4-7** (a) Cross section of an NMOS device. (b & c) 2-D perspective plots of the energy bands versus position of an ideal long-channel NMOS device when (b) $V_{GS} = 0V$ (flat-band condition), and $V_{DS} = 0V$; and (c) $V_{GS} > V_T$, $V_{DS} = V_{BS} = 0V$.

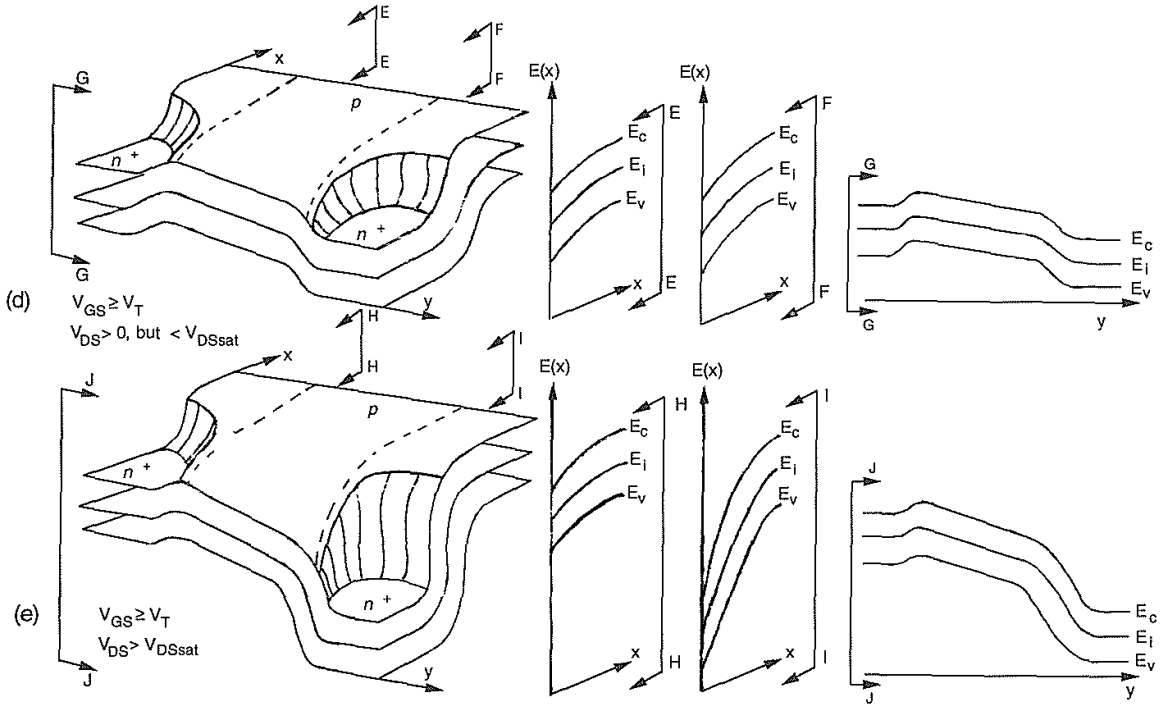


**Fig. 4-8** (cont.) (d & e) 2-D perspective plots of the energy bands as a function of position an ideal long-channel NMOS device when: (d) $V_{GS} \geq V_T$ and $V_{DS}$ is small (i.e., $< V_{DSsat}$); and (e) $V_{GS} \geq V_T$ and $V_{DS} > V_{DSsat}$. $V_{BS} = 0$ in both cases.

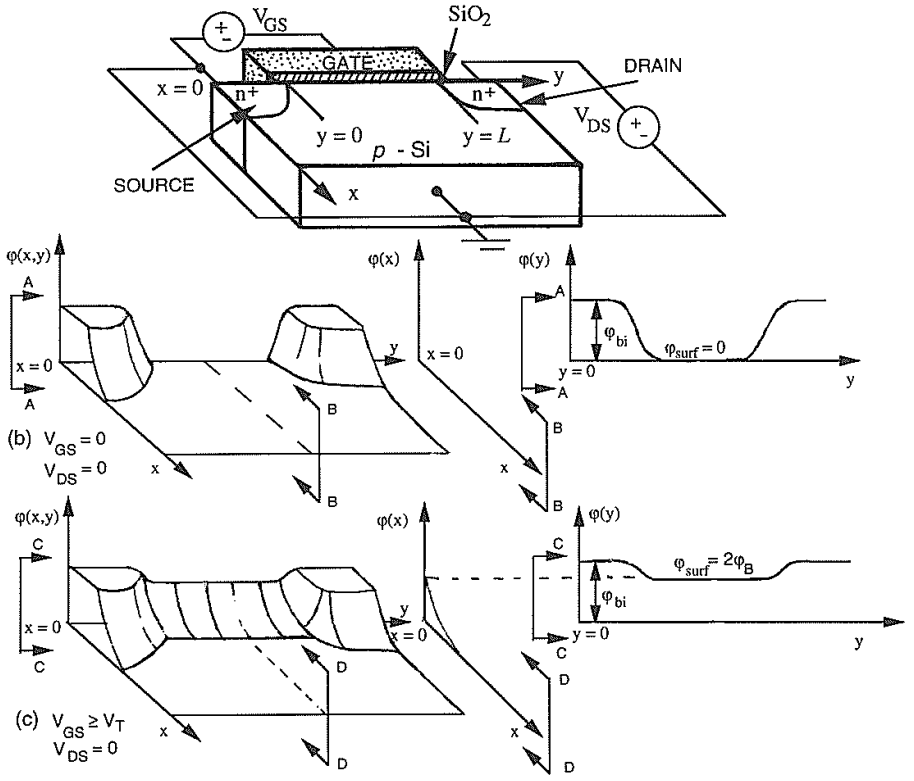


**Fig. 4-8** (a) Cross section of an NMOS device. (b & c) 2-D perspective potential versus distance diagrams of an ideal NMOS device when: (b) $V_{GS} = 0V$ (flat-band condition), and $V_{DS} = 0V$; and (c) $V_{GS} \geq V_T$, $V_{DS} = V_{BS} = 0V$.

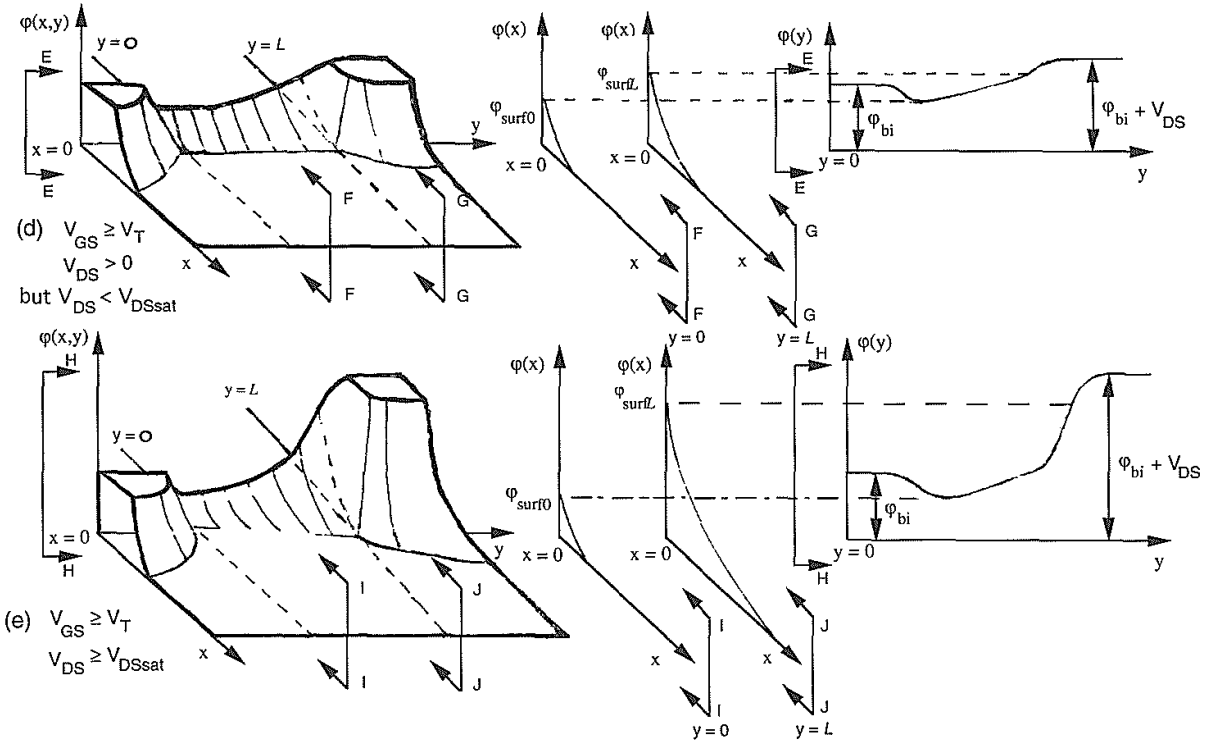


**Fig. 4-8** (cont.) (d & e) 2-D perspective potential versus distance diagrams of an ideal long-channel NMOS device when (d) $V_{GS} \geq V_T$ and $V_{DS} > 0V$, but $< V_T$; and (e) $V_{GS} > V_T$, and $V_{DS} > V_{DSsat} \sim V_{GS} - V_T$.

Thus, the circuit path between the $n^+$ source and drain regions effectively appears as an open circuit. This means that even if a voltage is applied between the source and drain ($V_{DS} \neq 0V$), essentially no drain current will flow. Moreover, if we apply either a negative $V_{GS}$ (or a positive $V_{GS}$ such that $V_{GS} < V_T$,) the gated region contains either an excess of holes (*accumulation*, when $V_{GS} < 0V$) or a deficit of holes and very few electrons (*depletion*, when $V_{GS} < V_T$). In this case, the circuit path between source and drain still appears essentially as an open circuit. That is, no current flows in the drain terminal even if a drain voltage is applied. For all of these conditions, the MOSFET is said to be in an "OFF" state.

If a positive $V_{GS}$ is applied such that $V_{GS} > V_T$, an inversion layer containing mobile electrons is formed adjacent to the Si surface throughout the entire gated region between the source and drain (here we still assume that $V_{DS} = V_{BS} = 0V$). Thus, the circuit path between source and drain now contains an induced "*n*-type" region (the inversion layer), as shown in Fig. 4-9. This means that a conducting path or *channel* exists between the source and drain. (However, if $V_{DS} = 0V$, no drain current will yet flow.) Now, if a drain voltage is applied (i.e., $V_{DS} > 0V$), drain current will flow. The device in this state is said to be "ON." Obviously, the larger the value of gate voltage ($V_{GS}$), the more electrons pile up at the Si surface, and the greater the conductance of this channel. This demonstrates that the input voltage to the MOSFET can induce a source-to-drain channel and will determine the maximum conductance of the channel.*

Figure 4-7c shows the energy band diagram of the MOSFET when $V_{GS} > V_T$ and $V_{DS} = V_{BS} = 0V$, and Fig 4-8c also shows the potential diagram for this case. Note that the bands along the *x*-direction in the gated region are no longer flat (see section B-B) and that $\varphi_{surf} > 2\varphi_B$ everywhere along the channel. The potential-energy barrier between the $n^+$ and *p* regions is also reduced (see the $E_c$ versus *y* plot in Fig. 4-7c). Hence, only a very low barrier to current injection exists between the source and the channel. The barrier height is smallest at the surface with its value controlled by the bias on the gate. At strong inversion and beyond, the barrier height is assumed to be remain constant at $\sim q(V_{bi} - 2\varphi_B)$, because $\varphi_{surf}$ is assumed to be clamped at $2\varphi_B$ in strong inversion. However, as $V_{GS}$ is increased, the inversion charge density continues to increase, increasing the conductance of the channel

## 4.4.2 Qualitative MOSFET Behavior when both Gate and Drain Bias are Applied

We now consider the variation of $I_D$ with $V_{DS}$. At first we assume that $V_{GS}$ is kept fixed at a single value while $V_{DS}$ is varied, and $V_{BS} = 0V$. Later we show how varying the value of $V_{GS}$ impacts the $I_D$-$V_{DS}$ characteristic. In this section we also assume that

* Note that when $V_{GS}$ is positive but smaller than $V_T$, the gated region can be in state of weak inversion. In weak inversion only small, so-called *subthreshold currents* are able to flow between the drain and source. These subthreshold currents are not large enough to be useful as driving currents for most applications, but they are sufficiently large to cause troublesome leakage - which can complicate the design of some circuits. We will describe subthreshold currents in more detail in section 4.7 and in chap. 5, as part of discussion on the quantitative behavior of the long-channel MOSFET and the submicron MOSFET.

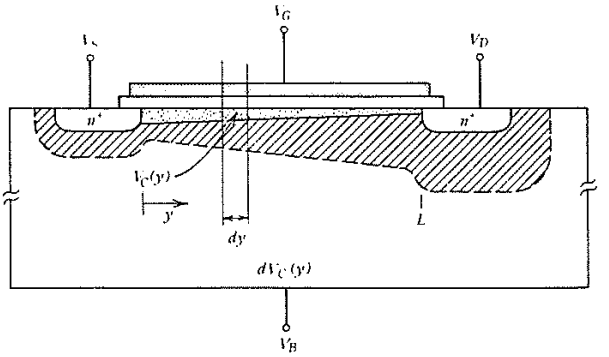


**Fig. 4-9** Depletion region width variation from source to drain end of a MOSFET when $V_{DS}$>0V.

sufficient gate bias is applied to ensure that the MOSFET is being operated in inversion (i.e., $V_{GS} > V_T$). We then describe what happens as a dc $V_{DS}$ is applied, with its value being increased in small steps, starting from $V_{DS} = 0V$.

As noted earlier, when $V_{DS} = 0V$, $I_D = 0$, even if $V_{GS} > V_T$ (see Fig. 4-10b). However, when $V_{DS}$ is increased slightly, $I_D$ starts to flow. When $V_{DS}$ is small (i.e., a few tenths of a volt or less), the surface channel behaves like a simple resistor (Fig. 4-10c). That is, an $I_D$ proportional to $V_{DS}$ flows into the drain. If a plot of $I_D$ versus $V_{DS}$ is used to demonstrate the $I_D$-$V_{DS}$ behavior, the response to small values of $V_{DS}$ is shown as the line from the point 0 to the point A in Fig. 4-10a.

When $V_{DS}$ is increased beyond a few tenths of a volt, the MOSFET exhibits a new phase of behavior. That is, current flowing in the channel gives rise to a significant voltage drop in the channel (unlike the case in the three-terminal structure introduced in section 4.2.1, where the channel voltage is constant along the entire channel length because essentially no current flows along it). Specifically, the *channel voltage* (introduced in section 4.2.1) is $V_{DB}$, at the drain end and $V_{SB}$ at the source end. If $V_{SB} = 0V$, the channel voltage at the source end will equal zero. But even with $V_{SB} = 0V$, the channel voltage at the drain end will not be zero, since we assume $V_{DS} > 0V$. As shown in Fig. 4-9 such a non-zero $V_{DB}$ causes the depletion region under the gate to widen toward the drain end of the channel. As described in section 4.2.1, this implies that the mobile charge concentration in the inversion layer simultaneously decreases. The smaller number of carriers causes the channel conductance to decrease, which in turn is manifested as a smaller slope in the $I_D$-$V_{DS}$ characteristic as $V_{DS}$ is increased. As the drain voltage is further increased, the depletion region continues to widen and the slope of the I-V characteristic continues to decrease (see Figs. 4-10a and 4-10c).

The energy-band and potential diagrams of the MOSFET when both a small $V_{DS}$ and a $V_{GS} > V_T$ are applied are shown in Figs. 4-7d and 4-8d, respectively. Even if the drain voltage is small enough so that the entire surface region remains in inversion, we see that near the drain the band bending is larger than at the source (see the $E_C$ vs. $y$ diagram in Fig. 4-7d). This implies that the depletion region under the gate is wider there. Since the gate-to-body voltage is constant across the entire gated region, less voltage is

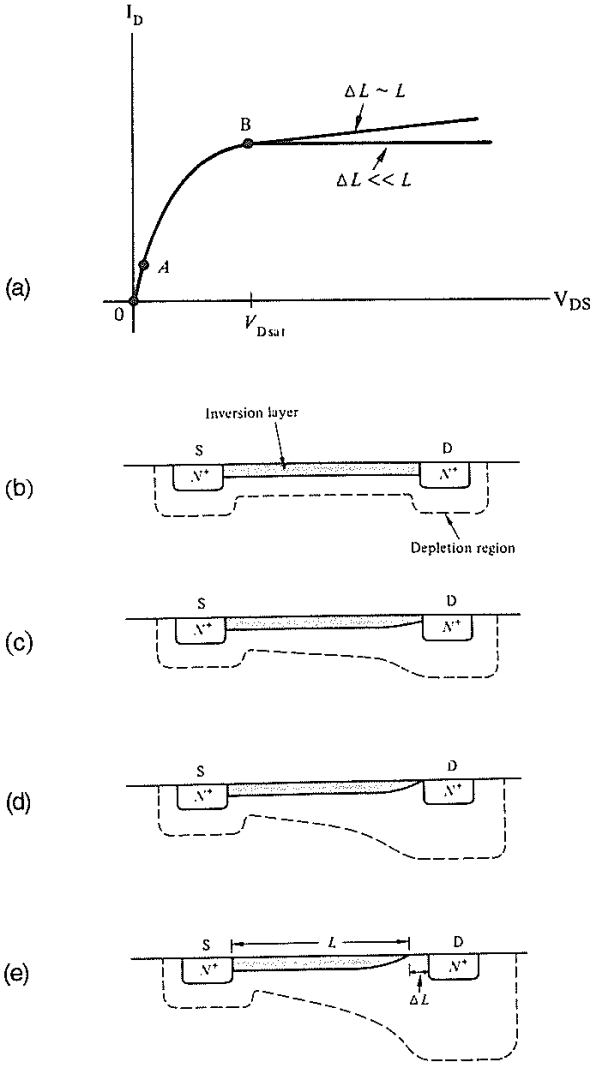


**Fig. 4-10** (a) $I_D$-$V_{DS}$ characteristic of a MOSFET being operated at a fixed $V_{GS}$, with $V_{GS}>V_T$. (b -e) Visualization of the various phases of $V_{GS}>V_T$ MOSFET operation: (b) $V_{DS}$ = 0V; (c) channel (inversion layer) narrowing under moderate $V_{DS}$ biasing; (d) pinchoff; and (e) post pinchoff ($V_{DS}>V_{DSsat}$).[30] Reprinted with permission of Addison-Wesley Pub. Co.

available near the drain to establish the inversion layer charge. Hence, inversion is less strong in the channel near the drain.

Eventually, if $V_{DS}$ is sufficiently increased such that $V_{DS}>(V_{GS} - V_T)$, the inversion layer ceases to exist near the vicinity of the drain. The disappearance of the inversion layer due to an increase in $V_{DS}$ is termed *pinch-off* (see Fig. 4-10d). The pinch-off point on the $I_D$-$V_{DS}$ characteristic is shown as point B in Fig. 4-10a. We see that the slope of the $I_D$ curve here has become approximately zero. Note, however, that pinch-off does *not* mean that $I_D$ vanishes as $V_{DS}$ exceeds the pinch-off voltage. In fact, it is the *gradual channel approximation* that is no longer valid in the region of the device in which pinch-off exists. That is, mobile charges still move through the depleted region near the drain, and drain current continues to flow. However, the equations for the charge distribution derived from the one-dimensional solution of the Poisson equation (which are valid for the case of the MOS-C) predict that no mobile charge exists in the pinch-off region. But in the depleted pinched-off region the one-dimensional Poisson equation is no longer valid. Instead, a two-dimensional numerical analysis (or an analytical expression based on a modified 1-D form of the Poisson equation - see section 5.4.3.3) must be used to calculate the potential and carrier concentrations in the pinched-off device region. A detailed numerical analysis of the saturation range has been carried out using the two-dimensional device simulator MINIMOS.[3] This work showed that for voltages greater than $V_{DSsat}$ the current stream of the carriers moving into the pinched off region is no longer confined to the inversion layer region near the surface, but begins to move away from the surface and into the bulk. Note that this physical picture is plausible because once $V_{DS}$ becomes larger than $(V_{GS} - V_T)$ the polarity of the vertical electric field in the pinched-off region is reversed. This tends to push any mobile carriers flowing in the channel *away* from the surface. Thus, in the region of the channel where $V_{DS}>(V_{GS} - V_T)$ the mobile carriers flow toward the drain *beneath* the surface.

Nevertheless, as the drain voltage increases beyond the pinch-off voltage $V_{DSsat}$ the pinched-off section of the channel widens from just a point into a segment $\Delta L$ in length (see Fig. 4-10e). Most of the voltage drop in excess of $V_{DSsat}$ is dropped across this pinched-off section $\Delta L$. $I_D$ remains approximately constant (*saturated*) for drain voltages greater then $V_{DSsat}$ so long as $\Delta L<<L$. If $\Delta L$ becomes comparable to $L$ (which is a condition that may occur in short-channel MOSFETs), the same voltage drop appears across a shorter channel $(L - \Delta L)$, and the post-pinch-off current $I_{Dsat}$ in such devices will increase somewhat as $V_{DS}$ is increased further beyond $V_{DSsat}$. Figures 4-7e and 4-8e show the energy-band diagrams and potential diagrams, respectively, for a long-channel MOSFET biased into pinch-off.

The response of the long-channel MOSFET to separate manipulation of gate and drain dc biases has been qualitatively described up to this point. This has allowed us to visualize the general variation of $I_D$ with $V_{DS}$ for a fixed value of $V_{GS}>V_T$. To allow the complete set of $I_D$ versus $V_{DS}$ characteristics to be obtained, we need to combine the results from the individual cases. These are as follows:

For $V_{GS}<V_T$, no channel exists and $I_D \approx 0$ for all drain biases below junction breakdown. For each value of $V_{GS}>V_T$, a characteristic of the form shown in

Fig. 4-10a will be observed. Since the conductance of the channel will increase as $V_{GS}$ is made larger, the initial slope of $I_D$ will also become steeper with increasing $V_{GS}$. Furthermore, since the inversion layer contains more electrons, a larger value of $V_{DS}$ is needed to produce pinch-off ($V_{DSsat}$ increases for increasing $V_{GS}$.). Based on these phenomena, the static $I_D$-$V_{DS}$ characteristics assume the form shown in Fig. 4-11.

Let us next consider quantitative models which allow these static (i.e., dc) $I_D$-$V_{DS}$ characteristics to be accurately simulated.

## 4.5 QUANTITATIVE BEHAVIOR OF MOSFETS: DC CIRCUIT MODELS OF LONG-CHANNEL MOSFETS

Although the discussion in the previous section provides a qualitative picture of how a MOSFET operates, we need to express this behavior in quantitative form. Specifically, to design circuits with MOSFETs we must be able to calculate how much current is carried in the "ON" state of a MOSFET and how much leakage current flows in the "OFF" state. In short, we need the current-voltage characteristics of the MOSFET, specifically the quantitative relationship between the drain current and terminal voltages.

In this section our goal is to derive relationships that allow the dc drain current $I_D$ of long-channel MOSFETs to be quantitatively predicted. Such $I_D$-$V_{DS}$ relationships are referred to as the *static (dc) circuit models* of the MOSFET. As is the case for the MOS-C, there exists a hierarchy of such long-channel MOSFET $I_D$-$V_{DS}$ models in terms of their generality, accuracy, and complexity. Our discussion in this section will derive four of these models, using as our foundation two of the five classical semiconductor equations introduced in chap. 2: the one-dimensional Poisson equation, and the one-dimensional drift-diffusion current density equation (as well as the three models of the MOS-C derived in chap. 3).

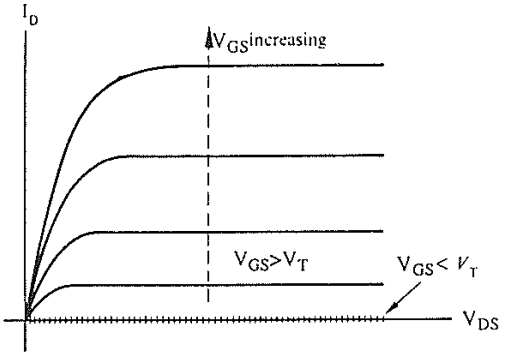


**Fig. 4-11** General form of the $I_D$-$V_{DS}$ characteristics expected from a long-channel MOSFET.

The first of these models is the *Pao-Sah* model, which is the most general and accurate of our four dc $I_D$ long-channel MOSFET models. Like the general MOS-C model, it also the most computationally complex (in that it requires numerical analysis techniques to calculate $I_D$ for a given set of terminal voltages). The three less-computationally complex long-channel models are derived from the Pao-Sah model by making suitable simplifying approximations. The first of these that we will study is the *charge-sheet MOSFET* model. It is based on the same assumptions used in the MOS-C charge-sheet model introduced in chap. 3. Unlike the Pao-Sah model, it provides an analytical expression for $I_D$ in terms of $V_{GB}$ and $\varphi_{surf}$, and thus involves much less computational effort. Nevertheless, it is only slightly less accurate than the Pao-Sah model provided the MOSFET is operated in inversion (i.e., this model is valid from weak through strong inversion). However, while this model provides an analytical expression for $I_D$, it still requires a numerical procedure to obtain the values of the surface potential needed to evaluate the $I_D$ expression. That is, $I_D$ is not explicitly stated in terms of the terminal voltages. (The terminal voltage values are used to first calculate $\varphi_{surf}$, which is then used to compute $I_D$.) Thus, the charge-sheet model is still too cumbersome to serve as a MOSFET model for most circuit-simulation applications.

By making suitable approximations that are valid over a more limited range of operation (namely, the strong inversion regime), two simpler long-channel MOSFET models have been derived that are extensively used in circuit analysis and design. They are the *variable depletion-charge* and the *square-law* models. These provide analytical expressions which give $I_D$ explicitly in terms of the terminal voltages. We show how they can be derived from the charge-sheet model by making additional simplifying assumptions. At the end of the section we compare these four models in more detail.

### 4.5.1 General Approach to Deriving the DC Drain-Current Relationships in Long-Channel MOSFETs

The derivation of the dc drain current relationship recognizes that, in general, the current in the channel of a MOSFET can be caused by both drift and diffusion current. In an NMOSFET we can accurately assume that only electrons contribute to the drain current. Thus, we only need to use Eq. 1-5a to describe the drain current density $J_D$

$$J_D = J_n = q\,\mu_n\, n\,\mathcal{E} + q\,D_n\,\nabla n \qquad (4\text{ - }16)$$

Within the conducting channel of a MOSFET the current flows almost exclusively in the *y*-direction, thus Eq. 4-14 can be simplified to the following one-dimensional form:

$$J_D \approx J_{ny} = q\,\mu_n\, n\,\mathcal{E}_y + q\,D_n\,dn/dy = -q\,\mu_n\, n\,d\varphi/dy + q\,D_n\,dn/dy \qquad (4\text{ - }16a)$$

Since we also assume there are no current sources or sinks inside the device, the current flowing through any cross-sectional plane within the channel must be constant, having some value $I_D$. We also assume that the current density is constant in the z-direction, but not necessarily in the *x*-direction. Hence, if $J_{ny}$ is integrated over Z we get

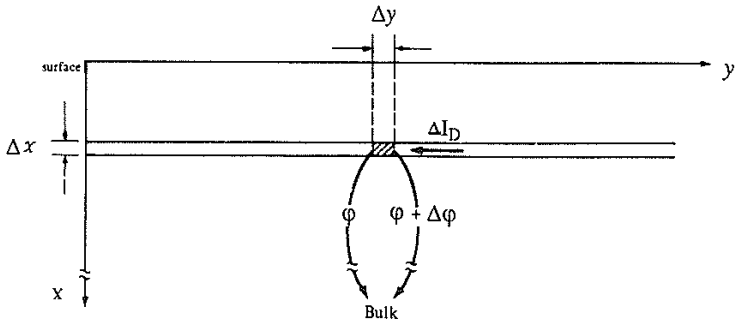


**Fig. 4-12** The drain current $I_D$ in a MOSFET can be modeled as the sum of currents in slices $\Delta I_D$ each having a thickness $\Delta x$ and a width Z. These slices exist from the surface to the depth at which the electron concentration becomes negligible.[5] Reprinted with permission of McGraw-Hill Book Co.

$$I_D = -\int\int J_{ny}\ dx\ dz = -Z\int_0^{x_c(y)} J_{ny}\ dx \qquad (4 - 17)$$

If the flow of electrons can be considered to be laminar, we can assume that the total current $I_D$ is the sum of elemental currents $\Delta I$, each flowing horizontally in an inversion layer slice parallel to the surface, having width Z and depth $\Delta x$, as shown in Fig. 4-12. If we allow $\Delta x$ to become a differential, the current in each slice $dI_D$ is

$$dI_D = dI_{Ddrift}(x,y) + dI_{Ddiff}(x,y) \qquad (4 - 18a)$$

Since $\mathcal{E}(y) = -d\varphi/dy$, the drift component of Eq. 4-18a can be written as

$$dI_{Ddrift}(x, y) = q\,\mu_n\,Z\,n(x, y)\,\partial\varphi(x, y)/\partial y \qquad (4 - 18b)$$

The diffusion component of Eq. 4-18b can also be rewritten as,

$$dI_{Ddiff}(x, y) = -Z\,q\,D_n\,\partial n(x, y)/\partial y = -Z\,\mu_n\,kT\,\partial n(x, y)/\partial y \qquad (4 - 18c)$$

since $D_n/\mu_n = kT/q$.

An expression for the total drain current for each of these components can be obtained by integrating each expression over the depth from $x = 0$ to a point below the surface at which the electron concentration is negligible, $x_c$ or

$$I_{Ddrift} = q\,\mu\,Z\frac{d\varphi}{dy}\int_0^{x_c(y)} n(x,y)\,dx \qquad (4 - 19)$$

$$I_{Ddiff} = -\mu Z kT \frac{d}{dy}\left[\int_0^{x_c(y)} n(x,y)\,dx\right] \qquad (4-20)$$

Since the charge per unit area due to carriers in the inversion layer, $Q_I$ is given by

$$Q_I(y) = -q\int_0^{x_c(y)} n(x,y)\,dx \qquad (4-21)$$

Thus, Eqs. 4-19 and 4-20 can be written as

$$I_{Ddrift} = \mu Z(-Q_I)\frac{d\varphi}{dy} \qquad (4-22)$$

and

$$I_{Ddiff} = \mu Z \frac{kT}{q}\frac{dQ_I}{dy} \qquad (4-23)$$

Our goal is to derive a model in which $I_D$ is expressed in terms of the terminal voltages $V_{GS}$ and $V_{DS}$. To do this we must integrate the sum of Eqs. 4-22 and 4-23. The integration is carried out by changing the variables of integration by multiplying both sides of Eqs. 4-22 and 4-23 by (dy). Since we recognize that $I_D$ is constant along the length of the channel, when we integrate the left hand side of the sum of Eqs. 4-22 and 4-23 (namely $I_D$[dy] from 0 to $L$) we get

$$I_D L = \int_0^L I_D\,dy \qquad (4-24)$$

Then we can write the total drain current $I_D$ as

$$I_D = \frac{\mu Z}{L}\int_{\varphi_{surf0}}^{\varphi_{surfL}} (-Q_I)\,d\varphi + \frac{\mu ZkT}{Lq}\int_{Q_{I,source}}^{Q_{I,drain}} dQ_I \qquad (4-25)$$

We see that the first term on the right hand side of Eq. 4-25 is no longer integrated with respect to position, but with respect to voltage. (In the *variable-depletion charge model* [section 4.5.4, Eq. 4-58], and the *square-law model* [section 4.5.5, Eq. 4-62], we assume that only the drift current term is needed to describe $I_D$. Hence, only this integral needs to be carried out to calculate $I_D$. By changing the variable of integration from position to voltage this integration becomes easy to perform, yielding Eqs. 4-58 and 4-62.) The limits of integration of the first term of Eq. 4-25 are the value of the surface potential at the source end $\varphi_{surf0}$ (which is usually set equal to zero), and the surface potential value at the drain end $\varphi_{surfL}$ (which is usually set to $V_{DS}$). The limits of the integration

of the second term are the value of the mobile charge density at the source end of the channel $Q_{Isource}$, and the value at the drain end $Q_{Idrain}$.

## 4.5.2 Pao-Sah Model

The *Pao-Sah* model,[4] published in 1966, was the first advanced long-channel MOSFET model to be developed. While it retained the gradual-channel approximation, it did not invoke the depletion approximation and permitted carrier transport in the channel by both drift and diffusion current. The formulation of the $I_D$ equation it develops is therefore quite general, but as a result requires numerical integrations in two dimensions. Such numerical complexity has limited the role of this model to theoretical analyses of the MOSFET. Other simpler models of the MOSFET have been developed for use in IC circuit design applications.

The Pao-Sah model follows the approach outlined in the previous section for deriving the $I_D$ relationship from the semiconductor device equations. However, the derivation is usually carried out using a more compact formulation, in which the drift and diffusion current expression are combined into a single equation. When we derive the charge-sheet MOSFET model we will return to calculating both current components separately, as this results in a simpler derivation. Here, the opposite is true, and so we also elect the single equation approach to deriving the Pao-Sah model. Note that the presentation of the derivation in this section, and the next, closely mimics the method proposed by Tsividis.[5]

We begin by noting that the Pao-Sah approach invokes the gradual channel approximation (like all long-channel MOSFET models), and assumes that $\mu$ is constant along the channel. In our derivation we also assume that the substrate doping is uniform and that an $n$-channel MOSFET is being treated.

To simplify the expression for $I_D$ so that it consists of one instead of two terms on the right hand side of Eq. 4-16, we start by noting that at the source end of the channel in the MOSFET (where $y = 0$), $n$ can be expressed in terms of $\varphi$ by

$$n\,(x, 0) = n_{po} \exp q[\varphi\,(x, 0) - V_{SB}]/kT \qquad (4 - 26)$$

and at the drain end by

$$n\,(x, L) = n_{po} \exp q[\varphi\,(x, L) - V_{DB}]/kT \qquad (4 - 27)$$

For an arbitrary position $y$ along the channel, $n$ is given by

$$n\,(x, y) = n_{po} \exp q[\varphi\,(x, y) - V_{ChB}(y)]/kT \qquad (4 - 28)$$

where $V_{ChB}\,(0) = V_{SB}$ and $V_{ChB}\,(L) = V_{DB}$. In Eq. 4-28, $V_{ChB}$ represents the potential corresponding to the difference between the quasi-Fermi level of the electrons in the inversion layer and the quasi-Fermi level of holes in the bulk, as shown in Fig. 4-13. That is, because the source and drain will in general be biased with respect to the substrate, the channel is also at some potential $V_{ChB}\,(y)$ relative to the substrate. Clearly this voltage is a function of position $y$ along the channel if $V_{DS} \neq 0$, because at the source end we have $V_{ChB}\,(0) = V_{SB}$ and at the drain end $V_{ChB}\,(L) = V_{DB}$.

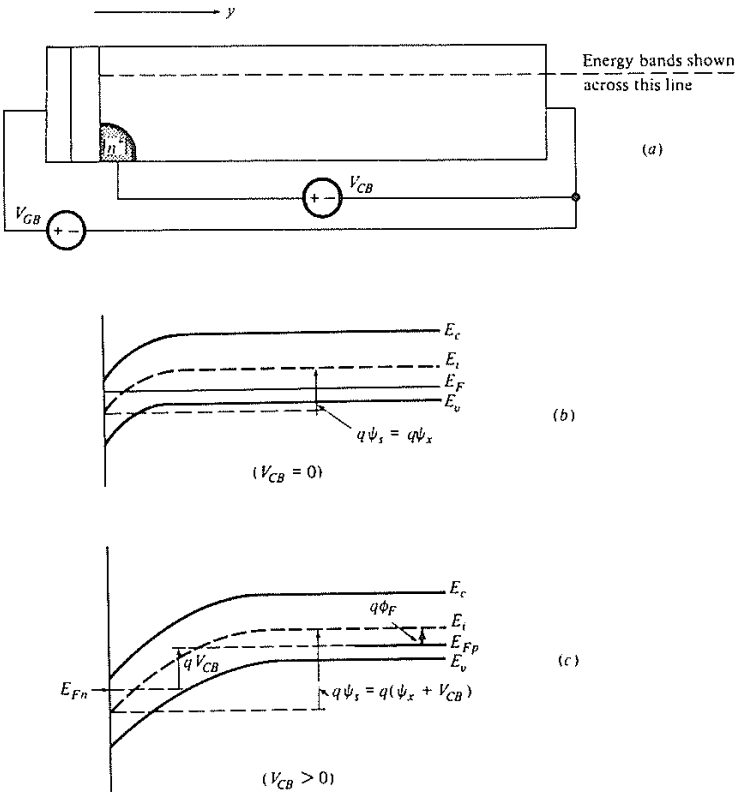


**Fig. 4-13** Energy-band diagram of a three-terminal MOS structure with a bias $V_{CB}$ (= $V_{ChB}$ in a MOSFET) showing how the applied bias $V_{CB}$ is related to the difference between the quasi-Fermi levels of the electrons in the inversion layer $E_{Fn}$ and that of the holes $E_{Fp}$.[5] Reprinted with permission of McGraw-Hill Book Co.

If Eq. 4-28 is differentiated with respect to $y$ we get

$$\frac{\partial n(x, y)}{\partial y} = \frac{q\, n(x, y)}{kT}\left[\frac{\partial \varphi(x, y)}{\partial y} - \frac{\partial V_{ChB}(y)}{\partial y}\right] \qquad (4\text{-}29)$$

Using Eq. 4-29 in Eq. 4-18 we obtain

$$d\, I_{Ddiff}(x, y) = -(Z\, dx)\, q\, \mu\, n(x, y)\left[\frac{\partial \varphi(x, y)}{\partial y} - \frac{\partial V_{ChB}(y)}{\partial y}\right] \qquad (4\text{-}30)$$

If Eq. 4-30 is inserted together with Eq. 4-17 into Eq. 4-16 it is seen that the $\partial\varphi/\partial x$ terms cancel out, leaving

$$d\,I_D\,(x, y) = (Z\,dx)\,q\;\mu\,n\,(x, y)\,\frac{dV_{ChB}(y)}{dy} \qquad (4 - 31)$$

As was done above for Eqs. 4-19 and 4-20, $I_D$ from Eq. 4-31 can be obtained by integrating from the surface to a depth $x = x_c$ beneath which the electron concentration is negligibly small

$$I_D = \mu\,Z\,\frac{dV\,(y)}{dy}\,q\int_0^{x_c(y)} n\,(x, y)\,dx \qquad (4 - 32)$$

From Eq. 4-21 we can write Eq. 4-32 as

$$I_D = \mu\,Z\,(-Q_I)\,\frac{dV\,(y)}{dy} \qquad (4 - 33)$$

Now, integrating over the channel length and using Eq. 4-24, we get

$$I_D = \frac{\mu\,Z}{L}\int_{V_{SB}}^{V_{DB}} (-Q_I)\,dV \qquad (4 - 34)$$

We can now rewrite the expression for $Q_I$ given by Eq. 4-21 as

$$Q_I = q\int_0^{x_c} n\,(x, y)\,dx = q\int_{\varphi_{surf}}^{\varphi_c} \frac{n\,(\varphi)\,d\varphi}{d\varphi/dx} \qquad (4 - 35)$$

If we define $\varphi_t = kT/q$ we can write $n\,(\varphi)$ in Eq. 4-35 as

$$n\,(\varphi) = N_A \exp\,[\varphi\,(x,y) - 2\varphi_B - V_{ChB}(y)]/\varphi_t \qquad (4 - 36)$$

because $p_{po} \approx N_A$, and $n_{po} = n_i^2/N_A$, and $\varphi_B = kT/q \ln\,(N_A/n_i)$. Thus,

$$(N_A/n_i)^2 = \exp\,(2\varphi_B)/\varphi_t \qquad (4 - 37)$$

Solving Eq. 4-37 for $n_i^2$ and substituting the result for $n_i^2$ into $n_{po} = n_i^2/N_A$, we get

$$n_{po} = N_A \exp\,(-2\varphi_B/\varphi_t). \qquad (4 - 38)$$

In addition, we recall that $\mathcal{E}(x) = -\,d\varphi/dx$. In chap. 3 we derived an expression for $\mathcal{E}(x)$ in a MOS-C in which both electrons and holes were allowed in the depletion region of the semiconductor. This expression, with $\varphi$ being replaced by $\varphi \dashrightarrow \varphi + V_{ChB}$, is the expression we use for $d\varphi/dx$ in the denominator of Eq. 4-35. That is, $\mathcal{E}(x)$ is now

$$-\frac{d\varphi}{dx} = \mathcal{E}(\varphi) = \sqrt{\frac{2q\,N_A}{\kappa_{Si}\varepsilon_0}}\sqrt{\varphi_t e^{-(\varphi + V_{ChB})/\varphi_t} + \varphi - \varphi_t + e^{-2\varphi_B/\varphi_t}\left(\varphi_t e^{-(\varphi + V_{ChB})/\varphi_t} - \varphi - \varphi_t\right)} \tag{4 - 39}$$

Then substituting Eqs. 4-36 and 4-39 into Eq. 4-35 we obtain the *Pao-Sah $I_D$ expression* *

$$I_D = \frac{q\,\mu\,Z\,N_A}{L}\int_{V_{SB}}^{V_{DB}}\int_{\varphi_{surf}}^{0}\left[\{e^{(\varphi - 2\varphi_B - V_{ChB})/\varphi_t}\}/\,\mathcal{E}(\varphi)\right]\,d\varphi\,dV \tag{4 - 40}$$

In this equation, we must first calculate the limit of integration $\varphi_{surf}$ by using

$$V_{GB} = V_{FB} + \varphi_{surf} \tag{4 - 41}$$

$$+\ \gamma\sqrt{\varphi_t e^{-(\varphi_{surf} + V_{SB})/\varphi_t} + \varphi_{surf} - \varphi_t + e^{-2\varphi_B/\varphi_t}\left(\varphi_t e^{-(\varphi_{surf} + V_{SB})/\varphi_t} - \varphi_{surf} - \varphi_t\right)}$$

where $\gamma = \sqrt{2\kappa_{Si}\varepsilon_0 N_A/C_{ox}}$. Note that this equation must be solved iteratively for $\varphi_{surf}$.

To solve for $I_D$ once $\varphi_{surf}$ is obtained, Eq. 4-40 must be solved numerically. This involves numerically evaluating the double integral in Eq. 4-40. This is a computationally lengthy procedure. Nevertheless, the Pao-Sah model has been found to accurately predict the $I_D$ in long-channel MOSFETs.

Figure 4-14 is an example of the $I_D$-$V_{DS}$ characteristics of a long-channel MOSFET

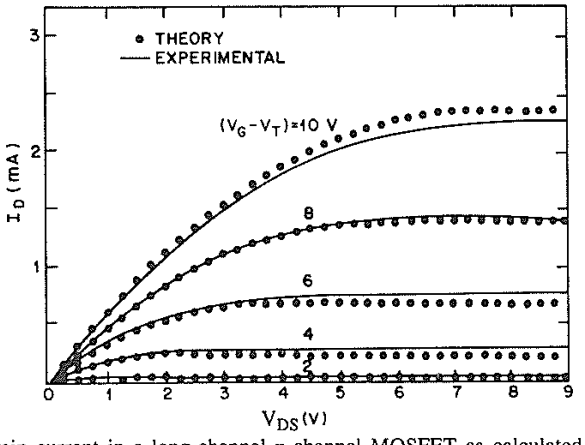


**Fig. 4-14.** Drain current in a long-channel *p*-channel MOSFET as calculated with the Pao-Sah model (dots) and as measured (solid lines).[4] Reprinted with permission of Solid-State Electronics.

* If $V_{BS} = 0V$, the limits of the voltage integral become 0 and $V_{DS}$, respectively.

calculated with the Pao-Sah model, together with experimentally measured results. We see that the agreement between measured and predicted $I_D$ values is excellent.

The computational complexity of the Pao-Sah model, however, makes it impractical for use as a MOSFET model in circuit simulation applications. Thus, we show how simpler analytical models can be developed by limiting the validity of the model to reduced regimes of operation. We also mention that an approach has been proposed to reduce Eq. 4-40 to a single-integral formula (which, however, must still be evaluated numerically).[6] However, we do not discuss this approach here.

### 4.5.3 The Charge Sheet Model

The limited practical utility of the Pao-Sah model motivated a search for an approximate advanced analytical model that still was accurate over a wider range of operating conditions than the earlier *variable depletion-charge* (introduced in 1964) and *square law* models, which are only valid if the MOSFET is operated in strong inversion. The charge-sheet MOSFET, introduced separately by Bacarani[7] and Brews[8] in 1978, has become the most widely adopted long-channel MOSFET model that is accurate over the entire range of inversion.

The charge-sheet model of the long-channel MOSFET makes some simplifying assumptions so the numerical analysis needed in the Pao-Sah model to calculate $I_D$ can be avoided. By doing so, it develops an analytical closed-form expression for $I_D$ in terms of $V_{GB}$ and the surface potential at the drain and source ends of the channel.* It is somewhat less general than the Pao-Sah model in that it is not valid if the MOSFET is operated in depletion or accumulation. However, it is only slightly less accurate than the Pao-Sah model if the MOSFET is being operated in inversion. Hence, by using this model it is possible to get quite accurate predictions of $I_D$ in these regimes without having to resort to the complex numerical analysis required by the Pao-Sah model.

We introduced the charge-sheet approximation for the MOS-C in chap. 3. The MOSFET model is based on essentially the same approximations, with a few more added to account for the current flow behavior of the MOSFET. That is, the charge-sheet approximation basically assumes that the inversion layer (both in weak and strong inversion) can be treated as an infinitesimally thin sheet of charge at the Si surface, and that the depletion approximation is valid for the depletion region below the inversion layer. As such, the inversion-layer charge density $Q_I$ can be found by subtracting the ionic charge in the depletion region $Q_B$ from the total charge in the semiconductor $Q_C$.

The other assumptions of the charge-sheet model of the MOSFET are the following:

1. The gradual channel approximation applies to the MOSFETs being treated by this model.
2. The drain current consists of both drift and diffusion components.
3. The mobility $\mu$ in the channel is proportional to the electric field and is constant with position along the channel.

* Although, as we shall see, a numerical iteration procedure must be used to determine these surface potential values from the terminal voltages.

We begin the derivation of the charge-sheet $I_D$ model by assuming that $I_D$ consists of both drift and diffusion current components. Since we also assume that the mobile charge is located in a very thin region near the surface, all the current is located at one depth (i.e., there is no $x$-dependence of current). Hence, Eq. 4-16 can be expressed as

$$I_D(y) = I_{Ddrift}(y) + I_{Ddiff}(y) \tag{4 - 42}$$

Now, we consider each of these terms separately. To express $I_{Ddrift}$, we treat a small element of the inversion layer between $y$ and $\Delta y$, as depicted in Fig. 4-15. The potential difference across this element is given by the difference of $\varphi_{surf}$ at the points $y$ and $y + \Delta y$, or $\varphi_{surf}(y + \Delta y) - \varphi_{surf}(y)$. Hence we can write an expression for the drift current using Eq. 4-22 with $\Delta\varphi(y)$ replaced by $\Delta\varphi_{surf}(y)$. In addition, we can express this equation in terms of the mobile charge density per unit area $Q_I$ instead of in terms of $n$ by multiplying the mobile charge density in the channel ($qn$) by the inversion layer thickness $t_{inv}$, or $Q_I = -q\, n\, t_{inv}$. Since $I_{Ddrift}(y) = A\, J_{drift} = Z\, t_{inv}\, J_{drift}$, $I_{Ddrift}(y)$ becomes

$$I_{Ddrift}(y) = \mu Z(-Q_I)\, \Delta\varphi_{surf}(y)/\Delta y \tag{4 - 43}$$

If we allow $\Delta y$ to approach zero we get

$$I_{Ddrift}(y) = \mu Z(-Q_I)\, d\varphi_{surf}/dy \tag{4 - 44}$$

The diffusion component of Eq. 4-42 can likewise be rewritten as

$$I_{D\,diff}(y) = Z D\, dQ_I/dy = Z \mu (kT/q)\, dQ_I/dy \tag{4 - 45}$$

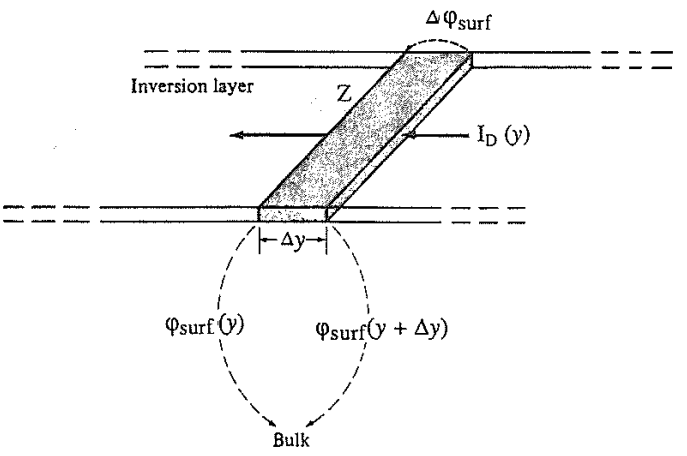


**Fig. 4-15** Small element of the inversion layer in a long-channel MOSFET.[5] Reprinted with permission of McGraw-Hill Book Co.

In the case of dc biasing, the total current in the channel must be constant for all points in the $y$-direction. Thus, Eq. 4-42 can be written as

$$I_D(y) = \mu Z(-Q_I)\, d\varphi_{surf}/dy + Z\mu(kT/q)\, dQ_I/dy \qquad (4-46)$$

If we designate $\varphi_{surf}$ at the source end of the channel ($y = 0$) by $\varphi_{surf0}$, and $Q_I$ there by $Q_{Isource}$, and the corresponding quantities at the drain end of the channel ($y = L$) by $\varphi_{surfL}$ and $Q_{Idrain}$, then by integrating from $y = 0$ to $y = L$ we get

$$\int_0^L I_D\, dy = \mu Z \int_{\varphi_{surf0}}^{\varphi_{surfL}} (-Q_I)\, d\varphi_{surf} + \frac{\mu Z kT}{q} \int_{Q_{I,source}}^{Q_{I,drain}} dQ_I \qquad (4-47)$$

or

$$I_D = \frac{\mu Z}{L} \int_{\varphi_{surf0}}^{\varphi_{surfL}} (-Q_I)\, d\varphi_{surf} + \frac{\mu Z kT}{L q} \int_{Q_{I,source}}^{Q_{I,drain}} dQ_I \qquad (4-48)$$

To perform the integrals in Eq. 4-47 and 4-48 we require an expression relating $Q_I$ and $\varphi_{surf}$. Equation 4-6 derived in section 4.2.2.1 is the appropriate expression we seek, and is repeated here

$$Q_I = -C_{ox}(V_{GB} - V_{FB} - \varphi_{surf} - \gamma\sqrt{\varphi_{surf}}) \qquad (4-49)$$

Using this in Eq. 4-48 for the drift current component of the drain current, performing the integration from $\varphi_{surf0}$ to $\varphi_{surfL}$, we get the following expression for $I_{Ddrift}$

$$I_{Ddrift} = (\mu C_{ox}Z/L)\,[(V_{GB} - V_{FB})(\varphi_{surfL} - \varphi_{surfo}) - (1/2)(\varphi_{surfL}^2 - \varphi_{surfo}^2)$$
$$- (2/3)\,\gamma\,(\varphi_{surfL}^{3/2} - \varphi_{surfo}^{3/2}) \qquad (4-50)$$

Using Eq. 4-49 for $Q_I$ (in which we let $\varphi_{surf} = \varphi_{surfo}$ at the source and $\varphi_{surfL}$ at the drain when we compute the values of $Q_I$ at the limits of integration), in the term of Eq. 4-48 for $I_{Ddiff}$, we get

$$I_{Ddiff} = (\mu C_{ox}Z/L)(kT/q)(\varphi_{surfL} - \varphi_{surfo}) + (kT/q)\,\gamma\,(\varphi^{1/2}_{surfL} - \varphi^{1/2}_{surfo}) \qquad (4-51)$$

The last step needed when computing $I_D$ with this model is to determine $\varphi_{surfo}$ and $\varphi_{surfL}$ from the terminal voltages $V_{GB}$, $V_{SB}$, and $V_{DB}$. It turns out that Eq. 4-4 is the appropriate expression for this task if $\varphi_{surf}$ and $V_{CB}$ are replaced with $\varphi_{surfo}$ and $V_{SB}$ at the source end of the channel, and with $\varphi_{surfL}$ and $V_{DB}$ at the drain end. Then we get

$$\varphi_{surfo} = V_{GB} - V_{FB} - \gamma\sqrt{\varphi_{surfo} + \varphi_t e^{(\varphi_{surf0} - 2\varphi_B - V_{SB})/\varphi_t}} \qquad (4-52a)$$

$$\varphi_{surfL} = V_{GB} - V_{FB} - \gamma\sqrt{\varphi_{surfL} + \varphi_t e^{(\varphi_{surfL} - 2\varphi_B - V_{DB})/\varphi_t}} \qquad (4-52b)$$

These equations for $\varphi_{surfo}$ and $\varphi_{surfL}$ however, are relatively complex transcendental equations which must be solved by iterative techniques to find $\varphi_{surfo}$ and $\varphi_{surfL}$.

Now, $I_D$ predicted by the charge-sheet model is a single expression given by the sum of Eqs. 4-50 and 4-51.

$$I_D\,(\text{charge sheet}) = I_{Ddrift}\,(\text{Eq. 4-50}) + I_{Ddiff}\,(\text{Eq. 4-51}) \qquad (4 - 53)$$

Experimental MOSFET characteristics are observed to agree very well with such predictions.

### 4.5.4 Variable Depletion-Charge (or Bulk-Charge) Model

As just described, the charge-sheet model for $I_D$ in its full form includes drift and diffusion current components, making it accurate over the MOSFET operating regimes from weak to strong inversion. However, the fact that neither Eq. 4-50 nor 4-51 is explicitly expressed in terms of the terminal voltages makes the full charge-sheet formulation too cumbersome for use in circuit design applications.

Nevertheless, it is possible to simplify the charge-sheet model formulation to obtain analytical expressions that explicitly give $I_D$ in terms of the terminal voltages. The price for such simplicity (while maintaining adequate accuracy) is that the resulting equations are only accurate over a limited operating range. Specifically, instead of being required to evaluate $I_D$ from Eq. 4-53 (which is a single, relatively complex equation, valid from weak to strong inversion), we develop two less complex approximations to Eq. 4-53, one which is only valid over the weak inversion regime (subthreshold), and the other only over the strong inversion regime. In this section we derive the strong-inversion approximation to Eq. 4-53, which is termed the *variable-depletion-charge* or *bulk-charge* model, and was developed in 1964.[9] In section 4.7 we develop the simplified $I_D$ equation valid for weak inversion. Note that in both of these models the charge-sheet and depletion approximations are still invoked.

We begin the derivation of the strong-inversion model by recalling that once a MOSFET is biased beyond the point of strong inversion, the diffusion current component of $I_D$ is negligible compared to the drift current component; thus we can approximate $I_D$ with only the drift current term of Eq. 4-53. In addition, we assume that beyond the onset of strong inversion $\varphi_{surf}$ remains fixed. That is, the surface potential at the source and drain ends of the channel in strong inversion is assumed to be clamped at the value possessed at the onset of strong inversion. In that case, $\varphi_{surf}$ can be approximated as

$$\varphi_{surfo} \approx 2\varphi_B + V_{SB} \qquad (4 - 54a)$$

and

$$\varphi_{surfL} \approx 2\varphi_B + V_{DB} \qquad (4 - 54b)$$

The final approximation we use to derive the variable-depletion-charge model is that if $V_{GS}$ is biased below strong inversion (i.e., $V_{GS} < V_T$), $I_D$ is assumed to be zero.

Invoking these approximations, $I_D$ in a MOSFET can now be approximated by Eq. 4-50, with the values of $\varphi_{surfo}$ and $\varphi_{surfL}$ in this equation given by Eqs. 4-54a and 4-54b. Thus, by substituting these into Eq. 4-50 we get

$$I_D = \frac{\mu C_{ox} Z}{L}(V_{GB} - V_{FB})(V_{DB} - V_{SB}) - \frac{1}{2}[(V_{DB} + 2\varphi_B)^2 - (V_{SB} + 2\varphi_B)^2]$$

$$- \frac{2}{3}\gamma[(V_{DB} + 2\varphi_B)^{3/2} - (V_{SB} + 2\varphi_B)^{3/2}] \qquad (4 - 55)$$

By rearranging terms, this equation becomes

$$I_D = \frac{\mu C_{ox} Z}{L}(V_{GB} - V_{FB} - 2\varphi_B)(V_{DB} - V_{SB}) - \frac{1}{2}[(V_{DB}^2 - V_{SB}^2)$$

$$- \frac{2}{3}\gamma[(V_{DB} + 2\varphi_B)^{3/2} - (V_{SB} + 2\varphi_B)^{3/2}] \qquad (4 - 56)$$

We observe that $I_D$ is now explicitly expressed in terms of the terminal voltages $V_{GB}$, $V_{DB}$, and $V_{SB}$. To put Eq. 4-56 into a form in terms of $V_{GS}$, $V_{DS}$, and $V_{BS}$, we recall that $V_{GB} = V_{GS} + V_{BS}$ and $V_{DB} = V_{DS} + V_{BS}$. This allows us to rewrite Eq. 4-56 as

$$I_D = \frac{\mu C_{ox} Z}{L}(V_{GS} - V_{FB} - 2\varphi_B)V_{DS} - \frac{1}{2}V_{DS}^2$$

$$- \frac{2}{3}\gamma\,[(V_{DS} + V_{BS} + 2\varphi_B)^{3/2} - (V_{BS} + 2\varphi_B)^{3/2}] \qquad (4 - 57)$$

If $V_{BS} = 0V$, Eq. 4-57 becomes

$$I_D = \frac{\mu C_{ox} Z}{L}(V_{GS} - V_{FB} - 2\varphi_B)V_{DS} - \frac{1}{2}V_{DS}^2 - \frac{2}{3}\gamma(2\varphi_B + V_{DS})^{3/2} - (2\varphi_B)^{3/2} \quad (4 - 58)$$

Equation 4-57 (and 4-58) is sometimes referred to as the *Ihantola and Moll model*, since it was initially developed by them in 1964.[9] The name *variable-depletion charge model* signifies that the model computes $Q_I$ as the difference between $Q_C$ and $Q_B$ (*bulk* charge), taking into account the variation of the depletion region width along the channel to compute $Q_B$. We will see that the square-law model assumes the depletion region width is constant from source to drain.

Equation 4-57 predicts that for a given $V_{GS}$ the drain current first increases linearly with $V_{DS}$ (the *linear* regime), then gradually levels off, approaching a saturated value (the *saturation* regime). Thus, it behaves quantitatively as depicted by the basic output characteristic of the idealized MOSFET of Fig. 4-11.

We noted in section 4.4.2 that as $V_{DS}$ is increased, the output characteristic levels off. This leveling off occurs because as $V_{DS}$ increases, the channel near the drain is driven toward pinch off. In terms of the gradual channel approximation, pinch off is the point at which $Q_I$ drops to zero. (In fact, once $Q_I$ gets very small, the gradual channel approximation breaks down and Eq. 4-57 no longer applies.) When the $V_{DS}$ reaches the

value at which pinch off has been reached, the measured $I_D$ value in long-channel MOSFETs *saturates*. That is, it becomes essentially constant as $V_{DS}$ is increased further. The $I_D$ value at that point is denoted as $I_{Dsat}$. Although Eq. 4-57 is no longer valid for this regime, we use the maximum value of $I_D$ found using Eq. 4-57 as $I_{Dsat}$. We denote the $V_{DS}$ value to just reach this condition as $V_{DS,sat}$.

Since $V_{DS,sat}$ is the $V_{DS}$ value when $I_D$ reaches its maximum, such a maximum can be found by setting $dI_D/dV_{DS} = 0$ from Eq. 4-57 and solving for $V_{DS} = V_{DS,sat}$

$$V_{DSsat} = V_{GS} - V_{FB} - 2\varphi_B + \frac{\gamma^2}{2} - \gamma\sqrt{V_{GS} - V_{FB} + V_{BS} + \frac{\gamma^2}{4}} \qquad (4 - 59)$$

The value of $V_{DS,sat}$ obtained from Eq. 4-59 is used in Eq. 4-57 to calculate $I_{Dsat}$.

Note that the linear and saturation regimes of MOSFET operation have been defined. Since we also assume in this model that $I_D = 0$ for $V_{GS}<V_T$, we define this bias range as the *cutoff* regime. In fact, a small but nonzero drain current exists even when $V_{GS} <V_T$, so it is more appropriate to refer to this regime as the *subthreshold* regime. Further details on this regime are given in section 4.7.

### 4.5.5 Square-Law Model

Equation 4-57 predicts $I_D$ values in long-channel MOSFETs (operated in strong inversion) quite accurately. However, even this formulation is mathematically too complex for use in hand calculations. Furthermore, when it is necessary to simulate the circuit behavior of digital IC circuits containing a large number of MOSFETs, using Eq. 4-57 in SPICE significantly slows the simulation time. For such applications, a simplified version of Eq. 4-57 could be useful, even at the expense of somewhat less accuracy. This can be obtained if $2\varphi_B + V_{BS}>>V_{DS}$. In this case, we can use the binomial expansion to get

$$(2\varphi_B + V_{SB} + V_{DS})^{3/2} = (2\varphi_B + V_{SB})^{3/2}\left(1 + \frac{V_{DS}}{2\varphi_B + V_{SB}}\right)^{1/2} \qquad (4 - 60)$$

$$\approx (2\varphi_B + V_{SB})^{3/2} + \frac{3}{2}(2\varphi_B + V_{SB})^{1/2} V_{DS} \qquad (4 - 61)$$

Thus,

$$I_D = \frac{\mu C_{ox} Z}{L}\left(V_{GB} - V_{FB} - 2\varphi_B - [2\kappa_{si}\varepsilon_o N_A(2\varphi_B + V_{BS})/C_{ox}]^{1/2} - V_{DS}/2\right)V_{DS} \quad (4 - 62)$$

which can be written more succinctly as

$$I_D = [\mu C_{OX} Z/L](V_{GB} - V_T - V_{DS}/2)V_{DS} \qquad V_{GS} \geq V_T \quad (4 - 63a)$$

$$V_{DS} \leq (V_{GS} - V_T)$$

since $V_T = V_{FB} + 2\varphi_B + [2\kappa_{si}\varepsilon_o N_A(2\varphi_B + V_{BS})/C_{OX}]^{1/2}$. Or, Eq. 4-63a can be written in an even more compact way (again assuming that $V_{BS} = 0$, in which case $V_{GB} = V_{GS}$),

as

$$I_D = k\,[(V_{GS} - V_T)V_{DS} - V_{DS}^2/2] \qquad (4\text{-}63b)$$

where $k$ (the so-called device transconductance parameter) is defined as

$$k = \mu\, C_{OX}\, Z/L \qquad (4\text{-}64)$$

For very small $V_{DS}$ values, Eq. 4-63 can be further approximated as

$$I_D = k\,(V_{GS} - V_T)\,V_{DS} \qquad (4\text{-}65)$$

For $2\varphi_B + V_{SB} >> V_{DS}$, the condition for saturation becomes

$$-C_{OX}\,(V_{GS} - V_{FB} - 2\varphi_B - V_{DS,sat}) + (2\kappa_{si}\varepsilon_0 q N_A[2\varphi_B + V_{BS}])^{1/2} = 0 \qquad (4\text{-}66)$$

so

$$V_{DS,sat} \approx V_{GS} - V_T \qquad (4\text{-}67)$$

In saturation, $I_D$ in this model is given by Eq. 4-62 evaluated at $V_{DS} = V_{DS,sat}$; that is

$$I_{Dsat} = k/2\,(V_{GS} - V_T)^2 \qquad V_{GS} \geq V_T: \qquad (4\text{-}68)$$

$$V_{DS} > (V_{GS} - V_T)$$

Since Eq. 4-68 predicts that $I_{Dsat}$ will vary as the square of the gate voltage above threshold, Eq. 4-62 is termed the *square-law model.*

Equation 4-68 is often used as the basis for measuring $V_T$. In this technique, the gate and drain of the transistor are tied together as shown in Fig. 4-16, and then the drain current is measured as a function of applied drain voltage. Because $V_{DS}$ is set equal to $V_{GS}$ in this circuit, the transistor is in the saturated region of operation. Now a plot of

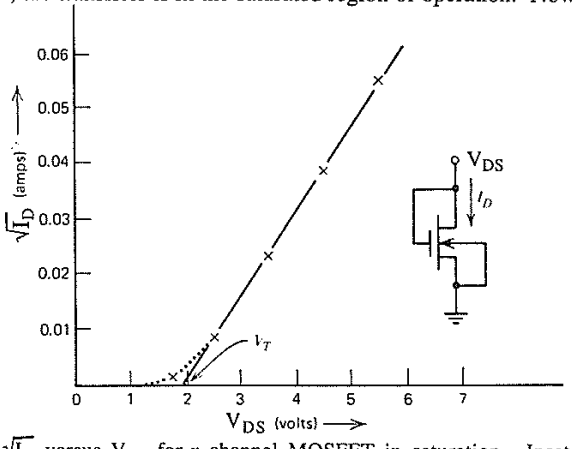


**Fig. 4-16** Plot of $\sqrt{I_D}$ versus $V_{DS}$ for $n$-channel MOSFET in saturation. Inset shows the circuit arrangement. The threshold voltage is indicated by the intercept of the straight line with the voltage axis.

$\sqrt{I_D}$ versus $V_{GS}$ should be a straight line with a voltage axis intercept equal to $V_T$. In fact, plotting $\sqrt{I_D}$ versus $V_{GS}$ is the most widely used method of determining $V_T$, yielding as will be discussed in section 4.6, the so-called *extrapolated threshold voltage* value.

From a physical perspective the square-law model can be derived by approximating that the channel depletion region has a constant width along the entire length of the channel (with a value equal to that near the source), even under $V_{DS} \neq 0$ biasing. This approximation is somewhat reasonable in strong inversion since the last term in the strong-inversion form of $Q_I$ (Eq. 4-10), namely $[\sqrt{2\kappa_{si}\varepsilon_o q N_A (2\varphi_B + V_{ChB})}]$, is small compared to the other terms. Since it is the only term that depends on the depletion-region charge, and this charge is much smaller than the mobile charge concentration under strong inversion, the variation of this term will not change the value of $Q_I$ much. That is, as long as the channel region remains inverted, $Q_I$ does not vary much from the source to the drain ends of the channel. Hence, approximating this term by a constant value (namely with the charge that would exist if the depletion region had a constant width, equal to the value it at has at the source end) does not change the value of $Q_I$ significantly. Yet it results in a much simpler form of the $I_D$ model.

At the source the depletion region width is $d_{max}$(source), which can be calculated from Eq. 4-8

$$d_{max}\,(\text{source}) = [2\kappa_{si}\varepsilon_o(2\varphi_B + V_{BS})/qN_A]^{1/2} \qquad (4\text{-}69)$$

Then

$$Q_B = [2\kappa_{si}\varepsilon_o N_A(2\varphi_B + V_{SB}]^{1/2} \qquad (4\text{-}70)$$

and using Eq. 4-10

$$Q_I = -C_{ox}[V_{GB} - V_{FB} - 2\varphi_B - V_{ChB} - \gamma(2\varphi_B + V_{BS})^{1/2}]$$

$$= -C_{ox}[V_{GB} - V_T - V_{ChB}) \qquad (4\text{-}71)$$

Thus,

$$I_D = \frac{\mu\, C_{ox}\, Z}{L}\int_{V_{SB}}^{V_{SB}+V_{DS}} (V_{GB} - V_T - V_{ChB})\, dV_{ChB} \qquad (4\text{-}72)$$

Integrating 4-72 from source to drain gives 4-62.

## 4.5.6 Comparison of the Four MOSFET Circuit Models

Let us summarize the characteristics of the four long-channel MOSFET dc circuit models just described, and make some further comparisons about their relative accuracies and utility. Recall first off that all are based on the long-channel (GCA) approximation.

The most general and accurate of the models is the *Pao-Sah* model. While it retains the gradual-channel approximation, it does not invoke the depletion approximation and permits carrier transport in the channel by both drift and diffusion current. The formulation of the $I_D$ equation it develops is therefore quite general, but also requires numerical integrations in two dimensions. Such numerical complexity has limited the role of this model role to theoretical analyses of the MOSFET. As a result the other three MOSFET models are more frequently used to calculate the $I_D$-$V_{DS}$ characteristics.

The *charge sheet* model allows $I_D$ to be calculated with much less computational effort than that of the Pao-Sah model and yet provides $I_D$ values very close to those predicted by the more complex model over the regime of inversion (both weak and strong). The accuracy of the charge-sheet model when compared to measured dc $I_D$-$V_{DS}$ characteristics of a MOSFET in inversion is about 1% or better. This model calculates the surface potential by solving the Poisson equation assuming the depletion approximation and the charge-sheet approximation. It also assumes that both drift and diffusion current can contribute to $I_D$. While not applicable to the depletion and accumulation regimes of operation, it is valid over all regimes of inversion. Although it accurately predicts $I_D$ over these regions of operation, it requires values of the surface potential to be calculated at the source and drain ends of the channel. These equations for $\varphi_{surf}$ are complex transcendental equations that require iterative techniques to solve them. As a result, the computational effort for determining $I_D$ is still too great for most circuit simulation applications, and thus the charge sheet model has not been incorporated into such popular circuit simulation programs as SPICE.*

Since the charge-sheet model is too complex to be used in most circuit simulation applications, the simpler bulk-charge and square law models are used instead. They both assume that the MOSFET is biased to strong inversion, and that only drift current contributes to $I_D$. As long as the MOSFET is biased into strong inversion ($V_H$ in Fig. 4-17) the results of the bulk-charge $I_D$ equation agree very well with the charge-sheet model results. That is, to allow the simpler analytical expressions of the bulk-charge (Eqs. 4-57 and 4-59) and square-law models (Eqs. 4-63 and 4-68) to be used to accurately calculate $I_D$, the allowable regime of operation must be reduced to the strong-inversion regime. If the MOSFET is operated in weak inversion, an alternate analytical expression (as derived in section 4.7) must be used to get an accurate value of $I_D$ in long-channel MOSFETs.

When comparing the utility of the *bulk-charge* and *square-law* models, the primary asset of the square-law model is its simplicity. It provides good insight into the device operation and is useful for obtaining first-order design data without an excessive amount of mathematical entanglement, particularly for the case of digital circuits. Most hand calculations for circuit design with MOSFETs therefore make use of the square-law model. It is also the model used for the simplest (Level-1) analyses of circuits containing MOSFETs in the SPICE program. The apparently arbitrary adjustment of $k$

* Note that the bulk-charge and square-law MOSFET models assume that the surface potential at inversion is fixed at $2\varphi_B + V_{CB}$. In reality this is the value of $\varphi_{surf}$ at which the surface just enters strong inversion. If the electron charge in the channel is substantial, the surface potential must be greater than this value (but not much more than a few kT above $2\varphi_B + V_{CB}$). Nevertheless, both these models must therefore consistently underestimate the $\varphi_{surf}$.

Now, if $\varphi_{surf}$ is underestimated, so is the magnitude of the depletion region charge $Q_B$. If $Q_B$ is underestimated, then from Eq. 4-1b $Q_I$ must be overestimated. The bulk charge model therefore consistently overestimates the amount of mobile electron charge in the channel, and thus overestimates the drain current - fortunately by less than 10 percent in most cases.

The charge sheet model, on the other hand does not make the above assumption, but instead calculates $\varphi_{surf}$. Hence, this error is avoided in the charge-sheet model approach.

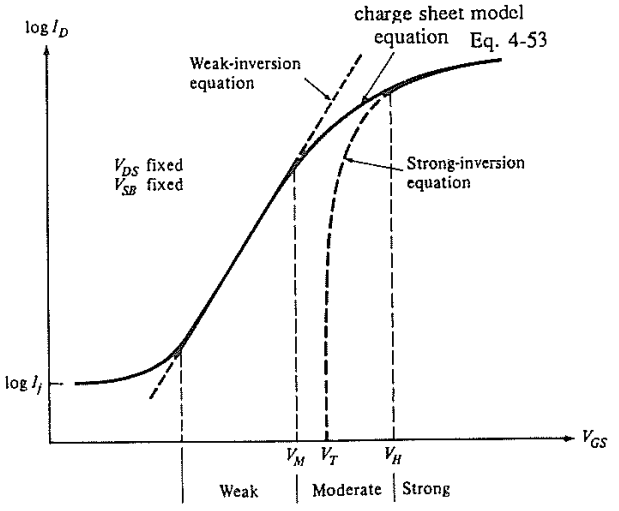


**Fig. 4-17** Log $I_D$ versus $V_{GS}$ for fixed $V_{DS}$ and $V_{BS}$, and comparison to weak- and strong-inversion equations.[5] Reprinted with permission of McGraw-Hill Book Co.

mentioned above is also not a practical problem since MOS processing procedures do not allow for the precise control of $\mu_n$, and the parameter must be extracted from measurements.

There are many cases of circuit design for which the increased accuracy of the bulk-charge model is not necessarily an advantage when computational complexity is considered. Often, for example, the designer is interested only in MOSFET operation in the saturated region (i.e., only the value of $I_{Dsat}$ is needed). To obtain $I_{Dsat}$ from the bulk-charge model, it is first necessary to calculate $V_{DSsat}$ from Eq. 4-59 and then use this voltage value in Eq. 4-58 to calculate $I_{Dsat}$. This lengthy process is greatly simplified in the square-law model in which $I_{Dsat}$ is calculated directly from Eq. 4-68.

The bulk-charge model is used when more accurate modeling of circuit behavior is needed. Measurements of $I_D$ versus $V_{DS}$ characteristics of long-channel MOSFETs are in reasonable agreement with the predictions of this model (i.e., usually within 10% of the measured data). However, the computational complexity is considerably increased, and hence it is typically implemented only in computer analyses. This model is available as the Level-2 model of the MOSFET in SPICE. Note that when comparing Eqs. 4-57 and 4-59 with 4-63 and 4-68, the added terms in the bulk-charge model equations are always negative and act primarily to reduce $I_D$ and $V_{DSsat}$ for a given set of operational conditions.

A plot of $I_D$ versus $V_{DS}$ (with $V_{GS}$ as a parameter) for a long-channel NMOS transistor calculated using both models is shown in Fig. 4-18. As can be seen the square-law model predicts larger values of $I_{Dsat}$ and $V_{DSsat}$ for each value of gate

voltage. The general behavior of both sets of curves is, however, similar. Note especially that in the linear region of operation both models give the same results, but that in saturation - for the same value of $k$ in both models - the bulk-charge model predicts a smaller value of $I_{Dsat}$.

**4.5.6.1 MOSFET Models of the SPICE Circuit Simulator.** The SPICE circuit simulator contains four MOSFET models which differ in the way they formulate the I-V characteristic. The simplest is the Level-1 model which is based on the rudimentary square-law model (Equations 4-63 and 4-68), with empirical adjustment. The most important adjustment it employs is the use of a coefficient in these equations to bring $I_{Dsat}$ into congruence with experiment and the more accurate models. That is, to obtain satisfactory results in circuit analysis and design using this model, measured data on samples of MOSFETs must be obtained. Measured data is fitted to the threshold voltage equation and Eqs. 4-63 and 4-65. Specifically $V_T$ and $k$ are determined from data obtained as shown in Fig. 4-16. Note that the extrapolated threshold voltage value $V_{T0}$ is used in SPICE because it is obtained by extrapolating the experimental curve of $\sqrt{I_D}$ versus $V_{DS}$ (with $V_{DS} = V_{GS}$) to zero drain current. The subscript "0" in the $V_{T0}$ symbol signifies that this is the extrapolated threshold voltage when $V_{BS} = 0V$.

The more-accurate Level-2 SPICE MOSFET model is based on the bulk-charge model equations (Eqs. 4-57 and 4-59). The Level-2 model also incorporates an approximate*

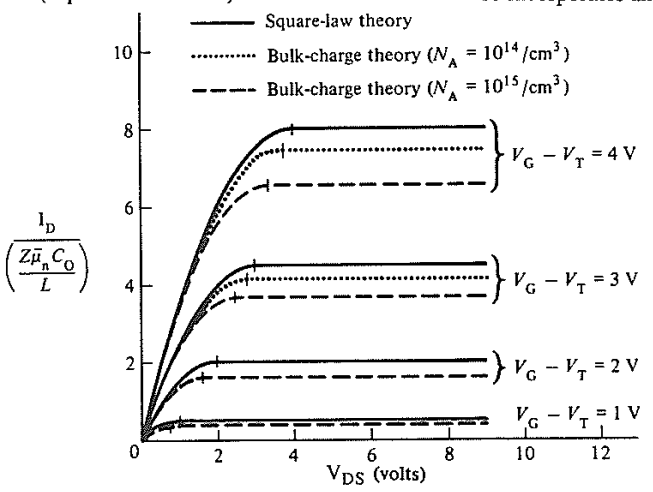


**Fig. 4-18** Theoretical predictions of $I_D$ versus $V_{DS}$ using the bulk-charge model equations (solid lines) and the square-law model equations (dashed lines). $I_D$ is taken to be equal to $I_{Dsat}$ for $V_{DS}>V_{DSsat}$.[30] Reprinted with permission of Addison-Wesley.

* For example, in the Level-2 MOSFET model, the carrier mobility is not treated as a constant. Instead, the mobility is modeled as being impacted by the gate-induced electric field (see chap. 5). The value used in the Level-2 model $\mu_{eff}$ is found using the expression Eq. 5-26.

treatment of some of the short-channel effects discussed in chap. 5 and is capable of computing the subthreshold current (in the manner as described in section 4.7).

The basic device structure parameters required to describe a MOSFET when using either the Level-1 or Level-2 model are the substrate doping, the gate oxide thickness, and the channel length and width. SPICE computes the threshold voltage from $N_A$ (NSUB in SPICE) and $t_{ox}$ using Eq. 4-12 (assuming $V_{FB} = 0$). Alternatively, the threshold voltage (for the case of $V_{SB} = 0$) can be input directly by supplying a value to the model parameter $V_{T0}$, in which case the internally computed threshold voltage is overridden.

The Level-2 SPICE MOSFET model, being based on the bulk-charge MOSFET model, has a three-halves-power dependence of $I_D$, rather than the square-law dependence of the Level-1 SPICE MOSFET model. Because the numerical handling of a fractional power requires significantly more computation time than if a power in integer form must be computed, circuit designers sought a model that was more accurate than the Level-1 model, but was faster to execute than the Level-2 model. Hence, the Level-3 model was developed and incorporated into SPICE.*

The Level-3 model not only removed the computational shortcoming of the Level-2 model, but was formulated to deal empirically with many other effects as well, including short-channel and narrow-channel effects. In fact, the Level-3 model represents an attempt to pursue a semi-empirical modeling approach, i.e., which only approximates device physics and relies on the proper choice of the empirical parameters to accurately reproduce device characteristics. As a result, a more physically based short-channel MOSFET model has also been developed for SPICE, known as the Berkeley Short-channel IGFET Model (BSIM). It has been implemented into the SPICE program as the Level-4 MOSFET model. We will describe BSIM in more detail in chap. 5.

**4.5.6.2 SPICE Models of the MOSFET Operated in Saturation.** As we noted in section 4.4.2, the value of $I_D$ may increase as $V_{DS}$ exceeds the pinchoff voltage value $V_{DSsat}$. This was modeled by assuming that the pinched-off region with a length $\Delta L$ makes the channel length appear shorter (i.e., $L - \Delta L$). To predict $I_D$ as $V_{DS}$ exceeds $V_{DSsat}$ the value of $\Delta L$ is needed. In the Level-1 and Level-2 MOSFET models

* The $I_D$ equation that constitutes the dc long-channel Level-3 model of the MOSFET[10] in the SPICE program is derived from Eq. 4-57 by employing a three-term binomial-series expansion for the second term in Eq. 4-57. This yields the Level-3 MOSFET equation for $I_D$ in the form:

$$I_D = \frac{\mu C_{ox} Z}{L}\left[(V_{GS} - V_T)V_{DS} - \left(\frac{1}{2} + \frac{\sqrt{\varepsilon_o q N_A/(-\varphi_B)}}{4 C_{ox}}\right)V_{DS}^2\right]$$

Notice by comparing it to the Level-1 expression, Eq. 4-63, that it differs only in the last term, a change that accounts for the ionic-charge variations that were ignored in the Level-1 model. Here, however, the square root term is only dependent on device structure parameters and not on $V_{DS}$, and hence this square-root term only needs to be evaluated once when calculating the $I_D$-$V_{DS}$ characteristics.

SPICE offers two possible approaches to calculating $\Delta L$. The first allows the *channel-length modulation parameter*, $\lambda$ (LAMBDA) to be specified, in which case $\Delta L$ is obtained from the simple empirical expression $\Delta L = \text{LAMBDA} \cdot V_{DS}$. LAMBDA can be used in either the Level-1 or Level-2 model. The value of LAMBDA is typically in the range of 0.1 to 0.01 $V^{-1}$. Empirical values of $1/\lambda$ can be obtained by finding an approximate intercept with the $V_{DS}$ axis of tangents to the $I_D$ curves beyond $V_{DSsat}$ in measured $I_D$-$V_{DS}$ curves.

If the value of LAMBDA is not specified in the Level-2 model, however, then $\Delta L$ is computed by using Eq. 5-47, which is based on the 1-D Reddi-Sah model of the MOSFET operated in saturation (see chap. 5, section 5.4.3.1).

## 4.6 THRESHOLD-VOLTAGE CONTROL IN MOSFETS

### 4.6.1 Measuring Threshold Voltage

Equation 4-1 calculates $V_T$ of real MOSFETs based on various device parameters. Yet, when devices are fabricated, they must be tested to ensure that the desired characteristics have been produced. Two approaches are used to obtain the $V_T$ values of MOSFETs from measurements. The first yields an *extrapolated-$V_T$* value, and the second, a *constant-current-$V_T$* value.

As described in section 4.5.5, the extrapolated $V_T$ is determined by connecting the drain and gate of a MOSFET together and measuring the drain current as a function of gate voltage (Fig. 4-16). Equation 4-68 predicts that a plot of $\sqrt{I_D}$ (with a linear $I_D$ axis) versus $V_{GS}$ should be linear. If $\sqrt{I_D}$ is plotted vs. $V_{GS}$, and the linear portion of the curve is extrapolated to intercept the voltage axis (corresponding to the condition that $V_{GS} = V_T$ in Eq. 4-68) the extrapolated-$V_T$ value is yielded. (Note that the dotted section of the curve in Fig. 4-16 results from currents that flow below the threshold voltage. Such *subthreshold currents* are discussed in section 4.7.)

The constant-current-$V_T$ is obtained by measuring the gate voltage at which a specific small drain current flows and this gate voltage is defined as $V_T$. For active MOSFETs, the gate voltage at which 1 $\mu$A of drain current flows per $\mu$m of drain width for $V_{DS}$ = 0.5V is the most common criterion applied when specifying constant-current-$V_T$. The constant-current-$V_T$ is generally measured in the IC production environment, while the extrapolated $V_T$ is preferred when the threshold voltage parameter is needed for circuit simulation (e.g., in a SPICE analysis). Note also that the extrapolated $V_T$ is typically 100 mV larger than the 1 $\mu$A/$\mu$m constant-current $V_T$.

### 4.6.2 Adjusting Threshold Voltage

As pointed out earlier, in many MOS IC applications it is critical to be able to establish and maintain a uniform and stable $V_T$. The factors that impact $V_T$ are given in Eq. 3-72. An examination of each term will reveal the device parameters that can be adjusted to provide practical control of $V_T$.

The $\varphi_{ms}$ term depends on the work-function difference between the gate, $q\varphi_m$(gate), and the semiconductor, $q\varphi_B$ (sub). While $q\varphi_m$(gate) for metal and heavily doped silicon

gates is constant, the parameter $\varphi_B$ (sub) depends on the substrate doping - but only in a logarithmic manner. Hence, each factor-of-10 increase in substrate doping will change the $\varphi_{ms}$ term by only 2.3 kT/$q$, or ~0.06 V (kT/$q$ = 0.026 V at 300K). Thus, changes in the substrate-doping concentration produce changes in $V_T$ through the $\varphi_{ms}$ term which are too small to provide the required degree of threshold-voltage control. The next term ($2\varphi_B$) also changes only slightly as a result of changes in the substrate doping concentration (for the same reason given for the $\varphi_{ms}$ term); thus, the $2\varphi_B$ term is also ineffective for controlling $V_T$.

Since every attempt is made to keep $Q_{tot}$ as low as possible through various processing procedures, and $C_{ox}$ is relatively large (since $t_{ox}$ is very thin in submicron MOSFETs), the $Q_{tot}/C_{ox}$ term is also very small in modern MOSFETs. Hence, this term must also be ruled out as a candidate for controlling $V_T$.

While is true that $C_{ox}$ could be varied (primarily by changing $t_{ox}$), this is not a practical approach to controlling $V_T$ in active devices, since $t_{ox}$ is normally made as thin as possible to maximize $I_D$. (In the field regions, however, large $V_{TF}$ values are needed to prevent inversion under the field oxide. A thick field oxide makes $C_{ox}$ small, allowing $V_{TF}$ to be increased Thus, $C_{ox}$ is one of the parameters normally used to control $V_{TF}$ in the field regions of the circuits.)

This leaves the $2\sqrt{\kappa_{si}\varepsilon_o q N_{sub}\varphi_B}/C_{ox}$ term as the remaining candidate for controlling $V_T$ in active devices. Since the change of $V_T$ in this term depends on $\sqrt{N_{sub}}$, it indicates that $V_T$ control is possible by exploiting this effect. In fact, Eq. 3-72 indicates that increasing the substrate doping (i.e., $N_A$ in $n$-channel devices, and $N_D$ in $p$-channel devices) will increase $V_T$. Figure 4-19 shows how $V_T$ varies in MOSFETs (both PMOS and NMOS) with substrate doping concentration (assuming the substrate is uniformly doped - i.e., no threshold adjust implant is used - and that $Q_{tot} = 0$), for various gate-oxide thicknesses.

Merely increasing the substrate doping, however, is not desirable since it will adversely impact other MOSFET characteristics, such as lower junction-breakdown voltages, larger junction capacitances, and lower carrier mobilities. Yet, prior to the development of ion implantation in the early 1970s, adjustment of substrate doping was the only practical *processing* approach for significantly controlling $V_T$ in active devices.

We showed earlier that a *circuit* approach based on applying a bias between the source and body (and hence known as body biasing) can also control $V_T$ (section 4.2.2.2, Eq. 4-12). Generally, an increase in $V_{BS}$ will raise $V_T$. Figure 4-20 gives an example of how the application of $V_{BS}$ can change the $V_T$ value in an NMOS device. The intercept of the channel conductance and the $V_{GS}$ axis when $V_{BS} = 0$ in this example is +0.99V. As $V_{BS}$ is increased from 0V to -5V, $V_T$ increases up to +2.3V. However, body biasing is an added complication, and is now avoided whenever possible as a technique for adjusting $V_T$, in favor of the ion implantation $V_T$-adjust method.

### 4.6.3 Ion Implantation for Adjusting Threshold Voltage

The development of ion implantation for $V_T$ adjustment removed the last obstacle to reliable production of $n$-channel devices for MOS ICs, as this procedure made it possible to select the substrate-doping value without having to consider its impact on $V_T$. That

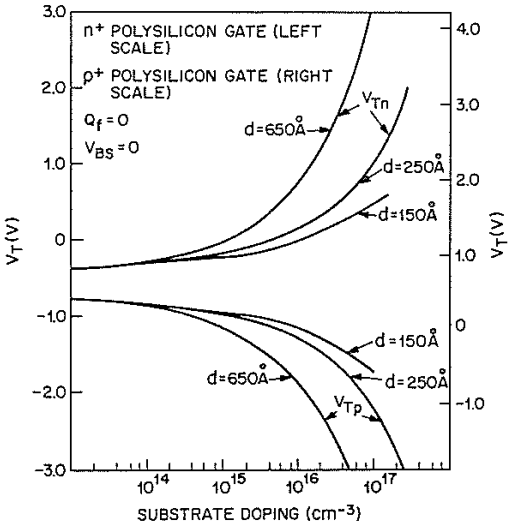


**Fig. 4-19** Calculated threshold voltages of $n$-channel ($V_{Tn}$) and $p$-channel ($V_{Tp}$) transistors as a function of their substrate's doping, assuming $n^+$ polysilicon gate (left scale) and $p^+$ polysilicon (right scale). Curves for gate oxide thicknesses $t_{ox}$ of 150 Å, 250 Å, and 650 Å are shown. From S. M. Sze, Ed., VLSI Technology, 2nd. Ed., Chap. 11, "VLSI Process Integration." Copyright, 1988 Bell Telephone Laboratories. Reprinted with permission of McGraw-Hill.

is, implantation can be used either to increase or to decrease (by compensation) the net dopant concentration at the silicon surface. As a result, substrate doping can be selected strictly on the basis of optimum device performance since $V_T$ can now be set by the $V_T$-

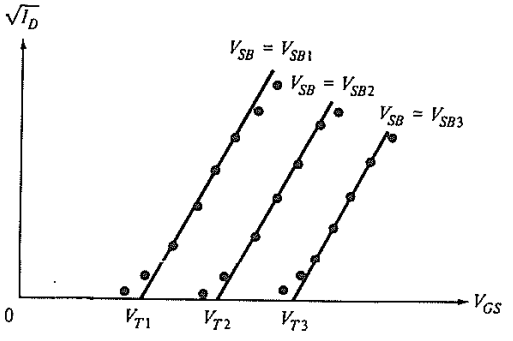


**Fig. 4-20** Plot of $\sqrt{I_D}$ vs. $V_{DS}$ for an NMOSFET showing the effects of a bias $V_{BS}$ between the source and the substrate. The observed shift in the threshold is predicted by Eq. 3-71.[16] Reprinted with permission of John Wiley & Sons.

adjust implant process. In addition, since dopants can be selectively implanted into the *field regions*, high-performance NMOS circuits can be fabricated on lightly doped substrates, without the possibility of inadvertent inversion of the surrounding field regions.

As mentioned earlier, the $V_T$-adjust-implant technique involves implantation of boron, phosphorus, or arsenic ions into the regions under the gate oxide of a MOSFET. Boron implantation produces a positive shift in $V_T$, while phosphorus or arsenic implantation causes a negative shift. For shallow implants, the procedure has essentially the same effect as placing an additional sheet of "fixed" charge at the $SiO_2$-Si interface.

To first order, if the implant and substrate are of the same type (e.g., boron into a *p*-substrate), and the effective depth of the implant $x_i$ (see Fig. 4-21) is less than $d_{max}$, the threshold-voltage change ($\Delta V_T$) can be reasonably well estimated from[11]

$$\Delta V_T\,(\mathrm{II}) = q\, D_I / C_{ox} \qquad (4 - 73)$$

**Example 4-1:** If the $V_T$ of a uniformly doped NMOS transistor is -0.41V and it is to be used in an application that requires a $V_T$ = 1.0V, calculate the B dose (to first order) needed to adjust $V_{T(nud,lc)}$ to this value.

**Solution:** The $V_{T(ud,lc)}$ of the device is -0.41 V. We wish to have a $V_T$ of 1.0 V. Thus, the threshold voltage must be shifted ($\Delta V_T$) by +1.41 V. Using Eq. 4-73, we see that the boron dose needed to cause this $\Delta V_T$ is

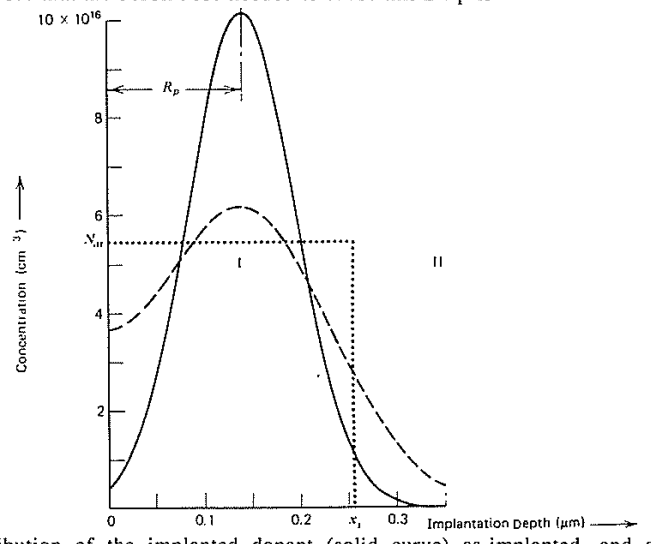


**Fig. 4-21** Distribution of the implanted dopant (solid curve) as-implanted, and after activating anneal and diffusions (dashed curve). The dotted "box" curve shows the distribution used to calculate the threshold voltage. (After Rideout, Gaensllen & LeBlanc in ref. 27.)

$$D_I = \Delta V_T(II)\, C_{ox}/q = [1.41V \times 2.3\times10^{-7}\ F/cm^2]/1.6\times10^{-19}\ C$$

$$= 2.1\times10^{12}\ \text{boron atoms}/cm^2.$$

where $D_I$ is the dose of the implanted ions (atoms/cm$^2$) which penetrate into the silicon. For example, Eq. 4-73 predicts that when $D_I = 5\times10^{11}$ ions/cm$^2$ and $t_{ox} = 25$ nm, a shift in $V_T$ of 0.58 V will be produced. Thus, Eq. 3-72 must be modified to account for threshold-adjust implants, as (where *nud* stands for non-uniformly doped)

$$V_{T(nud,lc)} = V_{T(ud,lc)} + \Delta V_T(II) \qquad (4-74)$$

A more exact formula for calculating for $V_T$ in this case (assuming $V_{BS} = 0$) is[12,13,14]

$$V_{T(nud,lc)} = V_{FB} + 2\varphi_B + qD_I/C_{ox} + \gamma_2\left(\sqrt{2\varphi_B + qD_I x_i/2\kappa_{si}\varepsilon_o}\right) \qquad (4-75)$$

where

$$\gamma_2 = \left(\sqrt{2q\kappa_{si}\varepsilon_o N_A}\right)/C_{ox} \qquad (4-76)$$

The $V_T$-adjust implant is often done through an oxide layer.* The implant energy is selected to place the peak of the implant slightly below the oxide-silicon interface (Fig. 4-21). After the implant-activating anneal, the implanted distribution is broader than the as-implanted profile.

Calculating the effect of the implant on $V_T$ is greatly simplified by approximating the actual distribution via a "box" distribution, as is also shown in Fig. 4-21 (in which the implanted dopant is assumed to have a constant density $N_A'$ from the surface to the depth $x_i$.) Figure 4-22 plots $V_T$ vs. effective implant depth $x_i$, and we can see that $V_T$ does not change much as $x_i$ is varied. Since the second term under the square root in Eq. 4-75 is the only one that depends on $x_i$, if we ignore it when calculating $V_T$ the results are still adequate for many applications. Thus, the first-order approximation of $\Delta V_T$ given by Eq. 4-73 is useful for hand calculations of $V_{T(nud,lc)}$.

Another slightly more complicated approach to calculating $V_T$ for this case is to solve the Poisson equation using a high-low step doping profile, which results in an effective concentration $N_{eff}$ given by[28]

$$N_{eff} = N_A' \frac{\varphi_s}{\varphi_i}\left[1 - \frac{N_A}{N_A'} + \frac{N_A'}{N_A}\sqrt{1 + \frac{N_A}{N_A'}\left(\frac{\varphi_s}{\varphi_i} - 1\right)}\right]^2 \qquad (4-77)$$

where $\varphi_s = kT/q\ [\ln(N_A'N_A/n_i^2)]$ and $\varphi_i = qN_A'x_i^2/2\kappa_{si}\varepsilon_o$. Here $\varphi_i$ is the potential corresponding to $x_i$ of the step profile. $N_{eff}$ is then substituted for $N_A$ in the body effect coefficient term $\gamma$ of Eq. 4-12, and then Eq. 4-12 with this value of $N_{eff}$ is used to calculate the value of $V_T$ in MOSFETs with implanted channels. This method for calculating $V_T$ in MOSFETs with non-uniformly doped channel regions is often called the *doping transformation procedure,* and reportedly gives excellent results.

Ion implantation can also be used to fabricate depletion-mode MOSFETs. Depletion-mode NMOS devices (i.e., in which $V_T<0V$) are commonly used in NMOS logic circuits. In order for the required negative threshold voltage for a depletion-mode NMOS device to be produced, *n*-type impurities are implanted into the *p*-type substrate to form a built-in channel between the source and drain. The dose required to shift the threshold voltage by the desired value may also be estimated using Eqs. 3-72 and 4-73.*

**4.6.3.1 Impact of the $V_T$-adjust Implant on the Body Effect.** The implanted layer also impacts the variation of $V_T$ with $V_{SB}$. This is shown in Fig. 4-23. We observe that for uniformly doped substrates [curves (a) and (b)] the variation of $V_T$ with $V_{SB}$ follows the data shown in Fig. 4-20. For shallow implants [curve (c)], the $V_T$ vs. $V_{SB}$ behavior approaches that for a delta function dose at the surface. That is, $V_T$ is observed to be merely shifted by $qD_I/C_{ox}$ from the $V_T$ values given by curve (a), and thus curve (c) is parallel with curve (a). However, for a deeper implant [curve (d)], the initial variation in $V_T$ with $V_{SB}$ is comparable to that for a uniformly doped region of concentration $N_A'$ [i.e., curve (b)]. However, as $V_{SB}$ is increased, the channel depletion region width d approaches and soon exceeds $x_i$, and the variation of $V_T$ with $V_{SB}$ thereafter behaves as if the substrate is doped with the bulk concentration $N_A$ [like curve (c)]. Since it is generally desirable to have $V_T$ exhibit a low substrate bias sensitivity

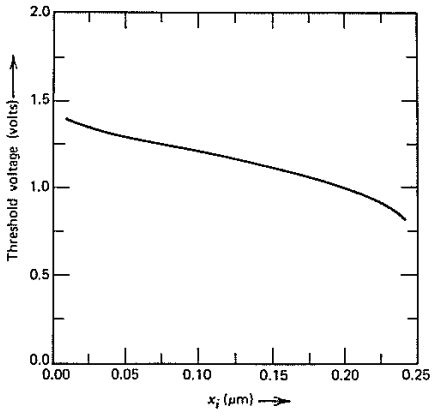


**Fig. 4-22** Dependence of the threshold voltage on the effective implantation depth $x_i$ as predicted by Eq. 4-75 for a MOSFET with an 87 nm-thick gate oxide, $Q_f/q = 10^{11}$ cm$^{-2}$, $D_I = 3.5\times10^{11}$ cm$^{-2}$, and $N_A = 2\times10^{15}$ cm$^{-3}$. Both the substrate and source terminal are assumed be grounded.[11] Reprinted with permission of John Wiley & Sons.

* Note that if $x_i$ is greater than $d_{max}$, $V_{T(nud,lc)}$ can be calculated using Eq. 3-72, with $N_A$ replaced by $N_A' = N_A + D_I/x_i$. However, this condition is generally avoided when choosing the $V_T$-adjust implant parameters, since the increased doping near the substrate edge of the source and drain junctions leads to higher junction capacitance, lower breakdown voltage, and a larger body effect.

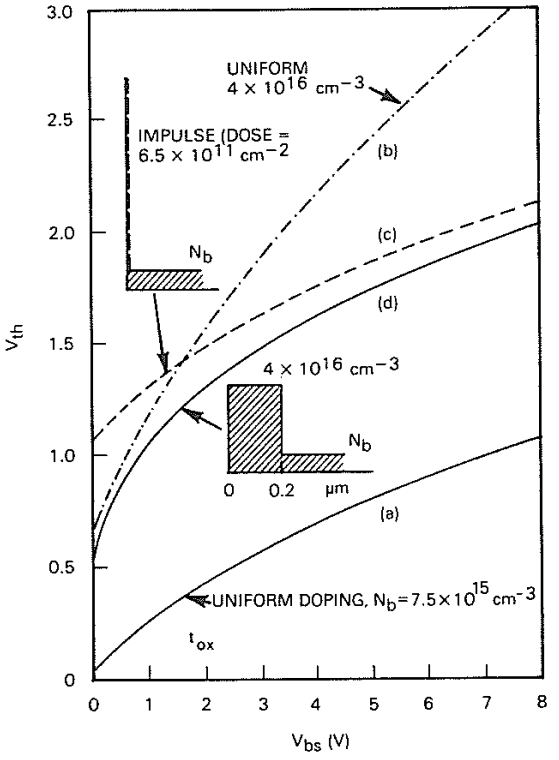


**Fig. 4-23** Calculated substrate sensitivity for various doping profiles. (After Rideout, Gaensllen and LeBlanc in ref. 27.)

(i.e., small body effect), Fig. 4-23 also demonstrates that a shallow implant with an appropriate dose can raise $V_T$ while maintaining a small body effect.

## 4.6.4 Impact of $V_T$-Adjust Implant on Other MOSFET Characteristics

By implanting ions near the Si surface, a nonuniformly doped channel region is produced. Besides shifting $V_T$, this alters the MOSFET behavior in several ways compared to devices having uniformly doped channels. First, the $V_T$-adjust implant introduces extra ions into the channel depletion region, causing its width to be modified. This effect is discussed here. In addition, the non-uniform doping profile changes the long-channel subthreshold characteristics (i.e., the slope of the log $I_D$ vs. $V_{GS}$ curves) as well as the punchthrough behavior of short-channel devices. These two latter effects will be discussed later, in chap. 5.

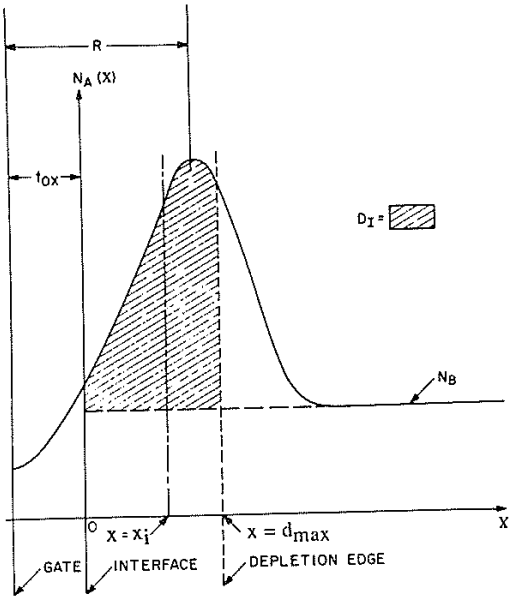


**Fig. 4-24** Schematic of the threshold adjust doping profile in an implanted MOSFET. The shaded portion of the profile is the portion of the implanted dose in the depletion region, whose depth extends to $d_{max}$. The effective depth of the implant (or centroid) is labeled $x_i$.[8,15] Reprinted with permission of Solid-State Electronics.

However, all of the above effects depend only upon the so-called *exposed dose* $D_I$ (i.e., the portion of the implant dose that ends up in the depletion region), and upon the *centroid* $x_d$ of the exposed dose. That is, those implanted ions which do not penetrate the screening oxide or which penetrate beyond the edge of the channel depletion region have no impact. Thus, these terms must be defined. $D_I$ (the shaded portion in Fig. 4-24), and $x_d$ are given in terms $N_{sub'}(x)$ and $N_{sub}$ by[15]

$$D_I\,(\text{cm}^{-2}) = \int_0^d [N_{sub'}(x) - N_{sub}]\,dx \qquad (4\text{-}78)$$

and

$$x_d = \frac{1}{D_I}\int_0^d [N_{sub'}(x) - N_{sub}]\,x\,dx \qquad (4\text{-}79)$$

where $N_{sub'}(x)$ is the true channel profile, including the implanted ions, and $N_{sub}$ is the uniform background doping of the substrate, as depicted in Fig. 4-24.

The change in width of the channel depletion region is most easily illustrated by replacing the actual implant profile shown in Fig. 4-24 with a simpler delta-function equivalent implant. That is, the equivalent doping profile $N_{sub'}(x)$ is given by

$$N_{sub'}(x) = N_{sub} + D_I\,\delta(x - x_d) \qquad (4 - 80)$$

Using such a delta-function replacement for the actual profile, the effects of the $V_T$-implant are illustrated in Fig. 4-25. Figure 4-25a shows a potential versus distance diagram [$\varphi(x)$ versus x] of a long-channel MOSFET with a non-implanted (i.e., uniformly doped) channel region. The channel depletion region width is d and the band bending is $\varphi_{surf}$. In Fig. 4-25b, the effect of varying the *dose* $D_I$ on the same depletion region is shown. The presence of $D_I$ at $x_d$ causes a larger voltage drop to occur between $x_d$ and the surface, leaving a smaller portion of $\varphi_{surf}$ to deplete the region behind the implant. Hence, the total width is reduced to $d_I = d_{DI}$. Doubling $D_I$ further reduces the width (in Fig. 4-25b to $d_{2DI}$). Eventually, for a value of dose termed the *effective* dose, $D_{eff}$, $d_I$ is reduced to a point $d_I = x_d$. Any increase of dose beyond $D_{eff}$ simply is neutralized in the bulk, and the condition of $d_I = x_d$ is maintained. In other words, $D_{eff}$ is the minimum dose needed to bring the depletion edge to that depth, making $d_I = x_d$.

Fig. 4-25c depicts the result of increasing implant *depth*. In this case, increasing $x_d$ also increases the voltage drop between $x_d$ and the surface, again reducing the width to a

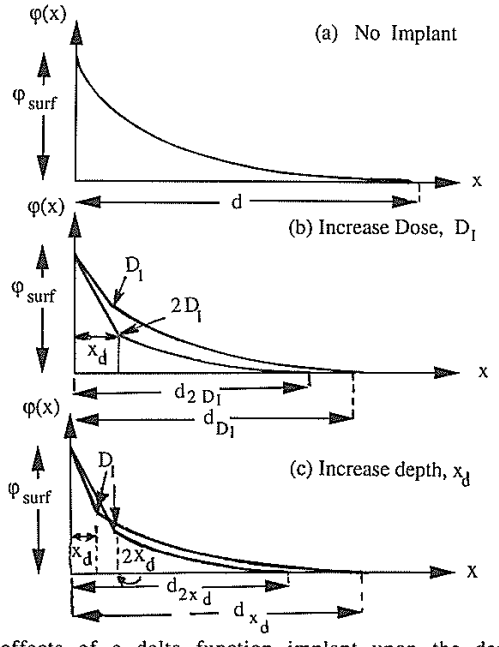


**Fig. 4-25** The effects of a delta function implant upon the depletion width. (a) Unimplanted, (b) Effects of changing dose, and (c) Effect of changing depth.[13] (© IEEE 1978)

smaller $d_I$. As a deeper $x_d$ is used, $d_I$ moves toward the implant. For example, in Fig. 4-25c, we see that for an implant with depth $x_d$, $d_I = d_{xd}$. This is deeper than $d_I$ due to a an implant with a depth $2x_d$ (here $d_I = d_{2xd}$). Ultimately, $d_I = x_d$, and $D_I = D_{eff}$, corresponding to this depth. Any further increase in $x_d$ carries the depletion region edge with the implant. The depletion region edge becomes *clamped* to the implant.

The quantitative variation of $d_I$ can also be simply expressed by again assuming a delta-function implant. That is, the depletion-region width in the presence of a $V_T$-adjust implant $d_I$ is calculated from

$$d_I = \sqrt{2}\, L_D\, [\varphi_{surf}/\varphi_t - D_I x_d/(N_{sub} L_D^2) - 1]^{1/2} \qquad (4 - 81)$$

where $L_D$ is the Debye length $\{[\kappa_{si}\varepsilon_o\varphi_t/qN_{sub}]^{1/2}\}$. Eq. 4-81 shows that the implant reduces the width, since in a uniformly doped channel the width d is given by

$$d = \sqrt{2} L_D\, [\varphi_{surf}/\varphi_t - 1]^{1/2} \qquad (4 - 82)$$

Likewise, $D_{eff}$ is given by

$$D_{eff} = N_{sub}\, (d^2 - x_d^2)/2x_d. \qquad (4 - 83)$$

## 4.7 SUBTHRESHOLD CURRENTS IN LONG-CHANNEL MOSFETs ($I_{Dst}$ when $V_{GS} < |V_T|$)

The small drain current which flows in the MOSFET channel below threshold (i.e., in weak inversion) is called *subthreshold current*, $I_{Dst}$. In most applications $I_{Dst}$ is far too small to be useful as a drive current. However, it can represent an unwanted leakage current, especially in ICs designed for low-power applications. It can also give rise to premature discharging of memory-cell capacitors or dynamic-logic circuit nodes, preventing these circuits from operating properly. The issues involving leakage currents in MOSFETs will become even more important with the proliferation of battery-powered (i.e., portable) electronic systems. The common range of $V_T$ in submicron digital CMOS ICs is 0.6-0.8V. Thus, when $V_{GS}$ = 0V the MOSFETs in these circuits may be close to weak inversion. Consequently, for many applications (especially those requiring low standby-power dissipation), subthreshold leakage must be well characterized so that the total IC leakage current of the chip can be predicted during the design phase of the product.

In actual MOSFETs, when $V_{GS}<V_T$ the minority carrier concentration in the channel (e.g., $n_{ps}$) is small (but not zero). That is, as $V_{GS}$ is increased from 0V and approaches $V_T$, the mobile charge concentration due to $n_{ps}$ remains smaller than the ionic charge of the bulk doping concentration, but continues to increase as $V_{GS}$ rises. In section 3.3.5 we defined *weak inversion* in terms of $\varphi_{surf}$, namely as $\varphi_B<\varphi_{surf}<2\varphi_B$.

The bulk-charge and square-law models of $I_D$ are not suitable for treating subthreshold behavior because they were developed to describe MOSFET behavior only in strong inversion. That is, both models assume that $I_D = 0$ if $V_{GS}<|V_T|$. While the Pao-Sah model can provide accurate predictions of $I_{Dst}$, it requires too much computation to be practical for circuit simulation applications. Thus, the charge-sheet model becomes the candidate for characterizing $I_{Dst}$. We noted in section 4.5.3,

however, that the $I_D$ expression of the charge-sheet model in its full form is also still too cumbersome for most circuit-design simulation tasks. Fortunately, by making some appropriate simplifying approximations, the general form of the charge-sheet model $I_D$ equation can be reduced to a less complex formulation that still provides accurate predictions of $I_{Dst}$ in long-channel MOSFETs.

Consider the case of a long-channel NMOSFET in which: (1) the source is grounded; (2) $V_{GS}$ approaches (but remains less than) $V_T$, and; (3) $|V_{DS}| \geq 0.1V$. Now recall that in inversion (i.e., when $V_{GS} > |V_T|$), the free-carrier concentration $n_{ps}$ in the channel is large (e.g., $n_{ps} \geq N_A$), and $I_D$ in this case is dominated by drift current. However, when $V_{GS} < |V_T|$, $n_{ps}$ is much smaller than $N_A$, but is not zero In addition, in weak inversion the drain voltage $V_{DS}$ drops almost entirely across the reverse-biased drain-substrate depletion region.

Figure 4-26a illustrates the variation of inversion-layer charge concentration versus channel position in a long-channel NMOSFET in weak inversion. Figures 4-26b and c depict $\varphi_{surf}(y)$ and a 2-D perspective plot of the potential $\varphi(x,y)$ diagrams in weak inversion, respectively. We see that the band bending in the *x*-direction is too small to establish a strongly inverted channel [i.e., $\varphi_B < \varphi_{surf} < 2\varphi_B$], thus the channel mobile charge density $Q_I$ is very small. In the *y*-direction most of the band bending occurs at the drain junction. Since the value of $\varphi_{surf}$ along the *y*-direction remains essentially constant over most of the length of the channel, the $\mathcal{E}$-field along the *y*-direction is also very small [i.e., $\mathcal{E}(y) = -\partial\varphi_{surf}/\partial y$ is very small]. The combination of a small lateral $\mathcal{E}$-field acting on a relatively small number of free carriers implies that the drift component of $I_{Dst}$ is negligibly small in weak inversion. In addition, in long-channel MOSFETs, the *gradient* of the $\mathcal{E}$-field in the *y*-direction along most of the channel length must also be very small. This means it is valid to apply the GCA when calculating $I_{Dst}$ in such devices. In short-channel MOSFETs, however, the gradient of $\mathcal{E}(y)$ can no longer be neglected, even in weak inversion, and thus the long-channel formulation of $I_{Dst}$ given here may not yield accurate estimates of $I_{Dst}$ in short-channel MOSFETs.

On the other hand, we shall show that the *gradient of the free carriers* along the *y*-direction in the channel in weak inversion can be relatively large. Since diffusion current is proportional to the carrier-density gradient, in such cases carrier diffusion can produce a significant $I_{Dst}$. In fact, diffusion is the dominant mechanism that establishes subthreshold current flow in long-channel devices. The expression for the diffusion current component is given by:

$$I_{diff} = A\, J_{diff} = A\, [q\, D_n\, dn\,(y)/dy] = Z\, t_{inv}\, [\, q\, D_n\, dn\,(y)/dy\,] \qquad (4 - 84)$$

where $D_n$ is the electron diffusion constant, A is the cross-sectional area of the electron flow, and $t_{inv}$ is the inversion layer thickness (or $A = Z\, t_{inv}$). We can express this equation in terms of the mobile charge density per unit area $Q_I$ instead of in terms of *n* by multiplying the mobile charge density in the channel (*qn*) by the inversion layer thickness $t_{inv}$. As shown in section 4.3.1.1, $t_{inv}$ can be approximated as $(kT/q)\mathcal{E}_{si}$ (x = 0), where $\mathcal{E}_{si}$ (x = 0) is given by $\sqrt{2qN_A\varphi_{surf}/\kappa_{si}\varepsilon_o}$, so

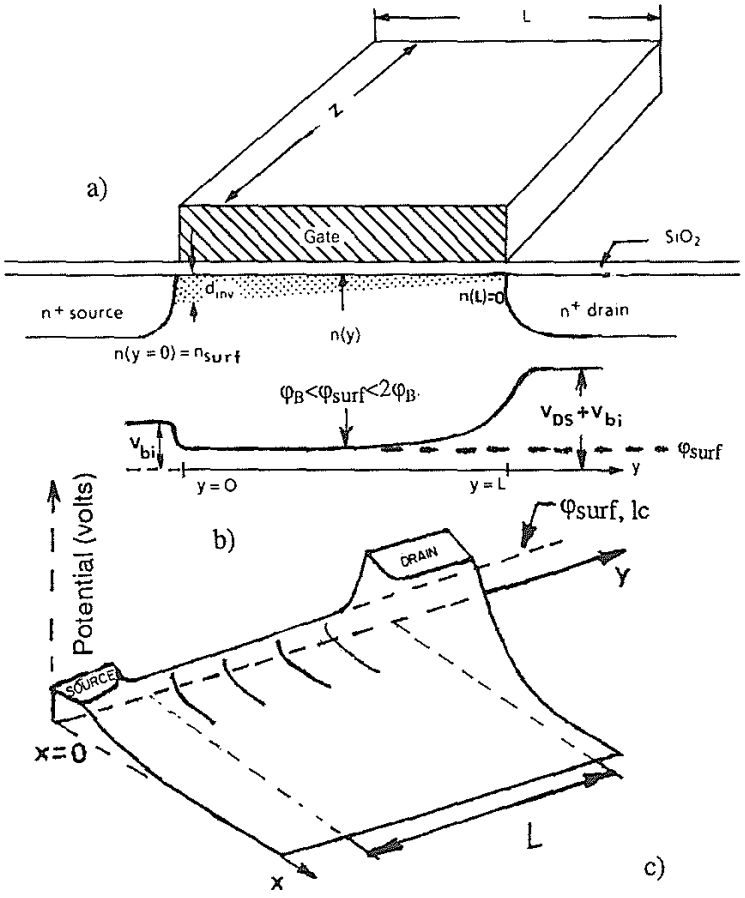


**Fig. 4-26** (a) Cross-sectional area of an NMOSFET in weak inversion showing the variation of inversion layer charge concentration versus position along the channel; (b) Plot of $\varphi_{surf}(y)$ versus y for the device of part (a); (c) 2-D perspective plot of potential versus position in a long-channel NMOSFET in weak inversion.

$$t_{inv} \approx \frac{kT}{q} \frac{\sqrt{\kappa_{si}\varepsilon_o}}{\sqrt{2q\, N_A\, \varphi_{surf}}} \qquad (4 - 85)$$

In addition, the carrier concentration in the inversion layer can be found using Eq. 3-13 (with $n_{po} = n_i^2/N_A$), or $n = (n_i^2/N_A)\exp(q\varphi_{surf}/kT)$. Using these relationships, $Q_I(y)$ can be expressed as

$$Q_I = q\, t_{inv}\, n(y) \approx q\, \frac{kT}{q} \frac{\sqrt{\kappa_{si}\varepsilon_o}}{\sqrt{2q\, N_A\, \varphi_{surf}}} \frac{n_i^2}{N_A} \exp\left(\frac{q\,\varphi_{surf}}{kT}\right) \qquad (4 - 86a)$$

By some algebraic manipulation this expression for $Q_I$ can be shown to be identical to the equation for the mobile charge density per unit area $Q_I$ in a MOS-C under weak inversion given in chap. 3 (i.e., Eq. 3-58, which we repeat here)

$$Q_I \text{ (weak inv)} \approx \frac{\sqrt{2q\, N_A \kappa_{Si} \varepsilon_o}}{2\sqrt{\varphi_{surf}}} \varphi_t\, e[\varphi_{surf}(GB) - 2\varphi_B]/\varphi_t \qquad (4 - 86b)$$

where the surface potential in the MOS-C is established just by the gate-body bias $V_{GB}$ (and $\varphi_t = kT/q$). We can include the effect of a bias between the channel and substrate in Eq. 4-85. That is, with the source grounded (i.e., $V_{BS} = 0V$, implying that $V_{DB} = V_{DS}$), $Q_I$ at the source and drain ends of the channel in a MOSFET under weak inversion, can be written using Eq. 4-86a as follows:

$$Q_{I,source} \approx q\, \frac{kT}{q} \frac{\sqrt{\kappa_{Si}\varepsilon_o}}{\sqrt{2\, q\, N_A\, \varphi_{surf}(source)}} \frac{n_i^2}{N_A} \exp\left(\frac{q\, \varphi_{surf}(source) - 2\varphi_B}{kT}\right) \qquad (4 - 87a)$$

$$Q_{I,drain} \approx q\, \frac{kT}{q} \frac{\sqrt{\kappa_{Si}\varepsilon_o}}{\sqrt{2\, q\, N_A\, \varphi_{surf}(source)}} \frac{n_i^2}{N_A} \exp\left\{\frac{q\, [\varphi_{surf}(source) - 2\varphi_B - V_{DS}]}{kT}\right\} \qquad (4 - 87b)$$

where $\varphi_{surf}(GB) = \varphi_{surf}(source)$ in this case, as $V_{BS} = 0V$. Since the diffusion current is constant along the channel, the gradient of $Q_I$ (i.e., $dQ_I/dy$) is also constant and can be approximated by the following expression, using Eqs. 4-87a and b:

$$\frac{dQ_I}{dy} = \frac{Q_{I,source} - Q_{I,drain}}{L} \approx \frac{Q_{I,source}}{L}\left[1 - \exp\left(\frac{-q\, V_{DS}}{kT}\right)\right] \qquad (4 - 88)$$

Then the expression for the diffusion component of the drain current in weak inversion $I_{Dst}$ can be written as

$$I_{Dst} = D_n\, Z \frac{dQ_I}{dy} = \frac{D_n\, Z\, Q_{I,source}}{L}\left[1 - \exp\left(\frac{-q\, V_{DS}}{kT}\right)\right] \qquad (4 - 89)$$

Now, if $|V_{DS}| \geq 0.1V$, at room temperature the term $\exp(-qV_{DS}/kT)$ in Eq. 4-88 is smaller than $e^{-4}$. Hence, this term in Eq. 4-89 will be much smaller than 1. As a result, if $V_{DS}$ exceeds a few $\varphi_t$ (i.e., a few $kT/q$, or at 300K, $\geq 0.1V$), we can consider $Q_{I,drain}$ to be negligibly small compared to $Q_{L,source}$.

In such cases, the expression for $I_{Dst}$ in long-channel MOSFETs can be approximated as $I_{Dst} \sim D_n Z Q_{Isource}/L$, or, in expanded form:

$$I_{Dst} \approx q\, D_n \frac{Z}{L} \frac{kT}{q} \frac{\sqrt{\kappa_{Si}\varepsilon_o}}{\sqrt{2\, q\, N_A\, \varphi_{surf}(source)}} \frac{n_i^2}{N_A} \exp\left(\frac{q\, \varphi_{surf}(source)}{kT}\right) \qquad (4 - 90)$$

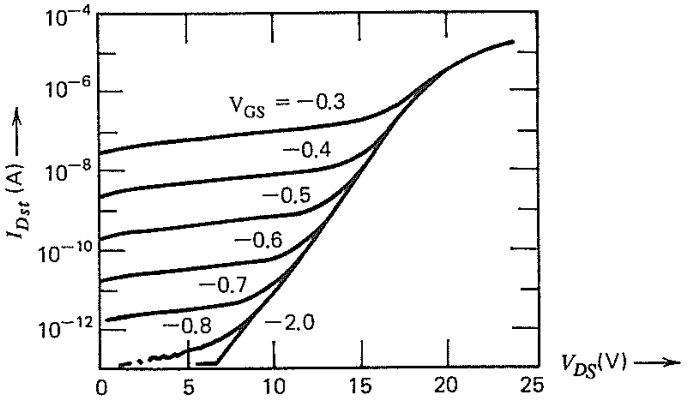


**Fig. 4-27** Experimental low-current characteristics for a MOSFET with $L = 2.1$ $\mu$m, with the source and substrate both tied to ground. For lower values of $V_{DS}$, $I_{Dst}$ is reduced by roughly one order of magnitude for each 0.1V reduction in $V_{GS}$ below the threshold value. At higher values of $V_{DS}$, a subsurface current flows that is independent of $V_{GS}$.[24] (© IEEE 1974).

Since $\varphi_{surf}$(source) is roughly proportional to $V_{GS}$ in the subthreshold region,[16] Eqs. 4-87 and 4-90 imply that $Q_{I,source}$ and $I_{Dst}$, respectively, are both exponentially dependent on $V_{GS}$.

In summary, Eq. 4-90 predicts that in long-channel MOSFETs $I_{Dst}$ will exponentially increase with $V_{GS}$ but will remain substantially independent of $V_{DS}$. Figure 4-27 illustrates this subthreshold behavior in a MOSFET with $L = 2.1$ $\mu$m. For values of $V_{DS}$ smaller than the punchthrough voltage (i.e., roughly the $V_{DS}$ value where the $I_D$ curves intercept the more steeply rising portion of the curve in Fig. 4-27), $I_{Dst}$ is seen to be essentially independent of $V_{DS}$ and increases exponentially with $V_{GS}$.

It turns out, however, that devices with gate lengths of ~2 $\mu$m are at the transition between long-channel and short-channel device behavior. That is, when $V_{DS}$ is sufficiently increased in MOSFETs with $L \leq 2$ $\mu$m, the source and drain depletion regions merge, and at that point $I_{Dst}$ starts to become dependent on $V_{DS}$ (as is also illustrated in Fig. 4-27 in the right side of the characteristics, where $I_{Dst}$ no longer depends on $V_{GS}$). This short-channel effect, known as *punchthrough*, is discussed in chap. 5. In general, however, punchthrough must be prevented from occurring in normal device operation, even in short-channel devices. That is, at the maximum operating $V_{DS}$ value the punchthrough current should be kept smaller than the long-channel $I_{Dst}$ value. One simple rule of thumb to accomplish this in a MOSFET that employs a $V_T$-adjust implant is to set the substrate doping concentration $N_{sub}$ at $>0.1N_I$, where $N_I = D_I/x_d$, and $D_I$ and $x_d$ are the threshold-adjust implant dose and the effective implant depth (or centroid), respectively.

It should also be noted that the $V_T$-adjust implant generally increases the subthreshold swing $S_t$, and this is one reason that $S_t$ in real devices is larger (~100 mV/dec) than the theoretically predicted value of ~60 mV/dec at 300K. A more complete discussion of $S_t$ is given in the upcoming section.

### 4.7.1 Subthreshold Swing $S_t$

Another important device characteristic in the subthreshold regime is the slope of log $I_D$ versus $V_{GS}$. This characteristic indicates how effectively a MOSFET can be turned OFF as $V_{GS}$ is decreased below $V_T$. The inverse of the slope is defined as the subthreshold swing $S_t$.[17] As voltage levels are reduced in an effort to save power and to use smaller devices, this characteristic becomes a limitation on how small a power-supply voltage can be used. In MOSFETs with uniformly doped substrates, $S_t$ is calculated from

$$S_t = \ln 10(d\ln I_D/dV_{GS})^{-1} = 2.3\ (kT/q)\ (1 + C_d/C_{ox}) \qquad (4\text{-}91a)$$

$$= 2.3\ (kT/q)\ [1 + \kappa_{si}t_{ox}/\kappa_{ox}d)] \qquad (4\text{-}91b)$$

$S_t$ is expressed in units of mV per decade. (The factor 2.3 comes from the conversion of ln(x) to 2.3 $\log_{10}[x]$). Let us consider the $S_t$ parameter in more detail.

Ideally, an abrupt change in $I_D$ should occur as $V_{GS}$ passes through $V_T$. If a MOSFET exhibits a steep decline in $I_D$ as $V_{GS}$ is decreased below $V_T$, its $S_t$ value will be small. Conversely, if a MOSFET structure is known to possess a small $S_t$, the implication is that only a small reduction of $V_{GS}$ below $V_T$ will effectively turn off the device; whereas if the device exhibits a large $S_t$ value (meaning a gradual slope in log $I_D$ vs $V_{GS}$) a significantly large $I_{Dst}$ may still flow in the OFF state (e.g., when $V_{GS} = 0$).

According to Eq. 4-91b, at 300K in the ideal limit of $t_{ox}$ --> 0, $S_t = (2.3kT/q)$ ~60 mV/dec. However, any nonidealities in an actual device (e.g., the presence of interface states, or a nonzero value of $t_{ox}$) cause $S_t$ to become larger than the 60 mV/dec value (also, note that if T increases, so does the value of $S_t$). The $S_t$ value of typical submicron NMOSFETs operating at 300K is ~100 mV/decade, and in such devices $I_D$ will drop from 1 $\mu$A to 1 pA for a 0.6V decrease in $V_{GS}$. Thus, if a MOSFET exhibits a *constant-current-$V_T$* of 0.6V (i.e., $I_D = 1\ \mu A/\mu m$ when $V_{GS} = V_T = 0.6V$), when $V_{GS} =$ 0V, $I_D$ will be reduced to 1 pA/$\mu$m. Thus, if $S_t$ is known, Eq. 4-91a can be used to estimate $I_{Dst}$ in long-channel MOSFETs in subthreshold operation (Fig. 4-28).[18] That is, circuit designers can readily calculate the gate bias required to keep the subthreshold leakage current below its specified maximum. Typically, to ensure that $I_{Dst}$ will be negligibly small, the maximum bias applied to the gate when the device is in the OFF state should be kept at least 0.5 V below $V_T$.

Equation 4-91 also indicates that $S_t$ can be made smaller by using a thinner $t_{ox}$ or a lower substrate doping concentration (which will make the channel depletion-region width d larger). In addition, Eq. 4-91 implies that $S_t$ increases with temperature (for example, at 100°C, the minimum theoretical value of $S_t$ is increased to ~100 mV/dec).*

* Note that in a non-uniformly doped channel (e.g., one which uses a $V_T$-adjust implant), the expression for $S_t$ is modified to

$$S_t = (kT/q) \ln 10\ [\ 1 + C_d/C_{ox}]/\{1 - [(\kappa_{si}/\kappa_{ox})(t_{ox}/L_D)]^2[C_d/C_{ox}]^2\} \qquad (4\text{-}92)$$

Basically, this equation indicates that the $V_T$-adjust implant causes $S_t$ to be somewhat increased (since the additional dopant in the channel reduces the depletion-region width, thus making $C_d$ in Eq. 4-91 larger). However, if the implant is deep enough, the depletion region

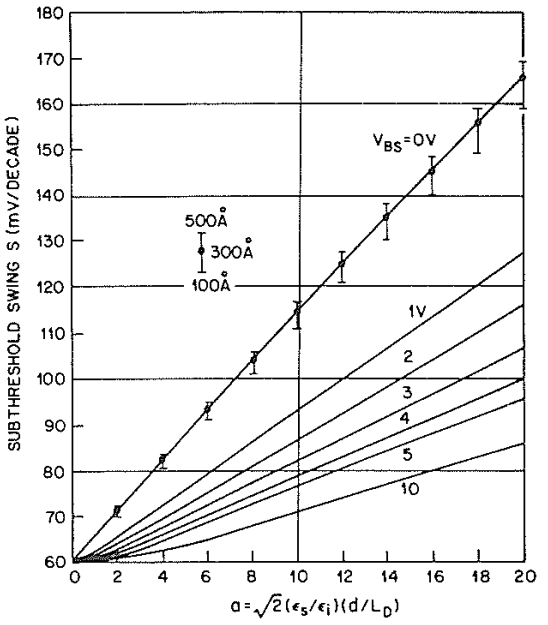


**Fig. 4-28** Subthreshold gate swing $S_t$ required to reduce the subthreshold current one decade versus the parameter $a = [\sqrt{2}\, t_{ox}/\kappa_{ox}q)][\kappa_{si}kT/\varepsilon_0 N_A)^{1/2}$. Vertical bars indicate the variation in $S_t$ at constant a when the oxide thickness is varied from 500 to 100 Å, and doping level and mobility adjusted accordingly. $V_{DS} >> kT/q$. [13] (© IEEE 1979).

Finally, it should be noted that because the depletion width increases when a substrate bias is applied, the subthreshold swing decreases according to Eq. 4-91b. This effect is shown in Fig. 4-29.[17,24]

Note that when the channel length gets small, the values of $I_{Dst}$ are larger than those predicted by the above model. This is due to so-called short-channel effects (discussed in chap. 5). As a result, measurements of $S_t$ versus channel length are used to detect the onset of these short-channel effects (punchthrough and surface drain-induced barrier lowering). Since the measurable $I_{Dst}$ is the sum of both the normal subthreshold and short-channel-induced components, an increase in the value of $S_t$ will signal the onset of the latter.

* (cont.) width will eventually be equal to that of the unimplanted device, and $S_t$ returns to the value exhibited by a device with no $V_T$-adjust implant. Nevertheless, the general dependences of $S_t$ on $t_{ox}$, T, and channel substrate doping exhibited in devices with uniformly doped channels still apply.

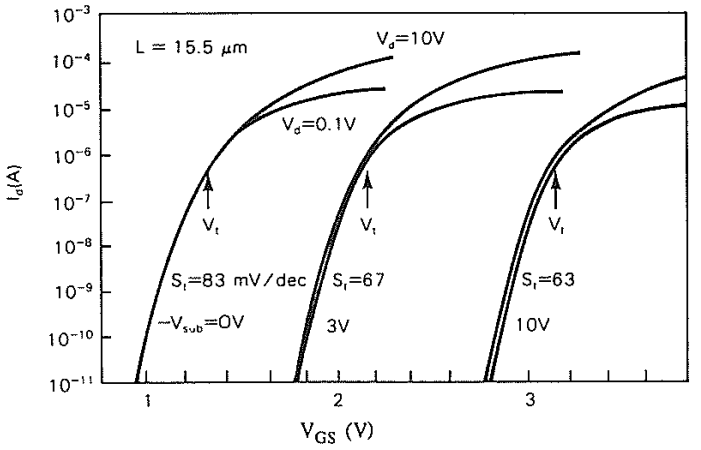


**Fig. 4-29** Experimental subthreshold characteristics for a long-channel device ($L$ = 15.5 $\mu$m).[24] (© IEEE 1974).

## 4.7.2 Gate-Induced Drain Leakage (GIDL)

Another form of leakage current observed in OFF-state MOSFETs is *gate-induced drain leakage (GIDL).*[19] The carriers responsible for GIDL originate in the region of the drain that is overlapped by the gate, and GIDL is occurs when the gate is grounded and the drain is at $V_{DD}$. A large electric field then exists across the oxide ($\mathcal{E}_{ox}$), which must be supported by charge in the drain region. This charge is provided by the formation of a depletion region in the drain as shown in Fig. 4-30a. If $\mathcal{E}_{ox}$ becomes sufficiently large, in addition to the depletion region, an inversion layer will attempt to form at the silicon surface of the drain. However, as the minority carriers arrive at the surface to form the inversion layer, they are immediately swept laterally to the substrate (which is a region of lower potential for the minority carriers). Hence, in this case, the depletion region under the oxide in the drain instead becomes a *deep depletion layer.** The zone near the surface where an inversion layer should be formed is referred to as an "incipient inversion layer." The current that flows as a result of the carriers being swept from this

* *Deep depletion* is a non-equilibrium condition where there are fewer minority carriers in a depletion region than would exist in equilibrium. Consider the case of an $n^+$MOS structure (i.e., the condition that exists in an NMOS drain region), that is biased so that an inversion layer of holes should exist at the surface (and a depletion layer exists below it). Under equilibrium conditions, this condition can persist indefinitely under appropriate dc bias. In the structure described above, a dc bias is applied that attempts to establish such an inversion layer of holes at the surface of the $n^+$drain. However, the potential of the substrate is lower for holes than the surface potential of the drain, and thus any holes arriving at the drain surface move laterally to the substrate region. Thus, the depletion region under the overlap area becomes a zone of deep depletion.

incipient inversion layer constitute the GIDL current.

The magnitude of GIDL current is independent of temperature, and hence it is believed that thermal generation of carriers in the incipient inversion region plays only a minor role in GIDL. Instead, it is proposed that when $\mathcal{E}_{ox}$ becomes large enough, the voltage drop in the deep-depletion layer becomes so large that various trap-assisted carrier-generation events become possible (Fig. 4-30b).[20] These include thermal emission of an electron from the valence band to a trap site (expressed as a vertical transition in the diagram) and then tunneling to the conduction band (horizontal transition), and trap-assisted tunneling from valence band to conduction band. For even larger fields (a few MV/cm), trap-free band-to-band tunneling may also occur (see also Fig..4-30b).

Like other forms of leakage current, GIDL will contribute to standby power, giving rise to the previously mentioned problems of excessive heat dissipation at large device counts and heavy current drain in portable systems. Hence, GIDL must be controlled so that it does not exceed some specified maximum value (typically, ≤10 pA/$\mu$m).

In order to control GIDL, the most important mechanisms that may cause it need to be identified. This allows processes involving these mechanisms to be avoided or modified to minimize GIDL. For example, it has been observed that shallow junction

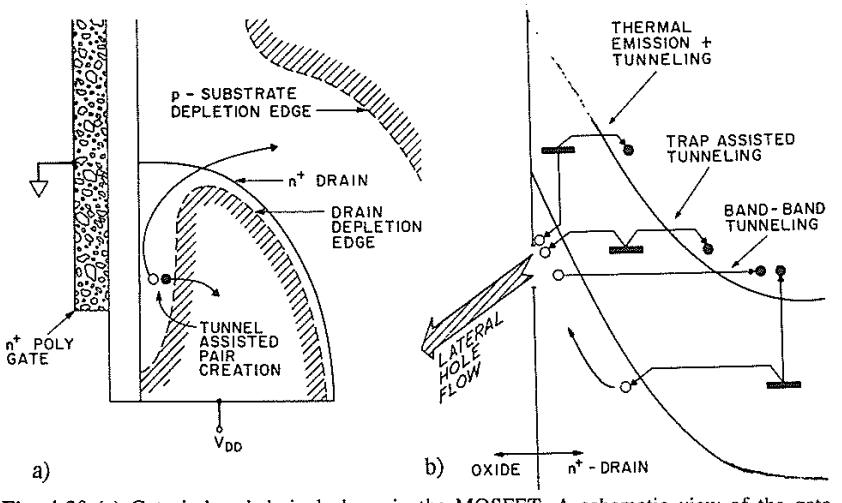


**Fig. 4-30** (a) Gate induced drain leakage in the MOSFET. A schematic view of the gate-drain overlap region for a grounded gate and the drain biased at $V_{DD}$. Tunneling created pairs lead to a lateral hole flow in the $n^+$ drain. This flow prevents formation of an inversion layer inside the drain. (b) Various mechanisms that can contribute to gate-induced drain leakage. Vertical transitions are thermal-emission processes. Horizontal transitions are tunneling processes. Holes are prevented from forming an inversion layer by lateral transport to the substrate. This flow is normal to the plane of the diagram, as indicated by the slanted arrow, lateral hole flow.[20] From J.R. Brews, "The Submicron MOSFET," Chap. 3, in *High-Speed Semiconductor Devices*, Ed. Sze. Copyright 1990, John Wiley & Sons. Reprinted with permission.

fabrication using Ge preamorphization introduces bulk midgap traps that increase GIDL.[21] Other reports indicate that interface traps caused by hot carrier injection,[22] or Fowler-Nordheim tunneling[23] increase GIDL by stimulating additional tunneling.

There are several general procedures that appear to be effective in reducing GIDL. First, the oxide thickness can be increased to reduce $\mathcal{E}_{ox}$ for a given voltage. But this is usually not implemented, since a thicker gate oxide will adversely impact other device characteristics. Second, the trap density in the near-surface area can be reduced, but such trap elimination generally requires a carefully controlled fabrication sequence. Third, the doping in the drain can be increased, as this will decrease the depletion region width and the tunneling volume. Unfortunately, the latter approach favors abrupt junctions, because graded or lightly-doped-drain (LDD) structures will lead to a significant lateral extension of the drain within which the doping is lighter, inviting greater GIDL. Tradeoffs of field reduction against GIDL may need to be considered. On the other hand, it has also been reported that LDD devices can suppress GIDL by suppressing the lateral field.

Nevertheless, it has been reported that GIDL sets a limit on the power supply voltage $V_{DD}$ of an LDD MOSFET of[25,29]

$$V_{DD} = 4 \times 10^6 \text{ V/cm} \times t_{ox} + 1.2\text{V} - V_{FB} \qquad (4 - 93)$$

A non-LDD MOSFET would have a much higher GIDL current. This implies that suppression of GIDL may be a strong reason to retain the LDD structure in MOSFETs even after $V_{DD}$ is reduced to suppress hot-carrier effects. (Note that in Eq. 4-93 $V_{FB}$ is ~0V for an $n^+$ polysilicon gate on an $n^+$ drain and about 1.1V for an $n^+$ polysilicon gate over a $p^+$ drain.)

## 4.8 SUMMARY OF LONG-CHANNEL MOSFET BEHAVIOR

The behavior of the long-channel as detailed in this chapter can be summarized by examining the I-V characteristics of the long-channel MOSFET in strong inversion (Fig. 4-31a), and in the subthreshold region of operation (weak inversion, see Fig. 4-31b).

In strong inversion we plot the output characteristics of the MOSFET ($I_D$ versus $V_{DS}$ with $V_{GS}$ as the parameter) on an axis with linear $I_D$ and $V_{DS}$ scales. We see that for a fixed value of $V_{GS}>V_T$, the drain current first increases linearly with $V_{DS}$. Eventually, as shown in Fig. 4-31a, the drain current saturates. Beyond the value of saturation voltage (i.e., when $V_{DS}>V_{DSsat}$), $I_D$ remains constant with increasing $V_{DS}$. The value of $I_{Dsat}$ is also proportional to $(V_{GS} - V_T)^2$ - as predicted by charge-control model. The values of $I_D$ versus $V_{DS}$ and $V_{GS}$ in the linear region, as well as the values of $I_{Dsat}$ and $V_{DSsat}$ can be calculated using any one of the four long-channel MOSFET models given in section 4.5, depending on the accuracy desired.

In the subthreshold region of operation, the behavior is described by plotting $I_D$ (with a logarithmic scale) versus $V_{GS}$ (with a linear scale). As shown in Fig. 4-31b, in long-channel MOSFETs the drain current $I_D$ drops exponentially once $V_{GS}$ becomes ~0.2V below $V_T$. Furthermore, in long-channel MOSFETs the slope of this log $I_D$-$V_{GS}$

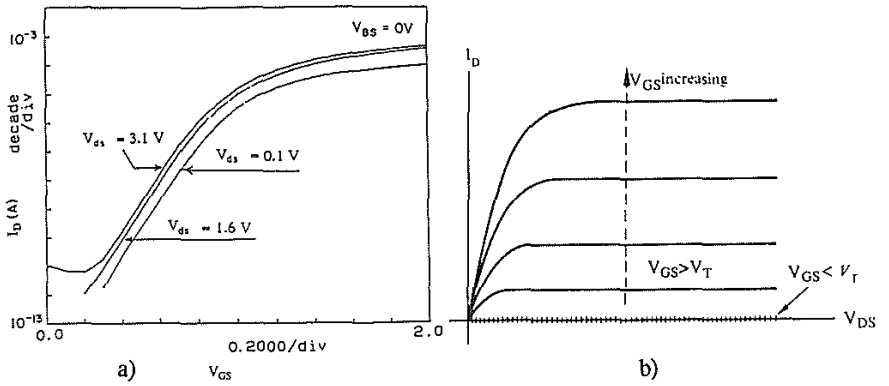


**Fig. 4-31** (a) $I_D$ versus $V_{DS}$ characteristics of long-channel MOSFETs beyond strong inversion. (b) $I_D$ versus $V_{GS}$ characteristics of a long-channel MOSFET below threshold (weak inversion).

characteristic does not change with increasing $V_{DS}$, nor does the value of $I_D$ increase at a fixed value of $V_{GS}$ as $V_{DS}$ is increased.

Finally, the threshold voltage of the long-channel MOSFET does not vary as $L$ is decreased, nor does it change with increasing $V_{DS}$, although this $V_T$ behavior is not indicated by either Fig. 4-31a or Fig. 4-31b.

## REFERENCES


1. D. A. Hodges and H. G. Jackson, *Analysis and Design of Digital Integrated Circuits,* McGraw-Hill Book Co., New York, 1983.
2. S. M. Sze, *Semiconductor Devices - Physics and Technology,* John Wiley & Sons, New York, 1985, p. 444.
3. S. Selberherr, A. Schutz, and H.W. Potzl, "MINIMOS-A two dimensional MOS analyzer," *IEEE Trans. Electron Dev.,* **ED-27**, p. 1540, 1980.
4. H.C. Pao and C.T. Sah, "Effects of Diffusion Current on Characteristics of Metal-Oxide (Insulator)-Semiconductor Transistors," *Solid-State Electron.* **9**, 927, (1966).
5. Y.P. Tsividis, *Operation and Modeling of the MOS Transistor,"* McGraw-Hill, New York, 1987.
6. R.F. Pierret and J.A. Shields, "Simplified long-channel MOSFET Theory," *Solid-State Electronics,* vol. 26, p. 143, 1983.
7. G. Baccarani et al., "Analytical i.g.f.e.t.model including drift and diffusion currents," *IEE Journal on Solid-State and Electron Devices,* vol. 2, p. 62, March 1978.
8. J.R. Brews, "A Charge-Sheet Model of the MOSFET," *Solid-State Electronics,* vol. 21, p. 345, 1978.
9. H.K. Ihantola and J.L Moll, "Design Theory of a Surface Field-Effect Transistor," *Solid-State Electronics* 7, 423 (1964).

**10.** A. Vladimirescu, A.R. Newton, and D.O. Pederson, *SPICE Version 2G.2 Users Guide,* Electronics Research Laboratory, University of California, Berkeley.

**11.** R.S. Muller and T.I. Kamins, *Device Electronics for Integrated Circuits,* 2nd. Ed., New York, John Wiley & Sons, 1986.

**12.** V.L. Rideout, F.H. Gaensslen, and A. LeBlanc, "Device Design Consideration for Ion-implanted *n*-Channel MOSFETs," *IBM J. Res. Dev.,* p. 50, (1975).

**13.** J.R. Brews *IEEE Trans. Electron Dev.*, **ED-26(11)**, 1696 (1979),

**14.** D. Antoniadis "Calculation of threshold voltage in nonuniformly doped MOSFETs," *IEEE Trans. Electron Dev.*, **ED-31,** p. 303, March 1984.

**15.** J.R. Brews, "The Physics of the MOS Transistor," in *Silicon Integrated Circuits*, Part A, Ed. D. Kahng, New York, Academic Press, 1981.

**16.** S. M. Sze, *Semiconductor Devices: Physics and Technology,*, John Wiley & Sons, New York, p. 213, 1985.

**17.** J.R. Brews, J. "Subthreshold Behavior of Uniformly and Nonuniformly Doped Long-Channel MOSFET," *IEEE Trans. Electron Dev.,* **ED-26** (9) p. 1282, Sept. 1979.

**18.** *ibid.* , (**16**), p. 470.

**19.** T. Y. Chan et al., 1987 IEDM Tech. Digest, p. 718.

**20.** J.R. Brews, "The Submicron MOSFET," chap. 3 in *High-Speed Semiconductor Devices,* S.M. Sze Ed., Wiley- Interscience, New York, 1990.

**21.** D.-S. Wen et al., "Tunneling Leakage in Ge-PreAmorphized Shallow Junctions," *IEEE Trans. Electron Dev.,* **ED-35** (7), 1107 (1988).

**22.** C. Duvvury et al., "Leakage Current Degradation in *n*-MOSFETs Due to Hot-Electron Stress," *IEEE Electron Dev. Lett.* **EDL-9** (11), 579 (1988).

**23.** I. C. Chen et al., "Interface-Trap Enhanced Gate-Induced Leakage Current in MOSFET," *IEEE* Electron Dev. Lett., **EDL-10**, (5), 216 (1989).

**24.** R.R. Troutman, "Subthreshold Design Considerations for IGFETs," *IEEE J. Solid-State Circuits,* **SC-9**, p. 55, (1974).

**25.** S. Parke et al., "Design for suppression of gate-induced leakage in LDD MOSFETs."

**26.** *ibid.,* reference **16** p. 444.

**27.** V.L. Rideout, F.H. Gaensslen, and A. LeBlanc, *IBM J. Res. Dev.,* **19**, p. 50, (1975).

**28.** N.D. Arora, *Solid-State Electronics*, **30**, p. 559, (1987).

**29.** H.-J Wann, P.K. Ko, and C. Hu, "Gate-Induced Band-to-Band Tunneling Leakage Current in LDD MOSFETs," *Tech. Dig. IEDM,* 1992, p. 147.

**30.** R.F. Pierret, *Field Effect Devices*, Vol. IV Modular Series on Solid-State Devices, Addison-Wesley Publishing Co. Reading, MA., 1983.

## PROBLEMS

**1.** Another way to model the drain current in a MOSFET is to note that it can be represented as mobile charge induced in the channel divided by the *transit time* (or average time required for an electron to move from the source to drain). For an *n*-channel MOSFET with a 250Å oxide, 1 $\mu$m channel length, 10 $\mu$m channel width, and $V_T = 1V$, operated at $V_{GS} = 5V$ and $V_{DS} = 0.1V$, calculate the total electron charges in the channel and the electron transit time. Then, show that this charge divided by the transit time is equal to the current calculated at the linear region as given by Eq. 4-65.

**2.** Evaluate the coefficient *k* of Eq. 4-64 for a MOSFET in which $\mu_n = 580$ cm$^2$/V sec, Z/L = 1 and (a) $t_{ox} = 50$ nm, and (b) $t_{ox} = 10$ nm.

**3.** Account qualitatively for the differing drain current $I_D$ predictions of the bulk-charge and square-law models of the long-channel MOSFET.

**4.** Describe how the saturation voltage $V_{DSsat}$ is defined and derive $V_{DSsat} \sim V_{GS} - V_T$ as a first order expression.

**5.** The sheet resistances of the source ($R_S$) and the drain ($R_D$) are both parasitic resistances (see Appendix B). Discuss why $R_S$ decreases $I_D$ more than does $R_D$ in the saturation region of operation. Also, derive an analytic expression of $g_m$ in the linear region as a function of $R_S$ and $R_D$.

**6.** If a circuit designer wants to ensure that a MOSFET exhibits no more than no more than 1 pA of leakage current in the off state, and also wants $V_T = 0.9V$ (where $V_T$ is defined as the gate voltage that causes 1 $\mu$A current), what maximum $S_t$ value must the device exhibit.

**7.** Verify that the expression for the capacitance of the surface space-charge region $C_d$ in Eq. 4-91 is correct (i.e., that $C_d = \kappa_{Si}\varepsilon_0/d$).

**8.** The $I_D$-$V_{GS}$ characteristics for a long *n*-channel MOSFET are shown in Fig. 4P-1. Using the square-law model and information available from the graph, compute the drain current $I_D$ when $V_{GS} = 3V$ and $V_{DS} = 5V$.

**9.** A MOSFET has been fabricated on a *p*-type substrate with doping concentration $N_A = 4\times10^{15}$ cm$^{-3}$. The gate oxide thickness is 50 nm, the gate is $n^+$ polysilicon, the oxide charge is $Q_{tot} = 2\times10^{10}$ cm$^{-2}$, and $V_T$-adjust implant of $2\times10^{12}$ boron atoms/cm$^2$ is performed through the gate oxide. Assume that Z/L = 1 and $\mu_n = 800$ cm$^2$/V sec, and $V_{BS} = 0V$. (a) Calculate the threshold voltage of the device; and (b) Calculate $V_{DSsat}$ and $I_{Dsat}$ for the MOSFET using: (i) the bulk-charge model and; (ii) the square-law model. Take $V_{GS} = 5V$. Comment on the accuracy of the square-law model.

**10.** Explain why we can approximate the thickness of the inversion layer as the depth beneath x = 0 at which $\varphi(x)$ has dropped to a value of $0.38\varphi_{surf}$.

**11.** Explain why $I_D$ does not become zero if $V_{GS}>V_T$ and $V_{DS}>V_{DSsat}$, as might be the conclusion based on the long-channel approximation used to calculated $I_D$.

**12.** Derive the I-V characteristics of a MOSFET with the drain and gate connected together and the source and substrate grounded. Can one obtain the threshold voltage from these characteristics?

**13.** An NMOSFET with $Z/L = 15$, $t_{ox} = 80$ nm and $\mu_n = 600$ cm$^2$/V sec is to be used as a controlled resistor: (a) What charge density is required for the device to exhibit a dc resistance of 3.5 kΩ between the source and drain in the saturation region? (b) What value of $(V_{GS} - V_T)$ is needed to obtain the desired resistance?

**14.** An Al gate enhancement-type NMOSFET has a substrate doping of $N_A = 6\text{x}10^{15}$ cm$^{-3}$ and a gate oxide thickness of 100 nm, and $Q_{tot} = 5\text{x}10^{10}$ cm$^{-2}$. Determine $V_T$ of this device. When the device is operated in the linear region with $V_{DS} = 0.5$V, calculate the gate voltage needed to obtain a drain current of 2 mA. Assume $L = 10$ $\mu$m, $Z = 100L$, and $\mu_n = 500$ cm$^2$/V sec.

# CHAPTER 5

## MOS TRANSISTOR DEVICE PHYSICS: PART 3

## THE SUBMICRON MOSFET

The two major goals of MOSFET scaling are to increase the *density* and *speed* of the digital ICs in which such scaled-down devices are used. Increasing *density* obviously means using smaller channel lengths and widths. To increase the *speed* of digital ICs, the MOSFET saturation drain current $I_{Dsat}$ must be increased (i.e., to allow faster charging and discharging of parasitic capacitances). From the long-channel MOSFET models given in chap. 4, a decrease in either the channel length $L$ or gate oxide thickness $t_{ox}$ will lead to an increase in $I_{Dsat}$. In fact, the long-channel MOSFET models predict that $I_{Dsat}$ should continue to increase indefinitely as $L$ and $t_{ox}$ are decreased, seeming to imply that only the limitations of process technology (and not device effects) prevent the manufacture of even smaller, higher-performing MOSFETs. In addition, the MOSFET models of chap. 4 also accurately describe many other device characteristics of long-channel MOSFETs, including threshold voltage, subthreshold current, and the $I_D$-$V_{DS}$ characteristics in strong inversion.

However, as process technology improved to the point where devices could be fabricated with gate lengths smaller than ~2 $\mu$m, it turned out that MOSFETs began to exhibit phenomena not predicted by the long-channel MOSFET models. Such phenomena were thus termed *short-channel effects.* One of the more surprising of such short-channel effects (which becomes especially pronounced as $L$ decreases below 0.5 $\mu$m) is that the drain current in saturation $I_{Dsat}$ shows far less increase as $L$ is decreased than is predicted by the long-channel models (see Fig. 5-1).[1,47] In fact, in the simple model to be presented in section 5.4, $I_{Dsat}$ is predicted to become independent of $L$ in extremely small MOSFETs, approaching instead, a constant value given by $Q_I v_{sat} Z$ (where $v_{sat}$ is the saturation velocity of the carriers, as described in section 5.4.1.2). In contrast, reducing $t_{ox}$ (which has the effect of increasing the oxide field, and in turn causes $Q_I$ to increase), yields a considerably greater increase in $I_{Dsat}$. Furthermore, as shown in Fig. 5-1 $I_{Dsat}$ will also increase more rapidly as $L$ is decreased if the MOSFET has a thinner gate oxide. This benefit provides even a greater impetus for making $t_{ox}$ as thin as possible as gate lengths are decreased further in the drive for higher density.

Since the quest for higher density still requires $L$ (and Z) to be further reduced, it will nevertheless be necessary to confront the other short-channel effects (besides the



MPS EX. 1008C - 144/295

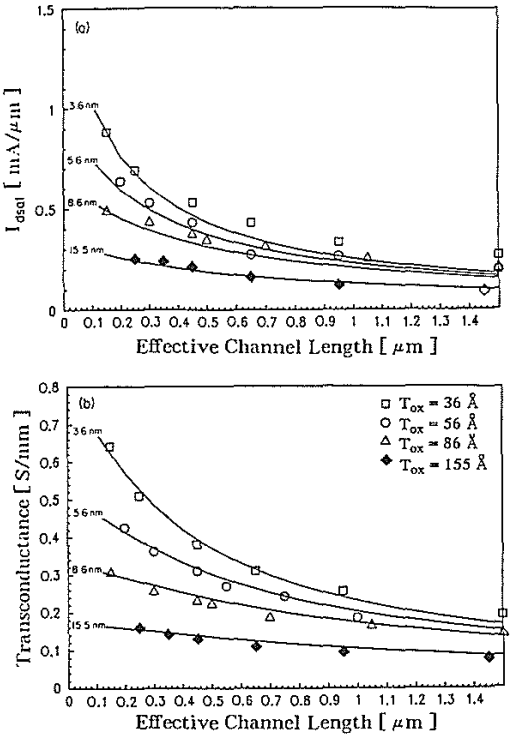


**Fig. 5-1** Measured and calculated $I_{Dsat}$ for an array of deep submicron NMOS transistors with four different gate-oxide thicknesses.[47] (© 1987 IEEE).

one of the $I_{Dsat}$ dependence on $L$ mentioned above). These other short-channel effects can be classified into two groups: (1) increased leakage current when the MOSFET is "off," and; (2) reliability problems associated with short-channel device structures.

Increased "off-state" leakage in short-channel MOSFETs is due to several phenomena, including: (a) lowering of the threshold voltage $V_T$ as $L$ is decreased and/or $V_{DS}$ is increased; (b) the onset of punchthrough at smaller drain biases as $L$ is decreased, and; (c) an increase in isolation leakage current as the isolation spacing is decreased. We will discuss $V_T$ lowering and punchthrough in this chapter, and isolation leakage phenomena in chap. 6.

The reliability problems that arise in short-channel MOSFETs include: (a) thin gate-oxide breakdown (to be discussed in chap. 7); (b) device degradation due to hot-carrier effects (to be discussed in chap. 9); and (c) reliability problems associated with the interconnects between MOSFETs (e.g., electromigration failures in the metal lines). The latter problem is treated in Vol. 2, chaps. 3 and 4.

**Table 5-1. Comparison of Long-Channel and Short-Channel MOSFET Characteristics**

| Long-Channel MOSFET Behavior | Short-Channel MOSFET Behavior |
|---|---|
| 1. The threshold voltage $V_T$ is independent of channel length $L$ and width Z. | 1. $V_T$ decreases as $L$ is decreased. $V_T$ may also be impacted by changes in Z. |
| 2. $V_T$ is independent of drain bias voltage. | 2. $V_T$ decreases with increasing $V_{DS}$. |
| 3. $V_T$ depends on $V_{BS}$ according to Eq. 4-12 (with $V_{BC}$ in Eq. 4-12 replaced by $V_{BS}$). | 3. $V_T$ increases less rapidly with $V_{BS}$ than predicted by Eq. 4-12. |
| 4. The subthreshold current $I_{Dst}$ increases linearly as $L$ decreases. | 4. $I_{Dst}$ increases more rapidly than linearly as $L$ decreases. |
| 5. $I_{Dst}$ is independent of drain bias. | 5. $I_{Dst}$ increases with increasing $V_{DS}$. |
| 6. The subthreshold swing $S_t$ is independent of gate length. | 6. $S_t$ increases with decreasing $L$. |
| 7. The drain current in saturation $I_{Dsat}$ is independent of $V_{DS}$. | 7. $I_{Dsat}$ increases as $V_{DS}$ increases. |
| 8. $I_{Dsat}$ is proportional to $(V_{GS} - V_T)^2$ | 8. $I_{Dsat}$ is proportional to $(V_{GS} - V_T)$. |
| 9. $I_{Dsat}$ is proportional to $1/L$. | 9. As $L \rightarrow 0$, $I_{Dsat}$ becomes independent of $L$. |

In this chapter we will also cover several device design scenarios developed to keep leakage currents sufficiently small as the MOSFET is scaled down. In addition, we describe the issues related to submicron PMOSFET design.

## 5.1 DEVICE CHARACTERISTICS OF LONG-CHANNEL VERSUS SHORT-CHANNEL MOSFETS

From the perspective of MOSFETs as circuit components, long-channel behavior has been specified in a number of ways. As a result, short-channel device effects can be so designated when a deviation from long-channel MOSFET behavior can be correlated with a reduction in the gate length (and/or gate width) dimension. Table 5-1 gives a list of long-channel device characteristics that undergo variation as the gate dimensions are decreased. As the behavior of the short-channel MOSFET is described later in this chapter, the terms associated with these characteristics will be defined and discussed in more detail.

From Table 5-1 we can see that the short-channel effects can be divided into the following categories: (a) those that impact $V_T$ (Items 1-3): (b) those that impact subthreshold currents (Items 4-6); and (c) those that impact $I_D$ when the MOSFET is operated in saturation [i.e., $V_{DS}>(V_{GS} - V_T)$], namely Items 7-9. In this chapter we

discuss these effects in detail, as well as measures that can be adopted to minimize their impact on MOSFET behavior.

## 5.2 EFFECT OF GATE DIMENSIONS ON THRESHOLD VOLTAGE

In this section we will describe three short-channel effects on the threshold voltage of MOSFETs, namely: (1) the short-channel threshold-voltage shift; (2) Narrow gate width effects on threshold voltage; and (3) the reverse short-channel threshold voltage shift.

### 5.2.1 Short-Channel Threshold-Voltage Shift

Experimentally, it is observed that as the dimensions of the gate are reduced, the threshold voltage of MOSFETs become less well predicted by the long-channel $V_T$ equation (Eq. 4-74). The error becomes significant as the *channel length dimension L* is reduced to less than 2 $\mu$m. Usually, $V_T$ decreases as $L$ is reduced.* In addition, in short-channel MOSFETs $V_T$ also decreases as $V_{DS}$ is increased. To get good agreement with measured data, a term $\Delta V_{TSC}$ must be subtracted from the value of $V_T$ obtained from Eq. 4-74. (In *n*-channel enhancement-mode MOSFETs the measured value of $V_T$ becomes less positive than that predicted by Eq. 4-74, while in *p*-channel enhancement-mode MOSFETs, $V_T$ becomes less negative.)

The decrease of $V_T$ with $L$ and $V_{DS}$ in short-channel devices is crucial because enhancement-mode FETs in CMOS are generally designed to operate with $V_T$ magnitudes of 0.6-0.8V. If the magnitude of $V_T$ drops even slightly below its designed value, the device may exhibit excessive drain leakage current when $V_{GS}$ = 0V. As discussed earlier, $V_T$ values of 0.6-0.8V in long-channel NMOS devices with lightly doped substrates can only achieved by increasing the doping concentration at the surface of the channel (i.e., with a $V_T$-adjust implant). If short-channel effects reduce $V_T$ below the long-channel values, the channel doping concentration must be increased even more to re-establish the desired $V_T$. Higher channel doping, however, generally degrades other device characteristics, such as carrier mobility and off-current. Thus, it is important to be able to model $\Delta V_{TSC}$ to facilitate reliable tradeoffs between process and electrical parameters and leakage current levels.

The failure of Eq. 4-74 to give good agreement with measured $V_T$ values in short-channel MOSFETs arises because this equation was derived assuming one-dimensional theory. That is, Eq. 4-74 assumes the space charge under the gate is controlled only by the vertical $\mathcal{E}$-field, $\mathcal{E}_X$. In that case, the channel depletion region charge will be influenced only by the charge on the gate. When the channel of a MOSFET is long, this is a reasonable assumption, as the influence of the drain and source junctions (and the influence of $V_{DS}$) on the quantity of channel charge can be neglected (Figs. 5-2a and b).

* In section 5.2.3, however, we will see that $V_T$ may initially increase as $L$ shrinks, before ultimately decreasing as described here. This unexpected effect is referred to as a *reverse short-channel effect* (RSCE), and will be described in section 5.2.3.

However, as $L$ approaches the dimensions of the source/drain junction depletion-region widths, a greater part of the channel-depletion region begins to consist of the space charge in the junction depletion regions (Fig. 5-2c and d). Hence, less gate charge (and a smaller vertical $\mathcal{E}$-field) is needed to cause inversion in short-channel MOSFETs than in long-channel MOSFETs (assuming each has the same substrate doping). This makes it appear that a smaller $V_T$ is needed to turn on a short-channel device. Furthermore, as the reverse bias applied to the drain ($V_{DS}$) is increased, the drain depletion region grows wider, leaving even less charge under the control of the gate.

There are four approaches that have been taken to establish quantitative values of $\Delta V_{TSC}$. They are the following:

1. *Numerical analysis* is used to find solutions of the two-dimensional Poisson equation for calculating the electric field and potential in the channel region.
2. Analytical expressions for $\Delta V_{TSC}$ are derived using the *charge sharing model.*
3. Analytical expressions for $\Delta V_{TSC}$ are derived using the drain-induced barrier lowering model, in which the 2-D Poisson equation is simplified to a one-dimensional form, making it solvable with analytical functions.
4. Analytical expressions for $\Delta V_{TSC}$ are derived using the drain-induced barrier lowering model in which a *quasi 2-D* approach is employed to analytically solve the Poisson equation.

While the numerical solution approach is the most accurate, this technique is not feasible for circuit simulation and statistical modeling. As a result, substantial effort has been expended to develop analytical models which provide rapid, inexpensive, and sufficiently accurate simulation of $\Delta V_{TSC}$. Hence, we devote most of our discussion to the latter three approaches.

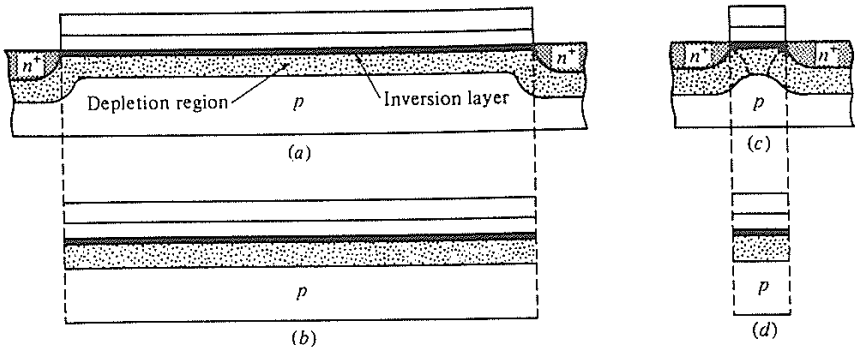


**Fig. 5-2** (a) Long-channel transistor; (b) the channel of (a) with edge effects neglected; (c) a short-channel transistor; (d) the channel of (c) with edge effects neglected. From Y.P Tsividis, *Operation and Modeling of the MOS Transistor*, McGraw-Hill, New York, 1987. Reprinted with permission.

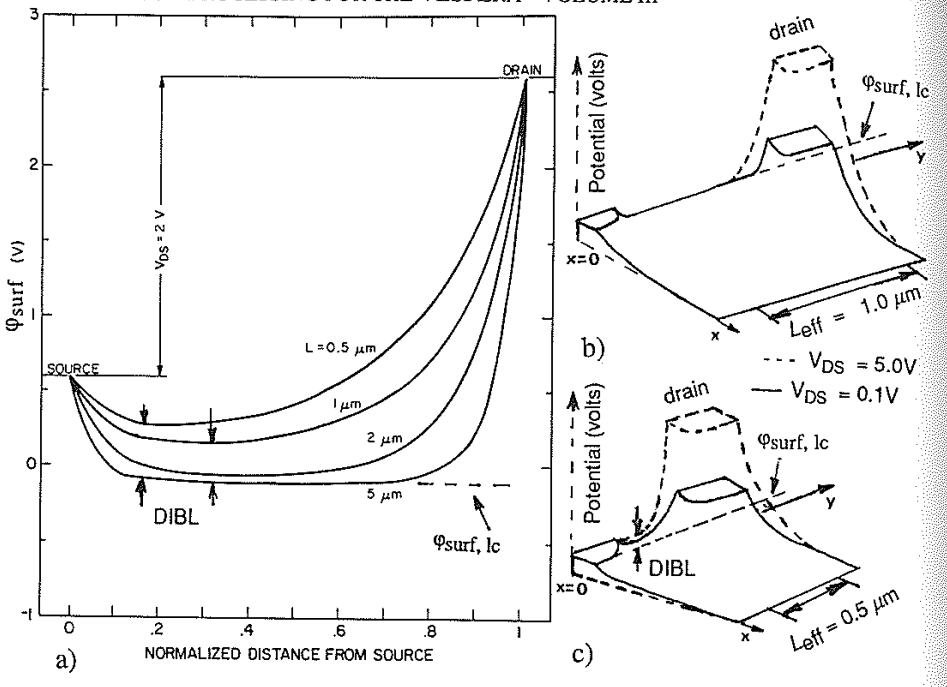


**Fig. 5-3** Simulated values of the surface potential $\varphi_{surf}$ along the channel for NMOSFETs with different channel lengths (note channel length is normalized). $N_A = 10^{15}$ cm$^{-3}$, $t_{ox}$ = 500Å, $r_j$ = 0.33μm, $V_{GS}$ = 0V, $V_{DS}$ = 2.0V, $V_{BS}$ = 0V.[109] (© 1979 IEEE). (b & c) 2-D potential variation for NMOSFETs with (b) $L_{eff}$ = 1.0 μm, and (c) $L_{eff}$ = 0.5 μm (see also Fig. 5-5). Solid line, $V_{DS}$ = 0.1V and dashed line, $V_{DS}$ = 5.0V.

**5.2.1.1 Numerical Solution of the 2-D Poisson Equation for Calculating $\Delta V_{TSC}$.** The most accurate method for simulating this effect is to solve the 2-D Poisson equation (i.e., as given here)

$$\frac{\partial^2\varphi(x,y)}{\partial y^2} + \frac{\partial^2\varphi(x,y)}{\partial x^2} = -\frac{\rho(x,y)}{\kappa_{si}\,\varepsilon_o} \qquad (5-1)$$

for the electrostatic-potential φ and the electric-field ℰ in the channel region. While exact analytical solutions of the 2-D Poisson equation are not possible, numerical methods can be used to obtain solutions of Eq. 5-1. As noted in chap. 2, several software programs have been developed which allow these methods to be implemented.[2,21] Specifically, such numerical Poisson solvers are available in device simulators (e.g., GEMINI, MINIMOS, and PISCES-II). However, numerical solutions of 2-D partial differential equations are computationally intensive (and hence time-consuming and expensive), and therefore as noted, are not suitable for use in circuit simulation applications in which the electrical behavior of large circuits must be simulated. Nevertheless, they serve as accurate benchmarks of $\Delta V_{TSC}$ against which the

values derived from the analytical models can be compared. Thus, they are a valuable tool for helping to develop more accurate analytical $\Delta V_{Tsc}$ models. Figure 5-3 shows such numerically calculated values of $\varphi_{surf}$ versus $y$ in NMOSFETs operated in subthreshold as $L$ is decreased from 5.0 $\mu$m to 0.5 $\mu$m.

**5.2.1.2 Charge-Sharing Models.** The *charge-sharing* perspective assumes that not all of the electric-field lines emanating from the charge under the gate terminate on the gate charge. Instead, some terminate on space charge in the source and drain depletion regions. The depletion charge under the gate is thus fractionally established by the source and drain (and in this sense, the channel charge is considered to be "shared" among the gate, source, and drain charge, see Fig. 5-4). Hence, less gate charge is required to cause inversion, making $V_T$ appear smaller. The fraction of the charge induced by the source and drain becomes significant as the channel length is of the order of the junction depletion region widths. Charge-sharing models seek to quantitatively determine the fractional charge induced by the gate.

In 1974, Yau proposed a simple, widely used analytical model based on the *charge-sharing* perspective.[3] This model assumes that the charge controlled by the gate is

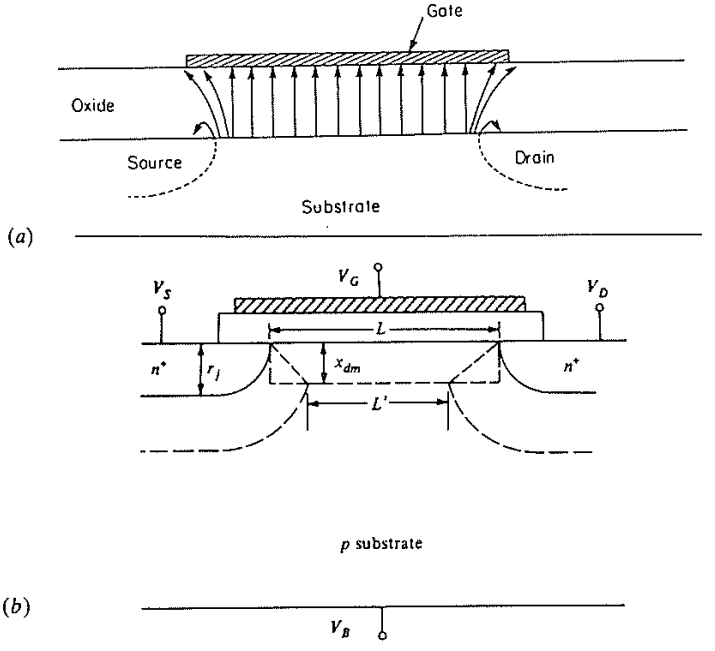


**Fig. 5-4** (a) Schematic showing perturbation of the electric field lines in the oxide near the source and the drain.[5] (© 1985 IEEE). (b) Yau's model of charge sharing.[3] Reprinted with permission of Solid-State Electronics.

reduced to the charge in the trapezoidal region of the channel shown in Fig. 5-4b. The resulting analytical expression based on this assumption allows the value of $\Delta V_{Tsc}$ to be calculated in devices with uniformly doped channels:

$$\Delta V_{Tsc} = \frac{q\, N_{SUB}\, d_{max}\, r_j \left( \sqrt{\left\{ 1 + \frac{2\, d_{max}}{r_j} \right\}} - 1 \right)}{C_{ox}\, L} \qquad (5 - 2)$$

where $d_{max}$ is the maximum width of the depletion region in the channel, and $r_j$ is the junction depth of the source/drain regions. According to Eq. 5-2, as $L$ decreases, $\Delta V_{Tsc}$ increases. Eq. 5-2 also implies that to keep $\Delta V_{Tsc}$ as small as possible, shallow source/drain junctions and thin gate oxides should be used ($C_{ox} = \varepsilon_{ox}/t_{ox}$). In addition, the channel depletion-region width should also be as small as possible. Although it will be seen that some of the assumptions used in Yau's model are generally invalid, the qualitative guidelines it yields for minimizing $\Delta V_{Tsc}$ appear to be correct as channel lengths are shrunk, regardless of the model employed for predicting $\Delta V_{Tsc}$. Yau's model also permits qualitative insight of $V_T$ lowering with decreasing $L$ to be gained, even if the quantitative $\Delta V_{Tsc}$ values do not accurately reflect experimental observations.

By modifying Eq. 5-2, Yau's model can also be used to estimate the effect of drain voltage on $\Delta V_{Tsc}$. That is, in Eq. 5-2 it is assumed that the width of the source, drain, and channel depletion regions are equal. However, under drain bias the drain depletion region grows wider. Thus these three depletion regions no longer have equal widths. To reflect the effect of drain-width variation on $\Delta V_{Tsc}$, Eq. 5-2 is reformulated as follows:[4]

$$\Delta V_{Tsc} = \frac{q\, N_{sub}\, d_{max}\, r_j \left( \left[ \sqrt{\left\{ 1 + \frac{2\, W_S}{r_j} \right\}} - 1 \right] + \left[ \sqrt{\left\{ 1 + \frac{2\, W_D}{r_j} \right\}} - 1 \right] \right)}{2\, C_{ox}\, L} \qquad (5 - 3)$$

Despite the appealing simplicity of the charge-sharing models, they fail to give good quantitative agreement with measured $V_T$ values in devices with very short channels (e.g., < 1 $\mu$m) or under large drain voltages. This apparently occurs because several of the assumptions used to derive the model are not valid, especially under short-channel and large $V_{DS}$ conditions. These include the following:

1. In Yau's model the induced charge is arbitrarily apportioned among the gate, source, and drain, whereas an accurate apportionment can only be accomplished by numerical integration of Poisson's equation and graphical analysis.

2. In the long-channel MOSFET model we assume that in subthreshold operation the entire $V_{DS}$ is dropped across the drain depletion region. Thus, the channel potential in the rest of the channel region is essentially independent of $V_{DS}$ and depends only on the gate bias. This also implies $\varphi_{surf}$ in this region is independent of position (i.e., its value is constant with position along the channel). However, as we shall see this assumption breaks down in the case of short-channel MOSFETs (and as is evident from the data shown in Fig. 5-3). Yau's model,

however, continues to assume that the potential in the channel region is constant with position. The portion of the charge that is shared is assumed to be distributed evenly under the gate to uniformly reduce the depletion charge density in the gate area. Obviously, this is not what actually happens physically.

These and other questionable assumptions of Yau's model are examined in ref. 5.

Nevertheless, despite the fact that charge-sharing models generally do not provide accurate quantitative results, they are still useful for providing first-order estimates of $\Delta V_{TSC}$, as well as for helping to intuitively visualize the physical basis of changes in $V_T$ as $L$ is decreased.

**5.2.1.3 Barrier-Lowering Models and DIBL.** The *barrier-lowering* perspective introduced by Troutman in 1979, provides a more rigorous foundation for deriving analytical models of $\Delta V_{TSC}$.[6] It seeks to determine the change in the potential energy barrier between the source and channel at the Si interface caused by the junction depletion region charges (which in turn arise from both the built-in *pn* junction $\mathcal{E}$-field and the reverse-bias drain voltage) as well as the gate charge.

Troutman made measurements of DIBL,[6] and he and others[1,2,6] performed numerical analysis of the Poisson equation (Eq. 5-1) to match experimental and theoretical results. As noted earlier, numerical analysis is necessary to obtain more accurate results. However, because of the extensive computational procedures required, this solution approach is not appropriate for applications involving computer-aided circuit design. As a result, other workers sought to develop approximate analytical solutions of Eq. 5-1 which would be suitable for such applications.

This is done by finding analytical models of the surface potential $\varphi_{surf}$ which relate it to the MOSFET structural parameters (e.g., $t_{ox}$, $r_j$, $L$), substrate doping levels, and applied biases. The value of $\varphi_{surf}$ from these models is used in the threshold voltage equation to calculate the modified $V_T$ value. The mathematical approach is to try and discover approximate analytical solutions to the 2-D Poisson equation, generally by converting it to a form that contains a differential term in only one dimension. This approach may be fruitful in this case, since we are only interested in finding the minimum value of $\varphi$ at the surface (i.e., of $\varphi_{surf}$) along the $y$-direction from source to drain, i.e., we want to determine $[\varphi_{surf}(y)]_{min}$. In most cases analytical solutions with approximate boundary conditions are proposed as the model. The accuracy depends on the degree of approximation in the boundary conditions.

Many DIBL-based analytical models have been developed. In general, they are more complex than the charge-sharing models. One of the simplest and most widely adopted is that of Hsu et al.[7] In this model, the 2-D Poisson equation is reduced to a 1-D equation by essentially approximating the $(\partial^2\varphi/\partial x^2)$ term of the 2-D equation as a constant. With the Poisson equation thereby converted into a 1-D form, it becomes possible to find an analytical solution, and Hsu's solution becomes the model for calculating $\Delta V_{TSC}$. Jain and Balk extend this model to include the effect of non-uniform channel width.[8] They also point out that both the Hsu model and their extension are expected to be accurate only for small values of DIBL (i.e., for devices having channels that are not too short and in which $V_{DS}$ is not too large). In addition, these models were derived for MOSFET structures with uniformly doped channel regions.

More recently, Skotnicki et al., reported another approach which allows the 2-D Poisson equation to be reduced to a 1-D equation using a so-called *voltage-doping transformation.* Using this technique they derived an analytical barrier-lowering model that is applicable to MOSFETs with non-uniformly doped channels.[9] Good agreement with measured data is also reported for devices with L as small as 0.8 $\mu$m (and in which $V_{DS}$ values are as large as 3V). A final approach, as described in the next section, also provides good agreement with measured data over the ranges of voltages studied.

Nevertheless, the accuracy of the barrier-lowering-based analytical models has not yet been confirmed for predicting the value of $\Delta V_{Tsc}$ in all device structures. As a result, it may still be prudent to use empirical measurements and/or numerical analysis to obtain accurate estimates of barrier lowering in specific device structures.

**5.2.1.4 Quasi-Two-Dimensional Analytical Solution for $\Delta V_{Tsc}$.** By using a quasi-2-D approach to solve the 2-D Poisson equation in the channel of the MOSFET, an analytical model has been derived that reportedly predicts $\Delta V_{Tsc}$ accurately, even for devices with channel lengths below 0.5 $\mu$m.[22] It begins by approximating the 2-D Poisson equation in the channel with the expression:

$$\frac{\varepsilon_{si}\, d_{max}}{\eta} \frac{d\mathcal{E}_y(y)}{dy} + \varepsilon_{ox} \frac{[V_T - V_{FB} - \varphi_{surf}(y)]}{t_{ox}} = q\, N_{sub}\, d_{max} \qquad (5\text{ - }4a)$$

or

$$\frac{\varepsilon_{si}\, d_{max}}{\eta} \frac{d^2\varphi_{surf}(y)}{dy^2} + \varepsilon_{ox} \frac{[V_T - V_{FB} - \varphi_{surf}(y)]}{t_{ox}} = q\, N_{sub}\, d_{max} \qquad (5\text{ - }4b)$$

where the parameters of this equation have been defined previously (except for $\eta$, which is a fitting parameter). The second term on the left-hand side is an approximation of the term $\partial\mathcal{E}_x/\partial x$ in the 2-D form of the Poisson equation. This quasi-2-D approach is also used in deriving a model for $I_{Dsat}$ and thus, the details involved in transforming Eq. 5-1 into a form akin to Eq. 5-4 are given in section 5.4.3.

The solution to Eq. 5-4, namely $\varphi_{surf}(y)$, under the boundary conditions $\varphi_{surf}(0) = V_{bi}$ and $\varphi_{surf}(L) = V_{DS} + V_{bi}$ is:

$$\varphi_{surf}(y) = V_{sL} + (V_{bi} + V_{DS} - V_{sL}) \frac{\sinh(y/l)}{\sinh(L/l)} + (V_{bi} - V_{sL}) \frac{\sinh(L - y)/l)}{\sinh(L/l)} \qquad (5\text{ - }5)$$

In Eq. 5-5 $V_{sL} = V_{GS} - V_T$, $V_{bi}$ is the built-in potential between the source-substrate and drain-substrate junctions, and $l$ is the characteristic length defined as

$$l = \sqrt{\frac{\varepsilon_{si}\, t_{ox}\, d_{max}}{\varepsilon_{ox}\, \eta}} \qquad (5\text{ - }6)$$

Equation 5-5 can now be plotted for a sufficient number of points between $y = 0$ and $y = L$ (e.g., 10 or more). From such plotted data, and a fitted curve, the minimum value of $\varphi_{surf}(y)$ can be found. By subtracting the long-channel value of $\varphi_{surf}$ at $V_T$ from $\varphi_{surf}(y)_{min}$, we can find $\Delta V_{Tsc}$. Figure 5-5 plots Eq. 5-5 for $\varphi_{surf}$ at a given $V_{GS}$, and for two values of $V_{DS}$ [i.e., $V_{DS} = 0.05$V (dashed lines) and $V_{DS} = 1.5$V (solid lines)] for

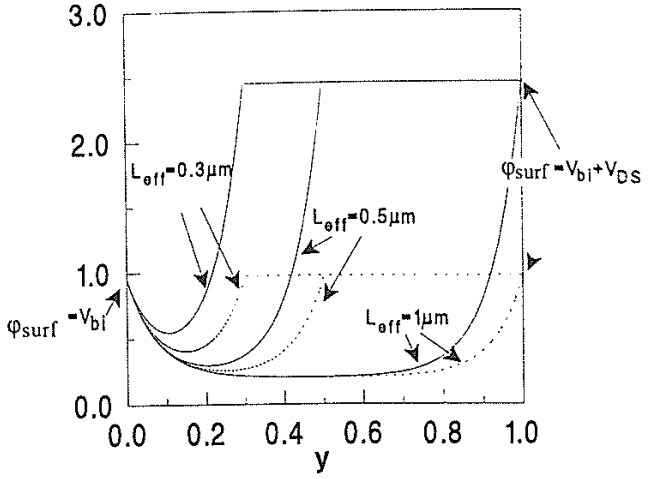


**Fig. 5-5** (a) Calculated surface potential along channel for different channel lengths using Eq. 5-5. The device parameters are $t_{ox}$ = 100Å, $N_{sub}$ = $N_A$ = $10^{16}$ $cm^{-3}$, $n^+$ = $10^{20}$ $cm^{-3}$, and $\eta$ = 1, i.e., $l$ = 0.1 $\mu$m.[22] (© IEEE 1993).

MOSFETs with different channel lengths. In this example, the device with $L_{eff}$ = 1 $\mu$m has a region where $\varphi_{surf}$ is constant as a function of position along a large fraction of the channel length (i.e., at a value of $\varphi_{surf}$ ~0.2V in this figure), and this value is determined merely by the gate bias (and not $V_{DS}$). A constant value of $\varphi_{surf}$ versus $y$ is indicative of long-channel behavior and $V_T$ in this device can thus be accurately found using Eq. 4-74.

In Fig. 5-5, devices with channel lengths 0.5 $\mu$m or smaller have a minimum value of $\varphi_{surf}$ greater than the long-channel $\varphi_{surf}$ value (i.e., $|2\varphi_B|$), and no region of constant $\varphi_{surf}(y)$ is evident, even for small values of $V_{DS}$. (This is different than the charge sharing approach, in which a region of constant [but somewhat larger] $\varphi_{surf}$ versus distance is assumed to exist even in very short length devices.) The results of Fig. 5-5 have been verified by 2D numerical simulation using such programs as MINIMOS and PISCES (e.g., as shown in plots of $\varphi_{surf}$ versus y for various $L$ values, see Fig. 5-3).

The minimum value of $\varphi_{surf}(y)$ is also seen in Fig. 5-5 to increase (i.e., the potential energy barrier for electron flow between source and drain will decrease) with decreasing channel length and increasing $V_{DS}$. If the minimum long-channel value of $\varphi_{surf}$ is subtracted from the minimum value calculated from Eq. 5-5 we get an expression for $\Delta V_{TSC}$. When $V_{DS}$ is small, this expression can be approximated as

$$\Delta V_{TSC} = [2(V_{bi} - 2\varphi_B) + V_{DS}](e^{-L/2l} + 2e^{-L/l}) \qquad (5-7)$$

Figure 5-6a shows the value of $\Delta V_{TSC}$ versus $L$ as calculated with Eq. 5-7 as well as with 2D numerical simulation. Agreement with the numerical simulation results is seen to be very good. It should also be noted that if $L > 5l$, then this equation reduces to a single exponential term, much like the one derived from the simpler barrier-lowering

models described in the previous section.* For most technologies $l$ is about 0.1-0.15 $\mu$m, hence these simple models give accurate results for $\Delta V_{Tsc}$ only if the channel length exceeds 0.5-0.8 $\mu$m.

When $V_{DS}$ is not small, the expression for $\Delta V_{Tsc}$ from this model is more complex, with its value when $L > 5l$ given approximately as

$$\Delta V_{Tsc} = 3(V_{bi} - 2\varphi_B) + V_{DS})\, e^{-L/l} + 2\sqrt{(V_{bi} - 2\varphi_B)(V_{bi} - 2\varphi_B + V_{DS})}\, e^{-L/2l} \quad (5 - 8)$$

Eq. 5-8 reduces to Eq. 5-7 for large $L/l$ and small $V_{DS}$ as expected. Figure 5-6b shows the results of calculating $V_T$ versus $V_{DS}$ for $L_{eff} = 0.3$ $\mu$m with Eqs. 5-7 and 5-8 as well as with 2D numerical simulation. Eq. 5-8 is seen to compare well with the 2D numerical simulation results, but Eq. 5-7 overestimates $\Delta V_{Tsc}$ at high $V_{DS}$. In Fig. 5-7 the value of $V_T$ is calculated versus $L$ using the charge sharing model, 2D numerical simulation, and Eq. 5-8. The results using Eq. 5-8 and numerical simulation are comparable. Finally, Fig. 5-8 compares the values of $V_T$ versus $L$ (with $V_{BS}$ as the parameter) calculated with Eq. 5-8 and with measured $V_T$ values in non-LDD

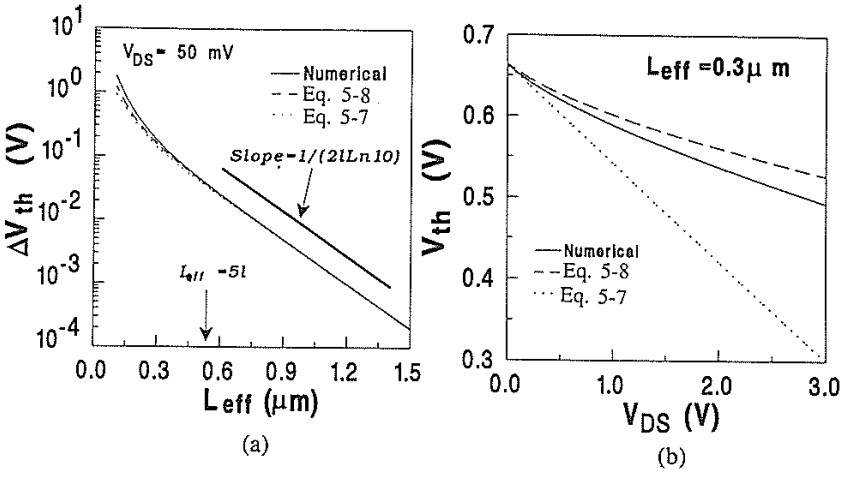


**Fig. 5-6** (a) The calculated $\Delta V_T$ shifts versus channel length at $V_{DS}$ = 0.005V. Note that the values obtained from the simple analytical models agree well with the numerical solution. The device parameters are the same as those in Fig. 5-5. Note that when $L > 5l$, all the curves have the same slope of $l$ ($2l$ in Eq. 5-8). (b) Comparison between simple analytical solutions and numerical solution of threshold voltage versus drain voltage. The solution based on $y_O = L/2$ (Eq. 5-7) overestimates the variation in threshold voltage.[22] (© 1993 IEEE).

* If $L = 5l$ then the first exponential term in Eq. 5-7 is $e^{-2.5}$ while the second term is $e^{-5}$, which is much smaller than $e^{-2.5}$. Thus, for $L>5l$, the second exponential term in Eq. 5-7 can be neglected, leaving an expression with only one exponential term. For cases where $L$ is smaller than ~$5l$, the second exponential term cannot be neglected, and the full Eq. 5-7 must be used to get accurate values of $\Delta V_{Tsc}$ when $V_{DS}$ is small.

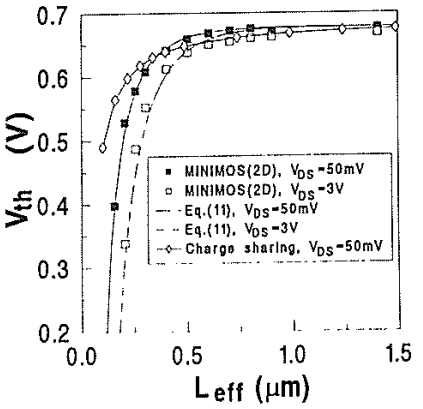


**Fig. 5-7** Comparison of the $V_T$ calculated using the charge sharing model, the two-dimensional numerical simulation (using MINIMOS), and the model of ref. 22. The device parameters are the same as those used in Fig. 5-5.[22] (© 1993 IEEE).

MOSFETs. Again, agreement is very good. The report describing this model also describes its application to LDD MOSFETs.

The characteristic length $l$ defined in Eq. 5-6 needs to be more exactly determined in order for this model to give accurate values of $\Delta V_{TSC}$. That is, due to the fitting parameter $\eta$ in Eq. 5-6, the value of $l$ from Eq. 5-6 only gives its correct order of magnitude. The exact value of $l$ needs to be extracted from $V_T$ data taken from actual MOSFETs.

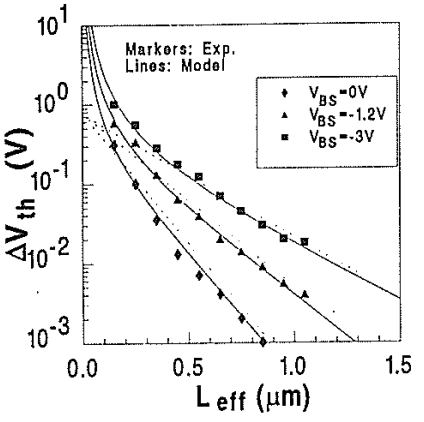


**Fig. 5-8** $\Delta V_T$ versus $L_{eff}$ at $V_{DS}$ = 0.005V and different $V_{BS}$ values for an non-LDD device. The solid lines are calculated results and the dashed lines are lines best fitting the experimental data of $L_{eff} >> 5l$. [22] (© 1993 IEEE).

An alternative form to Eq. 5-6 for expressing $l$ which allows its exact value to be empirically extracted is based on the empirical expression of Brews et al[23] for the minimum channel length $L_{min}$ a MOSFET must have in order to exhibit acceptable subthreshold behavior (see section 5.6.1.2 for more details on this expression):

$$L_{min} = 0.41\,(r_j\ t_{ox}\ d_{max}^2)^{1/3} \qquad (5 - 9)$$

If we assume $L_{min}$ is about $4l$, using Eq. 5-9 yields an empirical expression for $l$ as

$$l = 0.1\,(r_j\ t_{ox}\ d_{max}^2)^{1/3} \qquad (5 - 10)$$

According to this model, for an $n$-channel MOSFET with an $n^+$ poly gate, it can be shown that in order to maintain $V_T$ at 0.7V, i.e.,

$$V_T = 0.7V = V_{FB} + 2\varphi_B + \frac{t_{ox}}{\varepsilon_{ox}}\frac{4\,\varepsilon_{si}\,\varphi_B}{d_{max}} \qquad (5 - 11)$$

it is necessary that

$$d_{max} = \frac{t_{ox}}{\varepsilon_{ox}}\ \frac{4\,\varepsilon_{si}\,\varphi_B}{(V_T - V_{FB} - 2\varphi_B)} \approx \frac{2\,\varepsilon_{si}}{\varepsilon_{ox}}\ t_{ox} \qquad (5 - 12)$$

By substituting Eq. 5-12 into Eq. 5-10, $l$ can be rewritten as

$$l = 0.0007\ r_j^{1/3}\ t_{ox} \qquad (5 - 13)$$

where $r_j$ and $l$ are in $\mu$m and $t_{ox}$ is in Å. On the other hand, for an $n$-channel MOSFET with a $p^+$ poly gate,

$$d_{max} = 4\,(\varepsilon_{si}/\varepsilon_{ox})\ t_{ox} \qquad (5 - 14)$$

(assuming $V_T = 1.2V$). Therefore one has $l \sim 0.0011\ r_j^{1/3} t_{ox}$. This helps explain why buried-channel devices, either NMOSFETs or PMOSFETs generally have worse short-channel effects than comparable surface-channel N- or PMOSFETs.

**5.2.1.5 Measuring Surface-DIBL Effects.** Surface-DIBL in MOSFET structures with a fixed $L$ can be empirically characterized by measuring and plotting a set of log $I_{Dst}$ versus $V_{GS}$ curves with increasing values $V_{DS}$ as the parameter (as shown in Fig. 5-9). When analyzing such a set of curves, it must first be ascertained that subsurface-punchthrough current is not flowing (see section 5.3 for a discussion on punchthrough). For example, in Fig. 5-9 there is no indication that such punchthrough current occurs over the applied $V_{DS}$ range, since $S_t$ remains constant as $V_{DS}$ is increased.*

Once it is verified that punchthrough current is not significant, a quantitative estimate of surface-DIBL can be extracted from the shift in gate voltage $\Delta V_{GS}$ at a fixed drain current (typically 0.1 $\mu$A/$\mu$m) as the drain-source voltage is increased. That is, the

* If a device exhibits punchthrough current within the normal operating $V_{DS}$ range, the structure must be redesigned to eliminate this behavior. Devices exhibiting punchthrough will exhibit excessive leakage current at $V_{GS} = 0V$ (i.e., when the device is nominally OFF).

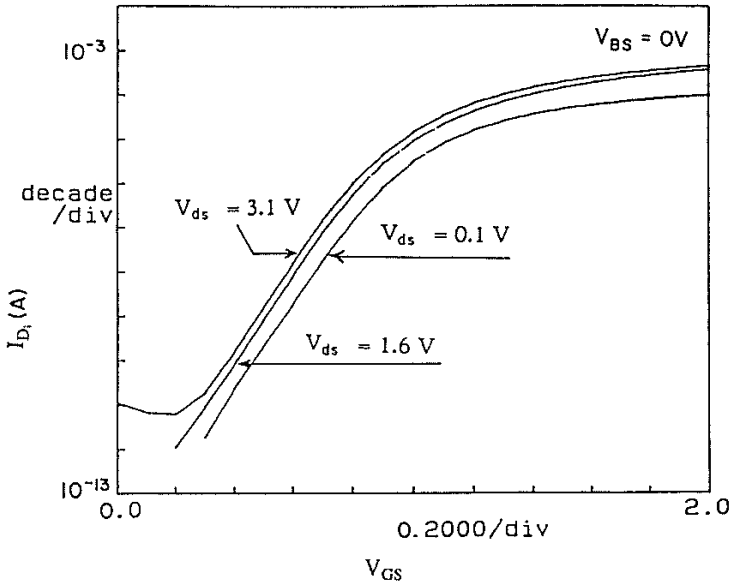


**Fig. 5-9** Plot of log $I_D$ versus $V_{GS}$ for an NMOSFET operated below threshold, with $V_{DS}$ as the parameter. The value of $\Delta V_{GS}/\Delta V_{DS}$ for a fixed value of $I_D$ (e.g., $1 \times 10^{-7}$ A/$\mu$m) is used to characterize DIBL.

$\Delta V_{GS}$ value represents a good first-order estimate of the expected shift in $V_T$ as a function of drain bias. The shift in $V_{GS}$ is normally expressed in normalized form as $\Delta V_{GS}/\Delta V_{DS}$. An acceptable value of $\Delta V_{GS}/\Delta V_{DS}$ is ~25 mV/V, depending on the circuit application and specific leakage requirements. $\Delta V_{GS}/\Delta V_{DS}$ is a strong function of channel length (Fig. 5-10) and must be guaranteed to at least 3-$\sigma$ below the target channel length.

An alternative method of evaluating DIBL is to measure the change in drain current as $V_{DS}$ is increased at some fixed gate voltage below $V_T$ (e.g., the change $\Delta I_D$ in Fig. 5-10 when $V_{DS}$ is increased from 0.1 [solid line in Fig. 5-10] to 5.0V [dashed line]). Because of its simplicity, this measurement is easily implemented on automated test equipment.

Another perspective on this last technique for measuring surface-DIBL is that such barrier lowering raises the electron density at the surface in subthreshold operation. That is, the electron density at the source end of the channel $n_S$(source) - where the surface potential is at a minimum - is increased due to surface-DIBL from its long-channel device value $n_S = (n_i^2/N_A)\exp(q\varphi_{surf}/kT)$ to

$$n_{SDIBL} = \left(\frac{n_i^2}{N_A}\right) e^{q\varphi_{surf}/kT} e^{q\Delta V_{T\infty}/kT} \qquad (5 - 15)$$

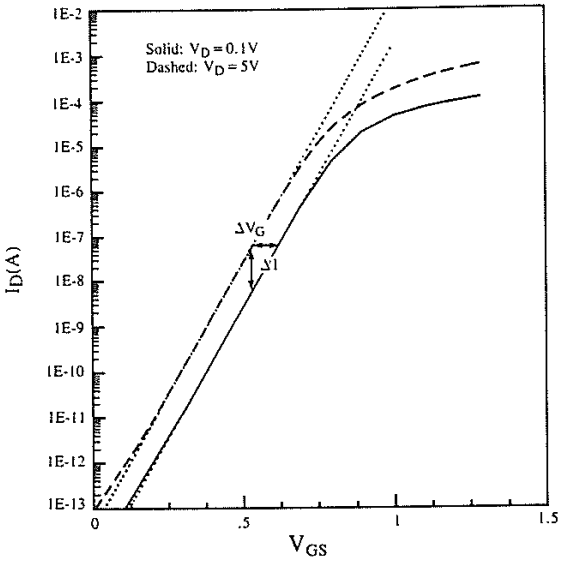


**Fig. 5-10** Simulated values of $I_D$ versus $V_{GS}$ for two values of $V_{DS}$ (0.1V and 5V) in a MOSFET with $L_{eff}$ = 0.7V. From J. Teplik, Chap. 2, "Device Design," in *BiCMOS Technology and Applications*, A. Alvarez Ed., Klewer Academic Publishers, Boston MA, 1989. Reprinted with permission.

where $\Delta V_{Tsc}$ will become larger as $V_{DS}$ is increased. This also implies that surface-DIBL will cause $I_{Dst}$ at a fixed value of $V_{GS}$ and $L$ to increase - by a factor of $\exp(q\Delta V_{Tsc}/kT)$ - above that expected in a long-channel device.* Experimental data can be plotted to depict this effect in the following way: As shown in Fig. 5-11, log $I_D$ is plotted versus $V_{DS}$ with $V_{GS}$ as the parameter. Figure 5-11a shows such characteristic curves for an NMOS device with $L = 2.1$ $\mu$m and Fig. 5-11b for a device with $L = 0.8$ $\mu$m. In both figures the curves exhibit two distinct regions. At low values of $V_{DS}$, $I_D$ depends primarily on $V_{GS}$ and increases only slightly with $V_{DS}$ (*but it is this change in $I_D$ that represents surface-DIBL*).** Eventually the $I_D$ curves intercept a more steeply

* Note, however, that as $V_{GS}$ is decreased, the value of $n_s$ at the source will decrease as quickly with decreasing $V_{GS}$ as in a long-channel device, because, the gate still has control of the charge giving rise to $I_D$. So, $S_t$ will not change, even though $V_T$ is smaller. But, when the device is in punchthrough, the gate no longer has the same control of charge flow as $V_{GS}$ is reduced. Hence, drain current doesn't decrease as quickly with shrinking $V_{GS}$, or $S_t$ gets larger in punchthrough.

** Note that according to the model of subthreshold behavior in long-channel MOSFETs at a fixed value of $V_{GS}$, $I_{Dst}$ is independent of the drain voltage $V_{DS}$ for $V_{DS}$>0.1V (see Eq. 4-90). But because of surface-DIBL, for a fixed value of $L$ and $V_{DS}$, $I_{Dst}$ increases as $V_{DS}$ increases, as described in earlier sections.

rising curve, and for $V_{DS}$ values beyond this point $I_D$ is no longer influenced by $V_{GS}$, but instead rises quickly as $V_{DS}$ is increased. The $I_D$ behavior in this latter region is indicative that subsurface-DIBL (punchthrough) has set in, as discussed in section 5.3.

**5.2.1.6 Dependence of $V_T$ on $V_{BS}$ in Short-Channel MOSFETs.** In long-channel, uniformly doped MOSFETs the threshold voltage depends on the body-substrate voltage $V_{BS}$ as given by Eq. 4-12 (repeated here for convenience)

$$V_T = V_{FB} + 2\varphi_B + \gamma(2\varphi_B + V_{BS})^{1/2} \qquad (5 - 16)$$

In short-channel MOSFETs, however, the effect on $V_T$ when a substrate bias $V_{BS}$ is applied is not well modeled by this expression. That is, as shown in Fig. 5-12, at shorter channels or higher drain biases, $V_T$ is less sensitive to $V_{BS}$ than predicted by Eq. 5-16. For example, in the case of $L = 1.5\ \mu$m and $V_{DS} = 8$V shown in Fig. 5-12, $V_T$ becomes almost independent of $V_{BS}$ at larger values of $V_{BS}$. In addition, for the case of $L = 0.7\ \mu$m, $V_T$ becomes independent of $V_{BS}$ for all values of $V_{BS}$.[10] This implies that the substrate tends to lose control of the channel (just as does the gate itself), at shorter channel lengths. The break in the slope of the $L = 1.5\ \mu$m curves in Fig. 5-12 occurs with punchthrough of the depletion regions of the source and drain (see sec. 5.3 for details on punchthrough). This is because punchthrough decouples the edge of the depletion region from the gate, thereby decoupling the channel from the substrate.

The data shown in Fig. 5-12 also implies that this effect can be modeled numerically by using a smaller body effect coefficient $\gamma$ (defined in Eq. 4-8a as $\gamma = [\kappa_{Si}\varepsilon_0/qN_A]^{1/2}$)

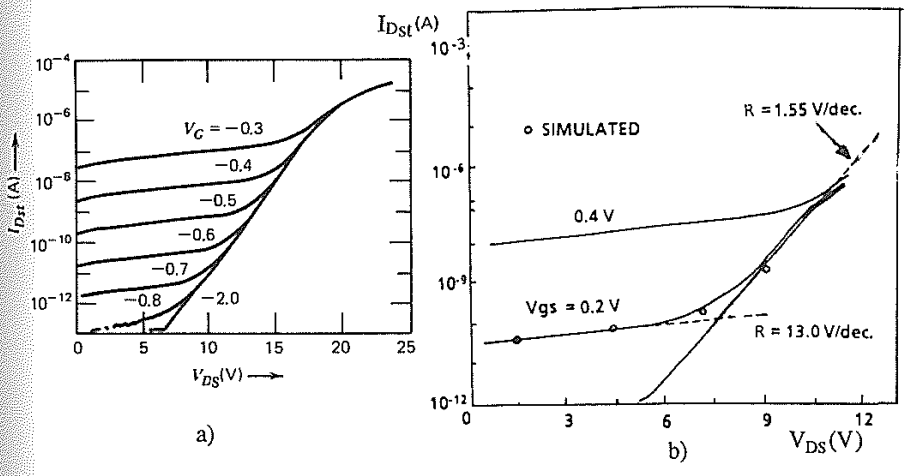


**Fig. 5-11** (a) Experimental $I_{Dst}$-$V_{DS}$ characteristics for a MOSFET with $L = 2.1\ \mu$m, $V_S = V_B = 0$V. For smaller values of $V_{DS}$, $I_{Dst}$ is reduced by roughly one order of magnitude for each 0.1V decrease in $V_{GS}$ below $V_T$. At higher values of $V_{DS}$, a subsurface punchthrough current flows that is independent of $V_{GS}$.[111] (© 1974 IEEE). (b) Experimental and simulated values of $I_{Dst}$ versus $V_{DS}$ for a 0.8 $\mu$m NMOSFET with Z = 20 $\mu$m.[74] (© 1988 IEEE).

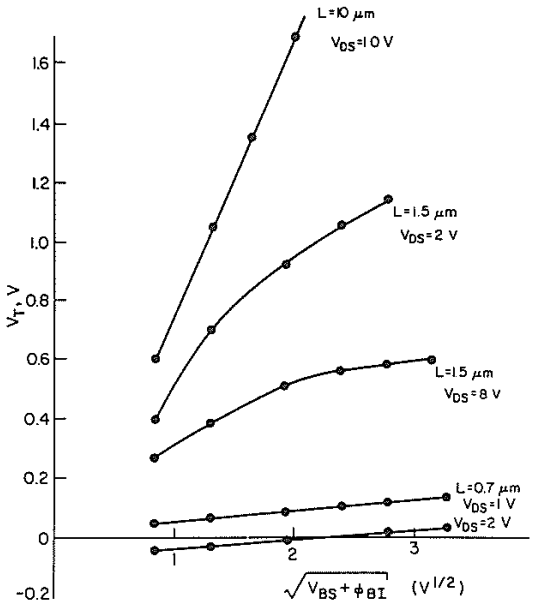


**Fig. 5-12** Variation of $V_T$ versus $V_{BS}$ for three different channel lengths: $L = 10\ \mu m$ (long channel); $L = 1.5\ \mu m$ (short channel); $L = 0.7\ \mu m$ (punched through at $V_{BS} = 0V$). $N_A = 10^{15}$ $cm^{-3}$, $t_{OX} = 1000Å$, $r_j = 1\ \mu m$.[10] Reprinted with permission of *Solid-State Electronics.*

in the threshold voltage equation. Similar results have been obtained by Sheu et al.[11] They, however, elected to model this effect in the short-channel MOSFET SPICE model (BSIM, see section 5.5) by including another empirical term in the $V_T$ equation (i.e., this new term is $P_2[2\varphi_B - V_{BS}]$, see Eq. 5-75). The coefficient $P_2$ of this term is empirically determined from measurements, and has a value of 0.8634 in BSIM.

## 5.2.2 Narrow Gate-Width Effects on Threshold Voltage

As device *widths* shrink, three additional effects begin to modify the expected $V_T$ behavior of such *narrow-channel* MOSFETs. Although these effects are less critical than short-channel effects, they cannot be ignored. The first two cause measured values of $V_T$ to *increase* above those calculated by Eq. 5-16 as the width is decreased (making the MOSFET appear narrower than its geometrical width).[12] The third causes $V_T$ to *decrease*, in effect making the device appear wider. The first two effects are exhibited by MOSFETs fabricated with either raised field-oxide isolation structures (in which the field oxide is grown and then etched to expose the active device regions, Fig. 5-13a) or with semi-recessed LOCOS isolation structures (see chap. 6) as shown in Fig. 5-13b.

The third effect occurs in devices which use fully-recessed-LOCOS or trench-isolation structures (in which the trench is filled with an insulator).

The first effect is the opposite of the short-channel $V_T$ shift effect. That is, at the source and drain ends of the channel (i.e., along the length dimension $L$), a depletion region exists at each *pn* junction (even at $V_{FB}$), requiring less voltage to be applied to invert the channel. As just mentioned, this leads to a *decrease* in $V_T$ in *short-channel* MOSFETs. However, at the ends of the channel perpendicular to the drain current flow, no *pn* junction exists (i.e., along the edges of the device in the *width* dimension). Hence, a gate bias that repels majority carriers must not only deplete such carriers in the channel in the vertical direction, but also in the lateral direction beyond the thin gate oxide. Because the lateral depletion region width in this region extends beyond the gate, an effective bulk charge width larger than the actual width is apparently present. If the width Z is small, these side regions represent a large percentage of the depleted volume. Hence, a larger $V_{GS}$ must be applied to invert the channel than if these edge regions did not have to be depleted. This leads to an *increase* in $V_T$.

The second effect arises from the encroachment of the channel-stop dopants under the edges of the sides of the gate. (In the case of NMOSFETs boron channel-stop dopants

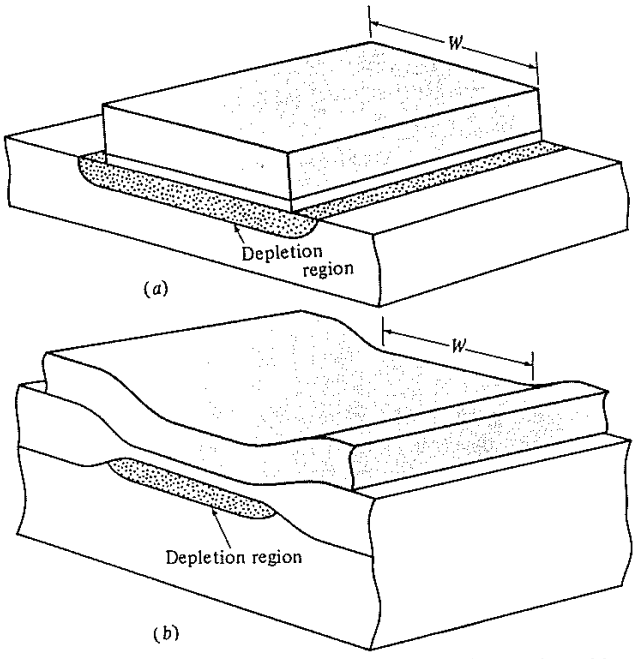


**Fig. 5-13** Effect of fringing field on spreading the depletion region sideways. (a) In MOSFET with field oxide grown and then etched to expose the active region. (b) In MOSFET having a semirecessed LOCOS field oxide. From Y.P Tsividis, *Operation and Modeling of the MOS Transistor*, McGraw-Hill, New York, 1987, p. 192. Reprinted with permission.

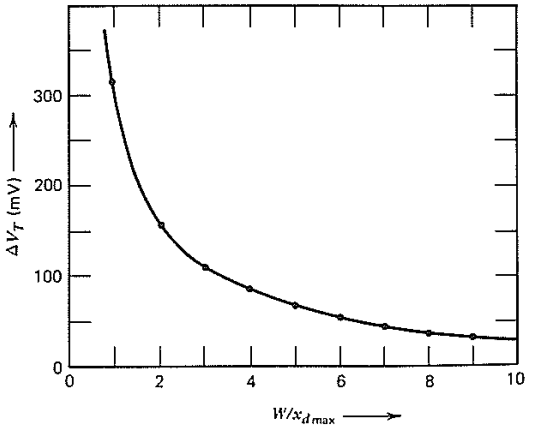


**5-14** Threshold voltage shift $\Delta V_T$ caused by this narrow-channel effect for a MOSFET with $N_A = 10^{15}$ cm$^{-3}$, and $t_{OX} = 50$ nm.[12] From G. Merkel, *Process and Device Modeling for IC Design,* (F. Van de Wield, Ed.), Noordhoff, Leyden, (1977). Reprinted with permission.

encroach under the gate edges. In the case of PMOSFETs, where a channel-stop implant may not be used, phosphorus pileup at the silicon surface during field oxidation produces *n*-type channel stop dopants at higher concentrations in the field regions. This also gives rise to subsequent encroachment into the active regions.) This has the effect of doping the channel at the edges along the width dimension more heavily than at the center (see Fig. 6-10). Again, a larger voltage must be applied to the gate to completely invert the channel than if the additional doping at the edges was not present (Fig. 5-14). From another perspective, the channel at the edges will be less turned on than the channel at the center. Thus, for the same ($V_{GS}$ - $V_T$), significantly less current may be conducted in a narrow-channel MOSFET with channel-stop dopant encroachment than in one without such encroachment.

In practice, the latter (encroachment-related) effect is more severe than the edge-depletion-region effect, especially in devices with heavy channel-stop implants. An analytical expression that models both effects in semirecessed MOSFETs is given in ref. 13. For more precise calculations, however, numerical analyses are required.[14] Several methods are described in chap. 6 for reducing the channel-stop encroachment and thus reducing this narrow-width effect.

Because the third effect *decreases* $V_T$, is often called the *inverse narrow-width effect.* As pointed out earlier, the effect occurs in MOSFETs with trench or fully recessed LOCOS isolation structures, as shown in Fig. 5-15. (Note that the narrow width effects described earlier does not occur in trench isolation structures. Since there is no semiconductor region beyond the edges of the gate in the width dimension, there is no region that is subject to depletion.)

Figure 5-15a depicts the edge of the channel, the trench field-oxide, and the gate (which always overlaps the channel to some degree). When the gate is biased, the field lines from the overlapping region are focused by the edge geometry of the channel. Thus, at the edges of the channel, an inversion layer is formed at lower voltages than at the center. As a result, *less* bias overall must be applied to the gate to invert the channel across its full width. From another perspective, a *corner parasitic MOSFET* in parallel with the main device is established. The parasitic device turns on at voltages lower that the main channel, resulting in a "hump" in the drain current versus gate voltage curves (Fig. 5-15b).[15] Thus, the parasitic device increases the subthreshold leakage current of the active device.

An analytical expression that simulates the narrow-width effect in an ideal isolation trench structure is given in ref. 16. A more general analysis of the narrow width effect that covers both the first and third effects is carried out in ref. 17. An even more recent model of the inverse-narrow-width effect in trench isolated submicron MOSFETs, including the impact of non-uniformly doped channels was proposed by Chung and Li.[18]

However, the inverse-width effect is also sensitive to several other factors,[19] including:

1. The *doping concentration in the sidewalls of the silicon*, which can be impacted by channel-stop dopant redistribution, dopant segregation during field-oxide growth, or intentional doping of the sidewalls by such processes as large-tilt-angle implantation.

2. The trench isolation spacing.

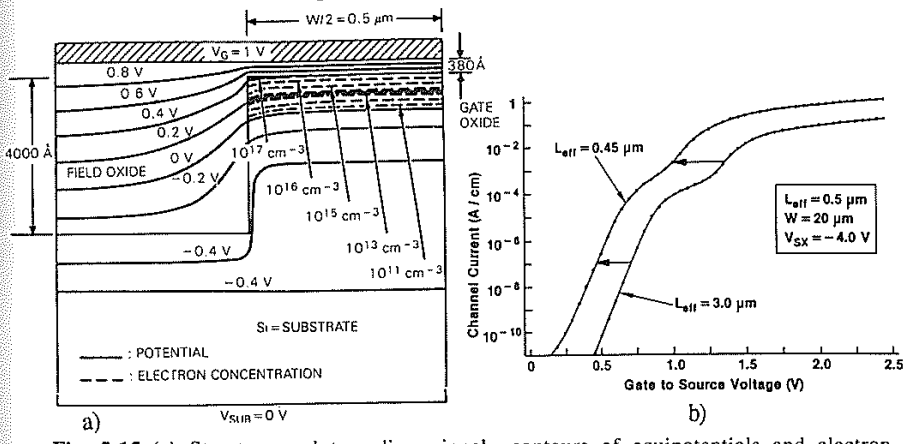


**Fig. 5-15** (a) Structure and two dimensional contours of equipotentials and electron concentrations for a MOSFET employing a trench or fully-recessed oxide isolation structure.[112] (© 1979 IEEE). (b) "Hump" in subthreshold $I_D$-$V_{GS}$ curve due to the inverse narrow width effect in trench isolated MOSFETs.[15] This paper was originally presented at the Fall 1988 Meeting of the Electrochemical Society held in Chicago IL.

3. The shape of the corner region at the edge of the gate. (If the top surface of the field oxide is depressed below the gate-oxide surface, the effect will be more severe than if the field oxide surface is raised above the gate oxide surface.)

Thus, if trench isolation is used, the planarization technology that determines the final wafer topology at the conclusion of the isolation structure fabrication will have to be tightly controlled to maintain precise control of $V_T$ (see also chap. 6).

**5.2.2.1 Devices Exhibiting Both Short- and Narrow-Width Effects.** In devices in which both effects are capable of causing a shift in $V_T$, neither the short-channel nor the narrow-channel models alone suffice to accurately predict the resultant $V_T$. Some simplified analytical expressions employing a three-dimensional approximation of the depletion regions have been developed,[20] but for cases involving various device voltages and non-uniform channel doping concentrations, numerical analyses are necessary.

## 5.2.3 Reverse Short-Channel Effects on Threshold Voltage (RSCE)

In the previous sections it was implied that the $V_T$ of a MOSFET decreases monotonically with decreasing channel length. This was explained by two-dimensional electrostatic field considerations, and various models for predicting such effects were described. However, in some situations it has been found that $V_T$ initially *increases* with decreasing channel length (beginning when $L$ ~2-3 $\mu$m), contrary to what is normally expected.[91,92] This phenomenon has been termed *reverse short channel effect (RSCE), $V_T$ roll-up,* or *anomalous threshold behavior.* After $V_T$ reaches a maximum value due to RSCE (at ~0.7 $\mu$m), it then declines as channel lengths are further decreased (*$V_T$ roll off*). Apparently the two-dimensional effects that are responsible for $V_T$ roll-off eventually compete with the effects causing $V_T$ roll-up and the former come to dominate at the shortest channel lengths. (In fact, the ultimate rate of $V_T$ roll-off with $L_{eff}$ is reported to be much faster than can be explained by conventional models of laterally uniform channel doping). The combined RSCE and $V_T$ roll-off effects result in a "hump" in the $V_T$ versus $L$ characteristics (Fig. 5-16). The initial rate of enhancement of $V_T$ with decreasing $L$ is also maximum at zero bias and decreases with increasing bias. As will be described in the next sections, different explanations have been given for the $V_T$ roll-up effect. However, while several models which seem to provide good quantitative agreement with experimental observations of RSCE have been developed, a consensus has not yet been reached as to which physical mechanism(s) are responsible for the effect.

**5.2.3.1 Model which Proposes RSCE is Due to Lateral Dopant Nonuniformity at the Channel Si-$SiO_2$ Interface (Arising from Enhanced Diffusion of Channel Dopants Caused by Interstitial Injection During Poly Reox, Salicide Formation, or Implant Damage).** The first explanation of RSCE is based on the fact that this effect was initially observed in NMOSFETs fabricated with two boron channel implants (i.e., a

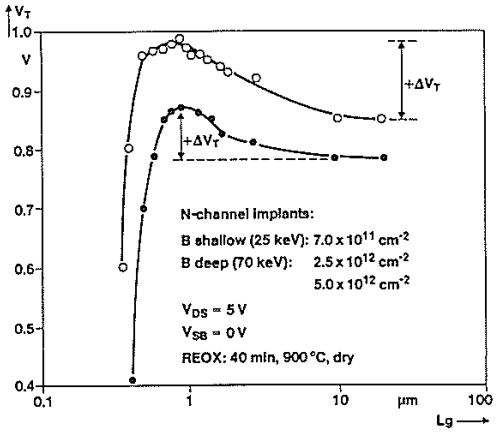


**Fig. 5-16** Experimental $n$-channel threshold voltage versus channel length.[92] (© 1987 IEEE).

shallow boron implant for adjustment of the threshold voltage, as described in chap. 4, and a deeper boron implant for suppression of punchthrough, as described in section 5.3).[92] The doping profile as a function of $x$ in the channel beneath the gate oxide resulting from these two implants is qualitatively depicted in Fig. 5-17a.

After the polysilicon gate is defined by etching and the source/drain regions are implanted, a thermal oxidation step (referred to as *reoxidation* or *re-ox*) is performed (see also chap. 9, sec. 9.7.1.4). This oxidation serves several purposes, including: (1) to re-oxidize the source/drain regions. (The source/drain implant is carried out with the gate oxide intact over these regions. The heavy implant is likely to damage and contaminate this oxide, and so it is stripped after the implant. The reoxidation step regrows a fresh oxide over the source/drain regions, as well as on and around the poly gate); (2) the thermal oxide on the poly serves as a diffusion mask which prevents boron dopants from the BPSG interlevel dielectric from diffusing into the $n^+$ poly during the BPSG flow and reflow processes; (3) to reduce the MOSFET gate-to-drain overlap capacitance and strengthen the gate oxide at the poly gate edge. The latter benefits are obtained because oxidation-induced encroachment gives rise to a so-called *gate bird's beak* - or *graded gate oxide* [GGO] - under the polysilicon edge, as shown in Fig. 5-17b. The thicker oxide due to GGO at the gate edge reduces the gate-to-drain overlap capacitance and relieves the electric-field intensity at the corner of the gate structure, thus enhancing the gate oxide integrity at its edge. However, the reoxidation step can also detrimentally impact the characteristics of MOSFETs which employ lightly-doped drains (LDD), and thus the re-ox step must be optimized for this type of device, as is described in more detail in chap. 9. Here only the proposed impact on $V_T$ due to the re-ox step is considered.

As described in chap. 7. vol. 1, the injection of interstitials which accompanies thermal oxidation causes oxidation-enhanced-diffusion (OED) of dopants in the vicinity of the growing oxide (see Fig. 5-17b). In the re-ox step, the diffusion of dopants is enhanced not only under the oxidizing (i.e., source/drain) regions but also in the adjacent

channel region (due to lateral diffusion of the injected Si self-interstitials into the channel region). The OED causes boron to diffuse more rapidly. This brings more boron from the deep buried peak to the surface near the edges of the channel (because the injected interstitial concentration is highest near the channel edges). As a result, the boron surface concentration becomes larger at the channel edges than if diffusion of the implanted boron profile had not been enhanced (see Fig. 5-18). The increased concentration of the boron in these regions gives rise to an overall increase in $V_T$ if $L$ becomes small enough to make these regions a significant fraction of the channel length.

The $V_T$ roll-up has also been observed in MOSFETs in which a salicide is fabricated[93] (i.e., a *salicide* is a self-aligned silicide formed on the source/drain regions to reduce the sheet resistance of the source and drain, see chap. 3, Vol. 2). Lu and Sung propose that during silicide formation vacancies are injected and these enhance the dopant diffusion of the boron in the dual-implant profile, again giving rise to a lateral nonuniform lateral distribution of boron along the channel surface. As in the OED model, this gives rise to an enhancement of $V_T$ as the MOSFET channel length is decreased.

An analytical model of RSCE based on nonuniform lateral boron surface concentrations arising from either (or both) of the above effects has been developed by Arora and Sharma,[94] although they model the RSCE as being due to a nonuniform buildup of oxide charge along the Si-$SiO_2$ interface (see also section 5.2.3.4).

**5.2.3.2 Model Which Proposes RSCE Arises from Boron Segregation to Implant Damaged Regions at the Edge of the Channel.** Although the above models appear plausible, $V_T$ roll-up has also been

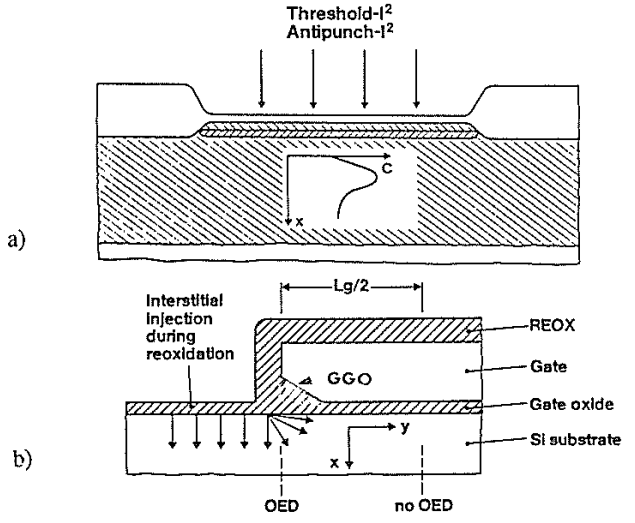


**Fig. 5-17** (a) Vertical doping profile in an NMOSFET channel which uses a punchthrough implant. (b) Conceptual diagram of local interstitial injection during reox.[92] (© 1987 IEEE).

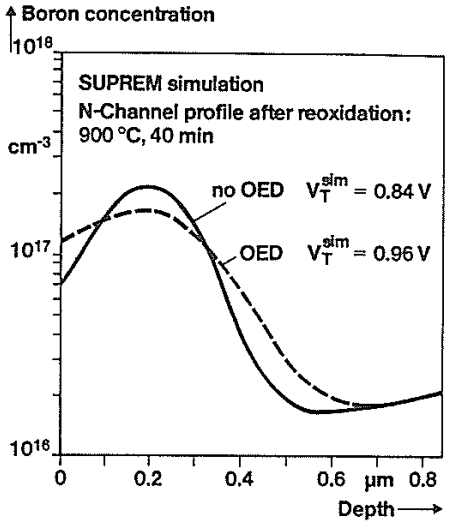


**Fig. 5-18** Simulated vertical $n$-channel profiles at x = 0 and x = $L/2$ with and without oxidation-enhanced diffusion (OED).[92] (© 1987 IEEE).

observed in MOSFETs with uniformly doped channel regions (Fig. 5-19). In such MOSFETs the above models would predict that boron surface concentrations would *decrease* near the edges of the channels. (That is, boron would segregate into the growing oxide, and then boron from the center of the channel would diffuse into these depleted regions, resulting in a loss of boron from the channel region). Thus, the model of section 5.2.3.1 predicts that $V_T$ would *decrease monotonically* with decreasing channel length in MOSFETs with nonimplanted (i.e., uniform) channel regions. Furthermore, when the channels get very short, (i.e., ≤0.3 $\mu$m) the observed $V_T$ *roll-off* is more rapid than that predicted by the 2-D DIBL numerical analyses assuming a laterally uniform channel doping. As a result, another phenomenon has been suggested as being responsible for the RSCE (including both the initial $V_T$ roll-up and the subsequent enhanced roll-off effects as the channel length is decreased), namely the depletion of boron from the channel region by strong segregation of the boron into the adjacent source and drain regions during the source/drain implant-activation anneal.[95, 96]

This segregation is thought to occur as a result of the presence of crystal defects caused by the source/drain implant step. (Such defects have, in fact, been detected using TEM micrographs of the source/drain regions after the source/drain implant step.) The boron is theorized to have a higher local solubility in the defective regions, and thus will diffuse to them during the anneal steps performed after the source/drain implant. Figure 5-19 shows the measured and calculated $V_T$ versus $L$ curves. The triangular data points in this figure are calculated using a 2-D device simulator assuming a uniform

lateral doping profile in the channel, and these show the conventional roll-off versus $L$ as described in section 5.2.1. The data points indicated by the squares and filled circles show the $V_T$ versus $L$ values calculated using the same device simulator, but with nonuniform lateral boron channel doping (see Fig. 5-20). The open-circle data points are the experimental data.

The $V_T$ roll-up is well predicted by this model, as is the enhanced $V_T$ roll-off for channel lengths shorter than about 0.3 $\mu$m. (This model also gives good agreement with RSCE in PMOSFETs.) For MOSFETs in which $L \leq 0.3$ $\mu$m the center of the channel is so small that the channel region depleted of boron extends across the entire channel length (see, for example, case where $L = 0.2$ $\mu$m in Fig. 5-20), and there is not sufficient dopant present in this region to cause the peaks of the boron concentration at the channel edges to rise to a degree that would offset the enhanced $V_T$ decrease due to the depletion effect.

The defects that give rise to the lateral dopant redistribution are observed to be eventually extinguished by a higher temperature anneal step (e.g., 900°C in $N_2$ for 5 min). Thus, it has been suggested that recrystallization of the defective regions using RTP could be carried out, such that the anneal would take place over a sufficiently short time as not to permit lateral dopant redistribution to occur.[95] If this is possible MOSFETs could be fabricated which would exhibit neither the $V_T$ roll-up nor enhanced roll-off effects. Another suggestion to alleviate the enhanced roll-off effect is to use a halo implant to increase the boron dopant concentration near the source and drain such that the B depletion would be counteracted.[96]

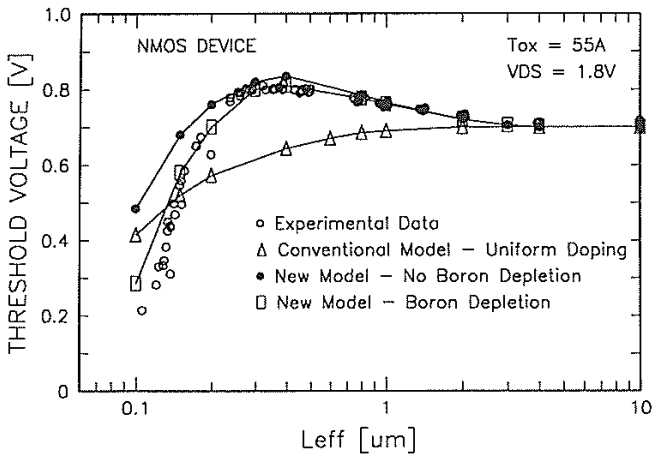


**Fig. 5-19** Measured and modeled $V_T$ versus $L$ curves. The conventional model results assume laterally uniform channel doping. The new model results assume box approximations for the lateral channel doping profile shown in Fig. 5-20. The boron depletion case assumes that the bulk doping is depleted into the source and drain regions within 0.1 $m$m of their edges.[95] (© 1993 IEEE).

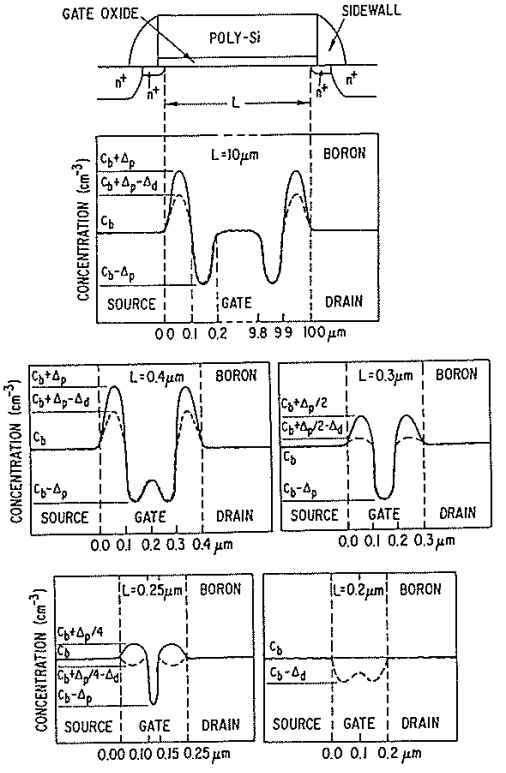


**Fig. 5-20** Conceptual schematic of the lateral channel doping profile of the present model for different channel lengths. The solid lines represent the case of no bulk depletion while the dotted lines represent the case of bulk depletion.[95] (© 1993 IEEE).

**5.2.3.3 Model Which Attributes RSCE to Transient Enhanced Diffusion of Channel Dopants to the Silicon Surface Arising from Implant Damage.** Another model that explains the occurrence of RSCE in MOSFETs with uniformly doped channel regions was developed by Rafferty et al.[98] In this model, it is proposed that the effect is associated with damage from the LDD implant. That is, point defects (interstitials) are assumed to be created by the LDD implant. They diffuse laterally into the channel region during the relatively low-temperature step used to deposit the CVD interlevel dielectric layer (needed to create the gate-sidewall spacers). As these point defects are primarily created at a depth corresponding to the end-of-range damage, the interstitial concentration peak exists beneath the surface. Thus, a retrograde profile of interstitials in the channel will arise. Since the dopant diffusivity is proportional to the interstitial concentration, the

retrograde interstitial concentration profile will cause a net boron diffusion flux toward the surface (i.e., during the source/drain activation anneal) even if a flat boron dopant profile exists in the vertical direction. As a result, boron piles up at the surface, leading to an increase in $V_T$. Experimental confirmation of such an impurity pile-up is found in SIMS analysis of flat profiles subjected to silicon damage and subsequent anneal.[99] The diffusion of boron toward the channel surface from this effect is a transient phenomenon because the interstitials are eventually annihilated during the anneal. Good agreement between this model and experimental data is also reported if the transient diffusion is modeled using a coupled impurity/point defect simulator.

**5.2.3.4 Model which Attributes RSCE to Silicon Interstitial Capture in the Gate Oxide.** Jacobs et al. note that $V_T$ can also be shifted by a change in fixed oxide charges $Q_f$ at the Si-$SiO_2$ interface.[97] Thus, they propose that RSCE in the absence of a vertical gradient in the channel dopant profile can be explained by the trapping of injected silicon interstitials by the gate oxide. These captured interstitials introduce the negatively charged complex in the oxide required for the observed $V_T$ roll-up). The oxide surface is known to be an effective sink for interstitials, and the process steps which supply the excess interstitials can be those mentioned above. The result is a position-dependent oxide charge distribution along the Si-$SiO_2$ interface, similar to the assumption of an exponentially decaying fixed charge variation made by Arora when deriving the analytical model of RSCE mentioned in section 5.3.2.1.[94]

## 5.3 PUNCHTHROUGH (Subsurface-DIBL) IN SHORT-CHANNEL MOSFETS

In chap. 4, section 4.7 we described the nature of subthreshold current in long-channel MOSFETs. We noted that in weak inversion $I_{Dst}$ flows at the surface of the channel region, and its value is calculated from Eq. 4-89. We also saw that the subthreshold-swing parameter ($S_t$) is an important characteristic of subthreshold behavior, and in long-channel, uniformly-doped-substrate devices it can be modeled using Eq. 4-91.

In short-channel MOSFETs, however, if $V_{GS}$ is fixed while $V_{DS}$ is increased, larger values of $I_{Dst}$ values than are predicted by the long-channel device equations are observed. This larger subthreshold current is due in part to increased $I_{Dst}$ flowing at the surface as a result of surface-drain-induced barrier lowering (DIBL), as described in section 5.2). If only surface DIBL is occurring in a MOSFET, $S_t$ values are observed to remain unchanged. However, another short-channel effect known as *subsurface punchthrough* can also give rise to an increase in $I_{Dst}$, and one manifestation of this effect is an increase in the measured value of $S_t$. That is, the gate has less control of the subsurface punchthrough current than it has over the surface subthreshold current. Thus, once a MOSFET enters subsurface punchthrough and such current starts to flow, the $S_t$ value of the MOSFET becomes larger than if only normal subthreshold current is flowing. Since the measurable drain current is the sum of both current components,

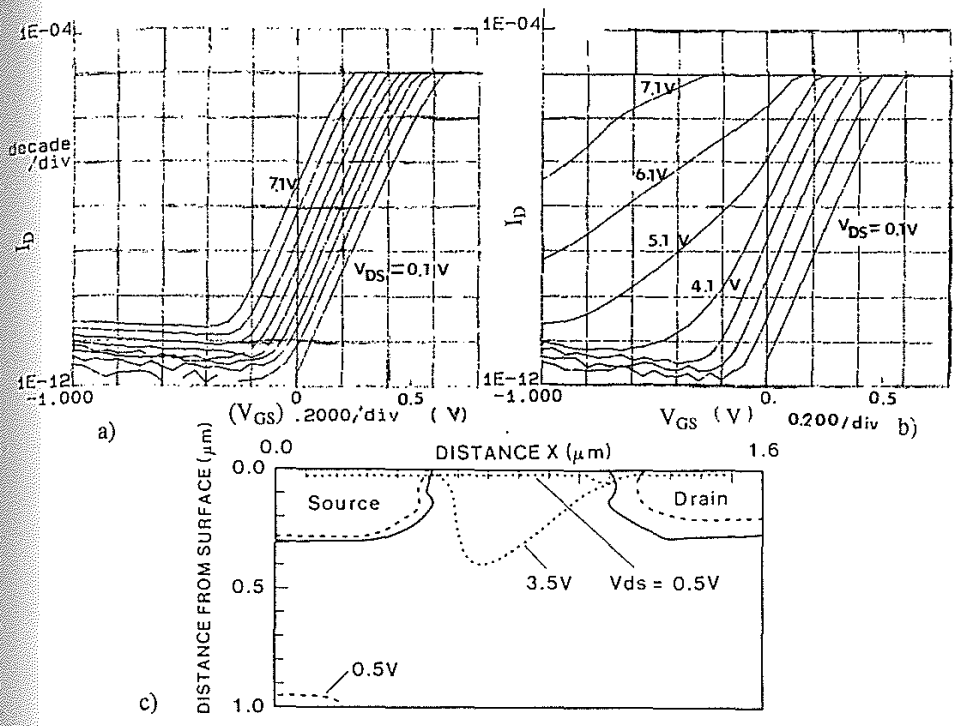


**Fig. 5-21** Two sets of log $I_D$ versus $V_{GS}$ curves for MOSFETs, with $V_{DS}$ varying in 1V increments. (a) No indication of punchthrough is observed, as $S_t$ remains constant for all values of $V_{DS}$. (b) Onset of punchthrough occurs as $V_{DS}$ reaches ~6V, as evidenced by an increase in $S_t$ that point. (c) Punchthrough current paths (dotted) in a surface-channel NMOSFET with $V_{DS}$ = 0.5 and 3.5V. Solid line shows the depletion region edge. The current path transfers from the surface to bulk as $V_{DS}$ is increased.[74] (© 1988 IEEE).

one technique for detecting the onset of punchthrough in a MOSFET is to monitor $S_t$ as $V_{DS}$ is increased. .

For example, in Fig. 5-21 two sets of $I_{Dst}$ versus $V_{GS}$ curves with $V_{DS}$ as the parameter are shown. In the MOSFET characterized by Fig. 5-21a $S_t$ remains constant as $V_{DS}$ is increased, indicating that no punchthrough is observed up to the maximum applied $V_{DS}$. In Fig. 5-21b $S_t$ increases as $V_{DS}$ is increased beyond ~4V, indicating that punchthrough sets in at about this value.

Punchthrough is a phenomenon associated with the merging of the source and drain depletion regions in the MOSFET. That is, as the channel gets shorter, these depletion region edges get closer (assuming that the channel-region doping is kept constant as $L$ is decreased). When the channel length is decreased to roughly the sum of the two junction depletion widths, punchthrough is established. (Note that punchthrough may

even exist in a short-channel device at $V_{DS} = 0$, depending on $L$ and the substrate doping.) Nevertheless, since the depletion regions of a *pn*-junction widen as reverse-bias is increased, all MOSFETs would eventually enter punchthrough if a high enough $V_{DS}$ could be applied. However, in MOSFETs with $L>2.0\ \mu m$, breakdown of the drain-substrate junction generally sets in before this punchthrough voltage is reached. As a result, in practice, punchthrough is not a limiting factor in long-channel digital MOSFET design. In shorter-channel devices (i.e., $L \leq 2.0\ \mu m$), however, punchthrough does represent a serious limitation.

Another factor also impacts punchthrough behavior in *n*-channel MOSFETs. That is, in submicron NMOSFETs a $V_T$-adjust implant is used to raise the doping of the surface-channel region above the doping of the substrate. (This can also be viewed as an increase in the electrostatic potential at that point near the source.) Thus, the source/drain depletion-region widening is greater beneath the surface due to the lighter doping there. A punchthrough condition would therefore be first established below the surface in such devices, and hence this effect is referred to as *subsurface punchthrough* (see Figs. 5-22 and 5-23). Note that in PMOSFETs fabricated with $n^+$ polysilicon gates the punchthrough problem occurs in a somewhat different manner, which we will describe in a later section dealing with this issue (i.e., section 5.8.2.3).

Once subsurface punchthrough occurs, any increase in the applied reverse-bias drain voltage (beyond that required to establish punchthrough) will lower the potential energy barrier for majority carriers in the source.[6] With a diminished barrier height, a larger number of source-region majority carriers (e.g., electrons in an NMOSFET) have enough energy to be injected from source to substrate. Some of these injected electrons are collected by the drain, causing $I_{Dst}$ to increase. The component of $I_{Dst}$ which flows as a result of subsurface punchthrough is known as *punchthrough current.* When designing MOSFETs one criterion of a successful device design is that the punchthrough current should be insignificant under normal bias conditions. That is, if sufficient punchthrough current is observed, the device structure must be redesigned to effectively suppress such current.

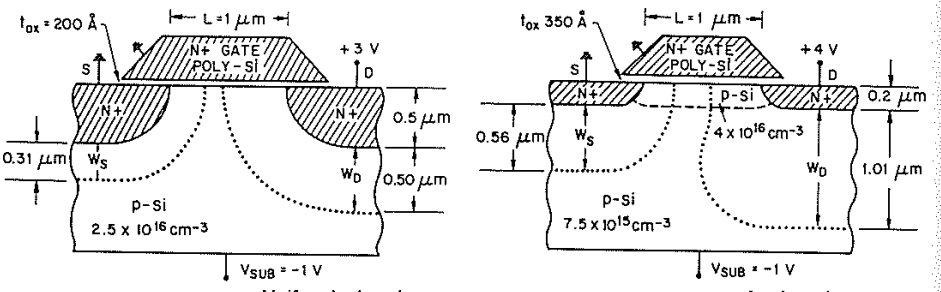


(a) Uniformly doped structure. (b) Implanted structure.

**Fig. 5-22** (a) NMOSFET without $V_T$-adjust implant. (b) NMOSFET with $V_T$-adjust implant, showing the bulging of the drain depletion region beneath the surface as $V_{DS}$ is increased, due to the lower doping concentration in the substrate below the depth of the $V_T$-adjust implant.

Two-dimensional simulations of the potential in the channel regions of short channel NMOSFETs with $V_T$-adjust implants support the view that depletion-region widening is greater beneath the surface. In addition, they indicate that the point of maximum source-substrate potential energy barrier lowering is also beneath the Si-$SiO_2$ interface (generally at approximately the same depth as the source/drain junction depths). Figures 5-23a, c, e and g show a "bird's eye" or perspective view of the electrostatic potential variation in a short-channel MOSFET computed using such 2-D numerical analyses, as $V_{DS}$ is increased from $V_{DS}$ = 3V to $V_{DS}$ = 9V. Figures 5-23b, d, f and h show contour plots of these same results. We can see that when the device enters punch-through the location of the electrostatic potential saddle point is beneath the surface, and the value of the potential at this saddle point may be higher than the potential minimum at the surface. Since electrons follow the potential peak (see Figs. 5-23g and i), in such cases the component of current due to subsurface punchthrough will be larger than the channel-current component, and the subsurface current will flow along the path indicated by the subsurface potential ridge connecting the source and drain. Figure 5-21c shows a simulation of the subthreshold current paths in an NMOSFET with $L$ = 0.6 $\mu$m for surface-DIBL (i.e., $V_{DS}$ = 0.5V) and for subsurface-DIBL (punchthrough, $V_{DS}$ = 3.5V). This shows that the subthreshold current path transfers from the surface to the bulk as $V_{DS}$ increases, which supports the view that at low $V_{DS}$ surface-DIBL is responsible for the increase in $I_{Dst}$ in short-channel NMOSFETs, but that at high $V_{DS}$ punchthrough becomes the primary cause of subthreshold leakage.

Subsurface punchthrough exerts the biggest impact on circuit operation when the MOSFET is OFF, since a tiny punchthrough current in this case can still represent intolerable leakage. However, the device parameter most commonly used to characterize punchthrough behavior is the *punchthrough voltage* $V_{PT}$ defined as the value of $V_{DS}$ at which $I_{Dst}$ reaches some specific magnitude (e.g., 1 nA/$\mu$m) when $V_{GS}$ = 0. The goal in designing a MOSFET is to have $V_{PT}$ exceed any possible operating $V_{DS}$. Thus, $V_{PT}$ is measured when the device is in subthreshold, as will be discussed in upcoming paragraphs. Note that $V_{PT}$ can be roughly estimated by determining the value of $V_{DS}$ at which the sum of the depletion widths $W_S$ under the source and $W_D$ under the drain (using the value of the doping concentration in the substrate as $N_{SUB}$) equals the channel length $L$, or from the expression[24]

$$V_{PT} \propto N_{SUB} (L - r_j)^3 \qquad (5 - 17)$$

Nevertheless, no accurate analytical model exists for estimating $V_{PT}$ as a function of implant dose and depth. A full numerical solution of the 2-D Poisson equation must thus be obtained to predict the variation of $V_{PT}$ for each device structure.

Several measures can be taken to prevent short-channel MOSFETs from entering subsurface punchthrough. First, the substrate doping can be increased to decrease the depletion-layer widths. A simple rule-of-thumb proposed by Klaasen[25] is to select a minimum substrate doping value according to $N_{SUB}>N_{ch}/10$, where $N_{SUB}$ is the uniform bulk-substrate doping/cm$^3$ and $N_{ch}$ is the average doping/cm$^3$ in the implanted region of the channel (e.g., $D_I/x_C$). This approach, together with a single $V_T$-adjust implant can produce appropriate threshold and punchthrough voltages for NMOSFETs

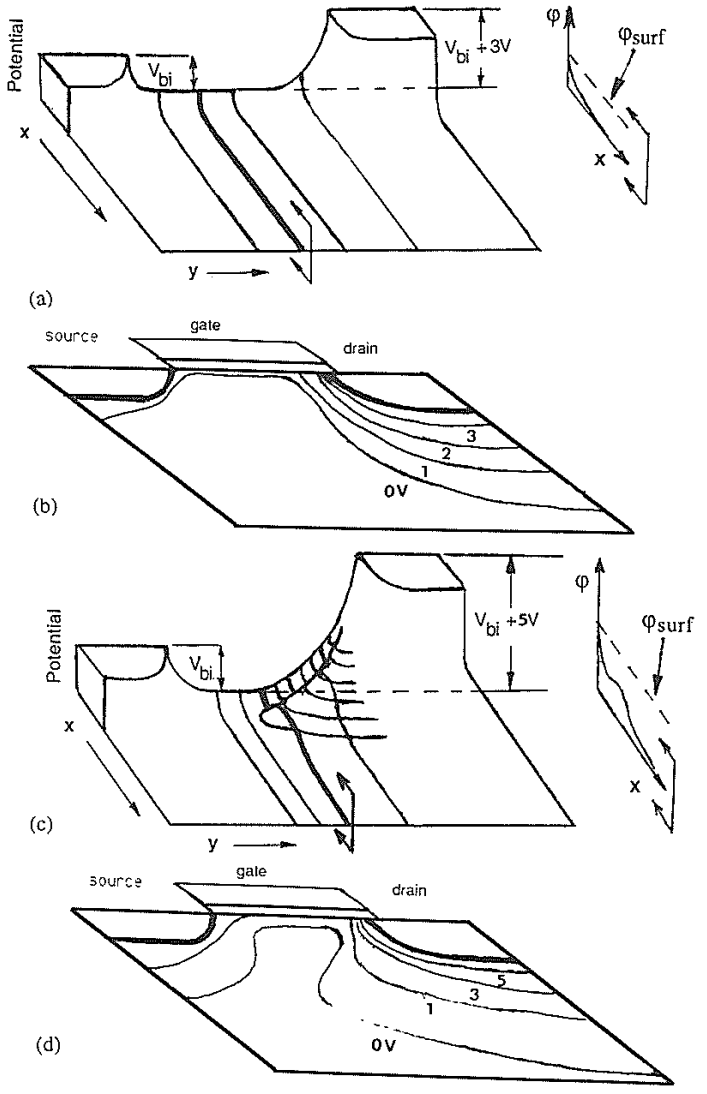


**Fig. 5-23** (a and c) 2-D perspective plots of the potential in an *n*-channel MOSFET with a drain bias of (a) 3 V and (c) 5 V, respectively. Channel length = 1 $\mu$m. (b and d) 2-D contour plots of the same cases. From K. M. Cham, et al., *Computer Aided Design & VLSI Device Development*. Copyright 1986 Kluwer Academic Publishers. Reprinted with permission.

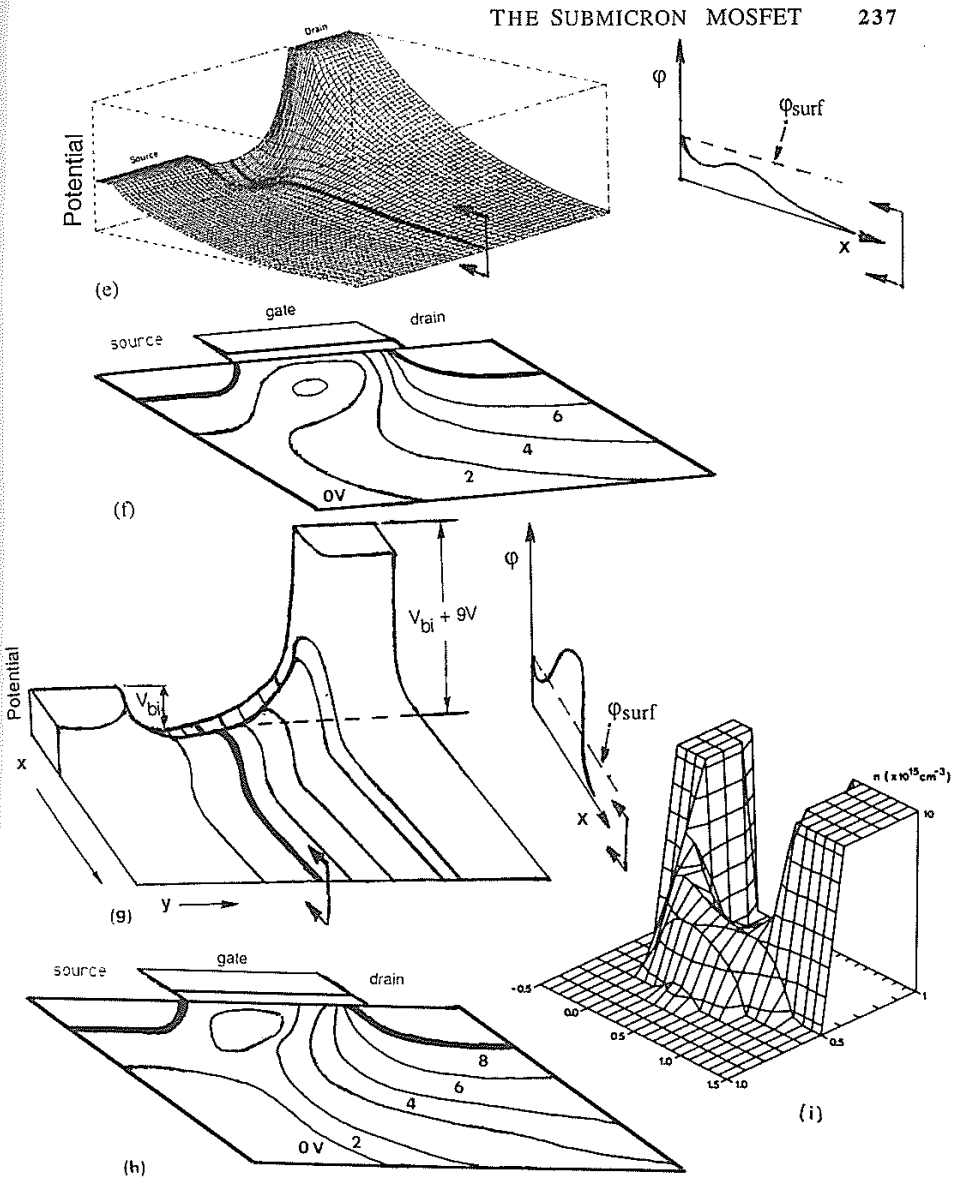


**Fig. 5-23** cont. (e and g) 2-D perspective plots of the potential in an *n*-channel MOSFET with a drain bias of (e) 7 V and (g) 9 V, respectively. Channel length = 1 $\mu$m. (f and h) 2-D contour plots of the same cases. From K. M. Cham, et al., *Computer Aided Design & VLSI Device Development*. Copyright 1986 Kluwer Academic Publishers. Reprinted with permission. (i) Electron concentration of the MOSFET in punchthrough, i.e., case g & h.

with drawn gate lengths of 1.3 $\mu$m nominally operated at 2.5V power supply (e.g., a single 20 keV $B^+$ implant at ~$9x10^{11}$ $cm^{-2}$). A similar process has also been applied to 1.25 $\mu$m CMOS devices using a 5V supply. Although some short-channel effects are observed, $V_T$ and $V_{PT}$ voltages are reasonable. However, for devices with drawn gate lengths of ~1 $\mu$m ($L_{eff}$ ~0.55 $\mu$m), a single $V_T$/punchthrough implant cannot adequately satisfy all requirements, especially if high resistivity (>10 $\Omega$-cm) substrates are used.

As a result, another approach using an additional implant known as a *punchthrough stopper implant* (or *punchthrough implant,* PTI) must be employed. The second implant peak concentration is located at a depth near the bottom of the source-drain regions. Fig. 5-24a qualitatively depicts such a MOSFET structure. The additional doping introduced by such an implant (e.g., boron in NMOSFETs) reduces the lateral widening of the drain-depletion region below the surface without increasing the doping under the junction regions. With such implants, the component of the punchthrough current can be suppressed to well below the long-channel $I_{Dst}$ value in MOSFETs down to 0.5 $\mu$m, while still maintaining a lower value of $N_{SUB}$ (for reduced values of $C_j$). However, precise control of the placement and dose of this implant within the channel region is required to achieve the intended enhancements. For example, Fig. 5-24b shows the as-implanted doping profile of the channel with (dashed line) and without (solid line) a punchthrough implant (i.e., prior to annealing the implants). In addition, it is important to keep the punchthrough implant profiles from spreading out appreciably during annealing (see Fig. 5-24c), since the additional doping above the well's value adds to the source/drain-to-well capacitance and the transistor's threshold voltage sensitivity to back biasing of the*p*-well. Thus, the post channel implant thermal cycles should be kept to a minimum. An example of such a punchthrough implant for a 1 $\mu$m NMOSFETs is a 70 keV $B^+$ implant at $6x10^{11}$ $cm^{-2}$.

A third technique is to locally implant *p*-type dopants (in NMOSFETs) under the lightly doped tip region of the LDD as shown in Fig. 5-25a, and such implants have been termed a "halo" implants. (The use of halo implants as punchthrough stoppers in PMOSFETs is discussed in section 5.8.1.1.) Because the implanted dopant raises the doping concentration only on the inside walls of the source/drain junctions, the channel length can be decreased without needing to use a higher-doped substrate. That is, punchthrough does not set in until a shorter channel length because of the "halo." A penalty in increased sidewall junction capacitance is paid, but this cost is smaller than that incurred should the bottom area of the junctions lie above heavily doped substrate material. The maximum halo doping is determined by the onset of low-level avalanche breakdown of the $pn^+$ junction as is shown in Fig. 5-25b.

A halo NMOSFET with $L$ = 0.35 $\mu$m, $t_{ox}$ = 15 nm, and operated at 3V has been reported.[26] The junction depth $r_j$ and *p*-halo peak doping were ~0.14 $\mu$m and ~$3x10^{17}$ $cm^{-3}$, respectively. A more recent report applied a large-angle tilt (LAT) implant of boron ions in NMOS and phosphorus in PMOS (Fig. 5-25c) to form a halo-like structure in each device (called a *self-aligned pocket implantation*). A tilt angle of 25-30° was used to implant the pocket dopants after gate formation, so that the gate structure acted as a self-aligned implant mask. Devices with channel lengths as small as 0.2 $\mu$m that still exhibited long-channel subthreshold $V_T$ behavior were fabricated.[27]

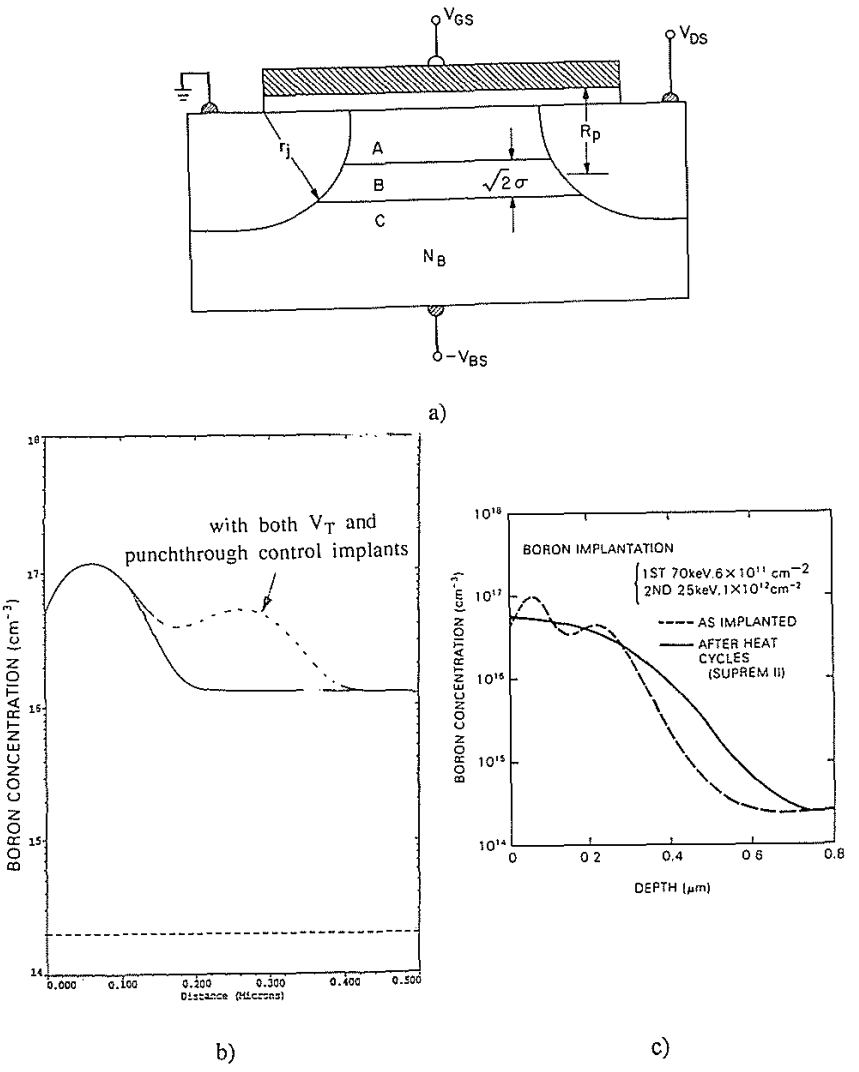


**Fig. 5-24** (a) An implanted NMOS structure with three regions of different doping. Level A contains the dopant from the $V_T$ implant. Level B contains the dopant from the punchthrough control implant, considered to be a Gaussian centered at a distance $R_p$ from the gate, with a straggle $\sigma$. Level C is the original substrate. (b) As-implanted channel doping profiles with (dashed line) and without (solid line) punchthrough implant. (c) Example of simulated channel impurity profile of an NMOSFET with both $V_T$ and punchthrough control implants - as-implanted (dashed lines), and after anneal (solid line).[113] (© 1982 IEEE).

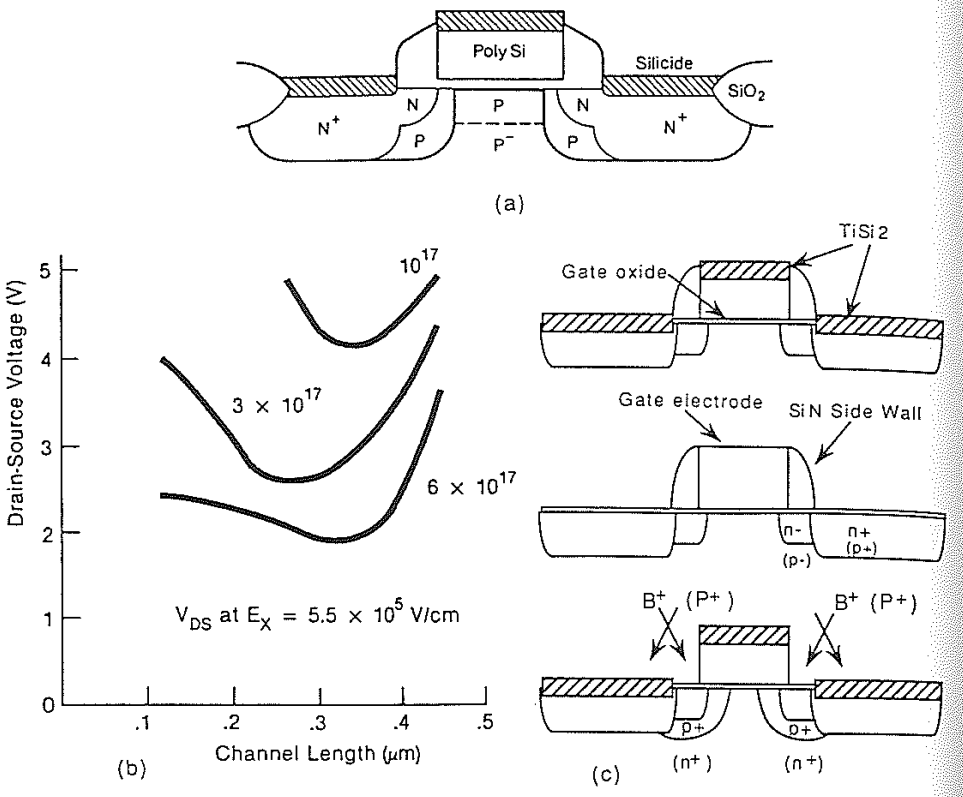


**Fig. 5-25** (a) "Halo" NMOS structure.[26] (© 1985 IEEE). (b) $V_{DSmax}$ limited by avalanche breakdown versus channel length for various peak halo doses.[26] (© 1985 IEEE). Process for producing "halo" NMOS structure using a Self-Aligned Pocket Implantation [SPI] technology is shown.[27] (© 1991 IEEE).

## 5.3.1 Experimentally Characterizing Punchthrough

The onset of punchthrough in a device can be measured in several ways. As mentioned at the outset of the discussion, for a specific device (i.e., one that has a single, specific channel length and channel doping profile), the onset of punchthrough over the operating range of $V_{DS}$ can be monitored by measuring log $I_{Dst}$ vs. $V_{GS}$ for different $V_{DS}$ values (Figs. 5-21a and b). If the curves look like those of Fig. 5-21a, the device does not exhibit subsurface punchthrough up to the maximum $V_{DS}$ applied (since the slope of the log $I_{Dst}$ curves remain constant as $V_{DS}$ is increased). The curves of Fig. 5-21b however, indicate that punchthrough is setting in, with its onset marked by the $V_{DS}$-curve having a larger $S_t$ value than that exhibited at small $V_{DS}$. (Note that since punchthrough current flows in parallel with ordinary $I_{Dst}$, $S_t$ will noticeably increase

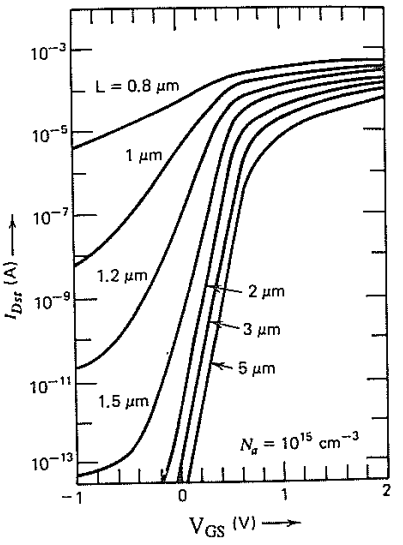


**Fig. 5-26** Simulated behavior of $I_{Dst}$ versus $V_{GS}$ for various channel lengths, $r_j = 0.33$ μm, $t_{ox} = 500$Å, $V_{DS} = 2$V, and $V_{BS} = 0$V.[109] Reprinted with permission of *Solid State Electronics.*

once punchthrough current exceeds a small fraction of the long-channel $I_{Dst}$ value.) Punchthrough voltage $V_{PT}$ (as defined earlier) can also be extracted with this procedure by continuing to increase $V_{DS}$ until the specified $I_{Dst}$ is reached at $V_{GS} = 0$.

One way to detect the onset of punchthrough in a family of devices with varying channel lengths is to plot log $I_{Dst}$ vs. $V_{GS}$ for a fixed $V_{DS}$ for the devices of different channel lengths on a single graph (Fig. 5-26). A second method is to measure $S_t$ at a fixed $V_{DS}$ for devices with different channel lengths, and then to plot these values as shown in Fig. 5-27. Here the impact of a punchthrough implant on $S_t$ versus channel length is depicted. A third way is to measure $I_D$ vs $V_{DS}$ at $V_{GS} = 0$, and to pick off the $V_{DS}$ value when $I_{Dst}$ reaches the specified value (e.g., 0.1 μA/μm).

An example of the impact of a punchthrough implant (as well as the impact of depth and dose) is shown in Fig. 5-28. Here a 1.2-μm MOSFET with a substrate doping of $1.9 \times 10^{15}$ cm$^{-3}$ (but without a punchthrough-stopping implant) shows a very large $S_t$ value (and hence a large $I_{Dst}$ when $V_{GS} = 0$ V - curve A). The large $I_{Dst}$ at $V_{GS} = 0$V indicates that the device is in punchthrough even when $V_{DS} = 0$V.[28] Implants of boron with a dose of $8 \times 10^{11}$ atoms/cm$^2$ and different energies are then performed in an attempt to produce a $V_T$ and an $S_t$ equal to the values exhibited by a long-channel (7.8 μm) device (curve B). If the punchthrough implant is too shallow, it has the effect of increasing the $V_T$ of the device to well beyond the desired value (curve C). When the energy is increased so that the implant is sufficiently deep, $S_t$ drops to a value comparable to that exhibited by the long-channel device (curves D and E). At the same time, the surface concentration remains essentially unchanged, so that $V_T$ is not

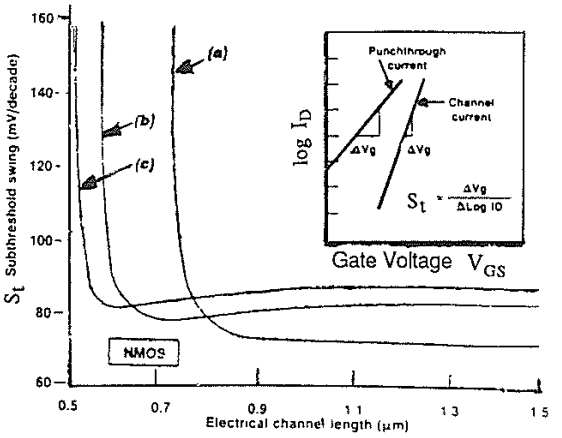


**Fig. 5-27** Subthreshold slope versus electrical channel length for NMOS devices $V_T = 0.7V$, having a common threshold adjustment implant and punchthrough implant doses of: (a) zero; (b) $2x10^{11}$ $cm^{-2}$; (c) $3x10^{11}$ $cm^{-2}$.[29] Reprinted with permission of Semiconductor International.

appreciably shifted. Note, however, that $S_t$ in the punchthrough implanted device is somewhat larger than that of the long-channel device.

In another example, the $S_t$ of a device without a punchthrough-prevention implant is measured as its length is varied (Fig. 5-27).[29] At an $L_{eff}$ of ~0.85 $\mu$m the $S_t$ starts to increase, indicating that punchthrough current begins to dominate $I_{Dst}$. By adding an implant that places boron atoms in subsurface region below the $V_T$-adjust implant, the punchthrough component of $I_{Dst}$ is suppressed so that it is not observed until $L_{eff}$ becomes nearly as small as 0.5 $\mu$m. Again, the price of an increased punchthrough implant dose is an increase in $S_t$. This tradeoff is discussed in more detail in the section on device scaling based on $I_{off}$ (that is, on $I_{Dst}$ at $V_{GS} = 0$).

## 5.3.2 Modeling Punchthrough

As discussed in the previous sections, punchthrough behavior can be measured in a number of ways, including measurements which determine $V_{PT}$. It is also often convenient to use punchthrough voltage ($V_{PT}$) as a device parameter during the tasks of device scaling and device design. Unfortunately, the amount of drain current used to define $V_{PT}$ is not universally standardized. Depending on the particular circuit application, this current level may vary from 1 pA for a DRAM to 1 nA for a static logic circuit. As a result, it would instead be useful to be able to predict the actual value of subthreshold surface-DIBL or punchthrough current in a MOSFET from the design parameters of the device prior to its fabrication. This, in fact, can be accomplished by using a 2-D device simulator which numerically solves both the Poisson equation and the carrier continuity equations to find $\varphi$, $n$, and $p$, and then uses these values to calculate the currents using the drift-diffusion current equations. Such an

entirely numerical approach, however, does not offer quantitative insight into the phenomenon of punchthrough, nor does it provide any information on trends in the device behavior as the terminal voltages are varied. However, a popular, hybrid approach that first employs a numerical method to calculate φ and then uses this solution in an analytical expression to calculate $I_{Dst}$ (instead of first solving the carrier continuity equations) has been implemented. This technique has been widely adopted for analyzing subthreshold behavior in MOSFETs because it offers some insight into the device physics, gives accurate results (provided its use is restricted to low-current operating conditions), offers a very computationally efficient approach to device analysis, and can handle both surface-DIBL and subsurface-DIBL (punchthrough) effects in MOSFETs.

This method uses the numerical techniques described in chap. 2 (with the aid of a computer and a 2-D Poisson solver software program), to find the solution of the 2-D Poisson equation. The electrostatic potential found in this manner is used in an analytical expression to calculate the value of $I_{Dst}$. That is, the value of the electrostatic potential at its minimum point, together with its variation in the vicinity of this minimum point, is used in the calculation of $I_{Dst}$, as described below. This technique was implemented in the device simulation program called GEMINI. The program has been used to analyze many aspects of MOSFET IC behavior including many of the

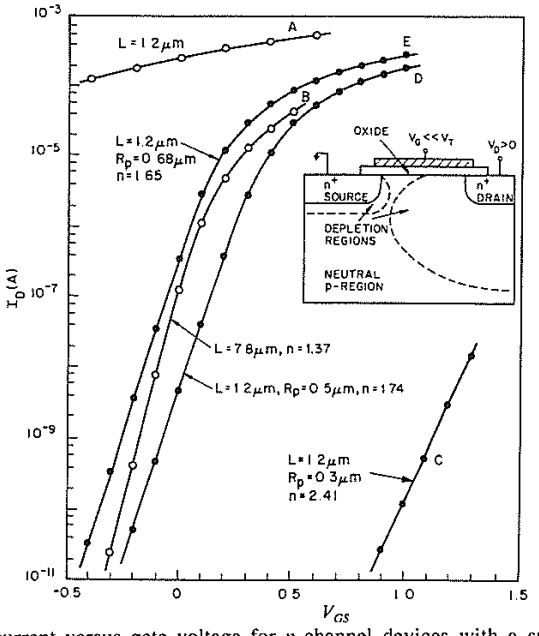


**Fig. 5-28** Drain current versus gate voltage for *n*-channel devices with a substrate doping of $1.9 \times 10^{15}$ atoms/cm$^3$, source/drain junctions are 0.47 μm deep, $t_{ox}$ = 575Å, and $V_{DS}$ = 5V, and $V_{BS}$ = 0V. Devices A and B have no channel implant, and devices C and E have a boron channel implant of $8 \times 10^{11}$ atoms/cm$^2$ at various energies.[28] (© 1978 IEEE).

topics discussed in this chapter and elsewhere in the book.[2,5,74,114,115,116]

The analytical expression for $I_{Dst}$ used in this approach is

$$I_{Dst} = -q\, D_n\, Z \frac{t^*}{L^*} \frac{n_i^2}{N_A} \exp\left[\frac{q}{kT}(\varphi^* - V_S)\right] \left\{ 1 - \exp\left(\frac{-qV_{DS}}{kT}\right) \right\} \qquad (5\text{ - }18a)$$

Note that this equation has the same basic form as the general expression derived for $I_{Dst}$ in long-channel MOSFETs in chap. 4 (i.e. Eq. 4-89). When $V_{DS} \geq 0.1V$ (the only operating condition of practical interest), Eq. 5-18a reduces to the following expression, which now has a form similar to that of Eq. 4-90 (but with some important differences):

$$I_{Dst} = -q\, D_n\, Z \frac{t^*}{L^*} \frac{n_i^2}{N_A} \exp\left[\frac{q}{kT}(\varphi^* - V_S)\right] \qquad (5\text{ - }18b)$$

That is, in Eq. 5-18, $\varphi^*$ is the value of the potential at the point P between the source and drain where it has its minimum value (i.e., along the surface when surface-DIBL dominates $I_{Dst}$, or at the saddlepoint in the bulk region when subsurface-DIBL [punchthrough] dominates $I_{Dst}$), and $V_S$ is the source potential. At P the lateral electric field (i.e., the direction of the field along the direction of current flow) becomes zero, and any current at that point must thus be due entirely to carrier diffusion. Point P is taken as the origin of a coordinate system ($r$,$\theta$) with the $r$ axis oriented along the current path and the $\theta$ axis oriented in the orthogonal direction at P (see Fig. 5-29). The

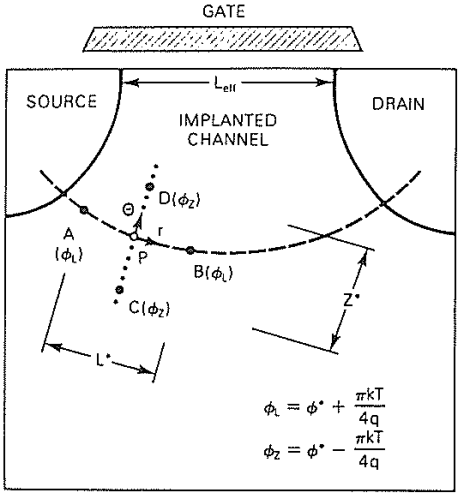


**Fig. 5-29** Cross-section of a MOSFET with a bulk current path showing the two axes (**r** and $\theta$) used to calculate the current. The points defining the approximate effective length $L^*$ and effective thickness $t^*$ are shown.[2] (© 1980 IEEE).

electrostatic potential $\varphi^*$ at P corresponds to a potential minimum along the $r$ axis and to a potential maximum along the $\theta$ axis. The value of $\varphi^*$ used in Eq. 5-18b is determined by numerically solving the 2-D form of the Poisson equation in the device region. The functional variation of the electrostatic potential at some point $(r,\theta)$ in the vicinity of point P with respect to the value $\varphi^*$ is $h\,(r,\theta)$. Hence, the electrostatic potential at point $(r,\theta)$ can be written as $\varphi(r,\theta) = \varphi^* + h\,(r,\theta)$.

In addition, the inversion layer thickness $t_{inv}$ used in Eq. 4-90, is replaced in Eq. 5-18 by $t^*$, and the channel length $L$ with $L^*$. These two terms represent, respectively, the *effective length* and *effective thickness* of the electron path near the point P, which controls the current transport. Note that when Eq. 5-18 is used to model surface-DIBL, the values of $t^*$ and $L^*$ are the same as in Eq. 4-90 (i.e., $t^*$ and $L^*$ in Eq. 5-18 in this case become $t_{inv}$ and $L$). Hence, the only difference between 5-18 when it is modeling surface-DIBL-induced $I_{Dst}$ and Eq. 4-90 is the use of $\varphi^*$ instead of $\varphi_{surf}$ (which was calculated using the analytical solution of the 1-D form of the Poisson equation).

On the other hand, when Eq, 5-18b is used to model punchthrough, $t^*$ and $L^*$ take on somewhat different meanings. Although the detailed derivations of their expressions is given in ref. 2, as shown in Figs. 5-29a and b, $L^*$ is the distance along the **r** axis between points A and B where $\varphi = \varphi^* + \pi kT/4q$, and $t^*$ is the distance along the $\theta$ axis between C and D where $\varphi = \varphi^* - \pi kT/4q$. The functional variation of $\varphi$ about point P found from the 2-D solution of the Poisson equation is used calculate $t^*$ and $L^*$.

Results obtained with this approach have been compared to solutions found from solving the carrier continuity equations as well as the Poisson equation, and with experimental data. Generally, good agreement has been found, if the operational limits of the approach are respected.[2,115]

### 5.3.3 Modeling the Simultaneous Occurrence of Surface-DIBL and Subsurface-DIBL

As a final note, we should recognize that up to now surface-DIBL and subsurface-punchthrough effects have been treated as separate, unconnected phenomena. However, when a device exhibits severe short-channel behavior, both phenomena are likely to be occurring simultaneously (see, for example, Figs. 5-23e & f), and the effects may be coupled. It may not even be possible to distinguish which one is dominant, either from a model or from measurements. In fact, the concepts of $V_T$ and $\Delta V_{Tsc}$ break down in devices that exhibit severe DIBL (surface and/or subsurface), because the log $I_D$ vs. $V_{GS}$ plots depend sensitively on the value of $V_{DS}$. That, is if a $V_T$ is defined as the $V_{GS}$ at which a specific $I_D$ flows, in severe short-channel-effect devices this will not be a unique value because the same specified current will be obtained at different gate voltages if $V_{DS}$ is changed. It is for this reason that a major goal of submicron MOSFET design is to produce devices without severe subthreshold short-channel behavior, and instead exhibit subthreshold behavior comparable to that of long-channel MOSFETs.

Nevertheless, it would still be highly useful to predict the degree to which each of these effects is occurring in a MOSFET, because each surface and bulk mechanism needs a different strategy for its suppression. One paper by Skotnicki et al. offers an analytical model that allows both surface and bulk punchthrough currents to be calcu-

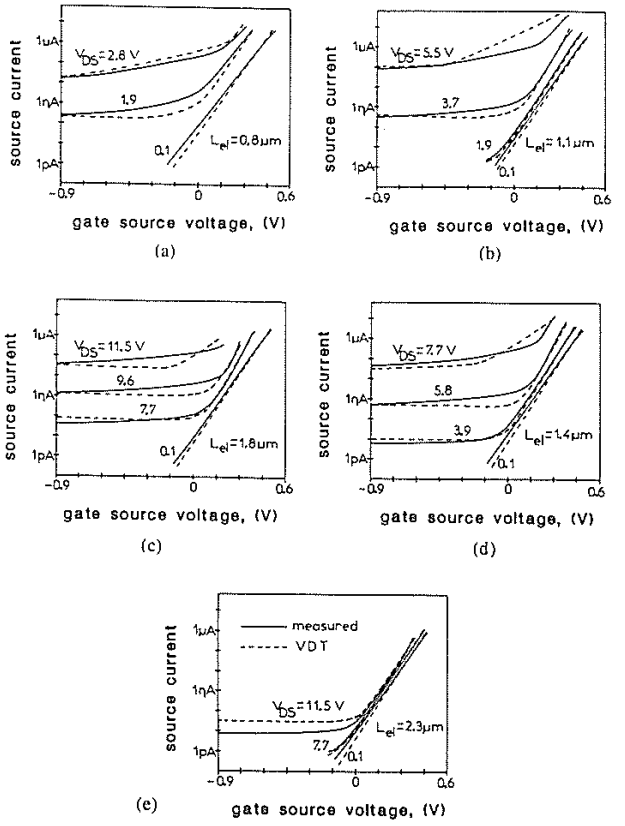


**Fig. 5-30** Measured (solid line) and analytically calculated (dashed lines) $I_{Dst}$ versus $V_{GS}$ characteristics at $V_{BS}$ = 0V and various $V_{DS}$ values for a series of MOSFETs with electrical channel lengths from 0.8 to 2.3 $\mu$m. The parameters in the VDT calculations are $r_j$ = 0.27 $\mu$m, $t_{ox}$ = 280Å, and Z = 50 $\mu$m.[30] (© 1988 IEEE).

lated simultaneously.[30] The same voltage-doping transformation (VDT) method introduced in ref. 9 is used to reduce the 2-D Poisson equation to a 1-D form. Using the VDT-method, the actual barrier heights at the surface and in the bulk can be calculated as a function of the applied voltages and channel length using the long-channel expressions where the doping concentrations in the channel $N_{ch}$ and $N_{SUB}$ are replaced by reduced values $N_{ch}^*$ and $N_{SUB}^*$. With the barrier heights known, the surface and bulk punchthrough currents can be determined. (This model is also valid in MOSFETs with non-uniformly doped channels.) Results reported show that good agreement with measured subthreshold currents is obtained for devices with gate lengths as small as 0. 8 $\mu$m and with $V_{DS}$ as large as 5.5V (see Fig. 5-30).

## 5.4 SHORT-CHANNEL EFFECTS ON THE I-V CHARACTERISTICS OF MOSFETS OPERATED IN THE STRONG INVERSION REGIME

Short-channel effects significantly alter the dc $I_D$-$V_{DS}$ characteristics of long-channel MOSFETs being operated in strong inversion in three ways. First, the combined effects of reduced gate length and gate width produce a change in $V_T$. Second, the mobility of the carriers in the channel is reduced by two effects, which in turn reduces $I_D$. These two effects are the *mobility-degradation factor* (due to the gate field), and the *velocity-saturation factor* (due to the lateral [channel] field). Third, the channel length is modulated by the drain voltage when the device is in saturation (i.e., when $V_{DS} > [V_{GS} - V_T]$), causing an increase in $I_{Dsat}$ with increasing $V_{DS}$ (*channel-modulation* effect). Figure 5-31 shows the I-V characteristics of an MOS device.[31] The curves in Fig. 5-31a are those of an ideal long-channel MOS device, while those in Fig. 5-31b show the effect of adding the channel modulation factor. Figure 5-31c shows the effect of adding the velocity saturation factor to the curves of Fig. 5-31b.

Here we describe some relatively simple models which allow an analytical dc model of the $I_D$-$V_{DS}$ characteristics of short-channel MOSFETs to be obtained. These analytical models allow circuit designers to estimate such dc parameters as $I_D$ and $g_m$ for various bias conditions using only hand calculations. They also allow an intuitive understanding of the short-channel electrical behavior to be developed, making such models useful for

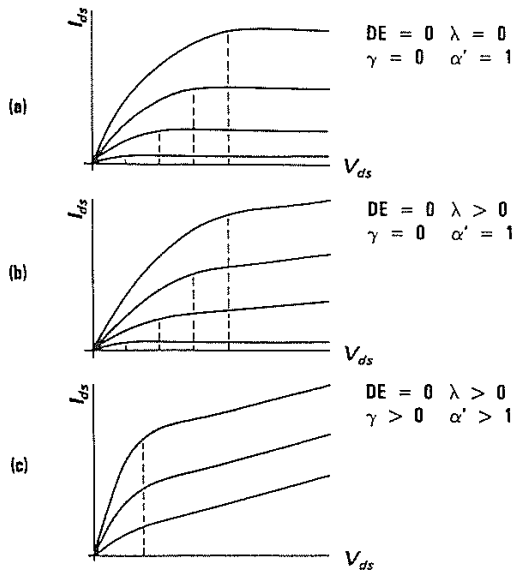


**Fig. 5-31** The I-V curves of an MOS device showing the effects of progressively increasing short-channel behavior on the operation of the device in inversion. (a) Long-channel behavior; (b) with channel-length modulation; (c) addition of velocity saturation.[31] (© 1986 IEEE).

device designers and process engineers who need to relate device and process parameters to circuit parameters. Finally, they allow $I_D$ to be calculated merely from a knowledge of device width Z, channel length $L$, the device threshold voltage $V_T$, the gate oxide thickness $t_{ox}$, the source/drain junction depth $r_j$, and with ($V_{GS}$ - $V_T$) as the independent terminal voltage parameter. On the other hand, to use the elaborate models provided in circuit simulators (such as BSIM the short-channel MOSFET model in SPICE, see the next section), it is necessary to determine a large number of model parameters. These model parameters must be derived from device measurements, often with the help of automated parameter extraction tools.

## 5.4.1 Impact of the MOSFET Electric Fields on Mobility

In deriving the long-channel dc MOSFET models (chap. 4) we assumed that the channel mobility was constant as a function of position along the channel. We also ignored any effect on the mobility due to the transverse and longitudinal electric fields acting on the carriers. In fact, both the gate-induced electric field (i.e., also called the vertical, normal, or transverse electric field), and the drain-induced electric field (i.e., referred to also as either the lateral, horizontal, or longitudinal electric field) influence the velocity of the moving carriers in the inversion layer of the channel. Since each effect can be modeled separately, this is done first. Later we show how both effects can be incorporated into the MOSFET models, allowing their impact on the $I_D$-$V_{DS}$ curves to be calculated. Before discussing how these electric fields alter the velocity of channel carriers, let us briefly review the concept of carrier mobility in a semiconductor.

The electron and hole mobilities ($\mu_n$ and $\mu_p$, respectively), are a measure of the ease of carrier motion in a semiconductor crystal. In the semiconductor bulk (i.e., at a point far away from the semiconductor surface), the carrier mobilities are typically determined by the amount of lattice scattering and ionized impurity scattering taking place inside the material. For a given temperature and semiconductor doping, these bulk mobilities are well-defined and documented material constants. (In lightly doped silicon at 300K, $\mu_n$ and $\mu_p$ are ~1350 cm$^2$/V sec and ~500 cm$^2$/V sec, respectively.)

Carrier transport in the MOSFET, however, primarily occurs in the surface inversion layer. The lateral electric field due to $V_{DS}$ acts to accelerate the carriers parallel to the Si-$SiO_2$ interface, whereupon they suffer scattering much as in the bulk. The transverse field, however, also causes the carriers to be accelerated toward the Si-$SiO_2$ surface. Thus, the carriers near the surface experience additional motion-impeding collisions with the silicon surface (see Fig. 5-32). As a result, the carrier mobilities at the surface are observed to be lower than in the bulk. (In the substrate doping range $N_A$, $N_D$<$10^{17}$ cm$^{-3}$, the mobilities of electrons and holes in the inversion layer at $V_{GS} = V_T$ are $\mu_{no}$ ~670 cm$^2$/V sec and $\mu_{po}$ ~160 cm$^2$/V sec, respectively.) The surface-scattering mechanisms include phonons, coulombic scattering sites, and surface roughness (see chap. 7). For a good quality Si-$SiO_2$ interface in strong inversion, phonon scattering is generally accepted to be the dominant scattering mechanism.

At low electric fields, the drift velocity of carriers in the bulk of a semiconductor is proportional to the electric field. The mobility is the proportionality constant in the

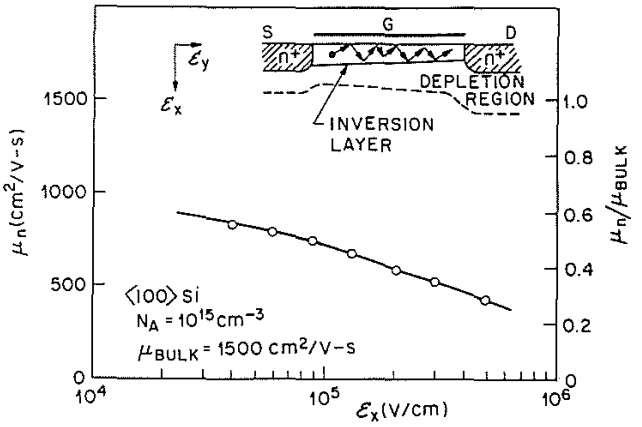


**Fig. 5-32** Visualization of surface scattering at the Si-$SiO_2$ interface.[119] Reprinted with permission of the American Physical Society.

equation which relates the drift-velocity to the electric field (at low $\mathcal{E}$–field values). However, experimental data indicate that if the electric fields get too large (i.e., >~$3x10^3$ V/cm in the bulk), the drift velocity no longer increases linearly with increasing field. In fact, at sufficiently high fields, the drift velocities approach a saturation velocity (~$10^7$ cm/sec for electrons in bulk Si).

Electrons and holes drifting in the channel also reach a saturation velocity if the lateral electric fields are high enough. In fact, in MOSFETs operating in the saturation regime, carriers moving in the pinched off region of the channel travel at this saturation velocity. The surface saturation velocity of electrons is estimated to be between $6x10^6$ to $1x10^7$ cm/sec, while that of holes is between 4-to-$8x10^6$ cm/sec.[32] These saturation velocities also appear to be relatively independent of the gate (transverse) field. In the next sections we discuss the quantitative models of both mobility degradation due to gate-induced field and the velocity-lateral field relationship (velocity saturation).

**5.4.1.1 Models of Mobility Degradation Due to Gate-Induced Electric Fields.** As the gate bias is increased, more carriers are drawn closer to the oxide-semiconductor interface. In addition, the stronger transverse (vertical) electric field acts on these carriers. This combination of effects is thought to enhance the phonon scattering of the carriers near the surface, which thereby lowers the average carrier mobility. According to Eq. 4-65 when $V_{DS}$ is small, i.e., $V_{DS}<<(V_{GS} - V_T)$, we can determine the mobility of the electrons in the MOSFET channel by measuring the slope of the $I_D$-$V_{DS}$ characteristic at fixed $V_{DS}$. When this is done, a reduction in the mobility of carriers near the surface is observed (compared to that in the bulk). Not only is the surface electron mobility under low lateral electric fields ($\mu_{no}$) found to be only one-half to two-thirds that of the low-field bulk electron mobility, but $\mu_n$ is also observed to decrease as the transverse field is increased.

An early, widely used empirical model introduced by Crawford for calculating the degree of degradation due to the transverse field (i.e., yielding an effective mobility $\mu_{eff}$)

is[33]

$$\mu_{eff} = \mu_o / [1 + \theta \mathcal{E}_x] \quad (5 - 18)$$

$$= \mu_o / [1 + \theta \ C_{ox} \ (V_{GS} - V_T) / \kappa_{si}\varepsilon_o] \quad (5 - 19)$$

where $\mu_o$ is $\mu_{no}$ for electrons and $\mu_{po}$ for holes, $\mathcal{E}_x$ is the transverse field in the silicon at the Si-$SiO_2$ interface, and $\theta$ is an empirical parameter found to be technologically and substrate-bias dependent. While it is difficult to assign a coherent physical interpretation to $\theta$, it's value has been empirically determined to be $10^{-7}$-$10^{-6}$ cm/V.

To improve the agreement between calculated and experimental values, an alternative empirical expression to that of Eq. 5-18 for the effective mobility was proposed, namely[34]

$$\mu_{eff} = \mu_o (\mathcal{E}_{crit}/\mathcal{E}_{eff})^{UEXP} \quad (5 - 20)$$

where $\mathcal{E}_{crit}$ and UEXP are empirically determined constants. This expression was used together with the results of Sabnis and Clemens,[35] who showed in 1978 that the channel carrier mobility on the (100) surface of silicon is a unique function of the *effective transverse field*, $\mathcal{E}_{eff}$ (which is defined as the field averaged over the electron distribution in the inversion layer). The expression of Sabnis and Clemens for $\mathcal{E}_{eff}$ is given by

$$\mathcal{E}_{eff} = [\ Q_B + (Q_I/2)\ ] / \kappa_{si}\varepsilon_o \quad (5 - 21)$$

Equation 5-21 can be understood as follows: The electric field at the Si-$SiO_2$ interface $\mathcal{E}_{si}$ (x = 0) can be written in terms of the total charge per unit area in the Si

$$\mathcal{E}_{si}\ (x = 0) = Q_C / \kappa_{si}\varepsilon_o \qquad \text{(Eq. 3-17)} \quad (5 - 22)$$

If an inversion layer exists, $Q_C = Q_B + Q_I$. If no inversion layer exists, $Q_C = Q_B$. Thus, $\mathcal{E}_{si1}(x = 0) = (Q_B + Q_I)/\kappa_{si}\varepsilon_o$ and $\mathcal{E}_{si2}\ (x = 0) = Q_B / \kappa_{si}\varepsilon_o$ when an inversion layer is present, or not, respectively. Also, if an inversion layer exists, the electric field at the boundary of the inversion layer $x_i$ and the depletion region is the same as at x = 0 if no inversion layer exists, or $\mathcal{E}_{si}\ (x = x_i) = Q_B / \kappa_{si}\varepsilon_o$. Thus, the effective transverse electric field within the channel can be approximated as the average of $\mathcal{E}_{si1}(x = 0)$ and $\mathcal{E}_{si}\ (x = x_i)$, or

$$\mathcal{E}_{eff} = [\mathcal{E}_{si1}(x = 0) + \mathcal{E}_{si}\ (x = x_i)]\ /2 \quad (5 - 23)$$

If we express Eq. 5-23 in terms of $Q_I$ and $Q_B$ we get

$$\mathcal{E}_{eff} = [Q_B + Q_I + Q_B] / 2\kappa_{si}\varepsilon_o = [\ Q_B + (Q_I/2)\ ] / \kappa_{si}\varepsilon_o \quad (5 - 24)$$

Eq. 5-24 can be approximated as

$$\mathcal{E}_{eff} \cong C_{ox}\,[V_{GS} - V_T]/\,(2\kappa_{si}\varepsilon_o) \qquad (5 - 25)$$

Then, if Eq. 5-25 is substituted into Eq. 5-20 the following expression is obtained

$$\mu_{eff} = \mu_o\,\{\,\kappa_{si}\varepsilon_o U_{crit}\,/\,(C_{ox}\,(V_{GS} - V_T)\}^{UEXP} \qquad (5 - 26)$$

where $U_{crit}$ is $2\mathcal{E}_{crit}$. Equation 5-26 is the model used to calculate $\mu_{eff}$ in the Level-2 MOSFET model in SPICE.*

In 1986 Liang et al[36] developed a modified form of the model of Eq. 5-26 for $\mu_{eff}$ also based on the concept of $\mathcal{E}_{eff}$. Their equation has the form:

$$\mu_{eff} = \mu_o\,/\{1 + (\mathcal{E}_{eff}/\mathcal{E}_{crit}]^{\nu}\,\} \qquad (5 - 27)$$

where $\mathcal{E}_{crit}$ and $\nu$ are empirically determined constants. Values for these parameters are shown in Table 5-2. Universal curves for $\mu_{eff}$ for electrons and holes at room temperature as a function of $\mathcal{E}_{eff}$ calculated using Eq. 5-27 are shown in Fig. 5-33.

Eq. 5-27 can also be expressed in a more useful form that explicitly relates $\mathcal{E}_{eff}$ to the device parameters and terminal voltages:

$$\mathcal{E}_{eff} \cong [(V_{GS} - V_T)/\,6t_{ox}] + [(V_T + V_a)/\,3t_{ox}] \qquad (5 - 28)$$

where it has been semi-empirically determined that $V_a \cong 0.5V$ in typical $n^+$ polysilicon gate MOSFETs (e.g., for NMOS and PMOS devices in an $n^+$ polysilicon gate CMOS technology with $V_{Tn} = 0.7V$ and $V_{Tp} = -0.7V$).[37] Note that in this equation it is assumed that $Q_I = C_{ox}\,(V_{GS} - V_T)$. Since this assumption overestimates $Q_I$ at low $(V_{GS} - V_T)$,[38] the $\mathcal{E}_{eff}$ according to Eq. 5-28 would be higher than its actual value. But, the error is small for $(V_{GS} - V_T)>1V$.

Using Eq. 5-27 and the parameter values in Table 5-2, the carrier mobilities for NMOS and PMOS devices are plotted in Fig. 5-34 for several gate oxide thicknesses as a function of $(V_{GS} - V_T)$. These curves are useful for rough estimates of device performance or as first-order calibrators in process monitoring and control. A theoretical explanation of the electron and hole mobility dependencies on the transverse electric field has been developed by Lee et al.[39]

**5.4.1.2 Models of the Carrier-Velocity Dependence on Drain Electric Field (Velocity Saturation).** As we noted earlier, the carrier velocities ($\nu$) near the Si-$SiO_2$ interface tend to saturate at high lateral electric fields, in a manner qualitatively similar to velocity saturation in the bulk. There have been

* In the Level-1 MOSFET model, however, the effective electron mobility is not explicitly expressed in terms of the field, but is treated as a fixed value.

**Table 5-2. Parameters for the Effective Mobility Models for Electrons and Holes[36]**

| | Electron (surface) | Hole (surface) | Hole (buried channel) |
|---|---|---|---|
| $\mu_o$ (cm$^2$/ V sec) | 670 | 160 | 290 |
| $\mathcal{E}_o$ (MV/cm) | 0.67 | 0.7 | 0.35 |
| $\nu$ | 1.6 | 1 | 1 |

several empirical models developed to describe the dependence of the carrier velocity on lateral field ($\nu$-$\mathcal{E}_y$).[40,41,42] Two of the most widely used are

Model I $$\nu = \mu_{eff}\,\mathcal{E} \;/\; \{1 + (\mathcal{E}/\mathcal{E}_{sat})^{\alpha}\}^{1/\alpha} \qquad (5 - 29)$$

where $\mathcal{E}_{sat}$ and $\alpha$ are empirically determined parameters (i.e., $\alpha = 2$ for electrons and $\alpha<2$ for holes). In Model II, the $\alpha$ term in Model I is taken to be unity, allowing Eq. 5-29 to become

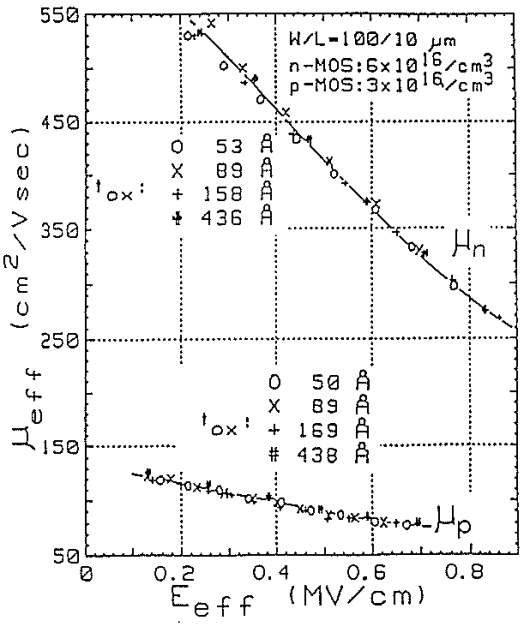


**Fig. 5-33** Measured universal $\mu_{eff}$ versus $\mathcal{E}_{eff}$ curves for electrons and holes in the inversion layer.[36] (© 1986 IEEE).

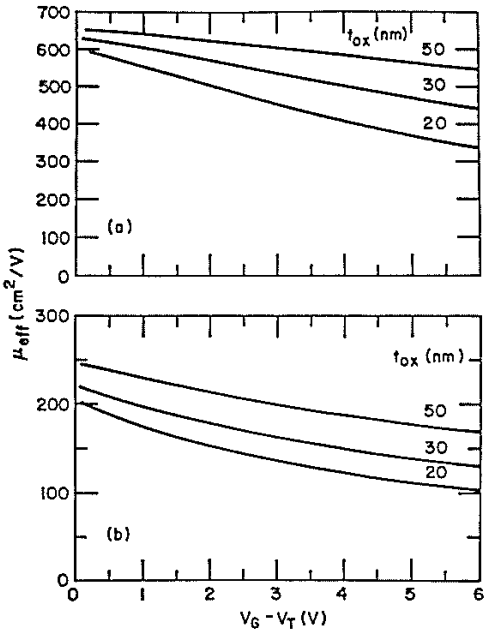


**Fig. 5-34** Calculated $\mu_{eff}$ of current carrier versus ($V_{GS}$ - $V_T$) for three different values of $t_{ox}$: (a) NMOS device and (b) PMOS devices. The "buried-channel" parameters in Table 5-2 are used for PMOS. (From [36] © 1986 IEEE) and[46] © 1988 IEEE).

Model II $$v = \mu_{eff}\,\mathcal{E} \;/\; \{1 + (\mathcal{E}/\mathcal{E}_{sat})\} \qquad (5 - 30)$$

A comparison of these two models with experimental data for electrons is shown in Fig. 5-35.[43] It is seen that Model I fits the measured data quite well, while Model II significantly underestimates the velocity at moderate fields (the same value of saturation velocity is used in both models plotted in Fig. 5-35). On this basis Model I would be preferred for estimating $v$. However, if Model I was inserted into an expression to calculate $I_D$, a solution could only be obtained by carrying out a prohibitively complex calculation.[44] Thus, to improve the accuracy of the carrier velocity model without incurring the complexity of Model I, a third, simpler, two-region piecewise model can be used. This model is defined by

Model III $$v = \mu_{eff}\,\mathcal{E} \;/\; \{1 + (\mathcal{E}/\mathcal{E}_{sat})\} \qquad \mathcal{E} < \mathcal{E}_{sat} \qquad (5 - 31a)$$

$$= v_{sat} \qquad \mathcal{E} > \mathcal{E}_{sat} \qquad (5 - 31b)$$

By using this model in the expression which calculates $I_D$ a closed-form solution of the $I_D$-$V_{DS}$ characteristics of the MOSFET is obtained. In addition, the carrier velocity saturates at $\mathcal{E}_{sat}$. $\mathcal{E}_{sat}$ can be expressed in terms of $v_{sat}$ and $\mu_{eff}$ by matching the carrier velocities given by Eqs. 5-31a and 5-31b at $\mathcal{E} = \mathcal{E}_{sat}$. Therefore,

$$v_{sat} = \mu_{eff}\, \mathcal{E}_{sat} / [1 + (\mathcal{E}_{sat} / \mathcal{E}_{sat})] \qquad (5 - 32)$$

or

$$\mathcal{E}_{sat} = 2\, v_{sat} / \mu_{eff}. \qquad (5 - 33)$$

This model is also plotted in Fig. 5-35 over a wide range of electric fields. Note that it slightly overestimates the carrier velocity near $\mathcal{E}_{sat}$.

## 5.4.2 A Simple, Analytic DC Circuit Model of the Short-Channel MOSFET in Strong Inversion

Now that we have described the influence of the transverse and lateral fields on the velocity of the channel carriers, we can use the models of these effects to modify the dc circuit models of the MOSFET operating beyond threshold. In this way we develop a simple analytical dc circuit model that is valid for short-channel MOSFETs beyond threshold, and which can be used for first-order, hand calculations of $I_D$-$V_{DS}$ and $g_m$ for devices with channel lengths down to ~1 $\mu$m.[45,46]

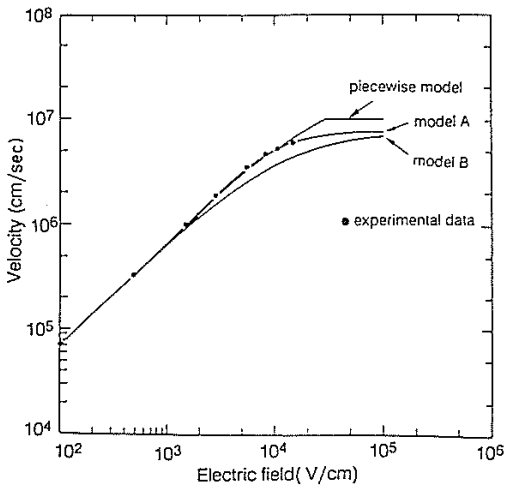


**Fig. 5-35** Comparison of velocity-field models: models A and B as given in Eqs. 5-29 and 5-30, respectively. The piecewise model is given in Eq. 5-31, and $\mu_0$ = 710 cm$^2$/V-sec, $v_{sat}$ = 1x10$^7$ cm/sec.[38] Reprinted with permission of *Solid State Electronics.*

We first note that the factors resulting from both mobility degradation due to transverse fields and velocity saturation effects are outside of the integral in the equations used to calculate $I_D$ (see Eqs. 4-16 and 4-19). Hence, they merely serve as multiplicative factors if incorporated into any of the long-channel dc models described in chap. 4. This means that any one of the long-channel models could be used to demonstrate the impact of these mobility effects the $I_D$-$V_{DS}$ characteristics. Here, for mathematical simplicity, we elect to use the square-law model of section 4.5.5 for this purpose. To complete the dc short-channel MOSFET model, however, we will later still need to add some discussion of the short-channel effects that occur when the MOSFET is operated in saturation (i.e., the effects of channel-length modulation).

**5.4.2.1 DC Circuit Model of the Short-Channel MOSFET in the Linear Regime.** As noted above, all of the long-channel MOSFET dc model equations can be modified in the same manner to take into account both effects described above. For simplicity, the square-law long-channel model is chosen to be modified. In the linear-region, the modified (i.e., short-channel) version of dc $I_D$-$V_{DS}$ equation of the square-law model (Eq. 4-68) is

$$I_D = \frac{\mu_{eff} C_{ox} \frac{Z}{L}}{(1 + \frac{V_{DS}}{\mathcal{E}_{sat} L})} \left[ (V_{GS} - V_T) V_{DS} - \frac{V_{DS}^2}{2} \right] \qquad (5 - 34)$$

Taking the ratio of the two currents given by Eqs. 5-22 and 4-68, we get

$$I_D\,(5\text{-}34)/I_D\,(4\text{-}68) = (\mu_{eff} / \mu_n)\,[1/\{1 + (V_{DS}/\mathcal{E}_{sat}L)\}] \qquad (5 - 35)$$

Note that since $\mathcal{E}_{sat}$ and $L$ appear as a product term in both Eqs. 5-22 and 5-23, a MOSFET is "long-channel-like" if either $\mathcal{E}_{sat}$ or $L$ is large. Therefore, a MOSFET with a thinner gate oxide is more "long-channel-like" because the thinner oxide will produce a larger transverse field, making the carrier mobility lower so that $\mathcal{E}_{sat}$ is high.

The saturation drain voltage $V_{DSsat}$ can next be calculated by equating the current at the drain to the current given by Eq. 5-34 when $V_{DS} = V_{DSsat}$. The current at the drain is given by the product of the carrier density and the drift velocity. The charge density at the drain, assuming that the GCA is still valid, is $ZQ_I = C_{ox}(V_{GS} - V_T - V_{DSsat})$ and the drift velocity is $v_{sat}$. Therefore the current is

$$I_D = Z\, v_{sat}\, C_{ox}\, [V_{GS} - V_T - V_{DSsat}] \qquad (5 - 36a)$$

$$= \frac{Z}{L\, \mu_{eff}\, C_{ox}} [V_{GS} - V_T - (V_{DSsat}/2)]\, V_{DSsat} \left[ \frac{1}{1 + (V_{DS}/\mathcal{E}_{sat}\, L)} \right] \qquad (5 - 36b)$$

After some algebra, an expression for $V_{DSsat}$ is obtained

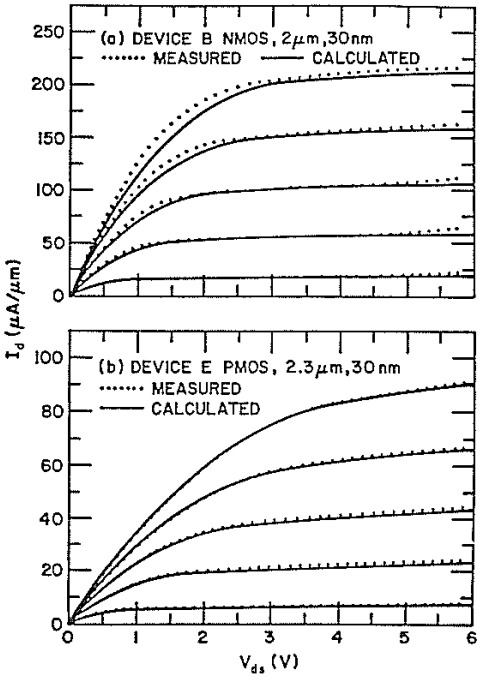


**Fig. 5-36** Measured and calculated I-V characteristics for a (a) NMOS device and (b) a PMOS device.[46] (© 1988 IEEE).

$$V_{DSsat} = \frac{\mathcal{E}_{sat}L\,[V_{GS} - V_T]}{(V_{GS} - V_T) + \mathcal{E}_{sat}L} \qquad (5 - 37)$$

where $\mathcal{E}_{sat}$ is the critical field for velocity saturation (~$4 \times 10^4$ V/cm).

The saturation drain current can be determined by substituting Eq. 5-37 into Eq. 5-36a to get

$$I_{Dsat} = Z\,v_{sat}\,C_{ox}\,\frac{[V_{GS} - V_T]^2}{(V_{GS} - V_T) + \mathcal{E}_{sat}L} \qquad (5 - 38)$$

The small-signal saturation transconductance $g_{msat}$ can be found by differentiating Eq. 5-36a with respect to $V_{GS}$:

$$g_{msat} = Z\,v_{sat}\,C_{ox}\,[1 - (\partial V_{DSsat} / \partial V_{GS})] \qquad (5 - 39)$$

Equations 5-36, 5-38, and 5-39 form the core equations of this simple model for calculating the dc drain characteristics for short-channel MOSFETs. Some modeling results using these equations are shown in Figs. 5-36a and b.[46] (Note that the $I_D$ values for $V_{DS} > V_{DSsat}$ in these curves are calculated using a saturation region model to be

described in the next section.) Good agreement with measured data is seen in these figures, and other work has shown good agreement for devices with channel lengths as small as 0.2 $\mu$m.[47] For example, agreement between calculated and measured values of $g_m$ is better than ±6 percent over most of the gate voltage range for channel lengths from 3 $\mu$m down to 1 $\mu$m.

Equation 5-37 indicates that as the channel length is decreased, the channel field at the drain end will reach $\mathcal{E}_{sat}$ at a lower value of $V_{DS}$. Thus, $V_{DSsat}$ is predicted to decrease with decreasing $L$ as well. When the gate oxide thickness is made smaller, $\mu_{eff}$ decreases because $\mathcal{E}_{eff}$ is larger (see Eq. 5-27). Consequently, $\mathcal{E}_{sat}$ will increase, and so will $V_{DSsat}$. MOSFETs with thin gate oxides thus appear more "long-channel-like," as was discussed earlier.

The short-channel dc model of the MOSFET given by Eq. 5-36 also predicts four effects that impact the value of $I_{Dsat}$ in short-channel devices not addressed by the long-channel dc models. First, mobility degradation reduces $I_{Dsat}$ in short-channel devices by a factor ($\mu_{eff}/\mu_o$). Since the effective mobility decreases as $V_{GS}$ increases, this indicates that $I_{Dsat}$ can be significantly reduced for large gate voltages. Second, $I_{Dsat}$ is also reduced by velocity saturation effects - to a value equivalent to the one predicted by the long-channel models (which assume a constant value of mobility, e.g., 4-68), except that the channel length appears longer than $L$ by the factor $V_{DS}/\mathcal{E}_{sat}$.

Third, Eq. 5-36 indicates that if the product $\mathcal{E}_{sat}L$ is large compared to $(V_{GS} - V_T)$, then $I_{Dsat}$ varies quadratically with $(V_{GS} - V_T)$. On the other hand, if $(V_{GS} - V_T) >> \mathcal{E}_{sat}L$ then $I_{Dsat}$ becomes linearly proportional to $(V_{GS} - V_T)$. Since one of the criteria in Table 5-1 for long-channel behavior is that $I_{Dsat} \propto (V_{GS} - V_T)^2$, long-channel behavior will be exhibited by devices in which either $L$ or $\mathcal{E}_{sat}$ is large. On the other hand, if $L$ or $\mathcal{E}_{sat}$ are both small, such that $\mathcal{E}_{sat}L << (V_{GS} - V_T)$, the saturation regime behavior of the MOSFET will be "short-channel-like." Note that even a very short-channel device will exhibit some long-channel behavior if $(V_{GS} - V_T)$ is small enough. The drain current under this situation is given by

$$I_{Dsat} = [\mu_{eff} Z C_{ox} / 2 L] (V_{GS} - V_T)^2 \quad \text{if } \mathcal{E}_{sat}L >> (V_{GS} - V_T) \qquad (5 - 40)$$

In shorter channel MOSFETs there is an observable trend toward a linear variation of $I_{Dsat}$ with $(V_{GS} - V_T)$ instead of the quadratic dependence, as is predicted without velocity saturation. This behavior is illustrated in Fig. 5-37a.

The fourth effect predicted by Eq. 5-36 (as noted in the introduction of this chapter) is observed in the limit of very strong velocity saturation (i.e., when the channel length is very short, such that $V_{DSsat}$ approaches zero). In such cases, Eq. 5-36 indicates that the drain current is independent of $L$, and $I_{Dsat}$ is given by

$$I_{Dsat} = [v_{sat} Z C_{ox}] (V_{GS} - V_T) \qquad (5 - 41a)$$

Under this condition, even the carriers at the source [whose density is given by $C_{ox}(V_{GS} - V_T)$] are velocity saturated.

However, $I_{Dsat}$ of a device with practical geometries is always lower than the maximum predicted by Eq. 5-41b. As a result, an ideality factor $K$ has been defined as a useful figure of merit which indicates how close $I_{Dsat}$ in a real device comes to that in an ideal device. This factor is inserted in Eq. 5-41b to yield

$$I_{Dsat} = K\,[v_{sat}\,Z\,C_{ox}]\,(V_{GS} - V_T) \quad \text{where } K < 1 \qquad (5\text{-}41b)$$

Then if we compare Eqs. 5-36 and 5-41b, we obtain a definition of as

$$K = (V_{GS} - V_T - V_{DSsat})/(V_{GS} - V_T) \qquad (5\text{-}41c)$$

This factor is a very handy parameter for device performance evaluation. That is, if an NMOS device with $t_{ox}$ = 60 nm and $L$ = 1 $\mu$m saturates at a $V_{DS}$ of 1.3V when $(V_{GS} - V_T) = 4.3$, the value of $K$ is $(4.3 - 1.3)/4.3 = 0.72$. This implies that shrinking the device would improve its driving current by no more than 30%. The $K$ factor given by Eq. 5-41c is plotted against $L$ for two different oxide thicknesses in Fig. 5-37c. The

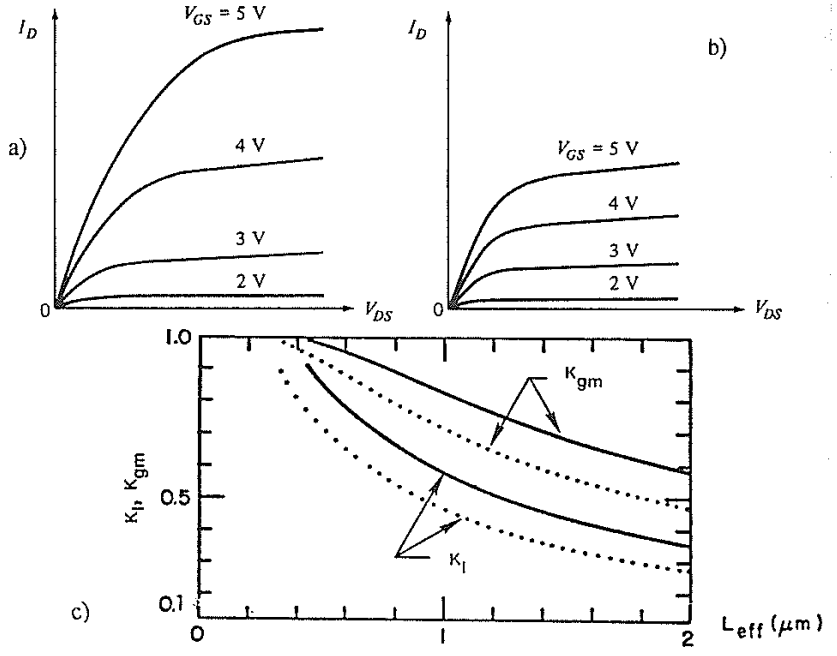


**Fig. 5-37** Device characteristics (a) in the absence and (b) in the presence of velocity saturation effects. From Y.P Tsividis, *Operation and Modeling of the MOS Transistor*, McGraw-Hill, New York, 1987, p. 180. Reprinted with permission. (c) The calculated drain current ideality factor $K_I$ versus $L$ for different gate-oxide thicknesses. Solid lines: $t_{ox}$ = 250Å; dotted lines $t_{ox}$ = 100Å.[46] (© 1988 IEEE).

$K$ of the thicker oxide device saturates at longer channel lengths. As a result, decreasing the channel length of a thick oxide MOSFET cannot significantly improve the current drive. On the other hand, as $L$ becomes very short (e.g., of the order of 0.25 $\mu$m), $K$ approaches unity independent of $t_{ox}$. Thus, $I_{Dsat}$ becomes proportional to $C_{ox}$. Since, in MOSFETs with very short channels, $I_{Dsat}$ becomes independent of channel length, the chief means of increasing $I_{Dsat}$ will be to make $t_{ox}$ as thin as possible (i.e., the device driving current will increase linearly with $C_{ox}$). Data and numerical simulation results support this argument.

As a last comment, note that because the value of $v_{sat}$ for electrons and holes is comparable, $n$-channel and $p$-channel MOSFETs tend to perform similarly under velocity saturation, other things being equal. This is not the case under normal operation. That is, because $I_D$ is proportional to $\mu_o$ in normal operation, and in this case the value of $\mu_o$ for holes in $p$-channel devices is one-half to one-fourth the corresponding value of $\mu_o$ for $n$-channel devices.

**5.4.2.2 Effects of Scaling on $g_{msat}$.** From Eq. 5-39 the maximum available value of $g_{msat}$ for a given $t_{ox}$ is given by

$$g_{msat} = Z\, v_{sat}\, C_{ox} \qquad (5 - 42)$$

This is the ultimate relationship for very-short-channel MOSFETs. However, the $g_{msat}$ of a device with practical geometries with finite channel length is always lower than this maximum. In general,

$$g_{msat} = K_{gm}\, Z\, v_{sat}\, C_{ox}, \qquad \text{where } K_{gm}<1 \qquad (5 - 43)$$

Compared to Eq. 5-39, $K_{gm}$ can be written as

$$K_{gm} = [1 - (\partial V_{DSsat} / \partial V_{GS})] \qquad (5 - 44)$$

It is observed that $g_{msat}$ of a short-channel device often peaks at some moderate gate bias, beyond which it appears to either remain flat or sometimes decrease slightly, as shown in Fig. 5-38. This is a consequence of the term $\partial V_{DSsat}/\partial V_{GS}$ in Eq. 5-44, which becomes almost constant beyond a gate bias roughly equal to $\mathcal{E}_{sat}L$.

**5.4.2.3 Comparing the Values of $I_D$ Calculated with the Long- and Short-Channel MOSFET Models as a Function of Channel Length.** The values of $I_{Dsat}$ as the channel length is reduced from 5 $\mu$m to 0.3 $\mu$m as calculated both by the charge-control dc circuit model of the long-channel MOSFET (Eq. 4-68), and the short channel dc circuit model (Eq. 5-38, whose basis is also the charge-control model) are given in Table 5-3. We observe that Eq. 4-68 predicts larger values of $I_{Dsat}$ than those calculated with Eq. 5-38 (and these in turn are much closer to the measured values). This reiterates the importance of choosing the correct device model when performing technology scaling studies.

**Table 5-3 Comparison of Drive Current Values versus Gate Length with the Long-Channel (Eq.4-68) and Short-Channel MOSFET Models.**

| | | | | | | |
|---|---|---|---|---|---|---|
| Technology/Gate Length ($\mu$m) | 5 | 3 | 2 | 1 | 0.5 | 0.3 |
| Gate Oxide (nm) | 100 | 60 | 40 | 20 | 12.5 | 7.5 |
| Calaculated $I_{Dsat}$ @ $V_{GS} = 5V$ Long-channel Model ($\mu$A/$\mu$m) | 1 | 2.61 | 6.25 | 20 | 99.3 | 206 |
| Calaculated $I_{Dsat}$ @ $V_{GS} = 5V$ Short-Channel Model ($\mu$A/$\mu$m) | 1 | 2.18 | 4.12 | 10.5 | 19.9 | 30 |

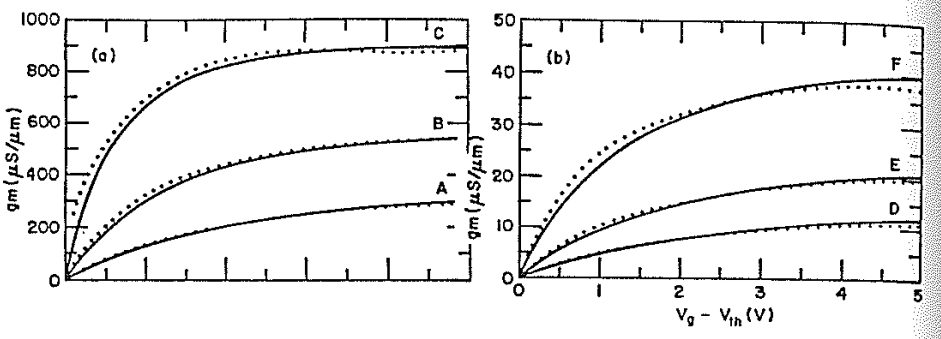


(a) (b)

**Fig. 5-38** Measured and calculated $g_m$ vs ($V_{GS}$ - $V_T$) @ $V_{DS}$ = 5V for (a) NMOS; & (b) PMOS devices with $L$ = 3 $\mu$m (A & D); $L$ = 2 $\mu$m (B & E); and $L$ = 1 $\mu$m (D & F).[46] (© 1988 IEEE).

## 5.4.3 Modeling the Saturation Region of Operation in Short-Channel MOSFETs

For drain voltages in excess of the pinch-off voltage ($V_{DSsat}$) the gate-to-drain voltage drops below the voltage value needed to establish an inversion layer (i.e., it becomes smaller than the threshold voltage). Hence, long-channel MOSFET theory implies that the inversion layer no longer exists in this case, and that there are no longer any mobile carriers present in the channel at such locations. The portion of the channel extending back from the drain over which the inversion layer is extinguished is called the *pinched-off region.* The length of the pinched off region is $\Delta L$, and its length increases as $V_{DS}$ grows beyond $V_{DSsat}$ (see Fig. 5-39). In addition, in saturation most of the drain voltage in excess of $V_{DSsat}$ is dropped across this region. From a modeling perspective this makes it appear as if the normal channel length (in which the GCA is still applicable, and in which mobile charges still exist) is growing shorter. The apparent shrinkage in channel length from this effect is known as *channel-length modulation.*

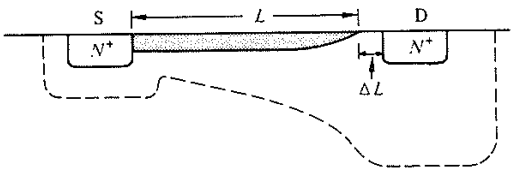


**Fig. 5-39** Visualization of the velocity saturation region in a MOSFET, having a length $\Delta L$.

In long-channel MOSFETs the length of the pinched-off region is much smaller than the original channel length (i.e. $\Delta L \ll L$), even at large values of $V_{DS}$. Thus, $I_D$ remains approximately constant for drain voltages in excess of $V_{DSsat}$. In short-channel MOSFETs, however, $\Delta L$ can be comparable to $L$. Thus, the same voltage drop ($V_{DSsat}$) will appear across a substantially shorter channel ($L - \Delta L$). Hence, when $V_{DS} > V_{DSsat}$ in short-channel MOSFETs, $I_D$ can increase significantly with increasing $V_{DS}$ (as is seen in Fig. 5-31b). Since $I_{Dsat}$ is proportional to $1/L$, the equation of drain current $I_D$ in saturation has the general form of

$$I_D\,(V_D > V_{DSsat}) = I_{Dsat}\,[L/(L - \Delta L)] \qquad (5\text{-}45)$$

To be able to predict the increase in $I_D$ in short-channel MOSFETs, the value of $\Delta L$ as a function of the terminal voltages is needed. The most general approach to calculate $\Delta L$, however, is to simultaneously solve the current transport equation (Eq. 1-4), and the two-dimensional form of the Poisson equation (Eq. 1-3) in the pinch-off region. Unfortunately, this general approach requires numerical solution of these equations, using such 2-D device simulators as MINIMOS or PISCES (see chaps. 1 and 2). To obtain an analytical expression for $\Delta L$ some approximations must be made to reduce the 2-D Poisson equation to a 1-D form. Analytical solutions of the Poisson equation can then be found, and these solutions can be used to derive analytical expressions for $\Delta L$. The analysis used to derive models for $\Delta L$ will also yield expressions that calculate the value of the channel electric field. These can be employed to find the magnitude of the maximum channel $\mathcal{E}$-field strength $\mathcal{E}_{ymax}$, a quantity that is needed when the subject of hot-carrier effects in MOSFETs is considered (see chap. 9).

For the purposes of modeling the MOSFET in saturation, the most common approach for reducing the 2-D Poisson equation to a 1-D form *assumes that* $\partial\mathcal{E}/\partial x$ (i.e., *the gradient of the electric field in the vertical (x) direction*) is much smaller than $\partial\mathcal{E}/\partial y$. In such cases, the $\partial\mathcal{E}/\partial x$ term in the 2-D Poisson equation can be dropped, turning a 2-D partial differential equation into the form of a one-dimensional (ordinary) differential equation. We note that this approach is opposite to the one taken in the GCA approximation. Namely, in the GCA approach the $\partial\mathcal{E}/\partial y$ term is considered to be much smaller than the $\partial\mathcal{E}/\partial x$ term, and thus it is the term dropped from the Poisson equation. Here we will derive three analytical models for $\Delta L$. The simplification of dropping $\partial\mathcal{E}/\partial x$ entirely from the 2-D Poisson equation is used in the first two.

**5.4.3.1 Modeling MOSFET Saturation Behavior Using the Abrupt Junction and Depletion Approximations.** The first and simplest approach to modeling saturation behavior in MOSFETs divides the MOSFET channel into two regions: one in which the long-channel $I_D$ models are still assumed to be valid, and the pinched-off region. This simple model also invokes three approximations in the pinched-off region, which are:

**a.** Only the drain field is assumed to be responsible for determining the current flow in the pinched-off region. (That is, the vertical field due to the gate is ignored.) In addition, the drain field is assumed to have only a horizontal component, $\mathcal{E}_y(y)$. Furthermore, its magnitude is assumed to be constant as a function of $x$. The map of the drain field in the pinched-off region is thus qualitatively depicted in Fig. 5-40. The strength of the field is indicated by the length of the arrows, and the field direction at each point by the direction of the arrow.

**b.** No mobile charge is present in the pinched-off region. That is, only the ionic charge [uniformly distributed with a concentration $\rho(x,y) = -qN_A$] is assumed to be present (i.e., the depletion approximation described in section 3.2.3 is once again invoked here).

**c.** The abrupt junction approximation is also invoked. This implies that $\mathcal{E}_y = 0$ at the leading edge of the pinched-off region $y = (L - \Delta L)_+$ (because the electric field at the edge of the depletion region in any abrupt junction is assumed to be zero).

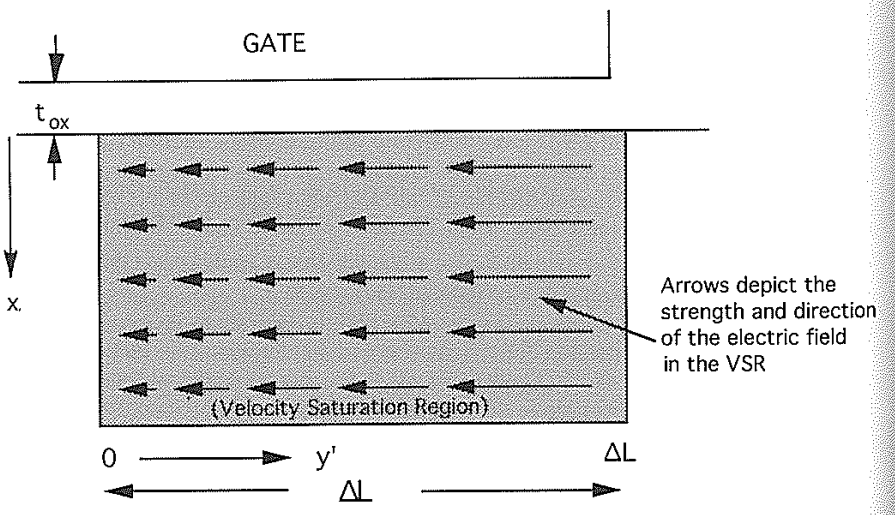


**Fig. 5-40** Map of the drain field in the VSR region.

Using these approximations the Poisson equation is reduced to the form:

$$\frac{d\mathcal{E}_y(y)}{dy} = \frac{q N_A}{\kappa_{si}\,\varepsilon_o} \qquad (5-46)$$

The expression for calculating the channel length modulation is found from Eq. 5-46 to be

$$\Delta L = \sqrt{\frac{2\varepsilon_{si}}{q N_A}(V_{DS} - V_{DSsat})} \qquad (5-47)$$

This equation for calculating $\Delta L$ was introduced by Reddi and Sah in 1965.[48]

Using this method to estimate $\Delta L$, however, leads to some physical inconsistencies in the value of $\mathcal{E}_y(y)$ as well as yielding values of $\Delta L$ that substantially overestimate its length (i.e., it predicts that $\Delta L$ can be larger than $L$, even in 2 $\mu$m MOSFETs under normal operating conditions). A more complex model must therefore be invoked to reconcile these apparently unphysical results, as well as to improve the predictive capability of the $\Delta L$ model. Before we describe such more-complex models let us first discuss the shortcomings of the Reddi-Sah $\Delta L$ model in more detail.

The variation of the channel electric field when the device is saturated provides some insight into the shortcoming of this $\Delta L$ model. We calculate the channel field using the approximations that led to the charge-control long-channel dc MOSFET model (adopted here again for the sake of mathematical simplicity). The channel field $\mathcal{E}_y(y)$ for $y < L - \Delta L$ can be found by substituting Eq. 4-63 into Eq. 4-22. Combining with the pinchoff conditions that led to Eq. 5-47, we get

$$\mathcal{E}_y(y) = \frac{V_{GS} - V_T}{2(L - \Delta L)} \frac{1}{1 - [y/(L - \Delta L)]} \qquad \text{for } y < L - \Delta L \qquad (5-48)$$

$$= \frac{q N_A}{\varepsilon_{si}} [y - (L - \Delta L)] \qquad \text{for } y > L - \Delta L \qquad (5-49)$$

These two equations for $\mathcal{E}_y$ are plotted as a function of $y$ in Fig. 5-41. Note from Eq. 5-49 that $\mathcal{E}_y$ increases linearly with $y$ in the pinched-off region. In addition, from Eq. 5-48 we see that the model predicts $\mathcal{E}_y$ goes to infinity at $y = L - \Delta L$. This occurs because at the point where the pinched-off begins (i.e., $y = L - \Delta L$), the inversion-layer charge concentration $Q_I$ becomes zero, as required by the pinchoff (and depletion-approximation) condition. To maintain current continuity when the mobile-charge concentration approaches zero, the electric field must approach infinity. In addition, Fig. 5-41 shows that $\mathcal{E}_y$ is discontinuous at $y = L - \Delta L$ (i.e., $\mathcal{E}_y$ is infinite at $[L - \Delta L]_-$, and is zero at $[L - \Delta L]_+$). Both of these predictions are, of course, unphysical. The problem lies with the pinchoff condition. That is, the concentration of mobile charges in the pinched-off region never actually becomes zero because of carrier velocity saturation. As a result, to derive a more accurate and physically correct model of the

MOSFET in saturation, a somewhat more complex formulation of the Poisson equation than Eq. 5-46 must be employed.

It should be noted that a completely empirical approach based on the Reddi-Sah model of $\Delta L$ was developed by Frohman-Bentchkowsky and Grove.[49] In this approach, Eq. 5-47 is still used, but two terms - each containing an empirically determined constant - are added as corrections to this equation to improve the accuracy with which it predicts the value of $\Delta L$. One of the correction terms is attributed to the fringing field between the gate and sidewall of the drain and the other to the fringing field between the gate and the end of the channel. These effects are not considered in the basic model represented by Eq. 5-47. Agreement with experiment is good for channel lengths from 2 to 4 $\mu$m and $N_{SUB} \sim 10^{15} - 10^{16}$ cm$^{-3}$.

**5.4.3.2 Constant-Field-Gradient Model.** The prediction of an infinite electric field strength at $y = L - \Delta L$ arises from the assumption that no mobile charge exists in the depletion region. If we remove this assumption (approximations **b** of the Reddi-Sah model), and also approximation **c** (which leads to the nonphysical discontinuity in the $\mathcal{E}$-field value at the leading edge of the pinched-off region), but retain approximation **a**, the formulation of the second of the three saturation models is obtained. That is, we now assume that a uniform mobile charge concentration (with a density $N_m$) exists to a depth $r_j$ in the pinched-off region, and also that these carriers are velocity saturated. Hence, it is appropriate to rename the pinched-off region as the *velocity saturation region* (VSR). Now, the mobile charge density in the VSR can be expressed in the following form[50] *

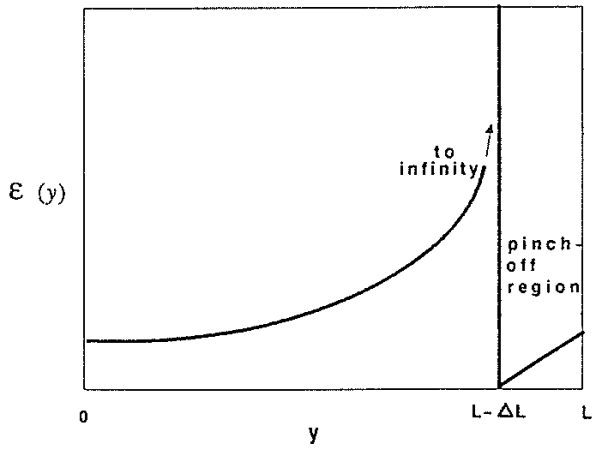


**Fig. 5-41** General behavior of $\mathcal{E}(y)$, the channel field, for a device in saturation according to the long-channel model.[45] Reprinted with permission of Academic Press.

* Note that Eq. 5-50 is similar to the more familiar drift current expression $I_{drift} = J_{drift} A = q\, n \langle v \rangle A$, where $N_m$ corresponds to $n$, $v_{sat}$ to $\langle v \rangle$, and $r_j Z$ to A.

$$q\,N_m = (A_{ph}\,I_D) / v_{sat}\,r_j\,Z \qquad (5 - 50)$$

where $I_D$ in this region is assumed to consist of velocity saturated carriers distributed uniformly into the bulk to a depth equal to the source/drain junction depths $r_j$, and $A_{ph}$ is a fitting parameter. With the total charge in the VSR now expressed as the sum of the ionic and mobile charges, the one-dimensional form of the Poisson equation (Eq. 5-46) becomes

$$\frac{d\mathcal{E}_y(y)}{dy} = \frac{q\,N_A}{\kappa_{si}\,\varepsilon_o} + A_{ph}\frac{I_D}{\kappa_{si}\,\varepsilon_o\,r_j\,v_{sat}\,Z} \qquad (5 - 51)$$

Using this equation, we can solve for the value of $\mathcal{E}_y(y)$ in the VSR. When removing approximation **c** we instead apply the boundary condition that $\mathcal{E}_y(0) = \mathcal{E}_{sat}$ at the leading edge of the VSR (instead of the boundary condition that $\mathcal{E}_y = 0$ at $[L - \Delta L]_+$, as is done in the Reddi-Sah model).

Since the terms on the right hand side of Eq. 5-51 are constant as a function of $y$, this model indicates that the gradient of the channel electric field in the $y$-direction in the VSR, $d\mathcal{E}_y(y)/dy$, is also a constant (hence the name, the *constant-field-gradient model*). As a result, $\mathcal{E}_y(y)$ is predicted by this model to increase linearly with $y$ in the VSR (as is also predicted by Reddi-Sah model). Since more charge is now assumed to exist in the VSR, however, the magnitude of the linear gradient in this model is larger. We plot this result over the channel position $\Delta L$ as the dotted line in Fig. 5-42.[54]

The channel field $\mathcal{E}_y(y)$ as calculated from a numerical solution of the two-dimensional form of the Poisson equation is also plotted in Fig. 5-42.[55] The numerical simulation predicts that $\mathcal{E}_y(y)$ exhibits a near-exponential-dependent rise towards the drain, implying that the constant-field-gradient model significantly underestimates the peak channel electric field. Because hot-carrier effects are extremely sensitive to the magnitude of the peak channel field, it has been concluded that this model is not sufficiently accurate for use in analyzing hot-carrier problems. Consequently, a more accurate analytical model of the saturation region is still needed.

**5.4.3.3 Pseudo-Two-Dimensional Model of the MOSFET Operating in Saturation.** The chief reason the constant-field-gradient model underestimates the maximum value of $\mathcal{E}_y$ in the VSR is that it ignores the effect of the gate field in the analysis. A pseudo-two-dimensional approach, which includes the effect of this field, has therefore been developed to obtain a more accurate analytical model of $\Delta L$ and $\mathcal{E}_y$ in the VSR. From these relationships a model for $I_{Dsat}$ as a function of $V_{DS}$ can also be obtained. The original pseudo-2-D model was introduced by Elmansy and Boothroyd in 1977.[51] Later, Ko et al. developed an enhanced version[52,53] that has also been applied to modeling hot-carrier effects and subthreshold MOSFET behavior (as outlined in section 5.2.1.4). Here we present a simplified version of this model, adapted from the description by Ko in references 52 and 53.

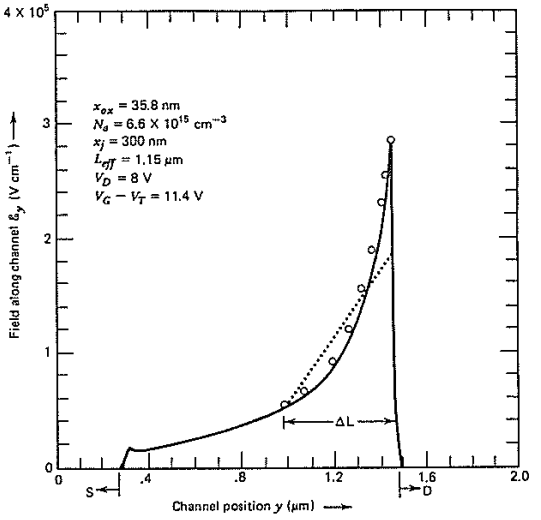


**Fig. 5-42** Calculated channel field region versus position in the channel near the drain end for three models ($t_{ox}$ =358Å, $N_A$ = 6.6x10$^{15}$ cm$^{-3}$, $r_j$ = 0.3 $\mu$m, $L_{eff}$ = 1.15 $\mu$m, $V_{DS}$ = 8V, ($V_{GS}$ - $V_T$) = 1.14V. Electrons in the channel have saturated velocities over the region $\Delta L$ which extends from the channel pinch-off point to the drain. From R.S. Muller and T.I. Kamins, *Device Electronics for Integrated Circuits*, 2nd Ed. Copyright John Wiley & Sons, New York, 1986. p. 491, Reprinted with permission.

In this approach we again remove approximations **b** and **c**, but also modify approximation **a** of the Reddi-Sah model. In Fig. 5-43a a schematic diagram of the VSR is shown. As in the previous approach the mobile carriers in this region are assumed to be velocity saturated and are uniformly distributed in the VSR to the depth of the source and drain junctions $r_j$ (with a concentration $N_m$). The VSR is thus approximated as a box bounded on the sides by ABCD. This box encloses all of the VSR mobile charges and most of the ionic charges of interest. The electric field and voltage at the leading edge of the VSR (point A) are assumed to have a values $\mathcal{E}_{sat}$ and $V_{DSsat}$, respectively. Since in steady-state the total number of mobile charges in the VSR is constant with time the phenomenon being analyzed is essentially an electrostatic problem, solvable using the Poisson equation.

Approximation **a** is modified as follows: First, let the coordinate system be selected such that $y = 0$ at A and $y = \Delta L$ at D. Next, we see that the charge enclosed in the VSR is the sum of the mobile charge and ionic charge concentrations, $qN_A$ and $qN_m$, respectively, or:

$$\rho\,(x,y) = qN_A + qN_m \qquad (5 - 53)$$

The drain $\mathcal{E}$-field is still assumed to have only a horizontal component $\mathcal{E}_y$ that varies with position $y$, but not with position $x$. The map of the drain field component in the

VSR bounded by ABCD is shown in Fig. 5-43b. The effect of the field due to the gate charge, however, is now also included in the Poisson equation. This field is assumed to have only a vertical component $\mathcal{E}_x$ which varies with position $y$ (i.e., $\mathcal{E}_x$ gets weaker as the drain is approached). $\mathcal{E}_x$ has a value at the Si-$SiO_2$ interface given by $\mathcal{E}_x(0,y)$ and is assumed to be zero at the bottom edge of the depletion region [$\mathcal{E}_x(d_{max},y) = 0$]. The value of $\mathcal{E}_x(r_j,y)$ is also assumed to be close to zero, even though $r_j$ is not as deep as $d_{max}$. (This latter assumption is plausible since the MOSFET is biased into strong inversion, making $qN_m$ in the VSR larger than $qN_A$. Thus, most of the total charge in the VSR region of the channel [i.e., from $y = 0$ to $y = \Delta L$], is confined within the depth from $x = 0$ to $x = r_j$). *It is now assumed that the value of* $\partial\mathcal{E}_x/\partial x$ *at each point y can be replaced by the average value of* $\partial\mathcal{E}_x/\partial x$ *from* $x = 0$ *to* $x = r_j$. This average value is given by [$\mathcal{E}_x(0,y) - \mathcal{E}_x(r_j,y)/r_j$]. Since $\mathcal{E}_x(r_j,y)/r_j \sim 0$, the average value of $\partial\mathcal{E}/\partial x$ can be approximated as just $\mathcal{E}_x(0,y)/r_j$.

The above modifications to approximation **a** result in the following important conclusion: *The term* $\partial\mathcal{E}/\partial x$ *in the Poisson equation can be approximated as* $\mathcal{E}_x(0,y)/r_j$. With this approximation, the 2-D Poisson equation which governs the relation between the electric-field and the charge density in the VSR, can be expressed as follows (with $\mathcal{E}_x(0,y)$ being written as $\mathcal{E}_{si}(0,y)$:

$$\frac{d\mathcal{E}_y(y)}{dy} + \frac{\mathcal{E}_{si}(0,y)}{r_j} = \frac{q\,N_A}{\kappa_{si}\,\varepsilon_o} + \frac{q\,N_m}{\kappa_{si}\,\varepsilon_o} \qquad (5\text{-}54)$$

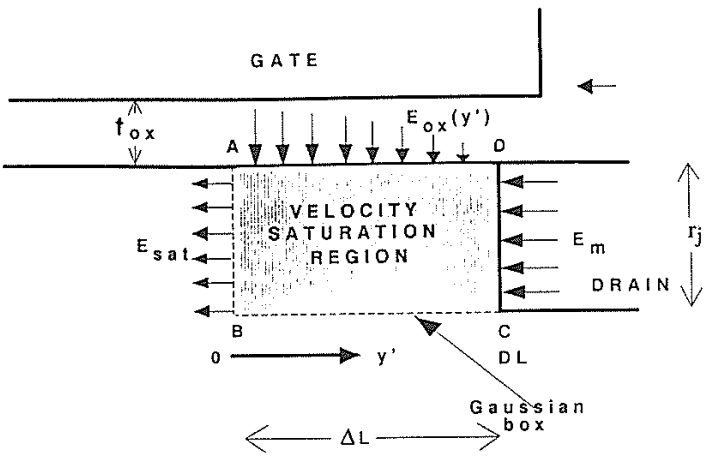


**Fig. 5-43** Schematic diagram to illustrate the analysis of the velocity saturation region (VSR). From P.K. Ko, "Approaches to Scaling," Chap. 1, in *Advanced MOS Device Physics*, N.G. Einspruch and G. Gildenblatt, Eds., Vol. 18 VLSI Electronics. Academic Press 1989. Reprinted with permission.

Thus, by using this modified approximation, not only is the Poisson equation reduced to a 1-D form (i.e., dependent only on $y$), but in addition, the effects of the both the vertical (gate) and the horizontal (drain) fields in the VSR are included. Consequently, the name chosen for this model (i.e., the *pseudo-2-D model*) is appropriate.

Now, we can further simplify Eq. 5-54 by noting that $\mathcal{E}_{si}(0,y)$ can be described in terms of $\mathcal{E}_{ox}$ (according to Eq. 3-15) as

$$\mathcal{E}_{si}(0,y) = (\varepsilon_{ox}/\kappa_{si}\varepsilon_o)\,\mathcal{E}_{ox}(0,y) \qquad (5-55)$$

Substituting the right hand side of Eq. 5-55 into Eq. 5-54 for $\mathcal{E}_{si}$, and then recalling that we since we can express $\mathcal{E}_{ox}(0,y)$ as

$$\mathcal{E}_{ox}(0,y) = [V_{GS} - V_{FB} - 2\varphi_B - V(y)]/t_{ox} \qquad (5-56)$$

[see Eq. 3-14, with $\varphi_{ox} = V_{GS} - V_{FB} - 2\varphi_B - V(y)$], we can make these both of changes in Eq. 5-54 to get

$$\frac{d\mathcal{E}_y(y)}{dy} + \frac{\varepsilon_{ox}}{\kappa_{si}\,\varepsilon_o}\frac{1}{t_{ox}}\frac{[V_{GS} - V_{FB} - 2\varphi_B - V(y)]}{r_j} = \frac{q\,N_A}{\kappa_{si}\,\varepsilon_o} + \frac{q\,N_m}{\kappa_{si}\,\varepsilon_o} \qquad (5-57)$$

Since $V(y = 0) = V_{DSsat}$ we can use Eq. 5-56 to write

$$\mathcal{E}_{ox}(y=0) = \frac{1}{t_{ox}}[V_{GS} - V_{FB} - 2\varphi_B - V_{DSsat}] \qquad (5-58)$$

In addition, since the GCA approximation is still valid at the leading edge of the VSR ($y = 0$), the total charge in the silicon ($Q_C$) at that point can still be calculated by Eq. 4-1c ($Q_C = \varphi_{ox}C_{ox}$), where $C_{ox} = \varepsilon_{ox}/t_{ox}$ and $\mathcal{E}_{ox} = \varphi_{ox}/t_{ox}$. Thus, since $Q_C$ ($cm^{-2}$) is ($qN_Ar_j + qN_mr_j$), and $Q_C = \mathcal{E}_{ox}\varepsilon_{ox}$, we can also write

$$\mathcal{E}_{ox}(y=0) = (q\,N_A\,r_j + q\,N_m\,r_j)/\varepsilon_{ox} \qquad (5-59)$$

Hence,

$$\frac{\varepsilon_{ox}}{\kappa_{si}\,\varepsilon_o}\frac{1}{t_{ox}}[V_{GS} - V_{FB} - 2\varphi_B - V_{DSsat}] = \frac{q\,N_A}{\kappa_{si}\,\varepsilon_o}r_j + \frac{q\,N_m}{\kappa_{si}\,\varepsilon_o}r_j \qquad (5-60)$$

Now we can substitute $(\varepsilon_{ox}/\kappa_{si}\varepsilon_o t_{ox}r_j)[V_{GS} - V_{FB} - 2\varphi_B - V_{DSsat}]$ for the right hand side of Eq. 5-57, allowing Eq. 5-57 to be simplified to

$$\frac{d\mathcal{E}_y(y)}{dy} = \frac{\varepsilon_{ox}}{\kappa_{si}\,\varepsilon_o\,t_{ox}\,r_j}[V(y) - V_{DSsat}] \qquad (5-61)$$

or

$$\frac{d\mathcal{E}_y(y)}{dy} = \frac{[V(y) - V_{DSsat}]}{l^2} \quad \text{where } l^2 = \frac{\kappa_{si}\varepsilon_o}{\varepsilon_{ox}}t_{ox}\,r_j \qquad (5-62)$$

or

$$\frac{d^2[V(y) - V_{DSsat}]}{dy^2} = \frac{[V(y) - V_{DSsat}]}{l^2} \qquad (5 - 63)$$

where the parameter $l$ is the effective length of the VSR.

A qualitative physical interpretation of equations 5-62 and 5-63 can be given as follows: At $y = 0$, where $V(0) = V_{DSsat}$, the charge in the VSR is still controlled entirely by the vertical field ($\mathcal{E}_x$). Since, for conditions of dc current flow the total charge density (i.e., the sum of the mobile and ionic charge densities) must remain constant along the VSR toward the drain, the total electric field at each point $y$ must also remain constant. However, the voltage $V(y)$ increases toward the drain. Thus, from Eqs. 5-55 and 5-56, we see that $\mathcal{E}_x$ must decrease toward the drain, and so must the amount of charge in the VSR controlled by it. According to the Poisson equation, this charge must be taken up by the gradient of $\mathcal{E}_y$. Thus, the gradient of $\mathcal{E}_y$ must increase toward the drain. In Eq. 5-62, the RHS is the amount of charge released by $\mathcal{E}_x$ as a result of the rise in the channel voltage [equal to $V(y) - V_{DSsat}$], while the LHS is the corresponding increase of the gradient in $\mathcal{E}_y$ in order to support these charges.

The general solution of Eq. 5-63 is:

$$[V(y) - V_{DSsat}] = A\, e^{y/l} + B\, e^{-y/l} \qquad (5 - 64)$$

By applying the boundary conditions: $V(0) = V_{DSsat}$, and $\mathcal{E}_y(0) = [\partial V(y)/\partial y]_{@y=0} = \mathcal{E}_{ysat}$, the coefficients in Eq. 5-64 are found to be $A = l\mathcal{E}_{sat}/2$ and $B = -l\mathcal{E}_{sat}/2$. Thus, we can write the expressions for $V(y)$ and $\mathcal{E}_y(y)$ in the VSR as

$$V(y) = V_{DSsat} + l\,\mathcal{E}_{sat} \sinh(y/l) \qquad (5 - 65a)$$

and

$$\mathcal{E}_y(y) = dV/dy = \mathcal{E}_{sat} \cosh(y/l) \qquad (5 - 66a)$$

Note that near the drain end of the VSR

$$V(y) \approx V_{DSsat} + l\,\mathcal{E}_{sat} \exp(y/l) \qquad (5 - 65b)$$

and

$$\mathcal{E}_y(y) \approx [(l\mathcal{E}_{sat})/l] \exp(y/l) \qquad (5 - 66b)$$

At the drain end of the channel $V(y)$ and $\mathcal{E}_y$ have their maximum values $V_{DSmax}$ and $\mathcal{E}_{ymax}$, as given by

$$V_{DSmax} = V_{DSsat} + l\,\mathcal{E}_{sat} \sinh(\Delta L/l) \qquad (5 - 67)$$

and

$$\mathcal{E}_{ymax} = \mathcal{E}(y = \Delta L) = \mathcal{E}_{sat} \cosh(\Delta L/l) \qquad (5 - 68)$$

Equations 5-67 and 5-68 can be combined to yield an expression for $\Delta L$

$$\Delta L = l \ln \frac{\{[V(y) - V_{DSsat}]/l\} + \mathcal{E}_{ymax}}{\mathcal{E}_{sat}} \qquad (5 - 69)$$

and

$$\mathcal{E}_{ymax} = \left[\frac{[V_{DS} - V_{DSsat}]^2}{l^2} + \mathcal{E}^2_{sat}\right]^{1/2} \qquad (5 - 70a)$$

Equations 5-66 to 5-70 describe important aspects of the behavior of the MOSFET in saturation. First, Eq. 5-66b indicates that $\mathcal{E}_y$ grows almost exponentially towards the drain, as was predicted by 2-D numerical simulation. In Fig. 5-42, Eq. 5-66a is plotted along with the results of the 2-D numerical simulation. Close agreement is observed. However, the parameter $l$ must be adjusted to give approximately the same peak channel field. We indicate below how this has been done using both experimental data and numerical simulation.

From Eq. 5-70, $\mathcal{E}_{ymax}$ is seen to depend explicitly on $[V(y) - V_{DSsat}]$, but the channel length $L$ only influences $\mathcal{E}_{ymax}$ indirectly. Furthermore, if $V_{DS}$ is more than about 2V greater than $V_{DSsat}$, $(V_{DS} - V_{DSsat})/l >> \mathcal{E}_{sat}$. In this case Eq. 5-70a for $\mathcal{E}_{ymax}$ is simplified to

$$\mathcal{E}_{ymax} \approx [V_{DS} - V_{DSsat}]/l \qquad (5 - 70b)$$

From experimental data and 2-D device simulations using MINIMOS the following expressions for $l$ that appear valid over a wide range of $t_{ox}$, $N_A$, and $r_j$ have been deduced:[1]

$$l \approx 0.22\, t_{ox}^{1/3}\, r_j^{1/3} \qquad \text{if } t_{ox} \geq 15 \text{ nm} \qquad (5 - 70c1)$$

and

$$l \approx 1.7\times10^{-2}\, t_{ox}^{1/8}\, r_j^{1/3} \qquad \text{if } t_{ox} < 15 \text{ nm} \qquad (5 - 70c2)$$

where $l$, $r_j$ and $t_{ox}$ are in centimeters.

By substituting Eq. 5-70c1 into Eq. 5-70b a simple, explicit expression for the maximum channel electric field is obtained

$$\mathcal{E}_{ymax} \approx [V_{DS} - V_{DSsat}]/0.22\, r_j^{1/3}\, t_{ox}^{1/3} \qquad (5 - 71)$$

where $V_{DSsat}$ is found using Eq. 5-37 and $\mathcal{E}_{sat}$ in that equation is taken to be the critical field for velocity saturation (~$5\times10^4$ V/cm). Equations. 5-71 and 5-37 can thus be used to estimate the peak channel electric field $\mathcal{E}_{ymax}$ as a function of device dimensions and bias voltages in conventional (i.e., non-graded drain) MOSFETs.

For example, by substituting some realistic values of $t_{ox}$ and $r_j$ into Eq. 5-71 (i.e., using values typical of 1-$\mu$m CMOS technology, namely, $t_{ox}$ = 250Å and $r_j$ = 0.2 $\mu$m), we get $l$ = 135 nm, and $1/l = 7.5\times10^4$ cm$^{-1}$. At low $(V_{GS} - V_T)$ values, $V_{DSsat}$~ 0. Using $\mathcal{E}_{sat} = 5\times10^4$ V/cm and $V_{DS}$ = 5V, from Eq. 5-71 we get $\mathcal{E}_{ymax} = 3.85\times10^5$ V/cm. Since $\mathcal{E}_{ymax}$ is proportional to $(1/r_j^{1/3}\, t_{ox}^{1/3})$, it is apparent that device scaling will magnify the high-field problems unless the power-supply voltage is also correspondingly reduced, or the MOSFET device structure is modified to reduce $\mathcal{E}_{ymax}$.

With an expression for $\Delta L$ also in hand (Eq. 5-69), a relationship for the drain current in saturation based on the pseudo-2D saturation model can now be derived, namely for $V_{DS}>V_{DSsat}$:

$$I_D(\Delta L) = I_{Dsat}\left[\frac{L}{L - \Delta L}\right]\left[\frac{V_{DSsat} + \mathcal{E}_{sat} L}{V_{DSsat} + \mathcal{E}_{sat}(L - \Delta L)}\right] \qquad (5 - 72)$$

## 5.5. SHORT-CHANNEL MOSFET MODELS USED IN THE *SPICE* CIRCUIT SIMULATOR

The simple, analytical short-channel MOSFET model described in section 5.4 is adequate for hand calculations. However, for computer-aided circuit analysis and design a more accurate model is needed, which also retains the benefit of simplicity to allow rapid circuit-simulation execution times. The Level-1 and Level-2 MOSFET models in SPICE are not suitable since they do not work well for small geometry transistors. Likewise, the Level-3 model relies too heavily on a semi-empirical approach. Thus, a simple and accurate, physically based, short-channel MOSFET model suitable for circuit simulation programs was needed.

Such a model has been developed and is incorporated in the circuit simulator SPICE. This model, named BSIM (Berkeley Short-channel IgFET Model), was introduced in 1987.[56] It is a modified version of the Bell Labs model CSIM with substantial enhancements (Compact Short-Channel IgFET Model).[57] BSIM is the Level-4 MOSFET model in SPICE, and BSIM2 (introduced in 1990) is the Level-5 MOSFET model.[58] By 1993, BSIM3 was developed and incorporated into SPICE.

BSIM is capable of simulating the drain current in short channel MOSFETs in both the strong-inversion and weak inversion regimes. It can model such short-channel effects as channel-length shortening, channel narrowing, mobility degradation, drain-induced barrier lowering, nonuniform channel doping for ion-implanted devices, subthreshold slope, and geometric dependencies. Terms with strong physical meaning are employed to model the fundamental physical effects while empirically derived parameters are judiciously used to embrace less-well-understood (and generally subtle) device characteristics. This approach is well-suited for circuit-analysis purposes, especially as two- and three dimensional small geometry effects become more important.

BSIM2 is an extension of the original BSIM model, but BSIM3 is essentially a new model. That is, while BSIM has about 60 parameters (17 for modeling the dc characteristics) and BSIM2 about 120, BSIM3 has 38 (the Level-1 and Level-2 SPICE models described in chap. 4 each have a total of about 15). It is generally conceded that while the Level-1 and Level-2 models had too few parameters, BSIM and BSIM2 had too many. BSIM3 is a compromise that seeks to use just the right number. In addition, many BSIM and BSIM2 parameters were put into the model strictly for curve fitting and did not have much physical basis. This makes it difficult to generate fast and slow models using BSIM or BSIM2. For the most part, the BSIM3 parameters are based on reasonable physical assumptions, and almost all have some connection with the real world, making the results of BSIM3 easier to interpret.

BSIM also includes a dedicated parameter extraction program, which together with the parameter-extraction system hardware (consisting of three major elements: a desktop computer, an H-P 4145 semiconductor parameter analyzer, and a probe station) allows the BSIM model parameters for a family of devices to be automatically extracted from measurements of actual test devices.

## 5.5.1 BSIM Model Equations

The formulation of BSIM can be broken down into the following aspects: (1) an equation for the threshold voltage $V_T$ of the short-channel MOSFET; (2) equations for the operation of the short-channel MOSFET in strong inversion; and (3) equations for the operation in weak inversion (subthreshold regime).

**5.5.1.1 BSIM Threshold Voltage Equation.** The equation used to model $V_T$ in long-channel MOSFETs (i.e., Eq. 4-12, with $V_{BC}$ replaced with $V_{BS}$), is modified in BSIM to allow the threshold lowering effect observed in short-channel MOSFETs to be modeled. The BSIM $V_T$ equation is

$$V_T = V_{FB} + 2\varphi_B + \gamma(2\varphi_B + V_{BS})^{1/2} - K_T(2\varphi_B - V_{BS}) - \eta V_{DS} \qquad (5-73)$$

We observe that in addition to the three parameters $V_{FB}$, $\varphi_B$, and $\gamma$, Eq. 5-73 contains two more for modeling $V_T$, namely $K_T$ and $\eta$. $K_T$ is the source and drain depletion charge sharing coefficient, and $\eta$ is the drain-induced barrier lowering coefficient (which is roughly inversely proportional to the channel length $L$). Together, $K_T$ and $\eta$ model the threshold lowering effect.

**5.5.1.2 BSIM Equations for $I_D$ when the MOSFET is Operated in Strong Inversion.** The BSIM $I_D$ equations contain three additional parameters to allow the mobility degradation and velocity saturation effects to be modeled. These are the vertical field mobility degradation coefficient $U_0$, the velocity saturation coefficient $U_1$, and the carrier mobility $\mu_0$. (Note that $\mu_0$ in BSIM is a function of the substrate and drain biases.) In order to speed up the circuit simulation time, instead of using $I_D$ in the form of the ionic charge model (i.e., of the form of Eq. 4-57 - which has a 3/2 power dependence of the drain current on the drain and substrate bias), a numerical approximation to the terms of Eq. 4-57 that contain $V_{BS}$ is used. The resulting BSIM equations for $I_D$ in the linear and saturation regions are:

*Linear Region:* [$V_{GS} > V_T$), and $0 < V_{DS} < V_{DSsat}$]

$$I_D = \frac{\mu_0}{[1 + U_0(V_{GS} - V_T)} \frac{C_{ox}\frac{Z}{L}}{(1 + \frac{U_1}{L}V_{DS})}\left(V_{GS} - V_T)V_{DS} - \frac{aV_{DS}^2}{2}\right) \qquad (5-74)$$

where

$$a = 1 + \frac{\gamma}{2\sqrt{2\varphi_B - V_{BS}}}\left[1 - \frac{1}{1.744 + 0.8364\,(2\varphi_B - V_{BS})}\right] \qquad (5-75)$$

If we compare Eq. 5-74 with the linear $I_D$ equation of the square-law model (Eq. 4-63b), we see that Eq. 5-74 is similar but that it also has some extra terms. The first fractional term of Eq. 5-74 models the vertical field mobility degradation effect, and has the same form as Crawford's mobility expression (Eq. 5-18). The denominator of the second fractional term models the velocity saturation effects. The last term of Eq. 5-74 is like the last term of Eq. 4-63b except that it also contains the empirical parameter 'a.' This formulation allows the terms of Eq. 4-57 containing $V_{BS}$ to be handled via a numerical approximation, rather than by having to compute terms to the 3/2 power (as would have to be done if Eq. 4-63 was used here instead to compute $I_D$). The values of $I_D$ computed with this approximation are quite close to the values that would be computed if the Eq. 4-57 was used instead (over a reasonable range of $V_{BS}$ and $V_{DS}$). See Appendix C to see how this approximation is derived, starting from Eq. 4-57.

*Saturation Region:* $[V_{GS} > V_T)$, and $V_{DS} \geq V_{DSsat}]$

$$I_D = \frac{\mu_o}{[\,1 + U_o(V_{GS} - V_T)} \; \frac{C_{ox}\frac{Z}{L}(V_{GS} - V_T)^2}{2aV} \qquad (5-76)$$

where

$$V = \frac{1 + v_c + \sqrt{1 + 2v_c}}{2} \quad \text{and} \quad v_c = U_1(V_{GS} - V_T)/a \qquad (5-77)$$

and

$$V_{DSsat} = (V_{GS} - V_T)/aV \qquad (5-78)$$

**5.5.1.3 BSIM Equations for $I_D$ when the MOSFET is Operated in Weak Inversion (Subthreshold Regime).** In BSIM the total drain current is modeled as the linear sum of the strong and weak inversion drain current components ($I_{D,S}$ and $I_{D,W}$, respectively) to allow proper matching of these two components at a transition point close to the threshold voltage. The weak inversion component is expressed as

$$I_{D,W} = (I_{exp}\, I_{limit})/(I_{exp} + I_{limit}) \qquad (5-79)$$

where

$$I_{exp} = \frac{\mu_o C_{ox} Z}{L}\left(\frac{kT}{q}\right)^2 e^{1.8}\, e^{(q/kT)(V_{GS} - V_T)/\eta}\left[1 - e^{-V_{DS}(q/kT)}\right] \qquad (5-80)$$

and

$$I_{limit} = \frac{\mu_o C_{ox} Z}{L}\left(3\,\frac{kT}{q}\right)^2 \qquad (5-81)$$

The factor $e^{1.8}$ is empirically chosen to achieve best fits in the subthreshold characteristics with minimum effect on the strong-inversion characteristics. The

subthreshold parameters $\eta_O$, $\eta_B$, and $\eta_D$ are used to model the subthreshold slope coefficient $\eta$, as:[59]

$$\eta = \eta_o + \eta_B V_{BS} + \eta_D V_{DS} \qquad (5 - 82)$$

The subthreshold swing $S_t$ is expressed as (Eq. 4-91)

$$S_t = (2.3kT/q)\,\eta = (2.3kT/q)\,(1 + C_d/C_{ox}) \qquad (5 - 83)$$

where $\eta$ is the subthreshold slope coefficient calculated from Eq. 3-82. As discussed in chap. 4 and earlier in this chapter, the subthreshold swing is a function of both substrate and drain biases, and this bias dependence is modeled in BSIM by the linear relation given by Eq. 5-82.

## 5.6 MOSFET SCALING

A roadmap of the scaling of MOSFET devices was proposed by Hu in 1993.[24] He assumed that a new generation of technology will continue to be developed every three years, with perhaps a slow-down to four years beyond the 0.35 $\mu$m generation. His proposal for MOSFET scaling is outlined as follows, with the result summarized in Table 5-4.

1. The IC industry/market will agree on the next power-supply voltage standard $V_{CC}$ several years in advance of introducing a technology/product using that voltage.

2. For a given $V_{CC}$, the thinnest gate oxide (i.e., from manufacturability, reliability and GIDL considerations) will be used to get maximum $I_D$.

3. Junction depths will be scaled aggressively to keep the short-channel effects (i.e., subthreshold leakage current) within a desired limit.

4. $V_T$ of general purpose technology will remain basically unchanged. A significant reduction in $V_T$ is unacceptable for channel subthreshold leakage.

5. The well doping concentration or punchthrough implant dose will be increased, and the gate length may be chosen to be larger than the minimum feature size in order to achieve acceptable leakage and standby current.

6. Drain engineered structures will be used as necessary to meet the constraints of hot-carrier reliability, breakdown voltage, and GIDL.

### 5.6.1 Design of Submicron MOSFETs: Scaling Guidelines

The fundamental issue of downsizing MOSFETs is to preserve long-channel characteristics after miniaturization. Several approaches have been proposed as roadmaps for designing submicron MOSFETs ($L$<1 $\mu$m) so that they exhibit such behavior.

**Table 5-4 MOSFET Technology Projection[24] (High-Speed Scenario)**

| | | | | | | |
|---|---|---|---|---|---|---|
| Minimum Feature Size ($\mu$m) | 0.5 | 0.35 | 0.25 | 0.18 | 0.13 | 0.09 |
| Year of Introduction | 1991 | 1994 | 1997 | 2001 | 2005 | 2009 |
| SRAM Density | 4M | 16M | 64M | 256M | 1G | 4G |
| $V_{CC}$ (V) (+10% for max $V_{CC}$) | 5 | 3.3 | 3.3 | 3.3 | 2.2 | 2.2 |
| MOSFET Gate Oxide (nm) | 13.5 | 9 | 8 | 7 | 4.5 | 4 |
| Junction Depth ($\mu$m) | 0.15 | 0.15 | 0.1 | 0.08 | 0.08 | 0.07 |
| Effective Channel Length ($\mu$m) | 0.40 | 0.30 | 0.25 | 0.2 | 0.15 | 0.13 |
| Threshold Voltage (V) | 0.7 | 0.7 | 0.7 | 0.7 | 0.7 | 0.7 |
| NMOS $I_{Dsat}$ @ $V_{GS} = V_{CC}$ (mA/$\mu$m) | 0.64 | 0.48 | 0.55 | 0.65 | 0.51 | 0.57 |
| PMOS $I_{Dsat}$ @ $V_{GS} = V_{CC}$ (mA/$\mu$m) | 0.31 | 0.22 | 0.26 | 0.32 | 0.24 | 0.28 |

Three of the most important scaling methodologies are the following: (1) constant electric-field scaling and its derivatives (constant voltage and constant electrostatic scaling); (2) scaling based on subthreshold behavior; (3) scaling to achieve a desired value of subthreshold current, $I_{off}$. Because subthreshold conduction is the dominant short-channel performance issue that limits MOSFET scaling,[60] the latter two have more applicability, but for completeness we also include a brief discussion of approach #1.

**5.6.1.1 Constant Electric-Field, Constant Voltage & Electrostatic Scaling.** The method of *constant electric-field scaling* for designing submicron MOSFETs was proposed by Dennard et al. in 1974.[61] In this approach, a successful larger device structure is selected (e.g., from the previous generation of ICs) and all its dimensions and voltages are reduced by a constant scaling factor $\lambda$ (>1). The new device dimensions are then $L' = L/\lambda$, $t_{ox}' = t_{ox}/\lambda$, and $W' = W/\lambda$, while the operating voltages are $V' = V/\lambda$. With this approach, operating speed increases, component density increases, and power density remains constant. Unfortunately, current density also increases by the scaling factor (a condition that aggravates electromigration failure in metal interconnect lines). In addition, the threshold voltage $V_T'$ is reduced to $V_T/\lambda$, which makes the subthreshold current larger at $V_{GS} = 0$. The worst shortcoming, however, is that the power-supply voltage must be reduced by the same factor as the channel length. This is not compatible with circuit requirements such as noise margin, current driving capability, and power-supply voltage compatibility from one generation to the next. Thus, this method has not been adopted in its original form.

Indeed, scaling of the power-supply voltage has not been implemented in digital ICs down to device dimensions of 0.8 $\mu$m. Instead, it has been maintained at 5.0 V, primarily to permit the next generation of semiconductor products to "plug in" to existing systems. Only for devices with smaller dimensions has a reduced power-supply voltage been implemented (3.3V). This has led to the consideration of *constant-voltage scaling* as a miniaturization alternative. In this approach, device dimensions are scaled by the same factor $\lambda$ as in constant-$\mathcal{E}$-field scaling, but the applied voltages remain constant. While this solves the circuit incompatibility problems, it leads to higher electric fields inside the device. These high fields cause mobility degradation, hot-carrier effects, oxide tunneling, and other reliability problems.

A compromise approach named *constant-electrostatic scaling* (or *quasi-constant voltage scaling*) was thus proposed by Bacarani et al.[62] Dimensions are still scaled by $\lambda$ but the potentials are allowed to be scaled by a separate factor $\kappa$ (e.g., $\kappa = \sqrt{\lambda}$). The operating voltages can then correspondingly decrease to $V' = V/\kappa$. This has allowed suitable fabrication parameters for MOSFETs to be derived for devices down to channel lengths of 0.25 $\mu$m (some degree of power supply voltage reduction is used).

However, even with the latter method, the depletion regions of the source and drain junctions scale by a factor less than $\lambda$, and hence devices specified according to this approach are subject to such two-dimensional problems as punchthrough and DIBL. In addition, subthreshold turn-off does not scale because it is dominated by the exponential dependence on potential of the carrier density (and the subthreshold current is dominated by a diffusion rather than a drift component). Thus, the subthreshold current does not scale with field. Consequently, the scaled down device fails to turn off at $V_{GS} = 0$ (because the voltage swing needed to drive the device "off" - which is in the range of 0.5-0.8V - cannot be scaled because the subthreshold portion of this swing $\{\Delta I_{Dst}/\Delta V_{GS}\}$ is invariant). As a result, the target $V_T$ value of a new, reduced-design-rule process will not decrease with the other physical parameters relative to an existing, larger-design-rule process. Hence, for ICs in which subthreshold leakage currents must be minimized, even this scaling method is not adequate.

**5.6.1.2 Subthreshold Scaling.** Another approach to scaling which overcomes the above difficulty was proposed by Brews et al.[63] They introduced an empirical formula which determines the minimum gate length a MOSFET can have so that its subthreshold behavior remains insensitive to drain bias. That is, by using this formula, a constraint upon each single combination of device parameters is identified, such that if this constraint is satisfied with this combination of parameter values, the resulting device exhibits long-channel subthreshold behavior.

We recall that when long-channel devices are operated in subthreshold, $I_{Dst}$ is independent of drain-to-source voltage once $V_{DS}$ exceeds a few kT/q (see Eqs. 4-87 and 4-89). Thus, the criterion selected to represent acceptable long-channel behavior was that no more than a 10% change in drain current could occur for a 0.5V change in $V_{DS}$ (e.g., $I_{Dst}$ should not vary more than 10% as $V_{DS}$ is increased from 0.5 to 1.0V).

Brews et al. found empirically that such subthreshold long-channel behavior will be preserved provided the channel length $L$ exceeds a minimum value $L_{min}$

$$L \geq L_{min} = A\,[r_j\, t_{ox}\, (W_S + W_D)^2\,]^{1/3} \qquad (5 - 84)$$

where, $r_j$ is the junction depth, $t_{ox}$ is the oxide thickness, $W_S$ and $W_D$ are the depletion widths of the source and drain (in a one-dimensional, abrupt junction for uniform doping). With $r_j$, $W_S$, and $W_D$ in microns, and $t_{ox}$ in angstroms, the fitting parameter is $A = 0.41\ \text{Å}^{-1/3}$. The substrate doping dependence is contained in the depletion-width equations, inasmuch as $W_S$ and $W_D$ (e.g., in an NMOSFET) are given by

$$W_S = \sqrt{2\kappa_{si}\varepsilon_0 V_{bi}/qN_A} \qquad (5 - 85)$$

$$W_D = \sqrt{2\kappa_{si}\varepsilon_0(V_{bi} + V_{DS})]/qN_A} \qquad (5 - 86)$$

According to Eq. 5-84, miniaturization requires shallower junctions ($r_j$), thinner oxides ($t_{ox}$), lower voltages, or heavier doping in the channel region (i.e, this will reduce $W_S + W_D$).

A set of experimental and computer-generated points were fitted to Eq. 5-84. The validity of the equation was established for gate lengths as small as 0.3 $\mu$m and for device parameters in the ranges of $100\text{Å} \leq t_{ox} \leq 1000\text{Å}$, $10^{14}\ \text{cm}^{-3} \leq N_A \leq 10^{17}\ \text{cm}^{-3}$, $0.18\ \mu\text{m} \leq r_j \leq 1.5\ \mu\text{m}$, and for drain voltages up to 5V. Figure 5-44 shows a plot of Eq. 5-84 for $L_{min}$ (solid line) compared with experimental measurements and computer simulations. For the ranges of device parameters examined, Fig. 5-44 indicates that Eq. 5-84 provides a reliable guideline for scaling MOSFET gate lengths down to 0.3 $\mu$m.

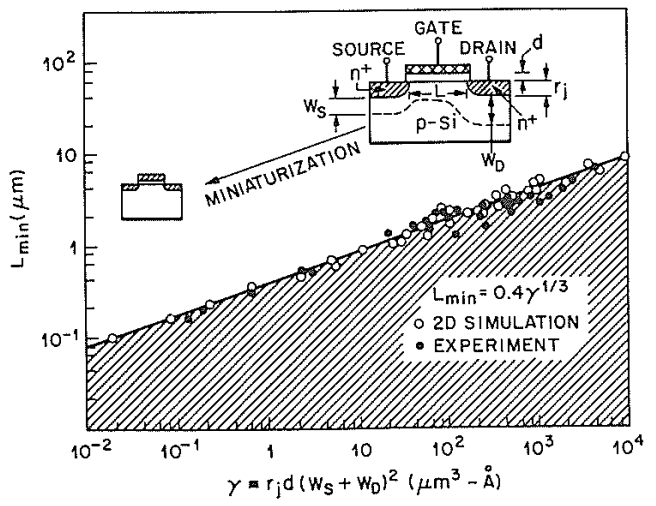


**Fig. 5-44** Equation 5-84 for $L_{min}$ compared with experimental measurements and computer simulations. The criterion for $L_{min}$ is that for $L = L_{min}$ a 10% variation in drain current occurs as $V_{DD}$ varies from 0.5 to 1.0V in the subthreshold regime of gate biases. The units of the abscissa reflect the choice of units: $d$ in Å, the other variables in $\mu$m.[63] (© 1980 IEEE).

This approach is also more flexible than the earlier ones because not all device parameters need to be scaled by the same factor $\lambda$. Instead, various device parameters can be adjusted independently as long as the value of $L_{min}$ remains the same. This is shown in Fig. 5-44, which also plots $L_{min}$ versus $\gamma$ [where $\gamma = r_j\, t_{ox}(W_S + W_D)^2$]. All devices with channel lengths lying above the line exhibit long-channel subthreshold behavior, while those below the line (crosshatched area) exhibit short-channel subthreshold behavior.

As an example, this figure shows that in order to design a MOSFET with $L_{min}$ = 0.5 $\mu$m, $\gamma$ should be 2. Once $\gamma$ is determined, $r_j$, $t_{ox}$, $W_S$, and $W_D$ can be chosen so that the resulting $\gamma$ does not exceed 2. Unlike electrostatic scaling, it is not necessary to start with an optimal large device and then scale it down by a single constant factor. Rather, any device that fits the criterion will be suitable. In addition, it allows voltages to be kept fixed or only reduced modestly, provided the other factors are changed to compensate.

To some degree Eq. 5-84 appears plausible. For example, it seems reasonable that $L_{min}$ should increase if the depletion widths increase, because such an increase enlarges the two-dimensional regions controlled by the source and drain at the expense of the region controlled by the gate. Similarly, increased junction depth increases the influence of source and drain regions, so we expect that shorter-channel devices will require smaller values of $r_j$ (i.e., shallower junctions). Finally, as $t_{ox}$ is increased, the screening effect of the gate is reduced, and the field lines emanating from the source and drain penetrate further into the channel region, and fewer of them terminate on the gate, causing $L_{min}$ to increase. However, while these simple ideas appear to support the validity of Eq. 5-84, the authors of this approach in fact admit that they do not know why it works.[65] In addition, Eq. 5-84 is known to be valid only over the fitted range, and has not been tested below 0.3 $\mu$m.

Nevertheless, Eq. 5-84 is useful in keeping DIBL under control. On the other hand, this approach still does not incorporate all of the necessary tradeoffs to handle such problems as hot-carrier degradation, or circuit-related constraints such as noise margin or off-current requirements. Consequently, the reduced devices designed with this criterion still need adjustments, especially as $L$ gets deeper below 1 $\mu$m.

Note as well, that in modern MOSFETs the substrate doping is not uniform. That is, ion implantation is used to increase the doping in the region between the source drain so that the doping there is heavier than in the substrate region beneath the source and drain. This allows a shorter source-to-drain spacing. With many MOSFET designs this surface doping is nearly uniform out to the junction depth. Thus, in Eq. 5-84 it is this doping concentration (i.e., $N_A$ in Eqs. 5-85 and 86) that must be used to calculate $W_D$ and $W_S$.

In addition, another aspect of modern NMOSFETs is the formation of shallow junction extensions by implantation using the gate as a mask (the LDD structure). It is the depth of this shallow junction extension that is used in Eq. 5-84. (The entire length of the junction is not made shallow, to avoid junction series resistance and junction leakage problems.)

Finally, Eq. 5-84 does not take into account the lateral ballooning of the drain depletion region in the lightly doped substrate beneath the source and drain regions. That is, this effect may allow bulk (subsurface) punchthrough to occur between drain and source. To prevent such subsurface punchthrough the substrate doping cannot be made as low as one would like in an attempt to reduce junction capacitance and threshold variation under source-to-substrate bias. A rough guideline for selecting the minimum value of substrate doping to avoid subsurface punchthrough has been suggested by Klaassen[64] to be

$$N_{SUB} \geq N_{ch}/10 \qquad (5 - 87)$$

where $N_{SUB}$ is the substrate doping and $N_{ch}$ is the doping in the region between the source and drain. Equation 5-87 sets a lower bound on the junction-to-substrate capacitance.

**5.6.1.3 Off-Current Scaling Approach.** Another scaling approach employing a more flexible criterion for acceptable "off"-state behavior (but which is also somewhat more complex than the previous subthreshold approach), has been recently proposed.[66] We will provide a brief outline of this method in this section. The crux of the procedure involves finding a channel doping profile which yields an acceptable combination of off-current $I_{off}$ ($I_D$ when $V_{GS} = 0V$) and $V_T$ in a device with as small an $L$ as possible. The following three parameters are varied to arrive at the appropriate channel doping profile: the exposed dose $D_I$ and centroid $x_c$ of the $V_T$ implant, and the substrate doping $N_{SUB}$. The profile is initially determined assuming that the device exhibits long-channel behavior (i.e., no significant punchthrough should be observed in the subthreshold operating region). However, the acceptable value of "off"-current in the long-channel device ($I_{off,lc}$) is deliberately picked to be smaller than $I_{off}$ in the short-channel device being designed - in anticipation of the increase in $I_{off}$ due to surface-DIBL in the shrunken device. The estimate of the increase in $I_{off,lc}$ due to surface-DIBL depends on the DIBL model chosen by the designer. To ensure that the subthreshold punchthrough current remains insignificant at maximum $V_{DS}$, a minimum $N_{SUB}$ is identified. Finally, in the process of selecting appropriate values of $D_I$ and $x_c$, the criterion that the channel depletion-region width d should be a minimum is applied (to keep $\Delta V_{TSC}$ as small as possible when $L$ is shrunk, as suggested by either Eq. 5-2 or barrier-lowering analysis).

In the report that describes this scaling strategy, the example to which it is applied is a symmetrical CMOS process (i.e., in which NMOSFETs are built with $n^+$-poly gates and PMOSFETs with $p^+$ poly gates), a technological approach that is gaining more popularity as $L$ is decreased to 0.5 $\mu$m or smaller. Let us now also consider this scaling strategy as applied to a symmetrical CMOS process in more detail.

First, the approach assumes that the following parameters are set by system and processing constraints: $V_{DD}$; the type of gate material (e.g., heavily doped poly); and minimum values of $t_{ox}$ and $r_j$. The minimum manufacturable $L$ is also limited by the lithographic process. However, $I_{off}$,$V_T$, and the actual value of $L$ are left as parameters that can be traded off later, based on the specific circuit or system application

requirements. The tradeoffs between $V_T$ and long-channel $I_{off}$ ($I_{off,lc}$) values are carried out with the aid of families of curves that relate $V_T$ and $I_{off,lc}$ for a fixed $t_{ox}$ (with $N_{SUB}$ as a parameter). Figure 5-45 is an example of one such family of curves, in which $t_{ox}$ = 100Å. Notice that the x-axis is expressed in $N_{off,lc}/N_{mg}$ instead of $I_{off,lc}$. However, since $I_{off,lc}$ is directly proportional to $N_{off,lc}$ (the latter being defined as the free-carrier density in the channel per unit area - e.g., per $cm^{-2}$ - when $V_{GS}$ = 0V) according to

$$I_{off,lc} = \mu\,(Z/L)(kT/q)qN_{off,lc} \qquad (5-88)$$

$I_{off,lc}$ is implicitly expressed in these curves. In Eq. 5-88, Z and $L$ are the device width and length, respectively. In addition, $N_{mg}$ is the free-carrier concentration per unit area in the channel at midgap,* and this value can be found from

$$N_{mg}\ (cm^{-2}) = n_i\,(\kappa_{si}/\kappa_{ox})(2kT/E_g)\,t_{ox} \qquad (5-89)$$

$N_{mg}$ is therefore the free-carrier density in the channel at the point when the surface is undergoing its field-induced reversal of polarity (e.g., from $p$-type to $n$-type). Thus, $N_{mg}$ represents the smallest free-carrier concentration in the channel in weak inversion. As is also indicated by Eq. 5-89, $N_{mg}$ is independent of $N_{SUB}$. In an Si-$SiO_2$ MOS device at 300K, Eq. 5-89 can be written to explicitly express the relation between $N_{mg}$ and $t_{ox}$ as

$$N_{mg}\ (@\ 300K,\ in\ cm^{-2}) = 10^{10}(cm^{-3})(11.8/3.9)\ 22.4\ t_{ox}(cm) = 1.33\times10^{9}\ t_{ox}(cm).$$

Thus, for a MOSFET with $t_{ox}$ = 15 nm = $1.5\times10^{-6}$ cm

$$N_{mg} \sim 2\times10^{3}\ cm^{-2}.$$

Thus, if $I_{off,lc}$ is given, and it is desired to relate this value to a point on a curve in which one axis is expressed in terms of $N_{off,lc}/N_{mg}$ (such as Fig. 5-45), it can be done as follows:

**Example 5-1:** If a maximum off-current $I_{off,lc}$ at 300K of 10 pA is required in an NMOSFET with $L$ = 3 $\mu$m, Z = 6 $\mu$m, $t_{ox}$ = 15 nm, and $\mu_n$ = 400 $cm^2$/Vsec, find the value of $N_{off,lc}/N_{mg}$ that corresponds to this $I_{off,lc}$ value.

**Solution:** Since $N_{off,lc} = I_{off,lc}/[\mu_n\,(Z/L)\,(kT/q)q]$

$$= 1\times10^{-11}\ A\ /\ [400\ cm^2/Vsec\ (6/3)\ (0.025V)\ 1.6\times10^{-19}C]$$

$$= 3.1\times10^{7}\ carriers/cm^2$$

* *Midgap* is the state of a MOSFET in which band bending is causing $E_F$ at the Si surface to co-incide with the energy level at the middle of the bandgap (which is also where $E_i$ resides). Also at midgap, $\varphi_{surf}/\varphi_t = \ln(N_{SUB}/n_i)$ as shown in Fig. 5-46. In the special case of midgap occurring at $V_{GS}$ =0V, $N_{mg}$ is the free-carrier concentration ($cm^{-2}$) in the channel for that condition.

and since $N_{mg}$ (300K, $t_{ox}$ = 15 nm) = $2x10^3$ $cm^{-2}$,

$$N_{off,lc}/N_{mg} = 1.5x10^4$$

To arrive at the $V_T$ values exhibited in a family of curves such as those in Fig. 5-45, we follow the general procedure given in section 4.6.3. That is, the value of $V_{Tud,lc}$ (assuming a uniformly doped channel region with a doping of $N_{SUB}$) is calculated using Eq. 3-71, and this is added to $\Delta V_T(II)$ using Eq. 4-73, to get $V_{Tnud,lc}$ (Eq. 4-74 or Eq. 4-75) However, to accurately determine $\Delta V_T(II)$ the value of both $D_I$ and $x_c$ must be specified. In addition, the impact of $N_{SUB}$ must included.

That is, in the simple long-channel analysis of a MOSFET in section it was assumed that $V_{Tud,lc}$ can be shifted by choosing $D_I$ and $x_c$ independent of $N_{SUB}$.

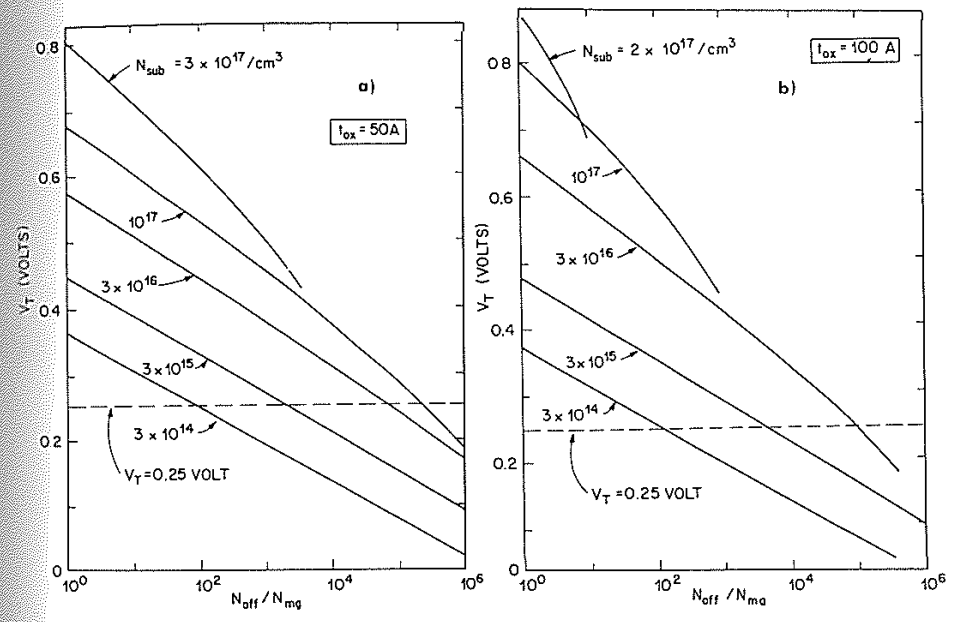


**Fig. 5-45** Threshold voltage for implanted structures with the indicated substrate doping as a function of $N_{off}/N_{mg}$. The dose and centroid of the implants are chosen for minimum depletion width. (a) $t_{ox}$ = 50Å; (b) $t_{ox}$ = 100Å. From J.R. Brews, K.K. Ng, and R.K. Watts, Chap. 1, "The Submicrometer Silicon MOSFET," in *Submicron Integrated Circuits*, R.K. Watts, Ed., Wiley-Interscience, New York, Copyright 1989 p. 34. Reprinted with permission.

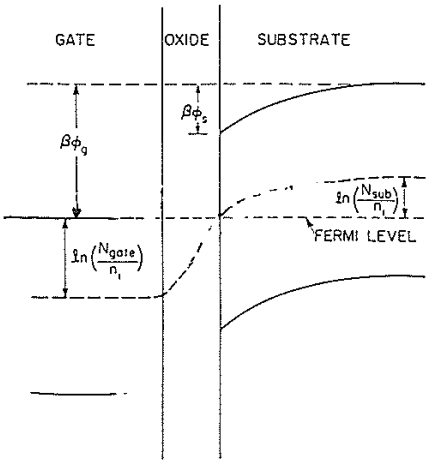


**Fig. 5-46** An MOS structure at zero gate bias with midgap level and the Fermi level at the surface being equal at zero bias (*midgap* occurs).

However, for the following reasons $N_{SUB}$ cannot be ignored, especially when designing short-channel devices: First, a minimum $N_{SUB}$ must be identified to prevent subsurface punchthrough, e.g., $N_{SUB} \geq N_{ch}/10$. (Note that in this analysis, the effect of a punchthrough implant is not considered, and hence only the substrate doping plays a role in preventing subsurface punchthrough.) Second, the choice of $N_{SUB}$ impacts $d_I$ (the channel depletion region width in the presence of an $V_T$ implant) in that larger values of $N_{SUB}$ will cause $d_I$ to decrease (see Eq. 4-80). To make $d_I$ smaller (i.e., to keep $\Delta V_{Tsc}$ as small as possible, as described earlier), larger $N_{SUB}$ values are needed.* Third, $N_{SUB}$ impacts $N_{off,lc}$, because $S_t$ depends on d (see Eq. 4-91b). In general, increasing the value of $N_{SUB}$ will cause the value of $S_t$ to increase. If $V_T$ remains the same, the consequence of an increase in $S_t$ is a larger $N_{off,lc}$ (as is also evident in Fig. 5-45). Obviously, the first two issues call for large $N_{SUB}$ values, while the third calls for smaller values. Hence, tradeoffs may be necessary.

Values for the exposed dose $D_I$ and the centroid $x_c$ that will produce a minimum value of d are plotted versus $N_{off,lc}/N_{mg}$ with $N_{SUB}$ as a parameter, and $t_{ox}$ = 50Å in Fig. 5-47. The value of $D_I$ is obtained from the following equation:

* The equations used to generate the $V_T$ versus $N_{off,lc}/N_{mg}$ curves are derived by invoking the constraint that the channel depletion width in weak inversion (d) must be a minimum. This constraint is derived from Eq. 5-2, and the fact that we want $\Delta V_{Tsc}$ to be as small as possible. Since it is assumed that the device will employ the smallest $t_{ox}$ and $r_j$ values allowed by process technology, the last parameter in Eq. 5-2 that can reduce $\Delta V_{Tsc}$ when the device is shrunk to its minimum *L*, is $d_{max}$.

$$qD_I = (Q/Q_{mg})\,(\kappa_{ox}\varepsilon_o/t_{ox})\,(kT/q)\,(\beta E_g/2q) \qquad (5\text{ - }90)$$

The value of $Q/Q_{mg}$ is found in terms of $N_{off,lc}/N_{mg}$ with the aid of Fig. 5-48.* (It turns out that for most cases of interest the substrate doping independence of $D_I$ assumed in section does in fact continue to hold to larger values of $N_{SUB}$ when the devices have thin oxides. Thus, Eq. 5-90, which is independent of $N_{SUB}$, continues to be valid for such cases). Once $D_I$ is known, its value is used to find $x_c$ from

$$x_c/d = -D_I/(N_{SUB}d) + \{(D/N_{SUB}d)^2 + 1\}^{1/2} \qquad (5\text{ - }91)$$

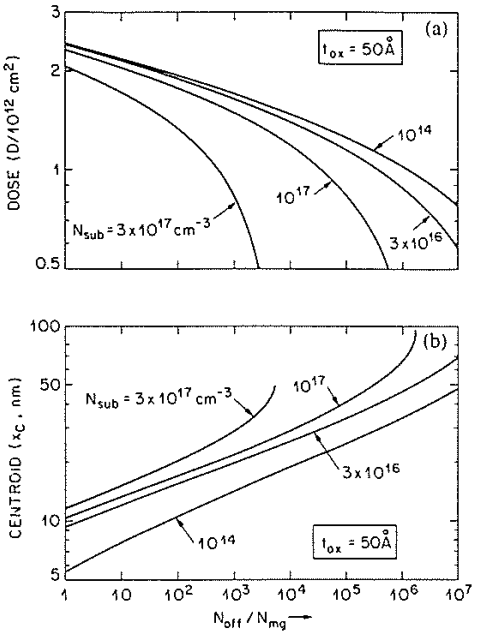


**Fig. 5-47** (a) Dose in units of $10^{12}/cm^2$ as a function of $N_{off}/N_{mg}$ with substrate doping as parameter. (b) Centroid or depletion layer width $x_c = w$ in nanometers versus $N_{off}/N_{mg}$. In both figures $t_{ox}$ = 50Å. From J.R. Brews, K.K. Ng, and R.K. Watts, Chap. 1, "The Submicrometer Silicon MOSFET," in *Submicron Integrated Circuits*, R.K. Watts, Ed., Wiley-Interscience, New York. Copyright 1989 p. 28. Reprinted with permission.

* Note that Q here is a dimensionless surface charge defined as by

$$Q = (D_I/N_{SUB}L_D) + (N_{off,lc}/N_{sub}L_D) + (d/L_D) \qquad (5\text{ - }92)$$

where $L_D$ is the Debye length, and $Q_{mg} = (\kappa_{ox}L_D E_g/2kT\kappa_s t_{ox})$. But for the purposes of our abbreviated description of this scaling strategy (described more completely in ref. 65), it suffices to note that $Q/Q_{mg}$ can be determined in terms of $N_{off,lc}/N_{mg}$ by using Fig. 5-48.

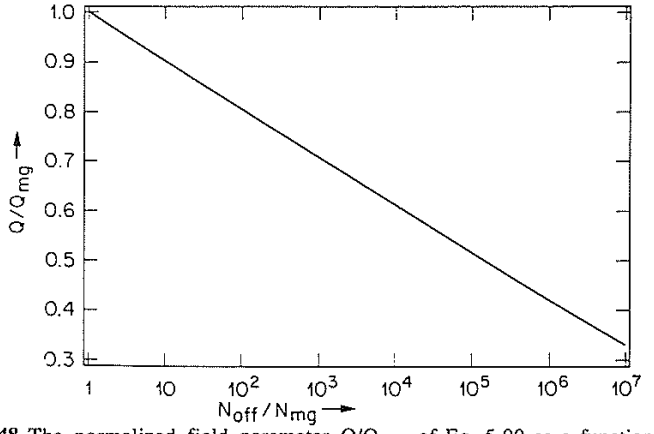


**Fig. 5-48** The normalized field parameter $Q/Q_{mg}$ of Eq. 5-90 as a function of zero-bias carrier density to midgap carrier density ratio $N_{off}/N_{mg}$. From J.R. Brews, K.K. Ng, and R.K. Watts, Chap. 1, "The Submicrometer Silicon MOSFET," in *Submicron Integrated Circuits*, R.K. Watts, Ed., Wiley-Interscience, New York, Copyright 1989 p. 28. Reprinted with permission.

Once $V_T$ is determined for an acceptable value of $N_{off,lc}$, a check is made to ensure that the chosen $N_{SUB}$ value exceeds the minimum substrate concentration identified as being able to provide adequate subsurface punchthrough protection. If $N_{SUB}$ is found to be large enough to prevent punchthrough, the design process can proceed to the next step - barrier-lowering analysis. (However, if the chosen value of $N_{SUB}$ cannot prevent punchthrough, a larger $N_{SUB}$ value may need to be accepted, which in turn may possibly require an adjustment of the maximum acceptable $I_{off}$.)

The barrier-lowering analysis examines the effect of shrinking $L$ to the minimum value that can be fabricated with the best lithographic process at hand. At that length the value of $\Delta V_{Tsc}$ is calculated, using the DIBL model of choice. The value of the long-channel off current $I_{off,lc}$ in the device designed using the strategy outlined above now becomes the basis for determining the short-channel device $I_{off}$, according to

$$I_{off} = I_{off,lc} \exp (q\Delta V_{Tsc}/kT) \qquad (5 - 93)$$

If $I_{off}$ is less than or equal to the target value, the device with that value of $L$ will succeed in meeting the circuit requirements and is deemed nominally manufacturable. If $I_{off}$ is too high, either the channel length will need to be increased, or a larger value of $I_{off}$ will need to be accommodated by changing the circuit design.

The term *nominally manufacturable* is used, because as the channel length is reduced, the sensitivity of $V_T$ to channel length variations increases. As already noted, the impact of channel length variation is to require a more conservative setting of nominal-$I_{off}$ so that devices with smaller than nominal $V_T$ values will still have acceptable off-currents. As the channel length is reduced, at some point this lowered $I_{off}$ estimate will encounter

the same punchthrough limit already discussed. If channel length is under very tight control, then $V_T$ variations from length variation remains small, and only variation due to changes in $V_{DS}$ will matter. However, it is more common that channel length variations will dominate the choice of $L_{min}$ as illustrated in the next section.

## 5.6.2 Manufacturing Considerations in Submicron MOSFET Device Design

As noted above, the "off"-current value in submicron MOSFETs must be maintained over the range of manufacturing tolerances. For example, assume that a typical 0.8 $\mu$m NMOS transistor (i.e., the drawn channel length $L$ is 0.8 $\mu$m) has an $L_{eff}$ of 0.7 $\mu$m and a 3-sigma manufacturing tolerance on patterned gate length of $\pm 0.12$ $\mu$m. Hence, the shortest $L_{eff}$ in a device that still meets the manufacturing tolerance (i.e., patterned gate length is 0.68 $\mu$m) will be 0.58 $\mu$m. At this gate length, the CMOS devices will still have to possess sufficient $V_T$ control, satisfactory hot-carrier reliability, and acceptable punchthrough characteristics. To enable a MOSFET to meet these requirements, $N_{SUB}$ will need to be raised to a value higher than that needed for the nominal device length. As a result, the performance of the nominal gate length device ($L = 0.8$ $\mu$m) will be degraded through increased source/drain junction capacitance and subthreshold turnoff.

The importance of manufacturing control on patterned gate length is illustrated in Fig. 5-49.[67] This figure plots the NMOS and PMOS device leakage in the "off" state

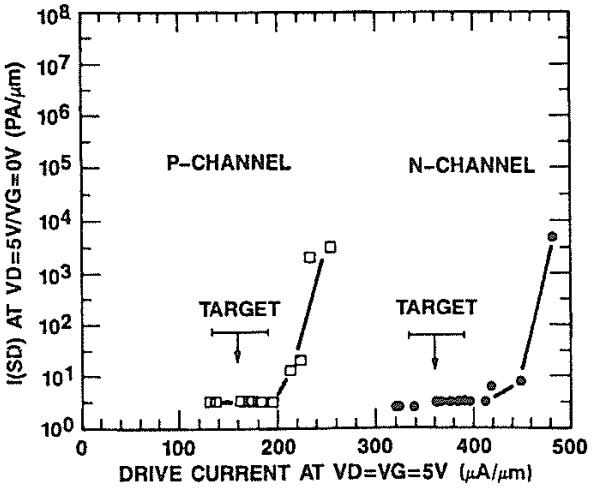


**Fig. 5-49** NMOS and PMOS drive current, defined as the drain current for 5V applied to the gate and drain, versus leakage in the off state with 0V on the gate and 5V on the drain. The parameter is gate length, with a target value of 0.8 $\mu$m. From R.A. Haken et al., "BiCMOS Process Technology," Chap. 3, p. 85, in *BiCMOS Technology and Applications,* A. Alvarez Ed. Klewer, Norwell MA, Copyright 1989. Reprinted with permission.

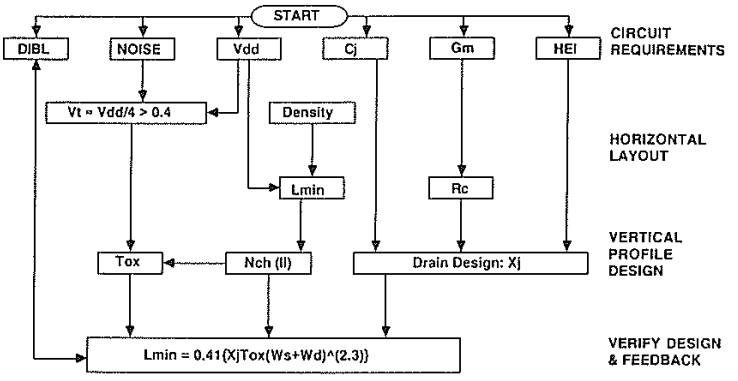


**Fig. 5-50** First order MOS device design methodology. Horizontal design generally precedes the vertical profile design. The horizontal design is set to optimize intrinsic device delay ($L_{eff}$, $R_{SD}$). Vertical profile design is set to minimize short-channel effects.[68] (© 1988 IEEE).

(in this figure $I_{SD}$ with 0V on the gate and 5V on the drain), versus drive current, defined as $I_D$ when $V_{DS} = V_{GS} = 5V$. Although $I_D$ is the $x$-axis variable, the actual parameter being varied is $L$, since $I_D$ is inversely proportional to $L$. In this example, for the $n$-channel device, when $L = 0.8$ $\mu$m ($L_{eff} = 0.7$ $\mu$m), $I_D$ is 400 $\mu$A/$\mu$m. The device design has been optimized for a patterned gate length of 0.8 $\mu$m with a manufacturing 3-$\sigma$ control on $L$ of $\pm 0.12$ $\mu$m. According to Fig. 5-49, as the 3-$\sigma$ manufacturing control limit is reached, the device leakage current increases to ~$10^4$ pA/$\mu$m (i.e., from Fig. 5-49 the leakage starts to rapidly rise when $I_D = 480$ $\mu$A/$\mu$m, which means it is occurring when $L = 0.68$ $\mu$m, or $L_{eff} = 0.58$ $\mu$m). Such high levels of device leakage might cause circuits to become nonfunctional, or could cause them to fail a particular circuit specification, such as maximum standby power.

## 5.7 DESIGN OF SUBMICRON NMOSFETS

We outline two approaches for the design of submicron NMOSFETs that have appeared in the literature. The first is fundamentally based on Eq. 5-87, while the second relies on the off-current scaling approach.

### 5.7.1 Design Methodology Based on the Subthreshold Scaling Equation

Figure 5-50 shows a flow-chart of the steps taken in the subthreshold-scaling approach to designing submicron MOSFETs in CMOS.[68] It assumes that the following circuit constraints on the device are defined (as dictated by the application being served): the power-supply voltage $V_{DD}$, the required drive current $I_D$ in $\mu$A/$\mu$m (or transconductance,

$g_m$), the required noise margin, the minimum intrinsic gate delay, and the maximum allowed device degradation (long-term) due to hot-carrier effects (HEI in the diagram).

The given $V_{DD}$ and noise-margin constraint determine the choice of $V_T$. $V_{DD}$ and the lithographic-processing capability limit the minimum channel length $L_{min}$. By thinning $t_{ox}$, $I_D$ can be increased, but minimum $t_{ox}$ is set by $V_{DD}$ and processing constraints.

The maximum allowed parasitic resistance $R_S$ depends on $g_m$ (which is really the inverse of $R_{ch}$). For example, $R_S$ may need to be kept smaller than 10% of $R_{ch}$. This may then dictate the minimum horizontal dimensions of the drain and source regions, and also the depth $r_j$ of the source and drain junctions. The required $R_S$ value may also determine the doping profile of the tip region of the LDD structure and may dictate whether or not salicided source/drains are necessary. The minimum gate delay $\tau_d$ will be impacted by the intrinsic device characteristics (i.e., $I_D$ through $L_{min}$, and $C_L$ through $C_{gate}$ and $C_j$). By minimizing gate area and source/drain junction areas, smaller $C_{gate}$ and $C_j$ can be realized. Lower substrate doping also decreases $C_j$.

The selection of the channel doping concentration ($N_{ch}$) will be impacted by the substrate concentration and the $V_T$-adjust implant. $V_T$ and $N_A$ will determine the $V_T$ adjust implant dose. The drain design (e.g., an LDD) is impacted by the desire to keep hot-carrier degradation to an acceptable value (see chap. 9). The depletion region widths of the source and drain junctions - $W_S$ and $W_D$ - are determined by $N_{ch}$ and the drain structure design.

Once the values of $t_{ox}$, $r_j$, and $W_S$ and $W_D$ are determined, they are inserted into Eq. 5-84. If the right hand side of the equation is a number smaller than $L_{min}$ with this group of parameters, then according to past experience it is likely that a MOSFET with this $L_{min}$ can be successfully fabricated (i.e., the device should satisfy the subthreshold leakage current criterion given in section 5.6.1.2). Hence, if some acceptable combination of manufacturable parameters meeting this criterion can be found, fabrication success is likely. If not, a larger value of $L_{min}$ may have to be accepted.

### 5.7.2 Design Methodology Based on Required Off-Current Value

The flow chart of the $I_{off}$ design strategy of submicron MOSFETs is shown in Fig. 5-51.[69] In summary, a MOSFET is designed by selecting what appears to be an appropriate set of $V_T$ and $I_{off}$ values, applying the principles of long-channel MOSFET physics to derive the channel doping profile. Then the device length is shortened and punchthrough analysis and barrier-lowering analysis is performed on the shortened device to ensure that the $I_{off}$ circuit specification is still met. If not, the design procedure must be repeated, trading off $V_T$ and $I_{off}$ against channel length until the best set of parameters for the application at hand is achieved. Details of the various steps in the flow chart were described in section 5.7.1.

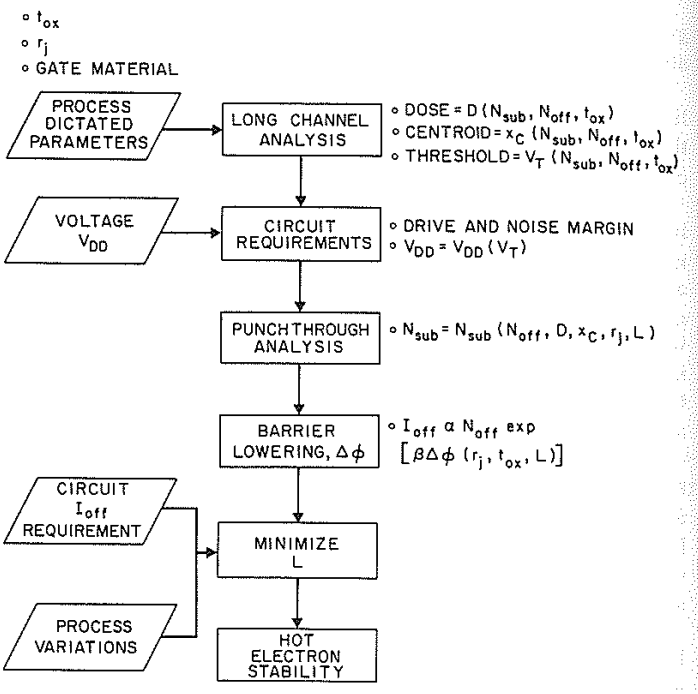


**Fig. 5-51** A flow chart of the $I_{OFF}$ strategy. From J.R. Brews, K.K. Ng, and R.K. Watts, Chap. 1, "The Submicrometer Silicon MOSFET," in *Submicron Integrated Circuits*, R.K. Watts, Ed.,Wiley-Interscience, New York, Copyright 1989, p. 24. Reprinted with permission.

## 5.8 SHORT-CHANNEL PMOS DEVICES IN CMOS

Early MOS ICs were built using PMOS technology, primarily because enhancement-mode MOSFETs with suitable $V_T$ values could only be fabricated as *p*-channel devices using aluminum or $n^+$-doped polysilicon gates and uniform lightly doped *n*-substrates. That is, at that time it was not possible to produce enhancement-mode *n*-channel MOSFETs using $n^+$-poly or Al gates on a uniform, lightly doped *p*-substrate because such structures exhibit a negative threshold voltage (see Fig. 3-20). However, with the advent of ion implantation it became possible to build NMOSFETs with positive $V_T$s by adjusting channel doping profiles. Thus, enhancement-mode and depletion-mode NMOSFETs could then be fabricated with little extra difficulty. Since *n*-channel transistors have greater drive current (and hence speed), NMOS naturally replaced PMOS as the dominant digital IC technology. During this era of NMOS dominance, interest in

$p$-channel MOSFETs languished. However, when CMOS arose to become the main technology for VLSI in the late 1980s, the need for enhancement-mode $p$-channel MOSFETs returned.

The fabrication of $p$-channel devices with short channels in CMOS, however, presents some unique problems which arise from having to build both NMOS and PMOS devices on the same chip. The problems revolve around the choice of a doping type for the polysilicon gate electrode and the impact that this choice has on the threshold voltage and other characteristics of PMOS devices.

### 5.8.1 PMOS Devices with $n^+$-Polysilicon Gates

To achieve high drive current it is necessary to make the threshold voltage of a MOSFET as close to 0V as possible (with the minimum value limited by noise margin and subthreshold-leakage considerations). When MOS IC technologies were initially being developed $V_T$ values with a magnitude of ~1V were acceptable. In early PMOS (and early $p$-well CMOS) it was relatively straightforward to build $p$-channel devices with $V_T$ = -1V since the doping in the $n$-substrates was in the range of 1-3x$10^{15}$ $cm^{-3}$. As seen in Fig. 3-20, $V_{Tp}$ of PMOS devices made on such substrates is -0.8V to -1.0V, which is well within the acceptable $V_T$ range.

However, in $n$-well CMOS (which was developed after $p$-well CMOS), as well as in twin-well CMOS, the situation changes. That is, in $n$-well CMOS the doping in the well is about 10x the doping in the substrate, making it at least 1x$10^{16}$ $cm^{-3}$. Twin-well CMOS becomes the well-architecture of choice as the gate lengths decrease below about 1 $\mu$m. For 1 $\mu$m MOS devices (both $p$- and $n$-channel) the substrate doping density must be 2-3x$10^{16}$ $cm^{-3}$. Thus, as shown in Fig. 3-20, the $V_T$ values of PMOS devices made with $n^+$-poly gates in either $n$-well or twin-well CMOS will be at least -1.5V, whose magnitude is too large. To make matters worse, in PMOSFETs with $L \leq 1$ $\mu$m, punchthrough effects are more severe than in comparably sized NMOSFETs (primarily due to the inability to make $p^+$ source/drain junctions as shallow as $n^+$ junctions, as will be described later). To suppress such punchthrough current it is necessary to increase the $n$-doping in the substrate (i.e., by an extra deep phosphorus implant into the channel of PMOS devices). The resultant increase in channel doping makes short-channel PMOS devices even more strongly enhancement mode (i.e., $V_T$ is increased even more).

For optimal logic-gate performance the threshold voltages of the $n$- and $p$-channel devices in CMOS circuits should also have comparable magnitudes. In addition, to allow for maximum current-driving capability, they should also be as small as possible. Thus, for 5V CMOS technologies, desirable threshold voltages are 0.6 to 0.8V for $V_{Tn}$ and -0.6 to -0.8V for $V_{Tp}$. Furthermore, as mentioned above, the most common choice for the gate material has historically been heavily doped $n$-type polysilicon. The work function of $n^+$ polysilicon is ideal for $n$-channel devices since these yield threshold voltages of less than 0.7 V for reasonable values of channel doping and oxide thicknesses.*

Figure 3-20 plots $V_T$ for long-channel, uniformly doped MOSFETs with $n^+$ poly gates (left scale)[70] as a function of $p$-substrate doping (assuming the substrate is uniformly doped and that $Q_{tot} = 0$). The value of $V_{Tn}$ is less than 1.0V for gate-oxide thicknesses of 25 nm or less and substrate dopings of less than $10^{17}$ $cm^{-3}$. Thus, $V_{Tn}$ can easily be adjusted to the desired values by implanting boron into the channel.

However, when $n^+$ poly is the gate electrode of a PMOS device, adjustment of $V_{Tp}$ to -0.7 V is not as simple, especially as the PMOS channel lengths shrink below about 2 $\mu$m. First, as we noted above, the magnitude of $V_T$ of PMOS devices when the substrate doping exceeds $2x10^{16}$ $cm^{-3}$ is significantly greater than -0.8V (e.g., -1.4V or larger). Even higher values of substrate doping will be needed as the channel lengths are decreased below 1 $\mu$m, implying that $V_T$ would be even larger in submicron PMOS devices with uniformly doped substrates. In addition, such short-channel PMOSFETs are more prone to punchthrough than NMOSFETs of the same channel length. This means that the substrate doping concentration will need to be increased even further in submicron PMOS devices to suppress these effects (e.g., by performing an additional deep $n$-type [phosphorus] implant into the channel region).

The increased susceptibility to punchthrough of scaled-down PMOS devices with uniformly doped channels is caused in part by the dopant used to form the source and drain regions of the PMOS device, i.e., boron. Boron diffuses much more quickly than the dopant used to form the source and drain junctions in NMOSFETs (arsenic). As a result, the junction depths of the $p^+$ regions in 1 $\mu$m PMOS are ~0.35 $\mu$m, whereas the $n^+$ regions in 1 $\mu$m NMOS are shallower (typically only ~0.2 $\mu$m deep). The deeper junctions accentuate the punchthrough susceptibility. The extra $n$-implant used to suppress punchthrough mentioned above must also place the additional doping at a depth below the source and drain depths to be effective (e.g., with a peak at ~0.15 $\mu$m and increased doping above the background level to a depth of ~0.5 $\mu$m). This extra implant, however, not only increases the $V_T$ value to about -2V, but also increases the source/drain-to-substrate capacitance.

In any case, it is obvious that the magnitude of $V_T$ in short-channel PMOS devices of advanced CMOS technologies needs to be reduced. However, implanting the $n$-doped substrate with more $n$-type dopant would only *increase* the magnitude of $V_{Tp}$, rather than bringing its value closer to the desired -0.7V. To reduce the magnitude of $V_{Tp}$ when an $n^+$ poly gate is used, a thin sheet of *negative* charges must therefore be placed at the Si-$SiO_2$ interface. This is accomplished by implanting a shallow layer of boron atoms, which as we know become negatively charged acceptor ions in the Si lattice. The boron dose must be heavy enough to overcompensate the $n$-surface so that a $p$-region (depleted of holes at $V_{GS} = 0V$) is formed. This shifts $V_{Tp}$ toward more positive values. In practice, the boron dose depends on the substrate doping, as shown

* Note that the polysilicon layer may be combined with a layer of silicide for sheet resistance reduction; since the polysilicon remains as the underlayer of the polycide, the work function of the gate electrode will not be changed.

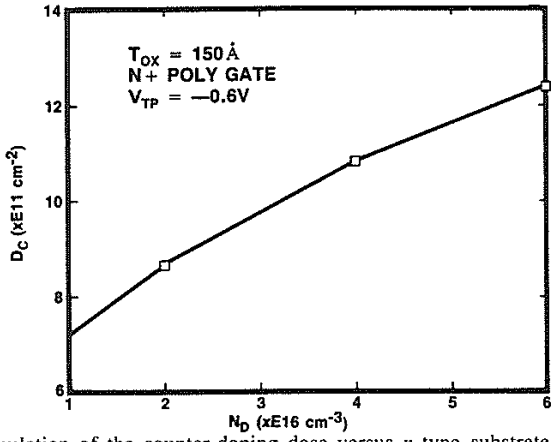


**Fig. 5-52** Simulation of the counter-doping dose versus $n$-type substrate concentration for a fixed $p$-channel threshold voltage of -0.6V.[115] (© 1984 IEEE).

in Fig. 5-52 for devices with $t_{OX}$ = 15 nm in which a $V_{Tp}$ = -0.6V is desired. Typical doses of such implanted layers are of the order of $5 \times 10^{11}$ cm$^{-2}$ at 25 keV.

The fact that boron is implanted to adjust both $V_{Tn}$ and $V_{Tp}$ in CMOS circuits with $n^+$ poly gates suggests that a single implant could be used instead of two separate implants. Figure 5-53 shows that this can be accomplished if the appropriate background dopings are chosen for the substrate and the well.[71] On the other hand, it may be decided to use two separate implants in order to achieve better short-channel behavior through individual optimization of the $n$- and $p$-channel devices. In the latter case, if the boron dose needed to adjust $V_{Tp}$ is smaller than the dose needed to adjust $V_{Tn}$, the former implant can be made into both the $p$- and $n$-channel regions without use of a mask. Then the second implant for adjusting $V_{Tn}$ is done with a mask that protects the $n$-well region. (A third boron implant may also be performed at that time to suppress punchthrough in the $n$-channel devices.) In other processes, however, it may be necessary to use a separate mask for both the $V_{Tp}$- and $V_{Tn}$-adjust implants.

## 5.8.2 Why PMOS Devices with $n^+$ Poly Gates and Implanted $p$-Surface Layers Exhibit Enhanced Susceptibility to Short-Channel Effects

The result of implanting boron atoms to adjust $V_T$ is that such PMOS devices exhibit worse short-channel effects than NMOSFETs with the same $L$. This susceptibility arises mainly because the implanted boron layer has a finite thickness (i.e., instead of being an infinitely-thin sheet of charge at the surface, as would exist in the ideal case). Figure 5-54 illustrates this fact, in which the channel doping profile of a PMOS device with such a boron implant is seen to extend well below the channel surface. The penetration of the $p$-layer into the $n$-substrate gives rise to two phenomena not observed

in surface-channel NMOSFETs: (1) a *pn* junction is formed beneath the gate oxide in the channel, extending to a depth $Y_j$ (as can also be seen in Fig. 5-54); and (2) the potential minimum is moved away from the surface. The latter effect gives rise to important device-behavior effects that differ from those of surface-channel MOSFETs. We explain this behavior by first comparing the location of the potential minimum in such boron-implanted-layer PMOSFETs to its location in surface-channel MOSFETs.

Figure 5-55 shows the one-dimensional potential diagrams of two PMOS devices, one with a $p^+$-polysilicon gate and a uniformly doped *n*-substrate ($3.4 \times 10^{16}$ cm$^{-3}$), and the other with a $n^+$-polysilicon gate and a shallow boron $V_T$-adjust implant. In both devices $V_{GS} = 0$V, and $V_{DS} = -5$V. The potential profile is taken at the point along the channel at which the longitudinal field vanishes (to match the fact that in a MOS-C there is also no longitudinal electric field). In the $p^+$-poly gate device the potential minimum is located at the surface, implying that such a device will operate much like the surface-channel NMOSFETs described in chap. 4. In the PMOS structure with the $n^+$-poly gate and boron $V_T$-adjust implant, however, we see that the potential minimum is away from the Si surface. The mobile carriers (holes) will thus be found at highest density near the location of the potential minimum. This implies that, unlike in the

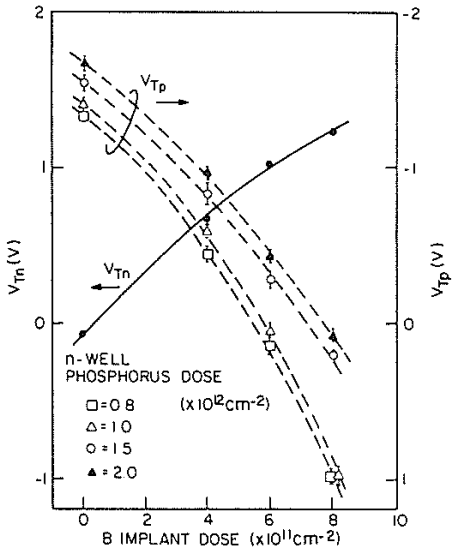


**Fig. 5-53** Threshold voltages of *n*-channel ($V_{Tn}$) and *p*-channel ($V_{Tp}$) transistors as a function of boron threshold-adjustment dose. The CMOS structure uses an *n*-well implanted into a *p*-substrate (whose doping level is $6 \times 10^{14}$ atoms/cm$^3$). $V_{Tp}$ results are shown for various implant doses of the *n*-well.[71] (© 1980 IEEE).

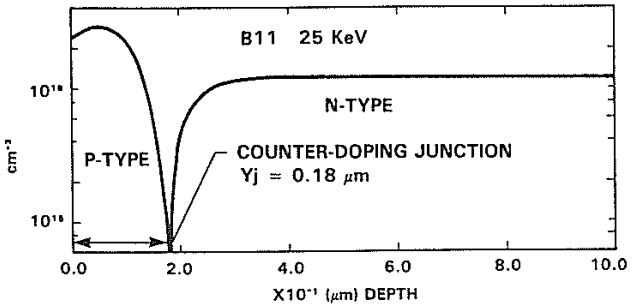


**Fig. 5-54** Simulated channel profile for a *p*-channel MOSFET with an implanted B dose at the channel surface.[115] (© 1984 IEEE).

case of conventional surface-channel devices, more current will flow in a channel *beneath* the surface of the device than at the surface.[72] Such PMOS devices are therefore referred to as *buried-channel* (BC) transistors. As also seen in Fig. 5-56 (which gives the calculated variation of the potential as a function of distance below the surface as the channel *pn* junction depth is varied), the potential minimum moves further into the substrate as the thickness of the implanted *p*-layer is increased. The mobility of carriers in the buried channel is ~15% higher than carriers at the surface, and thus BC MOSFETs exhibit a somewhat larger drive current than comparable surface channel FETs. While this is an advantage, it is outweighed by several other disadvantages exhibited by BC FETs. Let us examine how the presence of the channel junction and

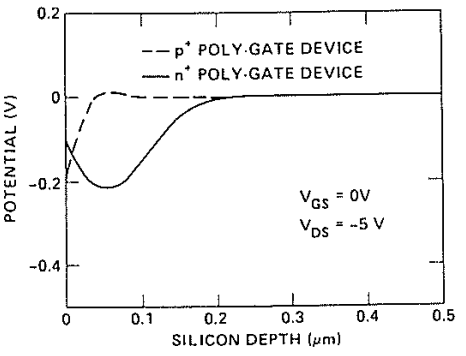


**Fig. 5-55** Simulations of the electrical potential perpendicular to the surface in the channel region of two long-channel PMOS devices using GEMINI and SUPREM III simulations of devices with $n^+$ polysilicon and $p^+$ polysilicon gates with effective gate lengths of 20 $\mu$m.[114] (© 1985 IEEE).

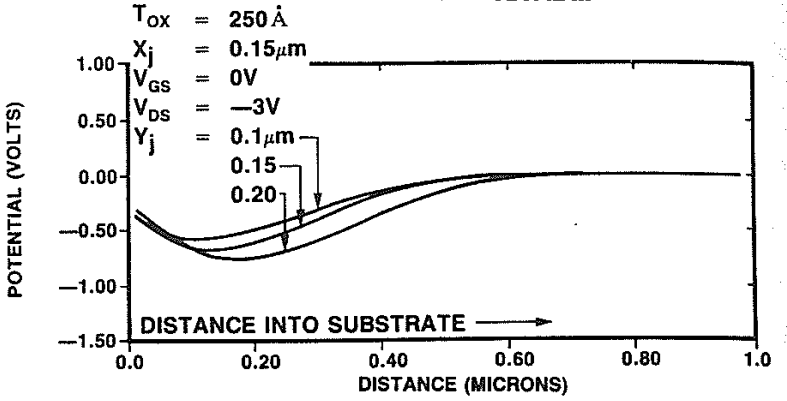


**Fig. 5-56** Channel potential profile versus vertical distance for a $p$-channel MOSFET with $Y_j$ = 0.1, 0.15, and 0.2 $\mu$m, and $V_{DS}$ = - 3V and $V_{GS}$ = 0V.[115] (© 1984 IEEE).

the shifting of the potential minimum beneath the Si surface worsen the susceptibility of the PMOS device to short-channel effects.

**5.8.2.1 Threshold-Voltage Roll-Off in Buried-Channel PMOS.** As the channel length of MOSFETs is decreased, the threshold voltage decreases from the value it exhibits in long-channel devices. This effect, as described in section 5.2.2, is referred to as *$V_T$-roll-off*. The $V_T$-roll-off effect is more severe in BC PMOS devices than in surface channel FETs (Fig. 5-57a).[114] This is due to an effect in BC FETs that does not occur in surface-channel FETs. That is, the implanted $p$-layer is a lightly doped $p$-region that extends entirely between the $p^+$ source and drain regions of the device. Holes diffuse from the regions of high concentration into the lightly doped layer as depicted in Fig. 5-57b.[106] The diffusion length $d_p$ is given by[107]

$$d_p = L_D \tan^{-1} [ (N_p^+/N_p^-)^{1/2}] \qquad (5 - 94)$$

where

$$L_D = [(2 \kappa_{si}\varepsilon_o kT)/(q^2 N_p^-)]^{1/2} \qquad (5 - 95)$$

and $N_p^+$ and $N_p^-$ are the doping levels in the $p^+$-source/drain and $p$-layer regions, respectively. If the diffusion length is smaller than half the channel length, the net effect of this hole diffusion is to increase the effective positive charge in the channel, thus making its threshold voltage smaller in magnitude. As the channel length is decreased, the proportionate contribution of the diffused mobile charge to the total channel charge increases, and as a result, the threshold is shifted to smaller values. Eventually, at short enough channel lengths, the diffused hole distribution from the source meets that from the drain.[108] When that occurs, the potential barrier between the source and drain is reduced, giving rise to poor subthreshold characteristics.

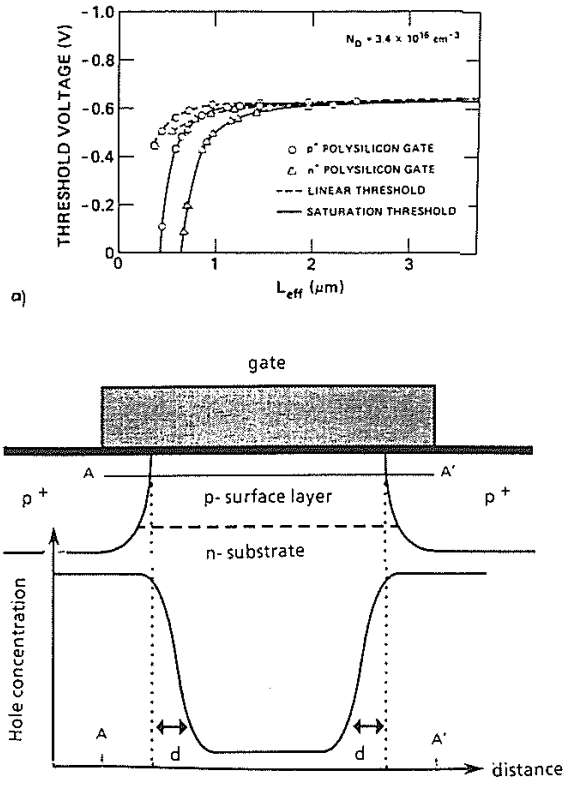


**Fig. 5-57** (a) Threshold voltage variation as a function of channel length $L_{eff}$ in surface-channel ($p^+$-poly gate) and buried-channel ($n^+$-poly gate) PMOSFETs.[114] (© 1985 IEEE). (b) The origin of short-channel threshold shifts in buried-channel PMOS transistors. From A.G. Lewis and J.Y. Chen, "Current Trends in MOS Process Integration," in N.G. Einspruch and G. Gildenblatt, Eds. *Advanced MOS Device Physics,* Academic Press, San Diego CA, 1989, p. 58. Reprinted with Permission.

Experimental values of $V_T$ in BC PMOS devices with a gate oxide thickness of 15 nm versus channel length are shown in Fig. 5-58a. As in Fig. 5-57a we see that the magnitude of $V_T$ decreases as $L$ is reduced. Simulation studies indicate that the severity of the $V_T$ roll-off is increased as $Y_j$ is made deeper (see Fig. 5-58b). This is due to the fact that more holes are able to diffuse into the thicker $p$-layer of the channel region from the source/drain regions as $Y_j$ is made deeper, accentuating the roll-off effect. As in surface channel devices, $V_T$ roll-off is decreased as $t_{ox}$ is made smaller (Fig. 5-58c). Thus, we conclude that smaller $Y_j$ and $t_{ox}$ values are needed to mitigate the $V_T$-roll-off effect in BC PMOS.

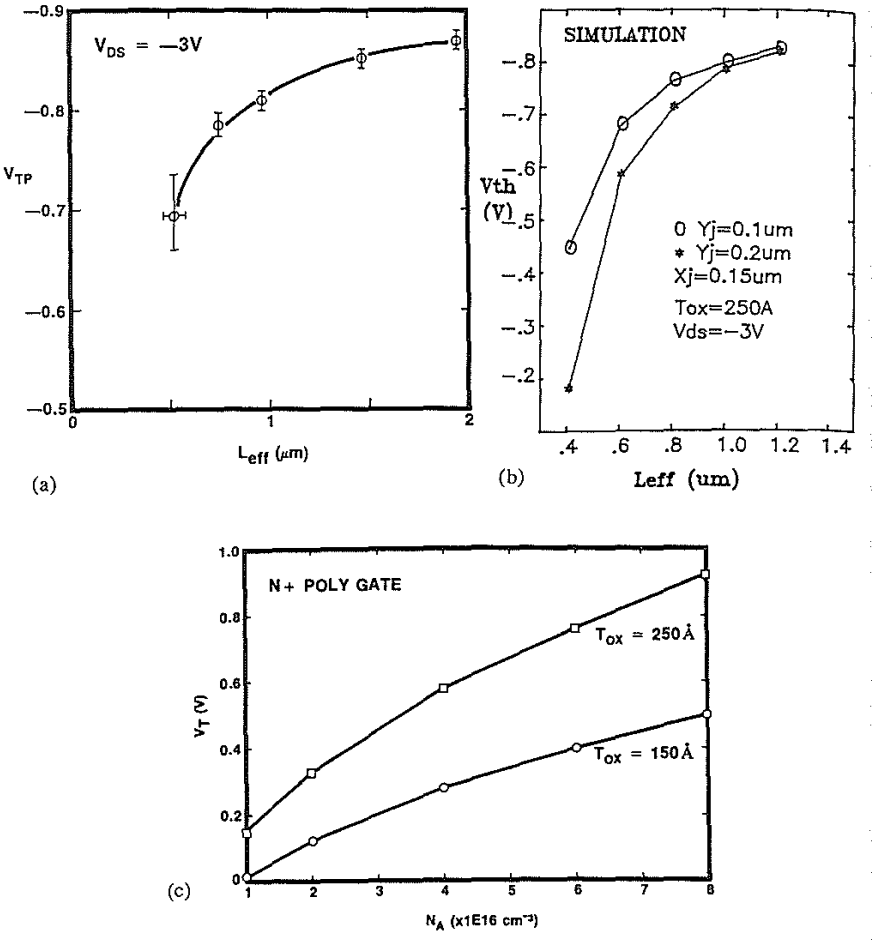


**Fig. 5-58** (a) Experimental data of $p$-channel threshold voltage versus $L_{eff}$ for gate oxide thickness of 15 nm. (b) Simulation of threshold voltage versus $L_{eff}$ for $p$-channel MOSFETs with different $Y_j$. (c) Simulated $p$-channel threshold voltage versus $L_{eff}$ for two different gate oxide thicknesses. From K. M. Cham, et al., *Computer Aided Design and VLSI Device Development*. p. 187-8, Copyright 1986 Kluwer Academic Publishers. Reprinted with permission.

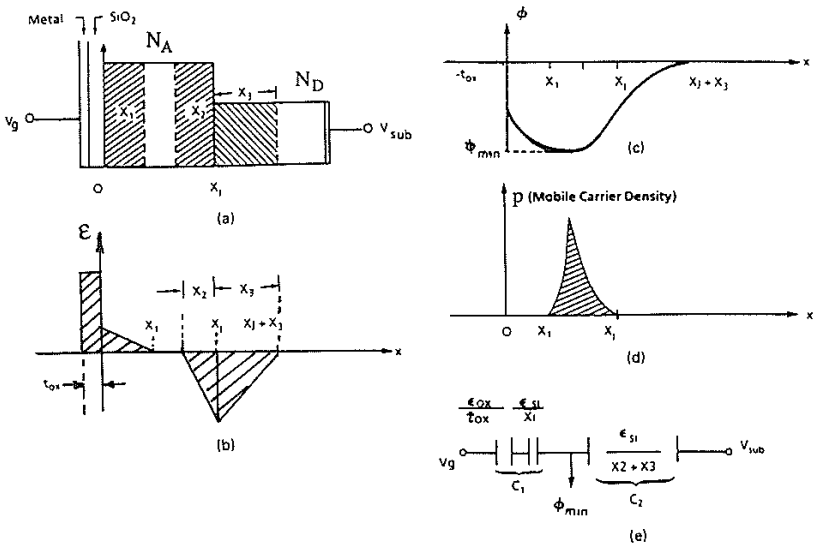


Fig. 5-59 Buried-channel PMOSFET when biased to inversion: (a) Doping profile and depletion regions; (b) electric field; (c) electron potential; (d) mobile carriers; and (e) equivalent capacitances in sub-pinchoff condition.[120] (© IEEE 1978).

**5.8.2.2 Subthreshold Swing ($S_t$) in Buried-Channel PMOS.** The PMOSFETs used in CMOS must be enhancement-mode devices; i.e., they need to be OFF when $V_{GS}$ = 0V. If such PMOSFETs are buried-channel devices, the entire implanted *p*-layer in the BC PMOS devices must be depleted of holes when $V_{GS}$ = 0V. On the other hand, upon applying a gate voltage equal to the threshold voltage, the *p*-layer of such devices is no longer depleted. That is, holes will have returned to the layer, forming a *p*-type conducting channel between the source and drain. But this channel will exist beneath instead of at the surface. Thus, for gate voltages greater than $V_T$, two depletion regions will be present in this *p*-layer; one that is formed between the surface and the buried channel (to a depth $x_1$) and the other due to the channel *pn* junction, as is shown in Fig. 5-59a. The BC MOSFETs thus have two capacitances in addition to the oxide capacitance $\kappa_{ox}\varepsilon_0/t_{ox}$; namely the depletion capacitance from the surface ($\kappa_{Si}\varepsilon_0/x_1$), and the depletion capacitance from the *pn* junction ($C_2 = \kappa_{Si}\varepsilon_0/[x_2 + x_3] \sim \kappa_{Si}\varepsilon_0/x_3$). The potential minimum is located in the position between these two capacitors, as shown in Fig. 5-59e. As also noted earlier, the location of the potential minimum causes most of the free carriers to appear in the bulk Si rather than at the Si-$SiO_2$ interface. It is expected that since the free carriers are now farther away from the surface they will be harder to modulate by the gate voltage. (In the same way that

carriers in a surface-channel MOSFET with a thicker gate oxide are harder to modulate - because of reduced gate-to-channel capacitive coupling - than in one with a thinner gate oxide.) Hence, to achieve the same degree of turn-off, the gate voltage will need to be reduced more than in the case of a surface-channel device. Thus, we expect that the turn-off characteristic will be less sharp, which means that $S_t$ will be larger.

Quantitatively the buried channel turn-off characteristic can be modeled by an expression that gives the subthreshold swing $S_t$ in a structure with two such depletion regions, i.e.,

$$S_t = 2.3\ (kT/q)\ (1 + C_2/C_1) \qquad (5 - 96)$$

$$= 2.3\ (kT/q)\ [1 + (\kappa_{ox}\varepsilon_o x_1 + \kappa_{si}\varepsilon_o t_{ox})/(\kappa_{ox}\varepsilon_o x_2 + \kappa_{ox}\varepsilon_o x_3)] \qquad (5 - 97)$$

where $C_1$ is the oxide capacitance ($C_{ox}$) in series with the depletion capacitance from the surface ($\kappa_{si}\varepsilon_o/x_1$), and $C_2$ is defined above. Let us compare Eq. 5-96 with Eq. 4-91 (which gives $S_t$ for the case of surface-channel MOSFETs, and is repeated here for convenience).

$$S_t = \ln 10(d\ln I_D/dV_{GS})^{-1} = 2.3\ (kT/q)\ (1 + C_d/C_{ox}) \qquad (5 - 98)$$

By noting that $C_1$ is smaller than $C_{ox}$, and $C_2$ is typically comparable in value to $C_d$, we see that $S_t$ is expected to be larger in BC devices. Experimental results confirm that $S_t$ is worse (i.e., larger) in buried channel devices, especially in short-channel PMOSFETs. That is, $S_t$ values in buried-channel PMOSFETs range from 0.5 to 1.5 V/decade, compared to the 70-120 mV/decade $S_t$ values observed in active NMOSFET devices. Figure 5-60 compares the subthreshold behavior of the two 0.8 $\mu$m BC PMOS

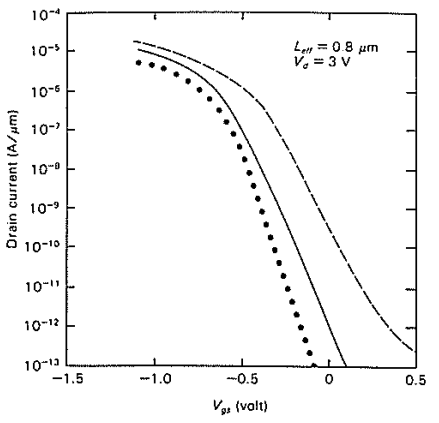


**Fig. 5-60** Subthreshold I-V curves in PMOS device in CMOS. Dashed lines: buried channel PMOS in a lightly doped substrate. Solid lines: buried-channel PMOS in a retrograde *n*-well. Dotted lines: surface channel NMOS drawn for comparison.[72] (© IEEE 1982).

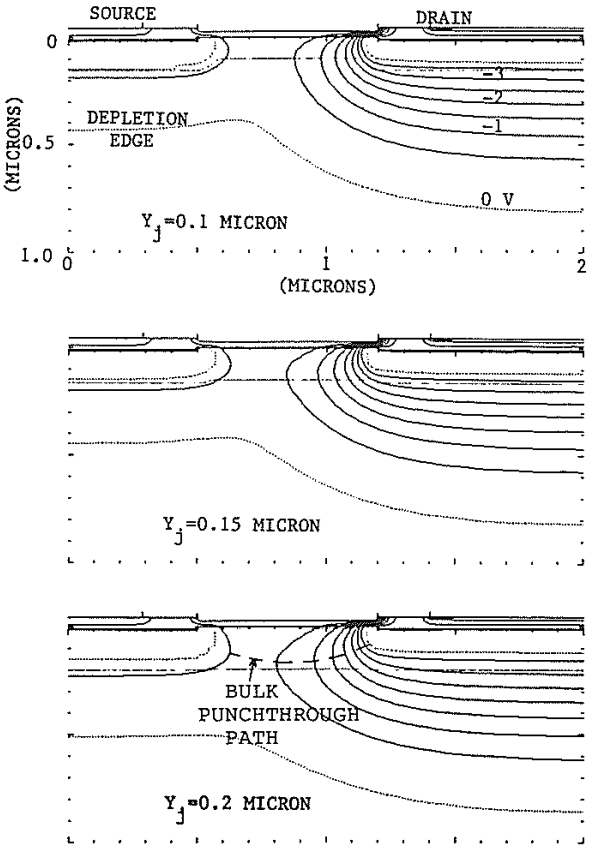


**Fig. 5-61** Simulated 2-D potential profile for *p*-channel MOSFET with $Y_j$ = 0.1, 0.15, and 0.2 $\mu$m. $V_{GS}$ = 0V and $V_{DS}$ = - 3V. [115] (© 1984 IEEE).

devices with that of a comparable surface-channel NMOSFET. (Note that the $V_{GS}$ scale for the NMOSFET should be +1.5V to -1.5V from left to right.) It indicates that $S_t$ is larger for the BC PMOS devices.

The effect on $S_t$ of the depths of the channel and source/drain junctions $Y_j$ and $r_j$, respectively, and of the gate-oxide thickness $t_{ox}$ has also been investigated with simulation studies. Figure 5-61 illustrates the 2-D simulated potential profiles for a 0.5 $\mu$m *p*-channel MOSFET as $Y_j$ is increased from 0.1 to 0.2 $\mu$m. It is observed that as $Y_j$ is increased the potential contours spread more from drain to source, and the bulk punchthrough path passes through the depletion region near the *pn* junction. Figure 5-62 shows the calculated values of $S_t$ for three $Y_j$ values (i.e., 0.1, 0.15, and 0.2 $\mu$m), as $r_j$ is varied in a BC PMOS device with an $L_{eff}$ = 0.5 $\mu$m, a $t_{ox}$ = 25 nm,

bulk punchthrough path passes through the depletion region near the *pn* junction. Figure 5-62 shows the calculated values of $S_t$ for three $Y_j$ values (i.e., 0.1, 0.15, and 0.2 $\mu$m), as $r_j$ is varied in a BC PMOS device with an $L_{eff}$ = 0.5 $\mu$m, a $t_{ox}$ = 25 nm, and $V_{DS}$ = -3V. Each curve corresponds to a fixed value of $Y_j$. The threshold voltage [defined as the gate voltage at which the drain current is 100 nA*(Z/*L*)] is specified at each point. The data shows that $S_t$ is strongly dependent on $Y_j$ and $r_j$. That is, as $Y_j$ is increased for a fixed value of $r_j$, $S_t$ increases. For a fixed value of $Y_j$, $S_t$ also increases as $r_j$ is increased. In Fig. 5-63 the simulated value of $S_t$ for two different gate oxide thicknesses is shown as $Y_j$ is varied. It is seen that $S_t$ improves for thinner gate oxides, but the dependence of $S_t$ on $Y_j$ is only slightly reduced. The overall conclusion from these studies is that small values of $Y_j$, $r_j$, and $t_{ox}$ are also needed to realize small values of $S_t$ in submicron BC PMOS devices.

### 5.8.2.3 Punchthrough Susceptibility of Buried-Channel PMOS.

The larger $S_t$ values exhibited by BC PMOS devices implies that they are susceptible to larger leakage currents in the OFF state. In fact, such relatively large leakage currents are commonly observed in short PMOSFETs, especially at high drain bias. For example, it has been shown that in submicron PMOS transistors ($L_{eff}$ = 0.8 $\mu$m), $I_{Dst}$ will increase by two orders of magnitude if $V_{DS}$ is increased from -1V to -10V.[74] In this case, if $I_{Dst}$ was 1 nA at -1V, it would increase to 0.1 $\mu$A if $V_{DS}$ was raised to -10V. It would be useful to be able to predict the value of $I_{Dst}$ prior to fabricating the device.

As described in section 5.3.1 an increase in $S_t$ has been correlated to the onset of subsurface punchthrough in surface-channel MOSFETs. The increase in $S_t$ in BC PMOS devices as a result of various device parameters (i.e., $L$, $Y_j$, $r_j$) discussed in the previous section can also be considered from the perspective of the phenomenon of punchthrough (subsurface-DIBL), which was introduced in section 5.3. However, we will see that the subthreshold leakage behavior in BC PMOSFETs differs from that observed in surface-channel FETs. To help explain this difference, we will once again

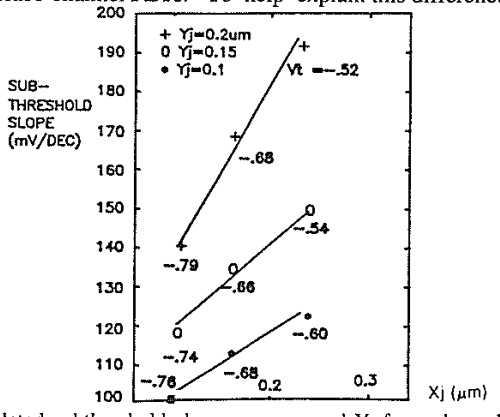


**Fig. 5-62** Simulated subthreshold slope versus $r_j$ and $Y_j$ for *p*-channel MOSFETs in which $L_{eff}$ = 0.5 $\mu$m, $t_{ox}$ = 250Å, and $V_{DS}$ = -3V. $V_T$ is the threshold voltage.[115] (© 1984 IEEE).

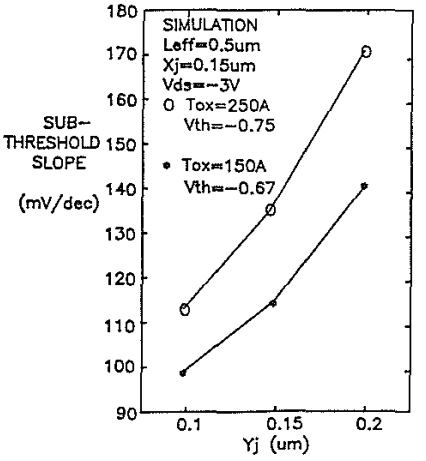


**Fig. 5-63** Simulated subthreshold slope versus $Y_j$ and $t_{ox}$.[115] (© 1984 IEEE).

employ the punchthrough modeling technique described in section 5.3.2, but here it will be applied to quantitatively model $I_{Dst}$ in BC PMOSFETs. The results of this analysis will permit us to compare the subthreshold leakage behavior of surface-channel and buried channel MOSFETs.

We recall that punchthrough current is determined by carrier injection over the potential energy barrier at the saddle point of the electrostatic potential in the bulk (see Fig. 5-64).[117] Therefore, analysis of the channel potential, especially the change of the potential at the saddle point P of the BC PMOS device with $V_{DS}$ is necessary. This analysis can be performed with the aid of 2-D device simulators,** and here we present the results of one report that performed such a study using the device simulator GEMINI.[74] The simulated potential along the direction from source to drain of a BC PMOSFET in an *n*-well with $L_{eff} = 0.55\ \mu m$ as $V_{DS}$ is increased is shown in Fig. 5-65. It is observed that the magnitude of $\varphi^*$ (the potential at the saddle point P), begins to drop as soon as $V_{DS}$ is increased above 0V. This is due to the fact that there is no *pn* junction along the channel region in a *p*-channel BC MOSFET. (Conversely, in the case of short, surface-channel MOSFETs, at low drain-bias values the $V_{DS}$ drop occurs almost entirely across the drain-channel junction, and the barrier at the source does not decrease as long as $V_{DS}$ remains small. Only when $V_{DS}$ becomes large enough to cause subsurface-DIBL does the barrier begin to drop as $V_{DS}$ exceeds this value.) The decrease of the potential barrier height ($\varphi^* - V_S$) in a BC PMOSFET as $V_{DS}$ is increased is plotted in Fig. 5-66. Here we see that ($\varphi^* - V_S$) is linearly proportional to the increase in drain voltage, even at low values of $V_{DS}$.

** Note that an entirely analytic model of punchthrough in PMOSFETs has also been published by Skotnicki et al.[117]

Once ($\varphi^* - V_S$) is found for a given value of $V_{DS}$, it can be used to calculate $I_{Dst}$ with the aid of an analytic expression (Eq. 5-18b) as discussed in section 5.3. This expression for $I_{Dst}$ is repeated here for the case of a PMOS device:

$$I_{Dst} = -q\, D_p\, Z \frac{t^*}{L^*} \frac{n_i^2}{N_D} \exp\left[\frac{q}{kT}(V_S - \varphi^*)\right] \qquad (5 - 99)$$

To exploit the results plotted in Fig. 5-66, we express Eq. 5-99 in logarithmic form as

$$\log (I_{Dst}) = \{\log [-q\, D_p\, Z\, (t^*/L^*)\, (n_i^2/N_D)]\} - q(\varphi^* - V_S)/k \qquad (5 - 100)$$

or

$$\log (I_{Dst}) = A - q\varphi_b/kT \qquad (5 - 101)$$

where $A = \log [-q\, D_p\, Z\, (t^*/L^*)\, (n_i^2/N_A)]$, and $\varphi_b = (\varphi^* - V_S)$. Now, Fig. 5-66 shows that the decrease in $\varphi_b$ is linearly proportional to $V_{DS}$, i.e.,

$$\varphi_b = (\varphi_{bo} - b\,|V_{DS}|) \qquad (5 - 102)$$

where $\varphi_{bo}$ is the barrier height at $V_{DS} = 0V$, and $b$ represents the slope of the curve of Fig. 5-66 (i.e., $d\varphi_b/dV_{DS}$). We also note that the values of both $\varphi_{bo}$ and $b$ can be determined from Fig. 5-66. Then we can write Eq. 5-101 as

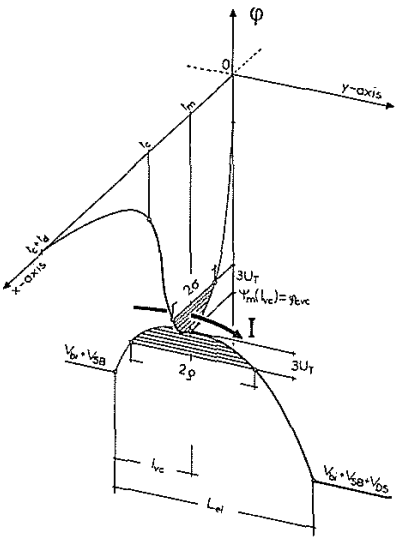


**Fig. 5-64** Perspective view of the electrical potential distribution in two perpendicular cross sections of the channel of a buried-channel PMOSFET. Shadowed regions are those corresponding to t* and $L^*$ in Eq. 5-99.[117] (© 1989 IEEE).

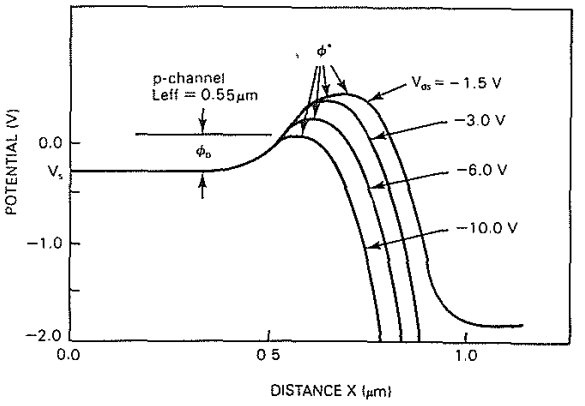


**Fig. 5-65** Simulated potential distributions along the buried channel of a PMOSFET for various drain voltages.[74] (© 1988 IEEE).

$$\log (I_{Dst}) = A - q(\varphi_{bo} - b\,|V_{DS}|)/kT \qquad (5 - 103)$$

or

$$= A' + V_{DS}/R \qquad (5 - 104)$$

where $A' = A - q\varphi_{bo}/kT$ and $R = kT/bq$. The parameter $R$ is the incremental voltage that the drain can sustain before $I_{Dst}$ increases by another order of magnitude ($R = \partial V_{DS}/\partial \log I_{Dst}$). The larger the value of $R$, the lower the DIBL rate, hence the better the MOSFET is able to maintain low subthreshold leakage as the drain bias rises.

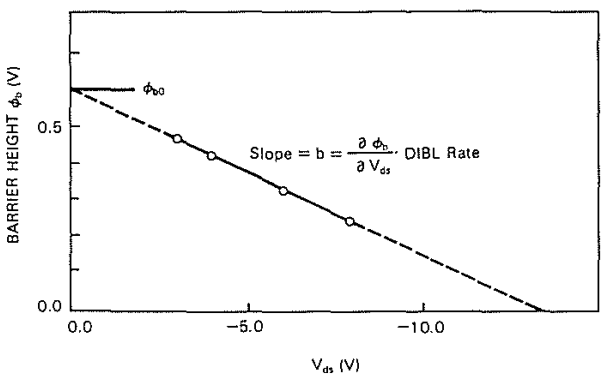


**Fig. 5-66** Potential barrier height as a function of drain voltage.[74] (© 1988 IEEE).

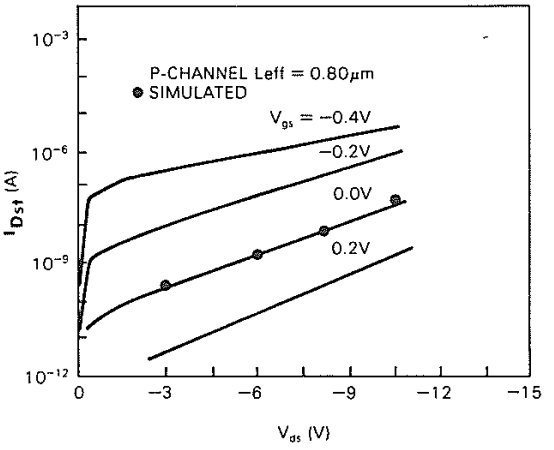


**Fig. 5-67** Subthreshold $I_{Dst}$-$V_{DS}$ characteristics for a submicron PMOSFET.[74] (© 1988 IEEE).

Equation 5-104 implies that the relationship between log $I_{Dst}$ and $V_{DS}$ should be linear in BC PMOSFETs operating in subthreshold. Figure 5-67 shows the measured log $I_{Dst}$-$V_{DS}$ curves for a 0.8 $\mu$m BC PMOSFET, together with some simulated $I_{Dst}$ values at $V_{GS}$ = 0V. The agreement between the experimental and simulated data is good. We also see that $R$ in this device is about -4.4V/decade for $V_{GS}$ = 0V. This means that if $I_{Dst}$ is 10 pA at $V_{DS}$ = -1V, it will increase to 10 nA at $V_{DS}$ = -10V.

Now we can compare the $I_{Dst}$ behavior of SC and BC MOSFETs with respect externally applied biases. We note that in the case of surface channel MOSFETs two regions of different slope are observed in the log $I_{Dst}$ versus $V_{DS}$ curves (see Fig. 5-11). At low values of $V_{DS}$ the value of $R$ is large (e.g., in Fig. 5-11b $R$ = 12.6V/decade when $V_{DS}$ <6.0V), but when $V_{DS}$ exceeds about 8.0V, the value of $R$ drops to about 1.0V/decade. This change implies that in surface-channel MOSFETs there is a transfer from surface-DIBL to subsurface-DIBL (punchthrough) - e.g., in the device of Fig. 5-11b at about 6.0V. Also, up to some value of $V_{DS}$ (e.g., $V_{PT}$), the drain bias has little effect on $I_{Dst}$. In BC PMOSFETs, however, the value of $R$ is relatively constant (e.g., it has a magnitude of $R$ = 4.4V/decade for all values of $V_{DS}$ in the case of the device characterized in Fig. 5-67). This implies that the nature of subthreshold leakage current in BC PMOSFETs does *not* undergo a change from surface- to subsurface-DIBL, but instead the DIBL phenomenon in a BC device is a combination of both effects. Furthermore, the intermediate value of $R$ also supports the view that *both* the gate and the drain voltages affect the potential of the $p$-type layer, and thus both can impact $I_{Dst}$ at all values. Finally, this indicates that the measured slope of log $I_{Dst}$ versus $V_{DS}$ (defined as $1/R$), reflects the effect of $V_{DS}$ on $\varphi_b$ through DIBL, and permits a comparison of the subthreshold leakage behavior of various PMOS device structures.

### 5.8.3 Techniques Used to Suppress Short-Channel Effects in Buried-Channel PMOS

**5.8.3.1 Techniques Used to Keep the Implanted *p*-Layer as Thin as Possible.** The most obvious solution to suppressing short-channel effects in PMOS devices is to increase the PMOS device channel length. This is done in many CMOS technologies, and it is the reason that the minimum channel lengths of PMOS devices are often larger than those of the NMOS devices on the same chip. But we also noted that to achieve small values of $S_t$, less $V_T$-roll-off, and larger punchthrough voltages in BC PMOS devices, the *p*-buried layer depth $Y_j$ must be as shallow as possible. That is, the thinner the *p*-layer, the more the device resembles a surface channel FET. Several methods have been reported to realize shallow *p*-layer implant profiles, including the following:

1. Using the lowest practical implant energy, which in ordinary medium-current implanters is typically 20-25 keV.
2. Implanting $BF_2^+$ (which produces shallower boron layers than implantation with elemental boron, see Vol. 1, chap. 9).
3. Using a high-energy *n*-implant (e.g., $P^+$ at 400 keV) to form a retrograde *n*-well in the regions where the PMOS devices are formed. This places more *n*-type dopant atoms beneath the channel *pn* junctions, and the more heavily doped regions absorb the drain voltage in a shorter distance, while simultaneously squeezing the channel *pn* junction toward the surface, as shown in Fig. 5-68.

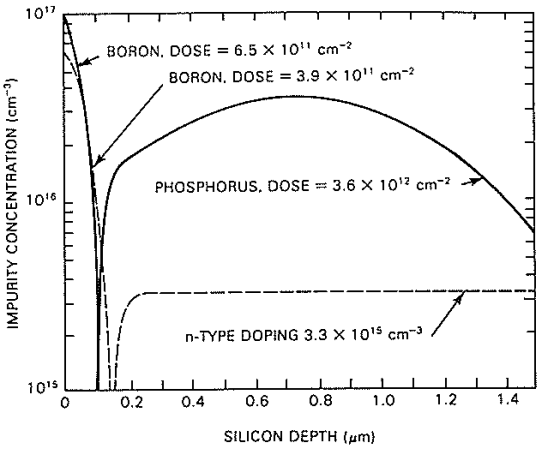


**Fig. 5-68** Simulated doping profiles in PMOS channel regions: dashed lines lightly doped substrate; solid lines, retrograde *n*-well.[72] (© 1982 IEEE).

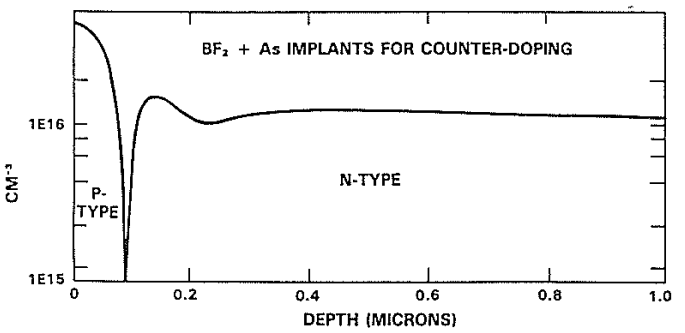


**Fig. 5-69** (a) Simulated channel profile for $p$-channel with $BF_2$ and As counterdoping.[115] (© 1984 IEEE).

4. An extra $n$-type implant (typically arsenic) can be performed into a conventional $n$-well or $n$-substrate, with it's peak located below the $p$-layer immediately following the $BF_2^+$ implant (Fig. 5-69a). The $n$-doping under the $p$-layer is thus raised, making the junction depth lie further up the tail of the boron distribution (and thereby making it shallower). The arsenic diffuses relatively slowly, and thus will largely remain in the vicinity of where it was implanted. This forms a steep profile at the counter-doping junction, and maintains a shallow junction depth. The simulation shown in Fig. 5-69a indicates that $Y_j$ with such an arsenic implant is ~0.09 $\mu$m. Such an extra implant can also be used with a retrograde $n$-well.

Two drawbacks of this technique are that since the boron channel implant is compensated by an arsenic implant very good process control must be maintained for it to be successful, and it also requires an extra masking step to prevent the arsenic implant from entering the $n$-channel transistor regions.

To prevent a shallow implanted-boron layer from growing thicker, it is necessary to use a reduced thermal budget in order to restrict boron diffusion following the implant. Specific steps for restricting boron redistribution include the following:[76]

1. Implanting the boron through the gate oxide. This avoids the oxidation-enhanced diffusion of boron that would occur during the growth of the gate oxide if the implant were performed first. In this case, it is necessary to prevent the gate oxide from becoming contaminated during implant, either by material sputtered by the beam line or by vaporized resist material used as a mask against the implant. To prevent such contamination, a thin layer of polysilicon may be

deposited on the gate oxide prior to the implant (in fact, immediately after the oxide is grown).[77]

2. After the implant has been performed, the remainder of the polysilicon film is deposited. In order to avoid the 900°C thermal cycle that would have to be used if the poly were doped following deposition, this polysilicon is doped *in situ* at ~600°C with phosphorus.

3. A BPSG glass layer is used as the dielectric between the gate and the first level of metal. A significantly lower temperature can be used to flow BPSG than PSG (e.g., 900°C versus 1000°C). A lower temperature cycle can thus be used to smooth the surface topography (flow step) and gently taper the contact holes after etch (reflow step).

**5.8.3.2 Shallow $p^+$ Source/Drain Junctions to Suppress Punchthrough in PMOSFETs.** As noted in our discussion of MOSFET scaling in section 5.6.1.2, reducing the source/drain junction depths also decreases the susceptibility to short-channel effects. By reducing the vertical depth of the source/drain junctions the lateral spread of the dopants in these regions beneath the gate also becomes smaller. Hence, a longer effective channel length is possible for a fixed drawn gate length. In addition, the lateral spread of source and drain depletion regions below the surface layer makes a MOSFET more prone to punchthrough. Consequently, shallow source and drains effectively suppress subsurface punchthrough paths.

In NMOSFETs, it is easier to fabricate shallow $n^+$ source/drain regions (i.e., $\leq 0.2$ $\mu$m in depth) because dopants with heavy ionic masses (usually arsenic) are implanted to form these regions. They yield implant profiles with small projected ranges and little channeling. Furthermore arsenic has a low diffusivity, so that little redistribution occurs during postimplant annealing. In PMOSFETs, however, the only practical $p$-type dopant for forming the $p^+$ regions is boron, and junctions formed with boron are much deeper than those formed with arsenic for several reasons. First, the projected range of the low-mass boron is relatively larger, even at low implantation energies. Ion channeling also causes the implanted boron profile to have a long tail, even if the target wafers are tilted to minimize this effect. Thus, the minimum junction depth which results when boron is implanted into a lightly doped $n$-type crystalline silicon wafer is about 0.35 $\mu$m.

The high diffusivity of boron compounds the problem. That is, in CMOS processes both the $n$- and $p$-implants that form the NMOS and PMOS source and drain regions, respectively, must be annealed. The anneal used for the arsenic implant will cause significant (>0.1 $\mu$m) redistribution of the boron implant. In CMOS technologies with channel lengths of 2 $\mu$m or longer, this issue does not arise because the boron can be implanted after the arsenic implantation and anneal steps (i.e., allowing the boron to be annealed only for the minimum time and temperature needed for full activation). Thus, boron redistribution after implantation can be minimized. However, in submicron CMOS processes it is generally not possible to perform the boron implant after the $n^+$ arsenic implant. This is because submicron NMOS devices usually use LDD structures,

in which the arsenic implant is performed after spacers have been formed. The boron $p^+$ implant, however, must be carried out before the spacers are formed for two reasons. First, this ensures that the boron implant sufficiently counterdopes the $n^-$ implant (used to form the LDD tip region) everywhere in the areas of the PMOS source and drain (i.e., the $n^-$ implant is typically done unmasked to maintain process simplicity). Second, this also guarantees that the $p^+$ doping will extend under the gate. Thus, in CMOS processes that use LDDs in the NMOS devices the $p^+$ regions must experience the same anneal cycle as the $n^+$ regions. Alternative approaches have been proposed to avoid subjecting the implanted boron to the $n^+$ anneal, as will be described below.

Techniques to decrease the $p^+$ junction depths fall into two groups: (1) those which set out to reduce the junction depth of the implanted boron profile; and (2) those which attempt to reduce the diffusion of the boron during the post-implantation anneals.

The approaches mentioned earlier when discussing techniques to reduce the depth of the as-implanted boron region in the channel of PMOS devices also apply to reducing the source/drain junction depths. These include use of $BF_2^+$ instead of atomic boron as the implant species, and implanting through a screen oxide. Pre-amorphizing the wafer surface region into which the junction dopants will be implanted to a depth of several tenths of a micron (with an earlier implant of silicon or germanium) has also been investigated (see Vol. 2, chap. 3). The amorphous layer effectively prevents channeling, and subsequent annealing at a low temperature is sufficient to achieve recrystallization by solid-phase epitaxy. Use of very-low-energy ion implanters (<5 keV) for implanting the boron has also been studied, as have techniques for implanting the boron into silicide layers formed above the source/drain regions and then diffusing the boron into the substrate from these silicide layers.

Several techniques to limit the redistribution of boron after implant have also been suggested. The first involves use of rapid thermal processing instead of a conventional furnace treatment following the implant. Relatively high temperatures are employed to realize adequate dopant activation, while keeping the times short enough so that boron redistribution is minimized. The second makes use of lower temperature flow and reflow steps by employing BPSG as the interlevel dielectric material instead of PSG. The third modifies the process sequence so that the boron implant is done after the arsenic implant. If the spacers required for NMOS LDD formation are in place, the boron implant must be sufficiently redistributed to ensure that the $p$-regions extend under the $p$-channel gates.[105] On the other hand, some process sequences have been reported in which the spacers are removed prior to implanting the boron. Other materials than $SiO_2$ must be used for such removable spacers (e.g., silicon nitride,[102] TiN,[103] or polysilicon[104]) since removing $SiO_2$ spacers would significantly thin the field oxide. Concerns about damaging the gate oxide at the gate edge have been raised if dry etching is used for such spacer removal. In the reports describing silicon nitride and TiN removable spacers, wet etching is used to remove them.

**5.8.3.3 LDD Structures in PMOS to Limit Punchthrough.** Another way to achieve a shallow junction in a PMOS device is to use an LDD structure. The junction depth of the lightly-doped LDD tip region is shallower than the heavily doped

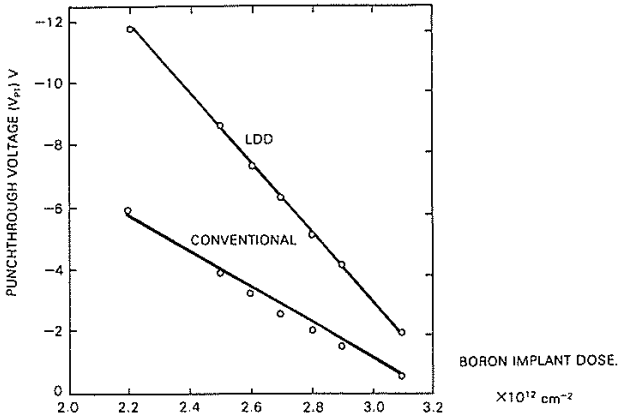


**Fig. 5-70** Punchthrough voltage as a function of boron implant dose for a 0.4 $\mu$m PMOSFET with and without LDD structure.[75] (© 1986 IEEE).

$p^+$ source/drain junction depth implanted at the same energy. Figure 5-70 indicates that the punchthrough voltage $V_{PT}$ is increased by 2-3V when an LDD is incorporated into a PMOS device. (The LDD structure, of course, may also be used to increase the hot-carrier resistance of the PMOS devices, especially as the channel length is decreased below about 0.8 $\mu$m.) The LDD, however, will generally reduce $I_D$ due to a rise in the series resistance of the drain region. Thus, a tradeoff analysis between an increase in $V_{PT}$ and a decrease in the drain current must be made.

Adding an LDD structure to a PMOS device in CMOS involves relatively straightforward changes to the process sequence. The gate sidewall spacers are already available from the creation of NMOS LDDs, but there is some increase in process complexity, (especially if the former process used a maskless $n^-$ implant to form the tip regions of the NMOS LDD). That is, to form both PMOS and NMOS LDDs four masking steps are generally needed ($n^-$, $p^-$, $n^+$, $p^+$), rather than just two. However, a two-mask process, which employs removable polysilicon spacers, has also been reported.[104]

**5.8.3.4 New PMOS Device Structures Designed to Suppress Punchthrough.** New PMOS device structures have also been proposed to minimize punchthrough current. For example, a small segment of an $n$-type region can be created by ion implantation between the $p$-type S/D and the channel as a punchthrough stopper (refer to Fig. 5-71). This structure has been termed a double-implanted or *halo structure*. One report of such a halo device with $L = 0.5$ $\mu$m used a phosphorus implant dose of $1 \times 10^{12}$ cm$^{-2}$ at 130 keV.[78] A sidewall spacer was used to form the lateral offset of the $n$-type region in this device. However, since the $p^+$ source/drain is offset from the gate by the sidewall spacer, this method of forming the local $n$-regions degrades the drive current and impairs hot-electron immunity.[79] Furthermore, as this technique also places a highly doped $n$-region adjacent to a highly doped $p$-region, the maximum halo doping

is determined by the onset of low-level avalanche at the chosen supply voltage and channel length.

A large-tilt-angle implant can be used to fabricate halo-type structures without a sidewall spacer, thereby gaining the benefits while avoiding the problems of the structure of Fig. 5-71.[79] The dopant is placed precisely between the $p^+$ source and the buried $p$-channel junction. The lateral penetration and depth of the $n$-type region are controlled by the implant energy and tilt-angle. The peak concentration is set by the dose. A typical implant sequence to form such a *large-angle tilt implanted punchthrough stopper* (LATIPS) structure as shown in Fig. 5-72 is: (1) implant phosphorus at 90 keV with a dose of $2x10^{13}$ $cm^{-2}$ at 25° tilt, in two segments, with the target rotated 180° between segments; then (2) implant $BF_2^+$ (source/drain) at 40 keV (no tilt) to a dose of $3x10^{15}$ $cm^{-2}$.[80]

Devices fabricated using the LATIPS process were compared to conventional PMOSFETs. LATIPS devices showed dramatically improved punchthrough characteristics for physical gate lengths as small as 0.5 microns. As an example, the OFF-state leakage current was eight orders of magnitude smaller (at -3V drain bias) than that of a conventional control device fabricated without the LATIPS structure. This dramatic improvement in punchthrough resistance was achieved without extreme scaling of the source/drain junction depth or the $n$-well background doping. That is, the $p^+$ source/drain junction depth was about 0.2 $\mu$m and the $n$-well concentration was $1x10^{16}$ $cm^{-3}$. Furthermore, the benefits were obtained without significant degradation of device performance. That is, no gate-oxide degradation was observed as a result of using $BF_2^+$ source/drain implants at 8 keV, even at doses of $5x10^{15}$ $cm^{-2}$. Better high-current drive capability than conventional devices was also exhibited, as well as a smaller body (back-gate bias) effect.

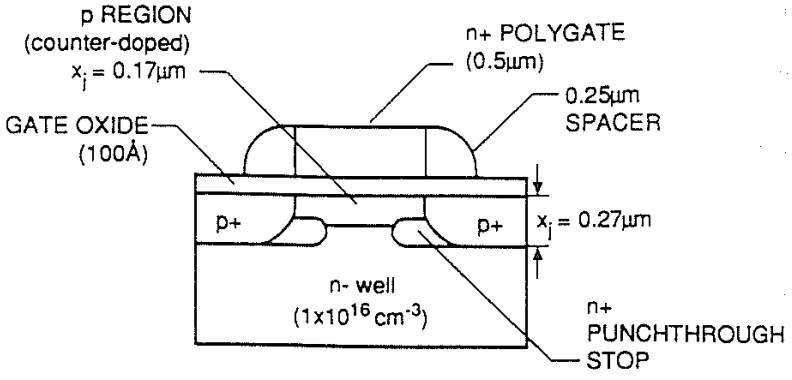


**Fig. 5-71** PMOS Punchthrough-stop structure.[78] (© 1985 IEEE).

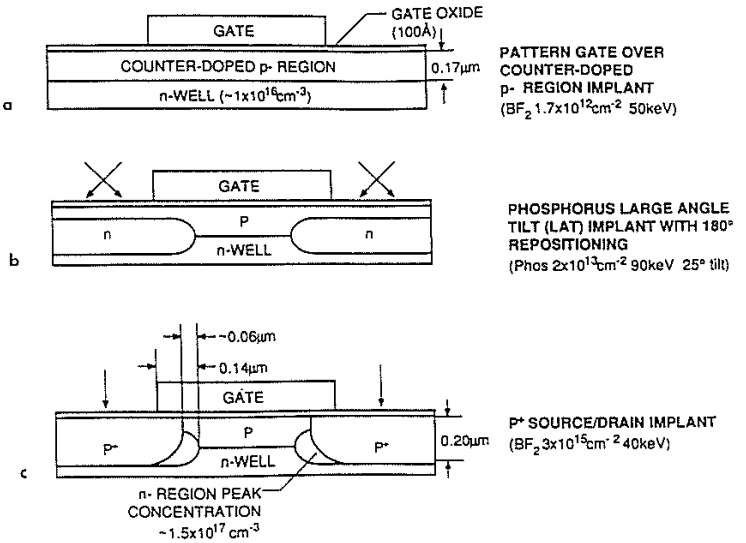


Fig. 5-72 LATIPS process sequence for PMOSFET: (a) Pattern gate over an $n$-well region that has been conterdoped with a $p$-type implant ($BF_2$); (b) Large angle tilt implant with phosphorus; (c) $p^+$ Source/Drain implant ($BF_2$).[79] (© 1988 IEEE).

## 5.8.4 PMOS Devices with $p^+$-Polysilicon Gates

The use of a boron implant to adjust $V_{Tp}$ becomes less feasible as devices use even thinner gate oxides, since larger doses of boron are needed. $Y_j$ thus becomes deeper, and the punchthrough problem worsens. In addition, buried channel devices are subject to more process variability stemming from the difficulty of controlling the compensating implant. Solutions involving the use of gate electrodes other than $n^+$ polysilicon must therefore be explored. One alternative is to use $p^+$ polysilicon for PMOS devices. This approach appears to become necessary for CMOS and BiCMOS once $L$ becomes smaller than 0.5 $\mu$m.

When $p^+$ polysilicon is used for the gate material, $V_{Tp}$ is shifted from the values that occur when $n^+$ polysilicon is used. Figure 3-20 also plots $V_{Tp}$ as a function of substrate doping when $p^+$ polysilicon is employed (using the scale on the right side of the figure). $V_{Tp}$ can be seen to be less negative than -0.7 V over the substrate doping range of $10^{15}$-$10^{17}$ cm$^{-3}$. Thus, $V_{Tp}$ can easily be made more negative through the implantation of phosphorus or arsenic into the channel. If $p^+$ polysilicon is used throughout the circuit, however, the NMOS device then has to be overcompensated in order for $V_{Tn}$ to be reduced to sufficiently small values. (Note that some reports have been published on the use of $p^+$ polysilicon alone.[81,82]) This implies it would be ideal

to use both $n^+$ and $p^+$ poly gates on the same chip (with $n^+$ poly for NMOS devices, and $p^+$ poly for PMOS devices).[83]

Such a dual-doped poly approach, however, adds process complexity, and also introduces other problems. One drawback of is that the sheet resistance of $p^+$ poly is ~3x higher than that of an $n^+$ poly film of the same thickness, because the mobility of holes is ~3x smaller than that of electrons in Si. A second problem arises from the need to connect the two types of poly (e.g., at the input of an inverter). Such problems occur when a silicide overlayer (or strap) is used to make the connection between $n^+$ and $p^+$ poly (as a method to avoid a separate, space-consuming metal contact). Because the silicide strap provides a very rapid diffusion path for boron and arsenic, one type of poly can be counterdoped by the other when the device is subjected to high-temperature excursions. This counterdoping can occur to the degree that a region of poly can change doping types (i.e., from $n^+$ to $p^+$). In such cases, the threshold voltage of devices with counterdoped poly will be shifted from their designed value.

If the processing temperature is limited to 800°C after the two types of poly have been connected by the silicide, such lateral diffusion does not produce significant shifts in $V_T$.[84] On the other hand, temperatures of 900°C will produce sufficient counterdoping to significantly shift $V_T$. Since one of the last high temperature steps in CMOS is activation of the source/drain implants, this would mean either using a lower-temperature activation step, or performing the step prior to formation of the silicide layer.

Another approach is to form a polysilicon electrode with an overlying conductor layer that suppresses such counterdoping. One such structure is a W-TiN-poly electrode structure.[85] The thin (30-nm) TiN film acts as a diffusion barrier to the dopants in the poly and also prevents reaction between the poly and the W. Very little of the dopant present in the poly is found to diffuse into the W, even following an anneal at 900°C for 1 hour.

Another problem encountered with $p^+$ poly gates when a thin gate oxide is used is poor $V_T$ process control in the PMOS devices, due to penetration of the boron into the oxide (or further, into the silicon). It is reported that boron will penetrate gate oxides that are ≤12.5 nm thick during a 900°C 30-minute post-implant anneal in $N_2$.[86] This implies that if $p^+$ poly gates are used, a lower processing temperature may be needed. If too low a temperature is used, however, the boron implanted into the polysilicon will not be sufficiently redistributed. The polysilicon dopant concentration at the polysilicon-gate oxide interface could thus end up being less than the mid-$10^{19}/cm^3$. This would make the work function of the polysilicon different from the desired degenerately doped value, creating $V_T$ control problems in the MOS devices.

It has also been found that the presence of fluorine in the gate oxide worsens the boron penetration problem (Fig. 5-73).[87,88] Such fluorine can be introduced into the gate oxide if the PMOS source drain regions are implanted using $BF_2^+$. Elemental boron is therefore considered inherently superior to $BF_2^+$ as the implant species for surface-channel PMOS devices in CMOS technologies that use $p$-doped polysilicon. A

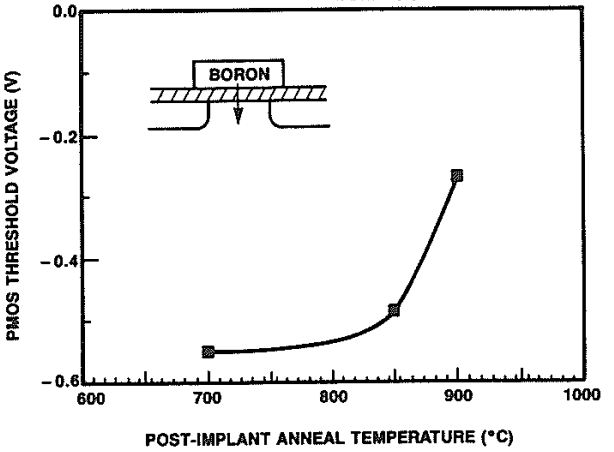


Fig. 5-73 Boron penetration through the gate oxide causes $V_T$ in $BF_2$ implanted PMOSFETs to shift positive at anneal temperatures above ~800 °C.[87] (© IEEE 1989).

study of enhanced boron diffusion through thin $SiO_2$ layers in a wet oxygen atmosphere is also reported in reference 89.

It also appears that nitrided oxides and reoxidized nitrided oxides (see chap. 9) are effective in blocking boron diffusion.[90] For this, and other reasons, they are being extensively studied for use as candidates to replace $SiO_2$ as the gate insulators in dual-gate CMOS processes. An alternative approach to introducing nitrogen into the gate oxide to block boron penetration is through ion implantation. Recently, ion implantation of nitrogen into the gate *p*- and *n*-doped poly electrodes of a 0.25 $\mu$m CMOS process has been reported. The heavy nitrogen dose ($1 \times 10^{15}$ $cm^{-2}$) resulted in the gate oxide incorporating high concentrations of nitrogen. This had the effect of suppressing boron penetration of the gate oxide.[110]

Hot carrier effects in $p^+$-poly 0.5-$\mu$m PMOSFETs have also been examined. Stress experiments showed significantly more electron trapping in short stress times than is observed in NMOSFETs. The device degradation due such trapping can be severe enough that it may pose a problem in such devices.[118]

## REFERENCES

1. J.E. Chung et al., "Performance and Reliability Design Issues of Deep Submicron MOSFETs," *IEEE Trans. Electron Devices* **ED-38**, March 1991, p. 545.
2. J. Greenfield and R. Dutton, "Nonplanar VLSI Device Analysis Using the Solution of Poisson's Equation," *IEEE Trans. Electron Dev.*, **ED-27**, p. 1520 (1980).
3. L..D. Yau, "A Simple Theory to Predict the Threshold Voltage in Short-Channel IGFETs," *Solid-State Electronics*, **17**, p. 1059, (1974).

**4.** W. Fichtner and H.W. Poetzl, "MOS Modelling by Analytical Approximations - Subthreshold Current and Subthreshold Voltage," *Int. J. Electronics*, **46**, p. 33, Jan. 1979.

**5.** C.R. Viswanathan, B.C. Burkery, G. Lubberts, and T.J. Treadwell, *IEEE Trans. Electron Dev.*, **ED-32**, p. 932, (1985).

**6.** R.R. Troutman, "VLSI Limitations from Drain-Induced Barrier Lowering," *IEEE Trans. Electron Dev.*, **ED-26**, p. 461, (1979).

**7.** F.-C. Hsu et al., *IEEE Trans Electron Dev.*, **ED-30**, p. 571 (1983).

**8.** S.C. Jain and P. Balk, "A Unified Analytical Model for DIBL ... in Short-Channel MOSFETs," *Solid-State Electronics*, **30** (5), p. 503, May 1987.

**9.** T. Skotnicki et al., *IEEE Electron Dev. Letts.*, **EDL-9**, p. 109, March 1988.

**10.** G.W. Taylor, *Solid-State Electronics*, **22**, p. 701, (1979).

**11.** B.J. Sheu, D.L. Scharfetter, P.K. Ko, and M.-C. Jeng, "BSIM: Berkeley Short-Channel IGFET Model for MOS Transistors," *IEEE J. of Solid State Circuits*, August 1987, p. 558.

**12.** G. Merkel, *Process and Device Modeling for IC Design*, (F. Van de Wield et al., Eds.), Noordhoff, Leyden, (1977), p. 705.

**13.** L. A. Akers et al., "A Model of a Narrow-Width MOSFET including Tapered Oxide and Doping Encroachment," *IEEE Trans. Electron Dev.* **ED-28**, p. 1490, 1981.

**14.** C.R. Ji and C.T. Sah, "Two-Dimensional Analysis of the Narrow-Gate Effect in MOSFET," *IEEE Trans. Electron Dev.*, **ED-30**, P. 635, June 1983.

**15.** T. Furukawa and J.A. Mandelman, "Process and Device Simulation of Trench Isolation Corner Parasitic Device," *Ext Abs. Mtg. Electrochem. Soc.*, Fall 1988, p. 329.

**16.** L. A. Akers, "The Inverse Narrow-Width Effect," *IEEE Electron Dev. Letts.*, **EDL-7** (7), p. 419, July 1986.

**17.** E.H. Li et al., "The Narrow-Channel Effect in MOSFETs with Semi-Recessed Oxide Structures," *IEEE Trans. Electron Dev.*, **ED-37** (3) p. 692, March 1990.

**18.** S. S. Chung and T.-C. Li, "An Analytical Threshold-Voltage Model of Trench-Isolated MOS Devices with Nonuniformly Doped Substrates," *IEEE Trans. on Electron Dev.*, March 1992, p. 614.

**19.** K. Ohe et al., "Narrow-Width Effects of Shallow Trench-Isolated CMOS with $n^+$-Polysilicon Gate," *IEEE Trans. Electron Dev.*, **ED-36** (6), p. 1110, June 1989.

**20.** G. Merkel, "A Simple Model of the Threshold Voltage of Short and Narrow Channel MOSFETs," *Solid-State Electronics.*, **23**, p. 1207, December 1983.

**21.** S. Selberherr et al., "MINIMOS - A Two-Dimensional MOS Transistor Analyzer," *IEEE J. Solid State Circuits*, **SC-15**, p. 605 (1980).

**22.** Z.-H. Liu et al., "Threshold Voltage Model for Deep-Submicrometer MOSFETs," *IEEE Trans. Electron Dev.*, **ED-40**, January 1993, p. 86.

**23.** J.R. Brews, W. Fichtner, E.H. Nicollian, and S.M. Sze, "Generalized Guide for MOSFET Miniaturization," *IEEE Electron Dev. Letts.*, **EDL-1**, p. 2, 1980.

**24.** C. Hu, "Future CMOS Scaling and Reliability," *Proceedings of the IEEE*, **81**, p.682, May 1993.

**25.** F.M. Klaasen, "Design and Performance of Micron-Sized Devices," *Solid-State Electron.*, **21**(3), p. 565 (1978).

**26.** C.F. Codella and S. Ogura, "Halo Doping Effects in Submicron DI-LDD Device Design," *Tech. Dig. IEDM*, p. 230, 1985.

27. A. Hori et al., "A Self-Aligned Pocket Implantation (SPI) Technology for 0.2 $\mu$m-Dual Gate CMOS," *Tech. Dig. IEDM,* p. 641, 1991.
28. H. Nihara et al., "Anomalous Drain Current in NMOS and its Suppression by Deep Ion Implantation," *Tech. Dig. IEDM,* p. 487 (1978).
29. L.C. Parrillo, "CMOS Active and Field Device Fabrication," *Semicond. International,* April 1988, p. 64.
30. T. Skotnicki, G. Merkel, and T. Pedron, "A New Punchthrough Current Model Based on the Voltage-Doping Transformation," *IEEE Trans. on Electron Dev.,* **ED-35**, July 1988, p. 1076.
31. C. Duvvury, "A Guide to Short-Channel Effects in MOSFETs," *IEEE Circuits and Systems Magazine,* November 1986, p. 6.
32. J. A. Cooper and D.F. Nelson, "Measurement of the high-field drift velocity of electrons in the inversion layer in silicon," *IEEE Electron Dev. Lett.,* **EDL-2**, July 1983, p. 169.
33. R.H. Crawford. *MOSFETs in Circuit Design*, McGraw-Hill, New York, 1967.
34. D. Frohman-Bentchkowsky, "On the effect of mobility in inversion and accumulation layers on thermally oxidized silicon surfaces," *Proc. IEEE*, **vol. 56**, p. 217, 1968.)
35. A.G. Sabnis and J.T. Clemens, "Characterization of Electron Velocity in the Inverted <100> Si Surface," *Tech. Dig. - IEDM*, p. 19, 1979.
36. M.S. Liang et al., "Inversion layer capacitance and mobility of very thin gate oxide MOSFETs," *IEEE Trans. Electron Dev.,* **ED-33**, March 1986, p. 409.
37. K.K Hung, *Electrical characterization of the Si-$SiO_2$ interface for thin oxides,* Doctoral Thesis, Hong Kong University, (1987).
38. C.G. Sodini, T. Ekstedt, and J. Moll, "Charge Accumulation and Mobility in Thin Dielectric MOS Transistors," *Solid-State Electronics*, **25**, p. 833, (1982).
39. K. Lee et al., "Physical Understanding of Low Field Carrier Mobility in Silicon Inversion Layer," *IEEE Trans. Electron Devices,* **ED-38**, August 1991, p. 1905.
40. S.R. Hofstein and G. Warfield, "Carrier mobility and current saturation in the MOS transistor," *IEEE Trans. Electron Dev.,* **ED-12**, p. 129, (1965).
41. F.N. Trofimenkoff, "Field-dependent mobility analysis of the field-effect transistor," *Proc. IEEE*, **53**, p. 1765, (1965).
42. D.M. Caughey and R.E. Thomas, "Carrier mobilities in silicon empirically related to doping and field," *Proc. IEEE*, **55**, p. 2192 (1967).
43. C.G. Sodini, P.K. Ko, and J.L. Moll, "The effect of high fields on MOS device and circuit performance," *IEEE Trans. Electron Dev.,* **ED-31**, October 1984, p. 1386.
44. E.A. Talkhan, I.R. Mansour, and A.I. Barboor, "Investigation of the effect of drift-field-dependent mobility on MOSFET characteristics," Parts I and II. *IEEE Trans. Electron Dev.* **ED-19**, August 1972, p. 899.
45. P.K. Ko, "Approaches to Scaling," Ch. 1, in *Advanced MOS Device Physics,* N.G. Einspruch and G. Gildenblatt, Eds. Academic Press, Orlando, FL., 1989, p. 1
46. K.Y. Toh, P.K. Ko, and R.G. Meyer, "An engineering model for short-channel MOS devices," *IEEE J. Solid-State Circuits,* August 1988, p. 950.
47. M.C. Jeng et al., "Performance and reliability of deep-submicron MOSFETs," *Tech. Dig. IEDM,* 1987, p. 710.

**48.** V.G. Reddi and C.T. Sah, "Source to Drain Resistance Beyond Pinchoff in Metal-Oxide-Semiconductor Transistor (MOST," *IEEE Trans. Electron Dev.*, **ED-12**, p. 108, (1969).

**49.** D. Frohman-Bentchkowsky and A.S. Grove, *IEEE Trans. Electron Devices* **ED-16**, p. 108, (1969).

**50.** G. Baum and H. Beneking, "Drift Velocity Saturation in MOS Transistors," *IEEE Trans. Electron Devices*, **ED-17**, June 1972, p. 481.

**51.** Y.A. Elmansy and A.R. Boothroyd, "A simple two-dimensional model for IGFET operation in the saturation region," *IEEE Trans. Electron Dev.*, **ED-24**(3), p. 254-62, (1977).

**52.** P.K. Ko, R.S. Muller, and C. Hu, "A Unified Model for Hot-Electron Currents in MOSFETs," *Tech. Dig. IEDM,* p. 600, 1981.

**53.** P.K. Ko, *Hot-electron effects in MOSFETs,"* Doctoral Thesis, University of California, Berkeley, (1982).

**54.** R.S. Muller and T.I Kamins, *Device Electronics for Integrated Circuits,* John Wiley & Sons, New York, 1986, p. 491.

**55.** T.Y. Chan, P.K. Ko, and C. Hu, "Dependence of Channel Electrical Field on Device Scaling," *IEEE Electron Dev. Lett.*, **EDL-6**, October, 1985, p. 531.

**56.** B. J. Sheu et al., "BSIM: Berkeley Short-Channel IGFET Model for MOS Transistors," *IEEE J. Solid-State Circuits,* Aug. 1987, p. 558.

**57.** B. J. Sheu, D. L. Scharfetter, and H. C. Poon, "Compact short-channel IGFET Model," Univ. of Calif., Berkeley, CA Memo. UCB/ERL M84/20, March 1984.

**58.** M.-C. Jeng, *Design and Modeling of Deep-Submicron MOSFETs,* ERL Memo No. ERL M90/90, Electronics Research Laboratory, University of California, Berkeley, October 1990.

**59.** A.H.-C. Fung, "A Subthreshold Conduction Model for BSIM," Univ. of Calif., Berkeley, Memo, UCB/ERL M65/22, March 1985.

**60.** B. Eitan and D. Frohman-Bentchkowsky, "Surface Conduction in short-channel MOS Devices as a limitation to VLSI scaling," *IEEE Trans. Electron Dev.* vol. ED-29, p. 254, Feb. 1982.

**61.** R. H. Dennard, et al., "Design of II MOSFETs with Very Small Physical Dimensions," *IEEE J. Solid-State Circuits,* **SC-9** (5), 256, (1974).

**62.** G. Bacarani, M. R. Wordeman, and R. H. Dennard, "Generalized Scaling Theory and its Application to a 0.25 $\mu$m MOSFET Design," *IEEE Trans. Electron Dev.*, **ED-31**(4), 452 (1984).

**63.** J.R. Brews et al., "Generalized Guide to MOSFET Miniaturization," *IEEE Electron Dev. Letts.*, **EDL-1**, January 1980, p. 2.

**64.** F.M. Klaassen, "Design and Performance of Micron-Size Devices," *Solid-State Electronics,* **21**, March 1978, p. 565.

**65.** J.R. Brews, K.K. Ng, and R.K. Watts, in "The Submicron Silicon MOSFET," Ch. 1, p. 19, *Submicron Integrated Circuits,* Ed. R.K. Watts, Wiley Interscience, New York, 1989.

**66.** *ibid.* pp. 23- 37.

**67.** R.A. Haken et al., "BiCMOS Process Technology," Chap. 3, p. 85, in *BiCMOS Technology and Applications,* A. Alvarez Ed. Klewer, Norwell MA, 1989.

68. A. Alvarez et al., "Application of Statistical Design and Response Surface Methods to Computer-Aided VLSI Device Design," *IEEE Trans. Computer-Aided Design,* **CAD-7**, February 1988, p. 272.
69. *ibid.* ref. 65, p. 24.
70. S.M. Sze, Ed. *VLSI Technology,* 2nd edition, chap. 11, McGraw-Hill, New York, 1988.
71. T. Ohzone et al., *IEEE Trans. Electron Dev.,* **ED-32**, 1789, (1980).
72. G.J. Hu et al., *Tech. Dig. IEDM*, 1982, p. 710.
73. K.M. Cham et al., *Computer-Aided Design and VLSI Device Development,* Boston, Klewer Academic Publishers, 1986, p. 182.
74. J. Zhu, R.A. Martin, and J.Y. Chen,, "Punchthrough Current for Submicrometer MOSFETs in CMOS VLSI," *IEEE Trans. Electron Dev.*, February 1988, p. 145.
75. A. Schmitz and J. Y. Chen, "Design, Modelling, and Fabrication of Submicron CMOS Transistors," *IEEE Trans. Electron Dev.*, **ED-33**, p. 148, (1986).
76. L.C. Parrillo, "CMOS Active and Field Device Fabrication," *Semicond. Internat.,* April 1988, p. 64.
77. R. A. Chapman et al., "A 0.8 μm CMOS Technology," *Tech. Dig. IEDM*, 1987, p. 362.
78. S. Odanaka et al., "A New Half-Micron P-Channel MOSFET with Efficient Punchthrough Stops," *1985 Symp.VLSI Tech., Digest of Tech. Papers*, p. 62.
79. T. Hori et al., "A New P-Channel MOSFET with Large Tilt Angle Implanted Punch-through Stopper (LATIPS)," *IEEE Electron Dev. Letts.,* **EDL-9,** Dec. 1988, p. 641.
80. M. Stinson et al., "Effects of Ion Implantation on Deep-Submicrometer Drain-engineered MOSFET Technologies," *IEEE Trans. Electron Dev.,* **ED-38,** March 1991, p. 487.
81. L. C. Parrillo et al., *Tech Dig. IEDM*, 1984, p. 418.
82. K. M. Cham et al., *IEEE Electron Dev. Lett.*, January 1986, p. 49.
83. C.Y. Wong et al., *Tech. Dig. IEDM*, 1988, p. 238.
84. S. J. Hillenius et al., "A Symmetric Submicron CMOS Technology," Tech. Dig. IEDM, 1986, p. 252.
85. P.-H. Pan, J.G. Ryan, and M.A. Lavoie, *Ext. Abs. of the Electrochem. Soc. Meeting*, Spring 1989, Abs. 138, p. 193.
86. M.L. Chen et al., "Constraints in *p*-Channel Device Engineering for Submicron CMOS Technologies," *Tech. Dig. IEDM*, 1988, p. 390.
87. F.K. Baker, et al., *Tech. Dig. IEDM*, 1989, p. 443.
88. J.M. Sung, *Tech. Dig. IEDM*, 1989, p. 447.
89. Y. Sato, K. Ehara, and K. Saito, *J. Electrochem. Soc.,* June 1989, p. 1777.
90. H. Fang et al., "Low-Temperature Furnace-Grown Reoxidized Nitrided Gate Dielectrics as a Barrier to Boron Penetration," *IEEE Electron Dev. Letts.,* **EDL-13** (4) p. 217 April 1992.
91. M. Nishida and H. Onodera, "An anomalous increase of threshold voltages with shortening of the channel lengths fro deeply boron-implanted *n*-channel MOSFETs," *IEEE Trans. Electron Dev.,* **ED-28**, p. 1101, 1981.
92. M. Orlowski, C. Mazure, and F. Lau, "Submicron short-channel effects due to gate re-oxidation induced lateral diffusion," *IEDM Tech. Dig.* 1987, p. 632.
93. C.Y. Lu and J.M. Sung, "Reverse Short-Channel Effects on Threshold Voltage in Submicron Salicide Devices," *IEEE Electron Dev. Lett.,* **EDL-10**, p. 446, October, 1989.

**94.** N.D. Arora and M.S. Sharma, "Modeling the Anomalous Threshold Voltage Behavior of Submicrometer MOSFETs," *IEEE Electron Dev. Lett.,* **EDL-13**, p. 92, February 1992.

**95.** H. Hanafi et al., "A Model for Anomalous Short-Channel Behavior in MOSFETs," *IEEE Electron Dev. Lett.,* **EDL-14**, p. 575, December 1993.

**96.** D. Sadana et al., "Enhanced Short-Channel Effects in NMOSFETs due to Boron Redistribution Induced by Arsenic Source and Drain Implant," *IEDM Tech. Dig.* 1992, p. 849.

**97.** H. Jacobs et al., "MOSFET Reverse Short Channel Effect Due to Silicon Interstitial Capture in Gate Oxide," *IEDM Tech. Dig.* 1993, p. 307.

**98.** C.S. Rafferty et al., "Explanation of Reverse Short Channel Effect by Defect Gradients," *IEDM Tech. Dig. 1993,* p. 311.

**99.** M.D. Giles, *Appl. Phys. Lett.,* **62(2)**, p. 1940, (1993).

**100.** J.Y. Chen, "An *n*-well CMOS with self-aligned channel stops," *Tech. Dig. IEDM* 1983, p. 526.

**101.** T.M. Liu and W.G. Oldham, *IEEE Electron Dev. Letts.,* **EDL-5**, 299 (1984).

**102.** J.R. Pfiester et al., "A Poly-Framed LDD Sub-half-Micrometer CMOS Technology," *IEEE Electron Dev. Letts.* **EDL-11,** November 1990, p. 529.

**103.** J.R. Pfiester et al., "An Integrated 0.5 $\mu$m CMOS Disposable TiN LDD/Salicide Spacer Technology," *Tech. Dig. IEDM,* 1989, p. 781.

**104.** L.C. Parrillo, "CMOS Active and Field Device Fabrication," *Semiconductor International,* April 1988, p. 64.

**105.** S. Meguro et al., *Tech. Dig. IEDM, 1984,* p. 59.

**106.** J.S.T. Huang, J.W. Schrankler, and J.S. Kueng, *IEEE Trans. Electron Dev.*, **ED-31**, 1889, (1984).

**107.** S. Ogura et al., *IEEE Trans. Electron Dev.,* **ED-27**, 1359 (1980).

**108.** Y. Omura and K. Ohwada, *Solid-State Electronics,* **24**, 301 (1981).

**109.** N. Kotani and S. Kawazu, *Solid-State Electronics,* **22**, p. 63, (1979).

**110.** T. Kuroi et al., "Novel NICE (Nitrogen Implantation into CMOS Gate Electrode and Source-Drain) Structure for High Reliability and High Performance 0.25 $\mu$m Dual Gate CMOS," *Tech. Dig. IEDM, 1993,* p. 325.

**111.** R.R. Troutman, *IEEE J. Solid-State Circuits,* **SC-9,** p. 55 (April 1974).

**112.** J.Y. Chen et al., "A Fully Recessed Field Isolation Technology Using Photo-CVD Oxide," *Tech. Dig. IEDM*, 1982, p. 233.

**113.** T. Shibata et al., "An optimally designed process for submicrometer MOSFETs," *IEEE Trans. Electron Dev.* **ED-29**, p. 531, (1982).

**114.** G.J. Hu and R.H. Bruce, "Design Tradeoffs Between Surface and Buried-Channel FETs," *IEEE Trans. Electron Dev.,* **ED-32**, March 1985, p. 584.

**115.** K.M. Cham and S.Y. Chiang, "Device design for the Submicrometer *p*-channel FET with $n^+$ polysilicon gate," *IEEE Trans. Electron Dev.,* **ED-31**, p. 964 (1984).

**116.** K.M. Cham et al., "Characterization and modeling of the trnch surface inversion problem for the trench isolated CMOS technology," in *IEDM Tech. Dig.,* p. 23, 1983.

**117.** T. Skotnicki, G. Merckel, and T. Pedron, "Analytical Study of Punchthrough in Buried-Channel PMOSFETs," *IEEE Trans. E.ectron Dev.*, April 1989, p. 690.

**118.** Y. Hiruta et al., "Impact of Hot Electron Trapping of Half-Micron PMOSFETs with $p^+$ Poly -Si Gate," *Tech. Dig. IEDM,* 1986, p. 718.

119. J. Cooper and D. Nelson, "High-Field Drift Velocity of Electrons at the Si-$SiO_2$ Interface as Determined by the Time-of-Flight Technique," *J. Appl. Phys.* **54**, 1445 (1983).

120. T.E. Hendrikson, "A Simplified Model for Subpinchoff Condition in Depletion Mode IGFETs," *IEEE Trans. Electron Dev.*, **ED-25**, p. 435 (1978).

## PROBLEMS

1. Calculate the threshold voltage (a) in 1 Ω-cm *p*-type silicon and (b) in 1 Ω-cm *p*-type silicon. The MOS devices for each case have : (i) $n^+$-polysilicon gate; (ii) $t_{ox}$ = 100 nm; and (iii) the oxide is free of charge except for a surface density of $Q_f = 5\times10^{10}$ cm$^{-2}$.

2. For exercise **1**, what are the threshold voltages if $p^+$ polysilicon is used for both the *n*- and *p*-channel devices.

3. Describe punchthrough current and subthreshold current and explain the difference between them.

4. An *n*-channel MOSFET has a tox of 20 nm, an $L_{eff}$ = 1 μm, $r_j$ = 0.2 μm, and $V_T$ = 0.6V. If the device is biased at $V_{GS}$ = 3V and $V_{DS}$ = 5V, calculate the saturation voltage $V_{DSsat}$ and the maximum electric field.

5. Use one-dimensional junction theory to estimate the punchthrough voltage of a MOSFET with a channel length of 1 μm. Assume a substrate doping of $3\times10^{16}$/cm$^3$, a substrate bias of 0V, and a uniformly doped substrate (no $V_T$-adjust implant).

6. Using Eq. 5-97, calculate the buried-channel $S_t$ value for $x_1$ = 500Å, $t_{ox}$ = 250Å, $x_2 << x_3$ = 3000Å and compare it with the $S_t$ value calculated for a surface-channel MOSFET with the same $t_{ox}$ and a channel depletion width of d = $x_3$.

7. How does a MOSFET's threshold change when constant field scaling rules are applied? Does it scale proportionately?

8. Consider a long-channel MOSFET with $L$ = 3 μm, Z = 21 μm, $N_A = 5\times10^{15}$ cm$^{-3}$, $C_{ox} = 1.5\times10^{-7}$ F/cm$^2$, and $V_T$ = 1.5V. Calculate $V_{DSsat}$ for the case when $V_{GS}$ = 4V. If a constant scaling factor is used to reduce the channel length to 1 μm, find the following scaled-down parameters: Z, $C_{ox}$, and $I_{Dsat}$.

9. A MOSFET with gate oxide thickness of 20 nm is to be fabricated on a *p*-type substrate of doping $N_A = 10^{16}$ cm$^{-3}$. The source/drain regions have a depth of 0.2 μm and $N_D = 10^{19}$ cm$^{-3}$. The device is to be operated with $V_{BS}$ = 0V, but $V_{DS}$ could be as large as 3V. From Eq. 5-84 estimate the minimum channel length this MOSFET can have while still exhibiting electrically long-channel behavior. (The gate length is the channel length plus twice the junction depth.) A smaller value of minimum channel length could be obtained if a larger $N_A$ was used. Suggest some undesirable side effects that such a choice could produce.

10. Qualitatively describe the differences between a surface-channel and a buried-channel MOSFET.

11. We have stated in this chapter that the saturation of electron velocity can limit the drain current in a MOSFET with a channel length of 1 μm or less operating from a 5-V supply. Examine this effect by using SPICE to generate the $I_D$-$V_{DS}$ characteristic of an NMOSFET with $L$ = 1 μm formed on a substrate of doping $N_A = 10^{16}$ cm$^{-3}$ with a 50 nm thick gate oxide. Set $V_{GS}$ = 5V and sweep $V_{DS}$ from 0 to 5V using the Level 2 model. First run a simulation in which VMAX is not specified, and then repeat the simulation with VMAX = $8\times10^6$ cm sec$^{-1}$, which corresponds roughly to the scatter-limited velocity of electrons in a MOSFET channel.

**12.** Qualitatively summarize why a surface channel NMOSFET is prone to suffering punchthrough only after the punchthrough voltage is exceeded, but that a buried-channel PMOSFET exhibits punchthrough current behavior even when drain voltages are very small.

**13.** Why does the subthreshold slope of the $I_D$-$V_{GS}$ curve appear to increase at the onset of subsurface punchthrough?

# CHAPTER 8

## WELL FORMATION IN CMOS

Both *n*- and *p*-channel transistors must be fabricated on the same wafer in CMOS technologies. Obviously, only one type of device can be fabricated on a given starting substrate. To accommodate the device type that cannot be built on this substrate, regions of a doping type opposite to that present in the starting material must be formed. These regions are called *wells* (or sometimes *tubs*) and are usually (but not always) the first features to be defined on a starting wafer. The well-formation process starts with a uniform, lightly doped *p*- or *n*-type substrate. Excess dopants of the opposite type are then selectively implanted or diffused to attain the proper well depth and doping profile in the well regions. The doping type in the wells becomes the identifying characteristic of the CMOS technology (e.g., *p*-well or *n*-well CMOS). Conventional well-implant doses range from $2x10^{12}$-$8x10^{12}/cm^2$ at energies from 100-200 keV. The term "conventional" in this sense refers to wells formed by low-energy (<200 keV) ion implantation and a thermal drive-in. Alternative well-formation techniques that do not require a drive-in will also be discussed separately. Epitaxial $n$-on-$n^+$ or $p$-on-$p^+$ starting substrates have also come into widespread use, since they help reduce the susceptibility of CMOS circuits to latchup.

As well as being of the correct doping type, the well and substrate must be electrically isolated from each other under every operating condition. As noted in chap. 6, to ensure that *pn* junctions are not forward-biased during circuit operation, if a *p*-type substrate is used as the starting material of an IC, the substrate must be connected to the most negative circuit voltage. If an *n*-type substrate is used, it must be connected to the most positive circuit voltage. When wells are present, however, the well regions must also be connected to the appropriate circuit voltages to prevent forward-biasing of the junctions within the well (and between the well and substrate). Because the wells are totally junction-isolated from the rest of the wafer, it is especially important that provisions for well connections be made at the top surface of the wafer. That is, in non-well technologies, it may still be possible to contact the substrate from the backside of the wafer even if no provision is made for a substrate contact from the top surface. Obviously, such backside connections cannot be established to the well regions.

The dopant concentration near the surface of the well is one of the factors that impact $V_T$, carrier mobility, source/drain capacitance, and field isolation. The well concentration deeper beneath the surface affects other characteristics of MOSFET behavior such as latch-up and vertical punchthrough (i.e., between drain and well-substrate junctions).*

* To ensure that vertical punchthrough will not occur, the depletion regions of the drain/well and well/substrate junctions must be prevented from merging. That is, the depth of the well/substrate junction must be deep enough (typically >1.5 $\mu$m) so that it is greater than the sum of the widths of the two depletion regions in the well, even when a reverse bias of $V_{DD}$ is



MPS EX. 1008C - 260/295

## 8.1 *p*-WELL, *n*-WELL, and TWIN-WELL TECHNOLOGIES

There are many trade-offs involved in the optimization of a CMOS process. The choices revolve around the highly interrelated parameters of circuit performance, layout density, fabrication cost, and susceptibility to latchup. As described in previous chapters, obtaining the best circuit performance from an MOS device involves maximizing the drive current and minimizing junction capacitances and body effect - all characteristics which favor lower doping concentrations in the device body. Optimizing density, however, requires raising these same doping concentrations (to avoid punchthrough and to achieve high values of threshold voltage in the parasitic field-transistors). Higher density is thus achieved by allowing closer packing of adjacent *n*- and *p*-channel transistors. Conversely, latchup tolerance can also be improved by keeping *n*- and *p*-channel transistors farther apart (see chap. 6, Vol. 2), but this in turn lowers circuit density.

These complex interacting tradeoffs converge on several processing configurations that are determined at the outset of the processing sequence through the selection of the type of well doping.[1,2] It is therefore useful to consider the ramifications of the well-type choice with respect to its impact on circuit applications. Because at least one of the device types must be located in the well, the selection of well architecture influences device and circuit behavior. In particular, the performance of devices in the well for the most part suffer as a consequence of the higher well doping. That is, they exhibit higher junction capacitance, increased sensitivity to body effect, and decreased transconductance (due to reduced carrier mobility). Furthermore, substrate current (e.g., due to hot-carrier effects) is harder to collect from the well regions. The issue thus becomes one of deciding which device type (if any) should be subjected to such performance degradation.

Figure 8-1 shows the five basic well structures employed in CMOS technologies. Figure 8-1a illustrates the *single p-well structure*, in which *p*-wells are fabricated in an *n*-type starting substrate. NMOS devices are made in the well, and PMOS transistors in the substrate. If the dopant types of the *p*-well technology are reversed, a *single n-well structure* is obtained (Fig. 8-1b). The structures in Figs. 8-1c to 8-1e involve approaches in which *both p*- and *n*-wells are formed. CMOS technologies employing such structures are called *twin-well, dual-well,* or *twin-tub CMOS.* The first two of these (Figs. 8-1c and 8-1d) are designed to be fabricated on a particular substrate type, like the single *p*- and *n*-well structures. The third of these twin-well technologies (Fig. 8-1e), however, is independent of starting material type.

In the next sections we will outline the pros and cons of both the single *p*-well and *n*-well configurations, as well as those of the more complex well configurations that have been developed (e.g., twin-well and retrograde-well CMOS).

* (cont.) applied to the drain (see example 8-1 in this chapter.). In conventional-well CMOS structures, this depth is achieved by a long, high-temperature drive-in (up to 1200°C) following the well implants. For example, in one twin-well process the well-implants are followed by a drive-in at 1100°C for 500 minutes (8 1/3 hours).[13]

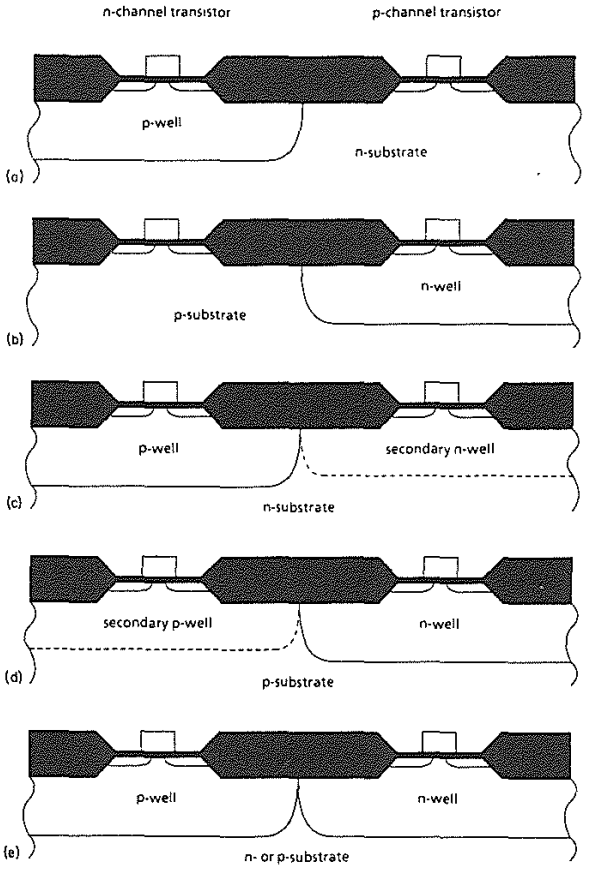


**Fig. 8-1** Well structures available for CMOS circuit fabrication: (a) *p*-well CMOS; (b) *n*-well CMOS; (c) *p*-well with secondary *n*-well (twin-well constrained to *n*-substrate); (d) *n*-well with secondary *p*-well (twin-well constrained to *p*-substrate); (e) twin-well CMOS on *n* or *p*-substrate. A.G. Lewis and J.Y. Chen, "Current Trends in MOS Process Integration," in N.G. Einspruch and G. Gildenblatt, Eds. *Advanced MOS Device Physics,* Academic Press, San Diego CA, 1989, Reprinted with Permission.

## 8.1.1 *p*-Well CMOS

The *p*-well process, illustrated in Fig. 8-1a, involves the creation of *p*-regions in an *n*-type substrate to permit the fabrication of NMOS devices. The *p*-wells are formed by implanting a *p*-type dopant into an *n*-substrate at a high enough concentration to overcompensate for the substrate doping and to give adequate control over the *p*-type

doping in the well. The starting *n*-type substrate, however, must also have sufficient doping to ensure that the characteristics of devices fabricated in the substrate regions are adequate (a minimum doping concentration of $3x10^{14}$-$1x10^{15}/cm^3$ is required). If the *p*-well is doped too highly, however, the performance of the *n*-channel devices will be degraded through lower carrier mobility, increased source/drain to *p*-well capacitance, and increased sensitivity to body-biasing effects. The *p*-well doping is therefore usually selected to be about five to ten times higher than the doping in the *n*-substrate.

*p*-well CMOS was the first type of CMOS that could be practically manufactured, and such circuits were introduced in the late 1960s. The first companies to commercially offer CMOS components produced many designs in *p*-well technology. As this experience was spread throughout the industry, *p*-well CMOS became widely established.

There were several reasons for choosing *p*-well CMOS at that time. First, the earliest MOS ICs were based on a metal-gate PMOS process which utilizes an *n*-substrate. The work-function of aluminum is such that enhancement-mode PMOS devices can be made in a lightly doped *n*-type substrate without the need for additional channel doping. Thus, when CMOS circuits were invented (to take advantage of the reduced power consumption possible with CMOS), it was simplest to manufacture them merely by adding a *p*-well to the basic PMOS process. Second, higher channel doping levels were needed to permit sufficiently large $V_T$ values to be established in the enhancement-mode NMOS transistors. Such higher doping was also needed in the field regions of the NMOS sections of the circuit to ensure adequate isolation (see chap. 6). These requirements are compatible with the need to have well surface concentrations five to ten times larger than the substrate doping level. Finally, it was relatively simple to manufacture *p*-wells with the existing process fabrication technology. That is, in the late 1960s ion implantation was not yet available and it was necessary to introduce the well dopants by chemical diffusion. At the doping levels required in the wells it was much easier to achieve adequate doping profile control using boron rather than phosphorus diffusion processes.

There are also several circuit and system advantages of *p*-well over *n*-well CMOS. First, *p*-well technology may be the better choice for pure-static logic, in which a good balance between the performance of both MOS device types is beneficial. (The performance of the PMOS and NMOS devices are "more balanced" because the carrier mobility reduction associated with higher well doping is compensated by forming the NMOS devices in the *p*-well; i.e., the electrons have higher mobility.) Second, it is attractive for applications that require an isolated *p*-region (such as those using an *npn* bipolar transistor as an on-chip driver or an *n*-channel FETs for an analog input). Third, *p*-well CMOS is less susceptible to field-inversion problems than *n*-well CMOS (which uses a lightly doped *p*-substrate), and can thus be slightly easier to fabricate. (We will describe later how *p*-well CMOS can use the inherent substrate and well doping as the channel stops, whereas *n*-well CMOS must use a separate substrate channel-stop process.) Fourth, if the so-called retrograde-well process (rather than a diffusion of a shallow implant) is used to form the wells, *p*-well technology is more feasible. It is easier to form a *p*-retrograde well than an *n*-retrograde well, since boron ions penetrate deeper than arsenic or phosphorus ions at the same implant energy. Finally, *p*-well

CMOS may be better for fabricating SRAMs. Since the alpha-particle-induced soft-error rate (SER) becomes significant even in SRAMs if feature sizes are scaled to submicron dimensions, the cells should be made inside a well. The sensing of the state of an SRAM cell depends on the current provided by the cell. As a result, high-gain NMOS devices are more desirable for the pass gates and drivers in the cell, and must be built in a *p*-well. Furthermore, it facilitates the use of polysilicon load resistors in 4-transistor memory cells and buried contacts.

Some of the disadvantages of *p*-well CMOS are the following: (1) Since NMOS transistors are fabricated in the *p*-well, their characteristics will be degraded compared to those made in a lightly doped substrate. In CMOS circuits that rely heavily on optimum NMOSFET behavior, this can lead to reduced circuit performance; (2) Substrate currents, the result of impact-ionization generated carriers in short-channel devices (see chaps. 7 and 9), are much larger in NMOS than PMOS devices. It is more difficult to collect these carriers from a well than from the substrate. Since the NMOSFETs in *p*-well CMOS are in the well, this represents a disadvantage of submicron CMOS *p*-well technology.

### 8.1.2 *n*-Well CMOS

By the late 1970s, the technological barriers that prevented enhancement-mode NMOS transistors from being manufactured were overcome. Primarily, the introduction of ion implantation made $V_T$ control in NMOSFETs a simple, straightforward procedure. As a result, NMOS technologies ousted PMOS in high-speed, high-packing-density ICs. By the mid-1980s, however, the power dissipation in VLSI NMOS ICs became intolerably high (see chap. 6, Vol. 2), and CMOS development was pursued as a mainstream replacement technology for NMOS. For those companies that had been producing NMOS as their main IC product, *n*-well CMOS appeared to be an attractive approach for making the switch to CMOS.

In the *n*-well process, shown in Fig. 8-1b, the *p*-channel devices are formed in the more heavily doped *n*-well, while the NMOS devices are made in the substrate. Since it was now feasible to build NMOS devices in lightly doped substrates, this made it possible to make *n*-channel devices in an *n*-well CMOS process that were identical to those made by NMOS technology. Thus, virtually all of the experience that had been amassed in fabricating high-performance NMOS could be transferred to an *n*-well CMOS process. Furthermore, CMOS circuits could be made that exploited existing NMOS device design. The availability of ion implantation for introducing well dopants into the substrate (instead of having to rely on diffusion), now made dopant control of *n*-wells much more feasible. This lead to the successful development of *n*-well CMOS technology.

As a result, virtually all EPROMs, microprocessors, and dynamic RAM designs in the generations of technology built with 1.25-2.0 $\mu$m dimensions were implemented with *n*-well CMOS. Mixed CMOS-NMOS designs were also made, in which the high noise immunity and negligible stand-by-power dissipation of CMOS was exploited in the input/output sections, and faster NMOS devices were used internally.

However, it should be noted that $n$-well technology also has some disadvantages. First, as mentioned earlier, it is more sensitive to field-inversion problems than $p$-well CMOS. Second, it may be more difficult to build pure-static, high-performance logic circuits with $n$-well CMOS.

### 8.1.3 CMOS on Epitaxial Substrates

As described in vol. 2, chap. 6, heavily doped substrates with a more lightly doped surface epitaxial layer have been utilized to suppress latchup in CMOS.[4] When such starting material is used with single-well CMOS, the epitaxial layer is doped to a concentration equal to that of the substrate in a nonepitaxial wafer used for that process. If a twin-well CMOS process is used, the epitaxial layer is doped to a level significantly lower than that required for building either the $p$- or $n$-channel MOSFETs (see section 8.1.4).

The epitaxial layer is made thicker than the well depth, since the dopants in the heavily doped substrate under the epi layer diffuse toward the surface as the well dopants are diffused toward the bulk (Fig. 8-2). Thus, some of the epitaxial layer becomes more heavily doped during the CMOS process flow. The process is designed so that the bottom of the well is eventually adjacent to the heavily doped substrate region.

Either $n$-epi on $n^+$ substrates or $p$-epi on $p^+$ substrates can be used, with each method having advantages and drawbacks. Because the problems with $n$-epi on $n^+$ are more serious, $p$-epi on $p^+$ is more widely used. The major limitation of the latter

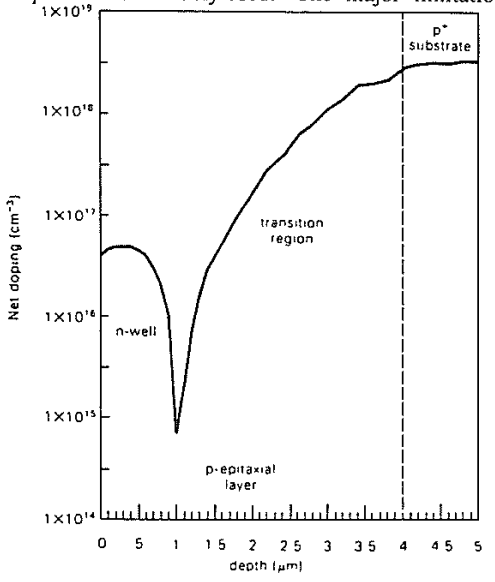


**Fig. 8-2** A $p$-on-$p^+$-epi doping profile and diffused $n$-well profile measured after the entire CMOS process has been completed. The as grown epi thickness is 4 $\mu$m and the final lightly doped epi thickness is about 2 $\mu$m.[3] (© 1987 IEEE).

approach is that the outdiffusion of boron from the $p^+$ is much more severe than is the outdiffusion of As or Sb in $n$-epi on $n^+$. (The reason for this is that boron diffuses much more rapidly than antimony, which is the most widely-used $n^+$ dopant material.) Thus, a thicker $p^-$- epitaxial layer must be used.

In addition, the transition region between the $p^+$ substrate and the $p^-$-epi layer is thicker, producing a larger series resistance ($R_{sub}$), which in turn reduces latchup immunity. On the other hand, the $p$-on-$p^+$ material is less sensitive to process-induced defects, and the $p$-type substrate provides higher conductivity under NMOS devices. Such additional conductivity is desirable, since it reduces the voltage drops caused by the substrate currents (generated as a result of the hot-carrier effects in short-channel devices). It is especially important in the regions containing NMOS devices, since the hot-electron substrate current is much higher in such devices than in PMOS devices.

The $n$-on-$n^+$ epitaxial substrates also offer some advantages. First, SRAMs are often built on $n$-type substrates, because the $p$-well-to-$n$-substrate junction provides protection from radiation-induced discharging of the memory's $n$-type storage nodes in the $p$-well.[5] Second, retrograde $p$-wells are easier to implement because their implantation energy requirements are much lower. Third, the $n$-to-$n^+$ transition region is smaller than that in $p$-on-$p^+$ substrates, and the smaller value of $R_{sub}$ provides improved latchup protection.

The limitations of $n$-epi on $n^+$ involve the process by which the heavily doped substrate is grown. Antimony (Sb) is the $n$-type dopant used, both because its diffusion coefficient is so low and because it exhibits much less lateral autodoping than arsenic (the other slow-diffusing $n$-type dopant). The problem with Sb is that its segregation coefficient, $k_O$, is very small (i.e., $k_{O,Sb} = 0.023$; see, Vol. 1, chap. 1), and a large quantity of Sb must therefore be put into the Si melt to ensure that a sufficiently heavily doped ingot will be produced. Furthermore, in even the most highly refined Sb there are high concentrations of unwanted heavy metals, which become incorporated into the growing silicon crystal. Finally, the oxygen content of the Sb-doped crystal is relatively small, due in part to the special growing conditions used when the Sb-doped ingot is pulled.[6,7] As a result, intrinsic gettering techniques that would immobilize the metals in the substrate are not as effective as they are in $p$-on-$p^+$ epi. For these reasons, $n$-on-$n^+$ substrates are less frequently chosen when epi-CMOS is implemented.[4]

A problem that exists with both types of epitaxial substrates for CMOS is that the wells cannot be made too deep, since the lateral diffusion would then take up too much area. On the other hand, if the wells are too shallow, vertical punchthrough (between the substrate and the source/drain regions of devices in the well) will ensue.[8] In this case, appreciable leakage current can flow along this vertical path. As noted, punchthrough can occur if the depletion regions of the $p^+/n$-well junction and the $n$-well/$p^+$-substrate junction merge. The problem is even more severe in the case of the heavily doped $p^+$ substrate, due to the high degree of boron outdiffusion. A major limitation is thus imposed on the minimum epitaxial-layer thickness.

Another problem of epi-CMOS is back-surface autodoping. For example $p$-type 20 $\Omega$-cm ($7 \times 10^{14}$ boron/cm$^3$) epi on a 0.005 $\Omega$-cm ($2 \times 10^{19}$ boron/cm$^3$) substrate is representative of epi for CMOS devices. If the back surface of the substrate is not

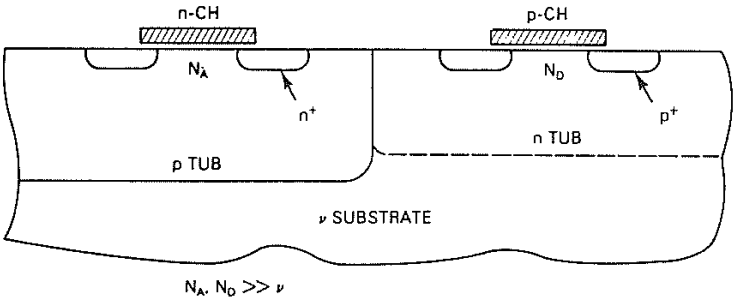


**Fig. 8-3** Cross section of a twin-well 1.2-$\mu$m CMOS structure.[5] Reprinted with permission of Semiconductor International.

sealed (e.g., by using a sealing layer such as undoped silicon dioxide or silicon nitride), boron evaporation from the substrate can contribute to autodoping on the front surface during the entire epi deposition cycle. This widens the epi/substrate interface and may even prevent the epi from reaching the 20 Ω-cm specified resistivity. Note that if silicon nitride is used as a sealing layer it should only be used in thin layers (e.g., less than 100 nm thick) since its high intrinsic stress causes it to bow the silicon.[9]

## 8.1.4 Twin-Well CMOS

With the twin-tub approach, two separate wells are formed for *n*- and *p*-channel transistors on a lightly doped substrate (Figs. 8-1c and 8-3). The substrate may be either a lightly doped wafer of *n* or *p* material, or a thin, lightly doped epitaxial layer on a heavily doped substrate. In either case, the level of the well surface doping is significantly lower than that required for building either the *p*- or *n*-channel MOSFETs. Each of the well dopants is implanted separately into the lightly doped surface region and is then driven in to the desired depth.

In twin-well CMOS, the doping profiles of each of the device types can be set independently, since the constraint of single-well CMOS does not exist (i.e., that the well doping must always be higher than the doping of the substrate in which one type of device is made). This was originally cited as an advantage of twin-well CMOS over single-well CMOS, with the argument made that both device types could thus be optimized.[12] This benefit for 1-2 $\mu$m CMOS has been questioned by Chen,[2] who points out that in modern single-well CMOS processes, an additional implant is used to prevent punchthrough without the need to raise the entire substrate-doping concentration. By incorporating this additional implant, it is possible to build higher-performance devices than can be achieved with the twin-well approach, in terms of junction capacitance and sensitivity to body effect.

Twin-well CMOS does offer some significant benefits for devices with submicron-channel lengths (although these advantages are gained at the cost of greater process

complexity). The first, and most important advantage arises when devices with submicron channel lengths are fabricated. Since it is recognized that the two device types perform similarly as channel lengths approach 0.5 $\mu$m, it is useful to provide symmetrical $n$- and $p$-channel devices. Furthermore, at submicron dimensions the body doping of both transistor types must be raised significantly to prevent punchthrough and to maintain adequate threshold-voltage levels. Thus, the advantage of having one type of MOS transistor in a lightly doped region (to optimize its performance at the expense of the other) disappears. It is instead more beneficial to produce two types of active device wells, each with its own optimized doping profile (i.e., formed by separate implants into a lightly doped substrate).*

The second advantage of the twin-well process is that it is compatible with the technologies of either isolation by selective epitaxial growth (SEG) or trench isolation.[1] Both approaches restrict the lateral diffusion of the dopants in each of the wells. In addition, sidewall inversion along the trench is less likely when both device sidewalls are butted against a trench that has been formed in a more highly doped well.[10] Finally, when deep trenches are used with a thin epitaxial layer on a heavily doped substrate, latchup can be eliminated. The combined use of the twin-well process and advanced isolation techniques allows $n^+$ to $p^+$ spacing to be dramatically reduced in comparison to single-well technologies.

A third benefit is that the combination of epitaxial substrates and the twin-well process allows either substrate type to be chosen with no effects on transistor performance and essentially no change in process flow. Such flexibility is useful since some applications are best met with $n^+$ substrates and others with $p^+$ substrates. This advantage may be important if a single process is needed for implementing designs with different applications.

Finally, self-aligned channel stops can be easily implemented in the twin-well approach, allowing the spacing between $n$- and $p$-channel devices to be reduced. Although this spacing reduction is not as great as it would be if trenches or SEG were used, the process is much less complex with the twin-well method.

A twin-retrograde-well 0.7-$\mu$m-CMOS process for fabricating 1-Mbit SRAMs has been reported.[11] The high energy implants also allow a restricted thermal budget to be used, thus reducing the up-diffusion from the $p^+$ substrate. This permits the use of a thinner epi layer (which also helps prevent latch-up), and allows implantation of the channel-stop dopants after the field oxide has been grown and planarized (consequently, minimizing lateral diffusion of the boron channel-stop dopants). We discuss retrograde-well CMOS in more detail in section 8.3.

* It is not useful to start with a substrate doped to the optimum level needed for just one of the submicron devices. If this were done, a single well of much higher doping would have to be established for the other type of submicron device, which would unnecessarily degrade the device performance. It is possible, with the twin-well approach, to have both types placed in a well of optimum doping profile.

### 8.1.5 Summary of CMOS Well-Technology Issues

The selection of a particular CMOS process depends largely upon circuit applications, and to a lesser degree on technology evolution. For VLSI circuits with 1-2 $\mu$m design rules *n*-well CMOS has been the more widely used single-well technology, both because *n*-channel devices can be optimized in the *p*-substrate and because most circuits use more NMOS than PMOS devices. In circuits that use transistor channel lengths smaller than 1 $\mu$m, twin-well and retrograde-well technology are more attractive. As noted, the price paid for their benefits is increased process complexity.

The optimum process-integration design strategy is to first select the well technology (and to decide whether or not to use epitaxial substrates), and then to select the isolation method. Once these decisions have been made, the well depth and doping profile can be determined. The well depth impacts the lateral-diffusion distance of the well and the vertical-punchthrough voltage. The doping profile affects transconductance, threshold voltage, source/drain punchthrough, junction capacitance, carrier mobility, source/drain-to-substrate breakdown, sensitivity to body effect, and hot-electron effects.

As previously discussed, early CMOS used lightly doped *n*-type wafers and diffused *p*-wells (in which the NMOSFETs were fabricated). The *p*-well approach was initially adopted because NMOSFETs could only be reliably produced in more heavily doped regions until ion implantation was developed in the mid 1970's (see chaps. 5 and 6, Vol. 2). Eventually, however, *n*-well as well as *p*-well single-well CMOS processes were implemented. Later twin-well processes were introduced, and these now dominate the newest CMOS fabrication lines (although older *n*- and *p*-well single-well technologies are still used to fabricate a variety of CMOS products).

The well-formation process was also one that quickly exploited the technology of ion implantation. The doping precision required in the well gave implantation a significant edge over diffusion as a method for introducing the dopants into the substrate. Advances in implantation technology are allowing development of processes involving multiple implants and higher energies to avoid the long, high-temperature drive-in and to form retrograde well profiles (as will be discussed in sections 8.3 and 8.4).

## 8.2 CONVENTIONAL FORMATION OF WELLS AND CHANNEL STOPS

There are several issues associated with conventional-well and channel-stop formation that are covered in this section, including: (1) alignment of subsequent patterns to the well locations; (2) process sequences for forming twin-well and channel-stop regions, and; (3) novel well-formation schemes that reduce mask count and process complexity.

### 8.2.1 Aligning Subsequent Patterns to the Wells

The wells are often the first features to be formed in the CMOS process flow. However, the implant process that introduces the well dopants does not produce visible features on the wafer surface. Thus, it is necessary to provide some indirect indication of the well locations so that subsequent layers can be aligned to them. Here we illustrate some

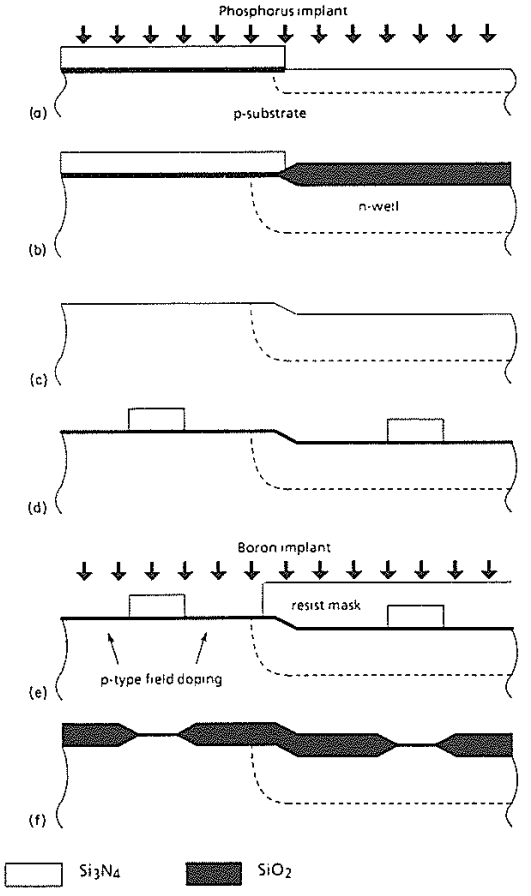


**Fig. 8-4** Conventional *n*-well architecture with *n*-well as first mask. (a) Pad oxide/nitride well mask and well implant. (b) Well oxidation and drive-in. (c) Nitride/oxide strip. (d) LOCOS pad oxide/nitride mask and active area definition. (e) NMOS field implant. (f) LOCOS field oxidation. A.G. Lewis and J.Y. Chen, "Current Trends in MOS Process Integration," in N.G. Einspruch and G. Gildenblatt, Eds. *Advanced MOS Device Physics,* Academic Press, San Diego CA, 1989, Reprinted with Permission.

methods that have been developed to provide such alignment marks. For simplicity we utilize an *n*-well CMOS structure in depicting the process flows, but later we show how these methods can be incorporated into twin-well CMOS processes.

In the first approach the wells are the initial features created on the wafer. Here a nitride mask is employed to both define the well locations and to serve as an oxidation mask (see Fig. 8-4a and 8-4b). That is, the patterned nitride/resist layer blocks the phosphorus *n*-well-implant from penetrating to the *p*-substrate (or *p*-well) regions. Part of the drive-in step after the implant is carried out in an oxidizing ambient with the nitride mask layer left in place. This causes a thermal oxide layer to be grown selectively over the *n*-well regions. At the conclusion of the drive-in process, this oxide is stripped. Since the oxide growth consumes some silicon in the *n*-regions and since no such silicon loss occurs in the regions covered by the nitride mask, a step is produced on wafer surface when the oxide is stripped (Fig. 8-4c). This step is also is self-aligned to the well edge, therefore providing a visible indication of the well boundaries that allows the active area features to be aligned to them. (Subsequent layers, however, are usually aligned to the active area.) The disadvantage of this approach is the step that is created on the wafer surface. In submicron processing such nonplanar topography is undesirable.

The second approach is a simpler process and it also avoids the creation of the step produced in the previous method (see Fig. 8-5). Here, however, the first features to be defined are the active areas (Mask #1). That is, a nitride mask stack layer is patterned first and all subsequent layers are aligned to the active area pattern. Then the well mask (Mask #2) is aligned to the active area pattern, and the well implant is performed. Note that the implanted dopants must penetrate the nitride mask stack. This does not present a serious difficulty, but it does mean that the *n*-well tends to be shallower and slightly less-heavily doped beneath active regions than under the field areas. Both the first and second approaches require three masking steps (including the boron channel-stop implant that is performed after the well implant - but prior to the LOCOS field oxidation process). However, the second approach offers the benefit of needing fewer oxidations and depositions.

The first method can be applied to a twin-well process by growing an oxide after the *n*-well implant (Mask #1), but not doing much of the drive-in step during this oxidation. Then the nitride mask is stripped and a second *p*-well mask is aligned to the *n*-well oxide (Mask #2). After doing the *p*-well implant the well drive-in process is performed. An even easier (i.e., one mask) procedure would be to use the *n*-well oxide to mask the *p*-well implant (instead of using the second mask). The second method can also be applied to a twin-well process but two masks must be used to create the twin wells. However, if a shallow *p*-well is acceptable, the same resist mask that is used to form the channel-stop region in Fig. 8-4e (Mask #3) can be used to form the shallow *p*-well. In this case the *p*-well implant must be performed at a higher energy than the field implant in order to penetrate the thin nitride mask layer.

The third method utilizes an initial alignment mark etched into the silicon surface prior to forming any device features. This mark is also used as an automatic alignment target by the wafer stepper. Figure 8-6 shows an example of such an alignment pattern.[16] The use of such initial alignment marks is likely to increase with the proliferation of automatic stepper alignment.

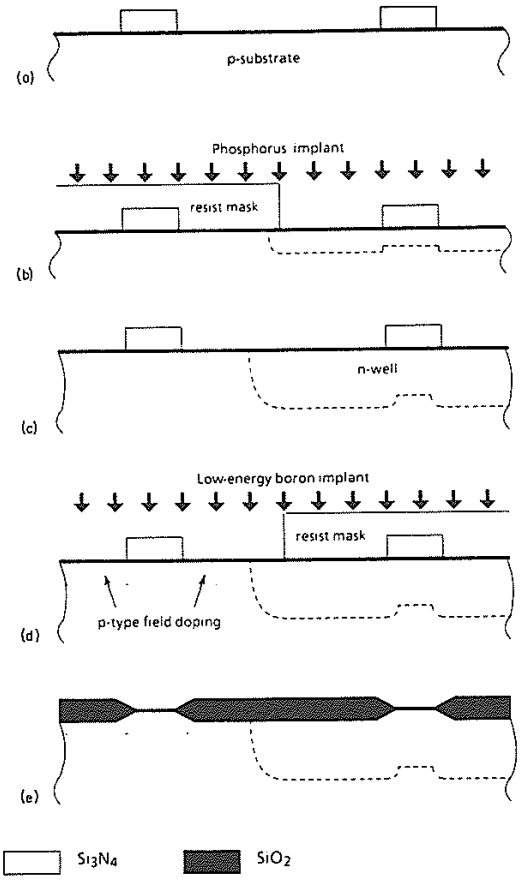


**Fig. 8-5** Conventional *n*-well architecture with active area as first mask. (a) Active area definition using LOCOS nitride mask. (b) *n*-well mask and implant. (c) *n*-well drive-in. (d) boron field implant, and (e) LOCOS field oxidation. A.G. Lewis and J.Y. Chen, "Current Trends in MOS Process Integration," in N.G. Einspruch and G. Gildenblatt, Eds. *Advanced MOS Device Physics,* Academic Press, San Diego CA, 1989, Reprinted with Permission.

## 8.2.2 Twin-Well and Channel-Stop Formation.

The most obvious method of forming twin wells is to use two masking steps, each of which blocks one of the well implants. A procedure for forming twin-wells with a single masking step, however, has also been suggested (see Fig. 8-7).[12] In this method,

a single mask is used to pattern a nitride/oxide film formed on the bare silicon surface (*Mask #1*). The openings in the film become the *n*-well regions, and phosphorus is implanted into them (e.g., at 80 keV). Next, a thermal oxide is selectively grown on the *n*-well regions, to a thickness that is sufficient to block the boron implant used to form the *p*-wells. (The nitride mask layer is used to prevent the oxide from growing in the *p*-well regions.) The pad-oxide/nitride mask layer is then stripped, exposing the silicon in the *p*-well regions. The *n*-well regions are however, still covered with the oxide grown earlier. Thus, during the *p*-well implant (e.g., at 50 keV), this oxide masks the *n*-well regions, permitting the boron to enter the silicon only in the *p*-well areas.

Next the wells are driven in (e.g., at 1100°C for 500 min). At the conclusion of this drive-in step the concentrations in the wells for an 0.8-$\mu$m-CMOS process are ~$1\times10^{16}/cm^3$ for the *p*-well, and ~$3\times10^{16}/cm^3$ for the *n*-well. The *n*-well is selected to have a higher doping concentration (i.e., to improve the punchthrough performance of the PMOS devices and to eliminate the need for a separate channel-stop implant for the *n*-well). A higher concentration in both wells would still produce devices with relatively low capacitances at the bottoms of the source/drain-to-well junctions.

The channel-stop implant procedure is also usually included in the part of the processing sequence in which the wells are formed. In one reported twin-well process,[13] only a *p*-well channel-stop implant (boron) is used, because the doping in the *n*-well is high enough ($3\times10^{16}$ $cm^{-3}$) that a separate channel stop implant is not required. In this case, an unmasked boron implant is performed following both well implants, but prior to field-oxide growth.

In a second approach,[14] an additional mask can be used to provide both *n*-well and *p*-well channel stops (Fig. 8-8a). Note that in this procedure, a mask is saved by

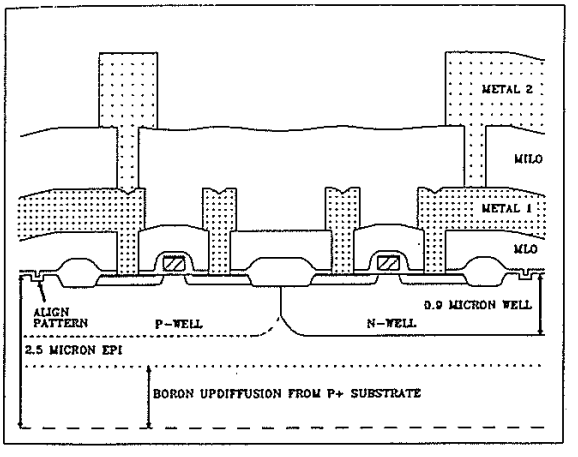


**Fig. 8-6** Twin-well CMOS showing initial alignment mark.[16] (© 1991 IEEE).

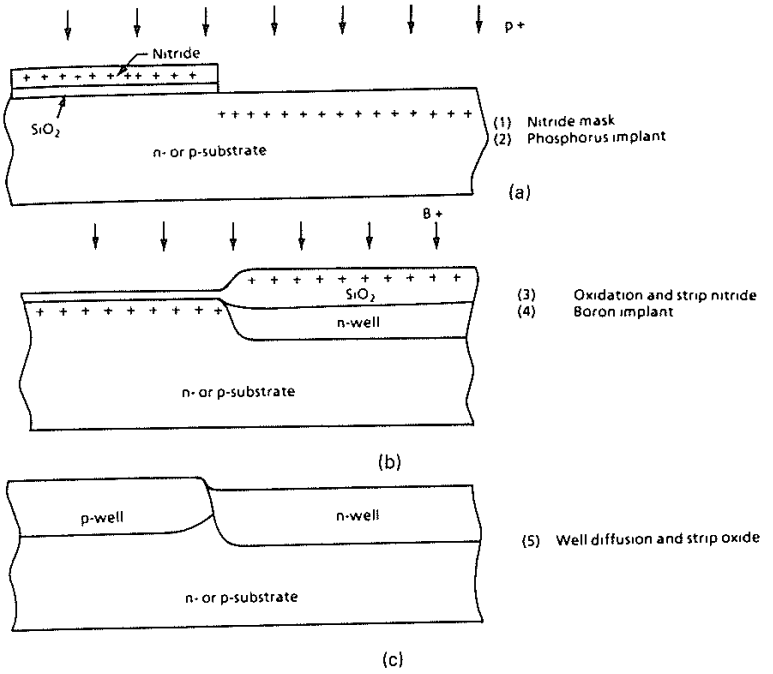


**Fig. 8-7** Twin-well CMOS process using a single mask to form both wells. (a) $P^+$ implant for the *n*-well. (b) $B^-$ implant to form the *p*-well (blocked by the *n*-well oxide). (c) well drive-in for both wells.[12] (© 1982 IEEE).

performing a blanket boron implant. As a result, the boron channel stop dopant ends up in the *n*-well as well as in the *p*-well. Hence, the phosphorus channel stop dose must be increased to compensate for the boron's presence in the *n*-well field regions. The disadvantages of this method include the additional alignment step between the channel stops and the well masks, the interdiffusion that occurs during the oxidation step, and the asymmetry of the doping profiles. (The latter is due to the increased phosphorus concentration that must overcompensate the nonselective boron channel stop).

A variation of this method that requires no masks at all to create the channel stops has been developed to overcome the above drawbacks (Fig. 8-8b).[14,15] In this sequence, both arsenic and phosphorus are co-implanted into the *n*-well regions. This places both the dopants that form the well and the channel stop into the *n*-well regions prior to implanting of the *p*-wells. An oxide is then selectively grown on the *n*-well regions and the boron dopant for the *p*-wells is implanted. After the wells have been driven in, the oxide over the *n*-wells is retained, and a second boron implant is carried out. This implant serves as both a channel stop in the *p*-well *field* regions and a punchthrough-prevention implant in the *active* regions of the *p*-well.

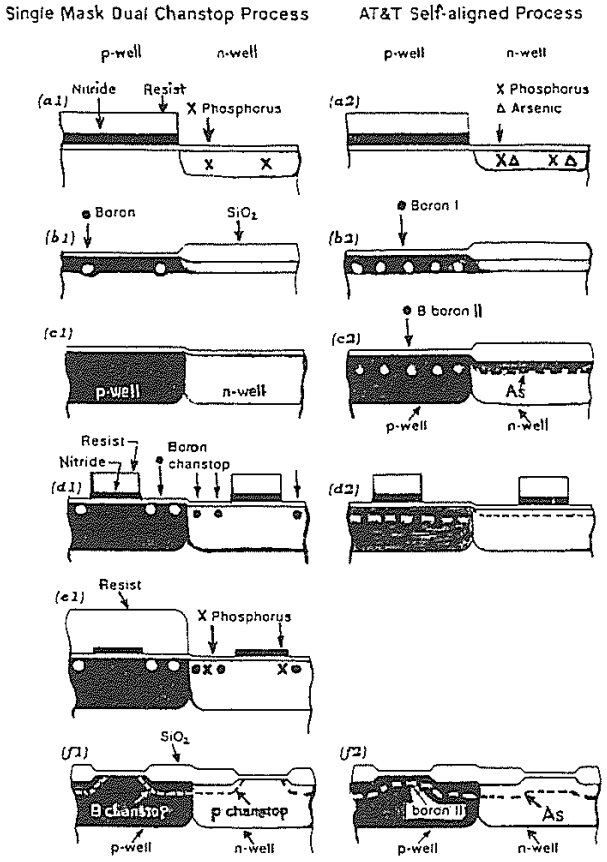


**Fig. 8-8** (a) Twin-well CMOS with a single-mask dual channel stop process. (b) ATT twin-well CMOS process which requires no masks to form the dual channel stops (self-aligned process.)[15] (© IEEE 1981).

It should also be noted that the minimum separation between two wells of the doping type at two different potentials is limited by electrical isolation. In single-well processes, to prevent punchthrough in the lightly-doped substrate between two such wells, adequate spacing between them must be allowed.

## 8.2.3 Split Well-Drive-In Process

In another report, the long, high-temperature drive-in step is performed in a novel manner, allowing the *p*-well transistors to be fabricated without use of a channel-stop

implant.[17] After the *p*-well implant is carried out, the field oxide is first grown without driving the implanted well dopants. During this step, some of the implanted boron impurities segregate into the field oxide, leaving a surface concentration as low as would exist after any field oxide step. Next, the remainder of the well drive-in step is performed in a non-oxidizing ambient. The well dopant deep in the bulk now back-diffuses toward the surface, raising the Si-$SiO_2$ interface concentration by a factor of 2-3 (to 2-3x$10^{16}$ $cm^{-3}$ in this case, see Fig. 8-9). The well concentration at surface of the field regions is only about 1.5x lower than at the surface in the active regions. $V_{TFiso}$s greater than 10 V (at $I_D$ at 0.5 pA/$\mu$m at $V_{DS}$ = 8V) can be produced for isolation lengths of 1.2 $\mu$m. It has been observed that for very narrow NMOSFETs (e.g., 0.35 $\mu$m) fabricated with the split-well drive-in scheme, $V_T$ is decreased by ~100 mV compared to wider channel devices (e.g., 5 $\mu$m). This occurs because boron also diffuses from the channel regions to the field regions during the post-oxidation drive-in step. Such diffusion occurs because, as described earlier, the boron concentration at the silicon surface in the field regions has been reduced during the field oxide step by boron segregation effects.

## 8.3 RETROGRADE-WELL CMOS

As previously discussed, conventional wells are formed in single- and twin-well CMOS technology by implanting the well dopants and then diffusing them to the desired depth. However, lateral as well as vertical diffusion occurs, which has the effect of reducing packing density. For example, since the lateral diffusion is ~0.7 times the junction

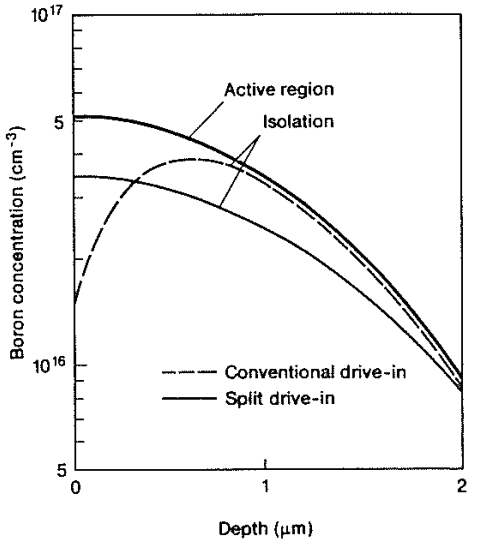


**Fig. 8-9** SIMS profiles of boron well underneath field oxide and in the active aréa for split and non-split drive-in. Implanted boron dose: 8x$10^{12}$ $cm^{-2}$. The active area profile is the same for both drive-in cases.[17] (© 1990 IEEE).

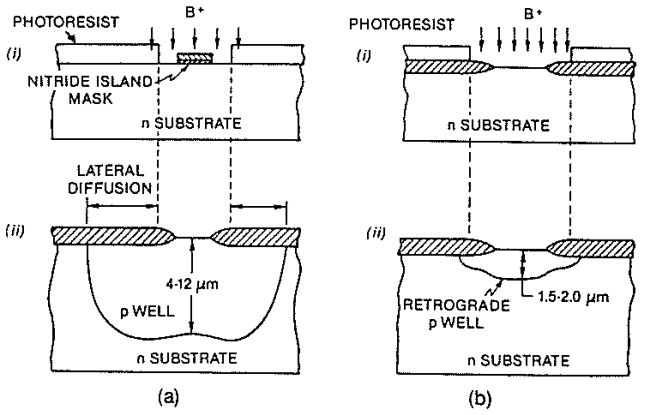


**Fig. 8-10** Formation of (a) conventional and (b) retrograde $p$-well CMOS structures.[19] (© 1981 IEEE).

depth, a typical diffused well of 3 to 4 $\mu$m results in a lateral spread of well dopant of ~2 to 3 $\mu$m. If a higher energy implant is used to place the dopants at the desired depth without significant additional diffusion (i.e., the high-energy implant is performed after the active area isolation structures [field oxide] is already in place, and only a short anneal at a relatively low temperature is used to activate the implant), much less lateral dopant spread occurs. This is because ion implantation is a more anisotropic dopant distribution process than diffusion. That is, the lateral implant straggle is ~0.7 $\mu$m and barely exceeds one micron after all thermal processing.[18] In addition, since the high-energy implanted wells are formed after the LOCOS isolation step, lateral spread of the well dopants is further reduced. Hence, the 7-9 $\mu$m $n^+$-to-$p^+$ spacing required for a twin-well 1.2 $\mu$m CMOS process which uses conventional wells, can be reduced to ~5 $\mu$m if retrograde wells are used instead.

Figure 8-10 depicts the cross-section of a high-energy implanted $p$-well in comparison with a conventional diffused well. In this example, the implanted $p$-well is formed by boron implantation at 400-600 keV, followed by a brief 30 min anneal at 1000°C (instead of the 6-20 hour drive-ins at 1100-1150°C used for conventional-well formation). Notice the lateral spread associated with the $p$-well is greatly reduced.

Such high-energy implants also cause the peak of the implant to be buried at a certain depth within the silicon substrate (depending on the implantation energy, but at roughly 1 $\mu$m for the energies most frequently used), and the impurity concentration decreases as the doping profile approaches the wafer surface (see Fig. 8-11). Since the well profile in this case is different from that of conventionally formed wells (in which the doping concentration after drive-in is highest at the surface, and decreases monotonically with depth), such deeply implanted wells are known as *retrograde wells*. It is estimated that, in order to avoid excessive spread of the active device electrical

parameters, the surface concentration after the retrograde implant should be at least five times smaller than its final value, which is set by shallower low-dose implants specifically designed for threshold and punchthrough control. Comparison of the doping profiles in conventional and implanted *p*-well profiles (obtained by simulation) is shown in Fig. 8-11.[19] The retrograde-doping profile is retained by minimizing the temperature cycles of later process steps (e.g., by using RTP). Retrograde wells can be implemented on both bulk and epitaxial wafers.[20]

Besides the potential benefit of increased packing density, retrograde wells offer the following advantages:[1]

**1.** A retarded electric field is created in the parasitic vertical bipolar transistor, thereby reducing its current gain. This affords some protection against latchup.

**2.** Susceptibility to vertical punchthrough is reduced without having to significantly raise the surface doping concentration.

**3.** The conductivity in the bottom of the well is increased, which also provides additional latchup protection.

**4.** A higher threshold voltage can be achieved in the field regions of the *p*-wells if the boron implant is done following field oxidation (i.e., the boron does not segregate out into the oxide during the field oxide growth step).[19]

**5.** Lateral diffusion of the channel-stop boron is also eliminated, thereby reducing encroachment of the boron into the active regions. This lessens narrow width effects in the active devices.

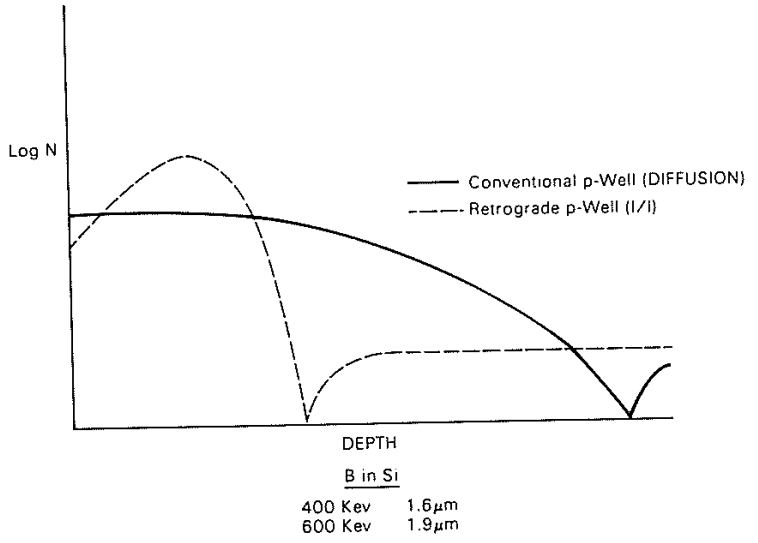


**Fig. 8-11** Comparison of conventional and retrograde well *p*-well profiles.[19] (© 1981 IEEE).

**6.** Greater flexibility exists in retrograde structures to optimize channel doping profiles for active device performance. That is, in conventional wells (especially shallow ones), the surface doping is primarily determined by the need to maintain sufficient vertical isolation. In retrograde structures, however, vertical isolation is secured by the high doping level towards the well bottom. Thus, it is possible to adjust the surface doping profile to a larger extent. This helps to achieve adequate short-channel device characteristics with retrograde wells.

**7.** The shallower well depth should also make the drain of the parasitic $n^+$-to-$n$-well (or $p^+$-to-$p$-well) parasitic FETs shallower. This should improve both the short-channel threshold roll-off and the punchthrough characteristics of these parasitic structures, as is discussed further in chap. 6.

However, several concerns associated with the retrograde process should also be mentioned. First, the process requires a thick photoresist as a masking material for the high-energy implant. Typical resist thicknesses are about 5 $\mu$m, and special exposure and development techniques are required for this process. Second, there is concern about the annealability of the damage caused by the high-energy implant. Third, the retrograde implant may cause both the junction capacitance and the body factor to be significantly increased. The $p^+$-to-$n$-well junction capacitances measured in retrograde-well structures formed with a 700 keV implant have been shown to be about twice the values obtained in conventional wells. While this can adversely impact the propagation delay, circuit performance is also impacted by a number of other parasitic capacitances, and the net result on typical CMOS circuit speed and power dissipation is often relatively small. For example, in a simulation of a 32-bit CMOS arithmetic logic unit (ALU), it was found that the circuit delay increases by about 7% as the $p$-channel junction capacitance increases by 30 percent.[1]

When the retrograde well is formed by means of very high-energy implants, however, the doping concentration under the bottom of the source and drain regions is decreased, which reduces the junction capacitance. This implies that if such high-energy ion implanters (~1 MeV) become available for production, some of the disadvantages of retrograde wells can be overcome.[18] In addition, the higher doping that will be required in the wells for fabrication of submicron CMOS devices may mean a less severe junction capacitance penalty.

Although both $p$-type[21] and $n$-type[22] retrograde wells have been demonstrated (see Figs. 8-12a and 8-12b,[20] and Fig. 8-12c,[23] respectively), the $p$-type technology has been more widely implemented. This is because at least 600-keV beam energies are required for the formation of $n$-type (phosphorus) retrograde wells suitable for 0.5-0.8 $\mu$m CMOS. As of 1994 such machines were commercially available, but had only begun to be introduced into mainstream production environments. Retrograde $p$-type wells adequate for 0.5 $\mu$m devices require implants with energies of ~300 keV at a dose of ~$1\times10^{13}$ cm$^{-2}$. Such $p$-well implants can be achieved by implanting singly ionized boron at 300 keV or doubly ionized boron at 150 keV. (The required $p$-well energy is smaller because boron has a larger projected range than either As or P; see Vol. 1, chap. 9). Although the doubly ionized boron approach is achievable with conventional

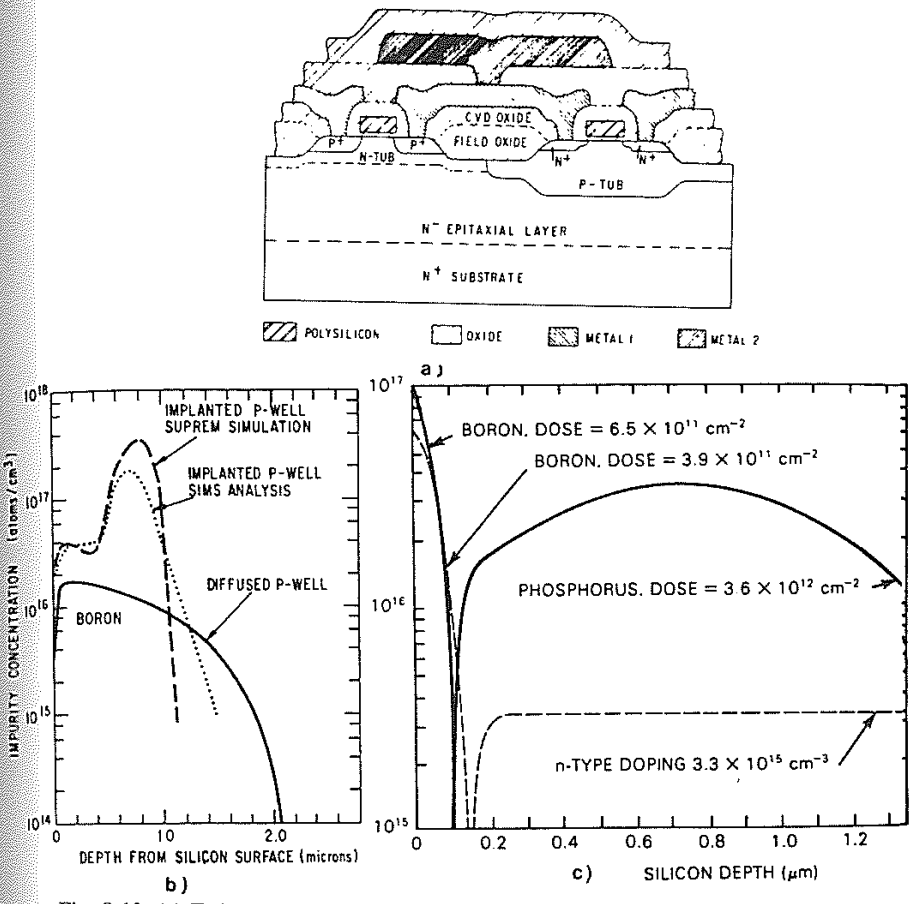


**Fig. 8-12** (a) Twin-tub device cross section in which a retrograde *p*-well is used. General Electric AVLSI Process. (b) Retrograded *p*-well implanted impurity concentration profile. General Electric AVLSI process. Also shown is a conventionally thermally diffused well.[20] (© 1986 IEEE). (c) Simulated doping profiles in PMOS channel regions: dashed lines, lightly doped substrate; solid lines, retrograde *n*-well.[23] (© 1982 IEEE).

production implanters it is not a routine process to implement.* Subject to the precautions mentioned in the footnote, retrograde well CMOS processes have been

* One problem is that a large fraction of double-ionized ions, as high as 20%, can interact with gas molecules at the entrance of the acceleration column and become single-charged ions because of partial neutralization. These ions would only penetrate into silicon about half the desired range, distorting the profile and causing abnormalities of the threshold

the successfully implemented in a production environment with good results. However, these have primarily been limited to custom and advanced system applications, where higher costs of retrograde well processing are justified by the higher density and performance benefits offered by the retrograde-well device structures.

Two examples in which a 300 keV boron implant is used to form a retrograde *p*-well CMOS structure have recently been published. In the first, this *p*-well structure (together with a 1.2 $\mu$m epi layer) allowed an NMOS device-to-device spacing of less than 1 $\mu$m to be used when an optimized field implant was employed.[25] In the second, the *p*-well was fabricated with a 320 keV implant (using, in fact, doubly-charged boron accelerated at 160 keV), and a 5 min 1100°C RTP anneal. Together with the use of a 2-2.5 $\mu$m epi layer, a sub-half micron CMOS structure was fabricated (which permitted an $n^+$ to $p^+$ spacing of less than 2.5 $\mu$m).[16]

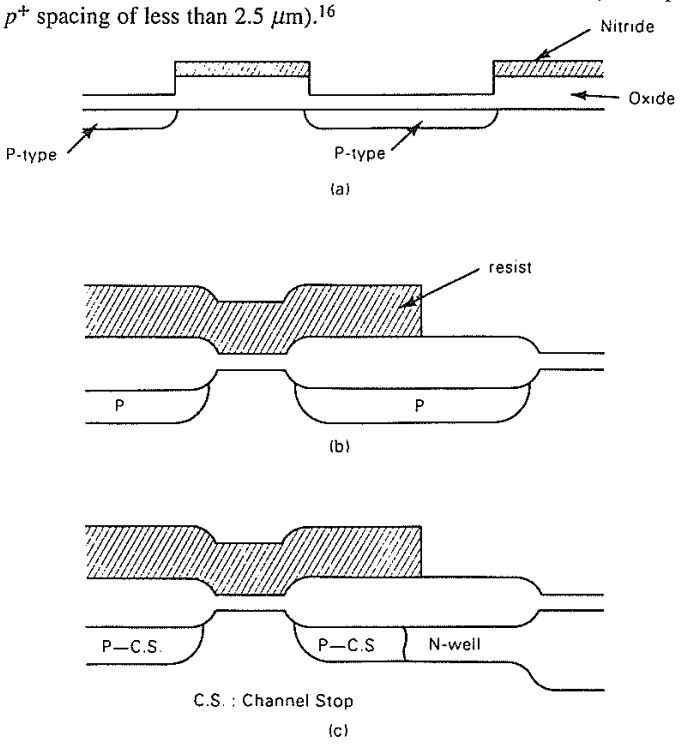


**Fig. 8-13** A simplified retrograde *n*-well process. (a) Nitride mask for active area and $B^+$ implant for *p*-type channel stop.; (b) photoresist mask for *n*-well; and (c) high energy $P^+$ implant and any additional shallow implants in the *n*-well.[18] (© 1986 IEEE).

* (cont.) voltage and other electrical parameters. Thus, if a high-current implanter is not available, a medium-current implanter of the post-analysis type should be used to eliminate single-charge ions before they reach the wafers.[24]

However, an $n$-well retrograde CMOS process using a 700-keV phosphorus implant has also been demonstrated.[18] The process sequence used to form this retrograde $n$-well CMOS structure (with the well implant performed after field oxidation) is shown in Fig. 8-13. The active areas are first defined using nitride masking. Next, a blanket low-energy boron channel-stop implant is performed. The field oxidation is then carried out and the retrograde $n$-well implant step is performed. A 30 minute, 1000°C anneal follows the implant. Note that the blanket boron channel-stop dopant is overcompensated in the $n$-well regions by the phosphorus implant. This retrograde-well process permits very small (~2 $\mu$m) $n^+$-to-$p^+$ spacings.

Some advanced twin-well CMOS processes with both retrograde $n$- and $p$-wells, (using short [~5 min] RTP well-drive-in steps), have also been reported for submicron applications.[26] Scaling CMOS to 0.5 $\mu$m and below reduces the well depths required to prevent vertical punchthrough and latchup. In addition, the well depth and well-dopant concentration can be reduced if additional, lower energy implants are precisely located with respect to the transistor structure to suppress punchthrough of the MOSFET channels and to enhance the field isolation characteristics.

One novel method of achieving such short well-drive-in times is to enhance the effective diffusion rate. It has been demonstrated that the diffusion of boron and phosphorus is substantially enhanced by oxynitridation in an $NH_3$ ambient with a thin oxide layer over the diffusion region.[27*] These factors combine to produce a trend of lower implant energy in retrograde wells for scaled devices at and below 0.5 $\mu$m.

A twin-retrograde-well 0.7-$\mu$m-CMOS process for fabricating 1-Mbit SRAMs on $p^-$-on-$p^+$ epi substrates has been reported.[11] The high energy implants also allow a restricted thermal budget to be used, thus reducing the up-diffusion from the $p^+$ substrate. This permits the use of a thinner epi layer (which also helps prevent latch-up), and also allows implantation of the channel-stop dopants after the field oxide has been grown and planarized (thus minimizing lateral diffusion of the boron channel-stop dopants).

The use of retrograde wells for both the $n$- and $p$-wells of a twin-tub CMOS process has also been reported.[29] The approach was called *quadruple-well CMOS* to emphasize the fact that for each type ($n$- or $p$-well), two wells were needed, one in the active area, and another, shallower one in the field region. The deep and shallow wells, however, are created simultaneously using the same higher energy implant steps. That is, since the implant is carried out after the field oxidation (and after the LOCOS nitride mask has been stripped), in regions of the wafer where no field oxide exists the implant penetrates deeply, but in regions where the implant must penetrate the field oxide, it enters the Si substrate less deeply (creating a shallower well there).

Another approach for fabricating retrograde wells without the need for very high ion implantation is to use epitaxy. Such a method for forming an $n$-well CMOS structure is shown in Fig. 8-14. Shallow, heavily doped wells are formed in the $p$-substrate by ion implantation of a slow diffusing dopant (typically arsenic) in order to prevent significant redistribution during subsequent processing. A $p$-type epitaxial layer is then grown to a thickness of a few microns, creating an $n^+$ buried layer. A low-energy phosphorus implant is then used to complete the $n$-wells. No drive-in is needed if it is

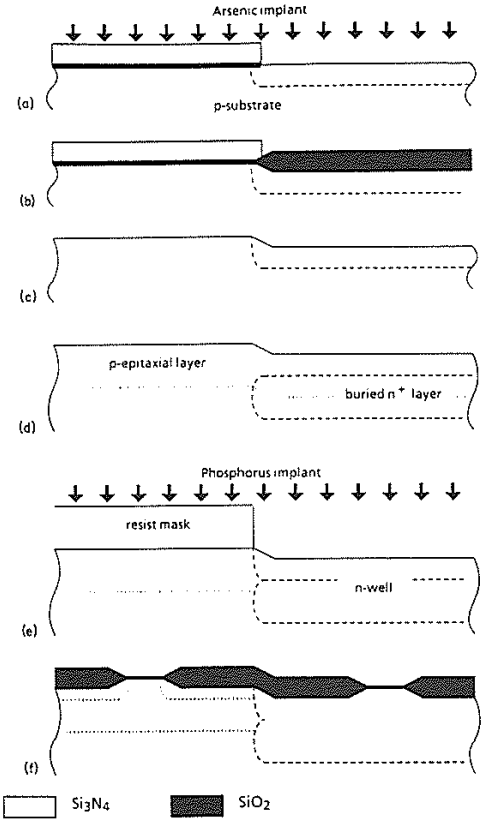


**Fig. 8-14** Retrograde *n*-well architecture based on epitaxy. (a) Oxide/nitride well mask and buried layer implant. (b) Well oxidation. (c) Nitride/oxide strip. (d) Epitaxial growth. (e) Surface *n*-well implant. (f) Boron field implant and standard LOCOS field oxidation. From A.G. Lewis and J.Y. Chen, "Current Trends in MOS Process Integration," in N.G. Einspruch and G. Gildenblatt, Eds. *Advanced MOS Device Physics,* Academic Press, San Diego CA, 1989, Reprinted with Permission.

arranged that the surface phosphorus implant merges with the buried layer to complete the *n*-well. The formation of buried layers in this way is especially well-suited to BiCMOS technologies.

### 8.3.1 Retrograde Well Technologies to Improve Isolation

Since retrograde wells are formed by a high-energy implantation step following the LOCOS oxidation growth process, lateral diffusion of the well dopants is greatly reduced compared to a conventional well process. This results in significant saving of layout space. Isolation among opposite type devices is also expected to be improved.

Here we present data that supports this latter claim, as a supplement to the material on isolation presented in chap. 6.

The comparison of isolation performance between conventional-well and retrograde-well CMOS structures was performed using an $n$-well process and aluminum-gate MOSFETs.[18] To establish a fair comparison, equal well depths were used in the active area of both the conventional-well and retrograde-well structures.

The process sequences used to form both the conventional-wells and retrograde-wells in an $n$-well CMOS process are shown in Figs. 8-15a and 8-15b, respectively.[30] The active areas are first defined in both structures using nitride masking. In the retrograde structures, a blanket low-energy boron channel-stop implant is performed next. In the case of the conventional well, the $n$-well resist mask is aligned to the patterned nitride, and the $n$-well implant (phosphorus) is carried out, followed by a blanket low-energy boron channel-stop implant. The field-oxide is now grown on both structures. In the retrograde-well structure, the $n$-well implant step is carried out after the field oxidation, followed by a short (~30 min) anneal at 1000°C. In both structures, the boron channel stop dopant is overcompensated in the $n$-well regions by the phosphorus implant.

Because the retrograde well is formed by high-energy ions penetrating the field oxide in the field regions the well depth there is only half of the well depth in the active regions. The shallower well depth in the field regions of the retrograde-well structure (compared to the well field-region depth in the conventional-well structure) is advantageous. That is, it creates a shallower drain for the $n^+$-to-$n$-well parasitic FET,

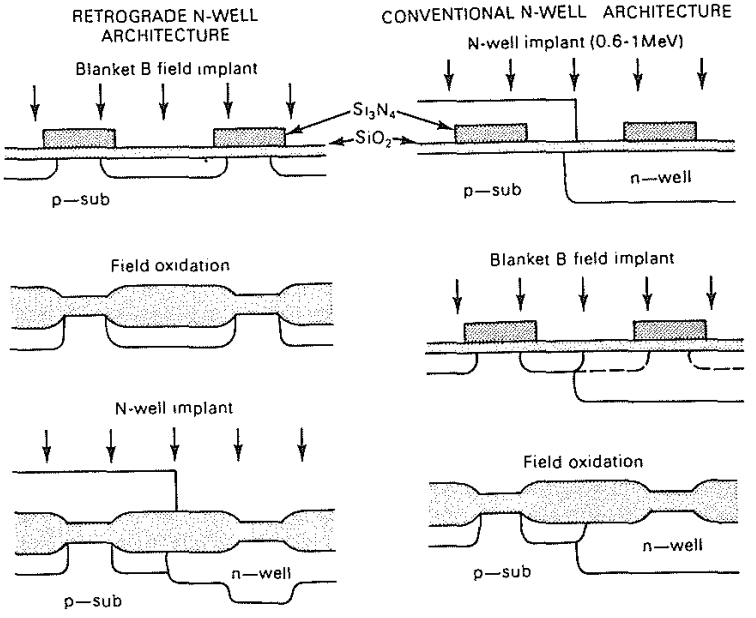


**Fig. 8-15** Process architectures for retrograde and conventional $n$-well CMOS structures.[30]

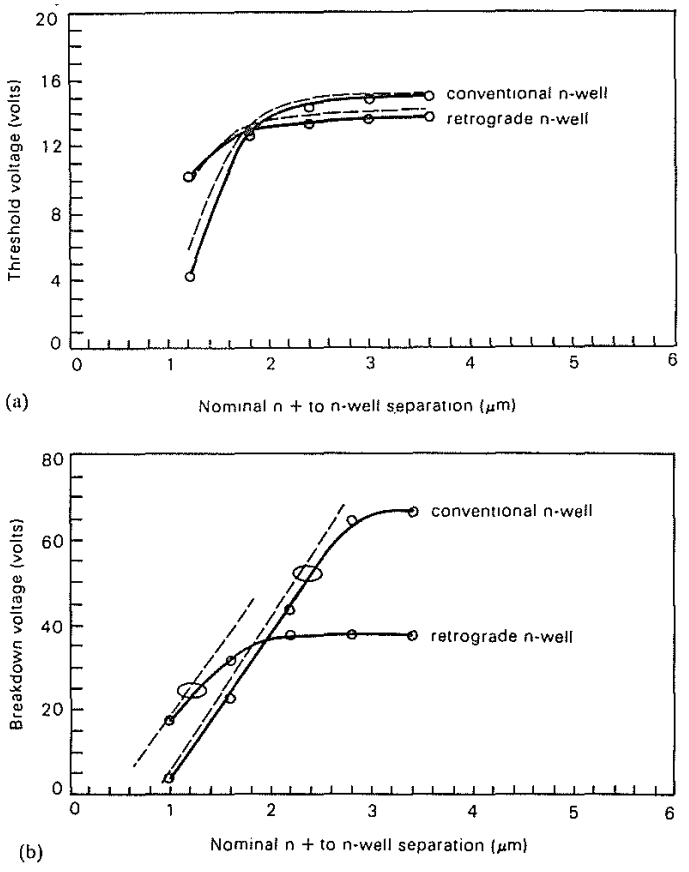


**Fig. 8-16** Comparison of retrograde and conventional well structures for $n^+$ to $n$-well parasitic FETs: (a) field threshold voltage; and (b) $n^+$-to-$n$-well breakdown voltage. Solid lines: experimental data, dashed lines: modeled results, breakdown voltage is modeled by punchthrough only.[37] (© 1987 IEEE).

thereby improving isolation. At the same time, the depth of the well in the active region is greater, so that the performance of the devices in the well are not significantly degraded because the $n$-well doping concentration near the surface remains sufficiently low. In addition, in the active regions the peak of implanted profile is near the bottom of the well, which is beneficial for vertical isolation. Meanwhile, the implant profile peaks near the Si surface in the field areas, which is again better for producing a channel stop and for preventing $p^+$-to-$p$-substrate lateral punchthrough.

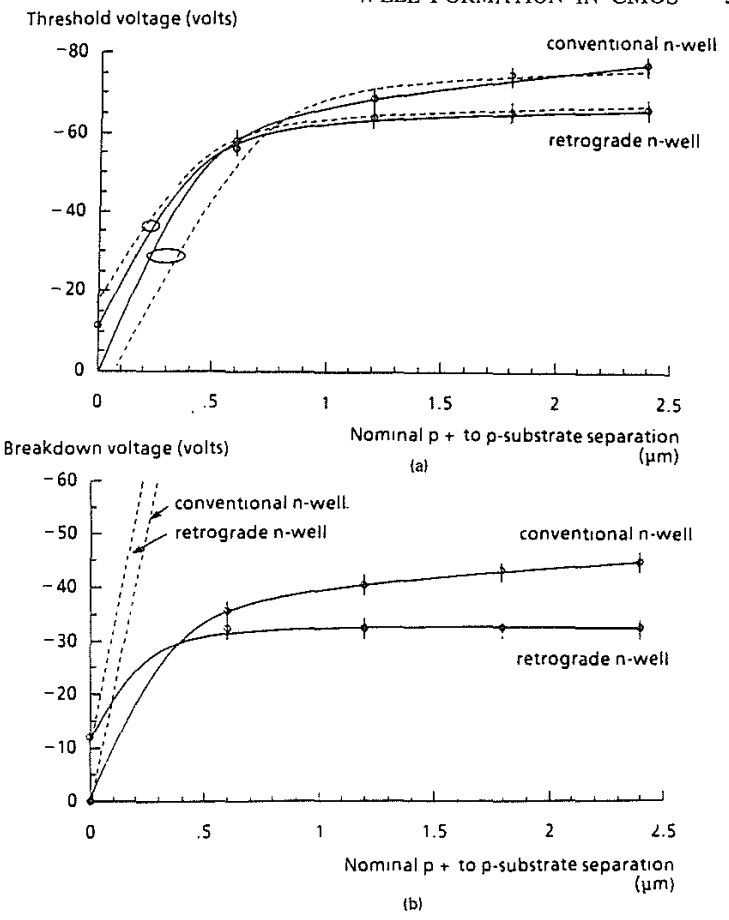


**Fig. 8-17** Comparison of retrograde and conventional well structures for $p^+$ to $p$-well parasitic FETs: (a) field threshold voltage; and (b) $p^+$-to-$p$ substrate breakdown voltage. Solid lines: experimental data, dashed lines: modeled results, breakdown voltage is modeled by punchthrough only.[37] (© 1987 IEEE).

The measured and simulated $V_{TFiso}$s and breakdown voltages (all defined at a drain current in the parasitic FET test structure of 10 pA) for $n^+$-to-$n$-well parasitic transistors in both the conventional and retrograde aluminum-gate CMOS test structures are shown in Figs. 8-16a and 8-16b. At large $n^+$-to-$n$-well separations, avalanche breakdown at the well-substrate junction occurs before lateral punchthrough occurs. The lower value of avalanche breakdown in the retrograde structures is attributed to higher well doping. As described earlier, shallower retrograde wells should exhibit less propensity to degradation

caused by short-channel effects (e.g., to threshold lowering and DIBL). These predictions are confirmed from the experimental $V_{TFiso}$ and punchthrough data.

Figure 8-17a gives the $V_{TFiso}$ values for lateral $p^+$-to-$p$-substrate parasitic devices. The absolute values are much larger than those for the $n^+$-to-$n$-well devices. These higher values are due in part to the greater field doping required in the $n$-well to guaranty sufficient compensation of the boron. The larger values are also partly caused by the fixed charge at the Si-$SiO_2$ interface, which is generally positive and thus increases the magnitude of the threshold voltage of the $p$-channel transistors. It is also evident that short-channel effects are much less severe in these $p$-channel parasitic devices, especially for the retrograde structures; the thresholds do not decrease until the channel length approaches 0.5 $\mu$m. This effect is caused by the higher channel ($n$-well) doping in these parasitic transistors, and to the drain (substrate) doping being lower than the channel ($n$-well) doping.

Figure 8-17b depicts the breakdown voltages exhibited by the same $p^+$-to-$p$-substrate devices, and comparison with Figs. 8-17a and b again shows the superior performance of these structures. In these types of parasitic FETs, the $p$-substrate, which is considered to be the drain, is not only deep but wraps around under the source (see Fig. 6-45). Thus, both lateral and vertical leakage paths may possibly exist between the $p^+$ source and the $p$-substrate. The limiting values of breakdown voltage for retrograde $n$-well structures is set by well to substrate avalanche breakdown, as is the case of the $n^+$-to-$n$-well transistors. In conventional wells, however, the limit is set by $p^+$-to-$p$-substrate vertical punchthrough breakdown. Thus, the maximum breakdown voltage shown on Fig. 8-17b for these devices is not the same as that shown in Fig. 8-16b, even though the drain-channel junction is in fact the same in both cases.

The application of retrograde wells for both the $n$- and $p$-wells to a twin-tub CMOS process has also been reported. The approach, as described in the previous section, was called *quadruple-well CMOS* to indicate that for each well type (i.e., $n$- or $p$-), two wells were needed, one in the active area, and another, shallower one in the field region (see Fig. 8-18). The two shallow wells actually function as self-aligned channel stops, in which the surface concentration of the well dopants is tightly restricted on each side of the well boundary. That is, as shown in Fig. 8-19 the reduction of the net impurity concentration is restricted to a small distance from the boundary of the well edge. Specifically, the surface doping concentration near the well boundary is decreased significantly only within a few tenths of a micron from the boundary, instead of a few microns, as occurs in a conventional twin-well structure (see Fig. 6-47). Experimental data shows that at a 4 $\mu$m $n^+$-to-$p^+$ separation, subthreshold leakage in the isolation region is <1 pA for gate voltages between -15V and +20V (Fig. 8-20). Simulation data indicate that it is possible to obtain adequate isolation with a 2 $\mu$m $n^+$-to-$p^+$ separation.

A CMOS process based on high energy implantations without epi-layers or trenches that allows $n^+$-to-$p^+$ spacings as small as 1.5 $\mu$m has been reported. To realize such small isolation spacing, the $n$-well was formed with 700 keV, $1 \times 10^{13}$ $cm^{-2}$ phosphorus and 1.5 MeV, $3 \times 10^{13}$ $cm^{-2}$ boron implantations. A unique feature of the well structure in this report is that these same two implantations simultaneously form not only the two retrograde wells and the $n$-well and $p$-well channel stops, but the boron implant also

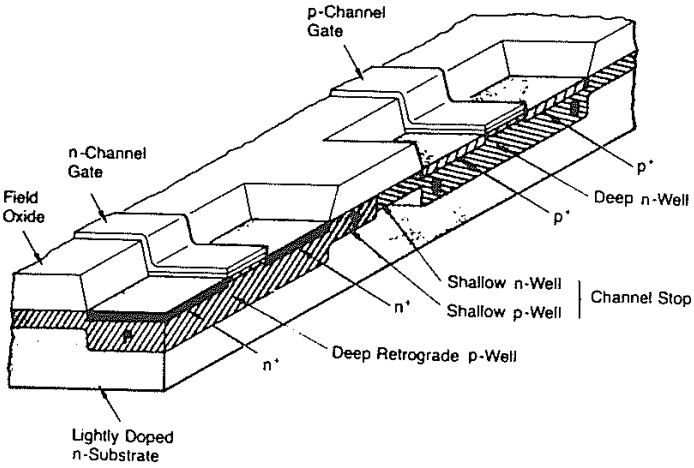


**Fig. 8-18** Cross section of a quadruple-well CMOS device.[36] Reprinted with permission of VLSI Design.

formed a deep, buried $p^+$ layer under the phosphorus $n$-well profile. The $p^+$ layer eliminates the need for substrates with an epi layer, since the low resistivity substrate required to suppress latchup is created by the high energy implantation. It was also reported that the high energy implantation did not induce any excess leakage or measurably degrade MOS transistor characteristics.

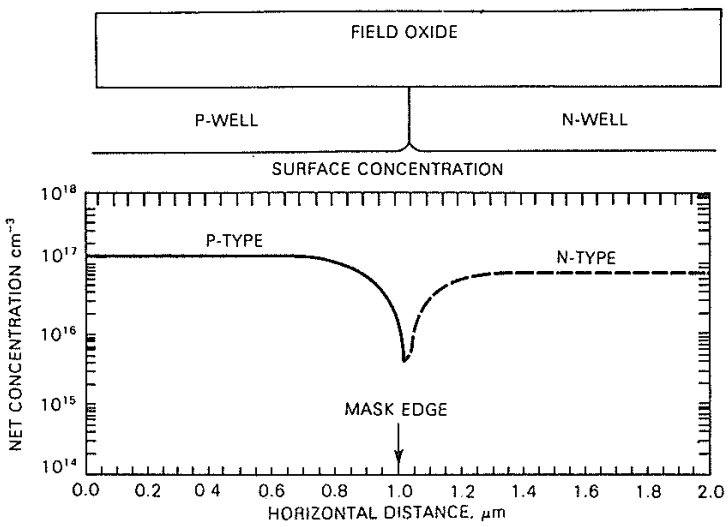


**Fig. 8-19** Surface impurity concentration at the boundary of the $p$- and $n$-retrograde wells in quadruple-well CMOS.[29] (© 1986 IEEE).

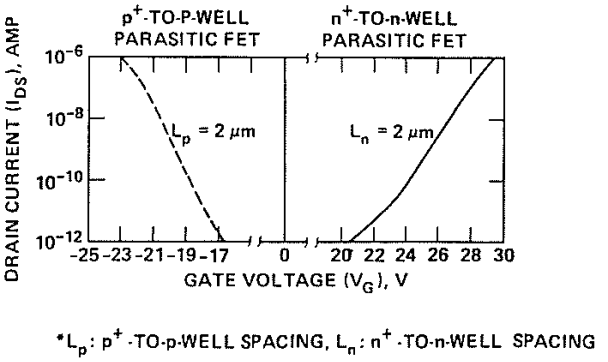


**Fig. 8-20** Subthreshold characteristics of symmetric parasitic FETs in quadruple-well CMOS.[29] (© 1986 IEEE).

## 8.4 FUTURE TRENDS IN WELL FORMATION

It seems that high-energy ion implantation will find more application for generating profiled wells. Profiled wells are achieved by multiple implants at varying energies. They offer the ability to independently control several MOSFET characteristics, including threshold voltage, hot-carrier generation, punchthrough voltage, junction capacitance, latchup susceptibility, soft-error immunity, and the body-effect coefficient. The optimization of well profiles for improving device performance has been termed "well engineering."[31]

Unlike a conventional well, which has an almost flat impurity distribution, a profiled well can have an impurity profile tailored to independently optimize a variety of device characteristics. Figure 8-21 shows the impurity profile of a multiply-implanted well and the relation of the device characteristics to the profile.[32]

In profile-implanted wells formed with high-energy implants, the wells are implanted after LOCOS isolation. In the *n*-well, multiple high-energy implants of phosphorus ions form a profiled well for active as well as isolation regions (with a thick photoresist serving as the *p*-well mask). Subsequently, low-energy implants are performed to adjust the PMOS $V_T$. A profiled *p*-well is next produced in the same way.

The deepest implant of the well in this example is fabricated with a 1 MeV implant. These implanted dopants form a heavily doped buried layer ($10^{18}$-$10^{19}$ $cm^{-3}$) at a depth of 2-4 $\mu$m that serves to reduce latchup susceptibility. Such a $p^+$ buried layer is more effective than an epitaxial layer in reducing substrate resistance and suppressing latchup, thus eliminating the need for an epi layer. The ability to use non-epi substrates when wafer sizes reach 150 mm and 200 mm represents a major cost savings, as the cost of 200 mm epitaxial wafers are ~$100 US higher than bulk-CZ wafers. The replacement of epitaxial wafers with MeV implantation processing also alleviates problems with autodoping control and backside sealing.[35]

The use of MeV implantation avoids the long (3-21 hour), high-temperature (1150-1200°C) well-formation drive-in step of the conventional process. This minimizes

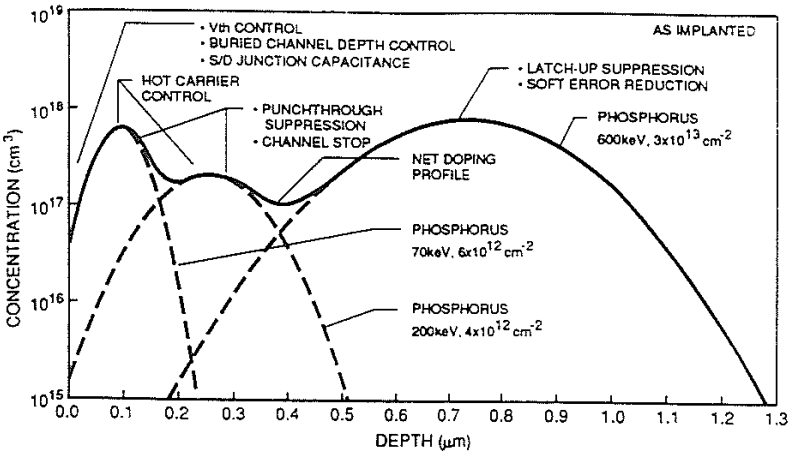


**Fig. 8-21** The relation between device characteristics and the impurity concentration at various depths in multiple implanted well.[32] Reprinted with permission of Solid State Technology.

thermally induced stress in large wafers that can cause wafer warpage, bow, and flatness degradation, as well as offering simplified processing with shorter fabrication times. Process simplification also results from the fact that the retrograde-well and field-isolation regions are formed by the same implant (after field oxidation). As noted in section 8.3.1, implantation through field oxide can also improve active device isolation characteristics. Employing MeV implantation to dope the bottom of the well more heavily leaves more room to tailor the doping profile at the top of the well in the channel area with lower energy implants.

Concern has existed that the high-energy implants may cause damage that will degrade device and circuit performance. Increased junction leakage is observed if the dose or energy are too low (i.e., $<3\times10^{14}$ cm$^{-2}$ and ~1-1.5 MeV, respectively). Recent studies, however, indicate that if the dose and energy exceed $3\times10^{14}$ cm$^{-2}$ and 1.5 MeV, respectively, leakage due to implant damage is dramatically reduced with both boron and phosphorus implantation. In fact, when an optimum combination of dose, energy, and annealing process is used, *less* leakage is observed than in control devices having no buried layer. This behavior is believed to be caused by gettering of electrically active damage or impurity defects away from the depletion regions of active transistors by secondary defects near the concentration peak of the buried layer. The effect is called "self-gettering." For all of the above reasons it appears that high-energy implantation will become more widely used to form wells in device generations at and below 0.5 $\mu$m.

## 8.5 AFTER-GATE IMPLANTATION (AGI)

An alternative technique which exploits high-energy implantation to reduce the complexity of CMOS process called *after-gate implantation* (AGI) has been suggested. That is, by performing all implantations after the gate electrodes are patterned (wells, channel-stop doping, and source/drain), the number of mask steps can be reduced.

Figure 8-22 illustrates this approach, in which only seven masks are required to form a single *p*-well CMOS structure.[33] The LOCOS-isolation field-oxide regions are formed first, then the polysilicon gates are deposited and patterned. Using a mask that obscures the PMOS regions, the NMOS *p*-well implant, multiple-channel implants, and the $n^+$ source/drain implants are carried out. Then a mask is used to cover the NMOS areas, and the PMOS-channel and $p^+$ source/drain implants are performed. Since the well and channel implantations must penetrate the field oxide and the polysilicon gate, they must be carried out at higher energies. The *p*-well implant energy is 600 keV (at a dose of $1 \times 10^{13}$ cm$^{-2}$), and the NMOS devices receive low-dose channel implants of 135 keV, 175 keV, and 215 keV. The channel of the PMOS devices receives two low-dose, higher-energy phosphorus implants (at 220 keV and 440 keV). Such multiple-channel implants are used in both NMOS and PMOS devices to avoid unacceptable $V_T$ variations caused by polysilicon gate thickness variations encountered in processing (and to improve the punchthrough resistance of the device structures). Studies also indicate

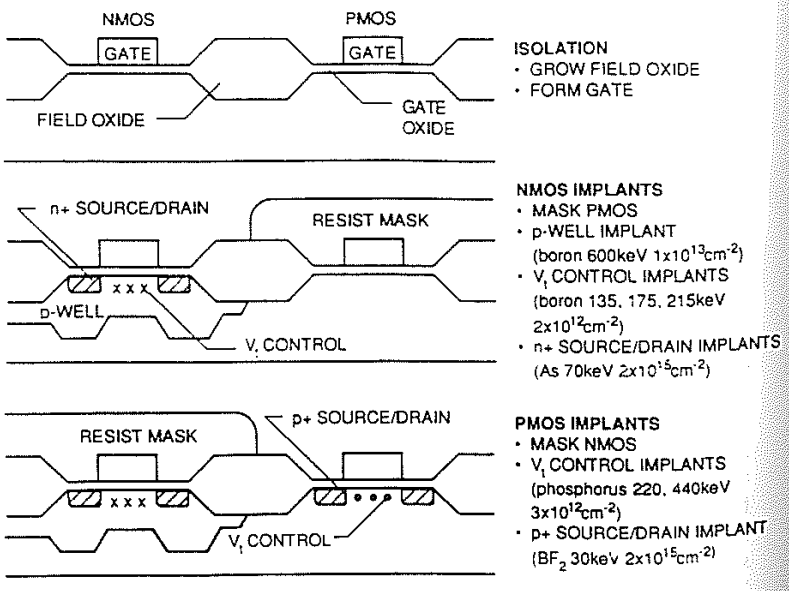


**Fig. 8-22** After-Gate Implant (AGI) process sequence.[33] (© 1986 IEEE).

that the high energy AGI does not degrade the gate oxide integrity[32] nor the MOS transistor characteristics.[34]

The AGI process thus offers the benefits of implantation processing freedom and flexibility, as well as reduced CMOS process complexity. The low doses required for the well and channel implantations can be performed with a medium-current implanter which may also have a higher energy implantation capability.

## REFERENCES


1. J.Y. Chen, "CMOS - The Emerging Technology," *IEEE Circuits and Devices Magazine,* March 1986, p. 16.
2. J.Y. Chen, *CMOS Devices and Technology for VLSI,* Prentice-Hall, Englewood Cliffs, N.J., 1990.
3. A.G. Lewis et al., *IEEE Trans. Electron Dev.,* **ED-34**, 2156, (1987).
4. T. Yamaguchi et al., *IEEE Trans. Electron Dev.,* **ED-31**, p. 205 (1984).
5. L.C. Parrillo "CMOS Active and Field Device Fabrication," *Semiconductor International,* April 1988, p. 64.
6. W. Wijaranakula et al., *J. Electrochem. Soc.,* December 1988, p. 3113.
7. H. Tsuya et al., *Japanese J. Appl. Phys.,* **22,** L16 (1983).
8. A. G. Lewis et al., "Vertical Isolation in Shallow *n*-Well CMOS Circuits," *IEEE Electron Dev. Lett.,* EDL-8, p. 107, 1987.
9. K. Tanno, F. Shimura, and T. Kawamura, *J. Electrochem. Soc.,* **128**, p. 395 (1981).
10. J. Manoliu and J.O. Borland, "A Submicron Buried Layer Twin-Well for High Density CMOS," *Tech. Dig. IEDM,* 1987, p. 20.
11. R. de Werdt et al., *Tech. Dig. IEDM,* 1987, p. 532.
12. L.C. Parrillo et al., "Twin-Tub CMOS-II," *Tech. Dig. IEDM,* 1982, p. 706.
13. R.A. Chapman et al., "A 0.8 μm CMOS Technology," *Tech. Dig. IEDM,* 1987, p. 362.
14. M.-L. Chen et al. *Tech. Dig. IEDM* 1986, p. 256.
15. S.J. Hillenius and L.C. Parrillo, U.S. Patent No. 4,554,726, Nov. 25, 1985.
16. R.A. Chapman et al., "High Performance Sub-Half Micron CMOS Using Rapid Thermal Processing," *Tech. Dig. IEDM* 1991, p. 101.
17. Ch. Zeller, C. Mazure, & M. Kerber, "Field-Implant-Free Isolation by Double-Well Split Drive-In," *IEEE Electron. Dev. Letts.,* p. 215, May 1990.
18. R. Martin and J.Y. Chen, "Optimized Retrograde *n*-well for 1 μm CMOS, *Proc. Custom Integ. Circuits Conf.,* 1985, p. 199.
19. R.D. Rung, C.J. Dell'Oca, and L.G. Walker, "A Retrograde *p*-well for High Density CMOS," *IEEE Trans. Electron Dev.,* ED-28, p. 1115, 1981.
20. D.M. Brown et al., "Trends in Advanced CMOS Process Technology," *Proceedings of the IEEE,* December 1986, p. 1646.
21. S.R. Coombs, "Scalable Retrograde *p*-well CMOS Technology," *IEEE Trans. Electron Dev.,* **ED-28**, p. 346, 1981.
22. Y. Taur et al., *IEEE J. Solid-State Circuits,* **SC-20,** p. 123, 1985.

23. G.J. Hu et al., "Design and Fabrication of *p*-channel FET for 1-$\mu$m CMOS technology," *IEDM Tech. Dig.* 1982, p. 710.
24. A. Stolmeijer, "A twin-well CMOS process employing high-energy ion implantation," *IEEE Trans. Electron Dev.*, **ED-33**, April, 1986, p. 450.
25. A. Shida et al., 3.3V BiNMOS Technology Using NPN Transistors without Buried Layers," *Tech. Dig. IEDM,* 1991, p. 93.
26. Y. Mochizuki, "Special Report: High Energy Ion Implantation Technology," Nikkei Microelectronics, (Dec. 1991), p. 92.
27. M. Moslehi and K. Saraswat, "Thermal Nitridation of Si and $SiO_2$ for VLSI," *IEEE Trans Electron Dev.* **ED-32**, p. 116, January 1985.
28. P. Fahey, R.W. Dutton, and M. Moslehi, "Effects of Thermal Nitridation Processes on Boron and Phosphorus Diffusion in <100> Silicon," *Appl. Phys. Letts.*, **43**(7), p. 683 July, 1983.
29. J.Y. Chen, "Quadruple-well CMOS for VLSI Technology," *IEEE Trans. on Electron Dev.*, **ED-31**, p. 910, 1984.
30. A.G. Lewis, R.A. Martin, and J.Y. Chen, "Retrograde and conventional *n*-well CMOS technologies: A Comparison," Internal Report, EIL-87-17, Xerox Palo Alto Research Center, Oct. 1986.
31. K. Tsukamoto et al., *Nucl. Instrumentation & Methods,* B59/60, p. 584 (1991).
32. K. Tsukamoto et al., "High Energy Ion Implantation for ULSI: Well Engineering and Gettering," *Solid State Technology* P. 49, June 1992.
33. H. Mikoshiba et al., "A Novel CMOS Process Utilizing After-Gate Implantation Process," *Dig. of Tech. Papers, 1986 Symp. VLSI Tech.*, p. 41.
34. J. Pfiester et al., "A Self-aligned Elevated Source/Drain MOSFET," *IEEE Trans. Electron Dev.*, September 1990, p. 365.
35. J.O. Borland and R. Koelsch, "MeV implantation technology: Next generation manufacturing with current generation equipment," *Solid-State Technology*, December 1993, p. 28.
36. J.Y. Chen, *VLSI Design* July 1984, p. 78.
37. A.G. Lewis et al., "Device Isolation in High Density LOCOS-Isolated CMOS," *IEEE Trans. Electron Devices,* **ED-34**, p. 1337, June 1987.

## PROBLEMS

**1.** An *n*-well $n^+$ polysilicon-gate CMOS process starts with a substrate doping of $3x10^{15}/cm^3$. The well doping near the surface of is approximately constant to a level of $3x10^{16}/cm^3$. The gate oxide thicknesses are both 40 nm, and $Q_{tot} = 3x10^{10}/cm^2$.

(a) Calculate the threshold voltages of the *n*- and *p*-channel transistors.

(b) Calculate the boron doses needed to shift the NMOS threshold to +1V and the PMOS threshold to -1V. Assume that the threshold shifts are achieved through shallow ion implantations.

**2.** In a *p*-well CMOS technology, the *n*-substrate has a doping concentration of $1x10^{15}/cm^3$, and a *p*-well concentration neat the surface of $5x10^{16}/cm^3$. Calculate the source/drain junction capacitances ($cm^{-2}$) and body effect coefficients for both *n*- and *p*-channel MOSFETs assuming the gate oxide is 20 nm thick in both devices.

**3.** Describe the split well-drive process, and the advantages it offers compared to the conventional well-drive process.

**4.** Comparing retrograde well to conventional well, what is the most important difference in process technology and finished device structure? How does it affect device isolation?

**5.** In a ($p^+$-diffusion)-$n$-well-($p$-on-$p$+ substrate)structure, the $n$-well is uniformly doped at $1 \times 10^{16}$ $cm^{-3}$ and is 1 $\mu$m deep, the $p$-epi thickness is 4 $\mu$m and is uniformly doped at $1 \times 10^{15}/cm^3$, and the $p^+$ diffusion is 0.4 $\mu$m deep. If a substrate bias generator is needed and the $p^+$ diffusion and $n$-well are both biased at 5V, what is the maximum (in absolute value) substrate voltage that can be applied before punchthrough occurs?